Conference Proceedings of the Society for Experimental Mechanics Series

Tom Proulx *Editor*

Sensors, Instrumentation and Special Topics, Volume 6

Proceedings of the 29th IMAC, A Conference on Structural Dynamics, 2011

SEM Springer

Conference Proceedings of the Society for Experimental Mechanics Series

For other titles published in this series, go to
www.springer.com/series/8922

Tom Proulx
Editor

Sensors, Instrumentation and Special Topics, Volume 6

Proceedings of the 29th IMAC, A Conference on Structural Dynamics, 2011

Springer

Editor
Tom Proulx
Society for Experimental Mechanics, Inc.
7 School Street
Bethel, CT 06801-1405
USA
tom@sem1.com

ISSN 2191-5644 e-ISSN 2191-5652
ISBN 978-1-4419-9506-3 e-ISBN 978-1-4419-9507-0
DOI 10.1007/978-1-4419-9507-0
Springer New York Dordrecht Heidelberg London

Library of Congress Control Number: 2011923650

© The Society for Experimental Mechanics, Inc. 2011
All rights reserved. This work may not be translated or copied in whole or in part without the written permission of the publisher (Springer Science+Business Media, LLC, 233 Spring Street, New York, NY 10013, USA), except for brief excerpts in connection with reviews or scholarly analysis. Use in connection with any form of information storage and retrieval, electronic adaptation, computer software, or by similar or dissimilar methodology now known or hereafter developed is forbidden.
The use in this publication of trade names, trademarks, service marks, and similar terms, even if they are not identified as such, is not to be taken as an expression of opinion as to whether or not they are subject to proprietary rights.

Printed on acid-free paper

Springer is part of Springer Science+Business Media (www.springer.com)

Preface

Sensors and Instrumentation Topics represents one of six clusters of technical papers presented at the 29th IMAC, A Conference and Exposition on Structural Dynamics, 2011 organized by the Society for Experimental Mechanics, and held in Jacksonville, Florida, January 31 - February 3, 2011. The full proceedings also include volumes on Advanced Aerospace Applications, Modal Analysis, Linking Models and Experiments, Civil Structures, and Rotating Machinery, Structural Health Monitoring, and Shock and Vibration.

Each collection presents early findings from experimental and computational investigations on an important area within Structural Dynamics.

Credit for much of the progress in the field of modal analysis over the last twenty five years is owed to substantial advancements in sensors, electronics and computing platforms. Many of those involved in modal analysis and testing have personal and professional interests in the associated equipment and sensors.

Achieving accurate test results depends on an adequate knowledge of the test equipment, its selection, use, and limitations. This series of tutorials, presented by a distinguished group of experts, is meant to offer readers an opportunity to learn more about their test instrumentation, and explore the application of emerging technologies such as wireless communication and fiber optics.

The organizers would like to thank the authors, presenters, session organizers and session chairs for their participation in this track.

Bethel, Connecticut

Dr. Thomas Proulx
Society for Experimental Mechanics, Inc

Contents

1 **Experimental and Numerical Investigation of Forming Limit Diagram for AA3105** 1
M. Safari, Islamic Azad University; S.J. Hoseinipour, Babol University of Technology; H.D. Azodi, Iran University of Science and Technology

2 **Multi-field Microphone – When the Sound Field is Unknown** 7
S. Gade, N.V. Bøgholm, Brüel & Kjær Sound & Vibration A/S

3 **Separating Three Sources of Changes in Structural Health Monitoring** 17
J. Kullaa, Aalto University School of Science and Technology

4 **Structural Damage Identification With Various Uncertainties** 27
J.-S. Lew, M. Williamson, Tennessee State University

5 **Excitation Techniques for Testing Bike Vibration Transmission in the Laboratory** 35
J. Lépine, Y. Champoux, J.-M. Drouet, Université de Sherbrooke

6 **Damage Detection Using Blind Source Separation Techniques** 45
V.H. Nguyen, J.-C. Golinval, University of Liège

7 **Application of Image Sensing to Motion Study of High-voltage Switchgear** 57
S. Marushima, Y. Ohda, M. Shimizu, H. Takagi, Toshiba Corporation

8 **CAE Based Approach to Understand a Behavior of Vibro-acoustic System** 65
K. Furuya, Chuo University; T. Yoshimura, Tokyo Metropolitan University; N. Okubo, T. Toi, Chuo University

9 **Verification of Coverage of Inverse-numerical Acoustic Analysis** 73
T. Koizumi, N. Tsujiuchi, A. Kobayashi, Doshisha University; H. Uehara, Yanmar Co., Ltd.

10 **Prototype WSN Platform for Performing Dynamic Monitoring of Civil Engineering Structures** 81
R. Aguilar, L.F. Ramos, P.B. Lourenço, University of Minho; R. Severino, R. Gomes, P. Gandra, M. Alves, E. Tovar, Polytechnic Institute of Porto

11 **Damage Identification in CRFP Laminates using a Statistical Method** 91
M.T.H. Sultan, K. Worden, W.J. Staszewski, The University of Sheffield

12 **High Intensity Noise Generation for Extremely Large Reverberant Room Test Applications** 103
A. Grewal, National Research Council of Canada; R. Ramakrishnan, Ryerson University/ Aiolos Engineering Corporation; W.O. Hughes, NASA Glenn Research Center; B. Woyski, TEAM Corporation; G. Elfstrom, Aiolos Engineering Corporation; C. Mech, Team Corporation; Y. Chen, National Research Council of Canada

13 **Human Induced Dynamic Loads Estimation Based on Body Motion** 119
P. Mazzoleni, E. Zappa, Politecnico di Milano

14 **In the Field Validation of Human Induced Loads Measuring Technique** 127
P. Mazzoleni, E. Zappa, Politecnico di Milano

15 **Optimal Selection of Artificial Boundary Conditions for Model Update and Damage Detection** 137
J.H. Gordis, Naval Postgraduate School; K. Papagiannakis, Hellenic Navy

16 **Use of Damping Solution for Acceleration Measurements in High Vibration Environments** 155
T. Connolly, Measurement Specialties, Inc.

17 **Efficiency Comparison of CMS Vibroacoustic Formulations for Uncertain Damped Problems** 161
M. Ouisse, E. Sadoulet-Reboul, University of Franche-Comté

18 **Nonlinear Parameteric Health Monitoring for Vibrating Structures Under Non-stationary Excitation** 177
T.A. Doughty, N.S. Higgins, University of Portland

19 **Displacement Based Approach for a Robust Operational Modal Analysis** 187
G. De Canio, ENEA; P. Andersen, Structural Vibration Solutions A/S; I. Roselli, M. Mongelli, ENEA; E. Esposito, Artemis srl.

20 **Effect of Systematic FRF Errors on Matrix Inversion Based Vibro-acoustic Analysis Methods** 197
P. Gajdatsy, P. Sas, W. Desmet, Katholieke Universiteit Leuven; K. Janssens, H. Van der Auweraer, LMS International

21 **Peri-prosthetic Fracture Vibration Testing** 207
J. Cruce, Oklahoma State University; J. Erwin, Middlebury College; K. Remick, University of Illinois Urbana-Champaign; P. Cornwell, Rose-Hulman Institute of Technology; R.M. Meneghini, Indiana University; J. Racanelli, Stryker Orthopaedics

22 **Performance Comparison of Fiber Optic Tips in Interferometric Displacement Measurements** 227
R. Grahn, University of New Mexico; H. Karimi, University of California, San Diego; K. Wilson, Rose-Hulman Institute of Technology; E. Moro, A. Puckett, Los Alamos National Laboratory

23 **Development of Polymer 'Chips' Used in Medical Diagnostics** 237
Z.G. Brush, Trinity University; L.M. Schultz, Georgia Institute of Technology; J.W. Vanness, Michigan Technological University; K.M. Farinholt, Los Alamos National Laboratory; S.A. Sarles, D.J. Leo, Virginia Polytechnic Institute and State University

24 **Acoustic Fluid-Structure Interaction of Cars and Ships (Tutorial)** 247
L. Gaul, University of Stuttgart

25 **The Testing Behind the Test Facility: The Acoustic Design of the NASA Glenn Research Center's World-class Reverberant Acoustic Test Facility** 255
W.O. Hughes, M.E. McNelis, A.D. Hozman, A.M. McNelis, NASA Glenn Research Center

26 **Detection of Damage in Space Frame Structures With L-shaped Beams and Bolted Joints Using Changes in Natural Frequencies** 263
K. He, W.D. Zhu, University of Maryland, Baltimore County

27 **Steels for Caribbean Steel Drums** 291
S.E. Maloney, Metal Industries Company Limited

Experimental and Numerical Investigation of Forming Limit Diagram for AA3105

Mehdi. Safari[a], S. J. Hoseinipour[b] , H. D. Azodi[c]

a

CRITERIA FOR DUCTILE FRACTURE

Based on various hypotheses, many criteria for ductile fracture have been proposed empirically as well as theoretically [5, 9]. It is well known that the forming limit of sheet metals depends greatly upon the deformation history. Therefore, the histories of stress and strain may have to be considered in the criteria. The energy or generalized plastic work criterion was first given by Freudenthal [10]:

$$
{}^{-}_{0} \quad - \quad - \qquad 1,
$$

extended. For the measurement of anisotropy coefficient specimens were cut at $0°, 45°$ and $90°$. These specimens were stretched in the range of uniform elongation and the dimensional changes were measured with the aid of a traveling microscope. R values were then determined from:

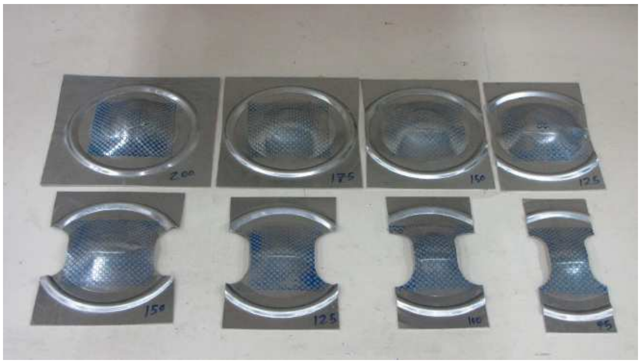

FIGURE 2. Stretched specimens of Aluminum alloy 3105

NUMERICAL WORK

Using commercially available finite element code ABAQUS/Standard simulation has done. In this state, experimental conditions were duplicated in numerical simulation. During simulation the analysis of data is done and the ductile fracture criteria used for this purpose. So, when the value of ductile fracture criteria receive to a critical value that obtained from experimental tensile test, necking has been occurred and simulation stopped. The punch, die and blank-holder are modeled as rigid bodies. The Coulomb friction model with a constant coefficient of friction, $\mu = 0$

the strains in the sheet vary over the stretched dome from a strain state close to plane strain near the flange of the sheet to one approximating balanced biaxial tension at the pole. In these situations, flow localization and failure site depend on the factors such as strain hardening, anisotropy behavior of the sheet metal, friction condition and strain gradient. During out-of-plane deformation, geometric and frictional effect comes into play with regard to their tendency to shift the site of strain localization away from the pole at which it was first initiated. The shift can also occur partly because of strain hardening and the development of a biaxial stress state in the neck.

TABLE 1. Measured R values

Alloy	0

In the numerical work, ductile fracture criteria used to prediction of necking. In Fig.5 FLDs obtained from these criteria compared with experimental results and it's shown that they are in good agreement together. Thus it is proven that ductile fracture criteria are useful to predict FLD for Aluminum alloy 3105.

CONCLUSION

In this work, forming limit diagram for Aluminum alloy 3105 was obtained experimentally using out of plane test. Also, forming limit diagram of this alloy predicted by ductile fracture criteria using commercially available finite element code ABAQUS/Standard. It is shown FLDs predicted by ductile fracture criteria are in good agreement with the results obtained from experimental work.

REFERENCES

S. P. Keeler and W. A. Bakhofen (1964) Plastic instability and fracture in sheet stretched over rigid punches,

Multi-field Microphone –
when the Sound Field is unknown

Svend Gade, Niels V. Bøgholm
Brüel & Kjær Sound & Vibration A/S, Skodsborgvej 307
2850 Nærum, Denmark

ABSTRACT

Only a small percentage of all acoustical measurements are performed in the well-defined and well-controlled environment of a calibration laboratory – on the contrary most acoustical measurements are done under non-controlled conditions which in many cases are not even known in beforehand. This is the reason that some acoustical standards such as the IEC 61672 series (the “Sound Level Meter standard”) specify the performance of the measuring microphone over a wide range of environmental conditions. Modern quality measuring condenser microphones often meet or exceed the requirements even under very varying conditions. However one important – and unfortunately in many cases major – source of error is often neglected: The response of the actual microphone type in the actual sound field. The influence of different sound fields on the measurement error is discussed in some detail with practical examples and it is shown how a worst-case error exceeding 10 dB @ 20 kHz is a real risk. After a brief discussion of a condenser microphone which drastically reduces the error caused by influence of an unknown sound field or varying angle of incidence. Finally, test results from production samples of the new microphone are shown.

INTRODUCTION

Only a small percentage of all acoustical measurements are performed in the well defined and well controlled (for example defined as: Temperature 23^{o}C deg., Relative Humidity 50 % and Ambient Static Pressure 101.3 kPa) environment of a calibration laboratory – on the contrary most acoustical measurements are done under non controlled conditions which are not often even known in beforehand.

This is the reason that acoustical standards such as the IEC 61672 series (the “Sound Level Meter standard”) specify the performance of the measuring microphone over a wide range of environmental conditions. When using high quality in-

T. Proulx (ed.), *Sensors, Instrumentation and Special Topics, Volume 6*, Conference Proceedings of the Society for Experimental Mechanics Series 9, DOI 10.1007/978-1-4419-9507-0_2, © The Society for Experimental Mechanics, Inc. 2011

strumentation and transducers the varying environmental conditions is normally not causing any problems at all.

However, one major source of error remains and that is the impact which the nature of the sound field will have on the measurement uncertainty. It is common practice to assume that the sound field in any measurement case will be either free, diffuse or pressure field.

SOUND FIELDS

Free field: There are no reflecting objects, only the microphone disturbs the sound field.

Diffuse field: There are so many reflecting surfaces, that the sound waves arrive with equal probability from all directions.

Pressure field: This is found in small confined spaces like calibration couplers.

Depending on the nature of the sound field an appropriate microphone is selected: A microphone which is "optimised" for the sound field in question. Unfortunately there are many practical situations where the sound field is not really of a well defined type. This may be the case inside buildings, during in-cabin noise measurements or measurements on multi or non- stationary sources. Often a free-field microphone is chosen more based on tradition than on real knowledge about the nature of the actual sound field. Fig. 1 shows a picture of the Multi-field microphone, which is suited for use in a free as well as in a diffuse field.

Fig. 1 Multi-field field microphone Type 4961

It is amazing how large the potential errors are if the conditions are non ideal.

Fig. 2 shows the response of a free-field microphone in a true free field; the frequency response is the ideal flat response. But the angle of incidence may not be zero (as assumed in Fig. 2) or the sound field may not be a true free field, say it actually was diffuse instead of free and the response will be as shown in Fig. 3.

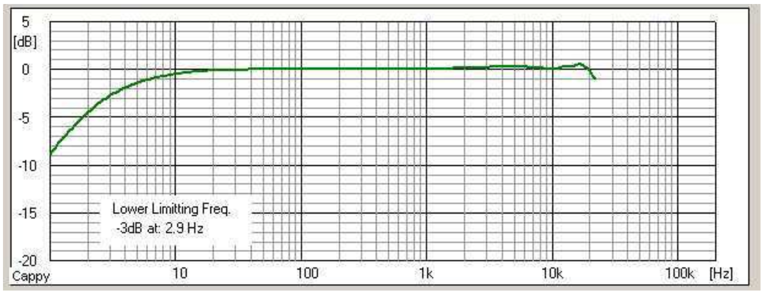

Fig. 2 Free-field response of a ½” free-field microphone

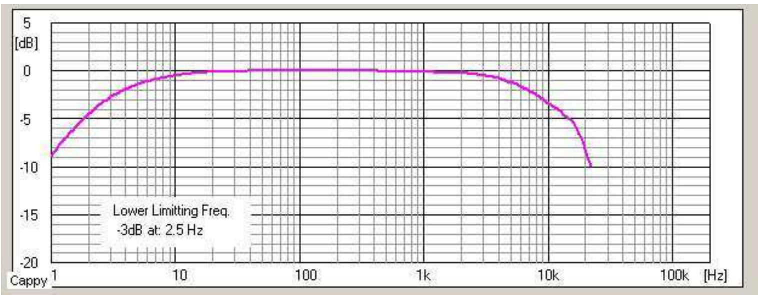

Fig. 3 Diffuse-field response of a ½” free-field microphone

Both Fig. 2 and 3 are valid for a typical ½” microphone with protection grid and (in Fig. 2) for zero degree of incidence (e.g. the microphone diaphragm is facing head on towards the sound source).

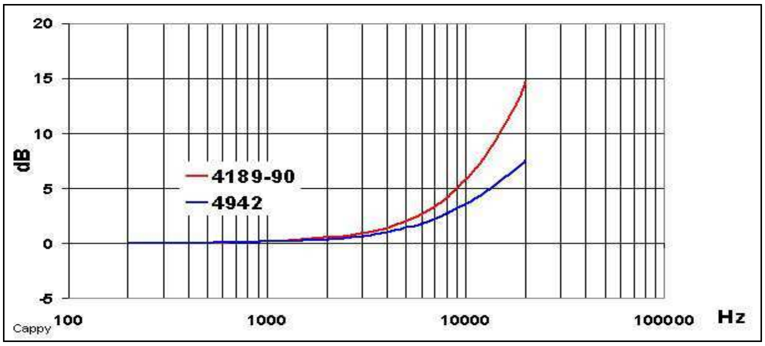

Fig. 4 Maximal error for free-field microphone type 4189/90 (upper curve) and diffuse-field microphone type 4942 (lower curve)

Actually taking not only the nature of the sound field but also the angle of incidence into consideration the potential error may be even larger.

Fig. 4 shows the maximal error as a function of frequency when a free-field (4189/90), respectively diffuse-field (4942) microphone is being used in a field or in an angle of incidence for which the actual microphone was not optimised.

As clearly shown in Fig. 4 the error is noticeable from 2 kHz and already at around 6 kHz the potential maximal error due to “unknown conditions” largely exceeds the influence of all other environmental influence factors and even exceeds the IEC 61672 tolerance of 3.5 dB not to mention the IEC 1094 + - 2 dB requirement.

IS THERE A CURE?

It has been known for many years (refs. [1, 3, 4]) that a microphone disturbs the sound field and that the issues addressed here are caused solely by the physical size of the microphone.

Generally speaking a microphone can be considered non-diffractive as long as $(\pi/\lambda) * 2a \leq 1$, where λ is the wavelength and 2a the microphone diameter. Therefore a ½” microphone can measure without disturbance of the sound field up to around 8 kHz, whereas a ¼” microphone can measure up to around 16 kHz. In reality, microphones can measure up to higher frequencies, because the measurement error at higher frequencies is predictable and the microphone frequency response can be compensated for (optimised) in the microphone itself. In this way, a flat frequency response can be achieved – but only in one given kind of sound field.

That is why there exist three different microphone types: Free-field, diffuse-field and pressure-field microphones. As mentioned above a ¼” microphone would be readily useable in all fields up to 20 kHz, but today unfortunately all commercial ¼” measuring microphones have less sensitivity and much higher noise floor than their ½ ” counterparts. A typical ¼” free - field microphone has a noise floor around 40 dB(A) opposed to 16 - 18 dB(A) for a typical premium quality ½” free-field microphone.

The limiting factors

In order to discuss the most important factors which determine the sensitivity of a condenser microphone we will introduce a set of simple equations which describe the sensitivity of a condenser microphone.

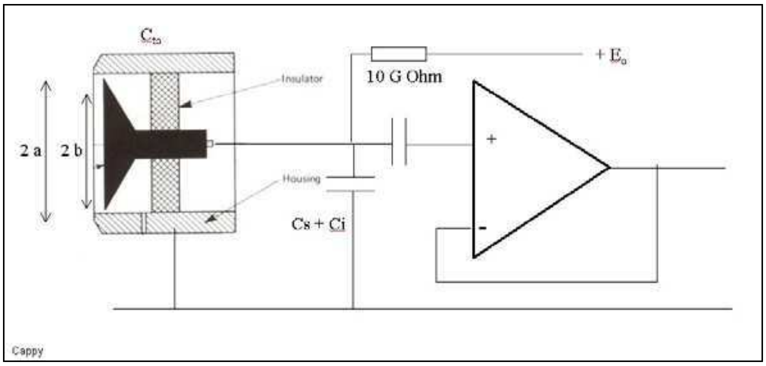

Fig. 5 Principal schematic of a condenser microphone with pre-amplifier

2a	is the diaphragm diameter
2b	is the diameter of the back-plate
h_0	is the distance back-plate to diaphragm
E_0	is the polarization voltage
C_i	is the pre-amplifier input capacitance
C_s	is the stray capacitance

Now the microphone mid range pressure sensitivity M_p (V/Pa) can be expressed as the product of two sensitivities $M_p = M_e * M_m$

Here M_e is the electrical transfer function in V/m and M_m is the mechanical transfer function in m/Pa and as one observes the dimension of M_p equals [V/m] * [m/Pa] which means that M_p is in V/Pa as expected.

As shown in the literatures see. f. inst. (ref. [2]) the following equations apply:

$$M_e = E_0/h_0 * [1 - b^2/2a^2)]*[1 + (C_i + C_s)/C_{to}] \quad (1)$$

Now in most practical cases b equals approximately 0.8 * a and typically
$C_i + C_s << C_{to}$ hence (1) is with good approximation

$$Me = [0.68 * E_0] / h_0 \quad (2)$$

For the mechanical transfer function in m/Pa (ref. [2]) shows that

$$Me = a^2/8T \quad (3)$$

Where T is the tension of the diaphragm in N/m, which depends on the radial stress s_{rr} (N/m^2) and the thickness d of the diaphragm accordingly to

$$T = s_{rr} * d \quad (4)$$

In practical cases T is often in the interval 2000 – 3000 Pa.
Combining (2) and (3) the simplified equation for the microphone mid range sensitivity is:

$$M_p = M_m * M_e = [0.11 * E_0 * a^2] / [T * h_0] \quad (5)$$

Using (5) and a polarization voltage of 200 V, 20 µm distance between the backplate and diaphragm and 2000 Pa tension (5) yields 3.3 mV/Pa for a ¼" microphone, which is in good agreement with practical values.

SUGGESTIONS ON HOW TO INCREASE THE SENSITIVITY OF A ¼" MICROPHONE

By inspection of (5) it is very easy to see how to increase the sensitivity of a microphone:

1 Increase the polarization voltage
2 Decrease the distance between the back - plate and the diaphragm
3 Reduce the diaphragm tension

Short comments and limitations to the suggestions:

Increased Polarisation voltage

For external polarized microphones the polarisation voltage must be 200 V in order to be compatible with existing front – ends on the market.

Besides there are practical limitations determined by the arching and static diaphragm deflection and for these and other reasons the polarization voltage can not be changed.

Reduce backplate to diaphragm distance

Reduction of the back-plate to diaphragm distance is also dangerous since this increases the electrical field strength with increased risk of sparks (excess noise in the microphone). Further the backplate to diaphragm distance at max SPL should ideally be larger than 50 % of the distance under quiescent conditions.

Lowering diaphragm tension

The last resort is to have a much *lower diaphragm tension* but here there are severe limitations when using the traditional cobalt base alloy as the diaphragm material.

Instead a solution has been found using a Titanium diaphragm; this diaphragm has the benefit that if it is processed properly the tension can be reduced to such a low value that the sensitivity of the ¼” microphone is very close to that of a normal ½” high sensitivity microphone.

The low tension means that the resonance frequency for this microphone is much lower than for a normal ¼” microphone around 26 kHz instead of say 70 - 100 kHz.

Additional sensitivity increase has been achieved by using more of the outer diameter (of the 6.25 mm) for the active part of the microphone e.g. a larger b value than in a normal ¼” microphone.

In order to achieve excellent temperature stability the cartridge was made “all Titanium” which brings additional benefits with respect to corrosion resistance and in-sensitivity to magnetic fields,

A new Titanium housed ¼” Constant Current Line Drive (DeltaTron) preamplifier with TEDS (Transducer Electronic Data Sheet) has been developed in order to be able to offer a complete all Titanium microphone with multi-field performance, see Fig. 1.

In summary, the microphone described here has the following key parameters:

Diameter	¼”
Sensitivity	60 mV/Pa
Noise floor	< 20 dB(A)
Frequency range	5 Hz – 20 kHz
Dynamic range	20 – 130 dB
Upper SPL limit	130 dB (3% distortion)
Max SPL	> 150dB (peak)
Temperature	-20 to +70°C (-4 to +158°F)

Fig. 6 shows the performance in unknown field for a multi-field microphone Frequency Response Function compared against IEC 61672 limits and compared with the already mentioned ½” microphones (worst cases) used today. Fig. 7 shows a typically Calibration Chart for a Multi-field Microphone.

SUMMARY

Using all Titanium technique it has now been possible to overcome the limitations which traditional technologies and materials have imposed on ¼” microphones so far. The result is a microphone which widely eliminates the influence of unknown measurement conditions and additionally it releases the user from the pain to be forced to choose between different microphones. Main uses are measurement in unpredictable sound field conditions, cabin noise measurements, near-field measurements and ad hoc sound measurements.

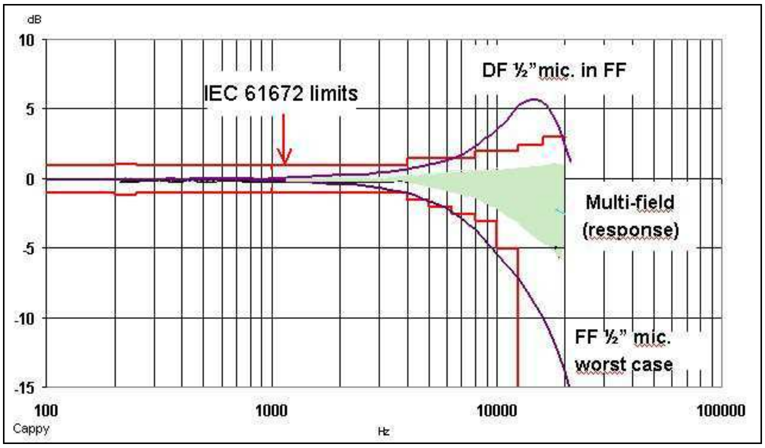

Fig. 6 Multi-field FRF compared against IEC 61672 limits and ½" microphones (worst cases), DF = Diffuse Field, FF = Free Field

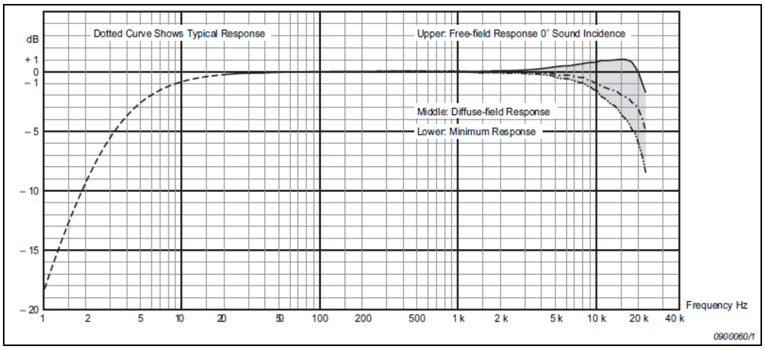

Fig. 7 Multi-field Frequency responses: Free-field response (upper), Diffuse-field response (middle) and minimum response (lower)

The multi-field measuring microphone, Type 4961, is the only ¼" measuring microphone in the world with a 20 dB noise floor and sensitivity exceeding 50 mV/Pa (nominal sensitivity is 60 mV/Pa) – enabling it to take accurate measurements in free, diffuse or diverse sound fields. Because Type 4961 is small and relatively insensitive to the angle of incidence, it simplifies the process of taking complex sound measurements, saving technicians' valuable time planning, setting up and analyzing results.

REFERENCES

1 Free Field response of Condenser Microphones
Brüel & Kjær Technical Review No.1 and 2, 1959
2 AIP Handbook of Condenser Microphones pg 43 and ff Edited by George S. Wong and Tony E. W. Embleton American Institute of Physics, New York
3 Microphone Handbook Vol. 1, Theory, BE1447-11, 1996, Brüel & Kjær Sound & Vibration Measurements A/S
4 Microphone Handbook Vol. 2, Falcon Range Microphones, BE1373-12, 1995, Brüel & Kjær Sound & Vibration Measurements A/S

Separating Three Sources of Changes in Structural Health Monitoring

Jyrki Kullaa

Department of Applied Mechanics,
Aalto University School of Science and Technology,
P.O. Box 14300, FIN-00076 Aalto, Finland
jyrki.kullaa@metropolia.fi
tel: +358-207836176
fax: +358-207836102

Abstract Discrimination between three sources of variability in a structural health monitoring system are investigated: environmental or operational effects, sensor faults, and structural damage. Different environmental or operational effects are included in the training data and can be accounted for by the model. Distinguishing between sensor fault and structural damage utilizes the fact that the sensor faults are local, while structural damage is global. A time domain approach is used to model the sensor network and the generalized likelihood ratio test (GLRT) is then used to detect and localize a change in the system. An experimental study is performed to validate the proposed method.

Keywords: environmental or operational effects; sensor fault; damage detection; minimum mean square error estimation; likelihood ratio test; structural health monitoring

Introduction

The objective of structural health monitoring (SHM) is to detect and identify damage in the structure utilizing the sensor data. New sensor technology makes it possible to monitor structures with a dense array of sensors. Damage identification can be approached by analytical or hardware redundancy [1]. If the number of vibration sensors is greater than the number of excited natural modes of the structure, hardware redundancy can be considered as an attractive alternative to analytical redundancy, because it is solely based on measurement data without a mathematical model of the structure.

However, in a dense sensor network with low-cost sensor nodes, it is quite probable that some nodes fail resulting in defective data for inference and decision.

T. Proulx (ed.), *Sensors, Instrumentation and Special Topics, Volume 6*, Conference Proceedings of the Society for Experimental Mechanics Series 9,
DOI 10.1007/978-1-4419-9507-0_3, © The Society for Experimental Mechanics, Inc. 2011

Also environmental (temperature, humidity, wind, etc.) or operational (traffic, rotating speed, joint positions, etc.) variability may result in changes in the system [2–8]. Both of the aforementioned effects can be incorrectly interpreted as structural damage.

Environmental or operational variability in the data can be removed from the features using latent variable models [9–22]. The advantage is that the measurement of the environmental or operational variables is not necessary. These methods use multivariable data with enough redundancy to remove the unwanted effects. Also sensor faults can be detected utilizing the redundancy in the measurement data [23–33].

In the present study, a unifying approach is proposed, which is able to distinguish between the aforementioned three sources causing changes in the system: environmental or operational effects, sensor faults, and structural damage. It is an automatic time domain method in the sensor space without a complex system identification algorithm.

The paper is organized as follows. Novelty detection and localization using minimum mean square error (MMSE) estimation and the generalized likelihood ratio test (GLRT) are first presented. An experimental monitoring test is performed to validate the proposed approach. Finally, concluding remarks are presented.

Novelty detection and localization

In this section, the application of the minimum mean square error (MMSE) estimation for novelty detection and localization is discussed. In MMSE estimation, each sensor is estimated in turn directly in the sensor space. The sensors are divided into observed sensors $\mathbf{v}$ and missing sensors $\mathbf{u}$:

$$\mathbf{x} = \begin{Bmatrix} \mathbf{u} \\ \mathbf{v} \end{Bmatrix} \tag{1}$$

with a partitioned covariance matrix $\mathbf{\Sigma}$ of the training data

$$\mathbf{\Sigma} = \begin{bmatrix} \mathbf{\Sigma}_{uu} & \mathbf{\Sigma}_{uv} \\ \mathbf{\Sigma}_{vu} & \mathbf{\Sigma}_{vv} \end{bmatrix} = \begin{bmatrix} \mathbf{\Gamma}_{uu} & \mathbf{\Gamma}_{uv} \\ \mathbf{\Gamma}_{vu} & \mathbf{\Gamma}_{vv} \end{bmatrix}^{-1} \tag{2}$$

where the precision matrix $\mathbf{\Gamma}$ is defined as the inverse of the covariance matrix $\mathbf{\Sigma}$ and is also written in the partitioned form. A linear MMSE estimate for $\mathbf{u}|\mathbf{v}$ ($\mathbf{u}$ given $\mathbf{v}$) is [31]:

$$\hat{\mathbf{u}} = E(\mathbf{u}|\mathbf{v}) = \boldsymbol{\mu}_u - \boldsymbol{\Gamma}_{uu}^{-1}\boldsymbol{\Gamma}_{uv}(\mathbf{v} - \boldsymbol{\mu}_v) \tag{3}$$

where $\boldsymbol{\mu}_u$ and $\boldsymbol{\mu}_v$ are the mean of **u** and **v**, respectively and $E(\cdot)$ is the expectation. The error covariance matrix is

$$\boldsymbol{\Phi} = \mathrm{cov}(\mathbf{u}|\mathbf{v}) = \boldsymbol{\Gamma}_{uu}^{-1} \tag{4}$$

Assuming Gaussian distribution, the conditional pdf of $\mathbf{u}|\mathbf{v}$ is

$$p(\mathbf{u}|\mathbf{v}) = |2\pi\boldsymbol{\Phi}|^{-1/2}\exp\left[-\frac{1}{2}(\mathbf{u} - \hat{\mathbf{u}})^T\boldsymbol{\Phi}^{-1}(\mathbf{u} - \hat{\mathbf{u}})\right] \tag{5}$$

The generalized likelihood ratio test (GLRT) [33, 34] can then be used for novelty detection using the hypothesis test for the MMSE parameters [31]. The test statistic is the log-likelihood ratio for each sample:

$$s = \ln\frac{p(\mathbf{u}|\mathbf{v}; H_1)}{p(\mathbf{u}|\mathbf{v}; H_0)} \tag{6}$$

where $p(\mathbf{u}|\mathbf{v}; H_i)$ is the probability according to hypothesis H_i, $i = 0, 1$. The hypothesis H_0 is that the parameters are the same as those of the training data (normal), and the hypothesis H_1 is that the parameters are different to those of the training data (anomaly). The distribution $p(\mathbf{u}|\mathbf{v}; H_1)$ is obtained by estimating the parameters from the current measurement, while the parameters of $p(\mathbf{u}|\mathbf{v}; H_0)$ are estimated from the training data.

Each sensor yields one test statistic s, resulting in a total number of variables equal to the number of sensors in the network. The dimensionality can be reduced by using principal component analysis (PCA) [35]. The variable used for novelty detection is finally the subgroup sample standard deviation S [36] of the first principal component scores. In this study, the subgroup consists of 100 subsequent variables.

If the novelty detector alarms, it may be due to any anomaly in the system. Here we distinguish between three different sources: sensor fault, structural damage, and environmental or operational variability. If a full range of environmental or operational conditions is included in the training data, normal variability should not result in an out-of-control signal.

Separating a sensor fault from structural damage is based on the fact that a sensor fault can be localized to a single sensor or a small number of sensors. On the other hand, structural damage cannot usually be localized to a single sensor, but several sensors measure the necessary information about damage.

The highest mean square of the log-likelihood ratios s is assumed to localize the anomaly to a single sensor. In order to infer the fault type, the sensor is first removed from the network and the novelty detection procedure is performed again for the remaining sensor network. If the control chart exhibits a similar pattern as before, it is an indication of a global change caused by structural damage. On the other hand, if the control chart shows a clearly visible change in the pattern, it indicates a fault in the removed sensor. The proposed approach is experimentally validated in the following section.

Experimental research

An experimental research was performed with a monitoring system built in the laboratory. The structure was a wooden bridge model shown in Fig. 1. Random excitation was applied to the structure to excite the lowest modes. Fifteen accelerometers measured the response at three different longitudinal positions. The sampling frequency was 256 Hz and the measurement period was 32 s. For sufficient redundancy, the data were low-pass filtered below 64 Hz and re-sampled.

The measurements were made during several days, and it was noticed that the dynamic properties of the structure varied due to environmental changes. Temperature and humidity variations were assumed to be the main influences on the wooden structure.

Damage was then introduced by adding point masses on the structure. The sizes of the masses were 23.5, 47.0, 70.5, 123.2, and 193.7 g. The point masses were attached on the top flange, 600 mm left from the midspan (Fig. 1). The last measurements were again from a healthy structure. The added mass was very small compared to the total weight of the structure (36 kg), less than half a percent.

For a sensor fault, precision degradation fault was introduced by adding random noise with a standard deviation of $\sigma = 0.01$ to sensor 3 during 10 measurements. No additional masses were present during sensor fault.

Spatiotemporal correlation with model order 5 was used to identify the MMSE model for each sensor [31]. With model order 0 (spatial correlation), damage detection was not successful indicating an insignificant change in the mode shapes. With a model order higher than zero, changes in the natural frequencies could also be detected.

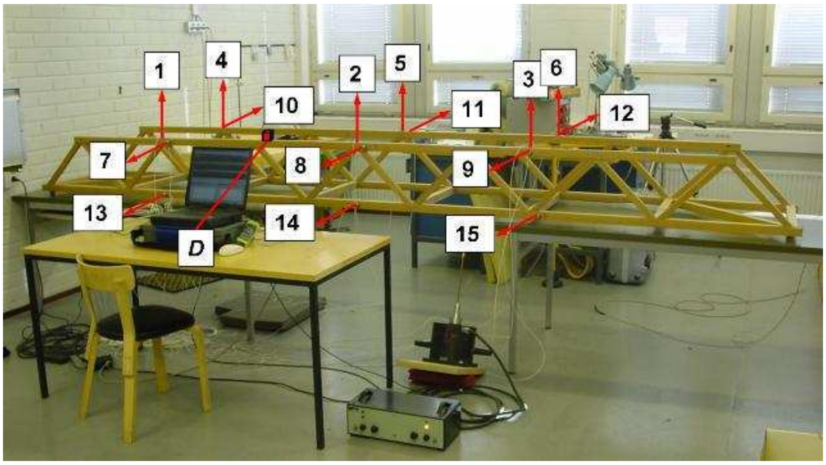

Fig. 1 Wooden bridge with the locations of sensors and damage (*D*) are indicated

The training data were the first 175 measurements, and the in-control data were the first 174 measurements. The test data consisted of measurements from both the healthy and the abnormal systems.

For a sensor fault, the *S* control chart for the first principal component of the log-likelihood ratios is plotted in Fig. 2a, clearly showing a change in the system during the last ten measurements. Sensor 3 showed the highest rms value of the log-likelihood ratios during those measurements. This sensor was then removed from the network and the remaining data were re-analysed resulting in a control chart shown in Fig. 2b. The pattern in the chart is clearly different to that in Fig. 2a. The plotted statistic now shows a similar pattern for the training and test data. In summary, the change in the system was correctly interpreted as a fault in sensor 3.

The effect of having data from a limited range of environmental conditions is demonstrated by analysing the healthy system with the first ten measurements only used as the training data. The control chart for novelty detection is shown in Fig. 3, from which it is seen that the environmental variability was significant resulting in serious difficulties in fault detection.

For structural damage, the *S* control chart for the first principal component of the log-likelihood ratios is plotted in Fig. 4a showing that an anomaly was detected. In addition, the increasing level of damage is visible. Notice also the last two measurements without the additional masses indicating again a normal condition.

The rms of the log-likelihood ratios of each sensor for the last measurements are depicted in Fig. 5a. Sensor 7 shows the highest value. This particular sensor was then removed from the network and the data were re-analysed resulting in a control chart shown in Fig. 4b. The pattern in the chart is similar to that in Fig. 4a, hence it is concluded that the change in the system was due to structural damage near sensor 7. Also the localization plot in Fig. 5b with sensor 7 removed indicates the largest discrepancy in sensor 8 locating also near the damaged region (Fig. 1).

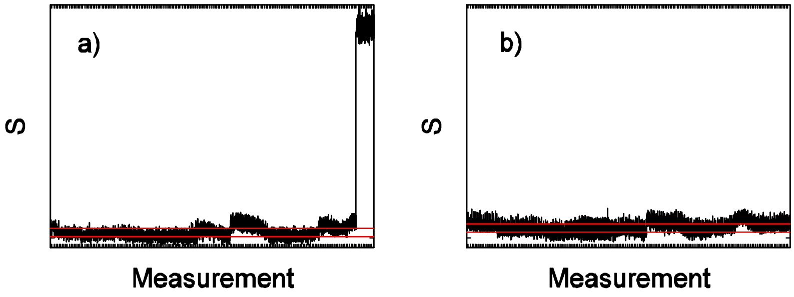

Fig. 2 *S* control chart for sensor fault detection a) with all sensors, b) sensor 3 removed

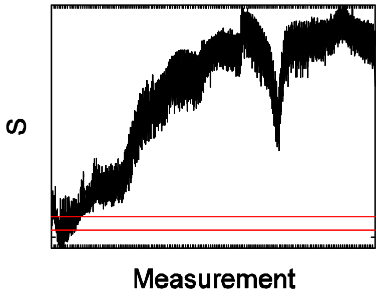

Fig. 3 *S* control chart for the healthy system. The training data are the first ten measurements

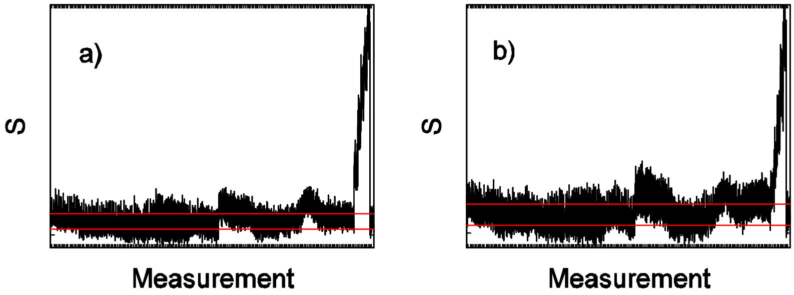

Fig. 4 *S* control chart for damage detection a) with all sensors b) sensor 7 removed

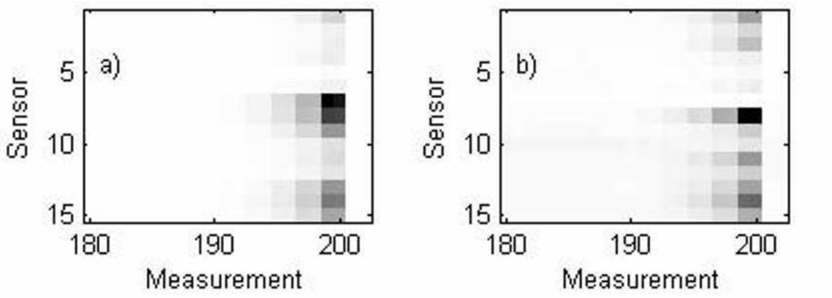

Fig. 5 Damage localization in the last measurements a) with all sensors b) sensor 7 removed

CONCLUSION

A method is proposed to distinguish between sensor fault, structural damage, and environmental or operational effects in a structural health monitoring system. It utilizes the hardware redundancy by modelling each sensor in the network using the others. The identification of the MMSE model is automatic and results in a conditional probability model of each sensor, which can then be used in the generalized likelihood ratio test to detect and localize a change in the system. The MMSE model takes into account the environmental or operational influences included in the training data. Both spatial and spatiotemporal correlation can be applied.

A procedure to distinguish between a sensor fault and structural damage was proposed, which is based on the fact that a sensor fault is local, while structural damage is global. If faulty sensors are removed from the network, the system should show similar performance as the original healthy structure. With structural damage, removing a sensor close to damage would not considerably affect the pattern in the control chart.

The advantages of the proposed time domain approach working directly in the sensor space are that (1) no complex system identification is needed, (2) damage can be distinguished from the sensor fault, (3) damage or faulty sensor localization is straightforward, and (4) the dimensionality of the data is relatively low. The main disadvantage is that the amount of data easily becomes high. It is therefore necessary to use recursive algorithms to estimate the statistical parameters. Also, for wireless sensor networks, the energy and time needed to transmit the data to the central computer are high, because no distributed computing is utilized. For the latter problem, damage detection from short time series could be applied [37].

Acknowledgments This research was performed in the Intelligent Structural Health Monitoring System (ISMO) project, funded by the Multidisciplinary Institute of Digitalisation and Energy (MIDE) research programme at Aalto University, Finland (http://mide.tkk.fi/en/).

REFERENCES

1. Simani, S., Fantuzzi, C., Patton, R. J. Model-based fault diagnosis in dynamic systems using identification techniques. Springer, London, 2003.
2. Wahab, M. A., De Roeck, G., Effect of temperature on dynamic system parameters of a highway bridge. Structural Engineering International, No. 4, 266–270, 1997.
3. Farrar, C. R., Doebling, S. W., Cornwell, P. J., Straser, E. G. Variability of modal parameters measured on the Alamosa Canyon Bridge. Proceedings of IMAC-XV: A Conference on Structural Dynamics, Orlando, Florida, 257–263, 1997.
4. Alampalli, S. Influence of in-service environment on modal parameters. Proceedings of the 16th International Modal Analysis Conference, Santa Barbara, California, 111–116, 1998.
5. Cornwell, P., Farrar, C. R., Doebling, S. W., Sohn, H. Structural testing series: Part 4. Environmental variability of modal properties. Experimental Techniques, Vol. 23, No. 6, 45–48, 1999.
6. Peeters, B., De Roeck, G. One year monitoring of the Z24 bridge: Environmental influences versus damage effects. Proceedings of IMAC-XVIII: A Conference on Structural Dynamics, San Antonio, Texas, 1570–1576, 2000.
7. Rohrmann, R. G., Baessler, M., Said, S., Schmid, W., Ruecker, W. F. Structural causes of temperature affected modal data of civil structures obtained by long time monitoring. Proceedings of IMAC-XVIII: A Conference on Structural Dynamics, San Antonio, Texas, 1–7, 2000.
8. Darbre, G. R., Proulx, J. The need for system identification techniques using ambient vibration data recorded on large dams. Proceedings of the International Conference on Structural System Identification, Kassel, Germany, 205–213, 2001.
9. Kullaa, J. Elimination of environmental influences from damage-sensitive features in a structural health monitoring system. Proceedings of the First European Workshop on Structural Health Monitoring, Paris, 742–749, 2002.
10. Manson, G. Identifying damage sensitive, environment insensitive features for damage detection. Proceedings of the Third International Conference on Identification in Engineering Systems, Swansea, 187–197, 2002.
11. Kullaa, J. Is temperature measurement essential in structural health monitoring? Proceedings of the 4th International Workshop on Structural Health Monitoring, Stanford, CA, 717–724, 2003.
12. Sohn, H., Worden, K., Farrar, C. R. Statistical damage classification under changing environmental and operational conditions. Journal of Intelligent Materials Systems and Structures, Vol. 13, No. 9, 561–574, 2003.
13. Vanlanduit, S., Parloo, E., Cauberghe, B., Guillaume, P., Verboven, P. A robust singular value decomposition for damage detection under changing operational conditions and structural uncertainties. Journal of Sound and Vibration, Vol. 284, 1033–1050, 2005.
14. Kullaa, J. Latent variable models to eliminate the environmental effects in structural health monitoring. Proceedings of the Third European Conference on Structural Control, Volume II, Vienna, Austria, S5-55–S5-58, 2004.
15. Kullaa, J. Damage detection under a varying environment using the missing data concept. Proceedings of the 5th International Workshop on Structural Health Monitoring, Stanford, CA, 565–573, 2005.

16. Yan, A.-M., Kerschen, G., De Boe, P., Golinval, J.-C. Structural damage diagnosis under varying environmental conditions—Part I: A linear analysis. Mechanical Systems and Signal Processing, Vol. 19, 847–864, 2005.
17. Yan, A.-M., Kerschen, G., De Boe, P., Golinval, J.-C. Structural damage diagnosis under varying environmental conditions—Part II: local PCA for non-linear cases. Mechanical Systems and Signal Processing, Vol. 19, 865–880, 2005.
18. Kullaa, J. Removing non-linear environmental influences from structural features. Proceedings of the third European Workshop on Structural Health Monitoring, Granada, Spain, 635–642, 2006.
19. Basseville, M., Bourquin, F., Mevel, L., Nasser, H., Treyssède, F. Merging sensor data from multiple temperature scenarios for vibration-based monitoring of civil structures. Proceedings of the third European Workshop on Structural Health Monitoring, Granada, Spain, 759–506, 2006.
20. Yan, A.-M., Golinval, J.-C. Null subspace-based damage detection of structures using vibration measurements. Mechanical Systems and Signal Processing, 20, 611–626, 2006.
21. Lämsä, V., Kullaa, J. Nonlinear factor analysis in structural health monitoring to remove environmental effects. Proceedings of the 6th International Workshop on Structural Health Monitoring, Stanford, CA, 1092–1099, 2007.
22. Gorinevsky, D., Kim, S.-J., Boyd, S., Gordon, G., Beard, S., Chang, F.-K. Optimal estimation of accumulating damage trend from series of SHM images. Proceedings of the 6th International Workshop on Structural Health Monitoring, Stanford, CA, 1340–1346, 2007.
23. Dunia, R., Qin, S. J., Edgar, T. F., McAvoy, T. J. Identification of faulty sensors using principal component analysis. AiChe Journal 42, 2797–2812, 1996.
24. Kerschen, G., De Boe, P., Golinval, J.-C., Worden, K. Sensor validation using principal component analysis. Smart Materials and Structures 14, 36–42, 2005.
25. Friswell, M. I., Inman, D. J. Sensor validation of smart structures. Journal of Intelligent Material Systems and Structures 10, 973–982, 1999.
26. Abdelghani, M., Friswell, M. I. Sensor validation for structural systems with additive sensor faults. Structural Health Monitoring 3, 265–275, 2004.
27. Abdelghani, M., Friswell, M. I. Sensor validation for structural systems with multiplicative sensor faults. Mechanical Systems and Signal Processing 21, 270–279, 2007.
28. Hernandez-Garcia, M. R., Masri, S. F. Multivariate Statistical Analysis for Detection and Identification of Faulty Sensors Using Latent Variable Methods. Advances in Science and Technology 56, 501–507, 2008.
29. Kullaa, J. Sensor fault identification and correction in structural health monitoring. Proceedings of ISMA2006, International Conference on Noise and Vibration Engineering, Leuven, Belgium, 873–884, 2006.
30. Kullaa, J. Sensor fault identification and correction in vibration-based multichannel structural health monitoring. Proceedings of the 6th International Workshop on Structural Health Monitoring, Stanford, CA, 606–613, 2007.
31. Kullaa, J. Sensor validation using minimum mean square error estimation. Mechanical Systems and Signal Processing 24 (5), 1444–1457, 2010.
32. Ray, A., Luck, R. An introduction to sensor signal validation in redundant measurement systems. IEEE Control System Magazine 11, 44–49, 1991.
33. Basseville, M., Nikiforov, I. V. Detection of abrupt changes - Theory and application. Prentice-Hall, Englewood Cliffs, NJ, 1993.
34. Kay, S. M. Fundamentals of statistical signal processing. Detection theory. Prentice-Hall, Upper Saddle River, NJ, 1998.
35. Sharma, S. Applied multivariate techniques. John Wiley & Sons, New York, 1996.
36. Montgomery, D. C. Introduction to statistical quality control, 3rd ed., John Wiley & Sons, New York, 1997.
37. Kullaa, J., Bocca, M., Eriksson, L. M. Energy-efficient SHM in wireless sensor networks by damage detection from short time series. Proceedings of the 5th European Workshop on Structural Health Monitoring, Sorrento, Naples, Italy, 943–948, 2010.

Structural Damage Identification with Various Uncertainties

Jiann-Shiun Lew and Michael Williamson

Center of Excellence in Information Systems, Tennessee State University, Nashville, TN 37209

This paper presents an investigation of structural damage identification with various uncertainty conditions. The model-based damage identification techniques compare the change of the identified model and the change of the analytical model, such as a finite element model, due to damage. The analytical model is different from the identified model because of errors from boundary conditions, material properties, and other variability. The uncertainty associated with identification errors and other random factors may also result in false indications of damage. In this study, we examine the damage identification with various uncertainties, such as boundary condition variation, temperature change, and environmental variation. Experiments of a beam structure under various uncertainties will be used to demonstrate the study.

INTRODUCTION

Uncertainty and variability in structures raise issues such as safety, reliability, and performance [1-4]. The structural uncertainty and environmental variation, such as boundary condition uncertainty and temperature variation, result in the uncertainty of analytical dynamic model and the variation of the identified parameters. This brings a challenging problem to vibration-based structural health monitoring (SHM) methods [5, 6], which compare the change of the identified modal parameters and the change of the analytical model due to damage. This paper presents an investigation of damage identification of a structure with various uncertainties.

The model-based damage identification techniques compare the change of the identified model with the change of the analytical model due to damage. The error of the analytical model affects the performance of damage identification and results in false-positive/-negative indications of damage. The error of the analytical model may be from the uncertainty of boundary condition, computational error, uncertainty of material properties, and environmental variation. The quality of the identified parameters is also crucial to the performance of damage identification. In this investigation, experiments of a cantilevered Euler's beam with various uncertainties are used to demonstrate the study. The uncertainties under study include boundary condition uncertainty, temperature variation, and operational variability.

Natural frequencies and mode shapes have been most frequently used in vibration-based methods. However, mode shape measurements require a large number of sensors, and the identified mode shapes may be subject to significant measurement error. The study of damage identification uses a correlation approach [6, 7], which is based on the comparison of the identified natural frequency change and the change of the natural frequencies of the analytical model due to damage. The natural frequencies are identified by using OKID [8, 9], a time-domain system identification technique, to synthesize the collected time-domain input/output data with the specified sine-sweep excitation. Experiments under various test conditions are conducted to investigate the effects of damage identification from various uncertainties. The temperature variation may have significant effects on structural dynamics and the identified parameters, and this leads to false identifications of damage [3]. The temperature effects on the identified natural frequencies are included in the damage identification process. The results demonstrate

T. Proulx (ed.), *Sensors, Instrumentation and Special Topics, Volume 6*, Conference Proceedings of the Society for Experimental Mechanics Series 9,
DOI 10.1007/978-1-4419-9507-0_4, © The Society for Experimental Mechanics, Inc. 2011

that the proposed technique can identify the location and intensity of the damage, which is simulated as the added mass to a beam, under various uncertainty conditions.

CORRELATION APPROACH

A brief description of correlation approach is given in this section. In this paper, the study is based on the analysis of the natural frequencies. The natural frequency vector of the first *n* structural modes is defined as

$$\boldsymbol{\omega} = [\omega_1 \quad \omega_2 \quad \cdots \quad \omega_n] \ , \tag{1}$$

where ω_j is the *j*th structural natural frequency. The changes of the natural frequency vectors for the *i*th referred damage case, such as the added weight at the *i*th position of the structure, are defined as

$$\Delta\boldsymbol{\omega}^i = \boldsymbol{\omega}^i - \boldsymbol{\omega}, \qquad i = 1, \cdots, m, \tag{2}$$

where $\boldsymbol{\omega}^i$ is the natural frequency vectors of the *i*th referred damage case. The correlations between the tested system with the weighted change vector, $\Delta\boldsymbol{\omega}_W$, which represents the difference of the identified parameters between the tested system and the healthy system, and the *i*th damage case with the weighted change vector $\Delta\boldsymbol{\omega}^i{}_W$ are defined as

$$C_i = \frac{\Delta\boldsymbol{\omega}_W\,(\Delta\boldsymbol{\omega}_W^i)^{\mathrm{T}}}{|\,\Delta\boldsymbol{\omega}_W\,||\,\Delta\boldsymbol{\omega}_W^i\,|}, \tag{3}$$

where the weight of each element is the standard deviation of the corresponding element due to all the considered *m* damage cases [7]. The correlation C_i represents the cosine between two vectors. The value of the correlation C_i is between -1 and 1. When the absolute value of C_i is close to 1, it indicates that element *i* is a damage candidate [6].
The magnitude ratios between the tested system and the *i*th damage case are defined as

$$R_i = \frac{|\,\Delta\boldsymbol{\omega}_W\,|}{|\,\Delta\boldsymbol{\omega}_W^i\,|}. \tag{4}$$

The magnitude ratios can be used to identify the intensity and location of damage [7].

DESCRIPTION OF THE TESTBED

The tested structure is a cantilevered aluminum Euler's beam, as shown in Figure 1. The beam structure is not clamped to the ground, and it is tied to an extension structure using a screw as shown in Figure 2. The extension structure is clamped to a table. As shown in Figure 1, two macro-fiber composite (MFC) transducers, developed by NASA Langley [10], are bounded on the surface of the beam structure. One transducer is used to excite the structure with the specified sine-sweep signal, and another is used to collect the signal of the excited vibration.

For data acquisition with a PC computer, the setup uses an Adlink 9111HR PCI board in a computer running Linux, and the free software library COMEDI for communicating with the board. A 'C' language program is used for recording output measurement and generating the actuator signal from the board D/A converter. The frequency of the actuator signal increases exponentially with time during the acquisition period. The signal is buffered by an op-amp, which drives the actuator. The amplitude of the beam vibration is then measured using the transducer signal. This signal is buffered with a TL082 op-amp and fed to an A/D channel of the 9111HR board.

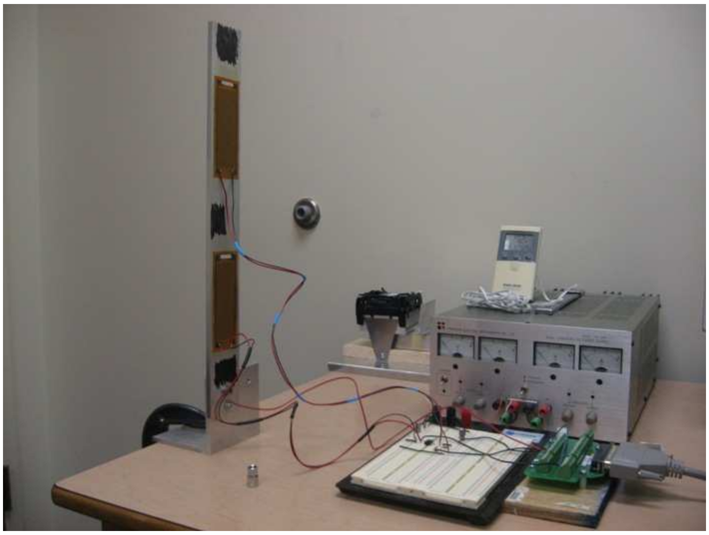

Figure 1. Beam structure for testing.

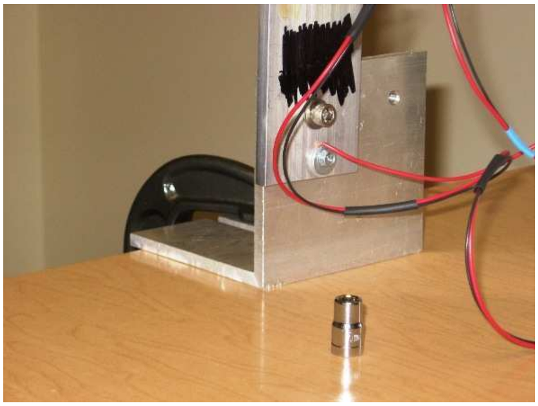

Figure 2. Beam tied with a screw.

The analytical model is based on the finite element analysis of the cantilevered beam with the length l= 41.5 *cm*, a rectangular section of 50x6 mm^2, Young's modulus E = 70 *GPa*, and density ρ = 2710 kg/m^3. There are various uncertainties that result in the model error of the analytical model. The major uncertainties are described as follows:

1. The measurements of the cross section are roughly estimated on purpose. The beam thickness measurement significantly affects the natural frequencies of the analytical model.
2. The beam is not exactly clamped to the ground, and it is screwed to an extension structure, which is clamped to a table.
3. The extension structure is excluded in the analytical model.

RESULTS AND DISCUSSIONS

In this study, first we investigate the identified natural frequency variations due to noise and other experimental random errors with minor temperature fluctuation. The sine-sweep signal with the log-scale frequency increase from 10Hz to 5000Hz is generated to excite the structure. The input/output measurements in 30 seconds at a sampling rate of 10K Hz are collected to get the identified model for each test. Input/output models of the system are identified using OKID [8] to synthesize time-domain data. Then, experiments are conducted for the damage case, where a load with the weight of 9 grams is attached to a position close to the free end. To simulate the boundary condition uncertainty, we loose the screw used to tie the beam. Experiments of undamaged and damaged cases are conducted for the beam with the loosed screw. Table 1 shows the natural frequencies of the first three modes of finite element models and the identified models for various conditions. The natural frequencies of the first three modes of the identified model for the healthy structure are 15.4%, 24.0%, and 27.6% lower than those of the analytical model, respectively. The relatively large weight of the extension structure may result in the decrease of natural frequencies. From the analytical models, the natural frequency reductions of the first three modes due to the added weight are 4.96%, 4.56%, and 4.25%, respectively. The results of the identified models show that the natural frequency reductions of the first three modes due to the added weight are 3.69%, 3.08%, and 3.76%, respectively, and these are lower than those based on the analytical models because the large weight of extension structure is excluded in the analytical model. The loose of the screw causes significant decreases of the natural frequencies of the first three modes. The reductions of the natural frequencies of the first three modes due to the loosed screw are 7.72%, 1.64%, and 2.68%, respectively.

Table 1. Natural frequencies of first three modes for various conditions.

Models	ω_1	ω_2	ω_3
Health (FE)	28.602	179.25	501.92
Damage (FE)	27.185	171.07	480.61
Health (ID)	24.208	136.20	363.48
Damage (ID)	23.315	132.01	349.82
Health (ID loosed screw)	22.339	133.97	353.74
Damage (ID loosed screw)	21.447	129.24	340.06

Figure 3 shows the identified natural frequencies of the first three modes of various tests for the healthy and damaged systems when the screw is tied or loosed. The loose of the screw results in the significant reductions of the natural frequencies of the first three modes. The identified natural frequency of each mode has relatively small variation due to the noise and other experimental random factors.

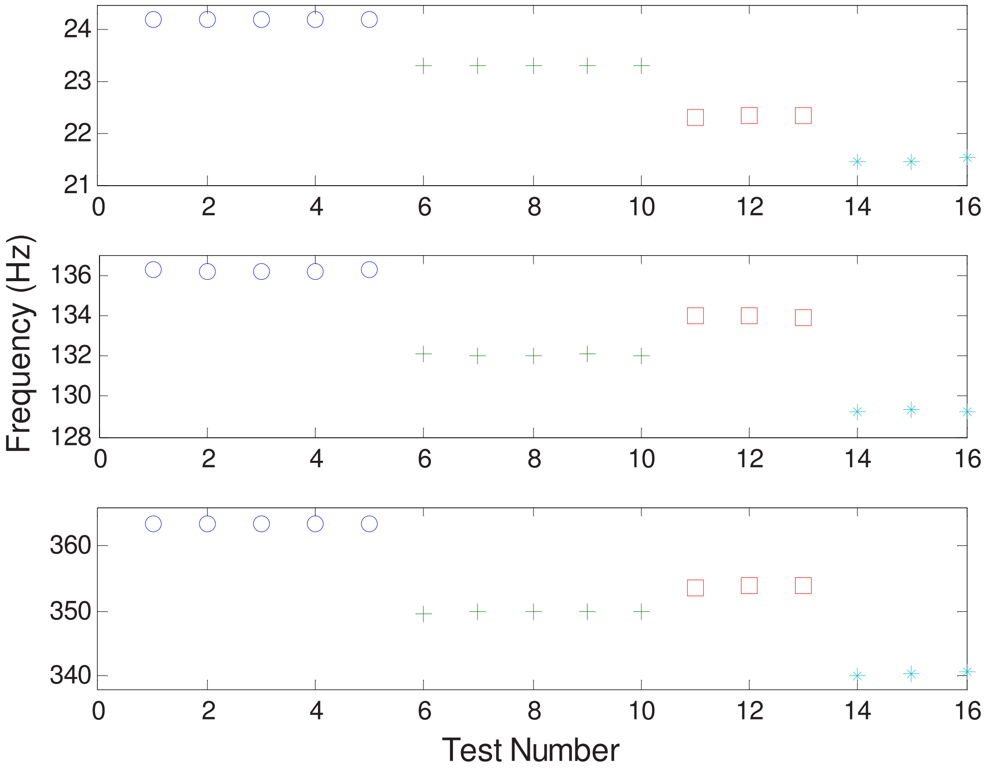

Figure 3. Identified natural frequencies of first three modes for various tests: o health (tied screw), + damage (tied screw), □ health (loosed screw), * damage (loosed screw).

Figure 4 shows the identified natural frequencies of the first three modes for the healthy structure with various temperatures. The effect of noise and other random factors on the identified natural frequencies of the first mode is more significant than that due to temperature variations in the range of 75^0F-83^0F. The natural frequency of the first mode of the health structure is computed as the average of the identified ones. For the second and third modes, temperature changes dominate the variations of the identified natural frequencies. For the second and third modes, solid lines represent the straight lines identified to curve fit the experimental data with the use of least-squares techniques. The identified straight lines well represent experimental data. The natural frequencies of the second and third modes of the health structure are computed as functions of temperature as

$$\begin{aligned} \omega_2 &= -0.05019T + 139.62, \\ \omega_3 &= -0.14821T + 373.41. \end{aligned} \tag{5}$$

Based on these functions, when temperature is 75^0F, the natural frequency of the second mode reduces 0.369% as temperature increases 10^0F and the natural frequency of the third mode reduces 0.409% as temperature increases 10^0F. The natural frequency reductions of these two modes due to 10^0F temperature increase are around 0.4%. The 0.4% change of the first natural frequency 24.2 Hz is around 0.097 Hz, which is close to the effect from other random factors.

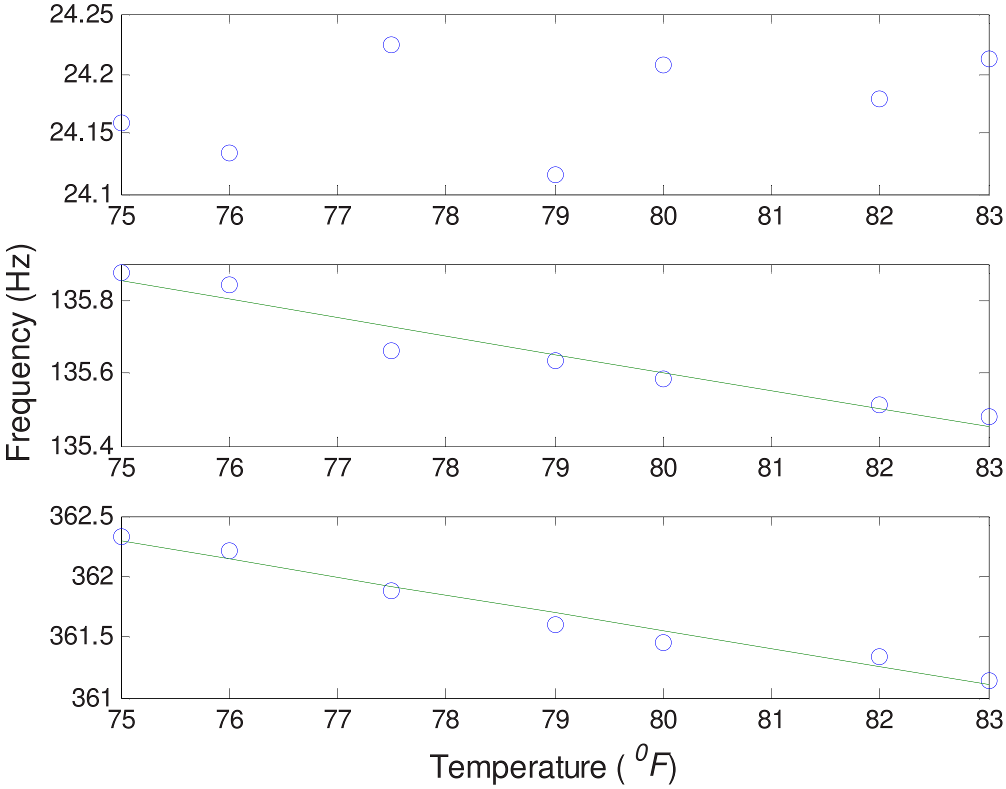

Figure 4. Identified natural frequencies of first three modes of healthy structure.

In this example, the damage identification process has the following steps:

1. Measure temperature T.
2. Use Eq. (5) to compute the natural frequencies of the second and third modes for healthy structure.
3. Use OKID to synthesize input/output data to get the identified natural frequencies of the tested system.
4. Compute the natural frequency deviation of the tested system

$$\Delta\boldsymbol{\omega} = \boldsymbol{\omega}_t - \boldsymbol{\omega}_h, \tag{6}$$

where $\boldsymbol{\omega}_h$ is the natural frequency vector of the healthy structure, and $\boldsymbol{\omega}_t$ is the natural frequency vector of the tested structure.

5. Use Eq. (3) to compute correlations.

Figure 5 shows the correlations of the damage case, where a mass is attached at the tip (close to location 15) of the beam, when the screw is tied. Solid line represents the correlations computed from the analytical models and the results correspond to the system without uncertainty. The dashed and dotted lines represent the results from two experiments of the damage case. The results of both experiments are close to the results based on the analytical models. For each test, correlation C_{15} is close to 1 and the damaged location is identified. Figure 6 shows the correlations of the damage case when the screw is loosed, which represents the beam with different boundary condition. The natural frequency vector $\boldsymbol{\omega}_h$ in Eq. (6) corresponds to the healthy structure with the loosed screw. Solid line represents the correlations computed from the analytical models with the tied screw. The dashed and dotted lines represent the results from two experiments of the damage case when the screw is loosed. The results of both experiments are close to the results based on the analytical models, correlation C_{15} of each test is close to 1, and the damaged location is identified. The results show that correlation approach can identify the damage location when the screw is tied or loosed.

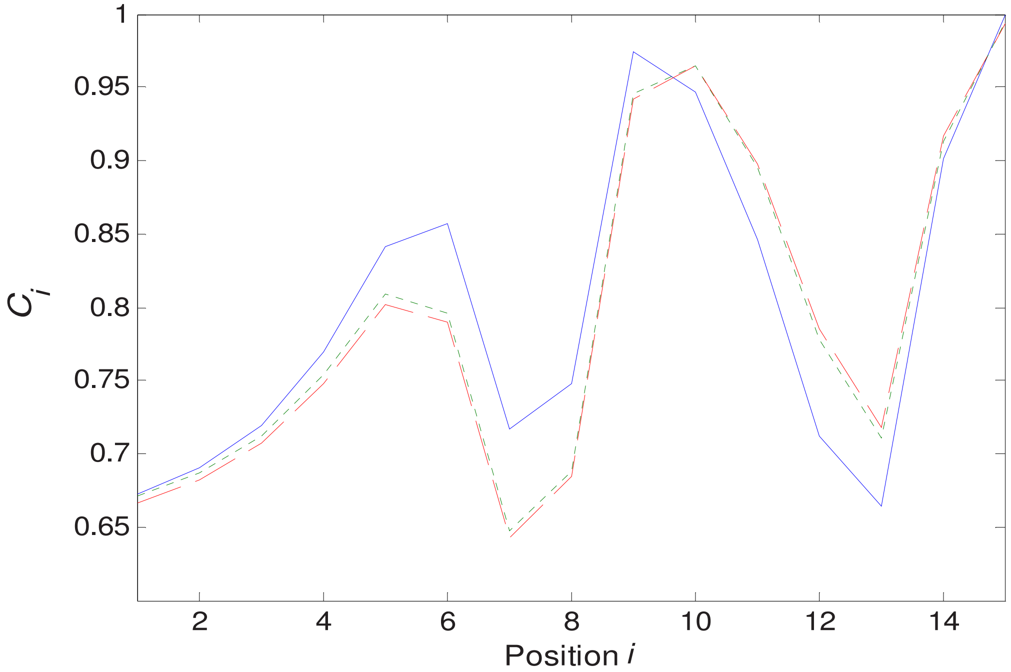

Figure 5. Correlation of beam with tied screw for position 15 damage case: —— analytical model, ⋯ 1st test, - - 2nd test.

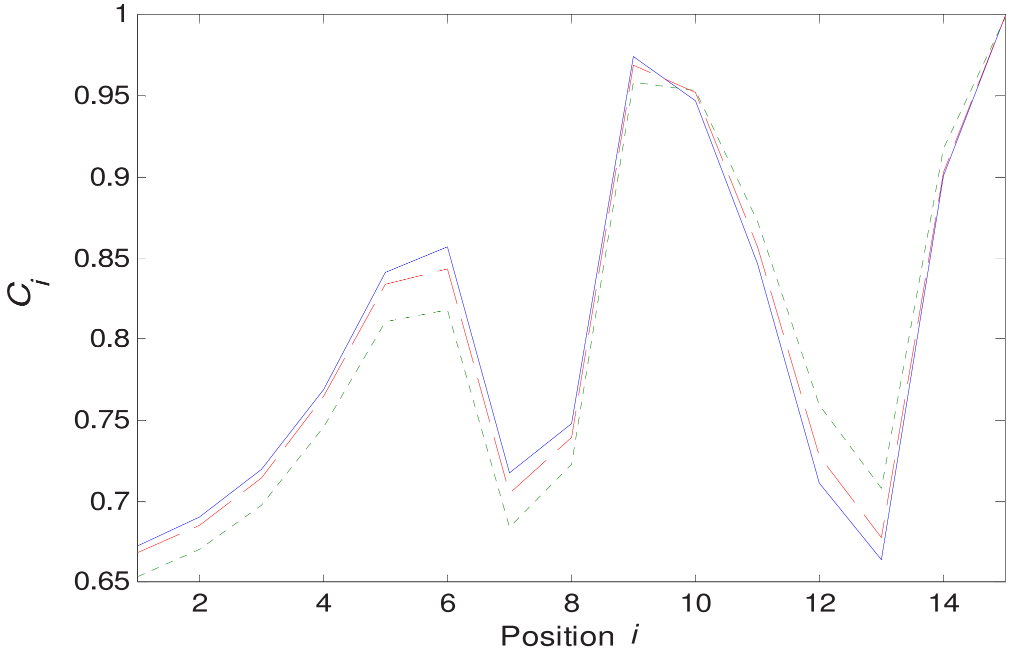

Figure 6. Correlation of beam with loosed screw for position 15 damage case: —— analytical model, ⋯ 1st test, - - 2nd test.

After the damaged location is identified, the intensity of damage is estimated to minimize the following cost function

$$J = (|\Delta \boldsymbol{\omega}_W| - |\Delta \boldsymbol{\omega}_W^i(\Delta m)|)^2 \tag{7}$$

where $\Delta \boldsymbol{\omega}_W$ is the weighted change vector of the identified parameters between the tested system and the healthy system, and $\Delta \boldsymbol{\omega}^i{}_W(\Delta m)$ is the weighted change vector of the analytical model due to the added mass Δm at location i, the identified damage position. The problem is to find Δm to make $|\Delta \boldsymbol{\omega}^i{}_W(\Delta m)|$ equate $|\Delta \boldsymbol{\omega}_W|$. Because the identified natural frequencies are around 20% lower than those of the analytical model, this factor is considered in the estimate of the added mass. When the screw is tied, the estimated weights for three experiments are 6.55, 6.61, and 6.52 grams, respectively. When the screw is loosed, the estimated weights for three experiments are 7.03, 6.75, and 7.04 grams, respectively. All the estimated weights are lower than the true one 9 grams. This is due to the model uncertainties, such as (i) the true weight of the beam is around 15% higher than the one used for the analytical model, and (ii) the relatively large weight of the extension structure makes the estimated weight lower.

CONCLUDING REMARKS

This paper presents a study of damage identification of a beam structure with various uncertainties. The results show that the correlation approach can identify the damage location with various uncertainties, such as the significant analytical model error and boundary condition variation. The temperature effect is also characterized and included in the damage identification process. The correlation approach is robust to various uncertainties under study, and it can also identify the intensity of damage. Further investigation of uncertainty and temperature effects will be conducted.

REFERENCES

[1] Mace, B. R., Worden, K., and Mason, G., "Uncertainty in Structural Dynamics," *Journal of Sound and Vibration*, Vol. 288, pp. 423-429, 2005.

[2] Red-Horse, J. R., and Paez, T. L., "Sandia National Laboratories Validation Workshop: Structural Dynamics Application," *Comput. Methods Appl. Mech. Engrg*., Vol. 197, pp. 2578-2584, 2008.

[3] Sohn, H., "Effects of environmental and operational variability on structural health monitoring," *Phil. Trans. R. Soc. A*, Vol. 365, pp. 539-560, 2007.

[4] Melchers, R.E., *Structural Reliability Analysis and Prediction*, Wiley, New York, 1999.

[5] Sohn, H., Farrar, C. R., Hemez, F. M., Czarneki, J. J., Shunk, D. D., Stinemates, D. W., and Nadler, B. R., "A Review of Structural Health Monitoring Literature: 1996-2001," *Los Alamos National Laboratory Report*, **LA**-13976-MS, 2002.

[6] Lew, J.-S., "Using Transfer Function Parameter Changes for Damage Detection of Structures," *AIAA Journal*, Vol. 33, pp. 2189-2193, 1995.

[7] Lew J.-S., "Optimal Controller Design for Structural Damage Detection," *Journal of Sound and Vibration*, Vol. 281, pp. 799-813, 2005.

[8] Juang, J.N., Horta, L.G., and Phan, M. "System/Observer/Controller Identification Toolbox (SOCIT)," *NASA Technical Memorandum* 107566, 1992.

[9] Juang, J.-N., *Applied System Identification*, Prentice-Hall, Englewood Cliffs, NJ, 1994.

[10] Wilkie, W.K., Bryant, G.R., High, J.W. et al. "Low-Cost Piezo-Composite Actuator for Structural Control Applications," *Proc. SPIE Int. Sym. on Smart Structures and Materials*, Newport Beach, CA, 2000.

Excitation techniques for testing bike vibration transmission in the laboratory

Julien Lépine, M.E. student
Dr. Yvan Champoux, Professor
Dr. Jean-Marc Drouet, Associate Professor
VélUS, Department of mechanical engineering
Université de Sherbrooke,
2500 boul. de l'Université, Sherbrooke (Québec),
CANADA J1K 2R1

ABSTRACT

Vibrations generated by road surface defects are a significant source of discomfort for cyclists. This paper presents two very different laboratory techniques for studying road bike vibration. The first technique uses a treadmill with a modified belt surface. The second technique is based on the use of a road simulator that was developed specifically to generate displacement excitation under the wheels of the bike. Broadband excitation generated by coarse pavement surface is also evaluated in this study.

The objective of this paper is to evaluate and compare the relative merits of these two approaches. For the purposes of evaluation, we have described a technique to obtain a realistic measurement of input in real road conditions.

Our results demonstrate that the road simulator succeeds in producing adequate displacement profiles in the vertical axis resulting in a vibration frequency spectrum that closely resembles the measurements in real road conditions. Limitations in current actuator capacity prevent to reproduce very coarse road conditions. Finally, more work is needed to develop an appropriate belt surface that can generate sufficient energy excitation above the 25 Hz range.

Introduction

Next to being lightweight, one of the most oft-mentioned desirable characteristics in a road bike is the capacity to filter vibrations. Because the cyclist has a very significant influence on the bike's dynamic behaviour due mainly to position and posture while cycling, laboratory excitation techniques are useful when we need to

T. Proulx (ed.), *Sensors, Instrumentation and Special Topics, Volume 6*, Conference Proceedings of the Society for Experimental Mechanics Series 9, DOI 10.1007/978-1-4419-9507-0_5, © The Society for Experimental Mechanics, Inc. 2011

obtain accurate and repeatable results. It is also important to use excitation signals that mimic road profiles, due to the non-linear behaviour of the cyclist's buttocks and hand-arm system. In this work, a rough granular pavement surface is considered to generate continuous random excitation.

The respective merits of two techniques are described and evaluated: one uses a treadmill with small wood studs glued onto the belt to create an uneven surface, while the second technique involves a road simulator apparatus that we developed specifically to generate road profile displacement under the bike's wheels. The same bike and same cyclist were used for all on-road and laboratory measurements. Acceleration signals are also measured at the same location in all tests.

In order to evaluate and compare the techniques, it was necessary to obtain a typical reference vibration signal on the bike and to carry out the measurements on the road. The technique to obtain this reference signal is described in the first section of this paper. Both techniques are presented in the second section, and the respective measured frequency spectrums are used to compare them. The final section of this paper compares and discusses the relative merits and limitations of both techniques.

Road reference signal measurement

The reference signal for evaluating the vibration replication fidelity of the two techniques was measured using the system shown in Fig. 1: the cyclist is sitting on a bike that is being towed by a car. A fixture connects the bike's front fork to the rear of the car, and a dummy front hub allows the fork to rotate freely along the front axle. The cyclist does not pedal and the chain has been removed. An instrumented stem monitors the vertical force applied by the cyclist on the handlebar. A triaxial accelerometer (PCB model 356B11) is secured to the left rear frame dropout of the bike. All cables are routed along the frame and connected to the power supply and data acquisition system installed in the car. This measurement technique is similar to the one used to rank road surfaces for cars [1]; it offers several advantages for bike testing, such as obtaining high quality signals related to road excitation. Speed is an important parameter that can be kept constant within ± 1 km/h; monitoring the leaning force [2] allows us to minimize the signal variability related to the cyclist's position and posture; gear and chain noise have been eliminated. The low natural frequency of the car's suspension system does not disturb the signal because it is below the selected frequency range of interest between 8 Hz and 100 Hz [3].

The measurements were repeated four times on the same 1.5 km section of the road located in Mont-Orford National Park (Quebec, Canada) at three different speeds: 26, 30 and 36 km/h. This road was selected because it does not have any major cracks or potholes and mainly because its surface is coarse enough to provide the desired random excitation.

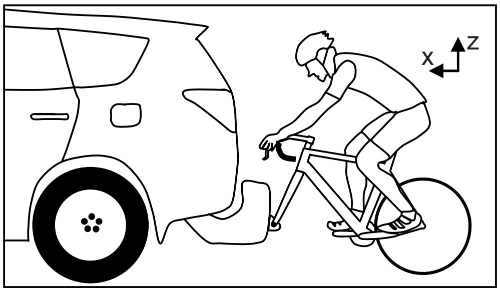

Fig. 1: Road test setup

The power spectral density (PSD) measured in the Z axis provided by the accelerometer are shown in Fig. 2 at all three speeds. Each curve represents the average spectrum over the 4 tests for each speed. The average absolute difference across all frequencies between the average spectrum and all curves at a specific speed is less than 0.5 dB. This shows that the technique provides repeatable measurements. The RMS and kurtosis values are also provided. The signals were bandpass filtered (8-100Hz) to calculate the kurtosis and RMS values. The frequency spectrums have the same smooth shape illustrating that there is no strong dynamic behaviour in the system. As expected, the spectrums as well as the RMS amplitudes increase along with speed. The maximum variation between the 20 and 36 km/h frequency spectrum curves is in the 4 dB range.

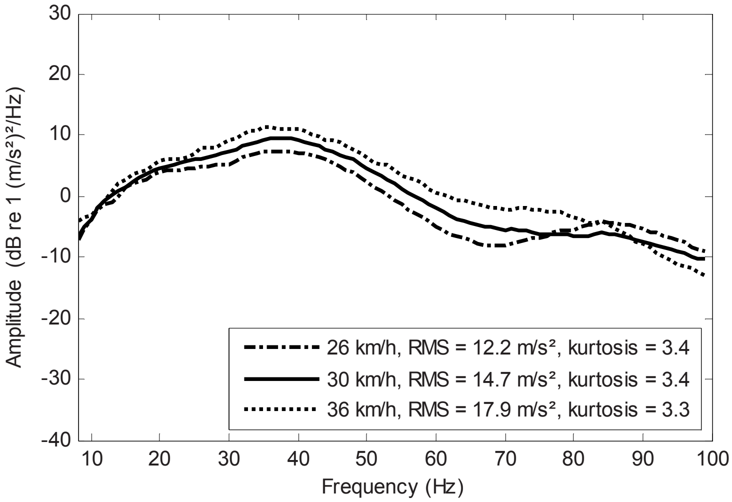

Fig. 2: Average PSD for the vertical accelerations (Z) at three speeds on the Mont-Orford National Park road.

The treadmill

For this research program, we custom-designed a treadmill to test road bikes mounted by cyclists in the laboratory [4]. It is powered by a 10 Hp variable speed electric motor. The rolling surface dimensions of 0.75 x 2 m provide enough space for the cyclist to move freely while pedaling normally. To reproduce road excitation, wooden dowels with diameters ranging from 6.4 mm to 7.9 mm were hot-glued onto the belt surface. The dowels are all approximately 30 mm long. The spacing between dowels follows a Gaussian distribution centred at 7 mm with a standard deviation of 3 mm. Fig. 3 shows the typical spacing of the dowels. Two rows with different span distribution were glued side by side to minimize the inherent periodicity provided by the treadmill. All parameters were selected according to road profile observation and road bike wheel dimension and with the goal of maintaining partial contact between the tire and the belt surface.

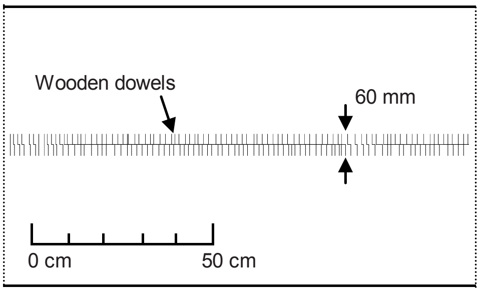

Fig. 3: Dowel distribution on the treadmill belt surface

During testing, the front wheel hangs above the rolling surface and does not touch the belt. This reproduces the same conditions used during on-road measurements for the reference signal. For this preliminary work, tests were carried out only at 26 km/h. The cyclist's position was also controlled for by monitoring the instrumented stem signal. An 8 channel LMS data acquisition system was used and the data was analysed using LMS Virtual.lab software package.

Fig. 4 shows a comparison of the reference signal frequency spectrum measured on the road and the average PSD of the vertical acceleration (z) measured on the treadmill. There are important discrepancies at high frequencies between the two frequency spectrums. The RMS and the kurtosis amplitudes are also quite different. The RMS level on the treadmill is 33% lower than the reference signal measured on the road. The modifications tested at the surface of the belt were not successful in replicating the high frequency content when compared to on-road measurements.

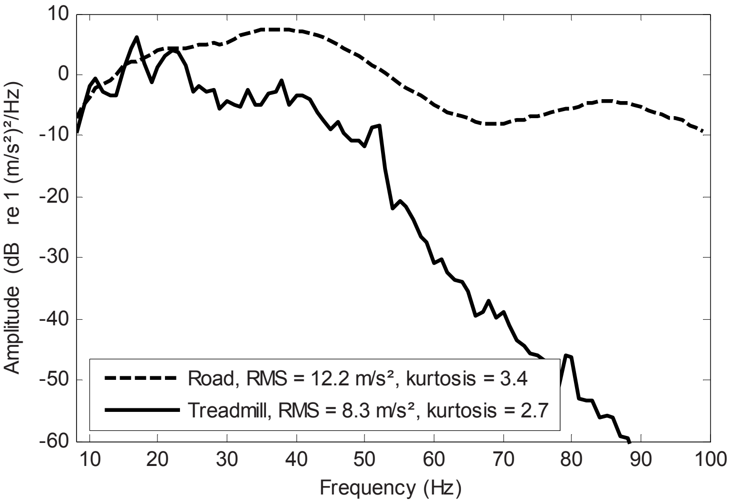

Fig. 4: Comparison of the average acceleration PSD measured using the treadmill and the PSD of the reference signal measured on the road. The speed is 26 km/h.

Road simulator

The second technique uses a road simulator (shown in Fig. 5) that was developed specifically for bike testing [5]. In the current stage of development, the bike wheels are not rolling and consequently the cyclist is not pedaling or steering the bike. Two motion actuators produce the required force to move a horizontal beam with one freely rotating end along a horizontal axis. At the other end of the beam this creates a displacement that is near-vertical to the wheel of the bike that rests on top of the beam. The actuators effective bandwidth ranges from DC to 100 Hz.

The driving signal is provided by the sound card output of a PC using a USB connector with an interface device. This feature eliminates the opportunity to use an analog closed loop field replication scheme that would have used the in-situ road acceleration measurement as a control signal. We therefore used a different approach developed to calculate the actuator's input signals. The ultimate objective here was to find the actuator input signal that would drive the simulator to ideally obtain the same rear drop-out acceleration measured on the road. We measured the system transfer function between the simulator's numerical signal input and the vertical acceleration at the rear dropout of the test bicycle mounted on the simulator. We used the same cyclist and the same bike as we used for on-road measurements. Cyclist posture was controlled by the stem force.

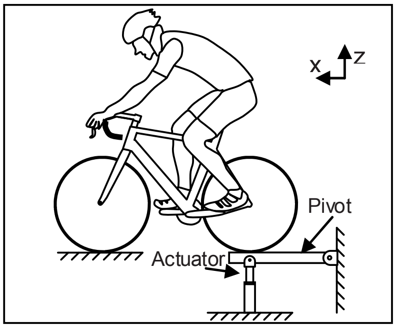

Fig. 5: Rear section of the road simulator

For non-linearity verification, the transfer function was measured six times with different signal amplitudes covering the full amplitude range of the device. Fig.6 reveals the average transfer function along with the transfer function with maximum and minimum amplitudes. The maximum amplitude variation span of the transfer function was less than 1 dB; this was satisfactory evidence by which to assume that the system behaves linearly.

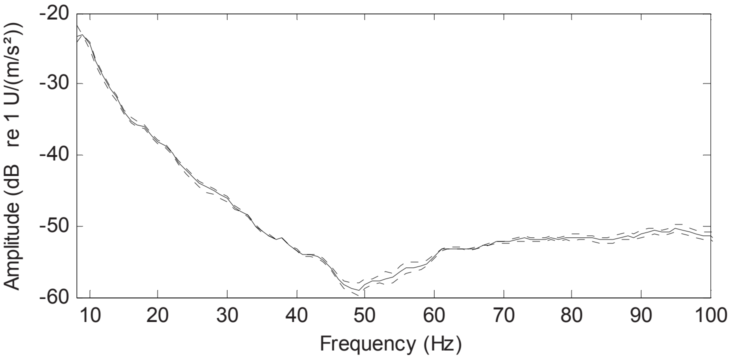

Fig. 6: Transfer functions between the simulator input signal and the vertical rear dropout acceleration (Z). Solid line: average transfer function Dashed lines: minimum and maximum limits of the transfer function

The impulse response corresponding to the system transfer function was calculated using the inverse Fourier transform. The resulting time signal corresponds to the FIR digital filter coefficients of the system. To calculate the required actuator input, the expected rear dropout acceleration time signal must simply be filtered.

To evaluate the road simulator's replication capability, road measurements at 26 km/h were used to calculate the input actuator signals. Due to actuator velocity limits, it was not possible to reproduce higher speed excitation. The simulator mainly creates vertical displacement under the wheels. This leads to speculation as to how well the horizontal acceleration can be replicated in view of vertical displacement only.

Results are shown in the two graphs of Fig. 7. These graphs compare the PSD of the road signal with the signal measured on the simulator. The top graph shows the horizontal acceleration (X) and the bottom displays vertical acceleration (Z).

The horizontal acceleration generated by the simulator is lower than the road values with an average difference of 7 dB. The RMS value is also 50% lower than road RMS value. The road and simulator vertical acceleration PSD and RMS are very similar with the curves showing a 3 dB difference in range. Using the correction with the transfer function to account for the dynamic response of the actuators thus provides reliable results. The simulator RMS value is only 6% below the road value. Kurtosis values are also similar.

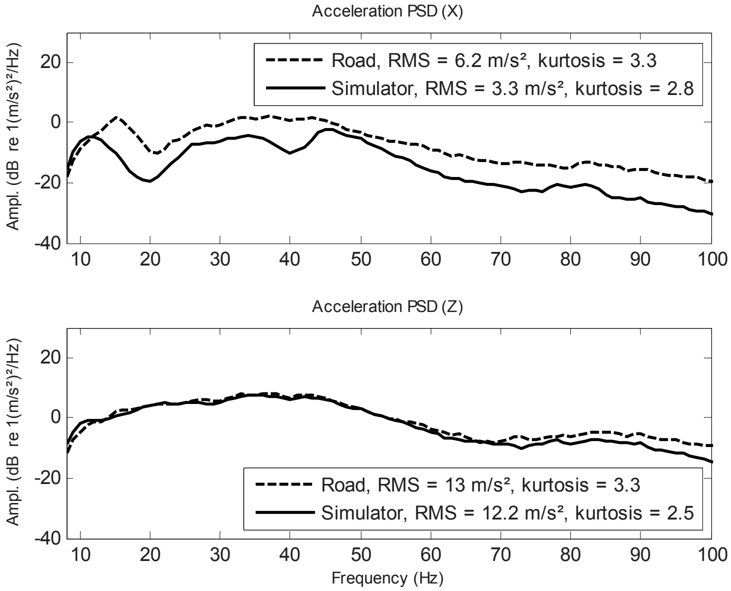

Fig.7: Comparison between the average measured PDS in the X and Z axes for the road and the simulator. The RMS and kurtosis values of the accelerations at the rear dropout are also provided. Bike velocity is 26 km/h

Discussion

In elucidating the physics related to the vibration behaviour of road bikes, it has been determined that road measurements are quite difficult to perform and results are often unreliable [2]. Several important parameters such as the cyclist's posture, speed, road profiles etc., all strongly influence vibration measurement. On the road, the cyclist's attention is focused on guiding and propelling the bike and it may be difficult to pay sufficient attention to other issues. This highlights the advantage of developing apparatus and techniques to "bring the road to the lab". Moreover, lab measurements can be performed in a controlled environment all year round. The input impedances related to the human body are known to be non-linear [6] and this is certainly the case for the hands and buttocks during cycling. To overcome this difficulty, one classical approach is to take measurements at the running condition amplitude [7]. Laboratory measurements enable control over the excitation amplitudes.

The techniques presented in this work both have limitations, advantages and disadvantages. Neither succeeds in perfectly mimicking road excitation. For example, more work is needed on the treadmill to modify the belt surface in order to increase high frequency content. This would however require a significant amount of work because surface modification is based on a trial and error approach and only a single profile would be obtained. The limited stiffness of the plate supporting the belt may be responsible for the high frequency limitation. Guaranteeing good measurement repeatability is a big challenge in bike testing. Measurement repeatability on the treadmill was found to be inferior to repeatability using the simulator. Notwithstanding these limitations, we believe that the realistic aspects provided by the cyclist pedaling and steering the bike under loading conditions makes the treadmill suitable for perception and qualitative testing.

On the road, vertical and horizontal forces are applied to the wheels of the bike. The simulator generates vertical displacement only. It should be noted that this is no different than what is used in NVH studies in the automobile industry. The requirement to generate accurate horizontal excitation is also somewhat alleviated by the fact that vertical forces predominate. The vertical acceleration average power measurement is 4 times greater than horizontal power.

The simulator technique requires that we use an in-situ road measurement to calculate the actuator's input signals. The displacement generated by the simulator can be associated with a specific "road profile". Different roads could conceivably be profiled to constitute a data bank for testing bikes in different conditions. This is likely the major advantage of the simulator. Moreover, when comparing dynamic behaviour, the simulator allows exactly the same profile to be played when different bikes are tested or when components are swapped.

Table 1 provides a summary of the major features of the two techniques tested in this research, based on the current stage of development of our testing apparatus.

Table 1: Features of the excitation technique tested in this study

	Treadmill	Simulator
Features	- Very similar to road conditions: wheels are rolling; the cyclist pedals normally -Vertical and longitudinal excitation forces - It is possible to test one wheel at a time	- Very good replication for Z - Road data bank available - Good repeatability - Good control over the excitation amplitudes and features - Ideal for bike comparison and perception evaluation.
Limitations	- Difficult to replicate variety in road conditions - Repeatability is average - Inherent periodicity in the excitation signal -Changing the road profile is costly and time-consuming	-Vertical excitation only; horizontal excitation is not replicated as accurately as the vertical one - Powerful actuators are required for rough-surface roads

Acknowledgments

The authors gratefully acknowledge financial support from the National Science and Engineering Council of Canada (NSERC) and the participation of Cervélo and Vroomen-White Design.

References

[1] Adams, D.E and al., “Lab Lessons Learned-Part 2: Road Quality Determination Using Vehicle Data”, Experimental techniques, vol. 30, no. 1, pages: 61-66, 2007.
[2] Richard, S, “Étude du comportement dynamique d’un vélo de route en lien avec le confort du cycliste”, MSc. Thesis, Université de Sherbrooke, 2005
[3] IS0 2631-1 (1997), Mechanical vibration and shock -Evaluation of human exposure to whole-body vibration -Part 1: General requirements
[4] Richard, S. and Champoux, Y., Evaluation of road bike comfort using classical and operational modal analysis, Proceedings of IMAC XXIII, 2005.
[5] Brassard, F, “Développement d’un simulateur de vibration pour vélo de route”, under revision, 2010
[6] Panzke, K.-J and Balasus, W , “Time dependence and non-linearity of the impedanceof the human hand-arm system while exposed to intense vibration”, Int Arch Occup Environ Health, 57 :35-45, 1985
[7] Ewins, D.J., “Modal Testing Theory, Practice and applicaton, 2nd edition Reseach Studies Press, 2000

Damage Detection Using Blind Source Separation Techniques

NGUYEN Viet Ha, GOLINVAL Jean-Claude
University of Liege,
Aerospace & Mechanical Engineering Department, Structural Dynamics Research Group,
Chemin des chevreuils, 1 B52/3, B-4000 Liège 1, Belgium
Email : VH.Nguyen@doct.ulg.ac.be, JC.Golinval@.ulg.ac.be

ABSTRACT

Blind source separation (BSS) techniques are applied in many domains since they allow separating a set of signals from their observed mixture without the knowledge (or with very little knowledge) of the source signals or the mixing process. Two particular BSS techniques called Second-Order Blind Identification (SOBI) and Blind Modal Identification (BMID) are considered in this paper for the purpose of structural damage detection or fault diagnosis in mechanical systems. As shown on experimental examples, the BMID method reveals significant advantages. In addition, it is demonstrated that damage detection results may be improved significantly with the help of the block Hankel matrix. The main advantage in this case is that damage detection still remains possible when the number of available sensors is small or even reduced to one.

Damage detection is achieved by comparing the subspaces between the reference (healthy) state and a current state through the concept of subspace angle. The efficiency of the methods is illustrated using experimental data.

1. Introduction

Blind source separation (BSS) techniques are applied in many domains, since they allow separating a set of signals from their observed mixture, without the knowledge (or with very little knowledge) of the source signals or the mixing process. Among the methods in the BSS family, one can cite for example Principal Component Analysis (PCA) or Proper Orthogonal Decomposition (POD), Smooth Orthogonal Decomposition (SOD), Independent Component Analysis (ICA) and Second-Order Blind Identification (SOBI). All of these methods have been exploited in many engineering applications owing to their versatility and their simplicity of practical use. For example, BSS techniques showed useful for modal identification from numerical and experimental data [1-4], for separating sources from traffic-induced building vibrations [5] and for damage detection and condition monitoring [6-8].

McNeil and Zimmerman [9] proposed recently a methodology for modal identification based on BSS techniques, called Blind Modal Identification (BMID). This method uses a BSS algorithm like SOBI to decompose an augmented and pre-treated dataset. BMID is distinct from other usual BSS methods as it allows to estimate complex mode shapes which may occur in real-world structures.

In reference [9], BMID has been shown more advantageous than some traditional methods for the purpose of modal identification. In the present paper, BMID is exploited to tackle the problem of structural damage detection or fault diagnosis in mechanical systems. Its performance is compared to another BSS method, namely the SOBI method. Thanks to the use of the block Hankel matrix, detection remains possible even if the number of available sensors is small. The proposed method is illustrated on experimental applications such as damage detection in an aircraft mock-up, fault diagnosis of rotating devices and quality control of welded joints.

T. Proulx (ed.), *Sensors, Instrumentation and Special Topics, Volume 6*, Conference Proceedings of the Society for Experimental Mechanics Series 9,
DOI 10.1007/978-1-4419-9507-0_6, © The Society for Experimental Mechanics, Inc. 2011

2. SOBI algorithm and its extension called BMID

2.1 SOBI algorithm

Second-order blind identification was introduced by Belouchrani

2.3 SOBI, BMID and the Hankel matrices

The so-called

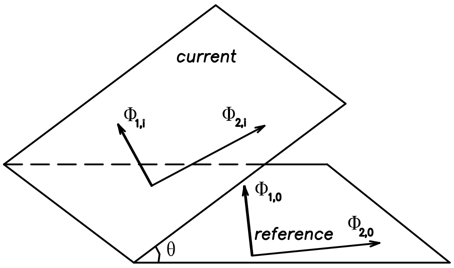

Figure 1: Angle θ formed by active subspaces (hyper-planes) according to the reference and current states, due to a dynamic change

4. Examples of application

4.1 Experiments in an aircraft model in different conditions

The first example consists in an aircraft model made of steel and suspended freely by means of three springs, as illustrated in Figure 2.

The fuselage is made of a straight beam of rectangular section and a length of 1.2 m. Plate-type beams connected to the fuselage form the wing (1.5 m) and tails (0.2 m). Their dimensions are detailed in Figure 3. The structure is randomly excited on the top of the left wing by an electro-dynamic shaker in the frequency range of 0-130 Hz. Eleven accelerometers are installed for capturing the dynamic responses of the structure in accordance with the set-up description given in Figure 3. Three levels of damage are simulated by removing, respectively, one, two and three connecting bolts on one side of the wing (Figure 2*b*). The data of this experiment was formerly used for illustrating damage detection methods based on Principal Component Analysis, Kalman model [12] and Null-subspace analysis [13]. Modal identification results were also given in [12].

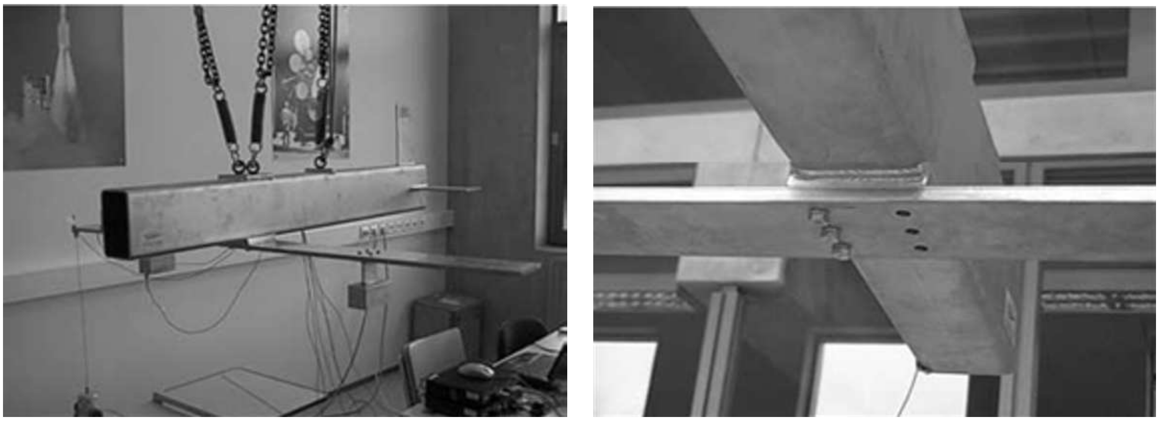

a) Aircraft model *b) removing of 1-3 connecting bolts*

Figure 2: An aircraft model (*a*) and the simulated damages (*b*)

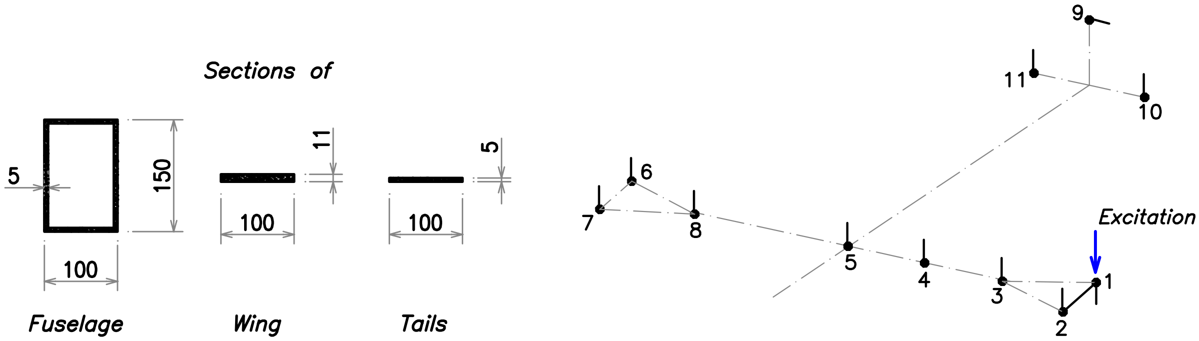

Figure 3: Dimensions (in millimeters) and location of the 11 sensors

❖ *Modal identification using SOBI or BMID*

For the sake of illustrating the sensitivity of SOBI to damage occurrence, resonance frequencies and mode shapes are first identified. Figure 4

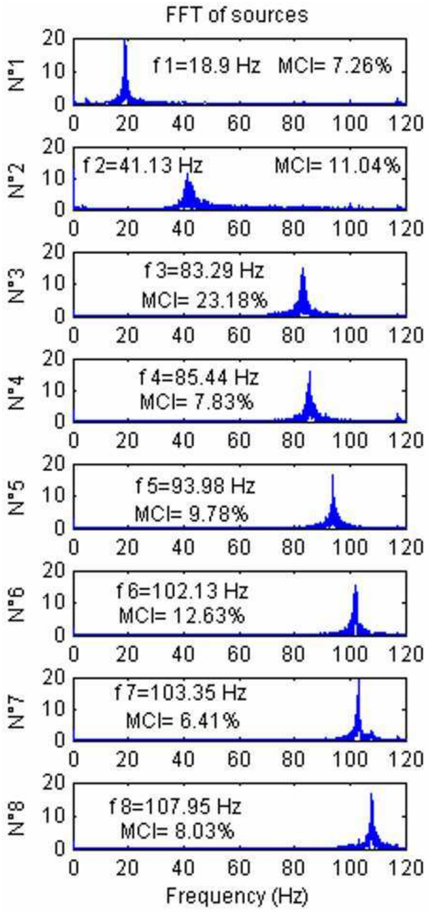
FFT of sources
N°1
f 1=18.9 Hz
MCI= 7.26%
N°2
f 2=41.13 Hz
MCI= 11.04%
N°3
f 3=83.29 Hz
MCI= 23.18%
N°4
f 4=85.44 Hz
MCI= 7.83%
N°5
f 5=93.98 Hz
MCI= 9.78%
N°6
f 6=102.13 Hz
MCI= 12.63%
N°7
f 7=103.35 Hz
MCI= 6.41%
N°8
f 8=107.95 Hz
MCI= 8.03%
0 10 20
0 20 40 60 80 100 120
Frequency (Hz)

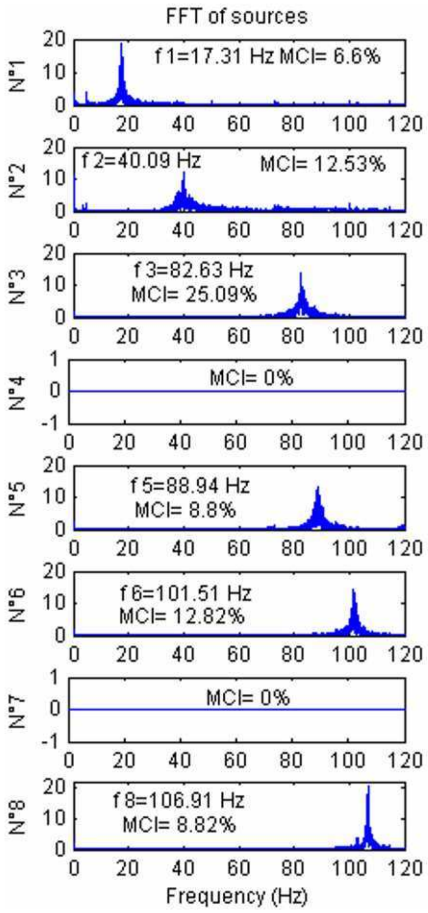
FFT of sources
N°1
f 1=17.31 Hz
MCI= 6.6%
N°2
f 2=40.09 Hz
MCI= 12.53%
N°3
f 3=82.63 Hz
MCI= 25.09%
N°4
MCI= 0%
-1 0 1
N°5
f 5=88.94 Hz
MCI= 8.8%
N°6
f 6=101.51 Hz
MCI= 12.82%
N°7
MCI= 0%
-1 0 1
N°8
f 8=106.91 Hz
MCI= 8.82%
0 10 20
0 20 40 60 80 100 120
Frequency (Hz)

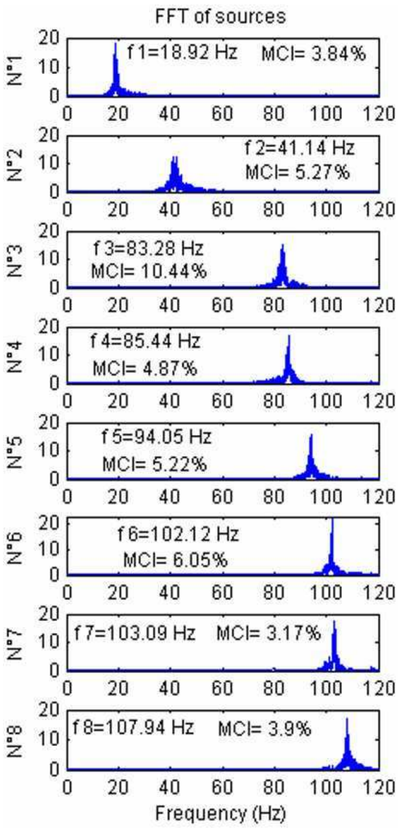
FFT of sources
N°1
f1=18.92 Hz
MCI= 3.84%
N°2
f2=41.14 Hz
MCI= 5.27%
N°3
f3=83.28 Hz
MCI= 10.44%
N°4
f4=85.44 Hz
MCI= 4.87%
N°5
f5=94.05 Hz
MCI= 5.22%
N°6
f6=102.12 Hz
MCI= 6.05%
N°7
f7=103.09 Hz
MCI= 3.17%
N°8
f8=107.94 Hz
MCI= 3.9%
0
10
20
0
20
40
60
80
100
120
Frequency (Hz)

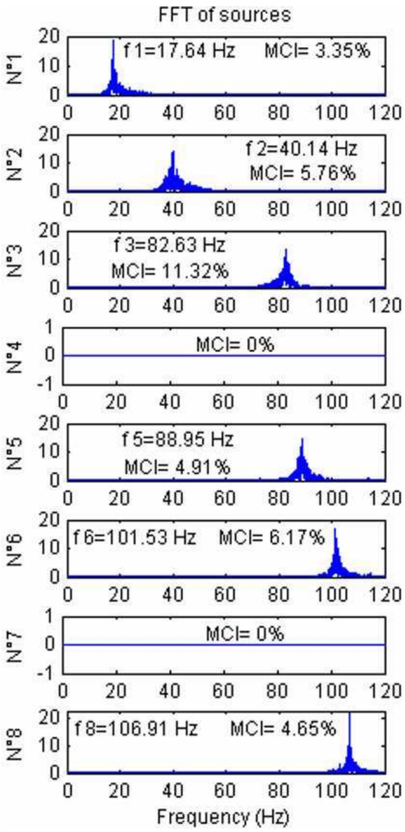
FFT of sources
N°1
f1=17.64 Hz
MCI= 3.35%
N°2
f2=40.14 Hz
MCI= 5.76%
N°3
f3=82.63 Hz
MCI= 11.32%
N°4
MCI= 0%
-1
0
1
N°5
f5=88.95 Hz
MCI= 4.91%
N°6
f6=101.53 Hz
MCI= 6.17%
N°7
MCI= 0%
N°8
f8=106.91 Hz
MCI= 4.65%
0
10
20
0
20
40
60
80
100
120
Frequency (Hz)

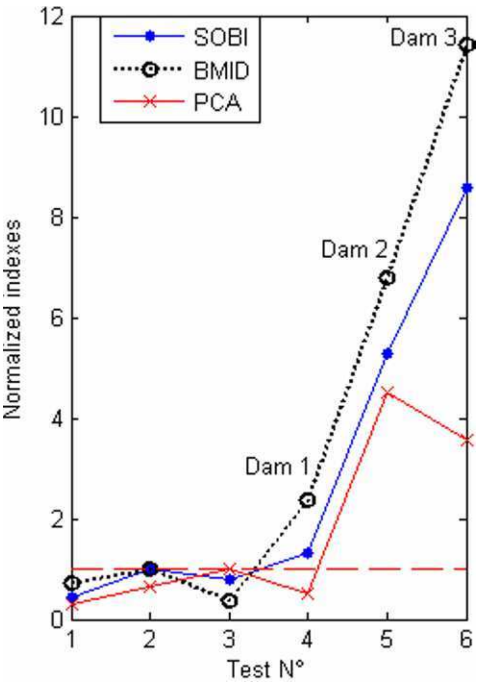
SOBI
BMID
PCA
Dam 3
Dam 2
Dam 1
Normalized indexes
Test N°
0
2
4
6
8
10
12
1
2
3
4
5
6

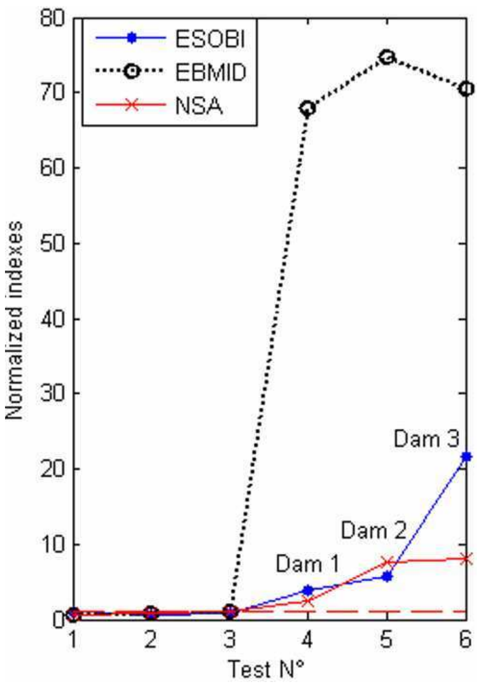
ESOBI
EBMID
NSA
Dam 3
Dam 2
Dam 1
Normalized indexes
Test N°
0
10
20
30
40
50
60
70
80
1
2
3
4
5
6

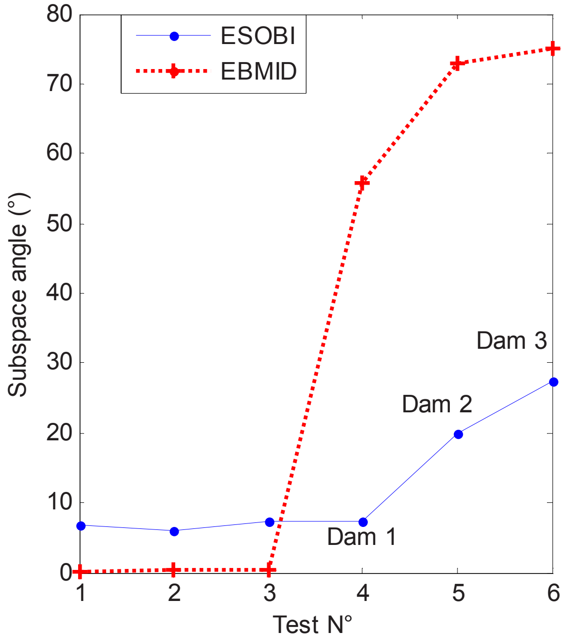

Figure 10: Damage detection by ESOBI and EBMID

Damage detection results based on the subspace angles are shown in Figure 10. ESOBI is able to detect damage levels 2 and 3 but is unable to detect damage level 1 while EBMID (using 8 block rows) is successful in distinguishing perfectly the healthy and damaged states. Thus EBMID looks more appealing when the number of sensor is small.

4.2 Damage detection in electro-mechanical devices

This industrial application concerns the case of electro-mechanical devices for which the overall quality at the end of the assembly line has to be assessed.

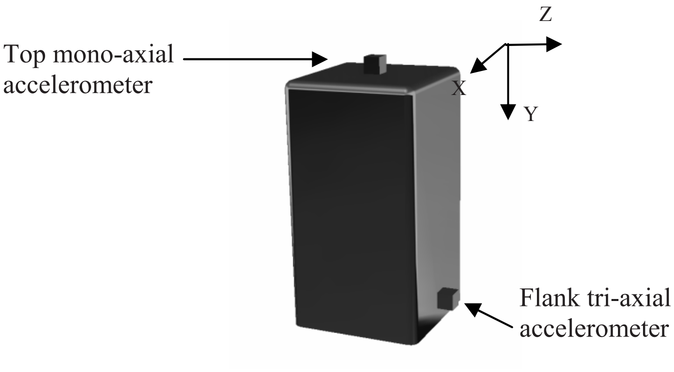

Figure 11: Location of the accelerometers on the electro-mechanical device: one mono-axial accelerometer on the top and one tri-axial accelerometer on the flank of the device

A set of five good (healthy) devices and four damaged devices was considered. Dynamic responses were collected by one mono-axial accelerometer on the top and one tri-axial accelerometer on the flank of the device as illustrated in Figure 11. Only data measured in one direction on the flank (X, Y or Z in Figure 11) or on the top of the device is used for the detection.

It is worth recalling that using the response measured by one sensor only, detection cannot be performed by subspace methods such SOBI and PCA. For this reason, fault diagnosis was realized in [17] using the Null subspace analysis (NSA) method based on block Hankel matrices. As it was found in [17] that fault detection is better when using the data in the Y direction, the data in this direction is exploited here to test the proposed methods.

As discussed earlier, it is also possible to construct a subspace even if only one response signal is available if BMID, SOBI are performed on the Hankel matrix. In this example, 8 block rows were used to construct the Hankel matrix. Figure 12 presents the results obtained on the whole set of electro-mechanical devices. Detection results using ESOBI and EBMID are given in Figure 12 well identified for welds A (-33% covering); D (-66% compensation); E1 and E3 (-10% current). However, the detection indicators show that they are not proportional to the severity of the defects in the welds.

Table 2: Welds realized with altered parameters (with respect to the nominal parameters)

Name	Modified parameter	Weld quality
Welding A	-33% covering	Acceptable
Welding B	-66% covering	Bad
Welding C	-33% compensation	Good
Welding D	-66% compensation	Acceptable
Welding E	-10% current	Acceptable
Welding F	-20% current	Bad
Welding G	-10% forging pressure	Good
Welding H	+5% forging pressure	Acceptable
Welding I	-66% covering and compensation	Bad

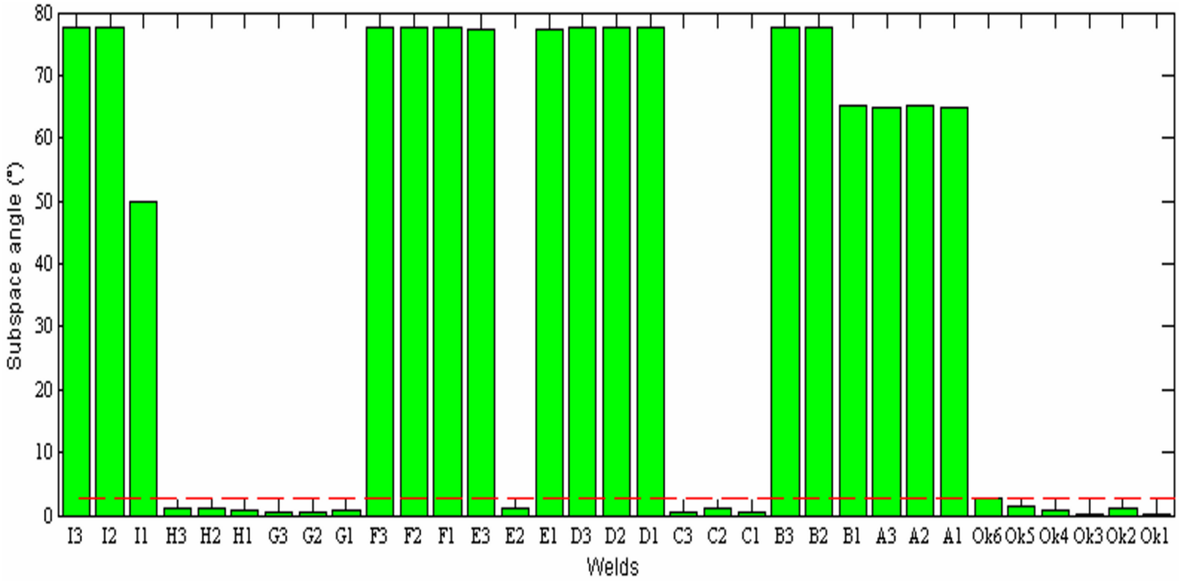

Figure 14: EBMID detection (the dash-dot line corresponds to the max value for healthy welded joints)

5. Conclusions

SOBI is well known as a modal identification method in the literature. It is appreciated because of its accuracy combined with its low computational cost and also because the selection of the model order is quite automatic. The accuracy of the method can be visually assessed by inspecting the modal responses (sources), for instance in the frequency domain. However, many works have shown that the main drawback of SOBI (or BMID) is the need of a number of sensors greater or equal to the number of active modes [2], [9], etc.

In this work, SOBI was applied to study the change in the dynamic behavior of mechanical systems under different conditions. The BMID technique which is an extension of SOBI has been proven to be very robust and suitable for structures with general damping. The examined examples show that the identification and detection problem using SOBI/BMID may be improved efficiently with the help of the Hankel matrices. Using ESOBI and EBMID, the detection remains still possible even if the number of available sensors is small or even reduced to one.

Acknowledgments

The authors are grateful to Jean-François Cardoso for making his extended Jacobi technique available. They would like also to thank the V2i Company for providing industrial applications.

References

[1] Kerschen G., Poncelet F., Golinval J.-C., “Physical interpretation of independent component analysis in structural dynamics”, Mechanical Systems and Signal Processing, 2007, pp. 1561-1575.

[2] Poncelet F., Kerschen G., Golinval J.-C., Verhelst D., “Output-only modal analysis using blind source separation techniques”, Mechanical Systems and Signal Processing 21, 2007, pp. 2335-2358.

[3] Zhou W., Chelidze D., “Blind source separation based vibration mode identification”, Mechanical System and Signal Processing 21, 2007, pp. 3072-3087.

[4] Farooq U., Feeny B. F., “Smooth orthogonal decomposition for modal analysis of randomly excited systems”, Journal of Sound and Vibration, 316, 2008, pp. 137-146.

[5] Popescu T.D., Manolescu M., “Blind Source Separation of Traffic-Induced Vibrations in Building Monitoring”, IEEE International Conference on Control and Automation, ICCA 2007, pp. 2101-2106.

[6] Zang C., Friswell M.I., Imregun M., “Structural damage detection using independent component analysis”, Structural Health Monitoring 3, 2004, pp. 69-83.

[7] Pontoppidan N. H., Sigurdsson S. and Larsen J., “Condition monitoring with mean field independent components analysis”, Mechanical Systems and Signal Processing 19, 2005, pp. 1337-1347.

[8] Jianping J., Guang M., “A novel method for multi-fault diagnosis of rotor system”, Mechanism and machine theory, 2009, vol. 4, n° 4, pp. 697-709.

[9] McNeil S.I., Zimmerman D.C., “Blind modal identification applied to output-only building vibration”, Proceedings of the IMAC-XXVIII, Florida, USA, February 2010.

[10] Belouchrani A., Meraim K.A., Cardoso J.F., Moulines E., “A blind source separation technique using Second - order statistics”, IEEE transactions on signal Processing 45, 1997, pp. 434-444.

[11] Overschee P. V., De Moor B., “Subspace identification for linear systems-Theory-Implementation-Applications”, Kluwer Academic Publishers, 1997.

[12] Yan A.-M., De Boe P. and Golinval J.-C., “Structural Damage Diagnosis by Kalman Model Based on Stochastic Subspace Identification”, Structural Health Monitoring, 3, 103, 2004, pp. 103-119.

[13] Yan A.-M., Golinval J.-C., “Null subspace-based damage detection of structures using vibration measurements”, Mechanical Systems and Signal Processing 20, 2006, pp. 611-626.

[14] Marchesiello S., Garibaldi L., “A time domain approach for identifying nonlinear vibrating structures by subspace methods”, Mechanical Systems and Signal Processing 22, 2008, pp. 81-101.

[15] Peeters B., De Roeck G., “Stochastic System Identification for Operational Modal Analysis: A Review”, Journal of Dynamic Systems, Measurement and Control, Transaction of the ASME, vol 123, December 2001, pp. 659-66.

[16] Golub G.H., Van Loan C.F., “Matrix computations” (3rd ed.), Baltimore, The Johns Hopkins University Press, 1996.

[17] C. Rutten, C. Loffet, J.-C. Golinval, “Damage detection of mechanical components using null subspace analysis”, 2th International Symposium ETE’2009 - Brussels, Belgium.

Application of Image Sensing to Motion Study of High-voltage Switchgear

Satoshi Marushima Yoshiaki Ohda Masaharu Shimizu Hirokazu Takagi
Toshiba Corporation
2-1 Ukishima-cho, Kawasaki-ku, Kawasaki
Japan

ABSTRACT

Video sensing method is applied to the motion study of high voltage switchgears, in which electric contacts are driven in high speed by hydraulic or spring powered mechanism in order to interrupt large current. The presented system combining high speed video and image processing algorithm realized precise measurement of linear or rotational motions of links, levers and cams that are too small to install conventional displacement sensors. Furthermore experimental properties as damping ratio and friction coefficient can be estimated by this method. By implementing those values in the multi-body motion analysis of operating mechanism, numerical simulation of motion shows excellent agreement with the prototype test.

1. INTRODUCTION

In recent years, given rising demand for substations in urban areas, including underground substations, high-voltage switchgears have been required to be more compact and to deliver higher performance.

Utilizing computer aided engineering (CAE), 3D-CAD and numerical simulations in the designing process of the operating mechanism, high-voltage switchgears have successfully realized a drastic down sizing. As equipment becomes more compact, however the measurement of motions of components is becoming more difficult with conventional sensors in verification tests. The location of potentiometer (displacement or rotation sensor) is frequently restricted by lack of space in small sized equipment. In case of noncontact laser displacement meters which need not to be attached directly on equipment, it can measure only linear motions at certain limited portions. When measuring the motions of multiple components, multiple sensors are required, which makes installation work more complicated.

In order to realize higher performance and reliability in high-voltage switchgear operating mechanism, it is necessary to analyze the high-speed motion of structural components, and evaluate vibration and impact effect on them. To this end, a noncontact-type motion measurement system that can simultaneously measure the complicated behavior of several components is needed.

Authors have developed an image measurement system, which combines a high-speed camera and image-processing technology, and applied the system to the development of an operating mechanism.

Frictional force at the joint unit and attenuation at the contact unit, which were calculated from comparisons of measured values using this image measurement system, and the results of a motion analysis[1] were reflected in the motion analysis model adopted. The resulting data are applicable to the future development of various equipment and devices that offer higher performance and greater reliability, as well as to diagnosing abnormalities in equipment.

In this paper, authors summarize the system characteristics and introduce measurement examples at the development stage of operating mechanism. The benefit of image measurement is also resented in updating numerical calculation models and in diagnostic process of prototype testing.

2. Image Measurement System

CAE-based design, popularly used in automobile and aerospace, has been also widely acknowledged [2] in the electrical power transmission and distribution industry. However, in addition to CAE design, a new trustworthy evaluation method is needed to guarantee the performance and the reliability of prototype as shown in Figure 1.

Therefore, authors developed an image measurement system, which is powerful in improving performance and

T. Proulx (ed.), *Sensors, Instrumentation and Special Topics, Volume 6*, Conference Proceedings of the Society for Experimental Mechanics Series 9,
DOI 10.1007/978-1-4419-9507-0_7, © The Society for Experimental Mechanics, Inc. 2011

quality controlling in prototype testing stage.The configuration and principles of the image measurement system is presented as follows.

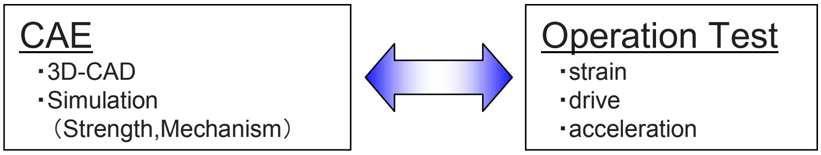

Figure 1 Development method

2.1. Summary of Image Measurement System

Figure 2 shows the configuration of the image measurement system combining a high-speed camera and image-processing technology.

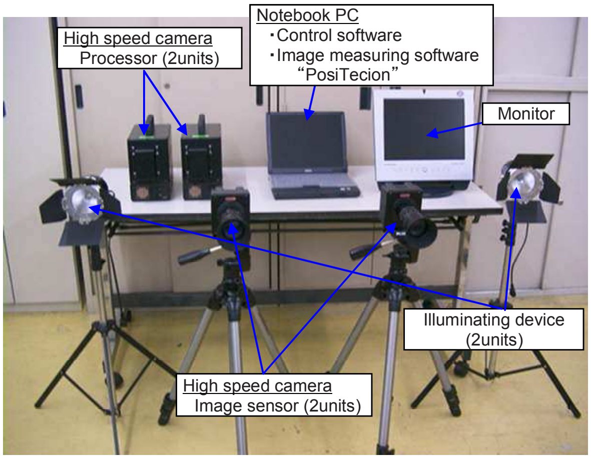

Figure 2 Image measurement system

The system configuration is as follows:

(1) High-speed camera

The image processors (2 units) and the image sensors (2 units) of the high-speed camera are connected with cables. The camera can be operated by its controller or by a notebook PC. During measurement, images are stored in the memory of the camera. After the images are stored, only those required are transferred to a notebook PC via an IEEE1394 interface port. Because the images are digital, there is no deterioration due to noise, and high-quality images can be obtained. In addition, because the camera head is lightweight and compact, the operator can respond to a variety of imaging conditions.

Using two camera units allows the operator to simultaneously record images at remote locations and take 3D displacement measurements using stereo images. Table 1 shows the specification of this camera system.

Table 1 Specifications of high-speed camera

Imaging method	CMOS image sensor
Storage capacity	8 GB (6144 frames recordable at the picture size of 1024 x 1024 pixels)
Imaging speed /Max. resolution	2000 fps/1024×1024 pixel -
	6000 fps/512×512 pixel
	15000 fps/256×256 pixel
	12000 fps/128×16 pixel
Density expression	30-bit color
Outside dimensions/Weight	Camera head: 110×120×92.2 mm / 1.0 kg
	Camera body: 140×213.1×308.8 mm / 5.5 kg

(2) Notebook PC
Two software products are installed in the notebook PC.

1) High-speed camera control software
This software is used to operate the camera and transfer and display images.

2) Image measurement software (manufactured in-house)
The behavior of components during the imaging process is measured automatically with this software. Details of measurement method and principles are explained later.

(3) Illuminating device
In high-speed imaging, an illuminating device is indispensable for gaining sufficient brightness of image in the extremely short exposure time. A halogen lamp is more suitable than a conventional incandescent lamp for its compactness and higher luminance. Because its luminescent temperature is higher, illumination with a color approaches white.
With the camera system configuration described above, the displacement of the respective components is measured using image measurement software installed in a notebook PC based on imaging data obtained by the high-speed camera. It takes a only few minutes to convert image data to physical displacement. Even spatial resolution less than 1 mm is possible depending on the imaging distance. Because this is a noncontact-type camera system, it is not necessary to attach a sensor; therefore, 2-dimensional motions and several components can be easily measured.

2.2. Newly developed “PosiTection” image measurement software

Image measurement software “PosiTection” is developed. This software realizes automatic measurement of displacement of each component from image data obtained by a high-speed camera. Figure 3 shows the start screen of this image measurement software and image measurement flowchart. The software is written in C++.

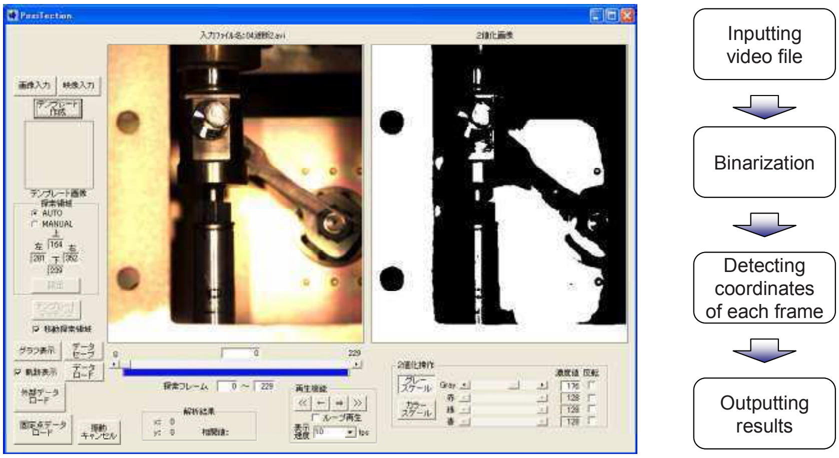

Figure 3 Image measurement software and image measurement flowchart

“PosiTection” software has the following features:

- Processes from imaging to displacement and speed measurement can be executed in a short time.
- The software can be run on almost all PCs, because no special image-processing board is needed and the software program needs only 200 Kbytes of memory.
- The software manufactured in-house can be handled flexibly by operators, and other functions can be added.
- External data such as current waveforms with corresponding images can be displayed simultaneously, and so it is easy to understand actual phenomenon.

The flowchart below explains the contents.

2.3. Image Measurement Flowchart

2.3.1. Inputting video file

Because video files are prepared in audio video interleave (AVI) format, which can be processed by standard PCs, the files can be input directly and read with the image measurement software.

2.3.2. Binarization [4]

As pre-processing of image, binarization is applied in order to facilitate the motion extraction in interested target area. Binarization is a process for converting multi-level images into binary images on the assumption that the pixel value of a corresponding output image is A (e.g. 1) if the pixel value is higher (or, brighter or whiter) than the threshold value, whereas it is B (e.g. 0) in other cases, with regard to the respective pixels of multi-level color and gray-scale images.

2.3.3. Detecting coordinates of each frame (Template matching[5])

Then the coordinates of the target is detected in each frame and arranged in time series. As shown in Figure 4, template matching is adopted. In template matching, a standard pattern (template) which represent particular shape of target is prepared. It determines the coordinate of target by searching location where the image difference between the template and the target is minimized.

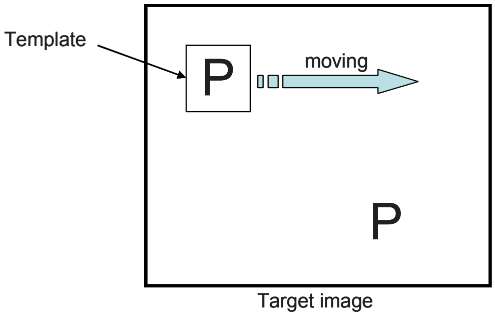

Figure 4 Template in target image

For template matching, it is important to determine what scale should be used to measure differences between two images. The software adopted the cross-correlation coefficient “C”. The cross-correlation coefficient C is obtained using the equation below, assuming that the template with image size M x N is T(i, j) and the partial image of the target image is I(i, j).

$$C = \frac{\sum_{j=1}^{N}\sum_{i=1}^{M}\{I(i,j)-\mu_I\}\{T(i,j)-\mu_T\}}{\left[\sum_{j=1}^{N}\sum_{i=1}^{M}\{I(i,j)-\mu_I\}^2\sum_{j=1}^{N}\sum_{i=1}^{M}\{T(i,j)-\mu_T\}^2\right]^{1/2}} \tag{1}$$

In Which, $\mu_I = \frac{1}{MN}\sum_{j=1}^{N}\sum_{i=1}^{M} I(i,j)$, $\mu_T = \frac{1}{MN}\sum_{j=1}^{N}\sum_{i=1}^{M} T(i,j)$ (2)

The coefficient C should be within the range of −1 to 1. As the value of C approaches 1, the difference between the two images decreases, thereby becoming the position where the corresponding template is drawn.

The precision of template matching declines unless the template-drawn image has a characteristic profile compared to other images. Consequently, to achieve higher measurement precision, a marker is commonly placed at the point where the position data should be detected.

Styrofoam ball with retro-reflective film (a kind of reflection according to which reflected light emitted from a light source is returned to the light source) is used as a marker. By irradiating light from the direction of the camera onto the marker, the marker’s luminance on the image increases, becoming appropriate for a template-drawn image. Even at positions where the marker cannot be attached, image measurement can be executed if its profile is characteristic.

2.3.4. Output results

After the analysis is completed, a graph with the frame number on the abscissa (X-axis) and the pixel number on the ordinate (Y-axis) is displayed automatically as shown in Figure 5. The graph displays measurement results in terms of X-axis, Y-axis, and moving distance of the measured portion. In addition, linking analyzed results with images is easy because an image corresponding to the frame number is displayed by dragging the mouse to move the frame bar. Furthermore, the measurement results can also be edited using spreadsheet software such as Excel, because the measurement results can be output as Comma Separated Value (CSV) files.

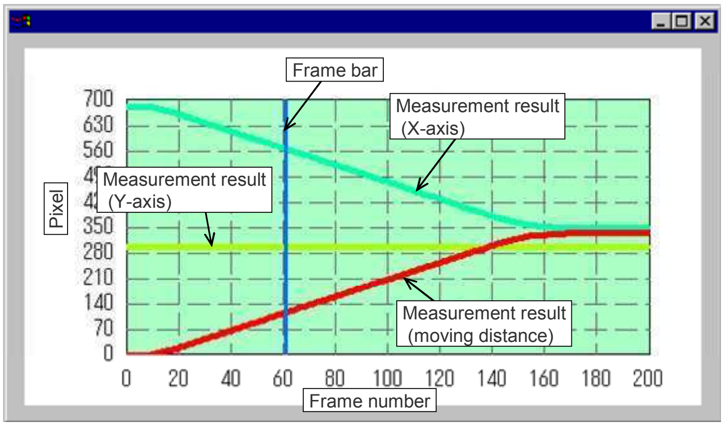

Figure 5 Graph of results

3. Image Measurement Examples

In following sections, some examples of image measurement are presented in the application of performance testing of prototype operating mechanism.

3.1. Measuring stroke

Stroke measurement by conventional rotary potentiometer and image processing are compared in the opening operation of high-voltage switchgear.

Figure 6 shows a schematic of high-voltage switchgear. The electrical contact installed inside of switchgear is switched to ON and OFF position by the motion of operating rod. The linear displacement of operating rod is called the stroke of high-voltage switchgear. Consequently, we installed the marker on the operating rod and took photographs using a high-speed camera within the range specified by dashed lines in Figure 6 below.

Figure 7 shows two images of a total of 230 frames at an imaging speed of 2000 fps taken by the high-speed camera. As can be seen in these photographs, when the high-voltage switchgear is in the opening operation, the marker moves linearly downward. Using this system, we measured the motions of the moving part, to which the marker was attached. Furthermore, we measured the motions of the fixed part, which is circled in the photograph at the left, because of taking into account vibrations of the entire equipment during its operation.

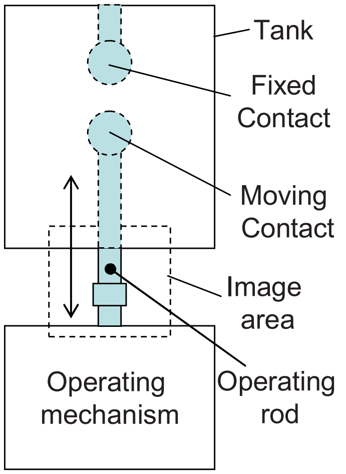

Figure 6 Schematic of
High-voltage Switchgear

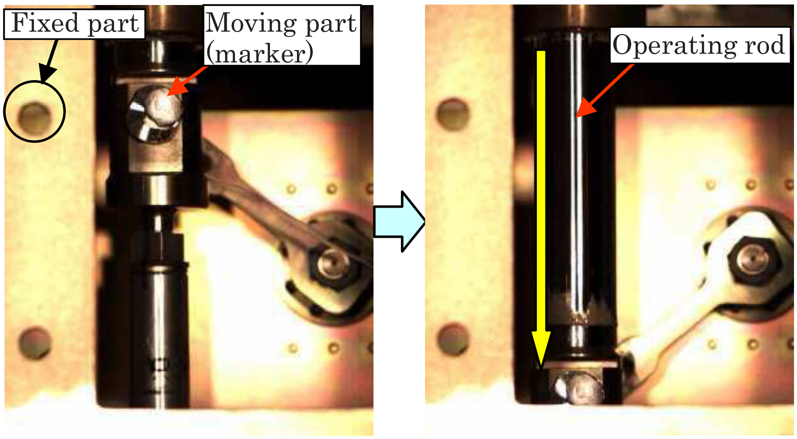

Figure 7 High-speed camera images (2000 fps)

We detected image coordinates of the moving part and the fixed part of each frame using the image measurement software and calculated the stroke with data on the relative positions of the moving part with reference to the fixed part position. In addition, we calibrated the real distance (mm) of the stroke with reference to the number of pixels by calculating the length per pixel from the part whose dimensions can be identified within the image. If no part whose dimensions are known is found within the image, the calibration above may be possible by taking photographs together with a part whose dimensions, such as scale, are identifiable under the same imaging conditions, such as camera position before or after measurement.

Figure 8 shows a comparison of measurement results between our image measurement system and a rotary potentiometer. Although minor errors were found just before completion of the cutoff motion, the results agreed well. The margin of error of the results is less than 1%, which means the precision of the image measurement system has been verified.

The time required for automatic detection with this software is approximately 90 seconds, which is a sharp reduction of 1/20 from the conventional sensor detection method with coordinates detected manually.

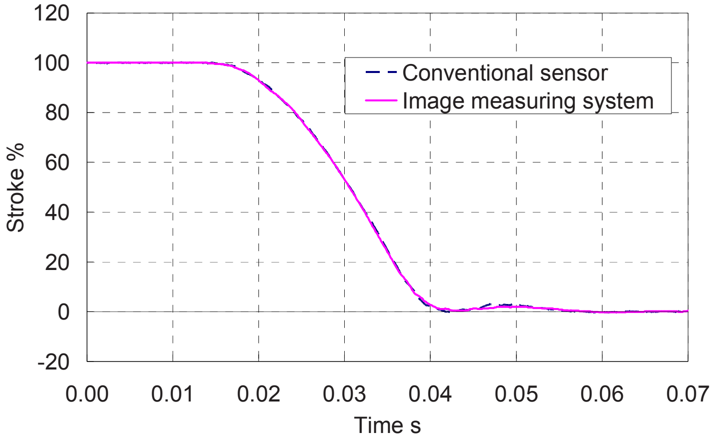

Figure 8 Comparison of measurement results

3.2. Measurement of parallel, rotational motions of trigger mechanism

Next, we explain how rotational motions of a trigger mechanism (prototype) at the openning operation are measured. It is important to understand the motion characteristics of a trigger mechanism, which retains and releases the force of a spring and quantitative measurements of the trigger mechanism when developing a high-voltage switchgear.

Figure 9 is a schematic of a trigger mechanism. The figure indicates the close status and the status just before the opening operation. When the opening operation starts, the lock lever is drawn in the direction ①, and rotates in the direction of the arrow ②. Along with these motions, the latch rotates in the direction ③. During the opening operation, the rotating center of the lock lever travels while the rotating center of the latch remains fixed.

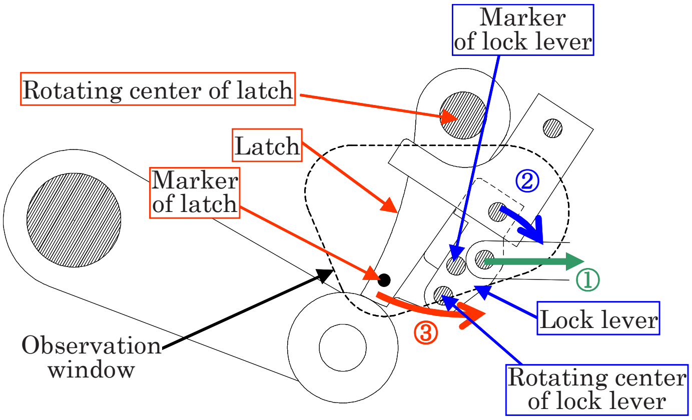

Figure 9 Schematic of trigger mechanism

Figure 10 shows two images of a total of 240 frames at the imaging speed of 2000 fps taken by the high-speed camera. These images were taken from an observation window especially cut in the frame of the prototype trigger mechanism. As the moving part of the respective components had no point at which the marker could be installed, a pen-drawn, black ball for the latch and a pin for the lock lever were used instead of the marker, and their respective motions were measured. The rotating center of both components (latch and lock lever) was also measured simultaneously to measure rotational movement. Because the rotating center of the latch could not be photographed temporarily in our experiment, we calculated the rotating center of the latch based on position data of the reference point.

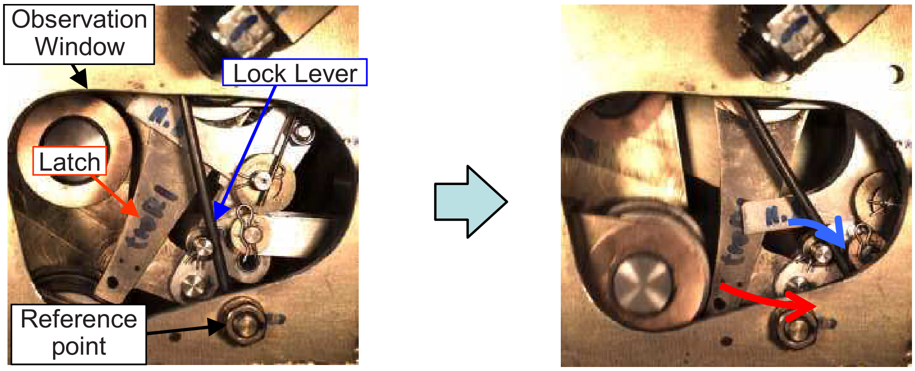

(a) Before Opening (b) Start Opening

Figure 10 High-speed camera images (2000 fps)

Figure 11 shows measurement results of the angular displacement of a latch and a lock lever. The complicated behavior of the two components, which were previously difficult to measure with conventional sensors, could be measured in cases where the rotating center travels. In view of the measurement results above, we collected data, including delayed start time, maximum displacement, reset time to the original position, and the effects of operating vibrations of the latch and lock lever.

As shown in Figure 12, it is possible to display a graph on which external signals such as command voltage and image measurement results overlap. By moving the frame bar on the graph, an image corresponding to the frame bar position can be displayed, which facilitates our understanding of phenomena.

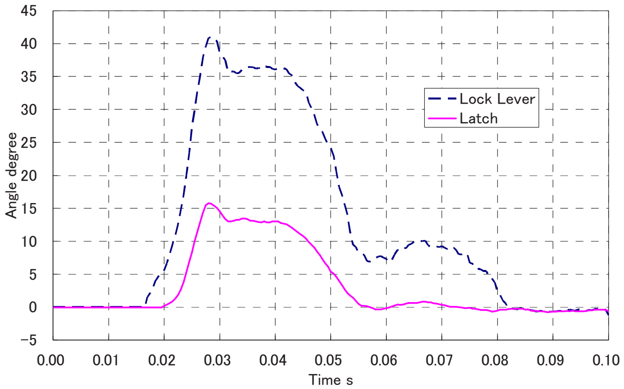

Figure 11 Angular displacement of lock lever and latch

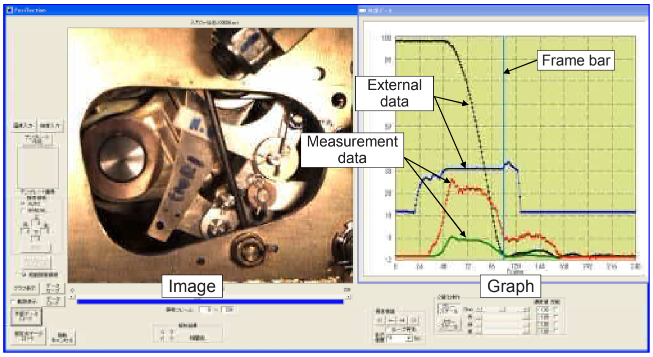

Figure 12 START screen of the software
(Simultaneous display of image and external data)

4. Numerical model updating with image measurement

Numerical simulation is popular in motion/structural analysis of equipment for the purpose of improving structural reliability, increasing mechanical strength and reducing development time. However, calculation accuracy is significantly reduced when theoretically uncertain parameters such as friction or damping cannot be neglected. With application of parameter estimation method, numerical model can be updated using estimated friction or damping from image measurement result.

Figure 13 shows a comparison of measured values and calculated values (before and after model updating) for the angular displacement of a latch, which was introduced in Section 3. In the circled portion, the original calculation without proper damping showed transient vibration, which was different from the measured curve. Meanwhile, updated model with proper damping factor showed consistency with measured values. Using a motion analysis model obtained with such high precision, it has become possible for us to search for new design parameters, which might contribute to the achieving higher equipment performance, and simulate the performance verification to check variations of quality.

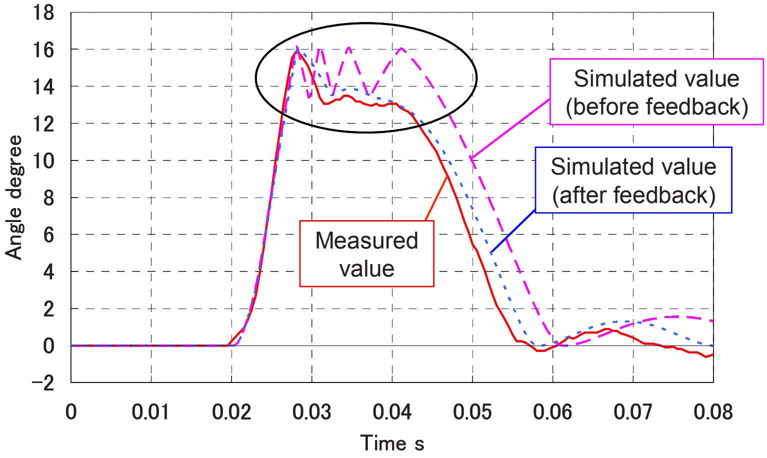

Figure 13 Comparison of measured and simulated values

5. Application of image measurement system to abnormality diagnosis

Image measurement system can be applied to diagnosing abnormalities in equipment already in operation. Although measuring stroke is one of the key items of an abnormality diagnosis, we have almost no equipment to which a sensor can be attached. Because a conventional contact sensor needs to be attached to equipment, equipment that is already in operation must be shut down temporarily. This makes it impossible to grasp the initial motion that is essential for a diagnosis. In contrast, the image measurement system allows us to measure the stroke with only the moving part visible, for example, by leaving the door of cabinet door open, thereby providing opportunities to obtain extensive diagnostic data.

The cause of a failure can be diagnosed by comparing the stroke between normal and abnormal statuses and the analysis results of a motion analysis model after which a failure mode is modeled.

6. CONCLUSIONS

In this paper, a new image measurement system combining a high-speed camera and image-processing technology is presented with applications on the operating mechanism of high-voltage switchgear.

From theses results, following are confirmed.

(1) The image measurement is powerful in the testing of operating mechanism of a high-voltage switchgear, and it will contribute to the improvement of performance and reliability.
(2) It is shown that the precision of numerical simulations can be improved by the feedback of measurement results to numerical model.
(3) Future application of the image measurement system for abnormality diagnosis can be anticipated.

7. REFERENCE

[1] Y.Taniguchi, H.Mizoguchi, Y.Ohda and S.Nishizumi: 'Development of spring operating mechanism for new 72/84kV GCB,' T.IEE Japan, Vol.120-B, No.1, 2000
[2] F.Leclerc, P.Chevrier, G.Charot, G.Gaudart and A.Giboulet: 'Compactness and Reliability of New Gas Insulated Switchgear with A Rated voltage of 420kV,' CIGRE Session 2006, Paris, 27 August-01 September 2006.
[3] J.P,Dupraz, R.Luescher and G.F.Montillet: 'A Hybrid Drive Merging a Servo-Controlled Motor and a Spring Mechanism,' IEEE, Vol.21, No.2,2006
[4] M. Inoue, N. Yagi, M. Hayashi, H. Nakasu, K. Mitani, M. Okui: ' practical Image Processing with C language,' Ohmsha. 1999
[5] Image Processing Editors: 'Image Processing,' CG-ART Society, 2003

CAE Based Approach to Understand a Behavior of Vibro-Acoustic System

Kohei Furuya
Assistant Professor, Department of Precision Mechanics, Chuo University,
1-13-27 Kasuga, Bunkyo, Tokyo 113-8551, Japan

Takuya Yoshimura
Professor, Department Mechanical Engineering, Tokyo Metropolitan University,
1-1 Minamiosawa, Hachioji, Tokyo, 192-0397, Japan

Nobuyuki Okubo
Professor, Department of Precision Mechanics, Chuo University,
1-13-27 Kasuga, Bunkyo, Tokyo 113-8551, Japan

Takeshi Toi
Professor, Department of Precision Mechanics, Chuo University,
1-13-27 Kasuga, Bunkyo, Tokyo 113-8551, Japan

Nomenclature

$\mathbf{A}_{SA}$	Coupling Matrix	$\mathbf{B}$	Dynamic Stiffness Matrix
$\mathbf{D}$	Damping Matrix	$\mathbf{K}$	Stiffness Matrix
$\mathbf{M}$	Mass Matrix	$\mathbf{p}$	Sound Pressure Vector
$\mathbf{Q}$, $\mathbf{q}$	Acoustic Transfer Matrix and Vector	r	Vibro-Acoustic Coupling Factor
$\mathbf{x}$	Displacement Vector	ϕ	Eigen Vector
λ	Eigen Value	Γ	coupling surface of structure and acoustics
$(\ )_A$	index of acoustics	$(\ )_S$	index of structure
$(\ )^H$	conjugate transpose	$(\ )^T$	transpose

Abstract

In this paper, a CAE based approach to understand a behavior of vibro-acoustic system is introduced. The sound pressure at an evaluation point in an enclosure can be described by inner product of (i)an acoustic transfer function from coupling surface to the evaluation point, and (ii)a structural vibration on the coupling surface. By addition of (iii)the correlation angle between above (i) and (ii), the sound pressure can be exactly estimated. In this paper, the correlation (iii) is called Vibro-Acousitc Coupling Factor (VAC). Using VAC, it is possible to understand not only the radiation efficiency, but also the interference of sound at the evaluation point. The proposing method explains the behavior of vibro-acoustic system using the frequency response of (i), (ii) and (iii). As an example, the proposing method is applied to FE model for improving the vibro-acoustic characteristic.

T. Proulx (ed.), *Sensors, Instrumentation and Special Topics, Volume 6*, Conference Proceedings of the Society for Experimental Mechanics Series 9,
DOI 10.1007/978-1-4419-9507-0_8, © The Society for Experimental Mechanics, Inc. 2011

1 Introduction

To reduce the noise in an enclosure like a vehicle cabin efficiently, Computer Aided Engineering tools (CAE tools) is widely used in design process. For low frequency range such as booming noise, Finite Element method (FEM) and structural optimization is used [1].

The structural optimization provides quasi-optimal structure, but is not capable of providing the information why sound pressure is reduced. A panel contribution analysis [2] is one of the methods providing such information. However, it is not easy to clearly understand the relationship between structural vibration and sound pressure in an enclosure. Furthermore, the countermeasure to reduce the sound pressure is not straightforward. For example in some cases, sound pressure is increased although structural vibration is reduced.

In this paper, quantitative understanding method of vibro-acoustic system and quantitative evaluation method of countermeasure which shows how sound pressure is reduced are introduced. In quantitative understanding method, to explain the relationship between structural vibration and enclosure sound, i.e., how they are coupled, the Vibro-Acoustic Coupling Factor (VAC) is defined in this paper. And the proposing method explains the behavior of coupling system using the frequency response of (i)an acoustic transfer function, (ii)a structural vibration and (iii) VAC. In quantitative evaluation method of countermeasure, to confirm the effect of the structural and acoustic modification easily, the optimal state chart which shows variation ratio of structural vibration and VAC is introduced. Applying the above proposing methods to FE model, it is shown the advantage of methods.

2 Relationships between Structural Vibration and Sound Pressure

2.1 Derivation

The equation of motion in vibro-acoustic system is expressed by [3]

$$\left(\begin{bmatrix}\mathbf{K}_{\mathrm{S}} & \mathbf{A}_{\mathrm{SA}}\\ \mathbf{0} & \mathbf{K}_{\mathrm{A}}\end{bmatrix}+j\omega\begin{bmatrix}\mathbf{D}_{\mathrm{S}} & \mathbf{0}\\ \mathbf{0} & \mathbf{D}_{\mathrm{A}}\end{bmatrix}-\omega^2\begin{bmatrix}\mathbf{M}_{\mathrm{S}} & \mathbf{0}\\ -\mathbf{A}_{\mathrm{SA}}^{\mathrm{T}} & \mathbf{M}_{\mathrm{A}}\end{bmatrix}\right)\begin{Bmatrix}\mathbf{x}\\ \mathbf{p}\end{Bmatrix}=\begin{Bmatrix}\mathbf{f}_{\mathrm{S}}\\ \mathbf{f}_{\mathrm{A}}\end{Bmatrix} \tag{1}$$

Physical meaning of coupling matrix $\mathbf{A}_{\mathrm{SA}}$ is array of normal vectors on the coupling surface between structure and acoustics. Assuming there is no sound source in acoustic system ($\mathbf{f}_{\mathrm{A}}$=0), the second row of Eq.(1) is solved with respect to **p**, which gives

$$\mathbf{p}(\omega)=\mathbf{Q}(\omega)^{\mathrm{H}}\mathbf{x}(\omega) \tag{2}$$

$$\mathbf{Q}^{\mathrm{H}}\equiv-\omega^2\mathbf{B}_{\mathrm{A}}^{-1}\mathbf{A}_{\mathrm{SA}}^{\mathrm{T}} \tag{3}$$

$$\mathbf{B}_{\mathrm{A}}\equiv\mathbf{K}_{\mathrm{A}}+j\omega\mathbf{D}_{\mathrm{A}}-\omega^2\mathbf{M}_{\mathrm{A}} \tag{4}$$

Q is called Acoustic Transfer Matrix and expresses the sound pressure response of the unit displacement input is applied to the coupling surface. From Eq.(2), sound pressure at an evaluation point *i* is given as follows inner product

$$p_i=\mathbf{q}_i^{\mathrm{H}}\mathbf{x} \tag{5}$$

$\mathbf{q}_i$ is a vector of column of matrix **Q** which corresponds point *i.* Elements of $\mathbf{q}_i$ are almost zero, except the elements on coupling surface Γ. Therefore, Eq. (5) can be rewritten as an inner product with respect to Γ

$$p_i=\mathbf{q}_{\Gamma i}^{\mathrm{H}}\mathbf{x}_{\Gamma}=\|\mathbf{q}_{\Gamma i}\|\cdot\|\mathbf{x}_{\Gamma}\|\cdot r \tag{6}$$

|| || denotes a vector norm. The vector $\mathbf{q}_{\Gamma i}$ is well known as Acoustic Transfer Vector (ATV[4]) and expresses transmission ratio from coupling surface Γ to the point *i.* The vector $\mathbf{x}_{\Gamma}$ expresses structural vibration on the Γ. Lastly *r* expresses the correlation angle between $\mathbf{q}_{\Gamma i}$ and $\mathbf{x}_{\Gamma}$ and it is defined as

$$r\equiv\frac{\mathbf{q}_{\Gamma i}^{\mathrm{H}}\mathbf{x}_{\Gamma}}{\|\mathbf{q}_{\Gamma i}\|\cdot\|\mathbf{x}_{\Gamma}\|} \tag{7}$$

In this paper *r* is called "Vibro-Acoustic Coupling Factor (VAC)". Eq.(6) shows that the sound pressure p_i is explained as multiplication of (i)amplitude of acoustic transfer vector $\|\mathbf{q}_{\Gamma i}\|$, (ii)amplitude of structural vibration $\|\mathbf{x}_{\Gamma}\|$, and (iii) the correlation angle r (VAC) exactly. Using those variables (i)(ii) and (iii), it is easy to understand which factor is most influenced to the sound pressure, and consequently it is able to decide the suitable countermeasure.

2.2 Physical Meaning of VAC

Assuming that the coupling surface Γ consists of some panels $\ell(\ell=1,\ldots,n)$, e.g. floor panel, fire wall of vehicle, the coupling matrix $\mathbf{A}_{\mathrm{SA}}$ is expressed as summation of the each panel's coupling matrices $\mathbf{A}_{\mathrm{SA},\ell}$.

$$\mathbf{A}_{\mathrm{SA}} = \sum_{\ell=1}^{N} \mathbf{A}_{\mathrm{SA},\ell} \tag{8}$$

Substitution of Eq.(8) into Eq.(3) gives

$$\mathbf{p} = \sum_{\ell=1}^{n} \mathbf{p}_{\ell} \tag{9}$$

$$\mathbf{p}_{\ell} \equiv -\omega^2 \mathbf{B}_{\mathrm{A}}^{-1} \mathbf{A}_{\mathrm{SA},\ell}^{\mathrm{T}} \mathbf{x} \tag{10}$$

$\mathbf{p}_{\ell}$ is called panel contribution [2] and expresses the sound pressure from the pane ℓ. Applying the same rule to the sound pressure p_i gives

$$p_i = \sum_{\ell=1}^{n} p_{i,\ell} \tag{11}$$

Eq.(11) shows that sound pressure p_i is expressed as summation of panel contribution $p_{i,\ell}$.
Assuming $\|\mathbf{q}_{\Gamma i}\| \neq 0$ and $\|\mathbf{x}_{\Gamma}\| \neq 0$, substitution of Eq.(11) into Eq.(6) gives

$$r \equiv \frac{1}{\|\mathbf{q}_{\Gamma i}\| \cdot \|\mathbf{x}_{\Gamma}\|} \sum_{\ell=1}^{n} p_{i,\ell} \tag{12}$$

If VAC r is zero, we obtain

$$\sum_{\ell=1}^{n} p_{i,\ell} = 0 \tag{13}$$

Generally, there are non-zero panel contributions $p_{i,\ell}$, because $\|\mathbf{q}_{\Gamma i}\| \neq 0$ and $\|\mathbf{x}_{\Gamma}\| \neq 0$. Therefore, $p_{i,\ell}$ are canceled out each other, when $r=0$ is attained. The value of r indicates the extent how cancellation is achieved.
On the other hand, the acoustic transfer matrix $\mathbf{Q}$ is expressed as summation of the acoustic resonance mode (acoustic only mode) ϕ_{A} and resonance frequency λ_{A}

$$\mathbf{Q}^{\mathrm{H}} \equiv -\omega^2 \mathbf{B}_{\mathrm{A}}^{-1} \mathbf{A}_{\mathrm{SA}}^{\mathrm{T}}, \qquad \mathbf{B}_{\mathrm{A}}^{-1} \cong \sum_{j=1}^{m} \frac{\phi_{\mathrm{A},j} \phi_{\mathrm{A},j}^{\mathrm{T}}}{\lambda_{\mathrm{A},j} - \omega^2} \tag{14}$$

Therefore, VAC (correlation between $\mathbf{q}_{\Gamma i}$ and $\mathbf{x}_{\Gamma}$) is contained the influence of correlation between ϕ_{A} and $\mathbf{x}_{\Gamma}$ also. The correlation between ϕ_{A} and $\mathbf{x}_{\Gamma}$ indicates the modal transmission (radiation) efficiently. Accordingly, the value of VAC r indicates the extent of coupling also.

3 Understanding Method of Vibro-Acoustic System

In this chapter, the understanding method of vibro-acoustic system with observing contributions of $\|\mathbf{q}_{\Gamma i}\|$, $\|\mathbf{x}_{\Gamma}\|$, r to the sound pressure p_{i}, is introduced.

3.1 Objective FE Model and Modes

Objective FE model, input force point and sound pressure evaluation point i are shown in Fig.1. The structure is a rectangular parallelepiped and consisted of thin shell elements(thickness 10mm). Four end points of bottom panel are constrained. The enclosed space by structure is modeled solid finite element as acoustic system. The model is coupling with the surface of structure and acoustics.

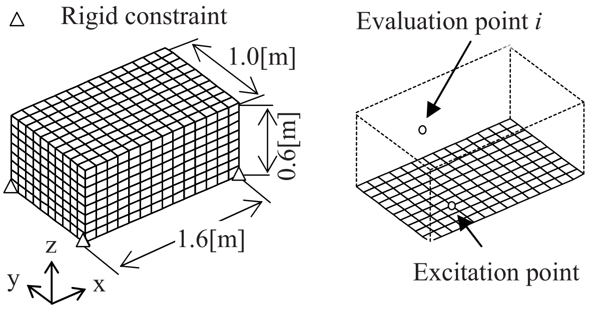

Fig. 1 Objective FE model

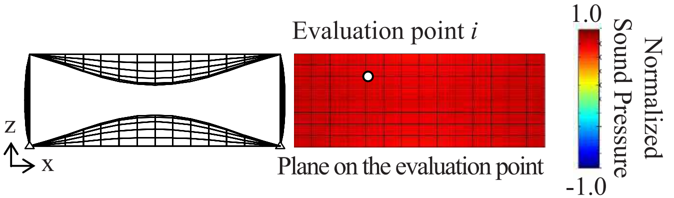

Fig. 2 1st mode of Vibro-Acoustic System (45.0Hz)

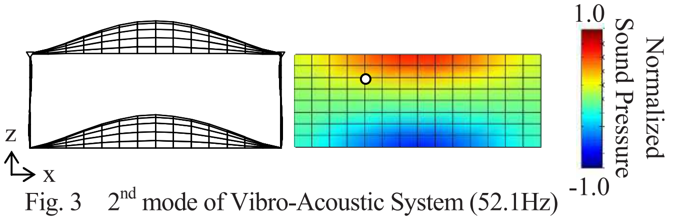

Fig. 3 2nd mode of Vibro-Acoustic System (52.1Hz)

1st and 2nd modes of vibro-acoustic coupling system are shown in Fig.2, 3 respectively. At the 1st mode (45.0Hz), the top and bottom panels deform in opposite directions each other, and the sound pressure distribution is almost uniform and high level, compared with 2nd mode's sound pressure distribution. At the 2nd mode (52.1Hz), the top and bottom panels deform in same directions, and the sound pressure is low level.

3.2 Acoustic Transfer Vector

The acoustic transfer vector $\mathbf{q}_{\Gamma i}$ of 45.0Hz is drawn in Fig.4 as a deformation. $\mathbf{q}_{\Gamma i}$ consists of acoustic only characteristic $\mathbf{B}_{\mathrm{A}}$ and $\mathbf{A}_{\mathrm{SA}}$ shown in Eq.(14), and around 45.0Hz, the major acoustic resonance mode ϕ_{A} is 1st rigid mode of 0.0Hz. Therefore the deformation of $\mathbf{q}_{\Gamma i}$ shows the expanding - shrinking mode which corresponded uniform (rigid) sound pressure distribution. And $\mathbf{q}_{\Gamma i}$ of 52.1Hz (near the 2nd coupling mode) is almost same deformation as 45.0Hz because there is no acoustic resonance mode from 10Hz to 100Hz. Above information indicates that if correlation of $\mathbf{q}_{\Gamma i}$ shown Fig.4 and structural deformation is high, the sound pressure p_{i} becomes high around 1st and 2nd mode frequency.

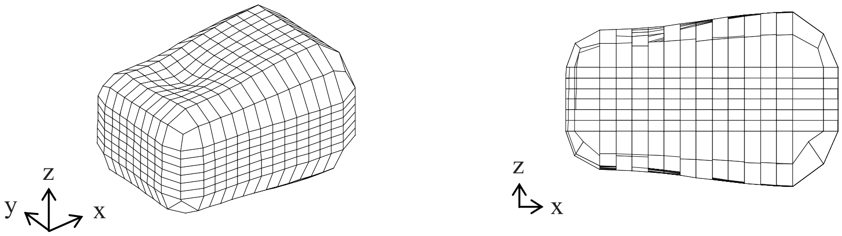

Fig. 4 Acoustic Transfer Vector $\mathbf{q}_{\Gamma i}$ of 45.0Hz

3.2 Quantitative Understanding Method using Frequency Response

In this section, the method to understand the behavior using frequency response of sound pressure p_i, amplitude of acoustic transfer vector $\|\mathbf{q}_{\Gamma i}\|$, amplitude norm of structural vibration on the coupling surface $\|\mathbf{x}_{\Gamma}\|$, and VAC r, is introduced. Those frequency responses of objective FE model are shown in Fig.5. The figure's frequency range is from 30Hz to 120Hz and assuming a modal damping ratio is $\zeta = 0.01$.

Amplitude of acoustic transfer vector $\|\mathbf{q}_{\Gamma i}\|$ has a peak at 2nd acoustic resonant frequency 107Hz, and it shows the transmission ratio from the coupling surface Γ to the evaluation point i is high around 107Hz. Around that frequency, amplitude of structural vibration on the coupling surface $\|\mathbf{x}_{\Gamma}\|$ is low level compared with the other frequency. Therefore it is difficult to reduce the sound pressure by decreasing the structural vibration $\|\mathbf{x}_{\Gamma}\|$. Accordingly Fig. 5 indicates that it is necessary to improve the $\|\mathbf{q}_{\Gamma i}\|$ or the VAC r, to reduce the sound pressure around 107Hz efficiently. These guides for reducing the sound pressure are well known experientially, but usually we have to realize the way from mode shapes implicitly. The proposing method provides those guides using $\|\mathbf{q}_{\Gamma i}\|$, $\|\mathbf{x}_{\Gamma}\|$, VAC quantitatively, and helps us to understand the phenomenon and decide the suitable countermeasure.

Fig. 6 shows those in frequency range from 30Hz to 70Hz. The sound pressure p_i at the 1st mode (45.0Hz) is high level than 2nd mode (52.1Hz). Around the 50Hz $\|\mathbf{q}_{\Gamma i}\|$ is flat characteristic and $\|\mathbf{x}_{\Gamma}\|$ is almost same level at the 1st and 2nd modes. However VAC is quite different and it is cause of difference of the sound pressure between 1st and 2nd mode. This information can be confirmed from Fig.2 to 4. It is able to predict that correlation of $\mathbf{x}_{\Gamma}$ of 1st mode and $\mathbf{q}_{\Gamma}$ is higher than 2nd mode from the deformation shown in figure. Using VAC, it is easy to evaluate the correlation quantitatively. Fig.6 indicates that that improving VAC or $\|\mathbf{x}_{\Gamma}\|$ is efficient to reduce the 1st mode sound pressure. On the other hand, for the 2nd mode, improving VAC is not efficient, and it is necessary to reduce the $\|\mathbf{x}_{\Gamma}\|$ keeping VAC is low level.

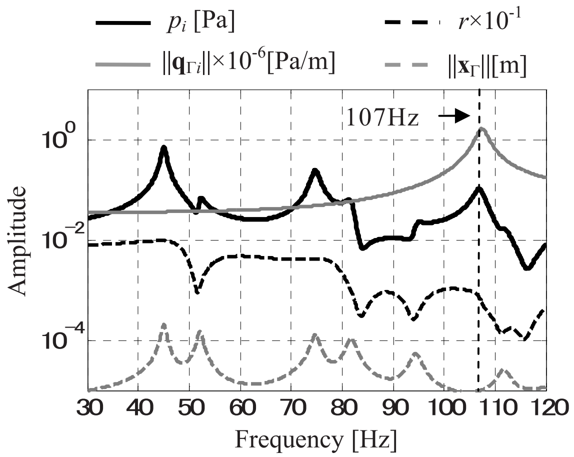

Fig.5 Frequency Response p_i $\|\mathbf{q}_{\Gamma i}\|$, $\|\mathbf{x}_{\Gamma}\|$, and r

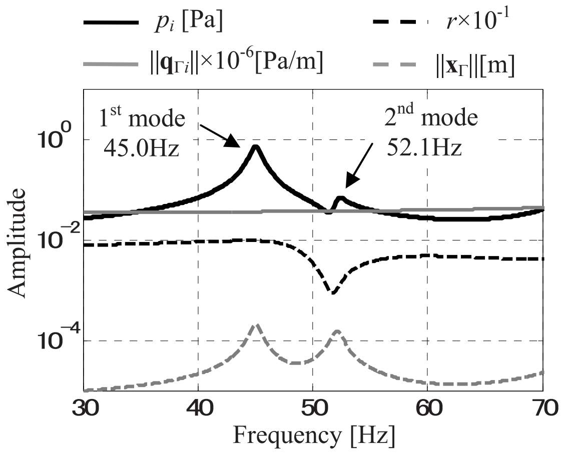

Fig.6 Frequency Response p_i $\|\mathbf{q}_{\Gamma i}\|$, $\|\mathbf{x}_{\Gamma}\|$, and r

4 Quantitative Evaluation Method of Countermeasure

4.1 Quantitative Evaluation Method

Using Eq.(6), normalizing the sound pressure of modified system by the initial sound pressure gives

$$p_{\mathrm{m}} = q_{\mathrm{m}} \cdot x_{\mathrm{m}} \cdot r_{\mathrm{m}} \tag{15}$$

$$p_{\mathrm{m}} \equiv \frac{\left|p_{i,\mathrm{mod}}\left(\omega_{\mathrm{mod}}\right)\right|}{\left|p_{i,\mathrm{org}}\left(\omega_{\mathrm{org}}\right)\right|} \qquad q_{\mathrm{m}} \equiv \frac{\left\|\mathbf{q}_{\Gamma i,\mathrm{mod}}\left(\omega_{\mathrm{mod}}\right)\right\|}{\left\|\mathbf{q}_{\Gamma i,\mathrm{org}}\left(\omega_{\mathrm{org}}\right)\right\|} \qquad x_{\mathrm{m}} \equiv \frac{\left\|\mathbf{x}_{\Gamma,\mathrm{mod}}\left(\omega_{\mathrm{mod}}\right)\right\|}{\left\|\mathbf{x}_{\Gamma,\mathrm{org}}\left(\omega_{\mathrm{org}}\right)\right\|} \qquad r_{\mathrm{m}} \equiv \frac{\left|r_{\mathrm{mod}}\left(\omega_{\mathrm{mod}}\right)\right|}{\left|r_{\mathrm{org}}\left(\omega_{\mathrm{org}}\right)\right|}$$

Index “mod” and “org” express after modification and initial respectively. The sound pressure variation ratio p_{m} is expressed as multiplication of variation ratios of q_{m}, x_{m}, r_{m}. In this section, the quantitative evaluation method which shows how structural and acoustic modification influence to q_{m}, x_{m}, r_{m}, and why sound pressure is improved, is introduced.

4.2 In Case of Structural Modification

Characteristic of $\|\mathbf{q}_{\Gamma i}\|$ shown Fig.6 is flat line in the low frequency because there is no acoustic resonance mode. And if the geometry of acoustic system is not changed or almost same under the structural modification (i.e. increase of thickness, addition of stiffener), it is able to assume the following equation.

$$q_{\mathrm{m}} \cong 1 \tag{16}$$

Therefore, the sound pressure ratio p_{m} can be explained in x_{m} and r_{m}.

Increasing the thickness of bottom panel 50% like Fig.7, the sound pressure of initial and modified system are shown in Fig.8. Natural frequency of 1st mode is lifted from 45.0Hz to 46.9Hz, 2nd mode's is lifted from 52.1Hz to 55.9Hz. And amplitude of sound pressure p_i of 1st mode is decreased as 60%, on the other hand 2nd mode's is increased about 100%. 1st and 2nd modes of modified system are shown in Fig.9, 10.

To explain how structural modification influence to x_m, r_m, and p_i, figure shown in Fig.11 is introduced. In this paper, the figure is called "Optimal State Chart". In the chart, the structural vibration ratio x_m is adopted as x-axis, and VAC ratio r_m is adopted as y-axis. The contour lines in the chart show constant sound pressure lines.

Fig.11 shows chart of 1st mode, it is easy to understand that x_m is reduced from 1.0 to 0.48 and r_m is reduced to 0.89 by the structural modification. And resultant sound pressure ratio p_m becomes 0.48×0.89 = 0.43.

$$x_\mathrm{m} \equiv \frac{\left\|\mathbf{x}_{\Gamma,\mathrm{mod}}(46.9\mathrm{Hz})\right\|}{\left\|\mathbf{x}_{\Gamma,\mathrm{org}}(45.0\mathrm{Hz})\right\|} = 0.48 \qquad r_\mathrm{m} \equiv \frac{\left\|r_\mathrm{mod}(46.9\mathrm{Hz})\right\|}{\left\|r_\mathrm{org}(45.0\mathrm{Hz})\right\|} = 0.89 \tag{17}$$

The chart of Fig.11 shows that the structural modification shown in Fig.8 influences to the structural vibration x_m mainly, and as a result of structural vibration reduction, sound pressure p_m is decreased.

Fig.12 shows chart of 2nd mode. It shows that r_m is increased to 2.12, although structural vibration is reduced to 0.90, and resultant sound pressure p_m becomes 0.90×2.12 = 1.91.

This example indicates there are same cases that sound pressure is increased, although structural vibration is reduced. The cause of the phenomenon is VAC or $\|\mathbf{q}_{\Gamma i}\|$ being increased. To avoid such case and to reduce the sound pressure efficiently, we are proposing the quantitative understanding method and quantitative evaluation method. In next section $\|\mathbf{q}_{\Gamma i}\|$ will be discussed.

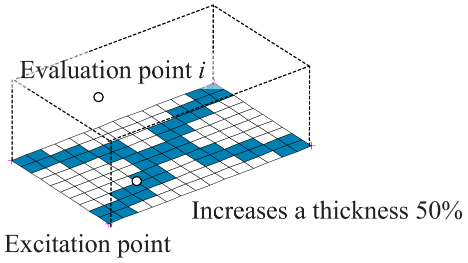

Fig. 7 Structural Modification

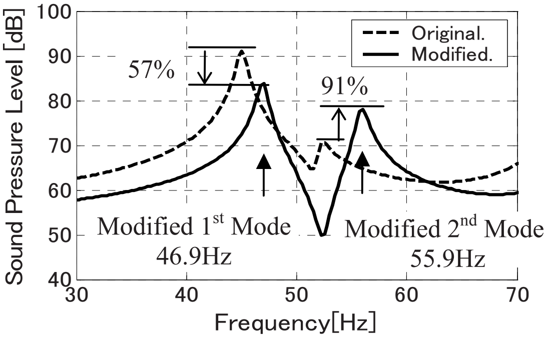

Fig. 8 Comparison of Objective Sound Pressure

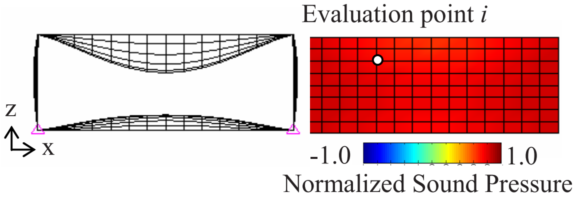

Fig. 9 1st mode of Modified System (46.9Hz)

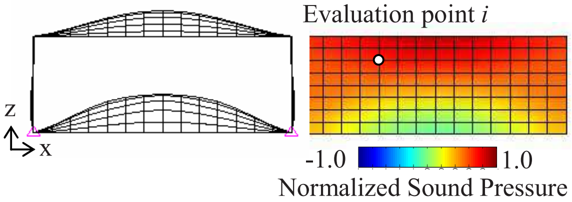

Fig. 10 2nd mode of Modified System (55.9Hz)

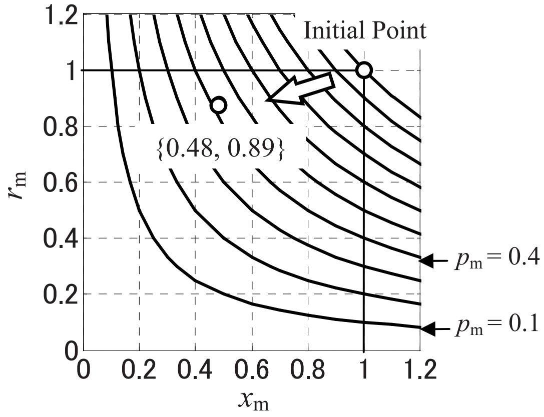

Fig.11 Optimal State Chart of 1st Mode

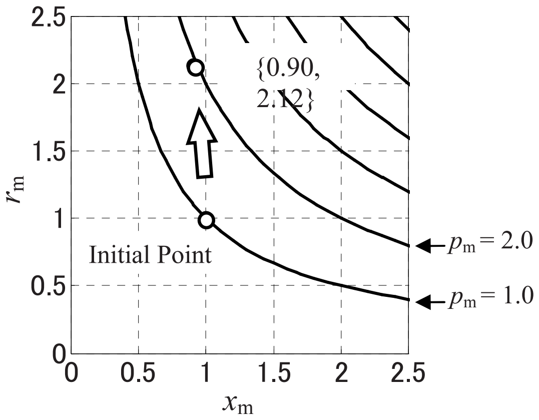

Fig.12 Optimal State Chart of 2nd Mode

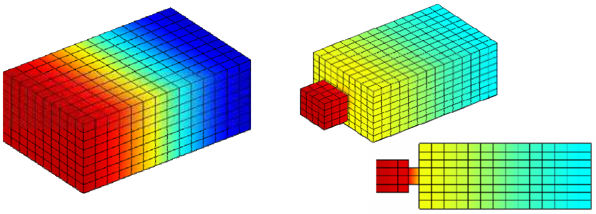

Original Model
1st Resonance Mode 107Hz

Helmholtz Resonator Model
1st Resonance Mode 95.1Hz

Fig.13 Acoustic Modification

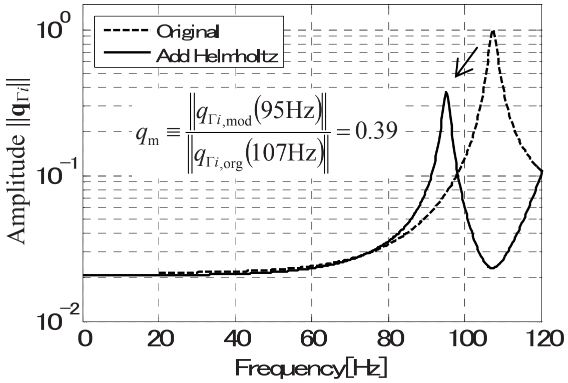

Fig.14 Frequency Response of $\|\mathbf{q}_{\Gamma i}\|$

4.3 In Case of Acoustic Modification

In this section, the acoustic transfer ratio q_m neglected previous section is explained. Adding Helmholtz's resonator to the side wall of the box shown Fig. 13, and that's acoustic transfer function $\|\mathbf{q}_{\Gamma i}\|$ is shown in Fig.14. Fig.14 shows that the 2nd acoustic resonance frequency is dropped from 107Hz to 95Hz, and amplitude of $\|\mathbf{q}_{\Gamma i}\|$ is decreased. The acoustic transfer ratio q_m becomes

$$q_m \equiv \frac{\left\|\mathbf{q}_{\Gamma i,\mathrm{mod}}(95.0\mathrm{Hz})\right\|}{\left\|\mathbf{q}_{\Gamma i,\mathrm{org}}(107.0\mathrm{Hz})\right\|} = 0.39 \tag{18}$$

Of course, structural vibration ratio x_m and VAC ratio r_m are influenced by addition of Helmholtz's resonator. Those variation are evaluated the Optimal State Chart in previous section.

This example indicates that it is possible to evaluate the effect of the all of countermeasure to the vibro-acoustic system using equation (15), i.e. increasing of thickness or stiffness, addition of Helmholtz's resonator, structural damper, sound absorbing material etc. There is no mention of structural damper and sound absorbing material in this paper, but they are expressed as $\mathbf{D}_S$ and $\mathbf{D}_A$ in Eq.(1), and theirs influence can be evaluated also.

In conventional design process, considering x_m, r_m and q_m at the same time is few case. Usually when we focus on modifying the structure, acoustic transfer ratio q_m and VAC ratio r_m haven't been taken care well. In the opposite, focusing on the acoustics, x_m and r_m haven't been taken care. For such conventional design process, there is an advantage to introduce the quantitative understanding method and quantitative evaluation method.

5 Conclusion

In this paper, to understand a behavior of vibro-acoustic system and to evaluate the effect of countermeasure, CAE based methods "quantitative understanding method" and "quantitative evaluation understanding method" are introduced. Those methods use the three variables, (i)acoustic transfer function, (ii)structural vibration, and (iii)the correlation between acoustics and structure, to explain the phenomenon. Applying the proposing methods to FE model, it is shown the advantage of the methods.

Recently, computer performance has been driven, and it is easy to apply the complex FE model with 10 million or more large degree of freedom to the engineering problem. On the other hand, the way to understand the phenomenon from the CAE results is same as 10 yeas ago. Moreover some of those ways are depending on the engineer's skill and experience. In the future, the CAE model and CAE method will be more detailed and more complex. In such feature, the benefit of the methods to understand the CAE result easily and surely will be recognized more.

Acknowledgments

[1] Donders, S. Hermans, L. Nauwelaerts, E. Chojin, S. Pluymers, B. Desmet, W., *CAE Technologies for Efficient Vibro-Acoustic Vehicle Design Modification and Optimization*, Proc. ISMA 2008, pp. 4127-4142, Leuven, Belgium, September 15-17, 2008.

[2] MSC software, *MSC.Nastran Reference Manual 2001*, pp580.

[3] R.Freymann, *Dynamic Response of Coupled Structural-Acoustic Systems*, Journal of Low Frequency Noise and Vibration, Vol.14, No.1, 1995.

[4] Michel Tournour, Luc Cremers and Pierre Guisset, *Inverse Numerical Acoustic Based on Acoustic Transfer Vectors*, Proc. ICSV-7, pp.221-229, Jul. 2000

Verification of coverage of inverse-numerical acoustic analysis

Takayuki KOIZUMI, Nobutaka TSUJIUCHI, Akihiro KOBAYASHI

Department of Engineering, Doshisha University,

1-3, Tataramiyakodani, Kyotanabe-city, Kyoto, 610-0321, Japan

Hiroshi UEHARA

YANMER Co., LTD.

1600-4 Umegahara, Maibara, Shiga, 521-8511, Japan

Abstract

This paper describes the influence of both air-borne noise and structure-borne noise (input) by using inverse-numerical acoustic analysis. Inverse-numerical acoustic analysis is a technique for calculating the vibration of the surface of the sound source by measuring sound pressure around the sound source. Therefore, vibrations with a high contribution to sound radiation can be identified by this technique. Moreover this technique can calculate the vibration of the engine with a complex shape. Therefore, this technique is a powerful method in acoustic problems.

However, accuracy of the identification result of the engine vibration might changes because of various factors. Therefore, Noise source's form must be considered. Noise source's form is whether the sound source contained in the structure-borne noise or the air-borne noise. Then, this paper focused on the oil pan that is penetrated by the combustion sound and the engine vibration easily. In addition, the accuracy using inverse-numerical acoustic analysis for oil pan was verified for the structure-borne noise or the air-borne noise respectively.

1. Introduction

Co-generation system (CGS) has a low consummation and effective for decreasing gas emissions that involves global warming, and the number of CGS installations is increasing every year1). CGS simultaneously and continuously obtains more than two kinds of energy, such as electricity and heat, from one fuel. Therefore, CGS is an ideal thermal energy system whose efficiency is excellent. In this system, a gas reciprocating engine is installed as the power source of a CGS. Therefore, CGS radiates noise that must be decreased.

To reduce the noise, modification of the enclosure is cost-effective2-3) because improvement of the engine requires cost and development period. In modification of the enclosure, a noise prediction technique by numerical simulation is useful. Thus, Construction of the sound source model of the engine is important.

In this study, we adopted inverse-numerical acoustic analysis as a modeling method. Inverse-numerical acoustic is a technique for identifying the surface vibration of sound sources from the measured surrounding sound pressure. Therefore inverse-numerical acoustic analysis is an effective sound source identification technique4-6).

However, accuracy of the identification result of the engine vibration might changes because of various factors. Thus, noise source's form must be considered. Noise source's form is whether the sound source contained in the structure-borne noise or the air-borne noise. This paper describes the influence of both air-borne noise and structure-borne noise, which are the input, by using inverse-numerical acoustic analysis. Moreover, this paper focused on the oil pan that is penetrated by the combustion sound and the engine vibration easily. In addition, the accuracy using inverse-numerical acoustic analysis for oil pan was verified for the structure-borne noise or the air-borne noise respectively.

T. Proulx (ed.), *Sensors, Instrumentation and Special Topics, Volume 6*, Conference Proceedings of the Society for Experimental Mechanics Series 9,
DOI 10.1007/978-1-4419-9507-0_9, © The Society for Experimental Mechanics, Inc. 2011

2. Inverse-numerical acoustic analysis

The relation between sound pressure and sound source can be written as following equation.

$$\{p\} = [H]\{v\} \tag{1}$$

When $\{P\}$ is the vector of sound pressure at m field points, $\{v\}$ is the vector of normal velocity at n surface points of sound source and $[H]$ is the $m \times n$ transfer matrix. To identify the surface velocity effectively, it is required for n to be the lager number than m.

Inverse-numerical acoustic method is the inverse problem of solving equation (1) for the unknown $\{v\}$ given the vector of measured pressure $\{p\}$. Surface vibration velocity $\{v\}$ can be obtained by the matrix inversion method. However, the inverse matrix of the matrix $[H]$ cannot always be obtained because $[H]$ is not usually a regular matrix. Instead of the inverse matrix, the pseudo inverse matrix is widely used in sound source identification as

$$\{v\} = [H]^{+}\{p\} \tag{2}$$

where $[H]^{+}$is the pseudo inverse matrix of $[H]$.

The applied method to set up the pseudo inverse matrix is based on a singular value decomposition of the transfer matrix, which is written as

$$[H] = [V][\Sigma][U]^{H} \tag{3}$$

where $[V]$ and $[U]$ are an $m \times m$ unitary matrix and an $n \times n$ unitary matrix satisfying $[V]^{H}[V] = [U]^{H}[U] = [I]$, and $[\sum]$ is a diagonal matrix containing the singular values of $[H]$ in non-increasing order. The total number of singular values is $min(m \times n)$, generally m. Here superscript H means the complex conjugate transposition.

From equation (3), the pseudo inverse matrix of $[H]$ can be obtained as

$$[H]^{+} = [U][\Sigma]^{+}[V]^{H} \tag{4}$$

In this calculation, the pseudo inverse matrix is sensitive to $[\sum]^{+}$. $[\sum]^{+}$contains huge value so that $[\sum]$ contains small values. This will generally lead to useless solutions when noise is present in the measured pressure vector. In order to avoid this problem, huge terms of $[\sum]^{+}$ calculated from small terms of $[\sum]$ are set to zero. A criterion for dropping small singular value is called for Tolerance. Tolerance is defined as

$$\text{Tolerance} = \sigma_i / \sigma_1 \tag{5}$$

where σ_1 is the maximum singular value in the singular matrix $[\sum]$ and σ_i is the maximum one of the singular values and σ_{i+1} are dropped from matrix$[\sum]$. Tolerance is determined from the L-curve criterion, which is based on a plot of the result norm versus the corresponding residual norm in a log-log scale[7)].

In this paper, the surface normal velocity $\{v\}$ is given as

$$\{v\} = [U]\begin{bmatrix} 1/\sigma_1 & & & & & 0 \\ & \ddots & & & & \vdots \\ & & 1/\sigma_i & & & \\ & & & 0 & & \\ & & & & \ddots & \vdots \\ 0 & & & & 0 & 0 \end{bmatrix}[V]^{H}\{p\} \tag{6}$$

Therefore it is significant to select appropriate tolerance for sound source identification because a small tolerance causes large error by huge values of inverse matrix and large one causes large error by information loss.

3. Experimental condition

This chapter explains the experimental object, the oil pan, which is the sound source. Moreover, we describe the excitation experiment to verify the influence of the air-borne noise and the structure-borne noise.

3.1. Experimental object

This paper focused on the oil pan which is penetrated by the combustion sound and the engine vibration easily. In addition, the accuracy using inverse-numerical acoustic analysis for oil pan was verified for the structure-borne noise or the air-borne noise respectively. Figure1 shows the oil pan used.

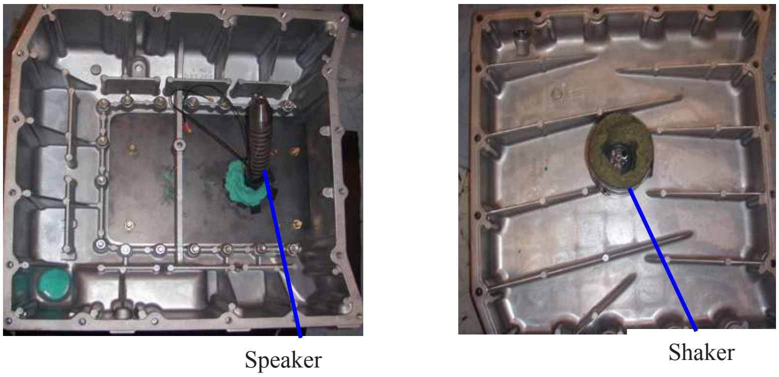

Figure1 Sound source

3.2. Excitation experiment

The Excitation experiment is done in a semi-anechoic room. The vibration input and the acoustic input were done by setting up the shaker of Wilcoxon Reserch Inc. as vibration source and the speaker of LMS international as sound source in the oil pan. In this study, combined acoustic input and vibration input are called combined input. The excitation frequency region of the oil pan was 400-2000Hz, and excited by a non-correlated random wave signal.

3.3 Radiated sound pressure measurement

To determine the frequency of an analytical object, we measured the radiated sound pressure from oil pan at 400-2000Hz .Measurement points are five points located on a hemisphere of 1m radius, centered on the oil pan. Figure2 shows averaged sound pressure level of all measurement points. According to Figure 2, the structure-borne noise is large in the low frequency, and the air-borne noise is large in the high frequency. Therefore, to verify influence of the structure-borne noise and air-borne noise, this study focused at 443Hz, 846Hz, and 1975Hz. Because frequency of 443Hz has large influence of structure-borne noise, frequency of 846Hz has large influence of both the structure-borne noise and the air-borne noise and frequency of 1975Hz has large influence of the air-borne noise.

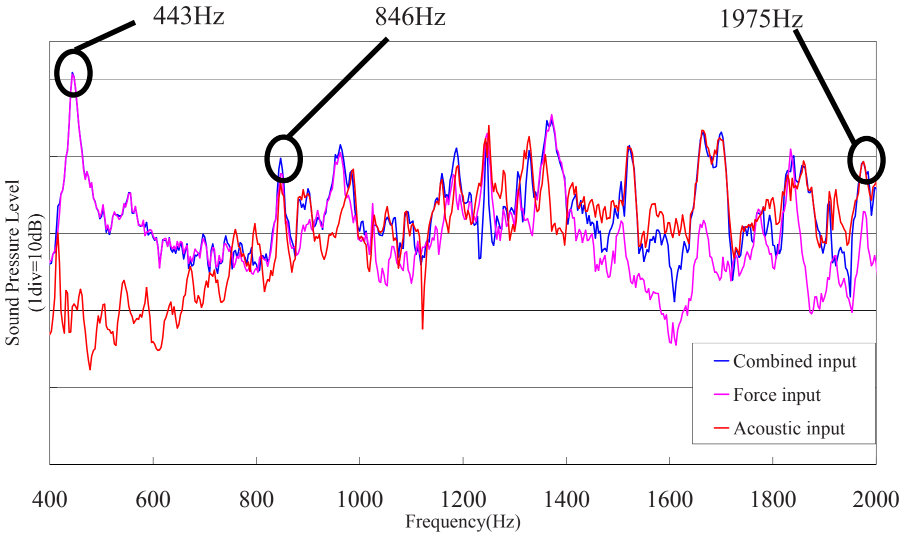

Figure2 Sound Pressure Level

4. Identification of sound source

To calculate inverse-numerical acoustic analysis, the boundary element model (BE model) of the sound source and field-point-mesh (FPM) of sound measuring point are used. We input the experimental results of sound pressure into the FPM. Then, we calculate surface vibration produced by the sound source using inverse-numerical acoustic analysis. In addition, we measured sound source surface vibration directly to verify the identification result.

4.1 BE model of oil pan

Concerning inverse-numerical acoustic analysis, the sound source's BE model and FPM for each sound pressure measurement point are necessary. BE model of oil pan is shown in Figure3. The length of each element was approximately 25 mm. The number of nodes and elements were 1262 and 1290, respectively.

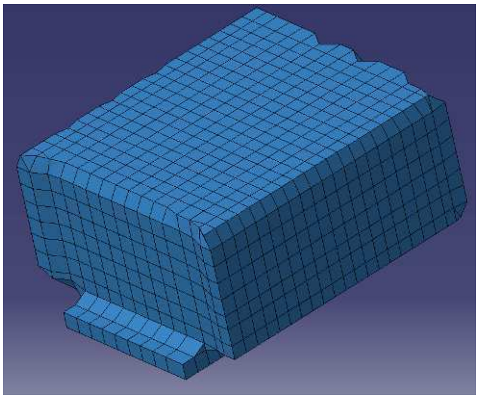

Figure3 BE model

4.2 Sound pressure measurement

We measured the sound pressure around the oil pan for the inverse-numerical acoustic analysis. Figure4 shows the position of the measurement point and the BE model of the FPM. The measurement point was a plane 60 mm from the oil pan's surface. We measured the sound pressure in five directions (top, right, left, back and front of the oil pan). The measurement point's pitch was 30 mm, and we measured the sound pressure of 798 points in total.

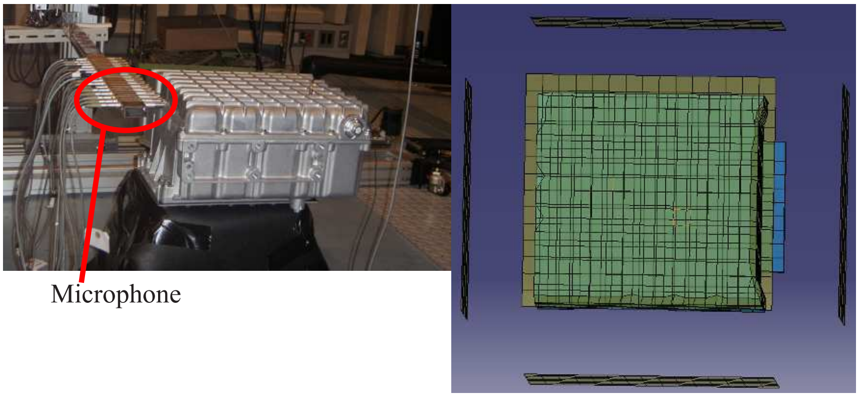

Figure4 (Left) Position of measurement points and (Right) FPM BE model

4.3 Verification of effectiveness of sound source identification

To compare with the identification results by using inverse-numerical acoustic analysis, the oil pan's surface vibration was measured using a laser Doppler vibrometer by Polytec. This vibrometer can accurately measure surface vibration for various objects because it measures the vibration without contact. Therefore, this vibrometer doesn't influence the object vibrations [8-9].

The sound source was identified using inverse-numerical acoustic analysis of boundary element model, sound pressure, and sound pressure measurement point model. The identification result was verified comparing it with the measurement results. The identification result in each input situation of 443Hz, 846Hz, and 1975Hz is shown in Figure 5, Figure 6, and Figure7 respectively.

According to Figure5, for a frequency with large influence of the structure-borne noise, measurement result can not specify the mode of vibration in the acoustic input. However, Identification result, using previously explained method, can specify the mode of vibration. Moreover, the sound source identification shows a tendency similar to the actual measurement result of the vibration input and combined input.

In the acoustic input, the vibration is small though the sound is radiated. Therefore, the measurement of the vibration became difficult. However, according to Figure6 and Figure7, identification results in all examination situations obtain tendencies similar to actual measurement result. From these results, for a frequency with a large influence of the structure-borne noise, measurement result can not specify the mode of vibration in the acoustic input. However, Identification result can specify the mode of vibration. Therefore, measurement result is necessary to verify sound pressure predicted from identification results.

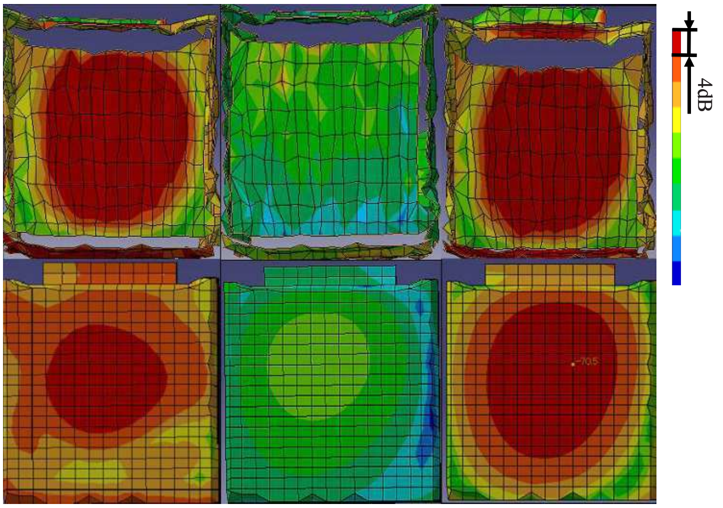

(a) Force input (b) Acoustic input (c) Combined input

Figure5 Sound source surface vibration at 443Hz (Upper-part) Measured, (Lower-part) Identified

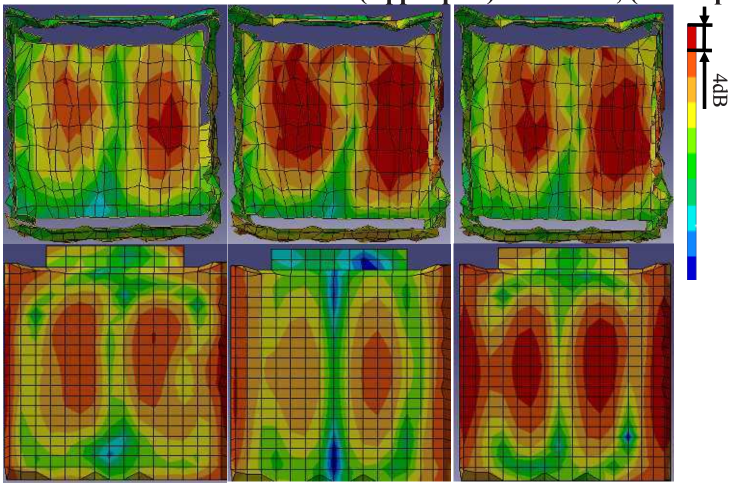

(a) Force input (b) Acoustic input (c) Combined input

Figure6 Sound source surface vibration at 846Hz (Upper-part) Measured, (Lower-part) Identified

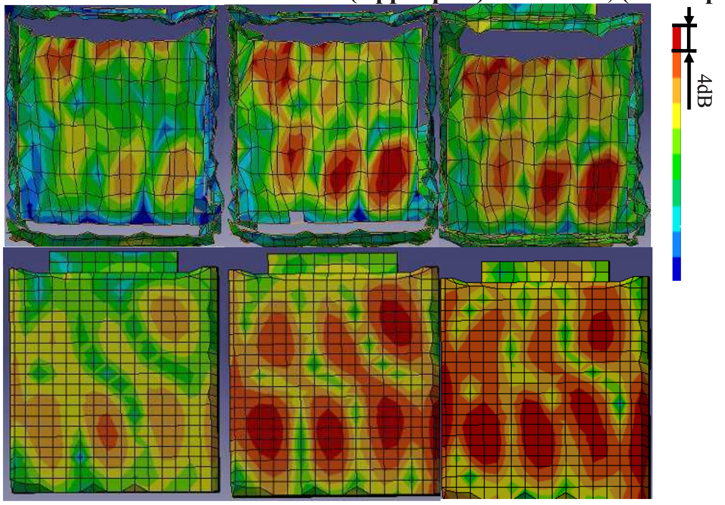

(a) Force input (b) Acoustic input (c) Combined input

Figure7 Sound source surface vibration at 1975Hz (Upper-part) Measured, (Lower-part) Identified

5. Prediction of sound pressure

Since we can not verify the vibration identification, we used this identification as an input in order to obtain the same sound pressure as an output. Using the vibration identification, we predicted the sound pressure and verify it with sound pressure measurement. Figure 8 shows the prediction result and the actual measurement result in 443Hz. A similar tendency can be seen on Figure 8 for all examination situations. Therefore, this study focused on combined input. Figure 9 shows the prediction value and the actual measurement value at 443Hz. Figure 9 shows the correlativity of the sound pressure distribution of prediction results and the measurement results in the sound pressure measurement point used in section 4.2.

When actual measurement value is x_i, prediction value is y_i and measurement point is n, correlation coefficient $\gamma_{x\,y}$ can be written as following equation.

$$\gamma_{xy} = \frac{\sum_{i=1}^{n}(x_i - \bar{x})(y_i - \bar{y})}{\sqrt{\sum_{i=1}^{n}(x_i - \bar{x})^2 \sum_{i=1}^{n}(y_i - \bar{y})^2}} \tag{7}$$

$\bar{x}, \bar{y}$ can be written as following equation.

$$\bar{x} = \frac{1}{n}\sum_{i=1}^{n} x_i$$
$$\bar{y} = \frac{1}{n}\sum_{i=1}^{n} y_i \tag{8}$$

According to Figure 9, the actual measurement value and the prediction value have good correlativity for each frequency. Moreover we predicted the sound pressure value on five-point of two hemispheres of 500mm and 1m radius respectively centered on the oil pan. The averaged prediction value and the averaged actual measurement value on each hemispheres are shown in Table 1 and Table 2 respectively. The prediction value and the actual measurement value correspond within 6dB from table1, table2.

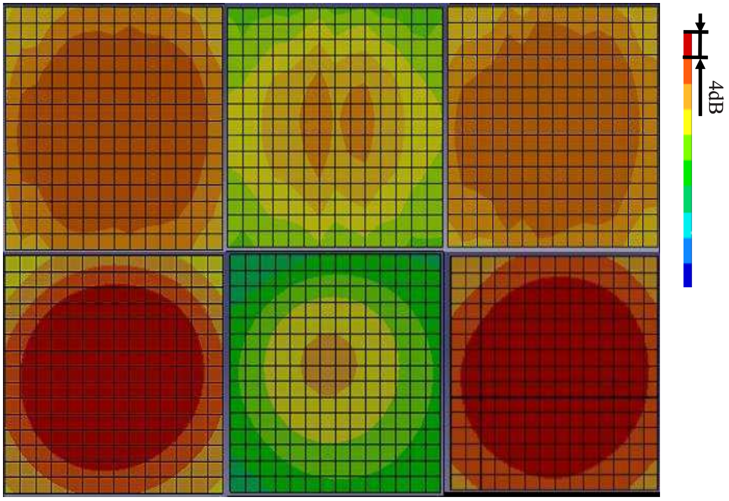

(a) Force input (b) Acoustic input (c) Combined input

Figure8 Sound pressure in field-point at 443Hz, (Upper-part) measured, (Lower-part) Predicted

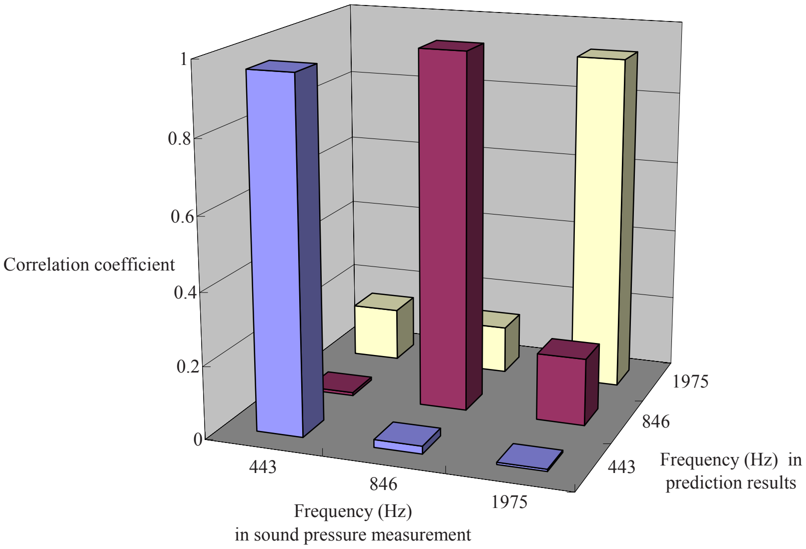

Figure9 Correlation coefficient to sound pressure distribution in combined input

Table1 Sound pressure at 500mm in combined input (Unit in dB)

Frequency (Hz)	Prediction	Measurement	Error
443	62.4	60.4	2.0
846	43.9	41.0	2.9
1975	36.0	41.9	-5.9

Table2 Sound pressure at 1m in combined input (Unit in dB)

Frequency (Hz)	Prediction	Measurement	Error
443	55.8	50.9	4.9
846	40.5	39.8	0.73
1975	36.1	39.4	-3.3

6. Conclusion

- Sound source distribution was identified by inverse-numerical acoustic analysis of an oil pan, in acoustic input, vibration input and combined input. As a result, for a frequency with large influence on structure-borne noise, measurement result can not specify the mode of vibration in acoustic input. However, Identification result can specify the mode of vibration. In the acoustic input, the vibration is small though the sound is radiated. Therefore, the measurement of the vibration became difficult. Then, the sound pressure was predicted from the identification result. As a result, similar tendency to the actual measurement value was obtained. From these results, when the sound source contains the air-borne noise, the sound source identification result is appropriated. However the vibration measurement results still have possibility to obtain different results. Therefore, measurement result is necessary to verify sound pressure predicted from identification results.
- We verified the correlativity between the sound pressure value predicted by using the sound source identification result and the actual sound pressure distribution measurement value. The actual measurement value and the prediction value have good correlativity for each frequency.
- We predicted the sound pressure value on five-point of two hemispheres of 500mm and 1m radius respectively

centered on the oil pan. The prediction value and the actual measurement value correspond within 6dB.

Reference

[1] Yuichiro Sugiyama, “Japanese energy journal,” 86-8, 628-638(2007).

[2] Yoshinori Takahashi, Toshiro Matsumoto, Kazuto Nakahira, Taishi Ohori, Masamichi Ipponmatsu, Hiroshi Fujimoto, Takaaki Kojima, and Masahiko Matsumura, “Takenaka technology research report,” 58, 43-48(2002).

[3] Takahide Osaka, “Acoustic technology, 35-3, 38-42(2006).

[4] Shinichi Nishimura, Yukihiko Hanzawa, Jun Kitahara, Hiroshi Nakahara, and Hiroshi Nakashima, Honda R&D Tech Rev, 16-2, 211-126(2004).

[5] Michel Tournour, Philippe Brux, Peter Mas, Xianchuan Wang, Colin McCulloch, and Philippe Vignassa, “Inverse Numerical Acoustics of a Truck Engine,” SAE 2003 Noise & Vibration Conference and Exhibition (2003).

[6] X. Chen, “Comparison of numerical methods for noise source identification,” Noise Control Eng. J, 54, 6, 420-428(2006).

[7] J. Morkholt, A. Schuhmacher, J. Hald, A. Omrani, M. A. Hamdi, X. Ouisse, F. Dupuy, and M. Mein, “Hotspot Identification Methods for the derivation of Acoustic Equivalent Source Models,” SAE 2003 Noise & Vibration Conference and Exhibition (2003).

[8] Saeed Siavoshani, Jay Tudor, and Dev Barpanda, “Vehicle Body Optimization of Structural Noise and Vibration Using a Hybrid Technique,” SAE2007 international, 2007-01-2327(2007)

[9] Matthias Schűssler and Georg Wirth, All Polytec GmbH, Germany, “3-D Scanning Vibrometry Enables Efficient Experimental Modal Analysis of Large and Complex Structures for NVH-Optimised Vehicles,” SAE2007, The Automotive Research Association of India, 2007-26-034(2007)

Prototype WSN Platform for Performing Dynamic Monitoring of Civil Engineering Structures

Rafael Aguilar, Civil Engineering PhD student, Department of Civil Engineering – ISISE, University of Minho, Campus de Azurém 4800 - 058 Guimarães, Portugal

Luis F. Ramos, PhD in Civil Engineering, Assistant Professor, Department of Civil Engineering – ISISE, University of Minho, Campus de Azurém 4800 - 058 Guimarães, Portugal

Paulo B. Lourenço, PhD in Civil Engineering, Full Professor, Department of Civil Engineering – ISISE, University of Minho, Campus de Azurém 4800 - 058 Guimarães, Portugal

Ricardo Severino, Electrical and Computer Engineering PhD Student, CISTER/IPP-HURRAY! Research Unit - School of Engineering Polytechnic Institute of Porto, 4200-072 Porto, Portugal

Ricardo Gomes, Junior Researcher, CISTER/IPP-HURRAY! Research Unit - School of Engineering Polytechnic Institute of Porto, 4200-072 Porto, Portugal

Paulo Gandra, PhD in Electrical and Computer Engineering, Researcher, CISTER/IPP-HURRAY! Research Unit - School of Engineering Polytechnic Institute of Porto, 4200-072 Porto, Portugal

Mario Alves, PhD in Electrical and Computer Engineering, Researcher, CISTER/IPP-HURRAY! Research Unit - School of Engineering Polytechnic Institute of Porto, 4200-072 Porto, Portugal

Eduardo Tovar, PhD in Electrical and Computer Engineering, Research Leader, CISTER/IPP-HURRAY! Research Unit - School of Engineering Polytechnic Institute of Porto, 4200-072 Porto, Portugal

ABSTRACT

Structural Health Monitoring represents the present and future of the civil engineering since, until few years ago, structural diagnosis works had been performed with few resources regarding to experimental techniques. Precisely in the field of monitoring sensors, the progress of new technologies based on wireless communications and Micro-Electro-Mechanical-Systems (MEMS) are of high interest for replacing the handle difficult wired sensors. However, three major limitations of the commercial off-the-shelf technology on WSN (combination of MEMS and wireless technology) for performing dynamic monitoring were identified by means of: (1) not enough sensitivity of the accelerometers; (2) low resolution of the ADC embedded; and (3) lack of synchronization algorithms implemented. This paper presents a new prototype system conceived for performing dynamic monitoring civil engineering structures. This system was jointly conceived by a team of civil, electrical and communication engineers and is a combination of the last technology on high resolution MEMS accelerometers and the state of the art of communication technologies. Despite the fact that the prototype system needs more improvements; the results of several rounds of validation experiences confirm the feasibility for its consideration as an alternative to the conventional wired based sensors.

T. Proulx (ed.), *Sensors, Instrumentation and Special Topics, Volume 6*, Conference Proceedings of the Society for Experimental Mechanics Series 9,
DOI 10.1007/978-1-4419-9507-0_10, © The Society for Experimental Mechanics, Inc. 2011

1. INTRODUCTION

According to Farrar and Worden [10], dynamic wired based monitoring systems are being widely applied to study civil engineering structures since the early 1980s. Most of those studies are related to large structures by means of bridges and tall buildings. In the case of existent masonry structures, there are also several applications such as the study of temples [13], and masonry towers [11; 12; 22; 23]. These systems were also used to study other types of masonry structures like arch bridges [8], churches [4; 5; 20] and minarets [21].

In the case of dynamic wireless based monitoring systems, the first case of study was the Alamosa Canyon Bridge in 1998 [24]. Afterwards, more case studies related with bridges were considered. These are the experiences in the Tokyo Rainbow Bridge in Japan [2], again the Alamosa Canyon Bridge in USA [15], a pedestrian bridge in the University of California-Irvine in USA [7], the Geumdang Bridge in Korea [16], the Gi-Lu cable-stayed bridge in Taiwan [25] and the Golden Gate Bridge in USA [18]. However, the only task reported in the literature related to large buildings is the dynamic monitoring of the 79 stories Di Wang Tower, located in Guangdong, China [17]. As masonry structures are difficult to excite and commercial MEMS have currently low resolution capabilities, only one case of dynamic wireless monitoring systems applications in existent masonry structures were reported. This study is the modal analysis of the Aquila Tower in Italy [6]. A novel contribution is given in this paper regarding the application of wireless based monitoring systems to other structures.

The paper starts by evaluating commercial off-the shelf WSN platforms in terms of its practical utility for performing structural dynamic monitoring works. Once the limitations of the available technology are stated, a new prototype system will be presented. Using this new prototype system, the results of several rounds of validations tests will be detailed. Finally, the conclusions as well as a draft of the future works are stated.

2. OPERATIONAL MODAL ANALYSIS USING COMMERCIAL OFF-THE-SHELF WSN PLATFORMS

Crossbow technology [9] was chosen as the best alternative for performing dynamic monitoring as it offers economical solutions including low powering boards and measurement platforms with microaccelerometers embedded. The selected Crossbow product (WSN professional kit) uses as gateway a Mica2 board in charge of the communication over the network in the radio frequency range of 868/916 MHz. To provide in-system programming and to supply energy to the devices, the system uses an interface board model MIB520 connected to a central computer trough an USB bus. The sensors' platform supplied by Crossbow is composed by a measurement board that works mounted on a Mica2 board. In this unit, the Mica2 board is not only in charge of the network communication but also in charge on supplying energy to the measurement board (using two AA batteries), as well as acquiring and converting the analogue measurements with an ADC resolution of 10 bits. There are several options of measurements boards available in the market, however; the one suitable for dynamic monitoring works is the MTS400. This measurement board has embedded four microsensors: biaxial microaccelerometer; light; pressure-temperature; and humidity-temperature. The location of the sensors in the MTS400 board and a view of the mounted measurement unit are shown in Figure 1. More details of the Data Acquisition (DAQ) process can be found at [1].

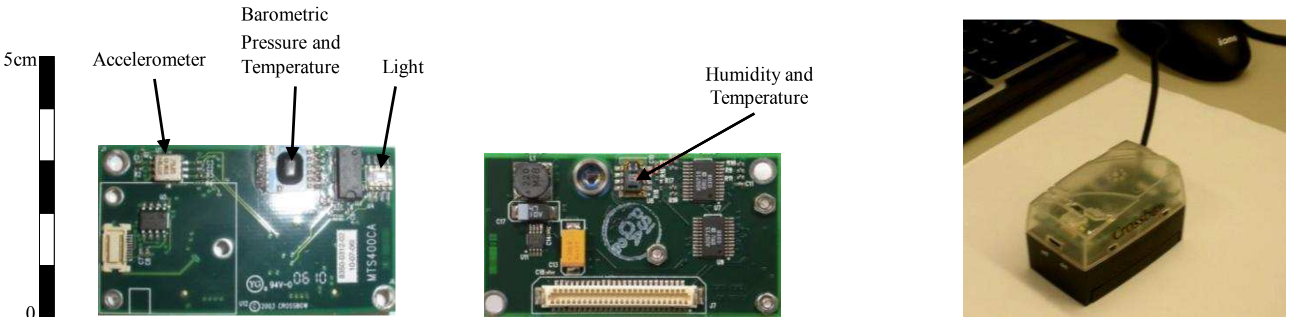

(a) (b)

Figure 1 - Crossbow sensors' platform: (a) front and back of the MTS400 sensors' board; and (b) mounted unit

A single degree of freedom structure represented by an inverted pendulum is one of the simplest examples that are used by civil engineers to explain the fundamentals of the dynamics of structures. In this work, this structure is also used as a tool to evaluate and understand the behaviour of the commercial wireless based platforms and their utility for engineering works. For comparison purposes, conventional wired based systems composed by high sensitive accelerometers with a measurement range of ± 0.5 g and sensitivity of 10000 mV/g as well as an ADC with 24 bits of resolution, were considered as references.

The initial test aimed at evaluating the time domain series recorded with these platforms. An impulsive force was applied to the pendulum five seconds after having started the acquisition process. The results of this first test (Figure 2) indicate the good performance of the commercial WSN platforms for measuring high amplitude vibrations. However as expected, for signals with amplitudes below 20 mg, the WSN platforms recorded only noise due to the low resolution of the microaccelerometers and ADCs embedded. Note that in this last scenario, it was even possible to observe the digitization lines (see left Figure).

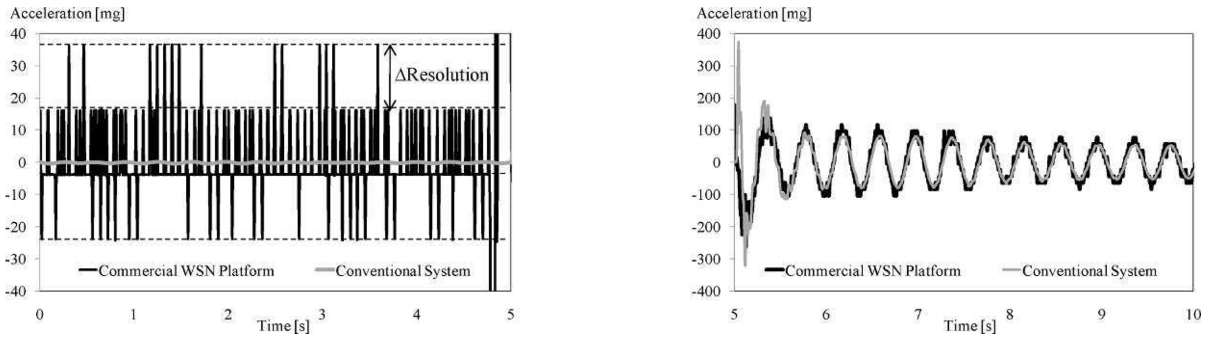

Figure 2 - Time series record of the response of the inverted pendulum under an impulse force test

A second round of evaluation tests was performed to study the accuracy of the wireless systems in tests with longer sampling periods. With this purpose, tests were performed under ambient noise and random impacts. Figure 3 shows the time series recordings and the resultant Welch spectrums, for each of the considered excitation scenarios. The time domain results evidence again the poor performance of the wireless systems for measuring low amplitude vibrations. On the contrary, in random excited tests, the similar response of the conventional and wireless systems is evident. It should be noticed that the results indicate that, due to the lack of implementation of communication protocols in the wireless systems, some data was lost in the recorded time series. For what respects to the frequency domain results, despite the expectable higher noise level of the data recorded with the wireless systems, similar frequency contents were found in both systems in the excited tests. In this scenario, the presence of two peaks, the first one in the band of 0 Hz - 10 Hz and the second one close to the band of 30 Hz, were clearly identified. Confirming the poor performance of the commercial WSN platforms in ambient noise tests, in the resultant spectrums no peaks were detected since these showed only noise.

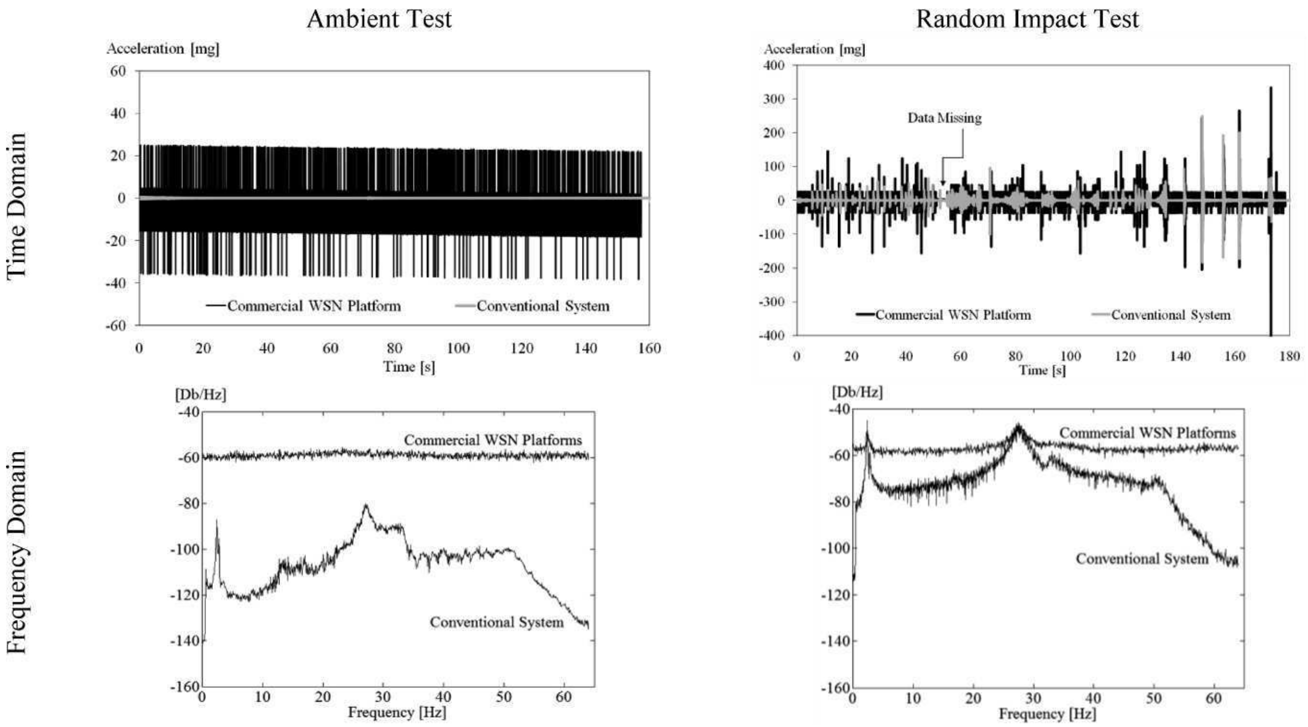

Figure 3 - Time and frequency series results from the data recorded in the inverted pendulum under an impulse force test

The results of the performed tests showed that the commercial off-the-shelf WSN platforms are not fully suitable for properly identifying the dynamic properties of civil engineering structures. This fact is mainly due to three reasons: 1) low resolution of the embedded microaccelerometers; 2) low resolution of the embedded ADCs; and 3) lack of communication protocols. It should be noticed that the problems related to the energy consumption were not considered since the use of these platforms for long term monitoring was outside the scope of this work.

3. NEW WIRELESS PLATFORM FOR PERFORMING STRUCTURAL HEALTH MONITORING OF CIVIL ENGINEERING STRUCTURES

One of the main objectives of the present work was to study the recent progresses on wireless technology and Micro-Electro-Mechanical-Systems (MEMS) in order to explore their possible inclusion in the Operational Modal Analysis (OMA) schemes for existent masonry structures. From previous experiences on OMA procedures in this type of structures, a main difficulty was observed related to the low levels of excitation registered in the experimental tests as a consequence of the high stiffness associated to these buildings. Therefore, if OMA tests are planned to be carried out in these structures, the characteristics of the measurement transducers and Data Acquisition (DAQ) equipments should be carefully chosen. From the experience gained on performing OMA in civil engineering structures using conventional and commercial off-the-shelf wireless sensors, the minimum requirements that the new WSN platform must fulfil were defined. According to this, the maximum frequency response range of the system was defined to be from 0 Hz to 100 Hz and the maximum sampling frequency to be of 200 Hz. Moreover, the maximum sampling drift must be lower than 5 ms (1/sampling frequency) and no samples should be lost during the acquisition and communication process. With respect to the measurement sensors, it was decided that triaxial MEMS accelerometers with a maximum measurement range of ±2g, typical resolution of 1 mg, and maximum resolution of 0.1 mg must be included. In the case of the DAQ board, this must include an ADC with at least 16 bits of resolution.

A WSN system can be understood as composed by two parts: the measurement units and the base station (a third part is not considered, the remote connection system, since traditional technology is used for this purpose). The prototype of the WSN platform developed in this work also matches with the mentioned definition following the system architecture presented in Figure 4.

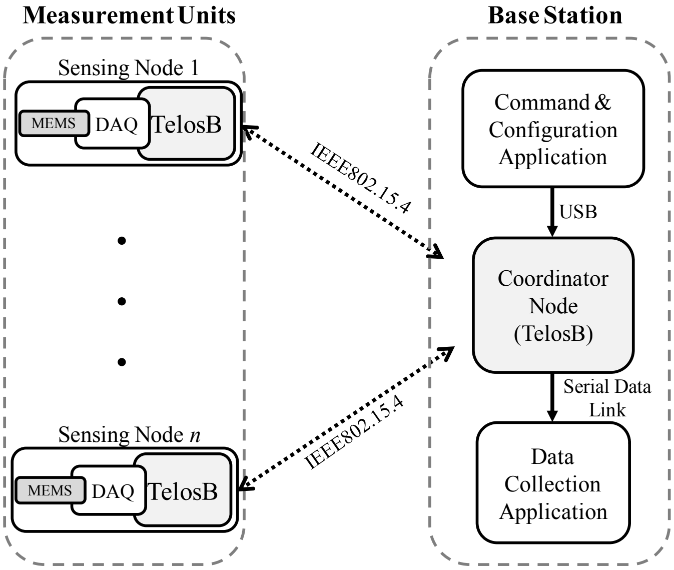

Figure 4 - Overview of the system architecture of the developed WSN platform

In the developed WSN, the wireless communication module in the measurement units and the base station was composed by TelosB platforms [9] working in the radio frequency range of 2.40/2.48 GHz. These hardware platforms feature an 8MHz TI MSP430 16-bit microcontroller, a CC2420 RF transceiver (IEEE 802.15.4 compliant), 48 kB of Program memory (in-system reprogrammable flash), 16 kB of EEPROM, and UART communication ports. They also include on-board light, temperature and humidity sensors, whose implementation was outside the scope of this work but; which might be useful in future developments for static SHM applications. The DAQ board was conceived for supporting a high resolution 24 bit ADC and a 32 MB serial flash memory for storing data samples. Both the ADC and the flash memory are managed by an 8 bits microcontroller (which also handles and pre-formats the acquired ADC samples) and accommodated an analogue 8th order Butterworth filter (to avoid undesired aliasing effects). The energy regulation and management circuitry is supplied from sets of four AA size batteries. From the commercial available solutions of MEMS accelerometers; two different types of capacitive triaxial transducers with a measurement range of ±2g were selected. The first one was the model ASC 5521-002 (called in this work as MEMS sensor Type A) and the second one the ASC 5631-002 (called as MEMS sensor Type B). The technical specifications' details of these sensors can be found at ASC [3].

With respect to the base station, and as mentioned before, it was composed by one TelosB platform acting as the system´s coordinator in addition to the command & configuration and data collection applications. The role of the coordinator node was to configure and synchronize the whole network using a beacon based solution contemplated in the IEEE 802.15.4 communication protocol. The coordinator node served also as interface between the network of sensors and the command & configuration application as well as reception point of the forwarded data. The available controls of the command & configuration application enabled full control over the acquisition configuration parameters (i.e. axis selection, sampling rate, sampling period, etc.) and also provided a quick evaluation of the presence of the system nodes. To complete the data reception process, a VI routine was developed in Labview [14] for data collection purposes. The data is transmitted from the measurement nodes in successive messages containing 8 measurements (4 bytes each one) in big-endian format. In this case, the developed application was also in charge of the interpretation and conversion into standard units of the received data as well as their local storage in the central station. More details can be found at [1].

The final appearance of the developed prototype platform is shown in Figure 5. In order to ensure the necessary energy resources in case of possible medium and long term monitoring studies, three sets of four AA batteries where included.

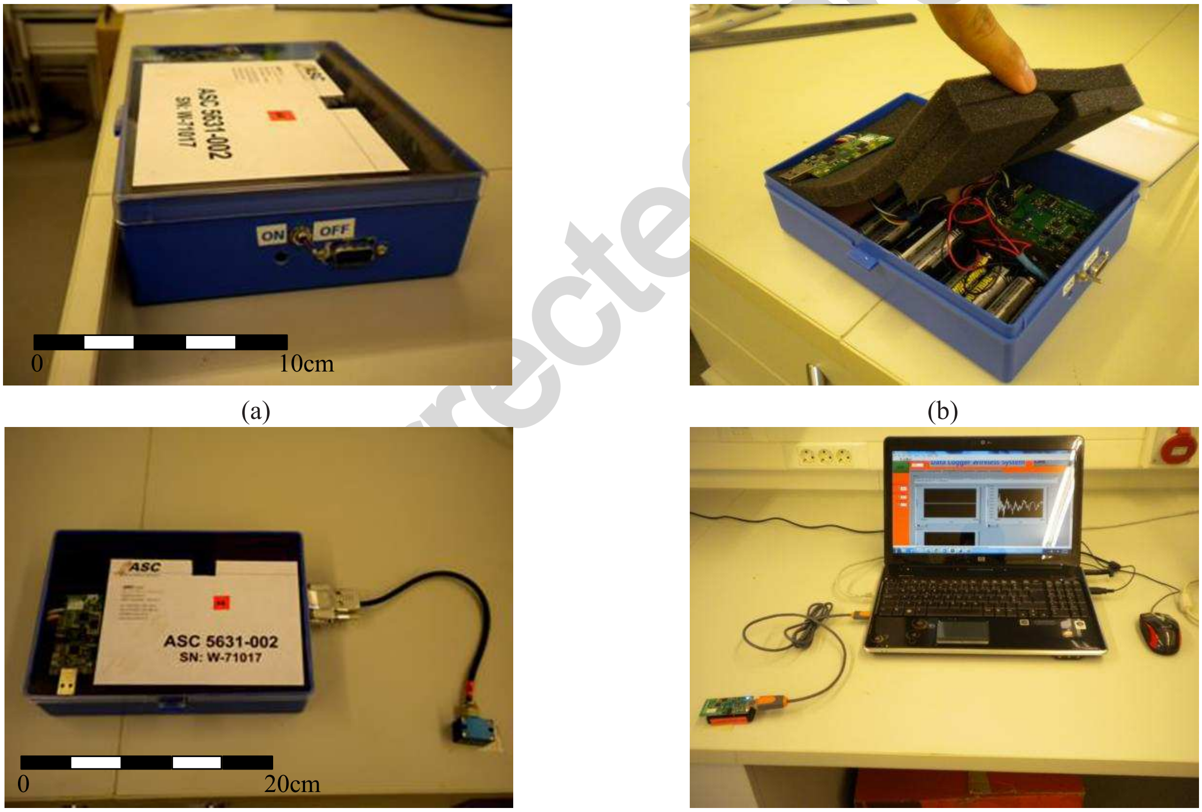

(a) (b)

(c) (d)

Figure 5 - Final appearance of the developed WSN solution: (a), (b), (c) measurement unit; and (d) base station

For the laboratory validation tests carried out in this work, the case study of the inverted wooden pendulum previously presented in section 2 was used again. Considering again the conventional wired based systems as reference (high sensitive accelerometers with high resolution ADC), numerous validation tests were carried out. In these experiments, the DAQ stations corresponding to both systems (conventional and wireless) were set for running in parallel aiming at performing measurements at the same instant of time using a common sampling rate of 100 Hz.

The initial time domain evaluation tests were carried out considering one measurement point at the top of the pendulum. As shown in Figure 6, one of each measurement units was located at that point (MEMS Accelerometers Type A and B as well as the conventional wired based transducers).

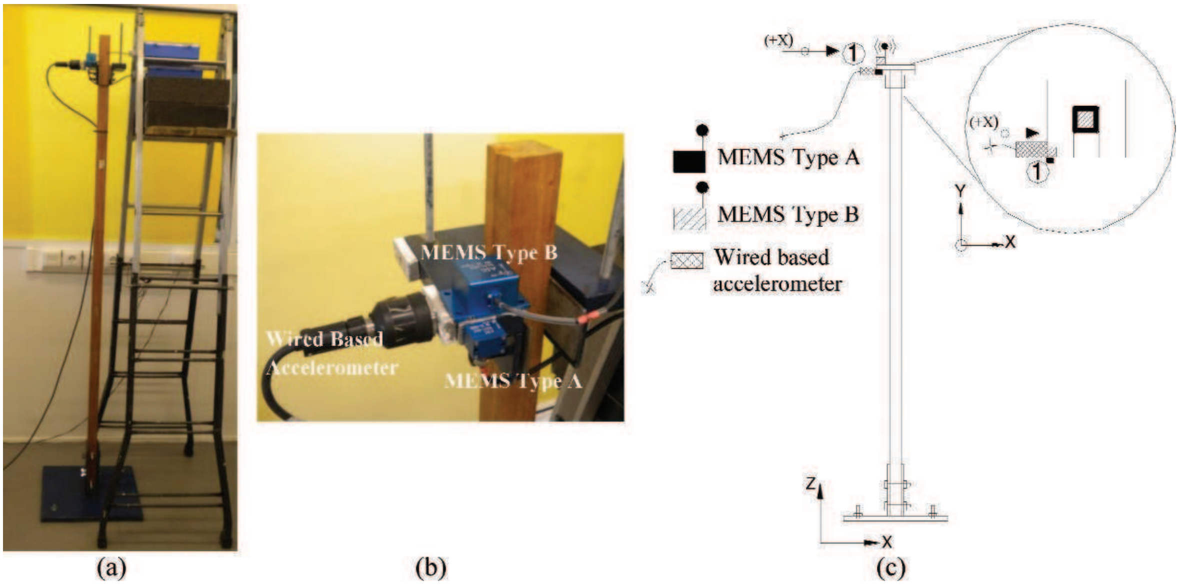

Figure 6 - Description of the arrangement of sensors for the time domain evaluation tests. (a) Inverted pendulum in the laboratory; (b) close up of the wired and wireless based sensors arrangement; and (c) scheme of the sensors deployment

The performance of the developed platforms in high and low amplitude excitations was evaluated when an impulse force was applied to the pendulum. For this test, a short sampling period of 10 seconds was considered. The time series recordings of the performed test are presented in Figure 7. The results indicated that for moderate amplitude vibrations (above 1 mg) the recordings of the three systems are very similar. However, as shown in the bottom left figure, for signals with amplitudes below this limit, the solution corresponding to the MEMS Accelerometer Type A has limitations. On the contrary, the system with MEMS Accelerometer Type B presents outstanding results maintaining a remarkable similitude with the conventional transducers, even in low noise environments. It is important to state that, even in the case of the MEMS Type A, the considered solutions had at least 20 times better performance in comparison to the commercial WSN solution presented in the previous section.

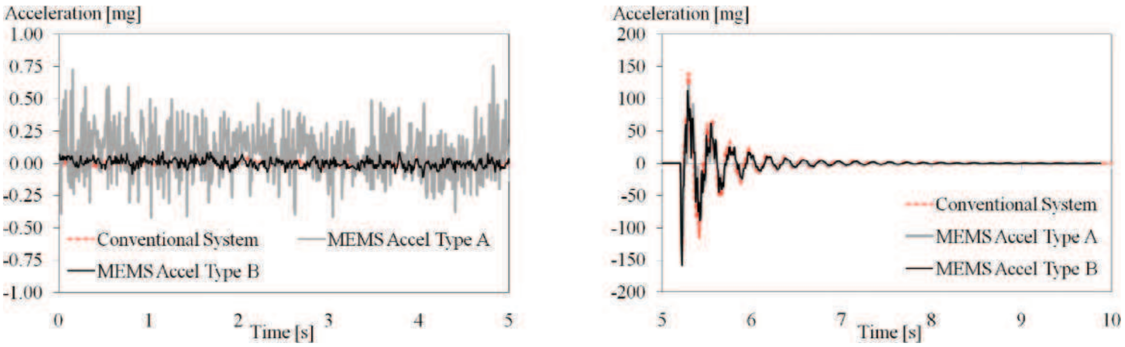

Figure 7 - Time series recordings of the response of the inverted pendulum under an impact force test – Validation Tests for New WSN Platforms

Next, the performance of the developed solution was evaluated considering tests with longer sample periods. Using the same deployment of sensors and 60 seconds for the sampling time, two rounds of tests were carried out: one considering light random impact excitations and the other ambient noise. Note that even if longer sampling periods of 1000 - 2000 times the structure’s first period are recommended for practical recommendations [19], shorter measurement times were considered due to time consuming data transmission process in this first prototype system. In this paper only the results of the solution using the MEMS accelerometers Type B will be presented since better performance in low noise environments was obtained. Figure 8 shows the time series recordings of the studied systems in each of the considered noise scenarios. The results showed the good performance of the developed system for registering low amplitude time domain events since vibrations with amplitudes above 0.1 mg were accurate acquired. For what respects to the frequency domain, the resultant spectrum of the wired and wireless based systems presented outstandingly similitude.

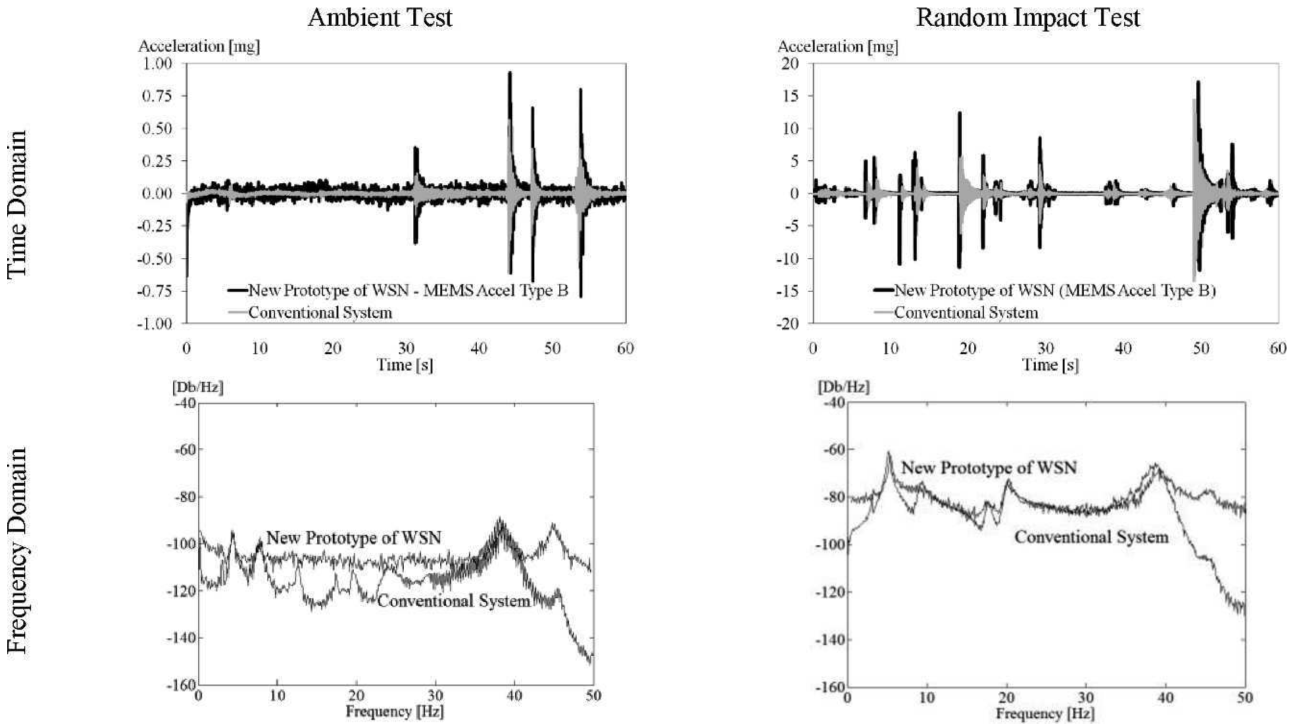

Figure 8 - Time and frequency series results from the data recorded in the inverted pendulum under an impulse force test

The modal validation tests considered the location of three measurement nodes at the top of the pendulum. In this case, the solution with MEMS accelerometers type A was considered since only one MEMS type B was available. As done before, the response of the pendulum was studied considering 60 seconds of sampling time and two excitation scenarios (moderate and low noise environments). In the collected time domain series acceleration peaks of 3.93 mg and 0.35 mg were registered, which corresponded to signals with RMS values of 0.23 mg and 0.03 mg for the medium and low noise environments, respectively.

For the modal identification process, it was considered that the information of interest is related only to the estimation of the first three structural mode shapes (translation in the two principal axes and rotation). Since the results of the developed platforms are imprecise in low noise environments, Figure 9 presents the results of the identified modal shapes only for the case of medium noise environments. The results of the medium excited environments evidenced the high accuracy of the measurements of the developed system. As it is possible to observe, the first two modes of the structure were identified with no uncertainties (MAC values close to 1) while for the case of the third mode, a slight difference with the results of the conventional systems was registered.

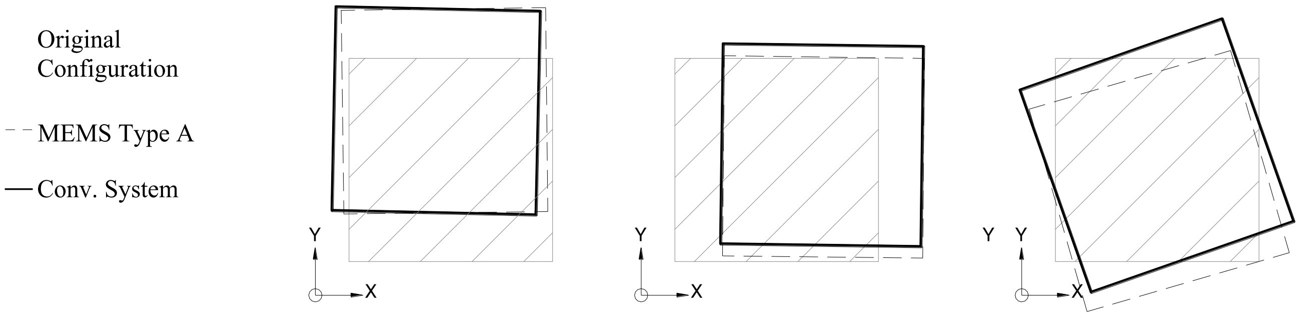

MAC 1-1 : 0.90 MAC 2-2 : 0.92 MAC 3-3 : 0.65

Figure 9 - First three mode shapes estimated from the experimental modal analysis tests in the pendulum first configuration – Validation Tests for New WSN Platforms

4. CONCLUSIONS

The present work explores the possible inclusion of Wireless Sensor Networks (WSN) in the Operational Modal Analysis (OMA) of civil engineering structures. With this purpose, the possibilities of the commercial off-the-shelf solutions on WSN platforms were first evaluated in detail. Several tests were carried out using these platforms and the results indicate that this technology, as it is commercialized, has no direct application in this type of studies. The main reasons are the low resolution of the accelerometers and the ADCs embedded and the lack of communication protocols that assure not only a proper synchronization among nodes but also reliability in the communication processes.

Once the limitations of the ready-to-use WSN solutions were identified, a joint team involving electronic and communication engineers developed a prototype WSN system aiming at fulfilling the demanding requirements of OMA tests in civil engineering structures. The laboratory and field validation tests carried out using the developed system indicate that this can be positively considered as alternative to the conventional wired based systems in monitoring works where vibrations with amplitudes over 0.10 mg are expected. In these scenarios, the results of the modal analysis process, by means of the detected frequencies and mode shapes evidenced outstanding accuracy comparable to the conventional wired based systems.

5. ACKNOWLEDGMENTS

The authors gratefully acknowledge Alban, European Union Programme of High Level Scholarships for Latin America, for the financial support of the PhD studies of the first author with the scholarship number E07D400374PE.

6. REFERENCES

[1] Aguilar, R. Dynamic Structural Identification using Wireless Sensor Networks. PhD Thesis, University of Minho, Guimaraes, (2010), Available at www.civil.uminho.pt/masonry

[2] Aoki, S.; Fujino, Y.; and Abe, M. Intelligent Bridge Maintenance System Using MEMS and Network Technology. Smart Systems and NDE for Civil Infrastructures - SPIE, San Diego, CA, Vol. 5057, (2003), pp. 37-42.

[3] ASC. Advanced Sensors Calibration. www.asc-sensors.de. Accessed December, (2009).

[4] Baptista, M.A.; Mendes, P.; Afilhado, A.; Agostinho, L.; Lagomarsino, A.; and Victor, L.M. Ambient Vibration Testing at N. Sra. do Carmo Church, Preliminary Results. Proc. of the 4th International Seminar on Structural analysis of Historical Constructions, Padova, Italy, (2004), pp. 483-488.

[5] Casarin, F.; and Modena, C. Dynamic Identification of S. Maria Assunta Cathedral, Reggio Emilia, Italy. Proc. of the 2nd International Operational Modal Analysis Conference, IOMAC, Copenhagen, Denmark, (2007), pp. 637-644.

[6] Ceriotti, M.; Mottola, L.; Picco, G.P.; Murphy, A.L.; Guna, S.; Corra, M.; Pozzi, M.; Zonta, D.; and Zanon, P. Monitoring Heritage Buildings with Wireless Sensor Networks: The Torre Aquila Deployment. International Conference on Information Processing in Sensor Networks, IPSN09, San Francisco, USA, (2009).

[7] Chung, H.C.; Enomoto, T.; Shinozouka, M.; Chou, P.; Park, C.; Yokoi, L.; and Morishita, S. Real-time Visualization of Structural Response with Wireless MEMS Sensors. 13th World Conference on Earthquake Engineering, Vancouver, BC, (2004).

[8] Costa, C.; Arêde, A.; and Costa, A. Caracterização Dinâmica e Análise da Ponte da Lagocinha. Proc. of the 6to Congresso de Sismologia e Engenharia Sísmica, Guimarães, Portugal, (2004), pp. 931-942.

[9] Crossbow. Crossbow Wireless Sensors Network. www.xbow.com. Accessed December, (2009).

[10] Farrar, C.R.; and Worden, K. An Introduction to Structural Health Monitoring. Philosophical Transactions of the Royal Society, 365, (2007) 303-315.

[11] Gentile, C.; and Saisi, A. Dynamic-based F.E. Model Updating to Evaluate Damage in Masonry Towers. Proc. of the 4th International Seminar on Structural analysis of Historical Constructions, Padova, Italy, (2004), pp. 439-449.

[12] Ivorra, S.; and Pallarés, F.J. A Masonry Bell-Tower Assessment by Modal Testing. Proc. of the 2nd International Operational Modal Analysis Conference, IOMAC, Copenhagen, Denmark, (2007), pp. 269-276.

[13] Jaishi, B.; Ren, W.X.; Zong, Z.H.; and Maskey, P.N. Dynamic and Seismic Performance of Old Multi-Tiered Temples in Nepal. Engineering Structures, 25, (2003) 1827-1839.

[14] Labview. LabVIEW User Manual, Release 8.0. National Instruments Corporation, USA, 2006.

[15] Lynch, J.P.; Sundararajan, A.; Law, K.H.; Kiremijdian, A.S.; Carryer, E.; Sohn, H.; and Farrar, C.R. Field Validation of a Wireless Structural Health Monitoring System on the Alamosa Canyon Bridge. Smart Structures and Materials: Smart Systems and Nondestructive Evaluation for Civil Infrastructures - SPIE San Diego, CA, Vol. 5057 (2003), pp. 267-278.

[16] Lynch, J.P.; Wang, Y.; Law, K.H.; Yi, J.-H.; Lee, C.G.; and Yun, C.B. Validation of a Large-scale Wireless Structural Monitoring System on the Geumdang Bridge. Proc. of the International Conference on Safety and Structural Reliability (ICOSSAR), Rome, Italy, (2005).

[17] Ou, J.P.; Li, H.; Xiao, Y.Q.; and Li, Q.S. Health Dynamic Measurement of Tall Building Using Wireless Sensor Network. Proc. of the Smart Structures and Materials, SPIE, San Diego, CA, USA, (2005), pp. 205-215.

[18] Pakzad, S.N.; Fenves, G.L.; Kim, S.; and Culler, D. Design and Implementation of Scalable Wireless Sensor Network for Structural Monitoring. Journal of Infrastructure Systems, 14(1), (2008) 89-101.

[19] Ramos, L.F. Damage Identification on Masonry Structures Based on Vibration Signatures. PhD Thesis, University of Minho, Guimaraes, Portugal, (2007), Available at www.civil.uminho.pt/masonry

[20] Ramos, L.F.; Alaboz, M.; Aguilar, R.; and Lourenço, P.B. Dynamic Identification and FE Updating of S. Torcato Church, Portugal. 28th International Modal Analysis Conference, IMAC. SEM, Jacksonville, Florida, USA, (2010).

[21] Ramos, L.F.; Casarin, F.; Algeri, C.; Lourenço, P.B.; and Modena, C. Investigations Techniques Carried out on the Qutub Minar, New Delhi, India. Proc. of the 5th International Conference of Structural Analysis of Historical Constructions, New Delhi, (2006), pp. 633 -640.

[22] Rebelo, C.; Júlio, E.; and Costa, D. Modal Identification of the Coimbra University Tower. Proc. of the 2nd International Operational Modal Analysis Conference, Copenhagen, Denmark, (2007), pp. 177-184.

[23] Schmidt, T. Dynamic Behaviour of Twin Bell Towers. Proc. of the 2nd International Operational Modal Analysis Conference, Copenhagen, Denmark, (2007), pp. 261-268.

[24] Straser, E.G.; and Kiremijdian, A.S. A Modular, Wireless Damage Monitoring System for Structures, The John A. Blume Earthquake Engineering Center, Report No.128, (1998).

[25] Weng, J.-H.; Loh, C.-H.; Lynch, J.; Lu, K.-C.; Lin, P.-Y.; and Wang, Y. Output-Only Modal Identification of a Cable-Stayed Bridge using Wireless Monitoring Systems. Engineering Structures, 30(7), (2008) 1820-1830.

Damage Identification in CRFP Laminates using a Statistical Method

M.T.H. Sultan, K. Worden, W.J. Staszewski
Department of Mechanical Engineering, University of Sheffield, Mappin Street, Sheffield, S13JD, United Kingdom

NOMENCLATURE

CFRP	Carbon Fibre Reinforced Polymer
SEM	Scanning Electron Microscopy
NDE	Non-Destructive Evaluation
BVID	Barely Visible Impact Damage
FRF	Frequency Response Function
OA	Outlier Analysis
EM	Envelope Mean
PSD	Power Spectral Density
RMS	Root Mean Square
MC	Monte Carlo
PCA	Principal Component Analysis
MC	Matrix Cracking
MB	Matrix Breakage
FC	Fibre Cracking
FB	Fibre Breakage

ABSTRACT

The purpose of this research is the detection and classification of impact damage in structures made from composite materials. This paper discusses classification of damage extent and type based on the use of X-ray analysis and a Scanning Electron Microscopy (SEM) technique. The composite material chosen for this research is a Carbon Fibre Reinforced Plastics (CFRP) laminate. The material was laid-up to produce plate specimens of 250 mm × 150 mm with 11, 12 or 13 layers. Piezoelectric sensors were placed on three different points of each test specimen in order to record the responses from impact events. An experimental modal analysis system was used to collect responses from both damaging and undamaging impacts. To perform the damaging impact tests, an instrumented drop test machine was used and the impact energy was set to range from 0.37 J to 41.72 J. The signals captured from each specimen were recorded for evaluation and the impacted specimens were X-rayed and SEM techniques were used to evaluate the extent and type of the damages. Statistical methods were used to classify the impact events into damaging and non-damaging and also to correlate the damage type and extent with the impact energy.

1. INTRODUCTION

Generally, damage can be defined as changes in physical properties that adversely influence the performance of a material. According to Farrar

Destructive or Non-Destructive Evaluation (NDE) techniques. Such hidden damage is commonly known as Barely Visible Impact Damage (BVID) [11]. In the types of composite laminates that are often used, damage can appear in various forms: matrix cracking, fibre fracture, fibre pullout and delamination. These are all possible damage mechanisms that composite laminates face in the event of a low-velocity impact.

Although visible damage can be clearly detected and remedial action can be carried out to maintain the structural integrity, the major concern is still the expansion of undetected hidden damage caused by the low-velocity impacts and fatigues [12]; those that cannot be clearly detected. Considering that impact damage can cause considerable reductions in performance of composite materials, understanding the characteristics of impact damage appearance, and crack growth, in such materials assumes great importance and is a major challenge to designers and end-users of these advanced composite structures. Therefore, there is a need to study their behaviour under impact loading since impacts do commonly occur. This all leads to the need for more reliable and responsive damage detection methods to overcome impact-related problems.

The ultimate objective of this research work, described in this paper, is to conduct an experimental investigation to detect and quantify impact damage in structures made from composite plates. The composite material chosen for the current research is a woven CFRP prepreg with a MTM57 epoxy resin system with CF2900 fabric. Two different approaches have been used to record the acceleration response signals resulting from the impact excitation. The first used the LMS Testlab

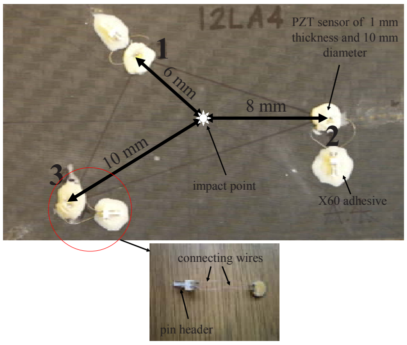

FIGURE 1. Layout of the three PZT sensors fixed on a test specimen

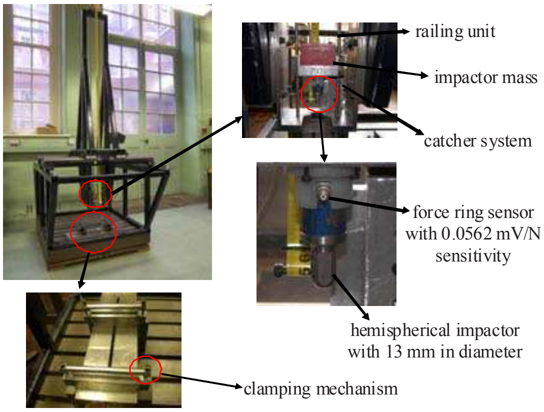
railing unit
impactor mass
catcher system
force ring sensor with 0.0562 mV/N sensitivity
hemispherical impactor with 13 mm in diameter
clamping mechanism

FIGURE 2. Instrumented drop-test rig

The impacted plate specimens were then examined using two different types of NDT approach, namely X-ray radiography and SEM fractography; from the SEM fractography, two different types of damages were observed. The first observation was on the surface defects of the impacted samples whilst the second type, usually categorised as destructive testing, visualised the cross-sectional defects to look at the internal damages. Cross-sectional fractography involves the process of sectioning the defected zone in a sufficient number of small sections at different impacted locations to look at the failure modes. The SEM was used to capture a series of microscopical images in the thin sections. These images were then used to visualise the progression and growth of the damages.

3. TEST RESULTS

The test results retrieved from the experimental work are presented in this section. Experimental results are divided into three main sections; results obtained from the force ring transducer, results from the X-ray radiography and results obtained from the SEM fractography. All these results were later used to evaluate the extent and type of the damages induced in the zone surrounding the impact location.

3.1 RESULTS FROM THE FORCE RING TRANSDUCER

The total test results conducted on the 12-layer specimens are summarised in Table 1. A range of 22 different impact energies was covered; this allowed the remaining 10 samples to be used to check the test repeatability by carrying out three further tests at the impact energies of 41.72 J and 20.86 J and two further tests at 31.29 J and 10.43 J, respectively. Table 1 confirms that the repeatability was excellent, at least in terms of peak contact force recorded. The reason for performing the repeatability test was to ensure that the contact force is behaving in a similar manner under the same impact conditions.

TABLE 1: Results for 12-layer samples in terms of contact peak force

CFRP specimen identifier	Impact energy, (J)	Peak contact force, (N) Impact 1	Peak contact force, (N) Impact 2 (repeatability)	Peak contact force, (N) Impact 3 (repeatability)	Peak contact force, (N) Impact 4 (repeatability)
12LA1	41.72	3589.7	3591.3 (12LC1)	3587.5 (12LC2)	3590.0 (12LF7)
12LA5	39.11	3562.2	-	-	-
12LA6	36.50	3555.0	-	-	-
12LA7	33.89	3235.0	-	-	-
12LA2	31.29	3059.9	3058.6 (12LC3)	3058.3 (12LC4)	-
12LA8	28.68	3022.9	-	-	-
12LB1	26.07	2848.4	-	-	-
12LB2	23.47	2656.3	-	-	-
12LA3	20.86	2470.2	2468.7 (12LC5)	2470.1 (12LC6)	2469.0 (12LF8)
12LB3	18.25	2205.9	-	-	-
12LB4	15.64	2069.0	-	-	-
12LB5	13.04	1958.2	-	-	-
12LA4	10.43	1927.2	1927.1 (12LC7)	1926.4 (12LC8)	-
12LB6	7.82	1187.2	-	-	-
12LB7	5.21	1064.2	-	-	-
12LB8	2.60	810.0	-	-	-
12LF1	2.22	714.0	-	-	-
12LF2	1.85	616.0	-	-	-
12LF3	1.48	413.2	-	-	-
12LF4	1.11	290.3	-	-	-
12LF5	0.74	119.0	-	-	-
12LF6	0.37	65.0	-	-	-

The results from the full test programme showed that the measured peak contact force showed an excellent correlation with the impact energy; this observation appeared to be true for the specimens with 11, 12 and 13 layers and the evidence is summarised in Figure 3. Previous studies also support the hypothesis made from this current work. Therefore, readers can consult [14-15] for more evidence.

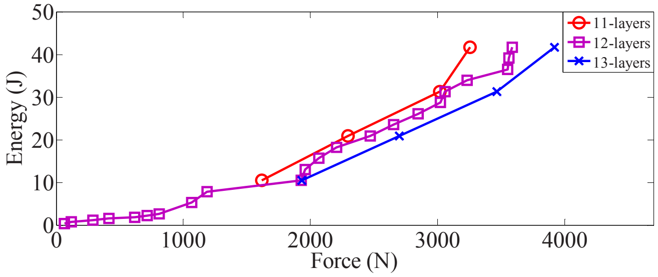

FIGURE 3. Correlation between impact energy and contact peak force for all layers

3.2 RESULTS FROM THE X-RAY RADIOGRAPHY

The ultimate aim of the research was to make inferences regarding the extent of the damage. To gather the appropriate information, two different methods were used to estimate the 'damaged area'. The first method used the naked eye and only considered the visible surface damage. This is clearly not a true measure of the subsurface area of the damage, however it was considered to be a possible proxy for the true damage when machine-learning approaches were applied later. The damaged area was assumed to be circular and was calculated from the surface diameter as measured with a vernier calliper. The second method used developed X-ray films. The damaged area was estimated as the rectangular area bounded by the width and length of the largest flaws visible parallel to the two plate axes. Table 2 summarises the results obtained for different types of estimations made on all of the specimens. Note that for the estimation method, which used X-ray images, the notation ND given in the table signifies 'Not Detected'. The damage due to the lower energy impacts did not allow sufficient entry of the penetrant into the sample; hence the term ND was used. From Table 2, it can be seen that damages were not captured in the X-ray film when the impact energy was below 10.43 J. This is because the damages below this energy level produced only surface defects consisting of only matrix cracks and matrix breakage. As a result, no images were recorded. Only when the energy level reached 20.86 J, the damages are visually captured for all specimens. Therefore, the X-ray radiography process was not carried out for specimens that were impacted at the lowest impact energies (0.37 J–2.22 J). The above results reveal that at the highest impact energy (41.72 J), the damaged area measured for the 11-layer specimen was the largest, followed by the 12-layer and 13-layer specimens. This is because specimens with a smaller amount of layers are prone to more damage compared to specimens with more layers. The general trend observed indicates that, as the plate thickness increases, the damage detected on the specimens decreases due to their ability to absorb the impact energy. Therefore, it can be concluded that the critical threshold for damage captured on X-ray film is above 20.86 J for all the specimens.

TABLE 2: The results for the two different estimates of damage area made for all the specimens

Impact Energy (J)	**Specimen Identifier**					
	11 Layers		**12 Layers**		**13 Layers**	
	Visual observation	**X-ray images**	**Visual observation**	**X-ray images**	**Visual observation**	**X-ray images**
41.72	16.62	224	15.90	195	12.57	90
39.11	-	-	15.21	180	-	-
36.50	-	-	13.86	144	-	-
33.89	-	-	13.20	100	-	-
31.29	11.95	120	12.57	70	10.75	40
28.68	-	-	11.95	60	-	-
26.07	-	-	11.34	54	-	-
23.47	-	-	10.18	40	-	-
20.86	10.18	60	9.62	30	9.08	18
18.25	-	-	8.55	ND	-	-
15.64	-	-	8.04	ND	-	-
13.04	-	-	7.55	ND	-	-
10.43	8.04	ND	7.07	ND	6.61	ND
7.82	-	-	6.16	ND	-	-
5.21	-	-	4.52	ND	-	-
2.60	-	-	3.80	ND	-	-

3.3 RESULTS FROM THE SEM FRACTOGRAPHY

Results from the SEM micrograph images allow the identification of three critical impact energy thresholds. The first threshold is for the onset of matrix cracking and breakage and was identified at the impact energy of 20.86 J. For fibre cracking the threshold was identified as between 20.86 J and 31.29 J. Finally, the third threshold for most of the damages was distinguished above 31.29 J. Readers can consult [16-17] for details. The overall failure modes observed from all the specimens are collected and presented in Table 3. A simple nomenclature was defined to identify the types of failure mode. The labelled MC, MB, FC and FB were named accordingly with matrix cracking, matrix breakage, fibre cracking and fibre breakage, whilst the labelled 1 and 0 indicates that the failure mode was 'observed' or 'not observed', respectively.

TABLE 3: Progression of failure modes for all the specimens

Impact Energy (J)	Specimen Classifier											
	11 Layers				12 Layers				13 Layers			
	MC	MB	FC	FB	MC	MB	FC	FB	MC	MB	FC	FB
41.72	1	1	1	1	1	1	1	1	1	1	1	1
39.11					1	1	1	1				
36.50					1	1	1	1				
33.89					1	1	1	1				
31.29	1	1	1	1	1	1	1	1	1	1	1	1
28.68					1	1	1	0				
26.07					1	1	1	0				
23.47					1	1	1	0				
20.86	1	1	1	0	1	1	0	0	1	1	0	0
18.25					1	1	0	0				
15.64					1	1	0	0				
13.04					1	1	0	0				
10.43	1	1	0	0	1	1	0	0	1	1	0	0
7.82					1	1	0	0				
5.21					1	1	0	0				
2.60					1	1	0	0				

4. STATISTICAL RESULTS

This Section discusses the statistical approach to damage detection using the outlier analysis (OA) method for 3-dimensional multivariate data. The reason for implementing the outlier detection is because the problem discussed here is a two-class problem; damage or no-damage, or matrix failure or fibre failure. The data from the no-damage and matrix failure states were used separately to build a statistical model of 'normality'; subsequent data can there be tested for conformality to the model, with deviations indicating the possibility of damage. The objective is to establish if new set of data are 'discordant' with the no-damage or matrix failure data in statistical terminology. For reasons of a large number of data sets, only results from the 12-layers test samples will be used and discussed here.

4.1 OUTLIER ANALYSIS FOR MULTIVARIATE DATA: SEPARATION OF UNDAMAGED AND DAMAGED DATA

In this section, the discussion will be focused on the OA for 3-dimensional features, mainly on features extracted from wavelet analysis. Readers can consult [18-19] for details on methods used for retrieving the Envelope Mean (EM), Power Spectrum Density (PSD) and Root Mean Square (RMS) from this analysis. As mentioned in Section 2 above, 10 hits were recorded for non-damaging impacts from the hammer tests on the undamaged specimens. From this data, only responses from 4 of the hits were used to calculate the statistics for the discordancy test. Although 10 hits were recorded, 4 hits were found to provide sufficient results to perform the OA.

To perform the OA on these features, the first stage is simply to make a three-component feature vector, which contains the EM, PSD and RMS for sensors 1, 2 and 3 from each of the impacts. These feature vectors (EM, PSD and RMS) are divided into training data for the undamaged condition and testing data for the damaged condition. Training data for the undamaged condition consisted of 60 observations from each of the sensors, whilst testing data consisted of 28 observations for each of the sensors. Meanwhile, for damaging impacts, only testing data was used, which consisted of 22 observations that were arranged in increasing order of impact energy. The following step is to calculate the damage index and to implement this, the Mahalanobis squared-distance as given in equation (1) was used. The statistics (mean vector and covariance matrix) from the training data were used to calculate the Mahalanobis squared-distance. To calculate the threshold value, a Monte Carlo (MC) method [20] was used and the threshold value calculated was 20 (1000 MC iterations, 3-dimentional feature space and 50 observations). Figure 4 illustrates the results obtained for the Mahalanobis squared-distance for each of the sensors.

$$(\{\quad\}\ \{-\})[\quad](\{\quad\}\ \{-\})$$

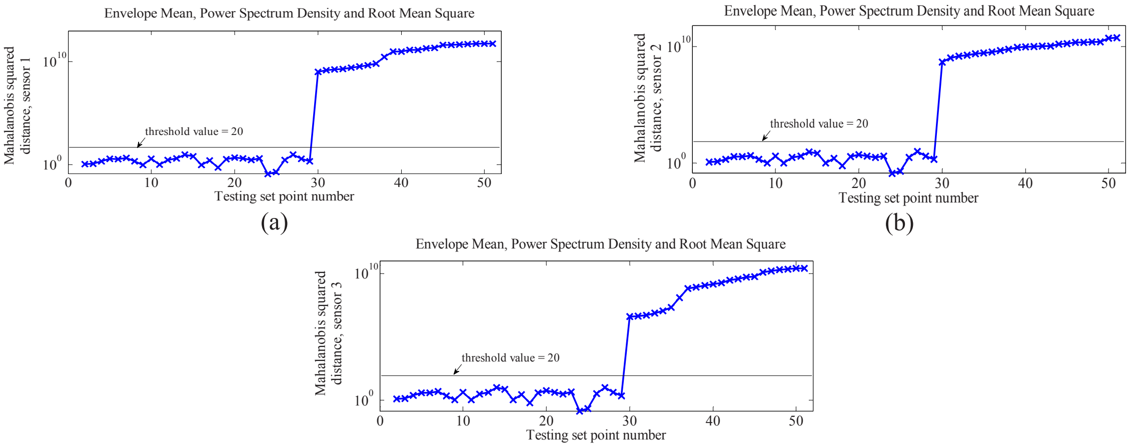

(a) (b)

(c)

FIGURE 4. Mahalanobis squared-distances for non-damaged and damaged cases for EM, PSD and RMS for, (a) sensor 1, (b) sensor 2, (c) sensor 3. (———) Threshold value

Referring to Figure 4, it can be seen that there is again a clear separation between the non-damaged data and damaged data. It is also obvious that there is a sudden jump between both the non-damaged and damaged data. The transition between these data is between points 28 and 29. Further, the discordancy also increases monotonically with respect to impact energy and therefore with the damage area. The monotonic pattern observed here supports the earlier results obtained from the wavelet analysis [18-19] where the univariate damage indices (EM, PSD and RMS) calculated also show a monotonic increase with increased impact energies. This monotonic behaviour is important when damage needs to be identified and detected directly from the impact response data.

Now, if one calculates the ratio of the highest damage index to the threshold value for each of the sensors, the sensitivity of the damage can be identified. It was found that, the corresponding ratio calculated for sensor 1 was approximately 10^{10} and 10^{9} for sensors 2 and 3. The corresponding ratio for these features is approximately eight orders of magnitude smaller for sensor 1 and seven orders of magnitude smaller for sensor 2 and 3 as compared to the threshold value, which in this case is 20. This means that, sensor 1 is more sensitive to detecting the damage as compared to sensors 2 and 3. The reason for this is due to sensor 1 being positioned closer to the impact point with the distance of sensor 2 following and with sensor 3 being positioned the furthest away from the impact (and hence damage) location. The following section will now discuss the effect of Principal Component Analysis (PCA) on these sets of data.

4.2 PCA FOR MULTIVARIATE DATA: SEPARATION OF UNDAMAGED AND DAMAGED DATA

Figure 5 illustrates the PCA results for EM, PSD and RMS for all the sensors. From these figures, it can be seen that, there is a clear separation between the two data sets: non-damaged and damaged, with the non-damaged data located to the far right (blue circles). There is also a sudden increase between these two data points; this is clearly marked on Figure 5 (a-c). All three graphs show a similar pattern where the damaged data moves away from the non-damaged data in a cyclic behaviour. This means that the first failure mode, which is the matrix cracking, moves in the high-variance direction where the Mahalanobis squared-distance grows slower than Euclidean distance. This is clearly illustrated in Figure 5 (a) where the first few data points are closely spaced. The second data point (which is the matrix breakage) shows a different pattern. As the impact energy increases, it can be observed that, the data point (matrix breakage) moves in the low-variance direction where the Mahalanobis squared-distance grows faster. This phenomenon is clearly exposed in Figure 5 (a). For the transition between the matrix failure and fibre failure, it can be noticed that the data point for fibre failure, again, moves in the high-variance direction before it settles down at the highest impact point. The point corresponding to highest impact energy, and severely damaged, is located in the bottom left. This observation is also true for sensors 2 and 3, which have a similar cyclic behaviour as depicted in Figure 5 (b-c).

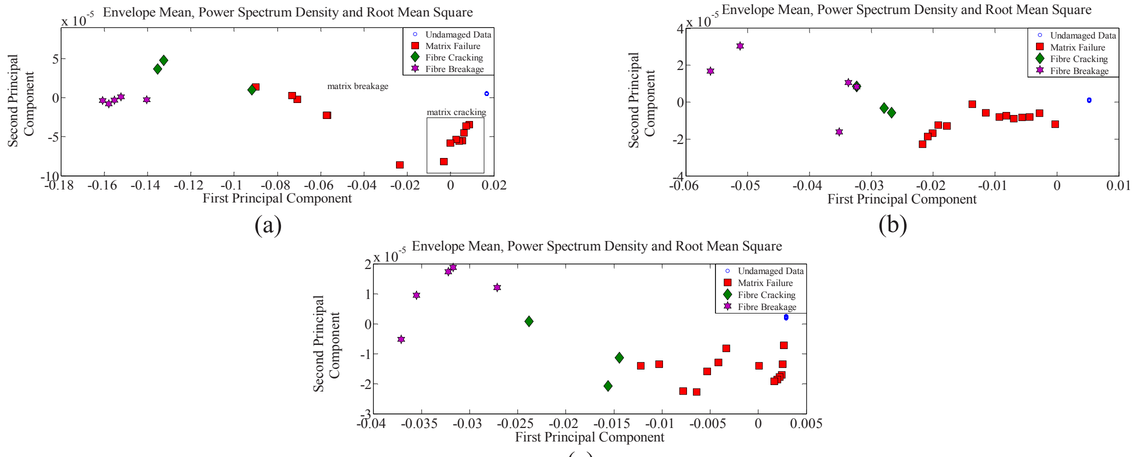

(a)

(b)

(c)

FIGURE 5. Principal Component Analysis for non-damaged and damaged cases for EM, PSD and RMS for, (a) sensor 1, (b) sensor 2, (c) sensor 3. (———) Threshold value

4.3 OUTLIER ANALYSIS FOR MULTIVARIATE DATA: SEPARATION OF MATRIX FAILURES AND FIBRE FAILURES

To perform the outlier analysis on the separation of the types of failure mode, the first stage is again to make a three-component feature vector containing EM, PSD and RMS from all the sensors (data points representing matrix failure and fibre failure). The EM, PSD and RMS used here were divided into two sets of data: training and testing data for the damaged state. Note that, at this stage, all the repeating tests data were also taken into account. The repeatability results data were retrieved at four selected impact energies: three test results, each at 41.72 J and 20.86 J, whilst two test results, were each at 31.29 J and 10.43 J. A total of 32 observations were used to perform OA, which includes 10 observations from the repeating test results. The training data contained 10 observations for the matrix failure, whilst the testing data contained 9 observations of the same failure mode. For fibre failure, the testing data contained 13 observations with the data sets being arranged in an increasing order of the impact energy (varied from 0.37 J up to 41.72 J). The following step is to calculate the Mahalanobis squared-distance (damage index) using equation (1) and the threshold value using the MC approach. The threshold value obtained here was found to be 10. This value corresponds to 100 MC iterations, a 3-dimensional feature space and 32 observations. Figure 6 illustrates the results for the Mahalanobis squared-distance obtained for the separation of matrix failures and fibre failures.

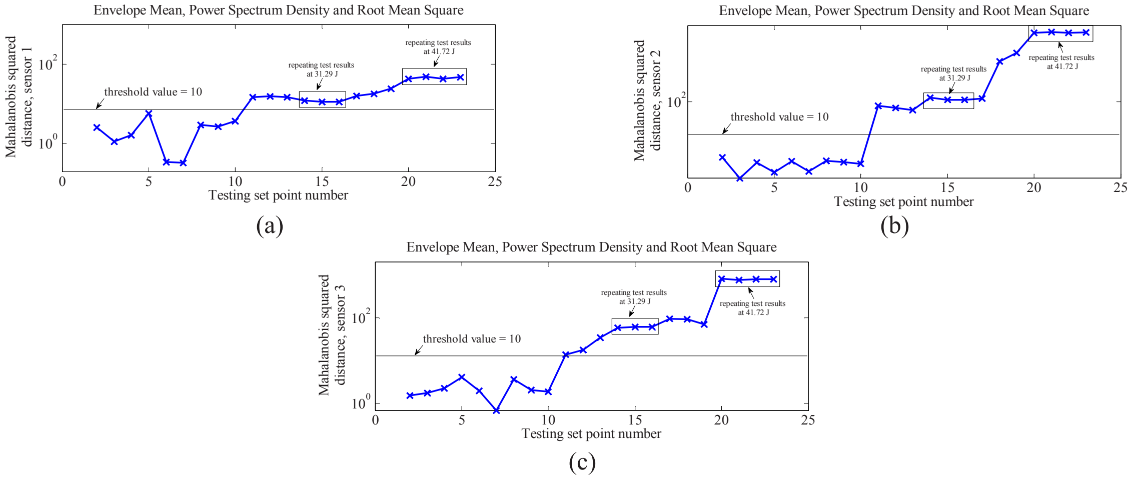

(a)

(b)

(c)

FIGURE 6. Mahalanobis squared-distances for matrix failures and fibre failures for EM, PSD and RMS for, (a) sensor 1, (b) sensor 2, (c) sensor 3. (———) Threshold value

Referring to Figure 6, one can clearly see that the type of failure mode is separated by the threshold value. All data points above this threshold are considered to be fibre failure, whilst data points below this line are categorised as matrix failure. From Figure 6 (a-c), one can also notice that there is again a sudden increase (between points 10 and 11). This is mainly because of the transition between these two failure modes. There is a large difference (in terms of damage severity and damage area measured) between these two failure modes. The sudden jump observed, from this transition, confirms that the amount of damage area measured, and the severity of damage, increases as the impact energy increases. This is verified with the results obtained from the SEM fractography and X-ray radiography. Due to this behaviour, one can clearly observe the sudden jump between these two failure modes. It is also observed, from Figure 6 (a-c), that all the data points that lay between 14 and 17, and between 20 and 23, confirm that the repeatability test conducted shows excellent results.

In terms of PCA results, it is again observed in Figure 7 that there is a clear separation between the fibre failure and matrix failure. The matrix failure points are assembled at the far right, whilst the fibre failure points are gathered at the far left. The data points for fibre failure (as shown in Figure 7 (a-c)) are again arranged in the similar cyclic pattern as observed in Figure 7. Furthermore, one can also observe from these figures that the repeatability again demonstrates convincing effects. This can be seen at the impact energies of 20.86 J, 31.29 J and 41.72 J, where the feature points are laid near to being on top of one another. The point corresponding to highest impact energy and the most damaged is in the bottom left. From these figures, it can be concluded that the Mahalanobis distance is weighted in different directions with respect to the variance of the normal condition data. Most of the matrix failures observed here move in the low-variance direction where the Mahalanobis squared-distance develops slower than the Euclidean distance. For the types of fibre failure (fibre cracking and fibre breakage), the feature points primarily grow in the high-variance direction before it moves again in the low-variance direction (as the impact energy increases).

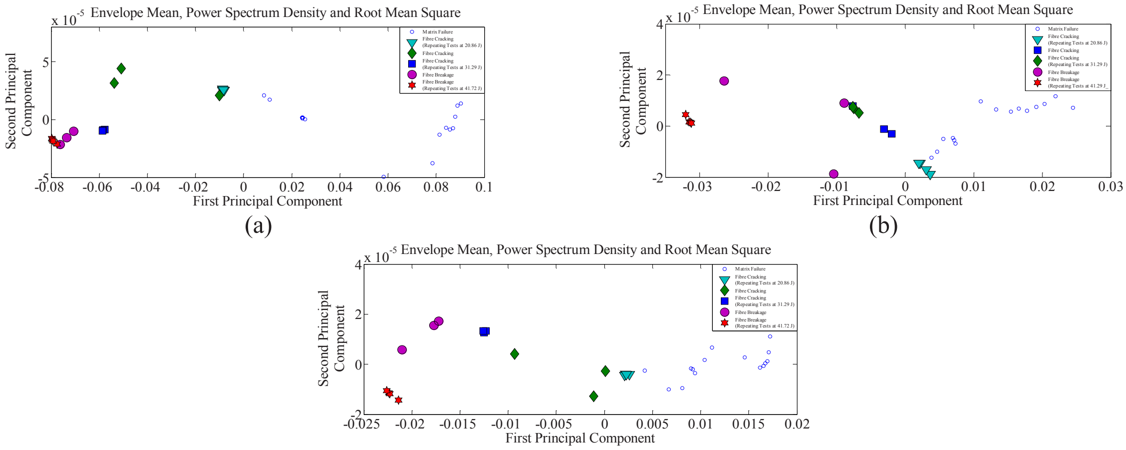

(a)

(b)

(c)

FIGURE 7. Principal Component Analysis for matrix failures and fibre failures for EM, PSD and RMS for, (a) sensor 1, (b) sensor 2, (c) sensor 3. (———) Threshold value

5. CONCLUSION

The main objective of this chapter was to describe the importance of using statistical methods to identify and categorise damaging or non-damaging impacts and also to categorise the types of failure modes (matrix failure and fibre failure) using only response data. A number of multivariate features extracted from basic surface-mounted sensors were used to provide enough information, which allows the development of diagnostics capable of inferring the impact damage extent. Results for the Mahalanobis squared-distance from the multivariate data revealed that, data for non-damaging and damaging impacts and also matrix failures and fibre failures were clearly separated by a threshold value. From the investigations carried out, it can be concluded that these multivariate features can be used as good damage indicators and proxies for the damage extent and type.

In terms of dimensionality reduction, PCA was found to be a powerful method for damage identification by reducing the number of monitored variables into a smaller scale of variables. Most of the damage features were recorded in the first two principal components. In terms of the results retrieved from PCA, it allows one to directly visualise the data and observe the distribution of damage mechanism precisely. Furthermore, it also allows one to monitor the pattern of the whole data set by looking at the separation between the damaged and non-damaged features, and also between the types of failure modes (matrix failure and fibre failure). From the analyses carried out in PCA, one can conclude that there is a clear separation between the damaged and non-damaged features. This observation was also true for the separation between the matrix failure (matrix cracking and matrix breakage) and the fibre failure (fibre cracking and fibre breakage).

REFERENCES

[1] C.R. Farrar., T.A. Duffey., S.W. Doebling and D.A. Nix., A Statistical Pattern Recognition Paradigm for Vibration Based Structural Health Monitoring. Proceedings of 2nd International Workshop on Structural Health Monitoring, Palo Alto, CA, 1999.

[2] C.R. Farrar., S.W. Doebling., and D.A. Nix., Vibration-Based Structural Damage Identification. Philosophical Transactions of the Royal Society of London. Series A: Mathematical, Physical and Engineering Sciences, 359(1778), 131-149, 2001.

[3] N.K. Naik., Y.S. Chandra., and S. Meduri., Damage in Woven-Fabric Composites Subjected To Low-Velocity Impact. Composites Science and Technology, 60(5), 731-744, 2000.

[4] Y.P. Siow., and V.P.W. Shim., An Experimental Study of Low Velocity Impact Damage in Woven Fiber Composites. Journal of Composite Materials, 32(12), 1178-1202, 1998.

[5] J.N. Yang., D.L. Jones., S.H. Yang., and A. Meskini., A Stiffness Degradation Model For Graphite/Epoxy Laminates. Journal of Composite Materials, 24(7), 753-769, 1990.

[6] N.H. Tai., C.C.M. Ma., J.M. Lin., and G.Y. Wu., Effects Of Thickness On The Fatigue-Behavior Of Quasi-Isotropic Carbon/Epoxy Composites Before And After Low Energy Impacts. Composites Science and Technology, 59(11), 1753-1762, 1999.

[7] B. Whittingham., I.H. Marshall., T. Mitrevski., and R. Jones., The Response of Composite Structures With Pre-Stress Subject to Low Velocity Impact Damage. Composite Structures, 66(1-4), 685-698, 2004.

[8] Z. Aslan., R. Karakuzu., and B. Okutan., The Response of Laminated Composite Plates under Low-Velocity Impact Loading. Composite Structures, 59(1), 119-127, 2003.

[9] T.J. Barden., D.P. Almond., S.G. Pickering., M. Morbidini., and P. Cawley., Detection of Impact Damage in CFRP Composites by Thermosonics. Non-destructive Testing and Evaluation, 22(2), 71-82

[19] M.T.H. Sultan., W.J. Staszewski., and K. Worden., Wavelet Feature Extraction for Impact Damage Analysis for CFRP Laminates. Proceedings of 10th International Conference on Recent Advances in Structural Dynamics, Southampton, UK, 2010.

[20] K. Worden., G. Manson., and N.R.J. Fieller., Damage Detection Using Outlier Analysis. Journal of Sound and Vibration, 229, 647-667, 2000.

High Intensity Noise Generation for Extremely Large Reverberant Room Test Applications

Anant Grewal[1], Ramani Ramakrishnan[2,3], William O. Hughes[4], Bill Woyski[5], Gary Elfstrom[3],
Chon Mech[5] and Yong Chen[1]

[1] *National Research Council Canada, Institute for Aerospace Research,1200 Montreal Road, Ottawa, ON, Canada, K1A 0R6, email: anant.grewal@nrc-cnrc.gc.ca*

[2] *Department of Architectural Science, Ryerson University, 350 Victoria Street, Toronto, ON, Canada, M5B 2K3*

[3] *Aiolos Engineering Corporation, Suite 100, 2150 Islington Avenue, Toronto, ON, Canada, M9P 3V4*

[4] *NASA Glenn Research Center, 21000 Brookpark Road, Cleveland, OH 44135, USA*

[5] *Team Corporation, 11591 Watertank Road, Burlington, WA 98233-3626, USA*

ABSTRACT

A recent operational need for the development of a large (101,000 ft^3) reverberant acoustic chamber at the Space Power Facility of NASA Glenn Research Center's Plum Brook Station with the requirement of generating sound pressure levels (SPL) as high as 163 dB has resulted in the need to re-examine the generation of noise in reverberant rooms. Early in the design stage, it was realized that the acoustic power level capability (10-30 kW) of conventional electrodynamic air modulators, such as those supplied by the Wyle Corporation, would be required in unprecedented numbers to meet the test spectra requirements. The design team then turned to a lesser known modulator, the hydraulically driven air modulator supplied by the Team Corporation, which has 150-200 kW acoustic power capability. The advantage to the project was a significant reduction in the number of modulators required to meet the requirements.

However, since only limited characterization of Team modulator's performance has been reported, a test program was required in order to mitigate the risk of the design of the RATF. Aiolos Corporation, which is responsible for the acoustic design of the RATF, and the Institute of Aerospace Research (IAR) of the National Research Council of Canada (NRC), entered into a collaborative agreement with the objective of characterizing, optimizing and investigating the controllability of the Team modulators. The test program was performed at the NRC-IAR reverberant chamber, a 19,000 ft^3 facility located in Ottawa, Ontario, Canada. The current paper provides details of the principle of operation of the Team modulators, including their servo control loops and provides of a summary of the characterization and controllability test program.

1.0 INTRODUCTION

The NASA Space Environmental Test (SET) Project is tasked to develop new environmental test facilities to support NASA's developing space exploration program. The Space Power Facility (SPF) at the NASA Glenn Research Center's Plum Brook Station in Sandusky, Ohio, USA is already the home of the world's largest thermal vacuum chamber. In order to provide the aerospace customer with one-stop testing for the suite of space environmental testing, the SPF is being augmented through the NASA SET Project Office with new reverberant acoustic [1], mechanical vibration [2], and modal test [2] facilities.

In August 2007, Benham Companies, LLC (Benham), located in Oklahoma City, Oklahoma, USA, won the NASA prime contract to design and construct the acoustic, vibration and modal test facilities, as well as to provide the high speed data acquisition system to support these facilities. Benham contracted with Aiolos Engineering Corporation (Aiolos), located in Toronto, Ontario, Canada to provide the acoustic design of the Reverberant Acoustic Test Facility (RATF).

The RATF will be a unique acoustic test facility due to its combination of very large chamber test volume and extremely high acoustic sound levels. Typically, the world's larger reverberant test chambers have a volume of ~ 50,000 to 76,000 ft^3, and can produce an empty chamber overall sound pressure level (OASPL) of approximately 152 to 157 dB. However the RATF has a volume of approximately 101,000 ft^3 and has been designed to produce an empty chamber test level of 163 dB OASPL. Amongst the world's active known reverberant acoustic chambers only the Lockheed Martin test facility located in

T. Proulx (ed.), *Sensors, Instrumentation and Special Topics, Volume 6*, Conference Proceedings of the Society for Experimental Mechanics Series 9,
DOI 10.1007/978-1-4419-9507-0_12, © The Society for Experimental Mechanics, Inc. 2011

Sunnyvale, California, USA is larger in volume at 189,200 ft^3 than RATF, but that test facility produces an empty chamber level of approximately 156.5 dB OASPL, which is at least 6 dB less than RATF's predicted capability. The RATF's combination of size and acoustic power was necessary to meet NASA's requirements to test the next generation of large space exploration vehicles whose acoustic environments have been predicted to be 163 dB OASPL or even higher.

2.0 RATF REQUIREMENTS

The key requirements for the RATF acoustic design were as follows:

a. The RATF shall be physically as large as possible within the given space limitations of SPF.
b. The RATF's test chamber shall be properly sized to acoustically test four space vehicle configurations, encompassing an 18-ft diameter test article, and a 47-ft tall test article.
c. The RATF's test chamber shall physically allow a 32.8-ft diameter test article weighing up to 120,000 pounds.
d. The RATF shall generate the empty chamber acoustic test spectra shown in Figure 1, for continuous test duration of 10 minutes. These eight (8) "C" spectra represent a wide range of current and future NASA missions, including five (5) spectra with a 163 dB OASPL.
e. The RATF shall include an independent, multi-channel digital acoustic control system capable of controlling the noise sources to the sound pressure levels (SPL) and spectra shown in Figure 1, within specified tolerances (+5dB below the 50 Hz one-third octave bands (OTOB), +3dB covering 50 Hz-2K Hz OTOB's, +5dB above 2K Hz OTOB's, +1.5dB on OASPL).

The physical size of the RATF was determined from the maximum available space within the SPF, along with following guidelines on proper room ratios and good acoustic test practices. Benham and Aiolos ultimately designed a reverberant acoustic test chamber with the following dimensions: 47.5-ft long x 37.5-ft wide x 57-ft high. After accounting for the main chamber door jamb structure the resulting chamber volume is 101,189 ft^3. A picture of the RATF under construction is shown in Figure 2.

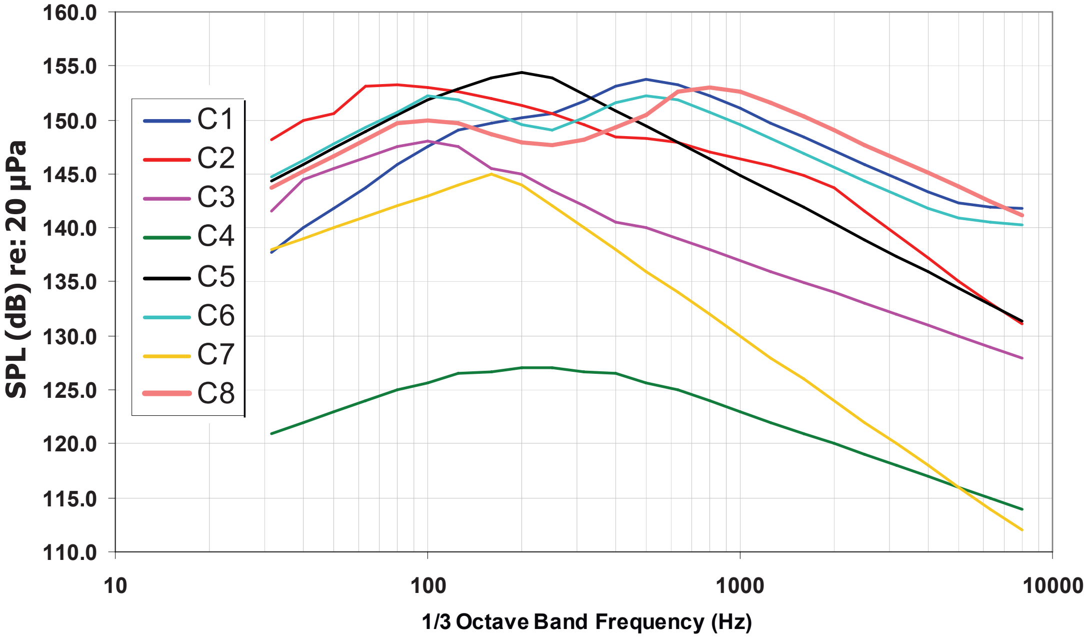

Figure 1: Acoustic Test Spectra Requirements

The next design issue was to determine the number and type of acoustic modulators or noise generators that would be needed to create the enormous sound power necessary to sustain the high SPL in this large chamber volume. Prior to the "C" acoustic spectra requirements becoming effective in September 2008, six other spectra were originally required including three spectra whose characteristics and SPL were very similar to the C2 spectrum, as shown in Figure 1. The common characteristic of the initial three spectra and C2 is very high SPL at frequencies at and below 100 Hz. The Wyle WAS3000 modulator, which has been in use since the 1960's, with an acoustic power generation capability of 30kW, was initially considered. Preliminary analysis showed that over fifty WAS3000 would be required to meet the initial three spectra. Most of these modulators would be paired with low frequency horns, which have very large dimensions at the horn mouth, the end result being a multitude of design problems in terms of integration with the chamber structure.

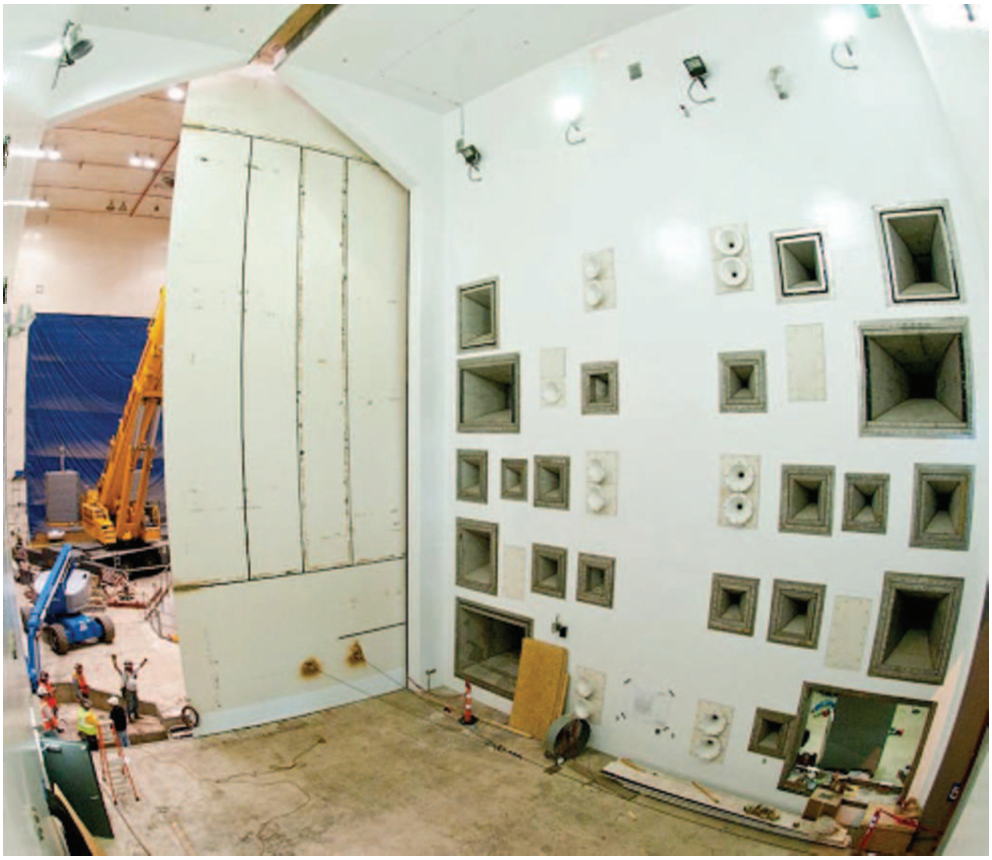

Figure 2: Ongoing Construction of the NASA Reverberant Acoustic Test Facility (RATF). The modulators are located behind the horn wall shown in the photograph.

The need was clear to reduce the number of horns by selecting higher power modulators. The only known commercially available high acoustic power modulators were the Team Corporation (Team) modulators with models known as the MK-VI and MK-VII. The Team modulators, although not widely utilized within the reverberant acoustic industry, are especially effective at the low frequencies (at or below the 125 Hz OTOB) with a rated modulator acoustic power of 150 kW (kilowatts) and 200 kW, respectively. These Team modulators were eventually paired with horns with six different cut-off frequencies (25, 35, 50, 80, 100 and 160 Hz) for the final RATF design. Benham later augmented the RATF design with several Wyle WAS-5000 modulators on 250 Hz horns to add to the high frequency capability of the RATF.

Although the Team modulators have been in service for over 40 years, there was not much acoustic characterization data available on them. To obtain Team modulator characterization data, and to qualify and mitigate any associated risk to NASA, Aiolos jointly with staff at the National Research Council of Canada (NRC) designed and conducted a series of test programs [3] at the Ottawa NRC 19,000 ft^3 reverberant acoustic test facility.

3.0 TEAM AIR MODULATOR

3.1 History

Team Corporation has been involved with the design, manufacture, application and installation of Air Modulators for more than 40 years. The Air Modulator is the evolutionary development of an acoustic generator designed in the early 1960s by Don Skilling at the Aircraft Division of Northrop Corporation. Skilling's early work focused on the use of electro-dynamic shakers as the motive force for opening and closing the poppet valve. It then became apparent to him that the superior force to mass ratio of the hydraulic shaker might open and close the air valve to even higher frequencies. He demonstrated that the use of hydraulic shakers did indeed extend the controllable acoustic spectrum out beyond 500 Hz.

Team Corporation worked with Northrop as a supplier and subcontractor from the initial design until Team purchased the product line in 1983. At Team, the MK-V model was dropped and the power of the MK-VI was increased from 85 kW (acoustic) to the current 150 kW (acoustic). The MK-VII Air Modulator was not altered significantly from the original design. Both the MK-VI and MK-VII benefited from Team's servo valve and servo controller improvements. The improvements eliminated the instabilities that the very early Northrop Air Modulators exhibited, with the result that current models are repeatable and reliable.

3.2 Modulator Design

Figure 3 displays the complete Air Modulator assembly. The Air Modulator comprises the hydraulic actuator, poppet valve and seat, and an air supply plenum. The poppet valve is housed in an air plenum designed to deliver a steady uniform source of air to the poppet valve. The plenum mounts to the throat of the acoustic horn. An air supply line is also connected to the plenum. The Air Modulator is designed to operate at air supply pressures between 40 and 200 psig.

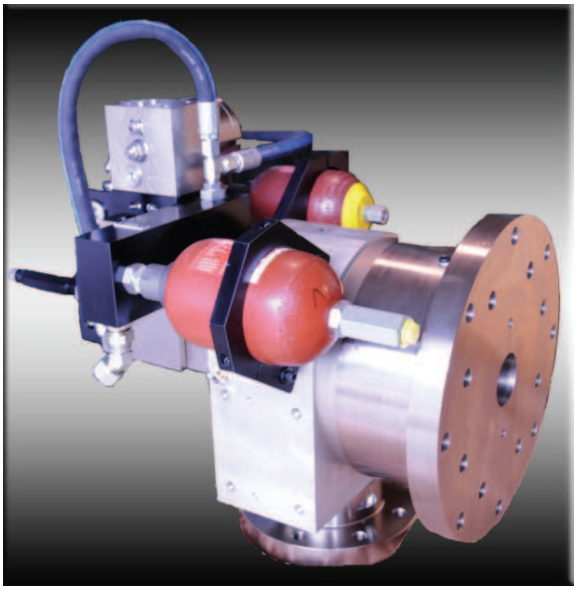

Figure 3: Team Air Modulator

The actuator is mounted on the plenum in such a way that it can drive the poppet valve via a short concentric shaft. The air valve is a reciprocating poppet valve that is driven by a special high response electro-hydraulic actuator (see Figure 4). The hydraulic actuator is driven by Team servo valves models V-20 and V-140. The V-20 valve, called the pilot valve, is a voice coil driven, four way spool valve. The V-140 valve, called the slave valve, is driven by the pilot valve and provides high flow to the actuator.

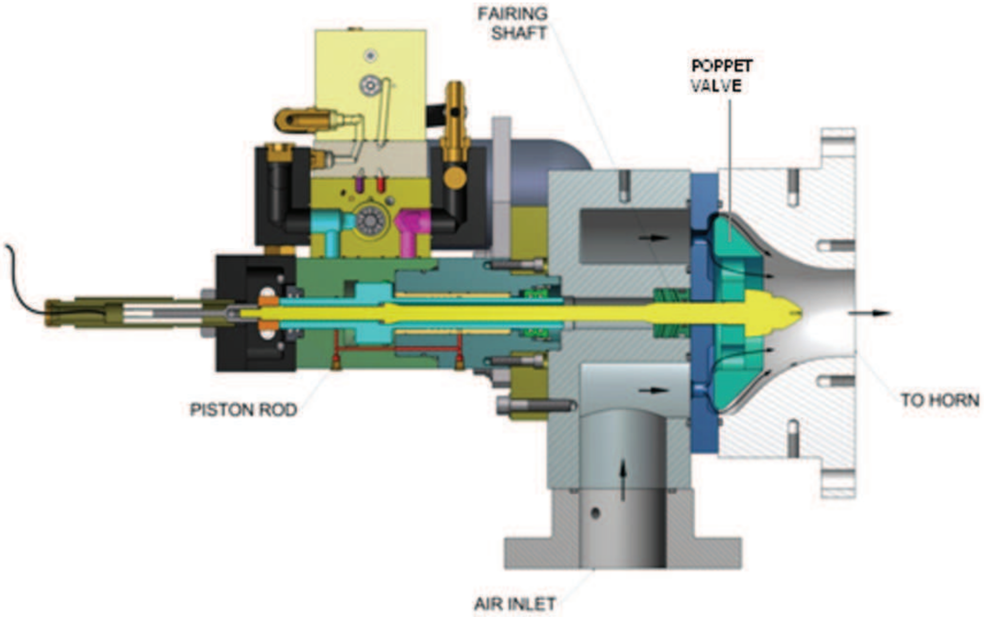

Figure 4: Acoustic Modulator Assembly cutaway with air flow paths.

The command signal can be generated by an automatic control system or a manual random noise shaping system. The voice coil signal is generated from the command with a position servo loop and a power amplifier. The poppet valve position is monitored, and fed back and serves as the control parameter.

The hydraulic actuator features hydrostatic bearings that prevent metal to metal contact and it uses no high pressure seals. This reduces the wear on parts and increases the longevity of the actuator. Additionally, the high frequency response dual stage voice coil driven servo valve allow air modulation out to high frequencies. The frequency response of the Team air modulators is shown in Figure 5.

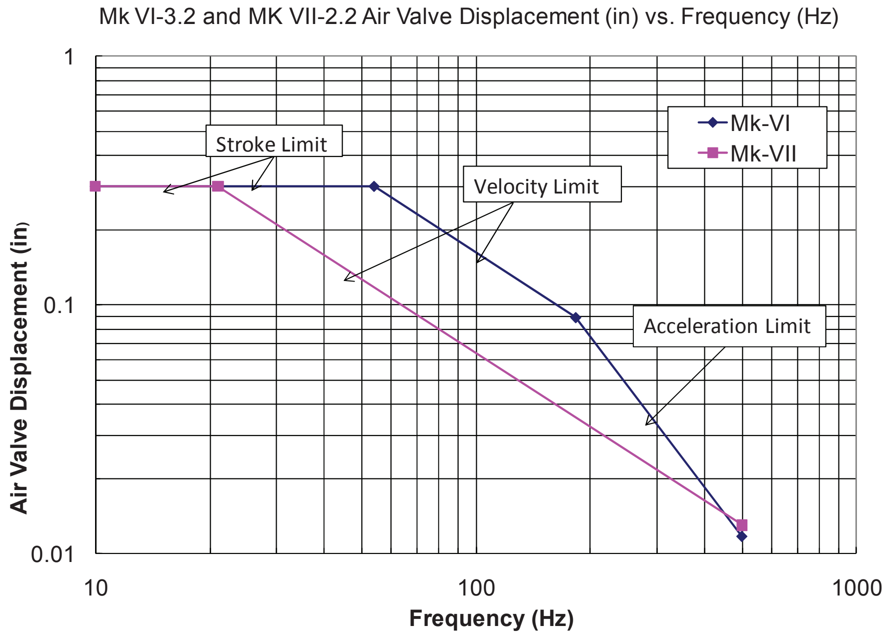

Figure 5: Team MK-VI and MK-VII Air Valve Displacement versus Frequency

3.3 Principle of Operation

3.3.1 Air Modulator

The Air Modulator system is developed specifically to generate broad band random noise. The main emphasis during the development was to maximize the efficiency and power output while keeping the mechanism simple and reliable. The acoustic power is given by the following equation [4]:

$$W_a = 0.166 \times Q \times E_a[(P_R)^{0.288} - 1]$$

Where W_a is the acoustic power in kilowatts; Q is the air flow in SCFM (standard ft^3 per minute); E_a is the air stream to acoustic power efficiency; 0.166 is a factor for units at standard condition; and P_R is the pressure ratio (i.e. the ratio of supply pressure to outlet pressure). The air modulator theoretical efficiency of air stream power to acoustic power is approximately 33%. The Team MK-VI and VII modulators can operate with either air or gaseous nitrogen as their pressurized gas source. The RATF will use gaseous nitrogen for its operation, whereas air was used for all testing at the NRC.

3.3.2 Air Modulation by Poppet Valve

High energy noise is produced by modulating the flow of a large quantity of high pressure gas with a mechanically driven poppet valve. The Team modulator differs from other air modulators in that it closes off the air stream completely when the poppet valve is shut and, if the supply pressure is high enough, generates a shock wave in the air stream when it opens. This creates the large pressure fluctuations required to produce 160 to 175 dB sound pressure levels in the test cell. The shock waves produce a broadband acoustic spectrum in the acoustic test cell, which can be a reverberant chamber or progressive wave tube.

During random operation, the Air Modulator normally produces a broad band random spectrum that is both smooth and continuous. The spectrum shaping is done in the traditional manner of shaping the input command spectrum up to about 500

Hz, after which the actuator can no longer produce sufficient displacement to modulate the open area of the poppet valve. The spectrum is also influenced to lesser extent by the air pressure, and force with which the poppet valve is held against its seat. The force needed to hold the poppet valve against the seat increases with increasing supply pressure, and this is accounted for with a servo bias applied toward the closed direction. A library of input settings and the resulting acoustic levels is accumulated to assist the operator in attaining a given test condition. The Air Modulator will repeat a given output if all the input parameters are duplicated.

3.3.3 MK-VI and MK-VII Specifications

The performance specifications for the MK-VI and MK-VII modulators are summarized in Table 1.

Table 1: Performance Specification of the Team MK-VI and MK-VII Modulators.

Parameter	**MK-VI 3.2**	**MK-VII 2.2**
Acoustic power output at rated hydraulic power supply of 30 gpm at 3000 psig	150 kW @ 2900 SCFM and 150 psig	200 kW @3800 SCFM and 150 psig
Poppet valve frequency response	20 to 500 Hz	20 to 500 Hz
Frequency Content of Acoustic Output	To 10 kHz	To 10 kHz
Servo valve flow capacity	140 LPM at 200 Hz	140 LPM at 200 Hz
Minimum hydraulic power supply	30 gpm at 3000 psig	30 gpm at 3000 psig
Recommended gas flow range	1500 to 3500 SCFM	1500 to 4500 SCFM
Recommended gas pressure range	120 to 200 psig	120 to 200 psig

4.0 MODULATOR TEST PROGRAM

The achievable performance such as, power output, spectral shape and amplitude control, for the Team modulators was determined by conducting a series of test programs at the reverberant test chamber at NRC-IAR in Ottawa, Ontario.

The aim of the test programs was to establish the behavior of the Team modulators with different parameters such as modulator gas supply pressure, the character of the broadband random input signal (including the dc bias of the servo-amplifier and the spectral shape), and the pressure of the hydraulic fluid.

The main acoustic parameters of interest were:

- The sound pressure level inside the reverberant chamber (both overall level and spectra);
- The acoustic power of the modulators at the horn mouth and at the modulator outlet; and
- The spatial variation of the sound inside the chamber.

The details of the test program are presented in this section.

4.1 Test Objectives

The acoustic test objectives can be summarized as follows:

- Determine the quantitative relationship of bias to modulator efficiency, flow, and acoustic output levels with the various horns;
- Demonstrate the repeatability of the modulator's acoustic performance;
- Demonstrate the controllability of the modulator to generate different spectral shapes by varying pressure, bias, input signal gain, and input signal spectrum; and
- Demonstrate the controllability of the modulator to generate consistent spectral shape output at full level and -6 dB settings.

4.1.1 Dynamic Range

The dynamic range of the modulator was determined as the signal within the test chamber was incremented slowly to the maximum desired specification. Ideally, the dynamic range should be at least -12 dB, with the desire to explore the range between -12 dB and -18 dB. Hence testing was performed with the modulator, whose powers were reduced from 0 to -18 dB in 3 dB increments.

4.1.2 Closed Loop Modulator Testing

The test objectives of Controlled Loop Modulator Testing were:

- Demonstrate that a Team modulator can be adequately controlled via acoustic feedback in a manner similar to other acoustic sound generators.
- Characterize the performance metrics of the Team modulators under closed loop control.
- Provide useful data for later inclusion in a performance specification for competitive bidding of an Acoustic Control System.

Acoustic closed loop testing was initially performed with a single MK-VII Team modulator coupled to the 25 Hz horn and then a single MK-VI Team modulator coupled to the 160 Hz horn in the NRC-IAR Reverberant Test Facility. The in-house NRC-IAR Acoustic Control System was employed with a total of 6 control microphones. For each target spectrum, the optimum bias was applied. The pneumatic pressure was within the range 150 to 175 psig. The closed-loop performance was characterized in terms of response time for each 1/3-octave band (25 Hz to 500 Hz) as well as the steady state error.

4.2 Modulator Hydraulic and Pneumatic Supply

For the characterization tests at the NRC, the hydraulic supply for a single modulator was provided by a MTS 30 gpm pump that was capable of supplying 3000 psig. When dual modulators were tested, a MTS pump rated at 70 gpm at 3000 psig was employed.

The air supply for the Team modulators is provided by a 8 MW compressor plant that fills three storage tanks with a total capacity of 50,000 ft^3 to a pressure of 300 psig. Note that this system is capable of filling the tanks to the aforementioned pressure in approximately 30 minutes. The air supply to the modulator was regulated using a 6” valve and delivered using 6” diameter piping. A 240 gallon accumulator was also placed in-line between the valve and modulator to reduce the pressure fluctuations within the pneumatic supply system. A schematic diagram of the air delivery system is shown in Figure 6.

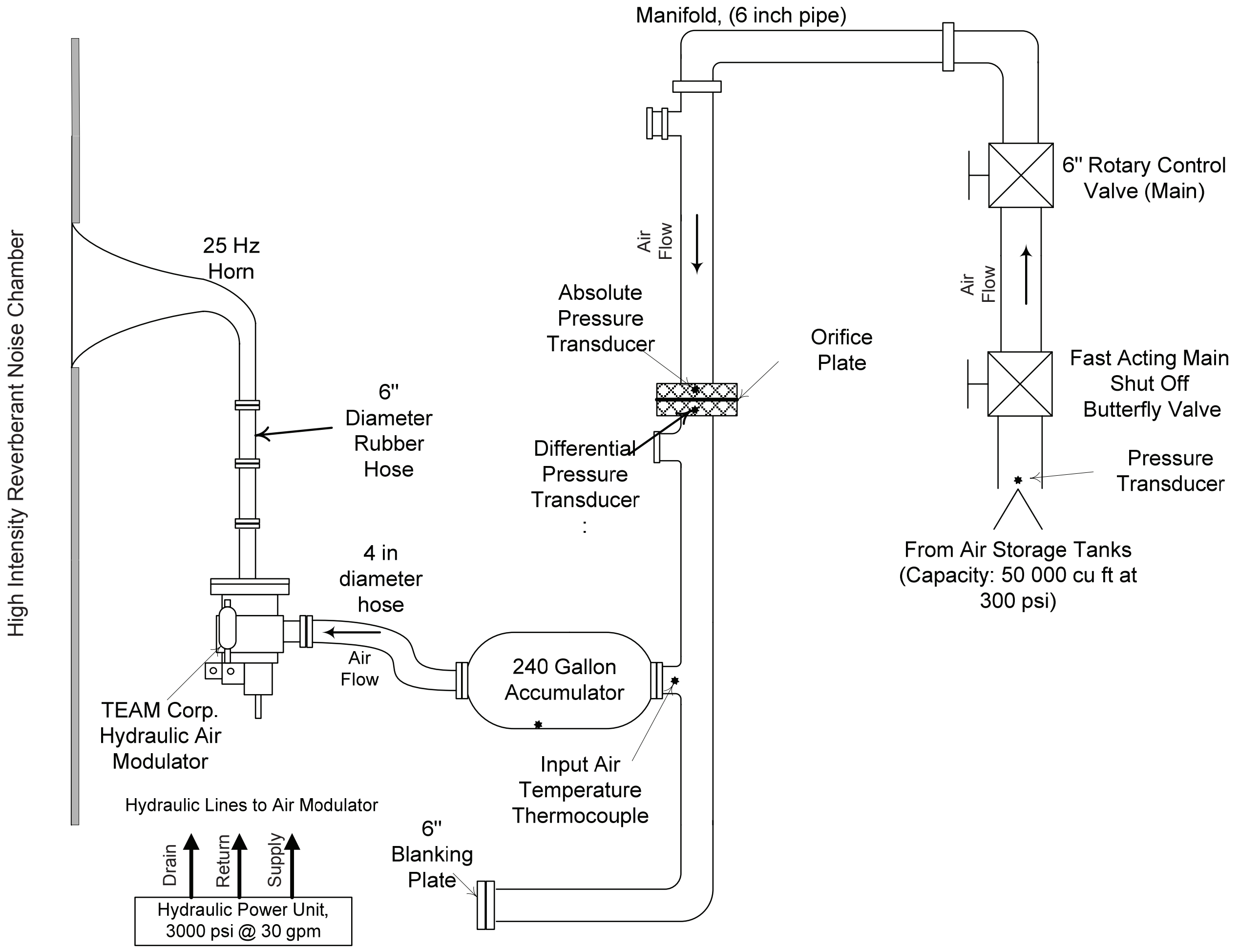
Manifold, (6 inch pipe)
6" Rotary Control Valve (Main)
Air Flow
Air Flow
High Intensity Reverberant Noise Chamber
25 Hz Horn
Absolute Pressure Transducer
Orifice Plate
Fast Acting Main Shut Off Butterfly Valve
6" Diameter Rubber Hose
Differential Pressure Transducer
Pressure Transducer
From Air Storage Tanks (Capacity: 50 000 cu ft at 300 psi)
4 in diameter hose
Air Flow
240 Gallon Accumulator
TEAM Corp. Hydraulic Air Modulator
Input Air Temperature Thermocouple
Hydraulic Lines to Air Modulator
6" Blanking Plate
Drain
Return
Supply
Hydraulic Power Unit, 3000 psi @ 30 gpm

Figure 6: Schematic of Air Delivery System used in Modulator Testing.

4.3 Data Acquisition Systems

There were two types of data collected namely acoustic and pneumatic/hydraulic data. The acoustic measurements were used to establish the sound power emitted from the modulators, while the principal use of the pneumatic data was to determine process parameters such as temperature, pressure and mass-flow, which were used to determine the efficiency of the modulators. The hydraulic data was mainly used in a monitoring capacity.

As expected, the sampling rate requirement for the two types of data were very disparate; the acoustic data was sampled at 25.6 k-samples/sec, while the process data was sampled at 100 samples/sec. The acoustic data was collected and processed using an LMS Test.Lab system, while a National Instruments/Labview system was used to collect and process the raw pneumatic measurements.

4.4 Acoustic Measurements

Each of the modulators with its support system and horn adapter was installed inside the horn/modulator room of the NRC test chamber in Ottawa, Ontario. A photograph showing the Team MK-VI modulator during testing at the NRC is shown in Figure 7. The supply gas was dry air at 20°C and was connected to the two modulators through a single T-junction connection. One of the modulators was connected to the 25 Hz horn and the other was connected to either a 100 Hz or 160 Hz horn. Tests were performed with each modulator operating alone on each of the two horns and also with both modulators operating at the same time. The gas pressure to each modulator was the same when two modulators were operating together.

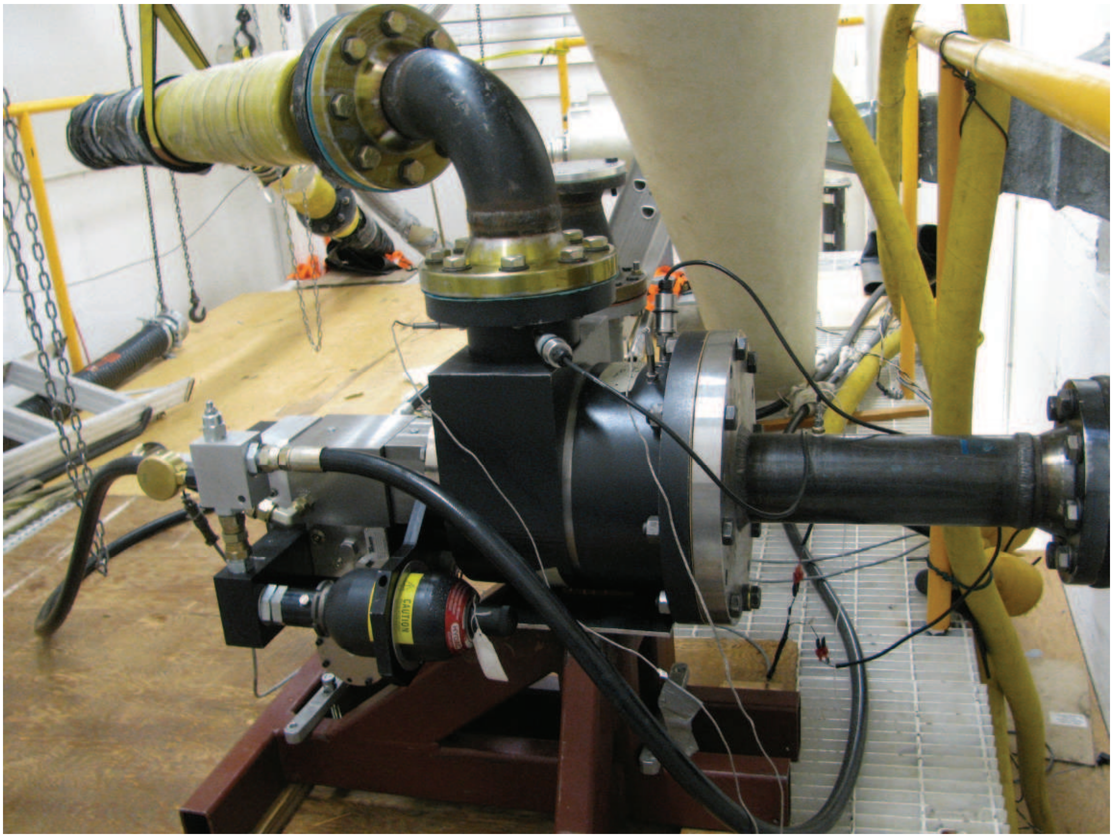

Figure 7: Team MK-VI Modulator during Testing at NRC.

The test process was as follows: the modulator was energized at a single pressure and a broad-band noise signal, set at a particular dc bias and shaped in 1/3 octave bands, was commanded to the servo-amplifier of the modulator to control the modulator valve. The resulting sound pressure level was measured inside the chamber using a minimum of six free field microphones. Time averaged (about 30 seconds) 1/3-octave band spectra were recorded from each of the microphones. The test at the set gas pressure was repeated with several modified 1/3-octave band noise signal inputs to the servo-amplifier. Tests were also performed with a different dc-bias value. The influence of the hydraulic fluid pressure was also evaluated for a few test conditions.

The above test was repeated for six pre-set gas pressures. This test procedure was repeated for a number of different modulator-horn combinations including: MK-VI on a 25 Hz horn, MK-VI on a 100 Hz horn, MK-VII on a 25 Hz horn, and MK-VII on a 100 Hz horn; both single and dual modulator operations were tested.

In addition, the chamber reverberation time was also measured in 1/3 octave bands from 50 Hz to 10,000 Hz and the relative humidity was kept below 5% for the reverberation time tests. The following parameters were recorded for each test condition:

- 1/3-octave band sound pressure levels from each microphone in the test chamber
- 1/3^{-}octave band sound pressure levels from a microphone placed in the horn room
- Test chamber pressure
- Test chamber temperature
- Chamber air humidity

4.5 Process Measurements

The following quantities also were also measured in order to allow for a complete characterization of the modulator performance:

- Modulator inlet and outlet air pressure
- Modulator inlet and outlet air temperature
- Modulator hydraulic supply and return pressure
- Modulator air mass flow

An orifice plate was installed in the manifold to allow for mass flow measurement during testing. The mass flow, $\dot{m}$, and volume flow (in Standard ft^3 per Minute, SCFM), Q_{SCFM}, are obtained from the orifice plate inlet pressure, P_s, differential pressure across the plate, ΔP_j, and the air temperature, T, as follows:

$$\dot{m} = CA_O\sqrt{\frac{2\Delta P_j P_s}{RT}}$$

$$Q_{SCFM} = \frac{CA_O}{P_{atm}}\sqrt{2RT\Delta P_j P_s}$$

R, is the gas constant for air, P_{atm}, is the atmospheric pressure, A_O, is the orifice area, and C is the discharge coefficient of the orifice plate, which is equal to 0.615. The mass flow computation allows for the evaluation of the air stream to acoustic power efficiency.

4.6 Acoustic Control System

The noise input to the NRC reverberant chamber is controlled using a proprietary acoustic control system, initially developed by NRC in the 1990's. The current implementation of the control system uses a high performance National Instruments (NI) PXI Embedded Real Time Controller for deterministic real-time operation. The system consists of a NI PXI-1042 chassis equipped with a PXI-8106 embedded controller and three PXI-4461 I/O modules, each of which has a pair of analog input and output channels with 24-bits A/D and D/A convertors. The control algorithm executes on the real time controller (running a real-time operating system, RTOS), while program I/O executes on a regular Windows-based PC. Communications between both computers occurs via an Ethernet connection.

The control target is specified in terms of 1/3-octave band levels from 25 Hz to 2000 Hz. A Gaussian white noise signal is filtered by a bank of 1/3-octave filters whose attenuation values are controlled by individual feedback control loops. The 1/3-octave filters are implemented in the digital domain using 10th order IIR filters that are ANSI and IEC compliant.

5.0 MODULATOR TEST RESULTS

The present section provides details of the experimental results collected during the test program. These include the modulator characterization tests as well as the closed loop tests.

5.1 Performance Characterization Test Results

In addition to measuring the acoustic output power as a function of various parameters, other aspects of the modulator behavior, including dynamic range, repeatability, and the effect of signal spectral properties were also evaluated.

5.1.1 Acoustic Power Output

The total modulator acoustic power was calculated from the averaged chamber sound pressure levels, the measured chamber reverberation time values and the various adjustment factors that are described below. The acoustic power level at the horn mouth, denoted as PWL_1 is given by the following equation:

$$PWL_1 = SPL + 10\log(S\alpha + 4\beta V)$$

where SPL is the averaged chamber sound pressure levels, S is total surface area including adjustments for vents and horns; α is the wall absorption coefficient, computed from the chamber reverberation time values, V is chamber volume and β is the air absorption coefficient of the chamber. The acoustic power level of the modulator, denoted as PWL_2 is related to PWL_1 by the following relationship:

$$PWL_2 = PWL_1 + 10\log(\varepsilon) + \text{Wall corner effects} + \text{Spill over} + \text{Horn Efficiency}$$

where ε is the coupling efficiency, defined as $\varepsilon = M/(M+1)$, where M is the Modal overlap Index, with $M = \eta\Delta$. η is the Modal density and Δ is the half power-pass band. The correction for wall corner effects is given by [5]:

$$\text{Wall Corner Effects} = 10\log(1 + Sc/8fV)$$

The spill-over loss is assumed to be 0.2 dB, based on typical values. The horn efficiency is assumed to be 30% for a typical exponential horn (the efficiency is usually between 30 and 35%). The acoustic powers of the modulator for typical test runs are shown in Table 2 below.

Table 2: The Sound Power Output of Team Modulators

Modulator Type	Test Run No	Modulator PWL, dB re 10^{-12} watts	Modulator Power, kW
MK-VI	#7	169	77
MK-VI	#8	172	150
MK-VII	#9	173	200
MK-VII	#18	172	152

The results of Table 2 clearly shows that the Team modulators are capable of producing 150 kW (MK-VI modulator) and 200 kW (MK-VII modulator) as advertised. Note that cases that yielded less than the maximum modulator power corresponded to non-optimal servo bias, input spectra and/or gas supply pressure settings.

5.1.2 MK-VI Modulator General Behavior

For the tests described in this section, the MK-VI modulator was coupled to a 100 Hz horn. The MK-VI is designed to have improved higher frequency performance, which inherently sacrifices its low frequency behavior.

A number of different input signals were applied to the modulator:

a) A flat white noise spectrum from 80 Hz to 800 Hz;

b) Several spectra obtained by shaping the flat 80 Hz to 800 Hz spectrum;

c) Individual 1/3-octave band or octave band signals.

The key acoustic results obtained for the MK-VI modulator are presented in Figure 8. The effect of modulator output with supply pressure is shown in Figure 8 (a). Between 125 and 225 psig, the supply pressure has a negligible effect on the acoustic output of the modulator. Note that for the cases in Figure 8(a), the shape of the input spectra was white noise between 80 Hz and 800 Hz. The effect of the spectral shapes of the input signal is shown in Figure 8 (b). The results show that the shaping of the input signal is reflected in the shape of the output spectra, indicating a high degree of spectral controllability. These results also illustrate the affect of the 100 Hz horn characteristics on the output for a flat white noise spectrum.

The effects of applying input noise exclusively within a single 1/3-octave band are shown in Figure 8 (c) and (d), where noise is contained only within the 100 Hz and 250 Hz bands, respectively. In each case, two signal gain values, as indicated in the figure legends, are applied. These results suggest that the desired modulator output spectra and levels can be readily obtained by adjusting the input spectra shape and levels. This again demonstrates that the modulator exhibits good controllability characteristics. This aspect will be examined in greater detail later in this paper. The repeatability of the Team MK-VI modulator was evaluated simply by repeating measurements with identical input spectra, gas supply pressure and the servo bias settings. In many cases, the repeated measurements were conducted on different days. In all cases the repeatability was excellent. Figure 8 (e) and (f) shows two such cases.

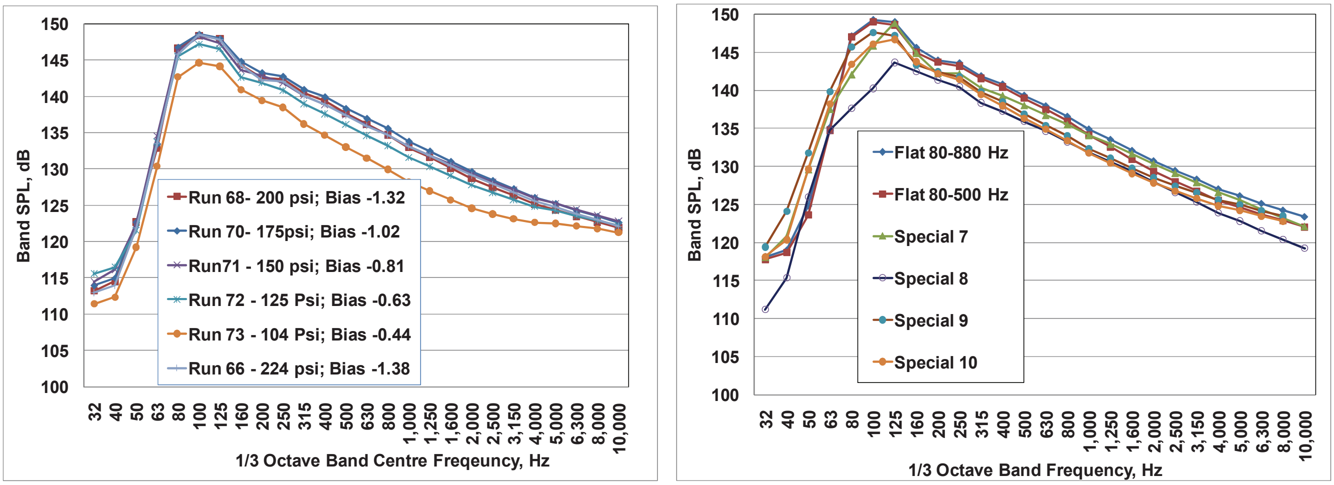

(a) Effect of Supply Pressure (b) Effect of Signal Shape

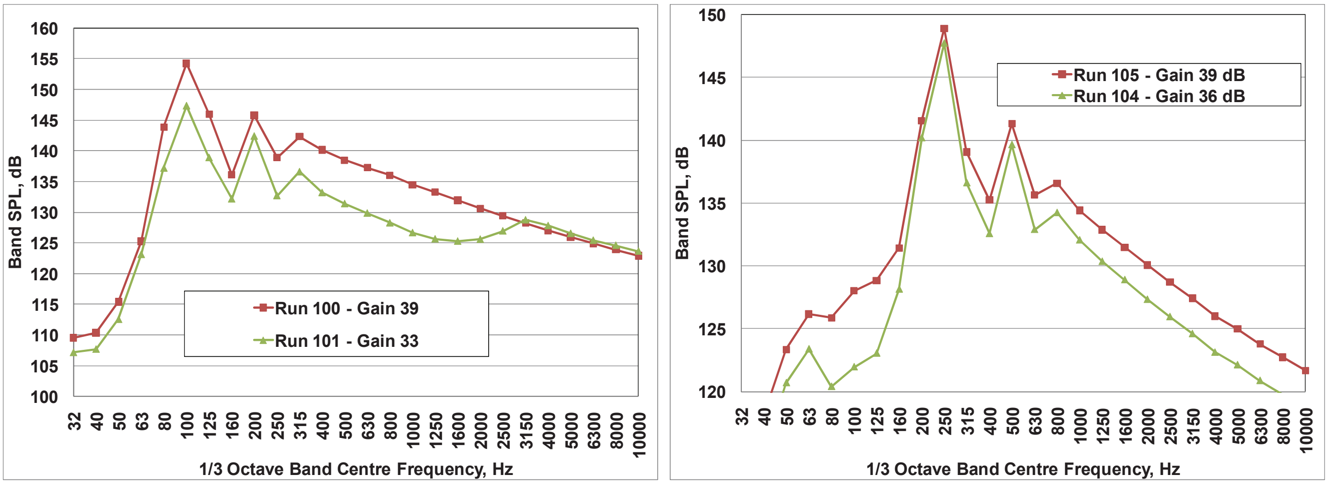

(c) Effect of Signal Gain and Signal Shaping, case 1 (d) Effect of Signal Gain and Signal Shaping, case 2

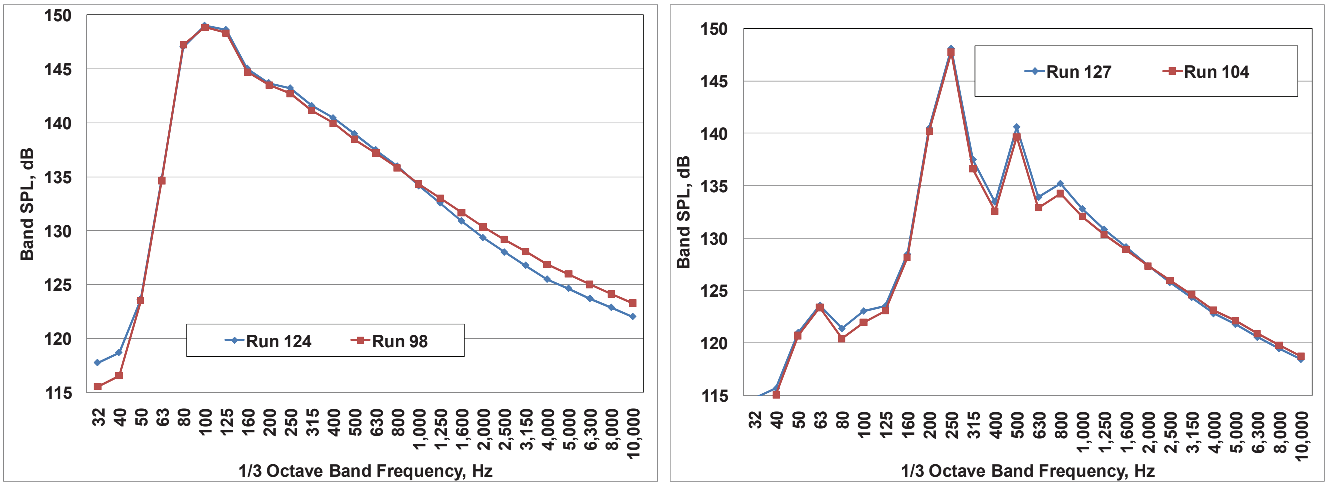

(e) Repeatability Test, trial 1 (f) Repeatability Test, trial 2

Figure 8: The behavior of MK-VI Modulator.

5.1.3 MK-VII Modulator General Behaviour

With the MK-VII modulator coupled to a 25 Hz horn, a few different combinations of the input signal were also applied:

a) A flat spectrum from 25 Hz to 800 Hz;

b) Several spectra obtained by shaping the flat 25 Hz to 800 Hz spectrum;

c) Individual 1/3-octave band or octave band signals.

Compared to the MK-VI, the MK-VII was typically tested with input signals that had greater energy content in the low frequency range to exploit its frequency response range. The effect of supply pressure on the performance is shown in Figure 9 (a). These results show that at and above a supply pressure of approximately 115 psig, the acoustic output of the MK-VII modulator is essentially invariant with pressure. The case shown with a low acoustic output is the result of an extremely low supply pressure, well below the rated minimum supply pressure of 120 psig. The variation of the output power spectrum with input signal spectrum is shown in Figure 9(b). In particular the additional energy content in the bands from 100 to 800 Hz is clearly visible when the corner frequency of the input signal is increased from 100 Hz to 800 Hz. Spectra 2 and 4 attenuate the baseline input spectrum (flat to 800 Hz) beyond 100 and 400 Hz by 3 dB per octave, and the effects are seen accordingly in the output spectra.

The combined effect of signal gain and narrowband performance is shown in Figure 9 (c) and (d). In the former case, input energy is only contained within the 50 Hz 1/3-octave band. Apart from some spill-over in the 100 Hz band, the output power is concentrated within the 50 Hz band. Furthermore, the effect of the input gain appears at the output in a linear fashion. The same can be said when the energy is contained within the 200 Hz 1/3-octave band, as shown in Figure 9 (d). The repeatability of the MK-VII is exemplified by the results shown in Figure 9 (e) and (f) for two representative cases.

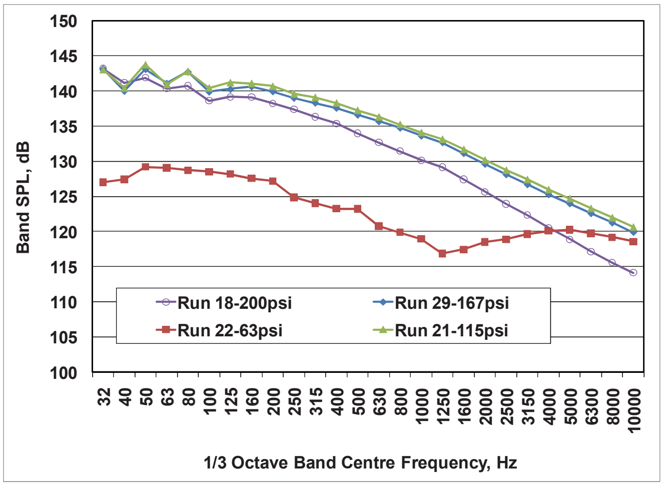

(a) Effect of Supply Pressure

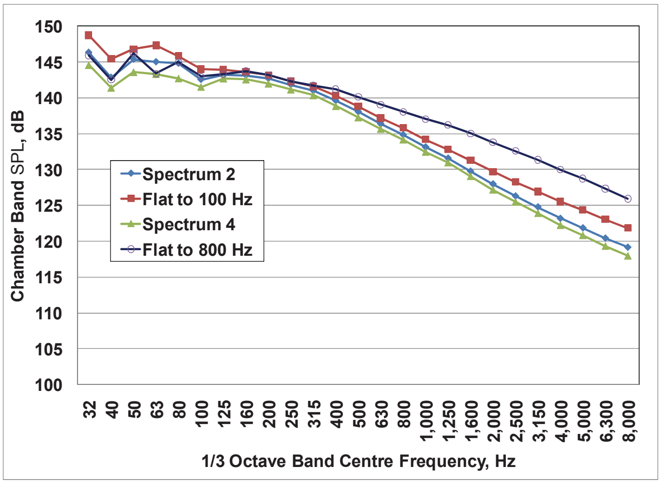

(b) Effect of Signal Shape

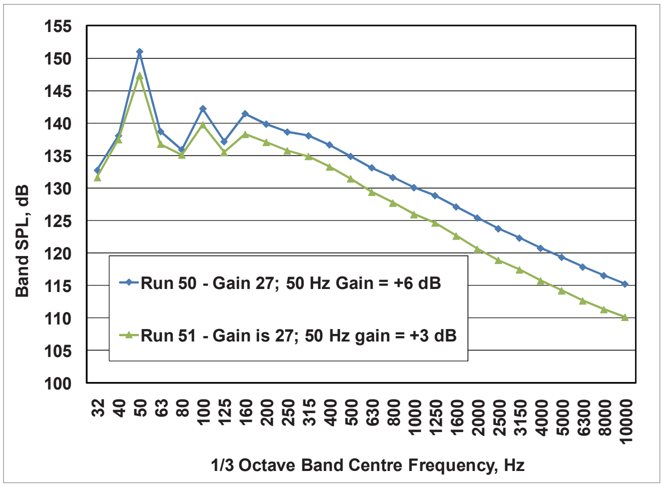

(c) Effect of Signal Gain and Signal Shaping, case 1

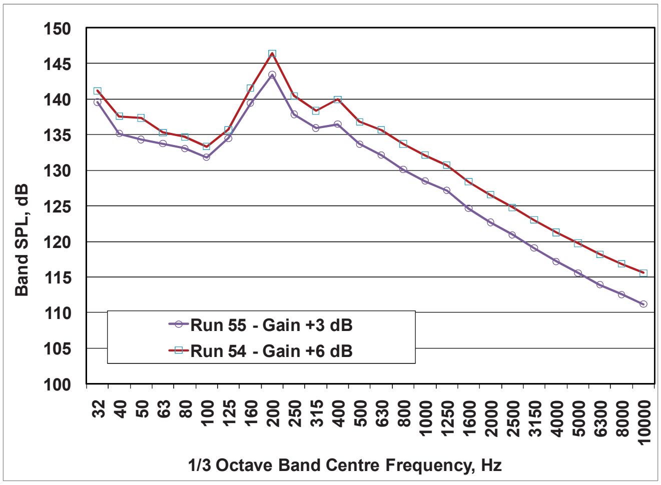

(d) Effect of Signal Gain and Signal Shaping, case 2

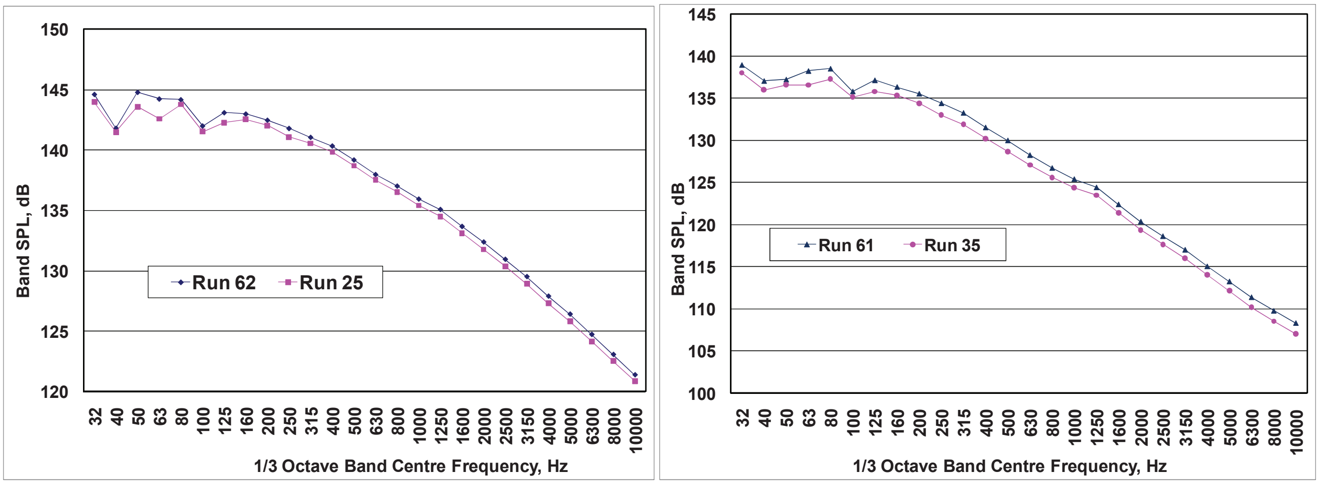

(e) Repeatability Test, trial 1

(f) Repeatability Test, trial 2

Figure 9: The behavior of MK-VII Modulator.

5.1.4 MK-VI Modulator Dynamic Range

The achievable dynamic range of a modulator is an important parameter that contributes to the complexity of the modulator layout required during a test program. A test program for a given test article invariably consists of testing to a series of spectral targets ranging from 15 dB below flight levels to in some cases several dB above. If a given modulator does not have sufficient dynamic range, a number of modulator configurations employing a varying number of modulators is required to encompass the range of spectral targets; the lower the dynamic range of a given modulator, the greater the number of required configurations.

Three spectral shapes were applied to characterize the dynamic range of the modulator. The results are shown in Figure 10 for two of the spectral shapes. The key observation is that the dynamic range that can be obtained for the MK-VI modulator is between 6 and 9 dB. Note that the dynamic range was found to be dependent on the input signal spectral shape.

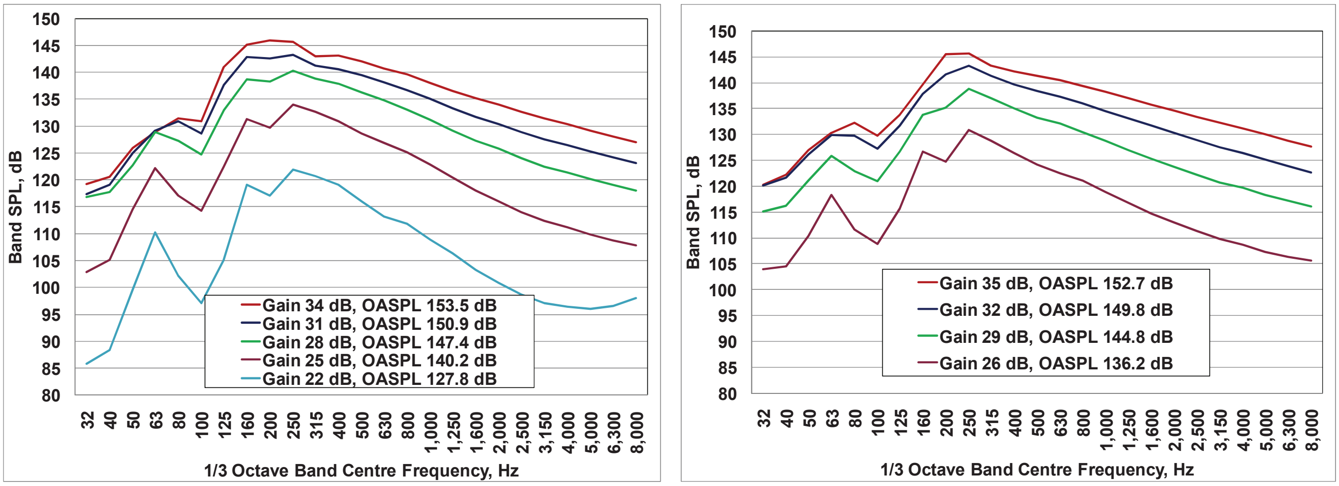

Figure 10: The Dynamic Range of MK-VI Modulator.

5.1.5 MK-VII Modulator Dynamic Range

Three spectral shapes were also applied to test the dynamic range of the modulator, and the results are shown in Figure 11 for two input spectral shapes. For the MK-VII modulator, the dynamic range is between 9 and 12 dB. As was the case with the MK-VI, the measured dynamic range is dependent on the spectral shape of the input signal.

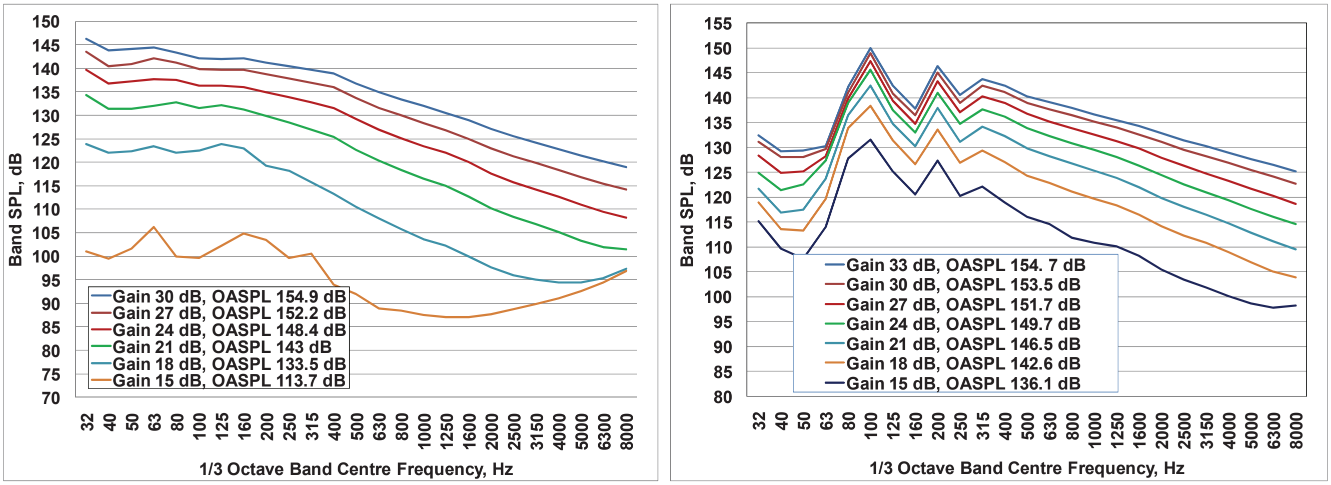

Figure 11: The Dynamic Range of MK-VII Modulator.

5.2 Controllability Test Results

The closed loop control for reverberant chamber acoustic spectrum control essentially involves applying an array of feedback loops to control the attenuation values of a bank of 1/3-octave filters. In typical control operations, the initial attenuation factors for each 1/3-octave frequency band would be pre-determined during an empty chamber calibration test to allow for quick convergence once the test article is placed in the chamber.

Since the initial attenuation factors were not known a priori for each test spectrum, the current control testing is to be considered as calibration mode testing, where large attenuation factors were used to begin the test. The above process was applied so that the noise levels do not overshoot the target sound levels. Five spectral shapes, each scaled to meet the achievable overall sound pressure levels in the NRC chamber with a single Team modulator, were used for the testing. Furthermore, the controllable frequency range for the chosen shape was adjusted to be within the operational range of the chosen modulator-horn combination. For example, the controllable range for the MK-VII on the 25 Hz horn is 31.5 Hz to 500 Hz. Similarly, the controllable range for the MK-VI on the 160 Hz horn is 125 Hz to 500 Hz.

The following process was applied:

- one of the chosen spectra was applied to the controller with the attenuators set at 100 dB below the target levels
- the controller was started
- the modulator takes a few seconds to initiate and once initiated it quickly rises to meet the target.
- The average of six microphone signals was used as the control parameter.

The time signals of all the microphones as well as the control signal, i.e., the six-microphone average, were recorded for at least two minutes after stabilization of the overall signal.

5.2.1 MK-VI Modulator Controllability

The results of the closed loop control tests for the MK-VI on the 160 Hz horn are presented as a time history to evaluate the rise time as well as the steady state statistics after the signal stabilizes to the set target. The average, standard deviation, deviation to maximum point, and deviation to minimum point were evaluated from the point of stabilization to the end of recording of that test. The results are shown in Figure 12 for one of the spectra tested.

For this specific closed loop test, the rise time is in the range of 25 to 35 seconds. Note: these rise times only represent those expected during initial empty chamber tests for a given spectrum. Once the appropriate attenuation factors are then applied for the actual test, these rise times would be reduced. The signal is seen to be reasonably steady with the standard error of one dB or less for most cases.

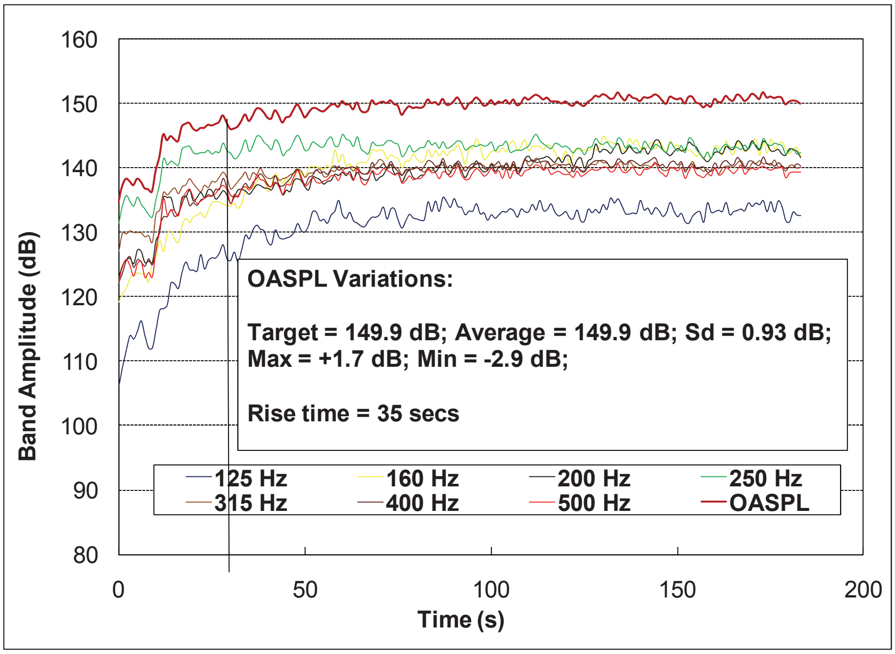

Figure 12: Closed Loop testing of MK-VI Modulator

5.2.2 MK-VII Modulator Controllability

The results of the closed loop control tests for the MK-VII on the 25 Hz horn are presented as a time history to evaluate the rise time as well as the basic statistics after the signal stabilizes to the set target. The average, standard deviation, deviation to Maximum point, and deviation to Minimum point were evaluated from the stabilization point to the end of recording of that test. The results are shown in Figure 13 for one of the spectra tested.

Once again, the rise time is in the range of 25 to 35 seconds and as was the case with the MK-VI, these are the rise times from a large attenuation initial state. Calibration runs will be employed to determine appropriate initial conditions for the controller to facilitate a much quicker response time. The steady state performance of the MK-VII in this case is slightly improved over the case presented for the MK-VI earlier.

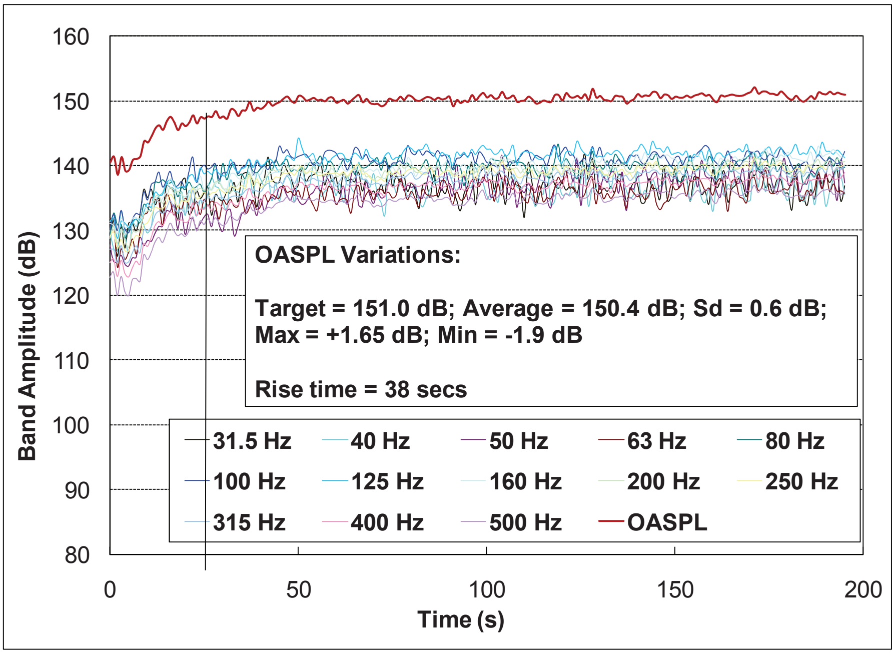

Figure 13: Closed Loop testing of MK-VII Modulator

6.0 CONCLUSIONS

An operational need for the design and development of a very large reverberant acoustic test facility at NASA Glenn Research Center with an extremely high acoustic power requirement necessitated the careful examination of the acoustic output power of available noise generators. Two models of modulators supplied by Team Corporation appeared to have the necessary acoustic output and frequency characteristics. However, a detailed characterization of these modulators was necessary to mitigate the risk of the proposed chamber design. Consequently, a series of test programs were performed that in addition to characterizing the generated noise, also examined the controllability, dynamic range and the optimal performance region of the modulator.

The test program was performed at the NRC-IAR reverberant chamber, located in Ottawa, Ontario, Canada and demonstrated that the modulators were capable of producing their rated acoustic power (150 kW for the Team MK-VI and 200 kW for the MK-VII), and had a dynamic range of between 6 and 9 dB for the MK-VI, and between 9 and 12 for the MK-VII. Furthermore, both modulators exhibited excellent repeatability and sufficiently controllability to allow for their control via currently available acoustic control systems.

7.0 ACKNOWLEDGEMENTS

The authors would like to acknowledge the contribution of their colleagues during the test program. In particular the NRC authors would like to thank Luc Hurtubise, Brent Lawrie, Viresh Wickramasinghe, David Zimcik, Sebastian Ghinet and Manouchehr Nejad-Ensan for their effort during the various test phases. Aiolos Engineering Corp would like to thank the engineering team members of Aiolos and Benham, headed up by Ralph Leitner and Neil Waggoner, respectively, for their many contributions to making this test program happen. The NASA author would like to acknowledge the NASA SET Project Office for their support and funding for this test program. He would also like to acknowledge the extensive and valuable engineering test support provided by Aron Hozman, Anne McNelis, and Mark McNelis from NASA GRC, and Dr. Jerome Manning and Dr. Patricia Manning from Cambridge Collaborative Incorporated. Team would like to acknowledge and thank Bob Tauscher from Team and Neil Waggoner from Benham.

8.0 REFERENCES

1. Hughes, W,O., McNelis, M.E., Hozman, A.D., and McNelis, A.M., “Status and Design Features of the new NASA GRC Reverberant Acoustic Test Facility (RATF)”, *Proceedings of the 2010 IEST Annual Technical Meeting, ESTEC 2010*, 3-6 May 2010, Reno, NV, USA.
2. Otten, K.D., Suarez, V.J. , and Le, D.K., “Status and Design Features of the new NASA GRC Mechanical Vibration Facility (MVF)”, *Proceedings of the 2010 IEST Annual Technical Meeting, ESTEC 2010*, 3-6 May 2010, Reno, NV, USA.
3. Hughes, W.O., McNelis, M.E., Hozman, A.D., McNelis, A.M., “The Testing Behind the Test Facility: The Acoustic Design of the NASA Glenn Research Center’s World-Class Reverberant Acoustic Test Facility”, NASA/TM-2010-216802, October 2010.
4. Fiala, W.T., Hilliard, J.K., Renkus, J.A., Van Houten, J.J., “Electropneumatic Acoustic Generator”, *Journal of the Acoustical Society of America,* Volume 38, Issue 6, pp. 956-964, December 1965.
5. Kutruff, H., *Room Acoustics*, 3rd Edition, Elsevier, London, 1991.

Human Induced Dynamic Loads Estimation Based on Body Motion

Paolo Mazzoleni[1], Emanuele Zappa[2]

Politecnico di Milano, Department of Mechanics
via Giuseppe la Masa 1, 20156, Milan (Italy)

[1]paolo2.mazzoleni@mail.polimi.it
[2]emanuele.zappa@polimi.it

ABSTRACT

Crowd motion on civil structures that host musical and sport events is one of the main causes of excessive vibrations. In scientific literature many works, related to the measurement of forces induced by a single volunteer, or few of them, can be found; but the extension of these results to a crowd is a non trivial operation because of crowd synchronisation effect; moreover obvious practical problems arise in measuring the forces due to many people. This work presents an innovative algorithm to estimate such an excitation without needing a direct force measurement but relying only on the knowledge of the motion of each subject in the crowd. As shown in a previous research, the motion of people in a crowd can be estimated through digital image correlation, starting from a movie of the stadia stand. The method proposed in this work was tested both for jumping and bobbing, within all the typical range characterizing these kinds of movements (1.5-3.5 Hz) and the obtained results are then validated with the signal acquired by a dynamometric platform. The results show an excellent correlation between expected and measured loads in the whole range, both for jumping and bobbing.

Introduction

The problem of human-structure interaction is becoming an increasing important matter in modern civil engineering. Such an issue can be decomposed into two main aspects [1]: on one hand the change of structural dynamic parameters due to the presence of crowd on the structure, on the other hand the effects of loads induced by the motion of the crowd itself.

Regarding the latter aspect, actions that are typically able to produce significant forces, that is eventually excessive vibrations, are: walking (problem related to pedestrian bridges), and jumping or bouncing, that can affect all those structures aimed to host sport events and, above all, musical performances, where the rhythm of the songs synchronizes the people movements.

The modern architecture propensity to realize more slender designs has resulted in an increase of stands flexibility, i.e. in lower natural frequencies of the structures, approaching the typical range of induced loads.

The well known case of the Millennium Bridge in London [2] is probably the most significant example concerning the pedestrian bridges. As for the large structures (mainly the stadia), problems of excessive vibrations due to human induced loads have been noticed, measured and study in many stadia: Maracana [3] and Morumbi [4] in Brazil, Feyenoord [5] in Nederland, Old Trafford, Highbury [6] and Anfield [7] in the United Kingdom, Meazza in Italy [8] and so on. The most important effects was probably the ones recorded at June 8th, 1985, at the Ullevy Stadium in Goteborg, Sweden, during a Bruce Spreesting concert: the induced vibrations were so high to damage the structure and a massively restructuring and structural changes were required after the event [9].

Without the reaching of such an extreme condition, excessive vibration could generate panic in the people or bring to cracks nucleation and propagation, and therefore it must be avoided.

Many papers present in scientific literature gives us important information regarding the characteristic frequencies of the motion induced loads [10,11,12,13,14]; such results can be summarized in a range between 1.5 and 2.8, as indicated by [15], neglecting higher frequencies where it is difficult for a crowd to maintain the synchronization.

Regarding the induced loads, Bachmann e Ammann proposed to model them as a semi sinusoidal pulse [16], while J.H.H. Sim [17] introduced a cosine-squared function to best represent the spectral characteristic of these forces. All the data collected for these and similar researches are direct measure of the induced loads, using dynamometric platforms and testing a high number of volunteers to create a solid statistic.

T. Proulx (ed.), *Sensors, Instrumentation and Special Topics, Volume 6*, Conference Proceedings of the Society for Experimental Mechanics Series 9,
DOI 10.1007/978-1-4419-9507-0_13, © The Society for Experimental Mechanics, Inc. 2011

Further works [17,18,19] try to forecast, starting from these data, the loads that can be induced by a crowd.
However there are two main aspects that make difficult this operation. The first one is the so called “crowd effect” [20] and it refers to a phenomenon for which is easier for a person to follow an acoustic rhythm if he can see other people doing the same. This behaviour is well known as an experimental evidence [14], but not yet analytically modelled. The second issue is the influence of structural movement on the jumping, that once again tend to increase the synchronization among people [21,22].
These two aspect are the main reasons that make the state of the art simulations of crowd induced loads not satisfactory [1,23] and prompted the authors to address the problem from a different point of view.
Previous researches carried out at the Mechanical Department of the Politecnico di Milano [24,25], successfully applied the digital image correlation technique to the crowd motion estimation.
This paper shows how it is possible to exploit these results in order to obtain a reliable estimation of human induced loads, both from jumping and bobbing, in the whole frequency range of interest.

Experiments: Design and Setup
Volunteers were asked to jump and bounce one by one following the rhythm marked by a metronome. A total of 42 tests (21 bobbing, 21 jumping) were performed, investigating a frequency range from 1.5 to 3.5 Hz, step 0.1 Hz, for both types of movement. For every test three different quantities were acquired:

- vertical force induce by the movement of the volunteer on the ground through a dynamometric platform;
- vertical acceleration of 8 parts of the body of the experimenter by means of 8 mems piezo-resistive accelerometer;
- a video of the motion of the volunteer, using a greyscale 1024x521 global shutter CCD camera.

Force and acceleration time histories were acquired at 300 Hz while the movies were captured with an acquisition frequency of 30 Hz; both the systems share the same trigger signal, ensuring synchronicity in the beginning of the acquisition.

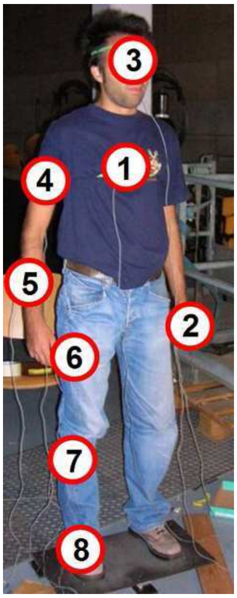

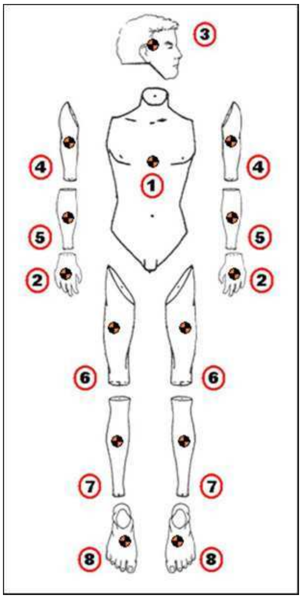

———·100

The sum of all these signal is used as the estimation of the induced load: in other words this means to assume that the induced force is manly due to gravitational and inertial contributions, considering only the movements along the vertical direction.

Fig. 2 Comparison between measured and estimated forces for both jumping and bobbing tests at 2.5 Hz; results in both time and frequency domain

In Fig. 2 we can find a comparison of the loads estimated with the described procedure versus the ones directly measured by the dynamometric platform. The figure shows a substantial correspondence between measured and estimated loads, both in time and frequency domain. The operation has been repeated for all the test; in order to have an idea of the trend of the results, the percentage error, $\delta^{\%}$, between the modules of the first spectral component has been chosen as index of the quality of the approximation:

$$^{\%} = \frac{_{1} \; - \; _{1}}{_{1}} \cdot 100$$

Data analysis and results II: accelerometers Vs digital image correlation

The goal of this chapter is to verify if the digital image correlation code is able to give a reliable estimation of the accelerations of the different parts of the body, in order to be able to substitute in the previously described method a non contact measuring technique, useful in the case of a crowd motion, when it is impossible to apply several accelerometers to every person.

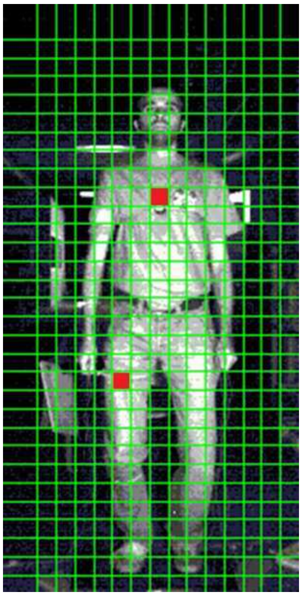

Fig. 4 Fist frame of a 2.5 Hz jumping test with DIC subset division superimposed; indicated the selected subsets for the comparison

Fig. 4 shows the subset division done by the DIC algorithm (subset size 64x64px overlap 50%). In order to verify the reliability of the measure, the time history of the two different subset indicated, corresponding to the position of the two accelerometers placed in the most significant position according with Fig. 1, has been extracted. The results have been converted from [px/frame] to [m/s] and numerically derived to [m/s^2]. The comparison among these results and the accelerometer signals is shown in Fig. 5.

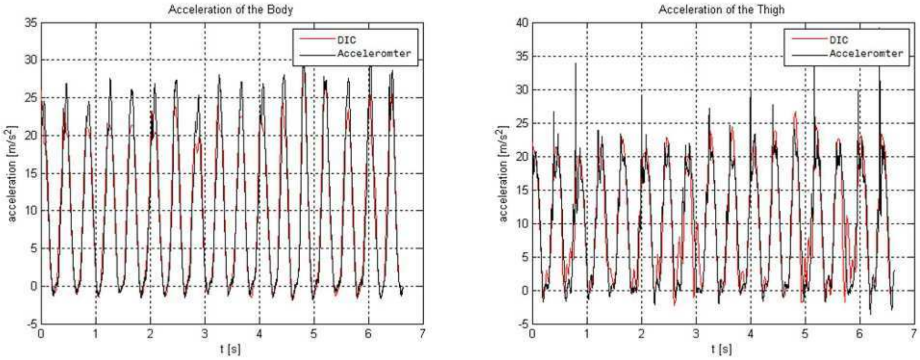

Fig. 5 Comparison between DIC results and accelerometer signals

The correspondence between the signal is clearly visible and analogous results are obtained for the others 6 sensors.

Data analysis and results III: loads from DIC Vs dynamometric platform

The first part of the data analysis showed how it is possible to obtain a reliable estimation of the induced force starting from the measure of vertical acceleration of the different parts of the body; the second one demonstrated that such a measure can be obtain using a non contact measuring technique. In this third part, the two contributions will be merged to obtain a evaluation of the loads relying only on a video of the motion of the subject.

In a real application it seems impossible to distinguish the different parts of the body of the jumper, so it has been decided to operate as follow: the DIC results are arranged in a 3D matrix (Fig. 6a), where rows and columns represent the region of the

field of view, while the velocity time history of each region is stored along the third dimension. The root mean squared velocity of each array has been evaluated, obtaining a 2D map (Fig. 6b).
It has been estimated that, with the zoom level used to grab the images, the upper part of the body of the volunteer is covered by approximately 100 subsets; this situation reflects what happens in a real environment, where the lover part of a person is covered by the people in front. So for every test the 100 subsets with the higher root mean squared velocity value are extracted (Fig. 6, b).

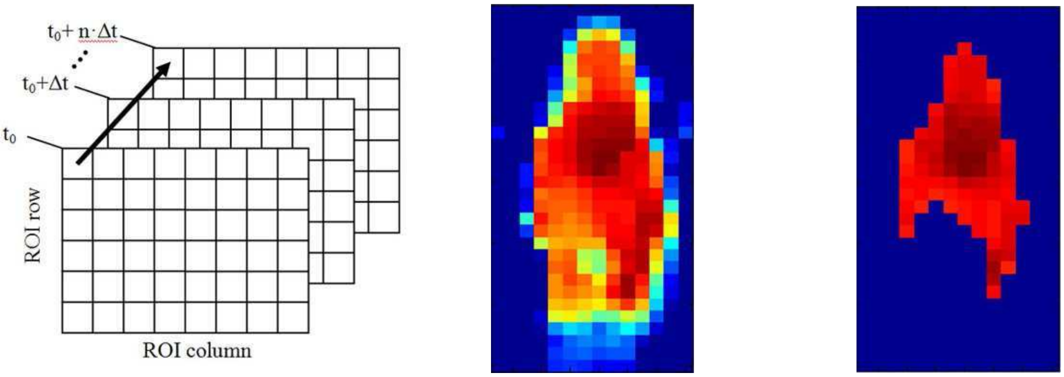

(a) (b) (c)

Fig. 6 (a) matrix of the DIC results; (b) R.M.S. map of the velocity for a 2.5Hz jumping test; (c) the same map filtered.

The mass of the volunteer is consequently equally divided into these subset, that is the time derivative of every time history (that is the acceleration) is multiplied by 1/100 of the volunteer mass. This operation imply the assumption that the mass distribution in the human body is equally spreads in the frontal area of the body itself. This is obviously an approximation but the previous chapter showed that the motion of the different parts of the body is very similar and so it's realistic to imagine that this assumption won't compromise the results. The sum of all these time histories of the inertial forces has been used as the estimation of the induced load. It is worth to notice that is operation is mathematically the same of calculating the average acceleration of the 100 subsets and multiplying it by the mass of the experimenter. As obvious, 100 is a number of convenience and linked to the zoom level used in this application, the same results are obtained selecting from 70 to 130 subsets, i.e. respecting the condition to take at least the upper part of the body correctly filtering the background.

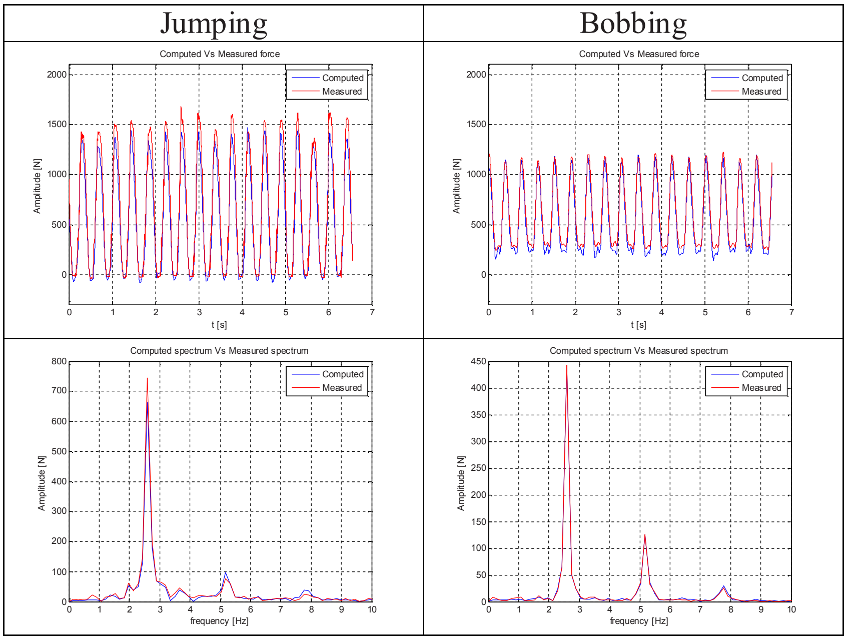

Fig. 7 Comparison between measured and estimated forces for both jumping and bobbing tests at 2.5 Hz; results in both time and frequency domain

As for the load evaluation computed with the accelerometer records, the measured and the estimated force signals show an high correspondence, both in time and frequency domain. Also in this case the percentage errors between the first spectral components has been evaluated.

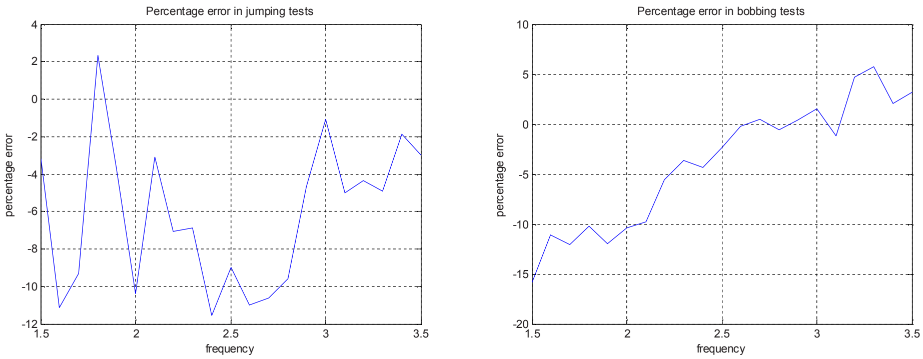

Fig. 8 Percentage error $\delta^{\%}$ trend in jumping and bobbing tests

The error analysis shows a reliability of the method even higher with respect to the ones found in the data analysis I chapter (that is using accelerometers), in particular for the higher frequencies. This is due to the fact that a non contact measuring techniques is not subjected to problems related to the sensor fastening. It remains instead an underestimation of the bobbing loads at lower frequency, likely related to the neglecting of rotation of some parts of the body in these kind of movements. Globally, the error is between 5 and 15%, with an average underestimation of about 5%, and with better results in the most important frequency range (2-3Hz). The general trend is very similar to the one showed in Fig. 3: in other words, the error is mainly associated to the model for the force reconstruction with respect to the uncertainty in the DIC measurements, in particular outside the 2-3 Hz range.

Conclusions and future developments

This paper proposes a new method to measure the dynamic load due to jumping and bobbing. The method is based on the motion analysis through a digital image correlation code and successive forces estimation starting only by a recorded video of the jumping people. Obtained results are encouraging: the error of the estimation of the first spectral component is less than 15% in all the considered cases, with further less discrepancy in the most significant range (2-3Hz). The use of a non contact measuring technique makes it attractive for applications in a real environment: future development will include test with more that one single volunteer in a real condition.

References

1. Sachse R., Pavic, A., Reynolds, P., Human-structure dynamic interaction in civil engineering dynamics: A literature review, Shock and Vibration Digest, v 35, n 1, p 3-18, January 2003.
2. Dallard P., Fitzpatrick T., Flint A., Low A., Smith R. R., Willford M., Roche M., London Millennium bridge: Pedestrian-induced lateral vibration Journal of Bridge Engineering, v 6, n 6, p 412-417, November/December 2001.
3. Batista R.C., Magluta C., Spectator-induced vibrations of Maracana stadium, Publ by A.A. Balkema, p 985, 1993.
4. Almeida P.A.O., Rodriguez J.F.S., Investigation of the vibrations induced by people in soccer stadiums, Proceedings of the International Modal Analysis Conference - IMAC, v 2, p 1417-1422, 1999.
5. Staalduinen V.P., Courage W., Dynamic loading of Feyenoord stadium during pop concerts, Symposium: Places of Assembly and Long-Span Building Structures, Birmingham, UK, 1994.
6. Rogers D., Two more wobbly stands, Construction News, August 2000.
7. Rogers D., Thompson R., Liverpool stand gets red card, Construction News, August 2000.

8. Cigada A., Caprioli A., Redaelli M., Vanali M., Vibration testing at Meazza stadium: Reliability of operational modal analysis to health monitoring purposes, Journal of Performance of Constructed Facilities, v 22, n 4, p 228-237, 2008
9. Erlingsson S., Bodare A., Live load induced vibrations in Ullevi Stadium-dynamic soil analysis, Soil Dynamics and Earthquake Engineering, v 15, n 3, p [d]171-188, Apr 1996.
10. Matthews C.M., Montgomery C.J., A dance floor with unsatisfactory dynamic response. Proceedings, Symposium/Workshop on Serviceability of Buildings (Movements, Deformations, Vibrations), Ottawa, Canada,1988.
11. Pernica G., Dynamic live loads at a rock concert, Canadian journal of civil engineering, v 10, n 2, p 185-191, Jun 1983.
12. Ginty D., Derwent J.M., Ji T., The frequency ranges of dance-type loads, Structural Engineer, v 79, n 6, p 27-31, March 20, 2001.
13. Littler J.D. , Frequencies of synchronized human loading from jumping and stamping, The Structural Engineer, 2003.
14. Agu E., Kaspersky M., A Random Load Model for Loads Induced by Coordinated Movements of Crowds, Proceedings of Eurodin, Paris, France, September 2005.
15. British Standards Institution (BSI). BS 6399: Part 1: Code of practice for dead and imposed loads. Londra, UK,1996.
16. Bachmann H., Ammann W., Vibration in structures: Induced by man and machines, Switzerland (Zurich), IABSE, 1987.
17. Sim J.H.H., Human-Structure Interaction in Cantilever Grandstands, thesis submitted for the degree of Doctor of Philosophy at the University of Oxford, 2006.
18. Parkhouse J. G., Ewins D. J., Crowd-induced rhythmic loading, Proceedings of the Institution of Civil Engineers: Structures and Buildings, v 159, n 5, p 247-259, October 2006.
19. Parkhouse J. G., Ewins D.J., Vertical dynamic loading produced by people moving to a beat Proceedings of the 2004 International Conference on Noise and Vibration Engineering, ISMA, p 821-835, 2004, Proceedings of the 2004 International Conference on Noise and Vibration Engineering, ISMA.
20. Ebrahimpour A., Fitts L. L., Measuring Coherency of Human-Induced Rhythmic Loads Using Force Plates, Journal of structural engineering New York, N.Y., v 122, n 7, p 829-831, Jul 1996.
21. Yao S., Wrigth J. R., Pavic A., Reynolds P., The effect of people jumping on a flexible structure, IMAC XXIV, Orlando, USA, 2003.
22. Yao S., Wright J.R., Pavic A., Reynolds P., Experimental study of Human-induced Dynamic forces due to jumping on a perceptibly moving structure, Journal of Sound and Vibration, v 296, n 1-2, p 150-165, September 12, 2006.
23. Dynamic performance requirements for permanent grandstands subject to crowd action, Interim guidance on assessment and design, Institution of Structural Engineers, UK.
24. Caprioli A., Cigada A., Sala R., Zappa E., Image based measurement of a stadium excitation due to jumping people, IMAC XXIV, 2006.
25. Caprioli A., Manzoni S., Zappa E., Crowd Motion Measurement Based on Image Processing, Wiley Interscience Journal, 2007.
26. Chandler R.F., Clauser C.E., McConville J.T., Reynolds H.M., Young J.W., Investigation of Inertial Properties of the Human Body. AFAMRL-TR-74-137, Aerospace Medical Research Laboratory, Wright-Patterson AFB, Ohio, 1974.

In the Field Validation of Human Induced Loads Measuring Technique

Paolo Mazzoleni[1], Emanuele Zappa[2]

Politecnico di Milano, Department of Mechanics
via Giuseppe la Masa 1, 20156, Milan (Italy)

[1]paolo2.mazzoleni@mail.polimi.it
[2]emanuele.zappa@polimi.it

ABSTRACT

Human induced vibrations on civil structures is a key problem in comfort and security design. The estimation of loads due to human motion is a critical and still unsolved problem, but it is fundamental for a correct design of new buildings and proper monitoring of existing. This work presents a validation of an imaged based measuring technique of these loads. The test-bed is the Meazza Stadium in Milan. The validation of the proposed technique is done as follows: some volunteers jump on a stand and the induced vibration is acquired; a video recording of the jumping crowd is acquired simultaneously. The video is analyzed using a digital image correlation (DIC) code in order to obtain a motion estimation and, starting from the DIC results, induced loads are predicted. Using the frequency response function of the stand, previously estimated through a dynamic characterisation of the structure, it is now possible to forecast the induced vibration and compare it with the acquired one. The results show a very high correspondence between the measured and estimated accelerations and, above all, the performances do not degrade increasing the number of volunteers.

Introduction

In the last decades, human-structure interaction has become an increasingly important aspect of the correct design of civil slender structures in terms of serviceability and safety. This issue includes all the aspects where the presence of human beings on a structure is able to 1)modify the dynamic properties of the construction, mainly modifying the mass and the damping parameters, or 2)induce loads that may result in excessive vibration of the structure itself [1].

This work deals with the second aspect of the human-structure interaction, focusing in particular on the loads induced by people jumping and bobbing on civil structure; this problem is particularly relevant in stadiums and large civil buildings that host sport and musical events [2,3,4]. In particular people motion during concerts is synchronized by music and this could result in loads that make the structure vibrate excessively [5,6,7].

Research carried out in the last years is focused on the investigation of this kind on loads. In addition to the mere description of the load typical frequencies [8,910] , some mathematical models have been proposed to reproduce the load induced by a single person jumping, as the "semi sinusoidal pulse model" [11] or the "cosine squared model" [12]. Further research went beyond, trying to forecast the load induced by a crowd, generalizing the results obtained with individual volunteers [12,13,14]. Such an operation is however very complex due to the intrinsic non linearity of the human being behaviour; there are two main aspect that it is difficult to take in account in these extrapolation procedures: the first one is the so called "crowd effect", that is the increase of a person's skill to follow a rhythm if they can see many people doing the same [12,15]. The second problem is related to how sensible movement of the surrounding structure can influence the motion of the occupants themselves [16,17]. The existence of these two phenomena has been experimentally verified in many tests, but at the moment there is not a model that can simulate, or mathematically reproduce, them. As a consequence, up to now there is not a reliable estimation of the load induced by a jumping crowd [1,18].

A research carried out in the Politecnico di Milano tried to face the problem from a different point of view: not a generalization of laboratory results from a single jumper to a crowd, but a measure of the loads themselves induced by a crowd. In this contest, the application of a digital image correlation (DIC) code to the "measure of motion" of a crowd has been successfully carried out [19,20]. The starting point is the acquisition of a movie of jumping people; the first frame of this movie is decomposed in small subsets and the algorithm looks for the most resembling zone of the second frame for each subset. Repeating the procedure for all the frames of the video is possible to extract the 2D displacement history of every subset, that is to have a motion estimation of the whole area framed by the camera.

T. Proulx (ed.), *Sensors, Instrumentation and Special Topics, Volume 6*, Conference Proceedings of the Society for Experimental Mechanics Series 9,
DOI 10.1007/978-1-4419-9507-0_14, © The Society for Experimental Mechanics, Inc. 2011

The next step of this research proposed a simple but effective method to estimate the induced loads starting from this motion measure [21]: assuming, as a first approximation, that the forces induced on the ground are only due to vertical inertia plus a constant value related to the gravity acceleration, it is possible to obtain an estimation of the loads multiplying the acceleration of every subset by the relative percentage of the total crowd mass. The sum of all these components gives the total induced loads.
This procedure has been successfully tested for a single jumper comparing the estimated loads with the ones recorded by a dynamometry platform. In this paper a "on the field" validation is proposed, with an increasing number of volunteers (from one to eight) . The validation of the method is done as follows: first of all the frequency response function of the used structure (a stand of the Meazza stadium in Milan) has been evaluated through the classical technique. Then some volunteers were asked to jump on this structure; a video to process is recorded in parallel with the vibration of the structure. From the video, using the proposed technique, it is possible to evaluate the induced loads and, thanks to the knowledge of the transfer function of the hosting structure, to forecast the stand accelerations. A comparison between the measured and computed structure vibrations gives the final validation to the technique.

Frequency response function estimation of a G. Meazza stadium stand

G. Meazza is the main stadium of the city of Milan; it hosts soccer matches of both the two main football teams in Milan and, during the summer, many musical events. Politecnico di Milano is in charge of the structure health monitoring of this structure. The structure is basically composed by three independent (from a dynamical point of view) "rings" (Fig. 1,a). The second ring is the one which showed higher vibration problems, mainly related to the cantilever beam structure of the stands; this is the reason why it has been chosen for the experiments of this work (Fig. 1,a). Once again, different stands are independent from a structural point of view.
In order to reconstruct the frequency response function (FRF), of a stand, the structure was excited step by step with a mono harmonic inertial load provided through a 120 kg mass moved in the vertical direction by an hydraulic actuator. The investigated range spans from 2 to 10 Hz, step 0.05 Hz. The piston is controlled in feedback through a linear variable differential transformer (LVDT) transducer. The acquisition of the LVDT signal allows, knowing the inertial mass, to estimate the force provided to the structure.

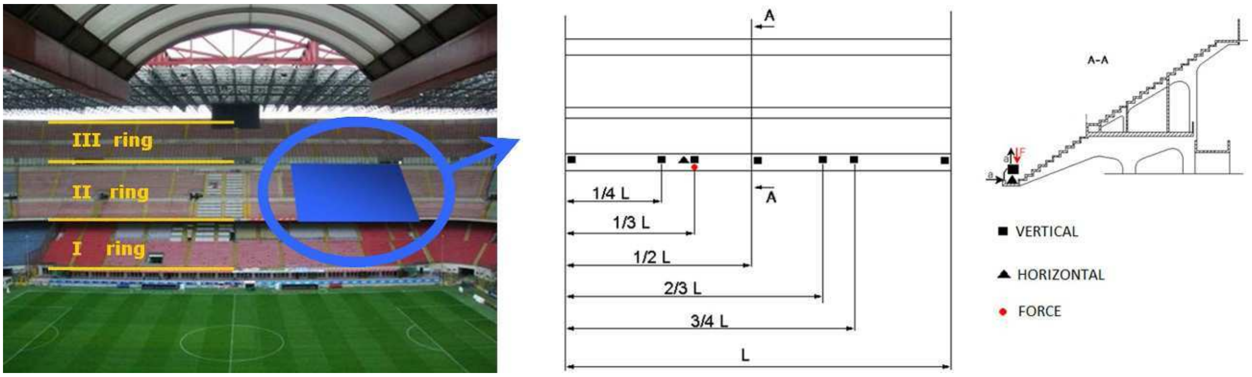

(a) (b)

Fig. 1 G. (a) Meazza stadium structure with highlighted the test stand; (b) measuring layout

To acquire the output of the system, i.e. the construction vibrations, the accelerations of the structure have been measured in 7 points, along the whole stand length, using servo accelerometers (Fig. 1,b). In correspondence of the actuator, horizontal vibrations are measured as well. Every record lasts 30 s, and the acquisition starts after the reaching by the structure of the steady state condition. The records are then processed to extract an integer number of sinusoidal cycles from each time history to avoid leakage problems. 8 frequency response functions are computed, one for every accelerometer.
Fig. 2 shows two of these computed curves: in all of the estimated FRFs it is possible to notice a low frequency zone, in the range of the first spectral component of exciting jumping loads (i.e. 2-3 Hz), in which the structure shows a quasi-static behaviour; at higher frequencies (above 4 Hz) a series of dynamic amplifications is present, in the typical range of the second and the third harmonics of a jumping load spectrum.

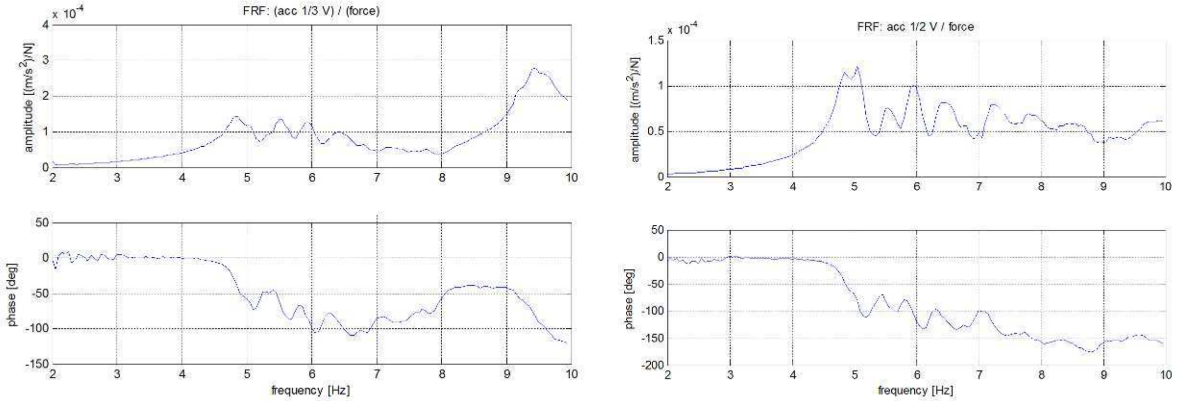

(a) **(b)**

Fig. 2 FRF: load Vs acceleration at 1/3 of the length of the stand (a) and load Vs acceleration at 1/2 of the length (b)

Experiments and results

An increasing number of volunteers, from one to eight, was asked to jump on the stand following the rhythm beaten by a metronome (3 test at 2.1, 2.3, 2.5 Hz for every volunteers number). The volunteers are 1/3 of the stand length, the same position of the hydraulic actuator of the previous paragraph. During each test a camera recorded a video of the people jumping (sampling frequency equal to 30 Hz) and 8 accelerometers (placed in the same points of the previous paragraph) the structure vibrations.

In each test, first of all the DIC algorithm is used to analyze the video in order to obtain a motion estimation of the framed zone [19,20]. After that, an rms (root mean squared) velocity map of the subsets allows to extract only the ones where people are present. Applying the load estimation method proposed in [21], i.e. multiplying every subset acceleration time history by the relative percentage of the whole volunteers' mass, it is possible to obtain an estimation of the induced loads. Switching to frequency domain, the product between the load complex spectrum and the FRFs estimated in the previous paragraph return a forecast of the structure vibration spectra, that can be compared with accelerometric signals. The next sub paragraphs show this procedure applied to 1,4,8 volunteers tests.

1 person tests

Fig. 3 shows all the steps that allow to select the subsets: the first frame of the video(a) is divided into 8x8 px subset (b). Analyzing the whole video with the DIC algorithm and evaluating the velocity rms for every subset time history, the rms map showed in (c) is obtained; it's interesting to notice that a rail is present just in front of the volunteer, and the algorithm doesn't see any motion in that zone as expected. Starting from this map, only the subsets in which the motion is significant are extracted (d) and used in the further steps (30 subset in total in this example).

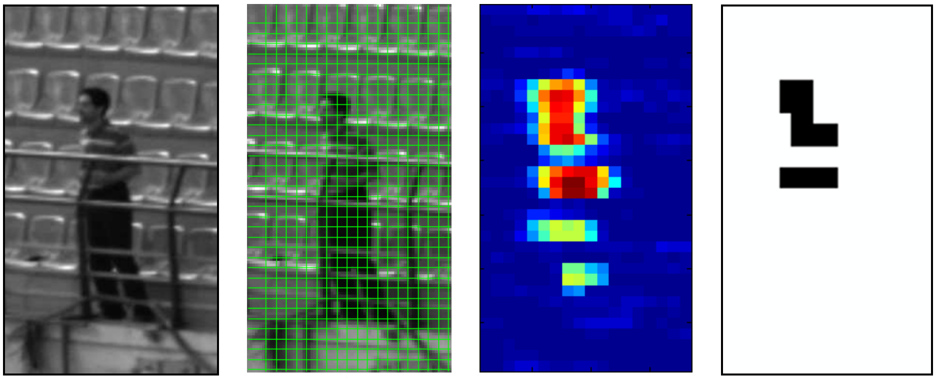

(a) (b) (c) (d)

Fig. 3 (a) first frame of the video; (b) subset division; (c) rms velocity map; (d) selected subsets for a single jumper 2.5 Hz test

The incremental displacement time histories resulting from the DIC analysis are converted from [px/frame] to [m/s], knowing the sample frequency and the camera calibration, and numerically derived to obtain accelerations [m/s^2]. Every subset acceleration is then multiplied by 1/30 of the volunteer total mass (65 kg): the sum of these time histories, with the addition of the gravitational contribution, returns the estimated induced load (Fig. 4).

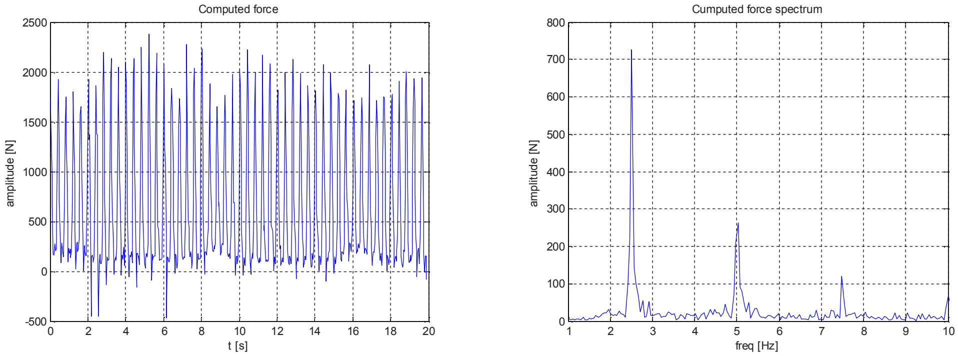

(a) (b)

Fig. 4 Estimated loads: time (a) and frequency (b) domain for a single jumper 2.5 Hz test

As well known in literature [12,13,14], the peak force for a single jumper induced load is roughly 3 times their weight and the spectrum of this load is well described by 3 spectral component.

Multiplying the complex load spectrum just estimated by the FRFs evaluated in the previous paragraph, it is now possible to forecast induced vibrations and compare them to the acquired ones (Fig. 5).

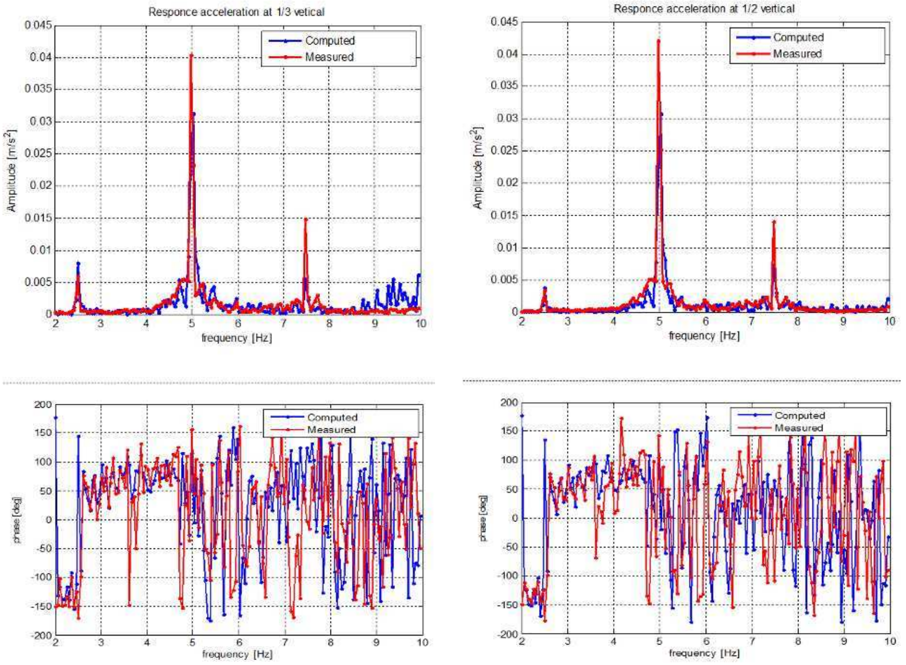

(a) (b)

Fig. 5 Computed Vs measured vertical vibration spectra at 1/3 of the stand length (a) and at 1/2 (b) for a single jumper 2.5 Hz test

Fig. 5 shows this comparison; it is worth noticing how the first spectral component, predominant in the force spectrum, loses importance compared to the second one thanks to dynamic amplification above 4 Hz in the FRF functions. The comparison between the measured and the predicted structure acceleration returns a high correspondence between the two curves.

Table 1 summarizes the results in terms of percentage discrepancy between the measured and the computed modulus and differences between the measured and the computed phase for the first and the second spectral components at two measuring points for three difference jumping frequencies. The average modulus percentage discrepancy for the first spectral component is 3% with a 21 % standard deviation. The average modulus percentage discrepancy for the second spectral component is -24% with a 5 % standard deviation. The average error on the phase is 4 deg for the first harmonic and 7 deg for the second one.

The third harmonics estimation results in higher errors; however, it will be shown in the next paragraphs why this component is negligible for a crowd.

Jumping frequency	Modulus [%]				Phase [deg]			
	I spectral component		II spectral component		I spectral component		II spectral component	
	1/3 L	1/2 L	1/3 L	1/2 L	1/3 L	1/2 L	1/3 L	1/2 L
2.1 Hz	-3	-17	-16	-27	5	1	0	-3
2.3 Hz	7	-19	-22	-31	5	6	-14	-17
2.5 Hz	38	12	-23	-27	8	0	-5	-15

Table 1 One volunteer jumping tests: discrepancies between measured and computed results

4 person tests

The same analysis described in the previous paragraph are carried out for a 4 person test (total mass equal to 260 kg). Fig. 6 shows the dynamic loading estimated considering the four persons; analyzing the load time history it can be noticed that the peak value of the force is less that 3 times the jumpers weight: this phenomenon indicates that the execution of the movements among the different volunteers is not perfectly synchronous, as can be seen in Fig. 6c, where four time histories (one for each jumper) are shown. In fact the time history of the force is never equal to zero, i.e. there is not a moment when all volunteers are in the air. Analyzing the frequency domain it can be noticed that the first spectral component, already higher for the single jumper with respect to the second and the third, gains here even more importance.

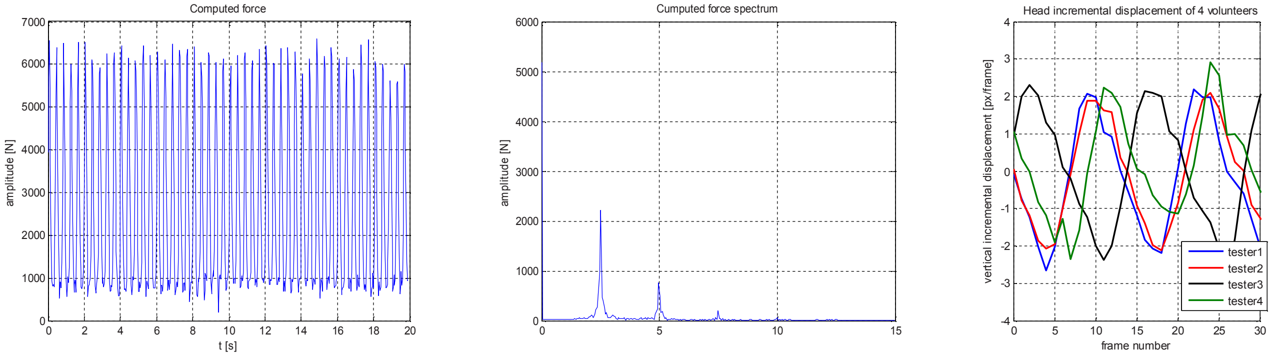

(a) (b) (c)

Fig. 6 Estimated loads: time (a) and frequency (b) domain for 4 jumpers 2.5 Hz test; incremental displacement of the heads of the 4 volunteers (c)

The increasing in the jumpers number does not result in a decreasing of the dynamic loading estimation performances (Table 2): if we focus on the first spectral component, that revealed more and more important increasing the volunteers, we find a maximum percentage discrepancy between the measured and the forecasted structure vibrations less than 15%, with a worst estimation of the phase angle of 17 deg.

Jumping frequency	Modulus [%]				Phase [deg]			
	I spectral component		II spectral component		I spectral component		II spectral component	
	1/3 L	1/2 L	1/3 L	1/2 L	1/3 L	1/2 L	1/3 L	1/2 L
2.1 Hz	12	9	-4	-18	-9	-2	50	-35
2.3 Hz	-6	-13	-30	-32	-4	17	-23	-15
2.5 Hz	12	8	2	1	-11	-9	-17	-22

Table 2 Four volunteer jumping tests: discrepancies between measured and computed results

8 person tests

The last test is carried out with 8 jumping volunteers (total mass equal to 600kg).

Fig. 7 shows, as for the single jumper test, the steps to select the significant subset. Once again it is possible to notice that no movement is measured in correspondence of the rail in front of the volunteers. The selected subsets belong to the upper part of the jumpers' body: this is done in order to reproduce the condition of a full occupied stand, when the lower part of the body of a spectator is hidden by the person in front of him.

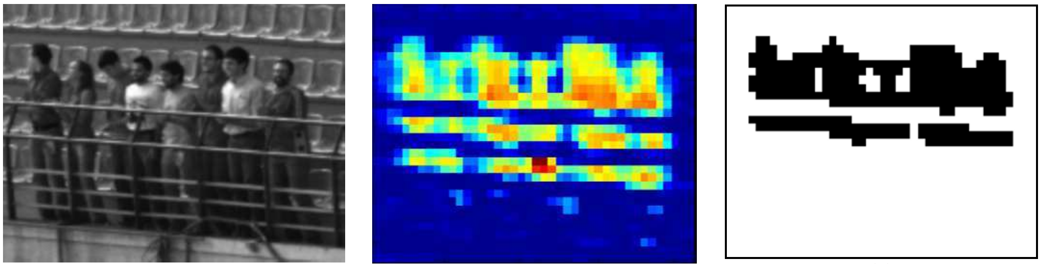

(a) (b) (c)

Fig. 7 (a) first frame of the video; (b) rms velocity map; (c) selected subsets for 8 jumpers 2.5 Hz test

The estimated loads (Fig. 8) confirm the expected trend: an increasing in the number of jumpers results in a higher importance of the first spectral component with respect to the other ones; at the same time the peak force (Fig. 8a) is much less than three times the total weight of the volunteers.

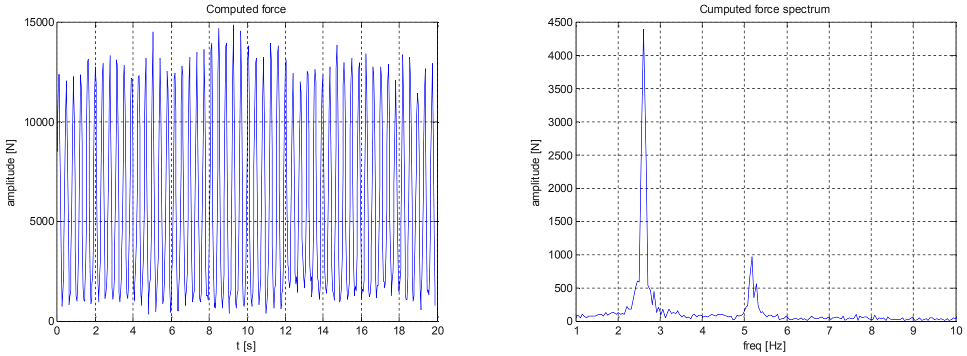

(a) (b)

Fig. 8 Estimated loads: time (a) and frequency (b) domain for 8 jumpers 2.5 Hz test

Fig. 9 shows the comparison between the measured and the computed structure accelerations; once again it can be noticed how the first spectral component, predominant in the force spectrum, loses importance compared to the second one thanks to dynamic amplification above 4 Hz in the FRF functions, but its importance is highly increased. The comparison between the measured and the predicted structure acceleration again returns a high correspondence between the two curves.

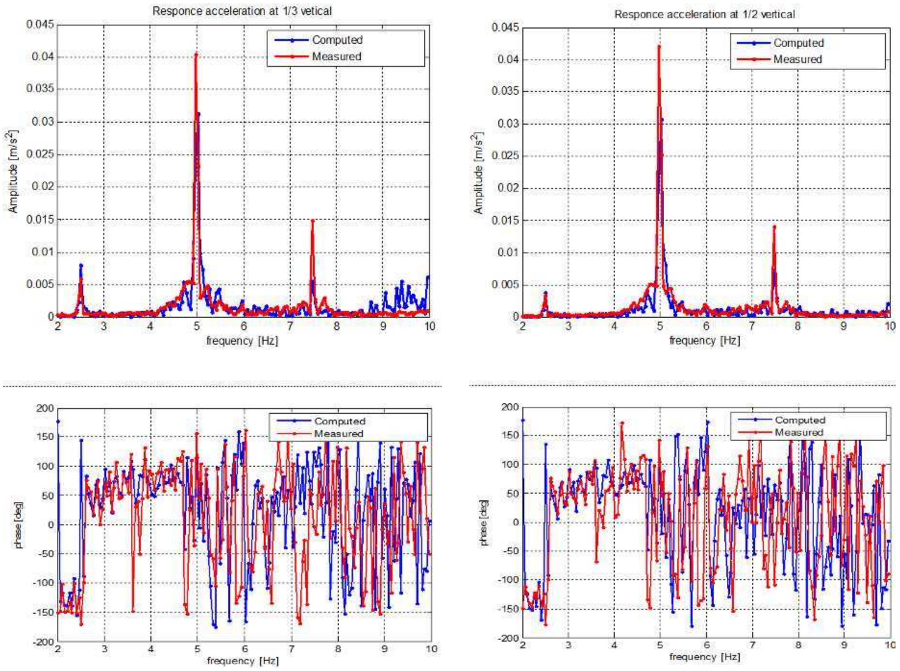

(a) (b)

Fig. 9 Computed Vs measured vertical vibration spectra at 1/3 of the stand length (a) and at 1/2 (b) for a 8 jumpers 2.5 Hz test

Table 3 summarizes the results in terms of percentage discrepancy between the measured and the computed modulus and the differences between the measured and the computed phase for the first and the second spectral component at two measuring points for three difference jumping frequencies. It is worth noticing that the trend seen in the 4 jumper test is here confirmed: the proposed method reliability does not decrease when increasing the number of volunteer. The maximum discrepancy between the measured and the computed spectra is around 30% and the maximum difference in the phase comparison is equal to 20 deg.

Jumping frequency	**Modulus [%]**				**Phase [deg]**			
	I spectral component		**II spectral component**		**I spectral component**		**II spectral component**	
	1/3 L	**1/2 L**	**1/3 L**	**1/2 L**	**1/3 L**	**1/2 L**	**1/3 L**	**1/2 L**
2.1 Hz	9	-9	-18	-20	13	3	-4	-10
2.3 Hz	5	-14	-25	-29	4	-6	20	-20
2.5 Hz	32	10	-11	-21	6	-6	-9	-10

Table 3 Eight volunteer jumping tests: discrepancies between measured and computed results

As conclusion of this data analysis, the comparison in time domain between the measured and the computed structure vibration is reported (Fig. 10). The high degree of correspondence highlighted in the frequency domain is obviously confirmed.

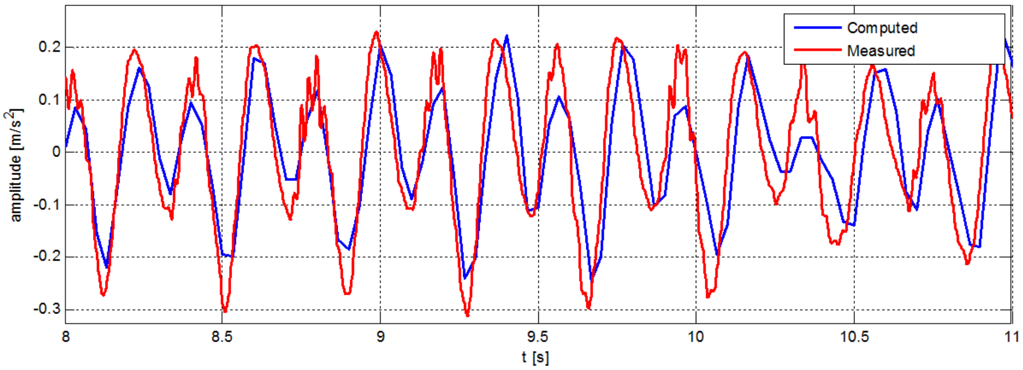

Fig. 10 Structural accelerations time history: comparison between measured and computed curves (1/3 of the stand length, 8 jumpers, 2.5Hz)

Conclusion

A new method for the load estimation of forces induced by the jumping and bobbing of a group of people is here validated through “in the field” experiments. A video of a jumping crowd is acquired and post processed with a digital image correlation algorithm in order to obtain a motion estimation of the crowd. The results of significant subsets are converted from px/frame to m/s and numerically derived in order to compute acceleration. All the acceleration time histories are then multiplied by the relative percentage of the total crowd mass: the sum of all of them gives us an estimation of the induced load. Knowing the frequency response function of the surrounding structure (a stand in G. Meazza stadium) it is possible to forecast the construction vibration and compare it with the measured one. This comparison shows an high correspondence between the computed and the measured vibrations: the percentage discrepancy in the first and the second spectral component is below the 30%, with a maximum error on the phases of 20 deg for a 8 jumper test.

As far as the authors know, this is the first method that proposes a way to measure the loads induced by a crowd; such an approach intrinsically overcame all the problems related to the generalization of many single jumpers tests, (namely the crowd effect and effects of a sensible moving structure below the jumpers), because it gives a measure of the forces taking in account automatically all these aspects.

Such a result is very important, due to the fact that it gives a method to fill a well known gap in human-structure interaction problem: it can be used to estimate a quantitative reliable value of a crowd induced load. Furthermore, in the future, it can open a new field in the structure heath monitoring: if it is possible to estimate induced load and to measure structure vibrations, therefore it is possible to estimate in real time the frequency response function of the structure. Changes in the FRFs, for example during a concert, can indicate significant structural modification, which is the approaching of a potentially dangerous situation.

References

1. Sachse R., Pavic, A., Reynolds, P., Human-structure dynamic interaction in civil engineering dynamics: A literature review, Shock and Vibration Digest, v 35, n 1, p 3-18, January 2003.
2. Batista R.C., Magluta C., Spectator-induced vibrations of Maracana stadium, Publ by A.A. Balkema, p 985, 1993.
3. Almeida P.A.O., Rodriguez J.F.S., Investigation of the vibrations induced by people in soccer stadiums, Proceedings of the International Modal Analysis Conference - IMAC, v 2, p 1417-1422, 1999.
4. Staalduinen V.P., Courage W., Dynamic loading of Feyenoord stadium during pop concerts, Symposium: Places of Assembly and Long-Span Building Structures, Birmingham, UK, 1994.
5. Rogers D., Two more wobbly stands, Construction News, August 2000.
6. Rogers D., Thompson R., Liverpool stand gets red card, Construction News, August 2000.
7. Erlingsson S., Bodare A., Live load induced vibrations in Ullevi Stadium-dynamic soil analysis, Soil Dynamics and Earthquake Engineering, v 15, n 3, p [d]171-188, Apr 1996.
8. Pernica G., Dynamic live loads at a rock concert, Canadian journal of civil engineering, v 10, n 2, p 185-191, Jun 1983.
9. Ginty D., Derwent J.M., Ji T., The frequency ranges of dance-type loads, Structural Engineer, v 79, n 6, p 27-31, March 20, 2001.
10. Littler J.D. , Frequencies of synchronized human loading from jumping and stamping, The Structural Engineer, 2003.

11. Bachmann H., Ammann W., Vibration in structures: Induced by man and machines, Switzerland (Zurich), IABSE, 1987.
12. Sim J.H.H., Human-Structure Interaction in Cantilever Grandstands, thesis submitted for the degree of Doctor of Philosophy at the University of Oxford, 2006.
13. Parkhouse J. G., Ewins D. J., Crowd-induced rhythmic loading, Proceedings of the Institution of Civil Engineers: Structures and Buildings, v 159, n 5, p 247-259, October 2006.
14. Parkhouse J. G., Ewins D.J., Vertical dynamic loading produced by people moving to a beat Proceedings of the 2004 International Conference on Noise and Vibration Engineering, ISMA, p 821-835, 2004, Proceedings of the 2004 International Conference on Noise and Vibration Engineering, ISMA.
15. Ebrahimpour A., Fitts L. L., Measuring Coherency of Human-Induced Rhythmic Loads Using Force Plates, Journal of structural engineering New York, N.Y., v 122, n 7, p 829-831, Jul 1996.
16. Yao S., Wrigth J. R., Pavic A., Reynolds P., The effect of people jumping on a flexible structure, IMAC XXIV, Orlando, USA, 2003
17. Yao S., Wright J.R., Pavic A., Reynolds P., Experimental study of Human-induced Dynamic forces due to jumping on a perceptibly moving structure, Journal of Sound and Vibration, v 296, n 1-2, p 150-165, September 12, 2006.
18. Dynamic performance requirements for permanent grandstands subject to crowd action, Interim guidance on assessment and design, Institution of Structural Engineers, UK.
19. Caprioli A., Cigada A., Sala R., Zappa E., Image based measurement of a stadium excitation due to jumping people, IMAC XXIV, 2006.
20. Caprioli A., Manzoni S., Zappa E., Crowd Motion Measurement Based on Image Processing, Wiley Interscience Journal, 2007.
21. Mazzoleni P., Zappa E., Human Induced Dynamic Loads Estimation Based on Body Motion, XXIX IMAC, Jacksonville, Florida, 2011.

Optimal Selection of Artificial Boundary Conditions for Model Update and Damage Detection

Joshua H. Gordis
Naval Postgraduate School
Dept. of Mechanical & Aerospace Engineering - Code ME/Go
700 Dyer Road Bldg. 245 Room 313
Monterey CA 93943-5146
(831) 656-2866 office
(831) 656-2238 fax
jgordis@nps.edu

LT Konstantinos Papagiannakis
Hellenic Navy
Athens, Greece

Abstract

Sensitivity-based model error localization and damage detection is hindered by the relative differences in modal sensitivity magnitude among updating parameters. The method of artificial boundary conditions is shown to directly address this limitation, resulting in the increase of the number of updating parameters at which errors can be accurately localized. Using a single set of FRF data collected from a modal test, the artificial boundary conditions (ABC) method identifies experimentally the natural frequencies of a structure under test for a variety of different boundary conditions, without having to physically apply the boundary conditions, hence the term "artificial." The parameter-specific optimal ABC sets applied to the finite element model will produce increased sensitivities in the updating parameter, yielding accurate error localization and damage detection solutions. A method is developed for identifying the parameter-specific optimal ABC sets for updating or damage detection, and is based on the QR decomposition with column pivoting. Updating solution residuals, such as magnitude error and false error location, are shown to be minimized when the updating parameter set is limited to those corresponding to the QR pivot columns. The existence of an optimal ABC set for a given updating parameter is shown to be dependent on the number of modes used, and hence the method developed provides a systematic determination of the number of modes required for localization in a given updating parameter. These various concepts are demonstrated on a simple model with simulated test data.

1. Introduction

In sensitivity-based finite element (FE) model updating and damage detection (here, collectively referred to as "updating"), there are typically a large number of physical parameters which need to be identified, either as "corrections" to the FEM in model updating, or as "flags" for potential damage in the test article in damage detection. The number of these updating parameters frequently exceeds the number of measured modes available for use in the updating process. This disparity between the number of available modes and the number of updating parameters has motivated much prior and current research into ways to increase the size of the available measured dataset, reducing this disparity. An increase in the size of the dataset, however valuable, does not directly address a fundamental limitation in the sensitivity-based approach to model updating. The updating solution for each parameter is dependent on the relative magnitude of its modal sensitivities, calculated from the FE model. Given the limited bandwidth of a modal test, the modal sensitivities calculated for the various updating parameters are of different magnitudes, and hence updating solutions are biased towards those parameters associated with higher sensitivity values. A low relative modal sensitivity of a given updating parameter will prevent the updating solution from localizing an error in this parameter, and prevent the estimation of the true error magnitude. In fact, without an accurate localization, it is in general not possible to accurately estimate the error magnitude. As has been noted previously [1], accurate localization is critical, as once the parameters in error have been identified, the updating can be carried out and the updating solution residual (however defined) between measured and calculated response minimized, or even driven to zero. This minimization can occur regardless of whether or not a "correct" selection of updating parameters

T. Proulx (ed.), *Sensors, Instrumentation and Special Topics, Volume 6*, Conference Proceedings of the Society for Experimental Mechanics Series 9,
DOI 10.1007/978-1-4419-9507-0_15, © The Society for Experimental Mechanics, Inc. 2011

(i.e. localization) has been made. A clear reminder is given in [2] that in sensitivity-based updating, a low sensitivity value does not imply that a parameter is not in error, but can impede both localization and estimation.

The use of artificial boundary conditions (ABC) addresses this fundamental limitation. Through the application of selected sets of ABC to the FRF data normally collected in a modal test, an accurate localization solution for a greater number of, and possibly all, individual updating parameters can be obtained. When the measured FRF are insufficient, either in spatial completeness or bandwidth, to localize the error in a given parameter, the method clearly indicates this insufficiency, for each updating parameter. As will be shown, this is accomplished through the application of multiple ABC sets, where a large number of alternative sensitivity matrices are generated, and these alternative sensitivity matrices are queried as to whether or not the localization of each updating parameter is possible. This large number of alternative sensitivity matrices made available by the method substantially increases the possibility of generating an accurate localization solution for each updating parameter. This application of multiple ABC sets also relaxes the demand on test bandwidth required (i.e. number of modes) for accurate localization.

2. Background

In a modal test of a structure, a single set of boundary conditions are typically used, due to the prohibitive demands in time, cost, and practicality of physically altering the boundary conditions and retesting the structure. The modal test yields spatially incomplete frequency response function (FRF) data at each frequency point in the measurement bandwidth. From this FRF data, the modal parameters of the structure can be identified. These parameters include a single set of natural frequencies and the associated mode shapes and damping ratios, and are specific to the "as-tested" configuration (e.g. boundary conditions) of the test article. Given the typically large number of physical parameters for which errors or damage need to be identified (updating parameters), the use of natural frequencies alone can therefore result in an underdetermined system of updating equations in the unknown parameters. A basic solution to an underdetermined problem is non-unique, while a least-norm solution tends to smear the identified location of errors, in that falsely non-zero values are produced for parameters other than those truly in error. One strategy for increasing the number of equations in the updating system is by the inclusion of mode shape sensitivity data, which can provide a sufficient number of additional equations such that the problem is rendered overdetermined. For an overdetermined problem, the least-squares solution also tends to smear error location. For brevity, we will refer collectively to FEM updating and damage detection as "updating," and to the solution of either problem as "errors" in the updating parameters.

The advantages of the use of natural frequencies only (excluding mode shape data) as a response metric are well known. These advantages include the higher accuracy with which natural frequencies can be identified as compared to mode shape data, the elimination of both the mode shape estimation process and the identification of real mode shapes from complex shapes. Despite the relative quality of the natural frequencies in the updating process, the limited number of measured natural frequencies can restrict the effectiveness of updating.

Another strategy for enlarging the measured data set is by the direct use of FRF data, due to the large amount of potentially useful data contained therein. This advantage is mitigated by the realization that not all FRF frequency points are of value, and a frequency selection algorithm is therefore needed. The use of antiresonance frequencies in addition to (or in place of) natural frequencies has also been explored; see for example [2-6]. Antiresonances are a potent response quantity for updating due to their being functions both of the (global) natural frequencies and the (local) mode shape elements specific to the excitation and response coordinates of the FRF. However, antiresonances are not without their peculiar limitations; it has been shown that antiresonances of transfer FRF are very sensitive to small changes in a structural model and excitation location, and that the robustness of the updating process is improved if restricted to the use of antiresonances from driving point FRF [4]. However, in a standard single-input modal test, only a single point FRF is measured. Other point FRF can be synthesized using the (incomplete) identified modes, and the resulting error in antiresonance locations (along the frequency axis) compensated for by the inclusion of low and high frequency residuals calculated from the model [6]. Furthermore, antiresonance sensitivities have been shown to be linear combinations of eigenvalue and mode shape sensitivities, and hence antiresonance data can replace, but not augment, mode shape data [3]. The overall performance of updating has been compared when using resonances versus using resonances along with some antiresonances. It was concluded that the improvement of the updating results upon inclusion of the antiresonances is dependent on the updating parameters selected as well as the location of the errors [7].

Yet another strategy for enlarging the data set for updating is by physically modifying the boundary conditions of the structure, and/or the addition or removal of mass and/or stiffness, generally referred to as perturbed boundary conditions. The physical alteration of the boundary conditions yields a distinct dynamic system with a different eigenvalue spectrum. Along with the similarly modified FE model, this provides independent rows for the sensitivity-based updating equation. This has been shown to be an effective strategy [8-12], but of course comes with the various demands of physically altering the boundary conditions.

3. Artificial Boundary Condition Sets

Both the antiresonance and perturbed boundary approaches to enlarging the data set do have significant benefits for updating. The method of Artificial Boundary Conditions [13] offers those benefits while avoiding some of their drawbacks. The theory of ABC originates in the concept of the omitted coordinate system (OCS) [14] which plays a central role in the underlying properties of advanced model reduction techniques and frequency domain updating; see for example, [15-21]. With respect to an experimentally derived model, an OCS is the dynamic system which results when some of the measured coordinates are restrained (i.e. "pinned" to ground). In [13], it is shown that the natural frequencies of the structure under test, from a potentially large number of different boundary conditions, are available from a square FRF matrix measured from the structure, without having to physically apply the boundary conditions, i.e. artificial boundary conditions (ABC). If we take "a" as the number of measured coordinates, then the total number of ABC sets available from a single FRF matrix of size a x a, and including the as-tested configuration, is given by the sum of the numbers of all k-combinations

$$C = \sum_{k=0}^{a} \binom{a}{k} \tag{1}$$

which is potentially a large number relative to the typical number of sensors used in a modal test. For example, if we use 10 accelerometers to measure the FRF matrix, and limit the number of coordinates at which to apply ABC to two, then the available number of ABC sets (and therefore OCS systems) is 55. If we include the as-tested configuration, the total number of distinct boundary condition sets is C = 56. If we increase the number of ABC coordinates to four, this total number of distinct boundary condition sets becomes 386. This potentially large number of ABC sets for which OCS natural frequencies can be identified leads to the primary focus of this work, which is how to select those sets which are most effective for model updating. The determination of optimal ABC sets has been previously explored [19] where genetic algorithms were used in the selection process. In that work, it was shown that effective updating is possible using a few low-order natural frequencies, and a few ABC sets. Here, we will also address the selection of optimal ABC sets, but rather than using optimization strategies, our selection will be based on an examination of underlying properties of the solutions to the parametric updating equations associated with a given ABC configuration.

4. Identification of Natural Frequencies for an Omitted Coordinate System

The full development of the theory can be found in [13,14]. The experimental identification of the natural frequencies of an OCS involves the elimination of the rows and columns of H_{aa} corresponding to the a-set coordinates to be artificially "pinned" to ground. The proper subset of the measured (a-set) coordinates which are to be artificially pinned are denoted as the "o-set" and the associated partition of H_{aa} is denoted H_{oo}:

$$\left[H_{aa}\right] = \begin{bmatrix} H_{a-o,a-o} & H_{a-o,o} \\ H_{o,a-o} & H_{oo} \end{bmatrix} \tag{2}$$

where a-o indicates the set complement, i.e. all coordinates in the a-set, but not in the o-set. The mass and stiffness matrices implicitly defined by $[H_{oo}]$ are obtained by the restraint of the a-set coordinates, and define an omitted coordinate system (OCS). The FRF matrix H_{oo} is then inverted yielding the impedance matrix $Z_{oo} = H_{oo}^{-1}$. If this is done as a function of frequency, peaks in the individual Z_{oo} will occur at the natural frequencies of the OCS. This has been demonstrated experimentally in [14,20]. The experimental study of the identification of OCS natural frequencies, reported in [20], demonstrated that OCS natural frequencies do indeed appear clearly as peaks in the OCS impedance spectra. It was also pointed out that with a significant noise content in the data can induce spurious spikes in the impedance spectra. It is noted that any measured FRF matrix represents a reduced-order realization of an infinite-dimensional system with a set of restraints (pins) at its (un-measured) a-set coordinates [21]. Note that the case where the p-set contains a single coordinate corresponds to an ABC set with a single "pin." In this case, from the eigenvalue separation theorem [22], the natural frequencies of associated OCS will interlace those of the baseline (as-tested) configuration. We also note that other strategies have been developed for identifying OCS natural frequencies that do not require a square matrix, but involve non-symmetric eigensolutions [4,23].

This procedure for identifying the natural frequencies of the OCS assumes that a square matrix H_{pp} is available. The direct measurement of a square FRF matrix requires the application of a suitable excitation at each response coordinate. This places an additional demand on the experiment. The synthesis of unmeasured FRF is possible once the measured FRF have been curvefitted. However, as the identification of OCS mode frequencies requires accurate FRF data at all frequencies in the bandwidth of interest, not just at modal peaks, the sensitivity of antiresonance frequencies to both the number and precision of estimated modes becomes a significant issue. This sensitivity was also shown to vary with distance from the driving point FRF. This was explored in some detail in [24], where both simulated and actual test data was used.

Here, we assume a square H_{pp} is available, to allow us to focus on two principle issues. The first issue is the development of a strategy for the selection of an optimal ABC set for the identification of specific updating or damage parameter(s). We will examine several updating metrics and show how they are minimized by the use of optimal ABC sets. The second issue pertains to the number of modes required in order for an ABC solution to identify errors in specific parameters. An ABC set can only be optimal if a sufficient number of modes are included in the identification.

5. The Updating Problem and its Solutions

The parametric updating problem can be constructed from the first-order structural eigenvalue sensitivities as

$$\{\delta\Lambda\} = [S]\{u\} \tag{3}$$

where $\{\delta\Lambda\} \in \mathbb{R}^{mx1}$ is a vector of the differences between the measured and calculated squared natural frequencies, $\{u\} \in \mathbb{R}^{nx1}$ is a vector of updating parameter changes (e.g. model "errors") to be identified, and $[S] \in \mathbb{R}^{mxn}$ is the matrix of eigenvalue sensitivities, calculated from the FE model. The number of modes used is "m" and the number of updating parameters is "n".

We again note that the identification problem requires both error localization and error magnitude estimation. With respect to {u}, the localization problem consists of identifying which elements are truly in error. The magnitude estimation problem consists of estimating the individual element magnitudes of {u}. Most commonly, the system Eq. (3) is underdetermined, i.e. n > m, as the number of model parameters which are in question exceeds the number of experimentally identified natural frequencies. We will here focus on this underdetermined case.

With regards to the solution of Eq. (3) with m < n, and rank([S]) = m, we will briefly review two possible solutions for {u}. The first of these is the least-norm solution, for which $\|\{u\}\|_2$ is a minimum, denoted $\{u_{ln}\}$. The least-norm solution minimizes the length of the solution vector, (in contrast to a least-squares solution, which minimizes the length of the residual [25]). The least-norm solution can be found from the pseudo-inverse, i.e.

$$\{u_{ln}\} = [S]^T \left([S][S]^T\right)^{-1} \{\delta\Lambda\} \tag{4}$$

Note that if [S] is full rank and well conditioned, the same solution is found from the SVD.

The second solution of relevance here is a *basic* solution, and can be found as follows. Given that [S] is m x n, we partition [S] into sets of basic and non-basic columns as follows:

$$[S] = [S_1 \quad S_2] \tag{5}$$

where a selection of m columns of [S] is made such that rank($[S_1]$)=m. These columns comprise the basis, and the corresponding elements of the solution vector are the basic parameters. The associated partitioning of {u}is written as

$$\{u\} = \begin{Bmatrix} u_1 \\ \hline u_2 \end{Bmatrix} \tag{6}$$

The solution of Eq. (3) can be written

$$\{u_1\} = [S_1]^{-1} \left(\{\Delta\omega^2\} - [S_2]\{u_2\}\right) \tag{7}$$

and Eq. (3) is satisfied for any choice of the vector $\{u_2\}$, which contains the non-basic parameters. Throughout, we will focus on the choice,

$$\{u_2\} = \{0\} \tag{8}$$

and which results in the following solution:

$$\{u_{QR}\} \triangleq [S_1]^{-1} \{\Delta\omega^2\} \tag{9}$$

We denote this basic solution with the subscript "QR" as this solution will be calculated from the QR decomposition of [S] with column pivoting [26]. As we will see, the set of pivot columns selected by the QR algorithm determines the ability of an ABC set to provide a localization solution.

5.1. Least-Norm vs. Basic Solutions

We first illustrate some distinguishing characteristics of the two important classes of solution to Eq. (3) described above. We will illustrate the difference between $\{u_{ln}\}$ and $\{u_{QR}\}$ with a simple numerical example. For [S], we will assume a random 3 by 4 matrix, corresponding to an updating problem using three modes and four updating parameters:

$$[S]=\begin{bmatrix}0.6557 & 0.9340 & 0.7431 & 0.1712\\ 0.0357 & 0.6787 & 0.3922 & 0.7060\\ 0.8491 & 0.7577 & 0.6555 & 0.0318\end{bmatrix} \tag{10}$$

We assume that a single error exists in the first updating parameter, and hence the "true" updating solution vector is:

$$\{u\}=\begin{bmatrix}1 & 0 & 0 & 0\end{bmatrix}^T \tag{11}$$

We first calculate the associated "true" mode frequency changes (i.e. the right-hand side), which is $\{\delta\Lambda\}$ = [S]{u} = $[0.6557, 0.0357, 0.8491]^T$. Assuming now that {u} is unknown, the problem to be solved is

$$\begin{Bmatrix}0.6557\\0.0357\\0.8491\end{Bmatrix}=\begin{bmatrix}0.6557 & 0.9340 & 0.7431 & 0.1712\\ 0.0357 & 0.6787 & 0.3922 & 0.7060\\ 0.8491 & 0.7577 & 0.6555 & 0.0318\end{bmatrix}\begin{Bmatrix}u_1\\u_2\\u_3\\u_4\end{Bmatrix} \tag{12}$$

We will compare the results of the two solutions, u_{ln} and u_{QR}. The two solutions are:

$$\{u_{ln}\}=\begin{bmatrix}0.9928 & -0.0503 & 0.0669 & 0.0116\end{bmatrix}^T \qquad \{u_{QR}\}=\begin{bmatrix}1 & 0 & 0 & 0\end{bmatrix}^T \tag{13}$$

and $||u_{ln}||$ = 0.9964 and $||u_{QR}||$ = 1. Comparing these two solutions to the true solution of Eq. (11), it is seen that in this case of a well-conditioned, full rank S, the least-norm solution u_{ln} fails to provide a localization (or magnitude) solution, while the basic solution u_{QR} (calculated using the QR decomposition with column pivoting) provides an exact localization (and magnitude) solution.

We will now repeat this calculation, with the only change being the location of the error. If we place the error in the third update parameter, i.e.

$$\{u\}=\begin{bmatrix}0 & 0 & 1 & 0\end{bmatrix}^T \tag{14}$$

We again first calculate the associated mode frequency errors, which are $\{\delta\Lambda\}$ = [S]{u} = $[0.7431 \quad 0.3922 \quad 0.655]^T$. Assuming that {u} is unknown, the system to be solved is,

$$\begin{Bmatrix}0.7431\\0.3922\\0.6555\end{Bmatrix}=\begin{bmatrix}0.6557 & 0.9340 & 0.7431 & 0.1712\\ 0.0357 & 0.6787 & 0.3922 & 0.7060\\ 0.8491 & 0.7577 & 0.6555 & 0.0318\end{bmatrix}\begin{Bmatrix}u_1\\u_2\\u_3\\u_4\end{Bmatrix} \tag{15}$$

and the two solutions are:

$$\{u_{ln}\}=\begin{bmatrix}0.0669 & 0.4680 & 0.3776 & -0.1075\end{bmatrix}^T \qquad \{u_{QR}\}=\begin{bmatrix}0.1075 & 0.7518 & 0 & -0.1726\end{bmatrix}^T$$

It is clear that in this case neither solution is able to locate the error; however, the least-norm solution in general cannot provide localization.

5.2. QR Decomposition with Column Pivoting for Subset Selection

The failure of the QR solution to provide the correct error location in this second example is due to the column of [S], associated with the updating parameter in error, not being included as a pivot column. We will describe the QR decomposition algorithm with pivoting as this, in effect, provides the subset selection strategy which identifies those updating parameters which can be localized by a given ABC set.

The QR decomposition of [S] is,

$$[Q][R]=[S][P] \tag{16}$$

where $[Q]\in\mathbb{R}^{mxm}$ is an orthogonal matrix, $[R]\in\mathbb{R}^{mxn}$ is an upper triangular matrix, and $[P]\in\mathbb{R}^{nxn}$ is a permutation matrix. We will refer to the set of pivot column indices as "p". Several methods are available for calculating the decomposition, such as Gram-Schmidt orthogonalization, Givens rotations, or Householder reflections [26]; the latter is used here. With respect to the use of Householder reflections, the key aspect of the algorithm is that at the ith iteration, prior to the ith Householder reflection, the norms of the columns of [R(i:m,i:n)] are calculated, and the ith column of [R(i:m,i:n)] is swapped with that column having the maximum norm. This procedure produces a decomposition with a column permutation identical to that of MATLAB [27]. This criteria for the permutation of the columns in effect selects updating parameters to serve as basic variables (subset selection). The underdetermined solution of Eq. (3) can only provide exact localization solutions for those updating parameters in this QR basis. Note that column pivoting in conjunction with the QR method is effective for dealing with near-rank deficiency, and can improve numerical accuracy, so its use as a subset selection strategy does not compromise the numerical aspects of the problem.

The reason for this difference in performance in the above examples lies in the set of column pivots (QR basis) which are a property of the matrix [S]. The QR decomposition of [S] above, Eq. (10), is:

$$[Q]=\begin{bmatrix} 0.6763 & -0.2813 & -0.6808 \\ 0.4915 & 0.8607 & 0.1326 \\ 0.5487 & -0.4243 & 0.7204 \end{bmatrix} \qquad [R]=\begin{bmatrix} 1.3810 & 0.4802 & 0.9269 & 1.0550 \\ 0 & 0.5460 & -0.5140 & -0.1495 \\ 0 & 0 & 0.1700 & 0.0183 \end{bmatrix} \tag{17),(18}$$

$$[P]=\begin{bmatrix} 0 & 0 & 1 & 0 \\ 1 & 0 & 0 & 0 \\ 0 & 0 & 0 & 1 \\ 0 & 1 & 0 & 0 \end{bmatrix} \qquad p=[2,4,1] \tag{19}$$

The first m=3 columns of the permutation matrix [P], Eq. (19), reveal that the QR basis includes the updating parameters (scalar elements of the solution), u_2, u_4, and u_1. We will refer to this parameter set as p = {2,4,1}. Element #3 is not included, and hence this sensitivity matrix [S] cannot localize a potential error in Element #3, as seen in the solution $\{u_{QR}\}$ above, Eq.(16).

The inability of the underdetermined solution of Eq. (3) to provide an exact localization solution for all updating parameters limits traditional (single boundary condition set) updating strategies. As seen above, this is due to the fact that a single sensitivity matrix can produce only one QR basis that satisfies the maximum column norm pivot criterion of the QR algorithm (described above). The ABC method directly addresses this problem by the fact that many different ABC configurations can be applied, using the same set of measured FRF data from the "as-tested" configuration. As the number of ABC configurations increases, the probability increases of generating a sensitivity matrix for which the QR pivot columns include a column associated with a given updating parameter. In other words, it is possible to find an ABC configuration which has sufficiently high modal sensitivities relative to a given updating parameter. This result guides the selection of ABC sets which are able to reveal errors for a given updating parameter. An optimal ABC set for an updating parameter "i" generates QR solutions with permutation set p, such that $i \in p$. Furthermore, the process clearly identifies the minimum number of measured modes required in order to identify a specific parameter, as will be demonstrated.

More generally, we can see that a related and broader requirement of a localization solution is that it be able to provide the necessary sparsity. A solution which maximizes sparsity, minimizes the zero-norm, $\|\cdot\|_0$, the number of nonzero components of the solution vector [28]. It has been shown [29] that for most large underdetermined systems, the sparsest solution (also) minimizes the 1-norm, $\|\cdot\|_1$. Therefore, the least-norm solution which minimizes the 2-norm is an inappropriate choice for localization. The two solutions shown in Eq. (13) demonstrate their relative ability to yield an appropriate sparsity to localize errors. While the basic solution (generated by the QR decomposition) is not a 1-norm minimizer, this solution can provide the necessary sparsity to reveal error locations. We demonstrate this more fully in what follows, with respect to ABC updating solutions.

6. Simulation Model and OCS Frequencies

Our simulated updating problem will make use of a cantilevered beam of length 3.048 m, cross-section area of 5.163×10^{-3} m^2, EI = 2.206×10^3 MPa, and density of 7.833×10^3 kg/m^3. The FE model, shown in Figure 1, is comprised of 10 two-noded elements with two DOF/node (lateral translation and slope). We will assume that a measured frequency response is available from every translational DOF, and that an excitation has been applied to every translational DOF, yielding a square 10x10 FRF matrix. The cantilevered boundary conditions constitute the "as-tested," configuration. All artificial boundary conditions (ABC) are relative to this as-tested (cantilevered) configuration. The first five elastic mode frequencies are 9.08, 56.92, 159.40, 312.58, 517.53 Hz.

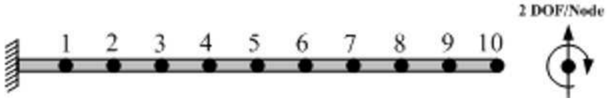

Figure 1. Simulation model - cantilevered beam

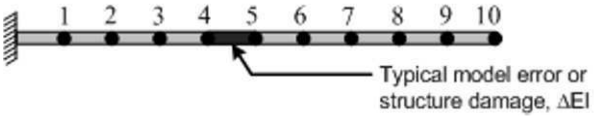

Figure 2. Typical parameter error, shown here in element #5

In order to examine the ability to localize model errors (or structure damage), EI errors will be placed in one element at a time, as shown in Figure 2. For localization, the updating parameters comprising the vector {u} will include the EI errors at each element. The goal is to select ABC configurations which include u_i in the QR basis, and thus have the ability to identify an error in element "i," e.g. $u_i \equiv \Delta EI_i$.

We here assume that all OCS frequencies of interest have been already been obtained (from simulated test data) in order to focus on the selection of ABC sets. However, we will demonstrate briefly the process of identifying the OCS frequencies from an FRF matrix. We start with a square, 10 x 10 FRF matrix, assumed measured from the as-tested configuration, or calculated from an FE model. Figure 3 shows a point FRF, $H_{11}(\Omega)$. The lowest five peaks correspond to the frequencies in Table 1.

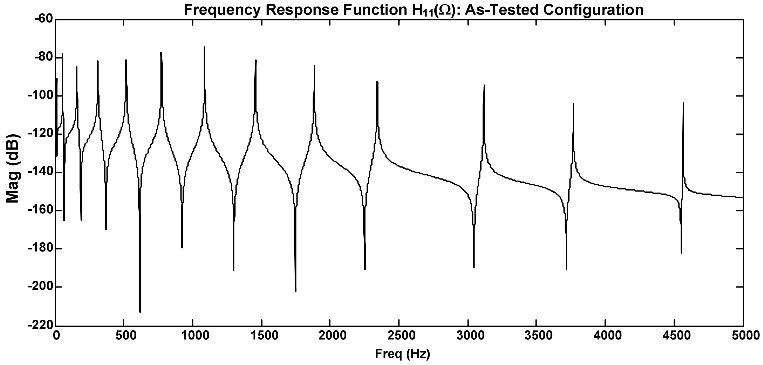

Figure 3. Point FRF from as-tested configuration

For a 10 x 10 FRF matrix, there are C(10,9) = 1024 possible ABC configurations (including the as-tested configuration). If we limit the number of ABC pins to two, then there are C(10,2) = 56 possible ABC configurations. For the purpose of illustrating the identification of OCS frequencies, we arbitrarily choose to artificially apply two pins, restraining the translations at nodes 9 and 10. This configuration is shown in Figure 4.

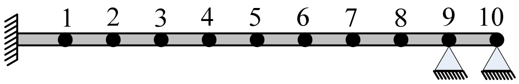

Figure 4. As-tested structure with ABC set comprised of two pins

The coordinate sets of Eq. (2) have the membership a = [1:10], and o = [9 10], all of which are translational DOF at the indicated nodes. The measured FRF can be written as:

$$[H] = \begin{bmatrix} H_{1:8,1:8} & H_{1:8,9:10} \\ H_{9:10,1:8} & H_{9:10,9:10} \end{bmatrix} \tag{20}$$

We invert $[H_{9:10,9:10}]$ at each frequency in the test bandwidth, and then plot one of the elements of the resulting 2x2 OCS impedance, $[Z^{ABC}]$, as shown in Figure 5.

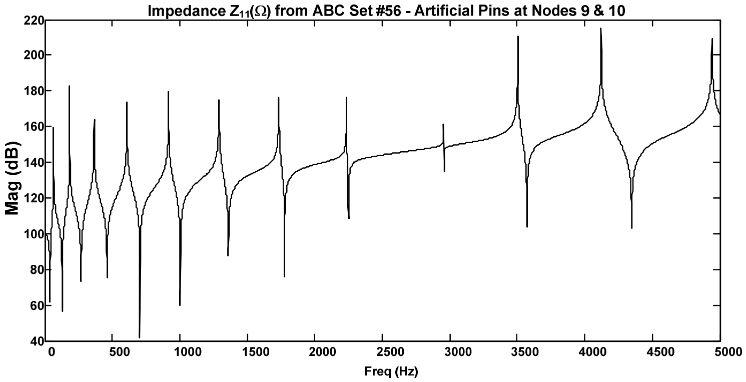

Figure 5. OCS impedance

If we apply these ABC to the FE model, the calculated lowest 12 mode frequencies match exactly the peaks in the impedance of Figure 5, and are 0.0671, 0.1860, 0.3667, 0.6098, 0.9172, 1.2914, 1.7344, 2.2347, 2.9546, 3.5029, 4.1222, 4.9415 (x10^3 Hz). This brief numerical example demonstrates how OCS natural frequencies for one of potentially many ABC sets can be identified from the FRF data acquired from a single test.

6.1. Generation of Artificial Boundary Condition (ABC) Sets

As discussed above, the imposition of a set of artificial boundary conditions (ABC) results in the definition of an omitted coordinate systems (OCS). Given the 10 measurement locations for the system shown in Figure 4, ABC sets are generated which include all combinations of the 10 measurement locations, taken both one, and then two, at a time (see Eq. (1)). These ABC sets are shown in Table 1, with Sets #15 through #54 removed to save space. In this table, a "1" indicates a node to be pinned, and a "0" indicates that the node remains free. Note that Set #1 shows no pins, as this set corresponds to the as-tested configuration.

Table 1. All ABC sets for 10 Nodes, taken one, and then two, at a time

	ABC Pin Location - Node #									
Set #	**1**	**2**	**3**	**4**	**5**	**6**	**7**	**8**	**9**	**10**
1	0	0	0	0	0	0	0	0	0	0
2	1	0	0	0	0	0	0	0	0	0
3	0	1	0	0	0	0	0	0	0	0
4	0	0	1	0	0	0	0	0	0	0
5	0	0	0	1	0	0	0	0	0	0
6	0	0	0	0	1	0	0	0	0	0
7	0	0	0	0	0	1	0	0	0	0
8	0	0	0	0	0	0	1	0	0	0
9	0	0	0	0	0	0	0	1	0	0
10	0	0	0	0	0	0	0	0	1	0
11	0	0	0	0	0	0	0	0	0	1
12	1	1	0	0	0	0	0	0	0	0
13	1	0	1	0	0	0	0	0	0	0
⋮					⋮					
55	0	0	0	0	0	0	0	1	0	1
56	0	0	0	0	0	0	0	0	1	1

For each of the above sets, the OCS natural frequencies are determined by the FRF matrix partition inversion process demonstrated above. Peak picking or curve-fitting can be used. We can plot the natural frequencies of the various OCS defined by the boundary conditions in Table 1. The lowest three mode frequencies of all 56 systems are plotted in Figure 6.

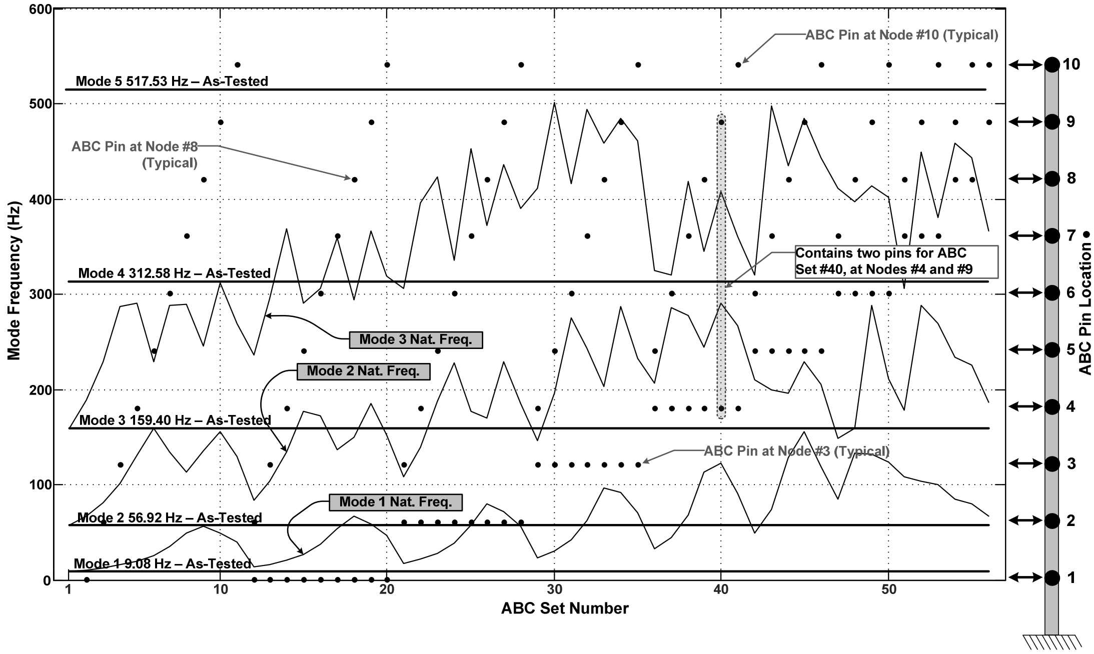

Figure 6. First three mode frequencies for all OCS systems defined by the 56 ABC configurations. ABC pin locations are indicated by the dots, which line up horizontally with the nodes on the beam to the right. For example, the shaded oval at ABC set #40 contains two black dots, which line up with Nodes #4 & #9 on the beam, indicating the artificial pin locations for this set. The as-tested beam natural frequencies are ABC set #1, and these frequency values are extended across the graph as the horizontal lines (as indicated).

In Figure 6, the horizontal lines, labeled "Mode i Nat Freq - As Tested," are the frequencies of the first five modes of the as-tested configuration (ABC Set #1). The jagged curves which depart from the lowest three of these horizontal lines are the mode frequencies for the various OCS systems defined by the ABC sets. As can be seen, the as-tested configuration mode frequencies are lower bounds for the frequencies of all OCS systems. Furthermore, for this system, all of the OCS systems have three modes within the bandwidth spanned by the lowest five modes of the as-tested configuration, indicating that the application of ABC do not necessarily move modes out of a reasonable test bandwidth.

We will now define a boolean flag which is set when an updating parameter index is included in the QR basis calculated from one of the OCS system sensitivity matrices. We will also define several updating solution performance metrics to gauge the effectiveness of an updating solution in both localization and magnitude estimation. We will refer to the quantities calculated for the cth OCS using a superscript. For example, $u^{(c)}$ indicates the solution for the updating parameters found from the cth OCS. Here, c = 1 corresponds to the as-tested configuration (no ABC). Again, for our example, C(10,2) = 56.

6.2. QR Basis Inclusion Flag

The ability of a solution, found from the application of a specific ABC set, to localize an error in a specific updating parameter is dependent upon whether the associated column of [S] is included in the QR basis (i.e. pivot column). We will quantify whether this criterion is satisfied for each ABC configuration, in the following manner. Associated with ABC set "c" is the updating problem,

$$\left\{\delta\Lambda^{(c)}\right\} = \left[S^{(c)}\right]\left\{u^{(c)}\right\} \qquad (21)$$

where $\{\delta\Lambda^{(c)}\}$ are the differences in natural frequency squared between the experimentally identified OCS and the similarly constrained FE model. The sensitivity matrix $[S^{(c)}]$ is calculated from this constrained model. The updating parameter vector $\{u^{(c)}\}$ is calculated from Eq. (21) using the QR method with column pivoting. The QR basis for $[S^{(c)}]$ is the parameter set p(c).

A boolean flag is used to signal whether the ith updating parameter is included in p(c).rendering error localization for this parameter possible, for updating problem "c". We define

$$QRB_c = \begin{cases} 0 \ if \ \ i \in p(c) \\ 1 \ if \ \ i \notin p(c) \end{cases} \qquad (22)$$

($QRB_c = 0$ indicates a "positive" result). This QRB flag will be plotted alongside several updating solution performance metrics, described in the following.

6.3. Updating Solution Performance Metrics

We will employ several metrics for comparing the effectiveness of each of the C = 56 OCS systems (and their solutions) for parametric updating. As we will see, the correlation between these metrics and the QRB flag reveals which ABC set (OCS system) can localize an error in a specific updating parameter.

Equation Residual e: From Eq.(21), we will calculate, for each solution,

$$e_c = \left\| \left\{ \delta\Lambda^{(c)} \right\} - \left[S^{(c)} \right] \left\{ u^{(c)} \right\} \right\|_2 \tag{23}$$

Note that to allow plotting of e_c on the same axes with the other metrics, the set of all e_c values is normalized such that $\max_c \left(e_c \right) = 1$.

Relative Magnitude Error (RME): For the true error in parameter "i" given as u_i^{true}, the relative magnitude error is calculated as

$$RME_c = abs\left(u_i^{(c)} - u_i^{true} \right) \Big/ abs\left(u_i^{true} \right) \tag{24}$$

Maximum False Alarm (MFA): This metric is a measure of the ability of a solution to suppress the reporting of false error locations

$$MFA_c = \max_{j,\, j \neq i} \left(abs\left(u_j^{(c)} \right) \Big/ u_i^{true} \right) \tag{25}$$

We will briefly mention the sensitivity matrix condition number ρ_c, and the angle between the subspace spanned by the columns of [S] and that spanned by [δΛ]. Neither the condition number nor this angle, calculated for each OCS, are correlated with the ability to localize the error or estimate its magnitude. The variation in the condition number and subspace angle is not correlated with any of the above metrics, and hence neither the condition number nor this angle are of use, with respect to our purpose of selecting optimal ABC configurations.

6.4. Simulation Results

One Mode Solution m=1: A single mode is assumed to have been identified from the measured FRF data for each ABC set, and is used to generate the sensitivity matrix and δΛ, as follows. We place a known EI error of 10% in element #1 of the system shown in Figure 1. The true solution vector for this case is $\left\{ u^{true} \right\} = \left\lfloor 0.1 \quad 0 \quad \cdots \quad 0 \right\rfloor^T$. For each OCS, the first-order eigenvalue sensitivity matrix is calculated for m=1 mode and for all n=10 updating parameters, which are the EI errors for each of the 10 elements. The solution $\{u^{(c)}\}$ is calculated using the QR decomposition. In Figure 7, the three metrics, (equation residual e; relative magnitude error, RME; and maximum false alarm, MFA), along with the QR basis flag, QRB, are plotted versus ABC set number. It is seen that the equation residual, e, drops to relative minimum values at only selected ABC sets. It is also seen that the RME and MFA also drop to minima at exactly the same ABC sets, indicating that the updating problems defined by these ABC sets produce accurate solutions for the identification.

Finally, it is seen that the QRB flag drops to zero at the identical ABC set numbers, indicating that an exact identification solution (localization and magnitude) is available for parameter "i" only when the ith column of the sensitivity matrix $[S^{(c)}]$ is included in the QR basis. From inspection of Figure 7, these optimal ABC sets for element #1 are $c_1^{QR} = \left\{ 1, 9, 10, 11, 48:56 \right\}$, Hence, the QRB flag being set "zero" is a condition which can be used to select ABC sets. Figure 7 makes it clear that only a subset of all the ABC sets can be used to locate error in Element #1, specifically, those ABC sets, c_1^{QR}, at which the QRB flag is zero.

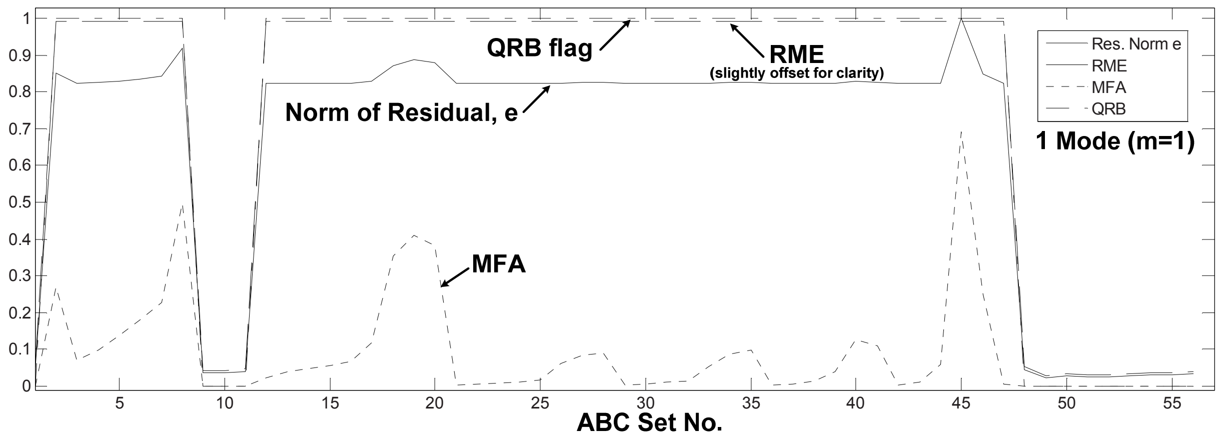

Figure 7. Solution metrics and QRB flag for Element #1, versus ABC set number, m=1 mode used.

We will plot the solution vector $u^{(c)}$ for several selected ABC configurations for which the QRB flag is zero (including the as-tested, i.e. c=1), and also for one ABC configuration for which the QRB flag equals one (failed solution). These four solutions are shown in Figure 8 through Figure 11. The as-tested configuration produces an accurate localization (Figure 8), as does ABC sets #9 & #48. These three solutions all have QRB = 0. The artificial pin locations are indicated by the small triangle. ABC set #33 does not produce an accurate solution, as predicted by QRB = 1.

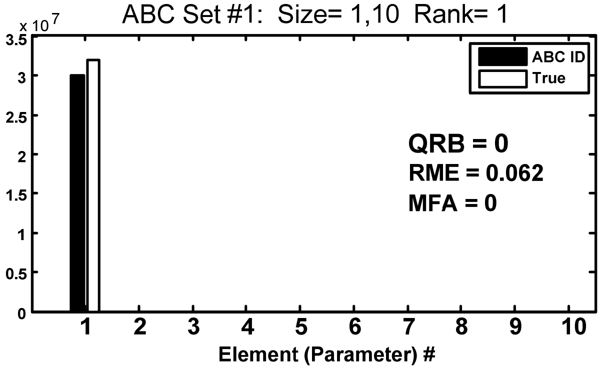

Figure 8. Localization is exact for As-Tested Configuration

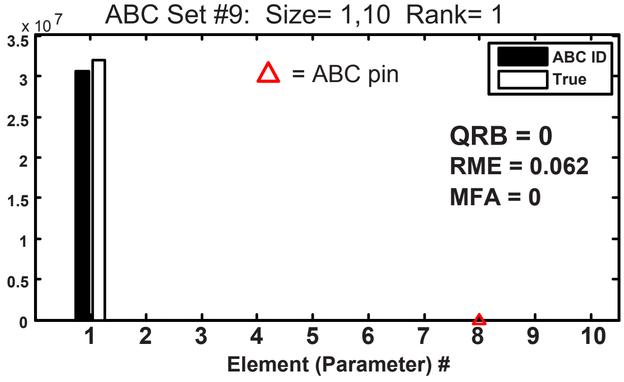

Figure 9. Localization is exact for ABC Set #9

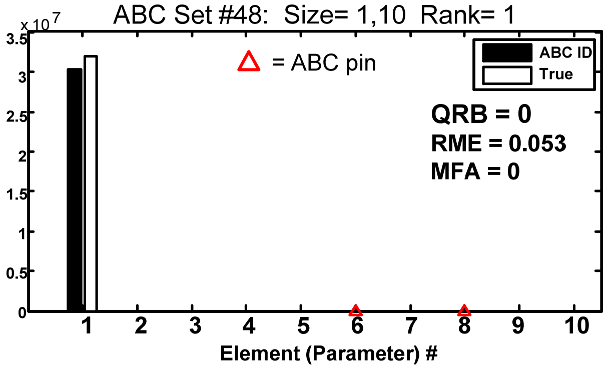

Figure 10. Localization is exact for ABC Set #48

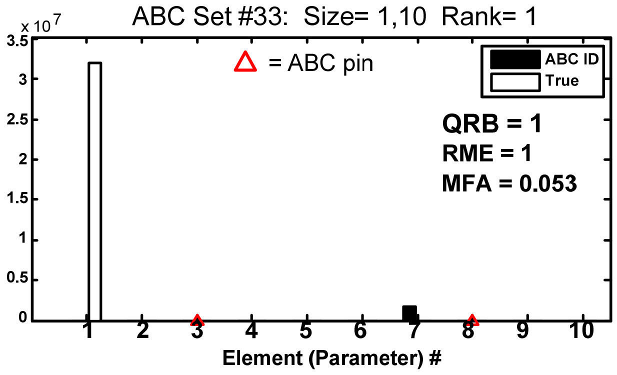

Figure 11. Localization fails for ABC Set #33 (QRB =1)

We can also ask, for a given updating parameter u_i, how many ABC configurations can localize a potential error? This is given by the histogram, shown in Figure 12, where again, only m=1 mode was used. This histogram shows the number of ABC sets for which each updating parameter is included in the QR basis, each basis having been calculated from one of the C=56 one-mode sensitivity matrices. For example, Figure 12 indicates that element #1 is included in the QR basis for 13 of the 56 OCS systems. These 13 systems are listed above as members of the set c_1^{QR}.

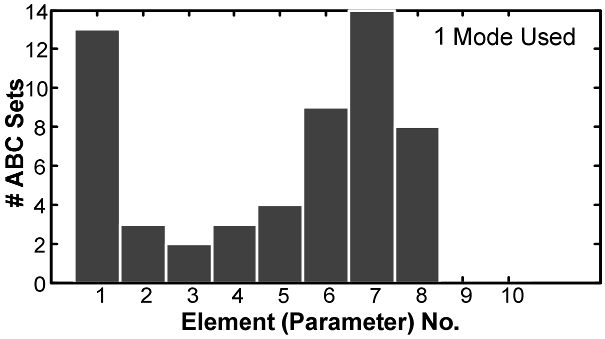

Figure 12. Histogram of updating parameter inclusion in QR basis sets, m=1 mode used

From Figure 12, it is also seen that none of the 56 OCS produce a QR basis which includes either element #9 or element #10, and hence none of these 56 OCS can be used to identify errors or damage in these two. Recalling that all of these updating problems were generated using a single mode, we will now repeat the identification calculations of Figure 7, with the only difference that we now include two modes in all solutions, m=2. This is shown in Figure 13. Comparing Figure 13 with Figure 7, it is seen that there is a greater number of ABC sets at which the QRB flag and solution metrics drop to a minimum. This reveals that the use of two modes (rather than one) increases the number of ABC sets which produce an updating system capable of localizing errors or damage in Element #1.

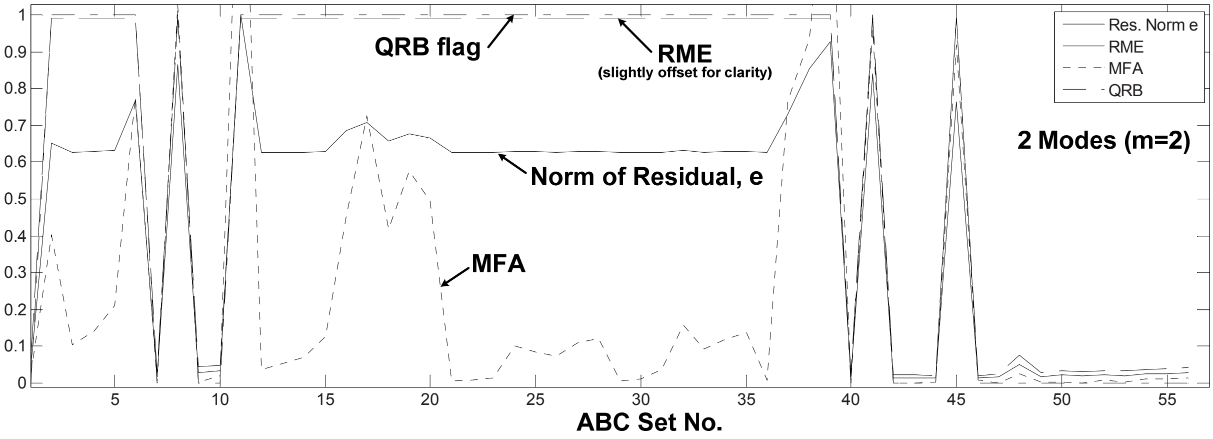

Figure 13. Solution metrics and QRB flag for Element #1, versus ABC set number, 2 modes (m=2) used.

Again plotting the histogram for m = 2 modes, shown in Figure 14, we see that there are now more ABC sets which can be used to localize errors in element #1. Using one mode to construct the updating problem yielded 13 optimal ABC sets (see Figure 12) for element #1, while using two modes increased this to 19 sets. Also, the use of two modes now produces six optimal ABC sets which are able to localize errors in element #9; the use of one mode had produced no ABC sets able to do so. The number of optimal ABC sets for element #2 actually decreases. Therefore, this procedure constitutes a means of determining modal sufficiency, for each potential updating parameter.

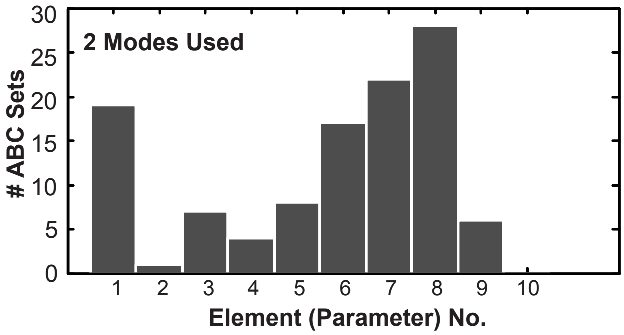

Figure 14. Histogram of updating parameter inclusion in QR basis sets, m=2 modes used

With an error placed in Element #9, we again calculate the solution metrics and QRB flag versus ABC set number, and we see in Figure 15 that there are precisely 6 ABC sets at which QRB = 0 (and at which the solution metrics drop to their respective minima).

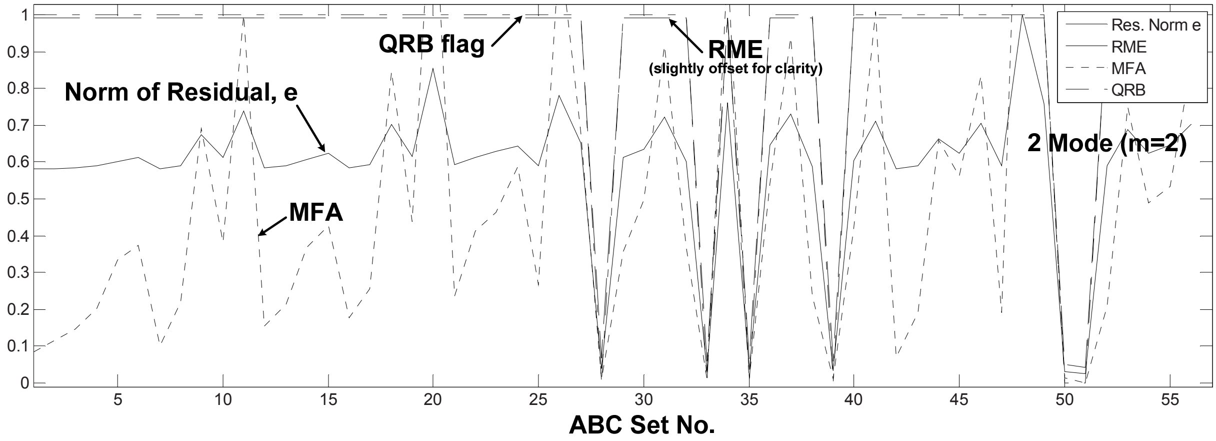

Figure 15. Solution metrics and QRB flag for Element #9, versus ABC set number, 2 modes (m=2) used.

Finally, we address the ability to localize errors in element #10. As this element is at the free end of the beam, it presents some difficulty for a sensitivity-based algorithm due to the greater number of modes required to generate sensitivities of sufficient magnitude. From the histograms shown in Figure 12 and Figure 14, it is seen that neither one mode nor two modes is sufficient to localize error in element #10. The use of three modes is still insufficient to identify errors in element #10, as shown in Figure 16. However, using four modes does produce three ABC sets at which QRB = 0, as shown in Figure 17. In other words, a minimum of four modes is required in order for element #10 to be included in the QR basis. This makes clear the correlation between the QR column pivot selection algorithm and obtaining a sensitivity matrix of sufficient sensitivity to errors in element #10.

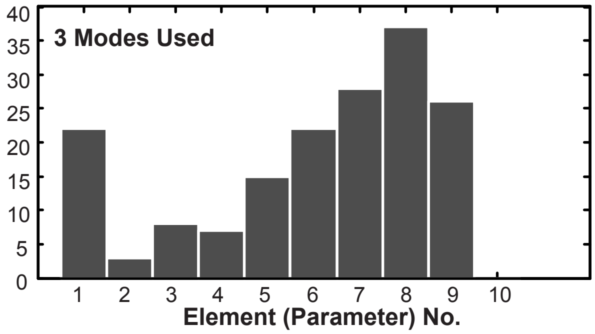

Figure 16. Histogram of updating parameter inclusion in QR basis sets, m=3 modes used. No optimal ABC sets for element #10 are produced.

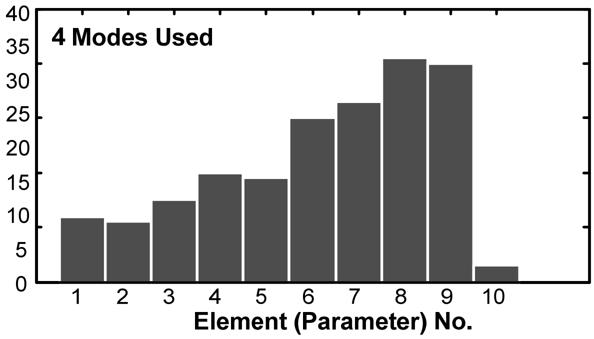

Figure 17. Histogram of updating parameter inclusion in QR basis sets, m=4 modes used. Three optimal ABC sets for element #10 are produced.

The solution metrics for an error in element #10, and the QRB flag, are plotted in Figure 18, where the three optimal ABC sets can be identified.

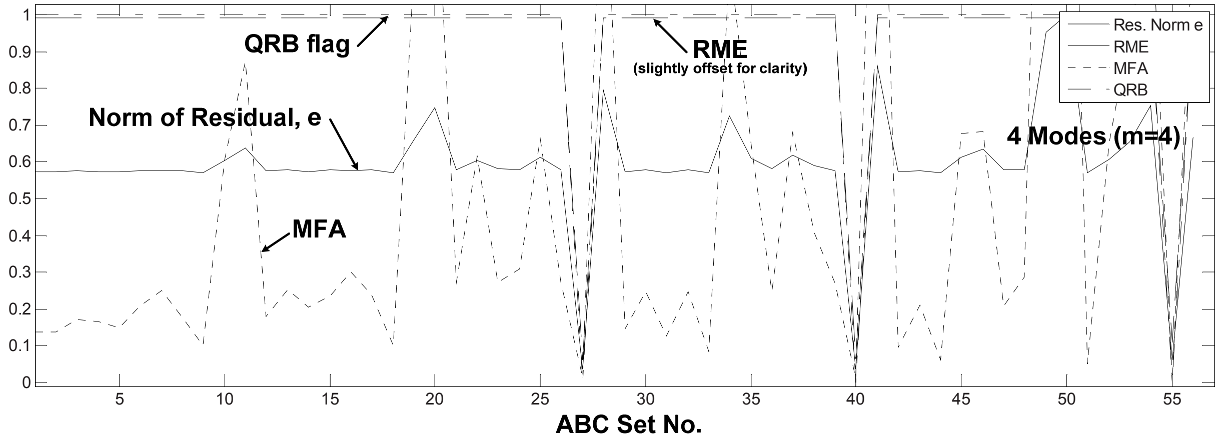

Figure 18. Solution metrics and QRB flag for Element #10, versus ABC set number, 4 modes (m=4) used.

6.5. Multiple OCS

The use of an updating system, Eq. (3), with m = 1 can uniquely identify a single parameter error; for two parameters errors, m ≥ 2 is required, and so forth. In order to identify multiple parameter errors, potentially in any, and possibly all, updating parameters, m ≥ n is required. A single updating system is assembled, comprised of rows selected from the c_i^{QR}, and i = 1,2,3,...,n.

We compile a database of optimal ABC sets for each element, based on the use of four modes, which was determined to be required to localize errors in all elements. We can tabulate this information in two useful ways. The first way tabulates, for each element "i" (updating parameter), the optimal ABC set indices, c_i^{QR}, i = 1,2,3,...,n. We provide an abbreviated list for illustration in Table 2, where for compactness of presentation, we limit the number of configurations displayed for each element to a maximum of 17. Table 2 shows the ABC set numbers for which an element is in the QR basis. For example, to identify an error in element #2, the OCS natural frequencies for ABC sets numbered 2, 4, 20, 29, etc., may be used. The sensitivity matrices calculated with these ABC applied to the FE model will result in element #2 being included in the QR basis. Alternatively, this information can be tabulated as shown in Table 3, where the membership of the QR basis set, for each ABC set, is shown. Again, four modes were used.

Table 2. Optimal ABC sets by Element Index (updating parameter). Only the first 17 configurations for each element are shown, for compactness. Four modes used.

Elem. No.	ABC Set Index, c																
1	1	7	36	37	39	41	47	49	50	53	54	55	0	0	0	0	0
2	2	4	20	29	30	31	32	33	34	35	48	0	0	0	0	0	0
3	3	5	8	9	12	14	18	38	40	42	43	44	46	51	52	0	0
4	4	13	15	16	20	21	23	24	26	28	42	43	44	45	46	48	51
5	5	6	7	14	15	16	18	20	22	25	26	29	31	32	47	48	49
6	1	2	3	7	8	9	10	11	12	14	16	17	18	19	20	23	24
7	1	4	5	6	9	10	11	13	14	17	19	21	22	25	26	28	29
8	1	2	3	4	6	7	8	9	10	11	12	13	15	16	17	18	19
9	2	3	5	6	8	10	11	12	13	15	17	19	21	22	23	24	25
10	27	40	55	0	0	0	0	0	0	0	0	0	0	0	0	0	0

Table 3. Updating parameters in the QR basis for each ABC set. Four modes used, m=4.

	Elem # in QR basis, m=4			
Set #	Row #1	Row #2	Row #3	Row #4
1	**8**	**7**	**6**	**1**
2	**9**	8	6	**2**
3	9	8	6	**3**
4	2	8	7	**4**
5	9	3	7	**5**
6	9	8	7	5
⋮	⋮			
54	9	7	6	1
55	**10**	7	6	1
56	4	5	7	8

The information contained in Table 3 identifies a minimum number of ABC sets for which updating systems (i.e. Eq. (21)) need to be generated. In fact, only selected rows from each of these selected ABC sets need be included. For our example problem, with 10 elements (10 updating parameters), we search Table 3 to find a minimum number ABC set indices such that each updating parameter is included once as a QR basis parameter. This not only down-selects the number of ABC sets, but from within each selected ABC set, down-selects the individual rows of $[S^{(c)}]$.

For our 10-element beam, the rows containing the shaded cells in Table 3 indicate those ABC sets which are selected, and the corresponding columns indicate the specific QR basic parameters (rows of $[S^{(c)}]$) which will be included. There are six ABC sets for which OCS need to be generated (which includes ten shaded cells). Therefore, it is not necessary to actually construct all of the OCS, beyond that needed to make this selection possible. From each of these six OCS, the selected rows of the sensitivity matrices are used to construct a final "composite" sensitivity matrix. This amounts to a total of 10 rows, which results in a square composite sensitivity matrix. Based on the shaded cells in Table 3, we use all four rows of the sensitivity matrix $[S^{(1)}]$ calculated from the FE model in the as-tested configuration (ABC set #1). These rows provide a basis for elements 8,7,6, and 1. For the remaining elements 2,3,4,5,9, and 10, we use rows 1 and 4 of $[S^{(2)}]$, calculated from the application of ABC set #2 to the FE model, and which represent elements 9 and 2. With the additional rows needed, the composite sensitivity matrix is illustrated as follows.

$$\begin{Bmatrix} \begin{Bmatrix} \delta\Lambda_1^{(1)} \\ \delta\Lambda_2^{(1)} \\ \delta\Lambda_3^{(1)} \\ \delta\Lambda_4^{(1)} \end{Bmatrix} \\ \hdashline \begin{Bmatrix} \delta\Lambda_1^{(2)} \\ \delta\Lambda_4^{(2)} \end{Bmatrix} \\ \hdashline \left\{ \delta\Lambda_4^{(3)} \right\} \\ \hdashline \left\{ \delta\Lambda_4^{(4)} \right\} \\ \hdashline \left\{ \delta\Lambda_4^{(5)} \right\} \\ \hdashline \left\{ \delta\Lambda_1^{(55)} \right\} \end{Bmatrix} = \begin{bmatrix} \begin{bmatrix} \cdots & S_{row1}^{(1)} & \cdots \\ \cdots & S_{row2}^{(1)} & \cdots \\ \cdots & S_{row3}^{(1)} & \cdots \\ \cdots & S_{row4}^{(1)} & \cdots \end{bmatrix} \\ \hdashline \begin{bmatrix} \cdots & S_{row1}^{(2)} & \cdots \\ \cdots & S_{row4}^{(2)} & \cdots \end{bmatrix} \\ \hdashline \begin{bmatrix} \cdots & S_{row4}^{(3)} & \cdots \end{bmatrix} \\ \hdashline \begin{bmatrix} \cdots & S_{row4}^{(4)} & \cdots \end{bmatrix} \\ \hdashline \begin{bmatrix} \cdots & S_{row4}^{(5)} & \cdots \end{bmatrix} \\ \hdashline \begin{bmatrix} \cdots & S_{row1}^{(55)} & \cdots \end{bmatrix} \end{bmatrix} \begin{Bmatrix} u_1 \\ u_2 \\ u_3 \\ u_4 \\ u_5 \\ u_6 \\ u_7 \\ u_8 \\ u_9 \\ u_{10} \end{Bmatrix} \tag{26}$$

Using this system shown, Eq. (26), we perform the identification for a known error installed successively in each element. The results of these 10 identification problems are shown in Figure 19. The composite system is able to precisely locate the error, regardless of its location. This is due to the composite system possessing a QR basis which includes every updating parameter, u_i. It should be noted that similarly constructed overdetermined systems will also localize the error, regardless of location, as long as the QR basis includes at least one row for each element.

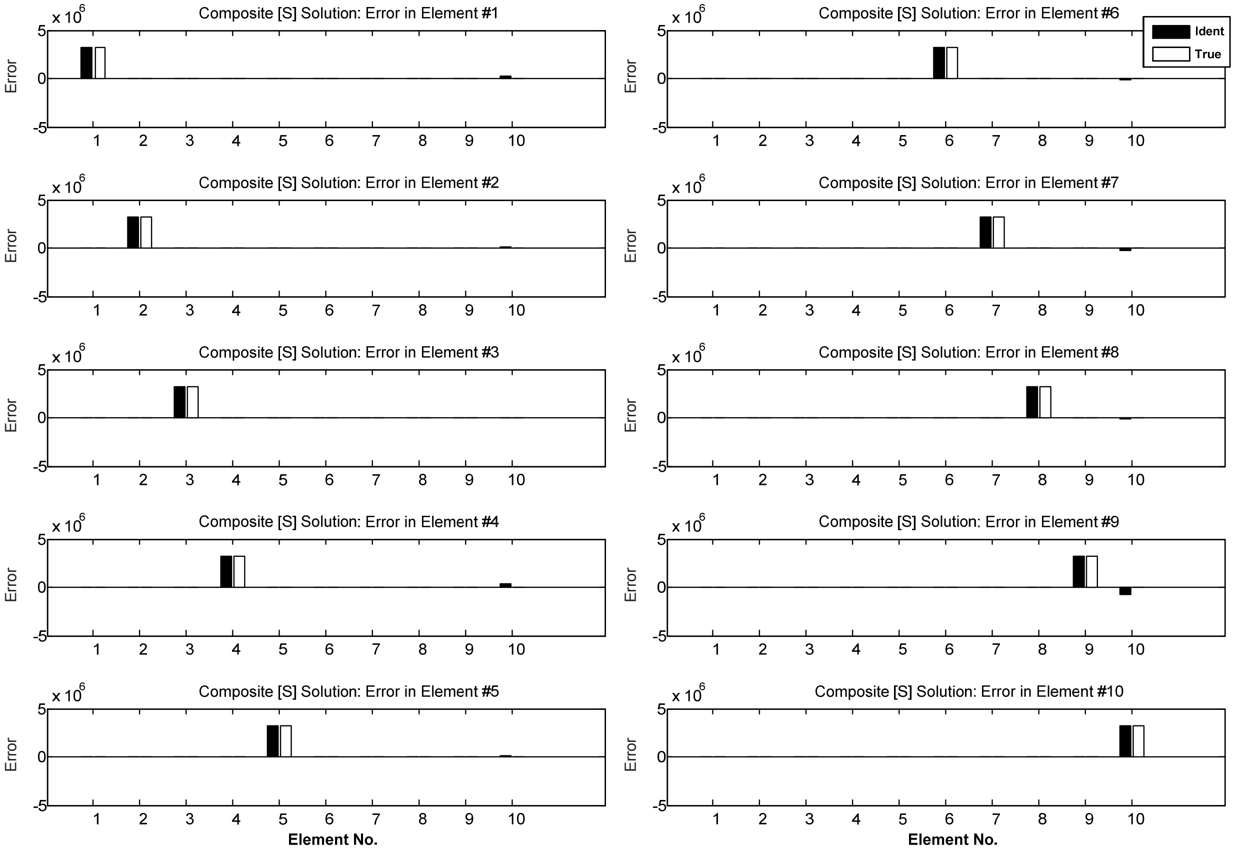

Figure 19. Solution using composite updating system assembled from multiple OCS. True error is installed in every element sequentially, demonstrating that the composite system is able to uniquely localize the error in every element.

7. Summary and Conclusions

A square experimentally measured FRF matrix can easily be processed to identify the natural frequencies for a potentially large number of distinct sets of artificial boundary conditions (ABC), the term artificial indicating that these boundary conditions need not be physically applied to the structure. A set of ABC defines an omitted coordinate system (OCS), which corresponds to the structure with additional restraints ("pins") artificially placed at some combination of a subset of the measurement locations. The number of combinations is given by the binomial coefficient. These same boundary conditions are easily applied to the FE model of the structure, starting in its "as-tested" configuration. From each OCS, a system of equations for model updating is defined which include a sensitivity matrix and a vector of differences in the square of the experimentally-identified and FE-calculated natural frequencies. Using a simple beam example with 10 simulated measured responses, the parametric updating systems were generated and solved for all combinations of two ABC pins. The solution was performed using the QR decomposition with column pivoting, which in the underdetermined case, provides a basic solution (not least-norm). The accuracy of these identification solutions were quantified using metrics defined for error localization and magnitude, the Relative Magnitude Error (RME) and Maximum False Alarm (MFA) . The RME and MFA were plotted versus ABC set number, and when the RME and MFA drop to zero, the updating parameter error location and magnitude are precisely estimated. It is shown that the ability of an OCS updating system (generated by a single ABC set) to successfully localize error in a specific updating parameter requires that the associated column of the sensitivity matrix be included in the QR basis. The permutation matrix of the QR decomposition reveals whether the updating parameter (i.e. its matrix column) is included in the basis. This inclusion in the QR basis is tracked, versus ABC set number, by a boolean flag, QR Basis (QRB), defined for this purpose. The QRB flag is shown to be exactly correlated with the RME and MFA. Therefore, the QR decomposition with column pivoting provides an effective updating parameter subset selection strategy. This strategy identifies those updating parameters for which errors can be localized by the OCS, resulting from a specific ABC set. We refer to these ABC sets as optimal ABC sets, but in fact they are not simply optimal, but for a given updating parameter, their use is required in order to localize errors. Conversely, there are updating parameters which cannot be localized by the updating systems produced by the non-optimal ABC sets. The use of ABC provides numerous updating systems and can significantly increase the likelihood of generating an OCS sensitivity matrix for which the QR basis includes each updating parameter of interest.

It is also shown that the minimum number of modes required to successfully perform model update is established by the requirement that, for every updating parameter, at least one ABC set have a QRB flag set to zero. This requirement translates into a requirement on the minimum number of modes needed to produce such an ABC set. The number of ABC sets with a zero QRB flag, for each updating parameter, was plotted as a histogram. The use of multiple OCS system sensitivity matrices, assembled into a composite updating system, was shown to uniquely localize a parameter error, regardless of its location. This ability is dependent simply on constructing a basis which includes representation from each updating parameter. The ability to generate many ABC sets greatly increases this practical possibility, with a moderate demand on the number of required modes.

References

[1] G. Lallement, J. Piranda, Localisation methods for parameter updating of finite element models in elastodynamics, 8th International Modal Analysis Conference. (1990) Orlando, Florida, USA. pp. 579-585.

[2] W. D'Ambrogio, A. Fregolent, Dynamic model updating using virtual antiresonances, Shock and Vibration, 11 (2004) 351-363.

[3] J.E. Mottershead, On the zeros of structural frequency response functions and their sensitivities, Mechanical Systems and Signal Processing. **12**(5) (1998) 591-597.

[4] W. D'Ambrogio, A. Fregolent, The use of antiresonances for robust model updating, Journal of Sound and Vibration 236(2) (2000) 227-243.

[5] K. Jones, J. Turcotte, Finite element model updating using antiresonant frequencies. Journal of Sound and Vibration 252(4) (2002) 717-727.

[6] W. D'Ambrogio, A. Fregolent, Results obtained by minimizing natural frequency and antiresonance errors of a beam model, Mechanical Systems and Signal Processing 17(1) (2003) 29-37.

[7] D. Hanson, T.P. Waters, D.J. Thompson, R.B. Randall, R.A.J. Ford, The role of anti-resonance frequencies from operational modal analysis in finite element model updating, Mechanical Systems and Signal Processing 21 (2007) 74-97.

[8] S. Li, S. Shelley, and D. Brown, Perturbed boundary condition testing, Proceedings of the 13th International Modal Analysis Conference, Vol. 1 (1995) 902-907.

[9] B.K. Wada, C.P. Kui, R.J. Glaser, Extension of ground-based testing for large space structures, Journal of Spacecraft, Vol. 23 No. 2 (1986) 184-188.

[10] B.K. Wada, C.P. Kuo, R.J. Glaser, Multiple boundary condition tests (MBCT) for verification of large space structures, AIAA Paper 86-0905 (1986).

[11] C.P. Kuo, B.K. Wada, System identification of a truss type space structure using the multiple boundary condition test (MBCT) method, AIAA Paper 87-0746 (1987).

[12] C.P. Kuo, B.K. Wada, Multiple boundary condition test (MBCT): Identification with mode shapes, AIAA Paper 88-2353. (1988).

[13] J. H. Gordis, Artificial boundary conditions for model updating and damage detection, journal of mechanical systems and signal processing, Vol. 13, No. 3 (1999) 437-448.

[14] J. H. Gordis, Omitted coordinate systems and artificial constraints in spatially incomplete identification." Int. J. Anal. Exp. Modal Anal, Vol. 11 No. 1-2. (1996) 83-95.

[15] J. H. Gordis, Spatial, frequency domain updating of linear, structural dynamic models, Proceedings of the 34th AIAA/ASME/ASCE/AHS/ACS Structures, Structural Dynamics, and Materials Conference, (1992) 3050-3058.

[16]] J. H. Gordis, An Analysis of the Improved Reduced System Model Reduction Procedure," Int. J. Anal. Exp. Modal Anal, Vol. 9 No. 4 (1994) 269-285.

[17]] J. H. Gordis, An exact formulation for structural dynamic model error localization, Int. J. Anal. Exp. Modal Anal, Vol. 10 No. 1 (1995) 19-33.

[18] E.J. Berman, M.S. Allen, D.C. Kammer, R.L. Mayes, Probabilistic investigation of sensitivities of advanced test-analysis model correlation methods, Journal of Sound and Vibration. 329(2010) 2516-2531.

[19] Z.Tu, Y. Lu, FE model updating using artificial boundary conditions with genetic algorithms, Computers and Structures, Vol. 86 (2008) 714-727.

[20] Y. Lu, Z.Tu, Artificial boundary condition approach for structural identification: a laboratory perspective, 26th International Modal Analysis Conference, Orlando, Florida USA (2008).

[21] A. Berman, System identification of structural dynamic models -theoretical and practical bounds, Proceedings of the AIAA/ASME/ASCE/AHS 25th Structures, Structural Dynamics, & Materials Conference, (1984) 123-128.

[22] J.H. Wilkinson, The Algebraic Eigenvalue Problem, Oxford University Press, 1965.

[23] D.A. Rade, G. Lallement, A strategy for the enrichment of experimental data as applied to an inverse eigensensitivity-based FE model updating method, Mechanical Systems and Signal Processing, **12**(2). (1998) 293-3078.

[24] C. Fernandez, Artificial boundary conditions in sensitivity based finite element model updating and structural damage detection, Master's Thesis. Naval Postgraduate School. Monterey, CA. 2004.

[25] S. Boyd, Lecture 8 Least-norm solutions of underdetermined equations, EE263 Autumn Stanford University 2007-08.

[26] G.H. Golub, C.F. Van Loan, Matrix Computations, The Johns Hopkins University Press, 3rd Ed. 1996.

[27] MATLAB® R2010A, The Mathworks, Inc. Natick, MA.

[28] M.J. Lai, On sparse solutions of underdetermined linear systems, Journal of Concrete and Applicable Mathematics. 2009.

[29] D.L. Donoho, For Most Large Underdetermined Systems of Linear Equations the Minimal L_1-norm Solution is also the Sparsest Solution, Communications on Pure and Applied Mathematics, Vol. LIX (2006) 0797–0829.

Use of Damping Solution for Acceleration Measurements in High Vibration Environments

Tom Connolly
Senior Design Engineer
Measurement Specialties, Inc.
32 Journey suite 32
Aliso Viejo, CA 92656

ABSTRACT

In many accelerometer applications, one can be faced with the challenge of making low amplitude, low frequency measurements in the presence of spurious high vibrations. Wideband, undamped accelerometers are commonly used for acceleration measurements in these applications but dynamic range must be sacrificed so as not to risk distortion and amplifier overload, or even damage to the device. A more suitable approach incorporates damping such that high frequency content above the passband of interest is directly mitigated. This paper contrasts and compares the effect of damping on the performance characteristics of piezoresistive MEMS and bonded strain gage accelerometers. It addresses the compromises that have to be made in terms of temperature response, phase delay, and noise for both fluid and gas damping. Also discussed are the inherent limitations of electronic filtering as an alternate approach for rolling off high frequency noise when using wideband accelerometers. A discussion of specific applications and test results are presented.

INTRODUCTION

Engineers and technicians are often confronted with measuring low level vibrations in a noisy environment that includes extraneous high frequency content. This can be random vibration over a broad spectrum or unwanted structural resonances outside the established passband.

Existing practice for flight test measurements is the use of accelerometers that have a wide bandwidth and a high Q (negligible damping) such as piezoelectric accelerometers. If the vibration in the installation contains frequencies that are near the natural frequency of the undamped accelerometer, a resonance peak occurs. This risks distortion of the waveform due to clipping in the user's data acquisition system if the gain is not set appropriately. On the other hand, scaling down the gain to compensate for the amplification at resonance can dramatically reduce measurement resolution at the desired low frequency.

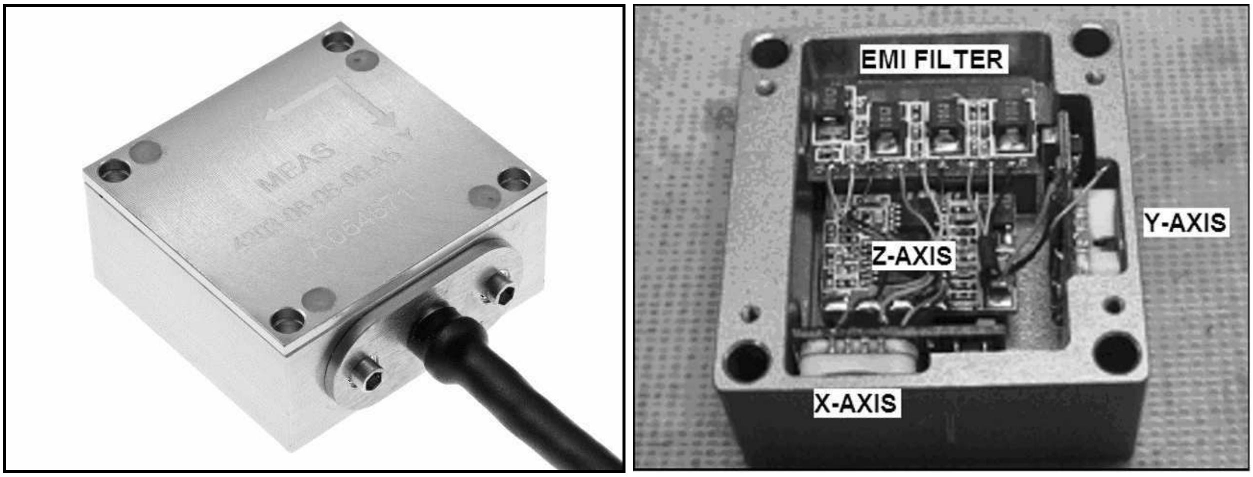

Fig. 1 – MEAS Model 4203 Triaxial Accelerometer Envelope and Interior View

T. Proulx (ed.), *Sensors, Instrumentation and Special Topics, Volume 6*, Conference Proceedings of the Society for Experimental Mechanics Series 9,
DOI 10.1007/978-1-4419-9507-0_16, © The Society for Experimental Mechanics, Inc. 2011

ELECTRONIC FILTERING

A common approach to addressing the issue of unwanted high frequency content and anti-aliasing is heavy low pass filtering on the front end of the user's data acquisition system. One example is the Measurement Specialties (MEAS) Model 4203 triaxial accelerometer designed primarily for race car monitoring as depicted in Figure 1. Its piezoresistive sensor element is responsive to vibration over a wide frequency band. However, Motorsports require a more limited passband in order to measure whole body motion.

Figure 2 shows a broadband spectral density plot from an actual NASCAR race that exhibits a spike at 155 Hz due to engine vibration. The filtering from the electronic circuit within 4203 eliminated this spike so the analysis can focus on low frequency content. For instance, the 30 Hz signal is due to contact patch loading variations due to tire rotation.

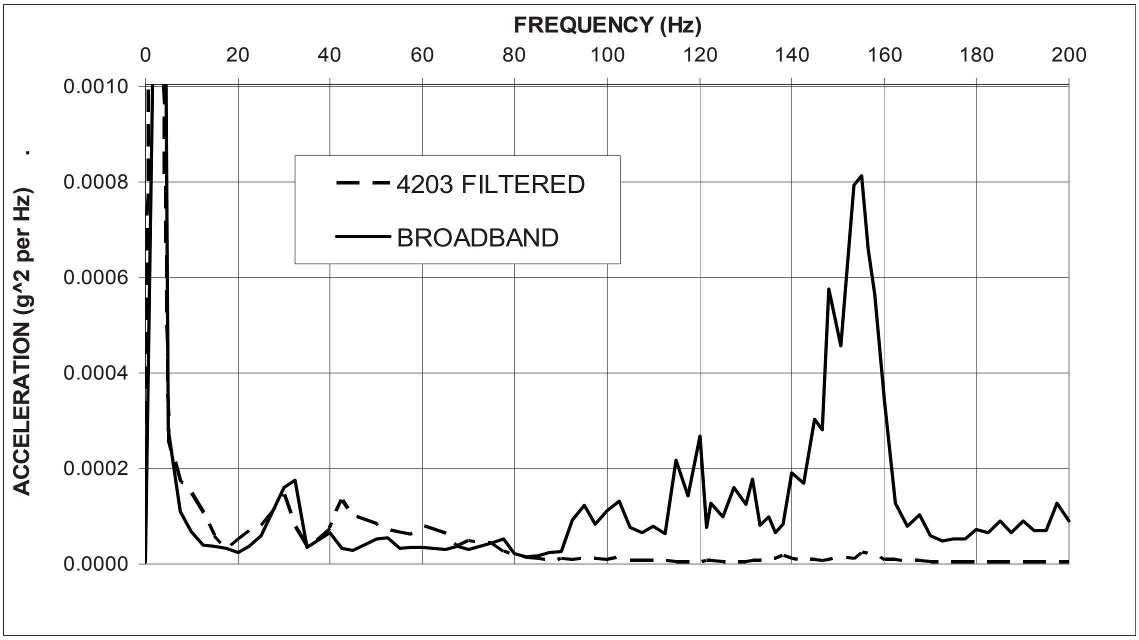

Fig. 2 – Spectral Density Plot from Race Track Run

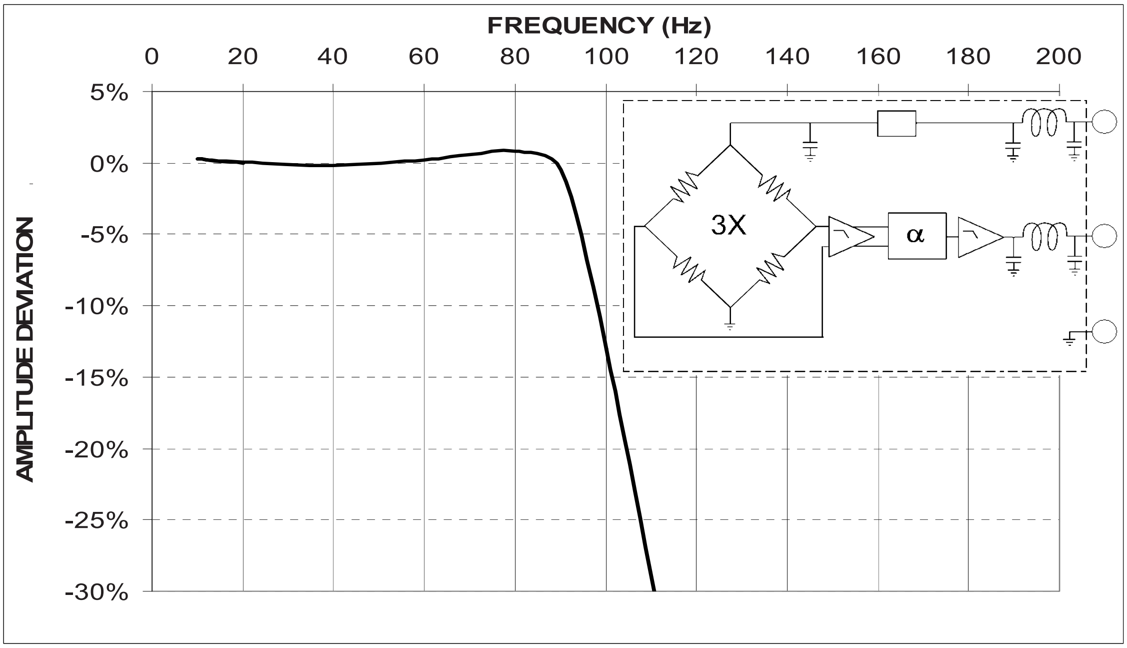

Fig. 3 – Model 4203 Frequency Response and Circuit Block Diagram

Figure 3 shows the signal being safely rolled off within the accelerometer without influencing low frequency content. The on-board signal conditioning provided a low pass eight pole Butterworth filter with a -3dB corner at 110 Hz.

This was accomplished by the judicious selection of over-travel stop locations in the sensor element and electrical filtering prior to the gain stage. This did require some sacrifice in measurement resolution because of the use of a sensor element with a higher full scale rating than that required for the actual measurement. Otherwise the proofmass could have engaged the mechanical stops whose deleterious effects may have been disguised by the filtering. Note that a brickwall filter can also create unintended distortions and errors in the time domain.

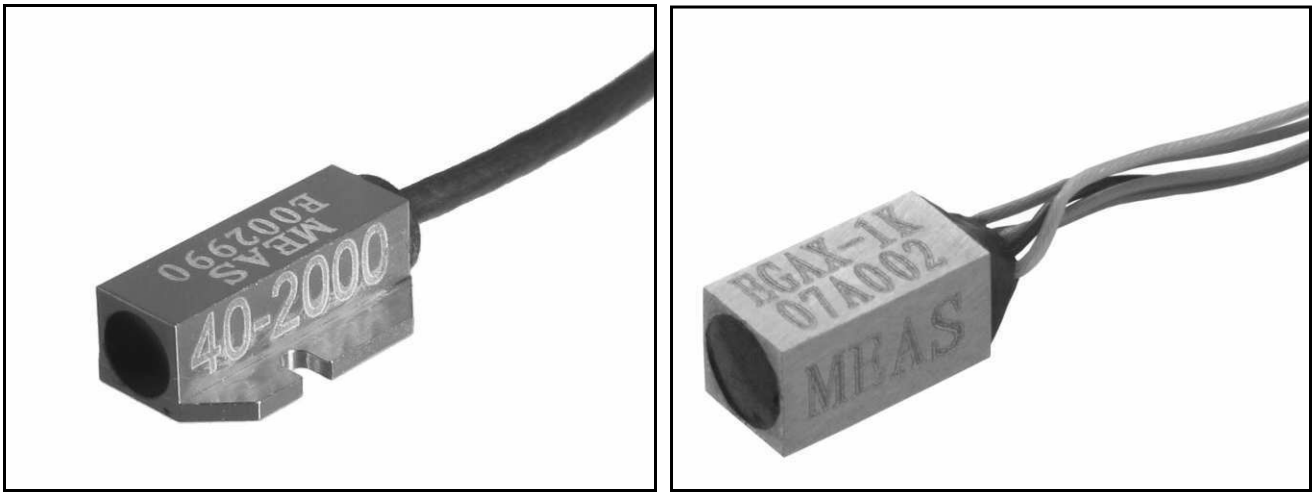

Fig. 4 – MEAS Fluid Damped Models 40 and EGAX

FLUID DAMPED PERFORMANCE

Unwanted high frequency content can be directly mitigated through the use of mechanical damping. MEAS has several fluid damped accelerometers that feature bonded silicon strain gage technology as depicted in Figure 4.

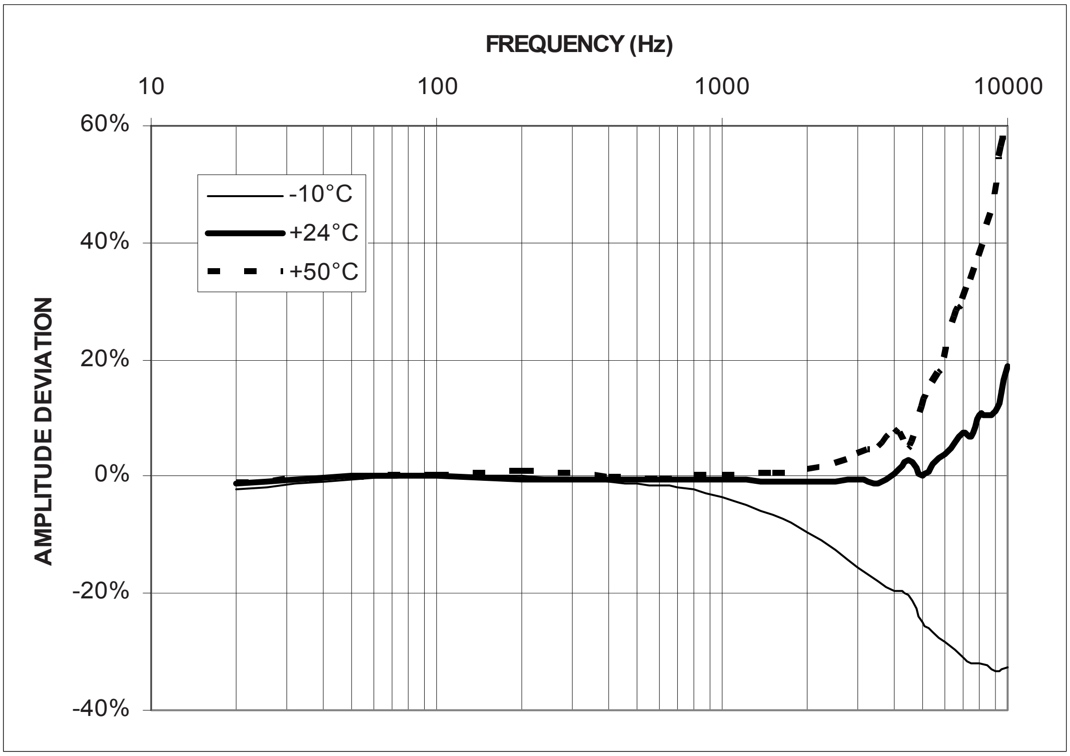

Fig. 5 – Fluid Damped Frequency Response versus Temperature

The deficiency of fluid damping is that it results in a significant change in the viscosity of the media over temperature. The frequency response becomes exceedingly overdamped going cold and significantly underdamped going hot. Figure 5 illustrates the effect of changing temperatures on the MEAS Model 40.

FLUID DAMPED CONSTRUCTION

A four leg fully active Wheatstone bridge is formed by adhesively bonding silicon gages to the flexures of a stainless steel cantilevered proofmass as seen in Figure 6. Two gages are mounted on the top surface of the flexure, and two on the bottom, so that two legs are in tension and two in compression when loaded. Mechanical stops prevent damage to the device by restricting overrange.

Damping is fine tuned to a nominal of 0.7 critical at room ambient by the mixing of silicone oils of selected viscosities and injecting into the sealed cavity around the proofmass. Construction requires an iterative approach of mixing silicone oils and frequency response testing in order to attain the optimum viscosity.

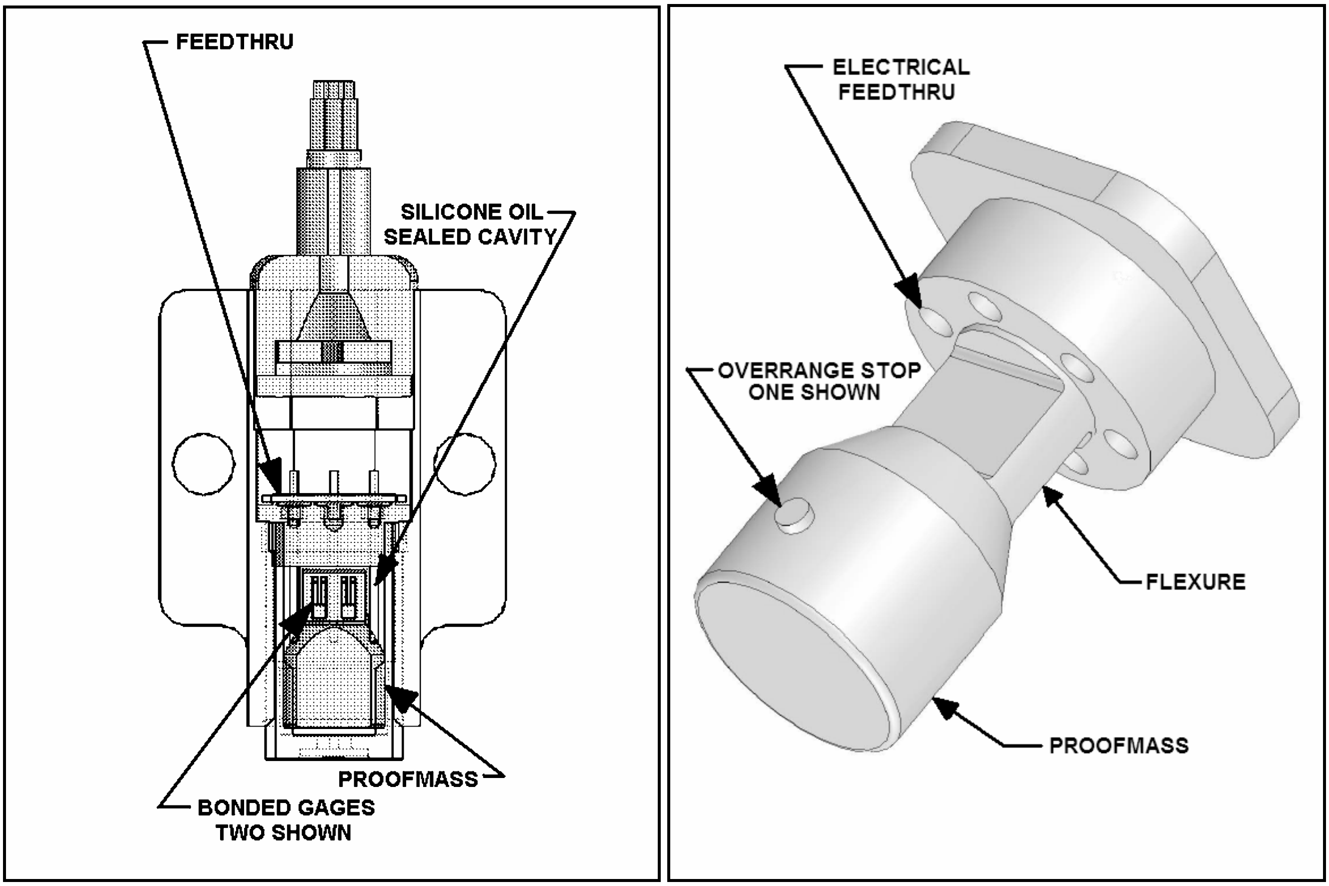

Fig. 6 – Model 40 Cantilevered Proofmass with Bonded Strain Gages

GAS DAMPING PERFORMANCE

The latest offering from MEAS is a family of accelerometers that uses squeeze-film gas damping in a miniaturized piezoresistive (PR) sensor element. A main advantage of gas damping is that the media experiences negligible changes in viscosity over temperature. This results in a damping ratio change of only 0.08% per degrees Celsius.

The control function of an accelerometer can be thought of as a single-degree of freedom device and is modeled as a mass-spring-damper system with a natural frequency and damping factor. A nominal damping of 0.7 critical was selected in order to prevent accelerometer resonance peaks and to optimize the flatness of the passband.

Damping can actually extend the usable passband for a given natural frequency as can be seen in the top chart of Figure 7. For a ±5% amplitude error (±0.43dB), the undamped natural frequency must exceed the maximum frequency to be measured by a factor of five due to the rise experienced from the high Q. On the other hand, an accelerometer with 0.7 critical damping can have the maximum frequency of interest within half of the natural frequency. Thus, the damped device has a 2.5 times increase in usable bandwidth over the undamped. Additionally, a damped device is more rugged than an undamped one which enhances reliability.

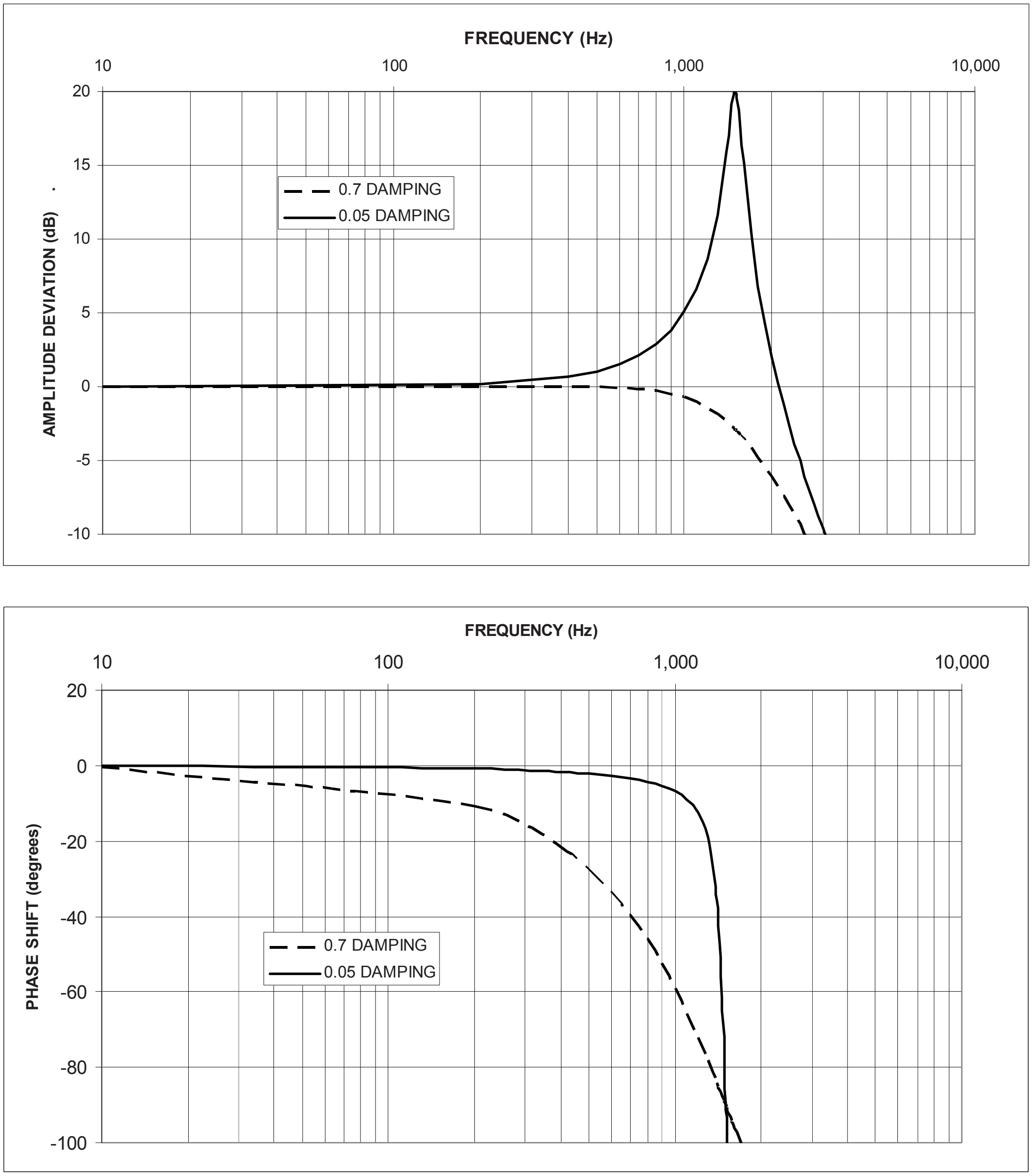

Fig. 7 – Damping Comparison

A potential disadvantage of damping is phase shift. For an undamped accelerometer, there is minimal phase shift in the passband and the change occurs rapidly as it goes through resonance. The phase of a damped device changes gradually over frequency. This is shown in the bottom chart of Figure 7. However, the waveform is preserved as long as the phase change is linear over frequency though it will be time delayed.

One illustration of the advantage of mechanical damping is that of a commercial aircraft manufacturer who wanted to make sway measurements of the engine during take-off and landing. They attempted to take measurements of a few hundred milli-g's over a bandwidth of 0.5 to 5 Hz. However, the engine generated 100g spikes at a frequency of 300 Hz which saturated the undamped accelerometer. MEAS provided a damped solution that mechanically filtered the unwanted engine noise and accurate measurements were attained.

GAS DAMPING CONSTRUCTION

The proofmass of the MEAS piezoresistive sensor is sandwiched between two fixed parallel surfaces, formed by the cap and base, with gas filling the small gaps in between. Damping is controlled by the depth of the cavities facing the proofmass that are etched into the cap and base. If the proofmass moves slowly, the gas film experiences little compression. When the proofmass moves at a high frequency, the gas is effectively trapped in the gap and compressed. This is an action that dissipates mechanical energy and results in damping.

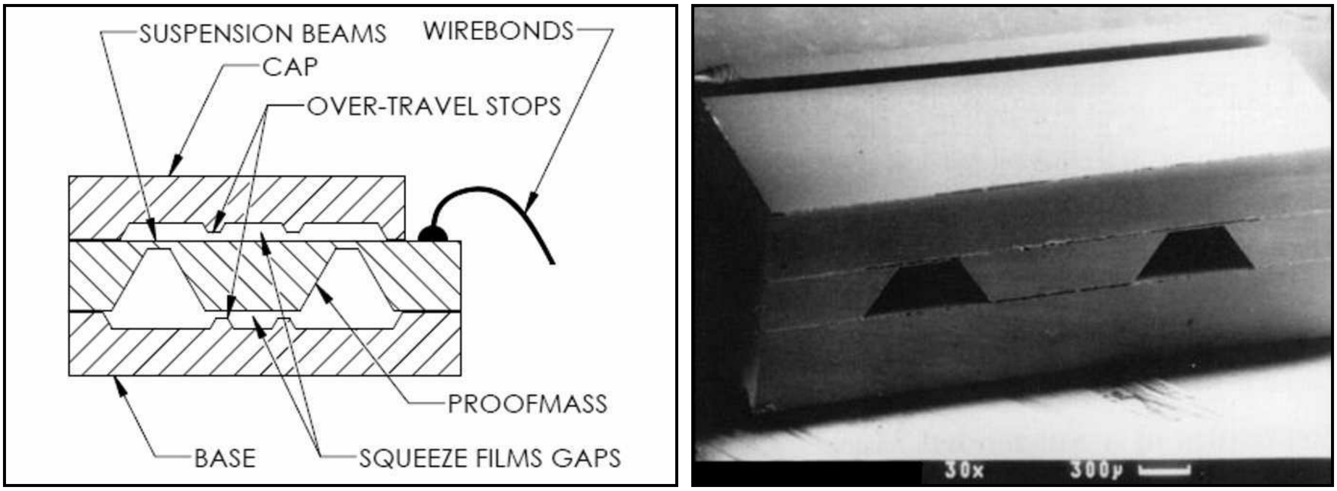

Fig. 8 – Piezoresistive Sensor Element Cross-section

The sensor features Micro Electro Mechanical Systems (MEMS) technology using bulk micromachining. The middle layer is contained between a silicon top cap and a base cap that, along with the frame, form an enclosure around the proofmass. The caps provide squeeze-film gas damping. The etch depths of the cavities in the caps are important in determining damping. This mechanically suppresses resonant peaks.

Figure 8 is a cross-section of the sensor element. The middle layer contains the proofmass suspended from a frame by four beams, approximately 10 microns thick, in a double cantilever configuration. This arrangement provides rectilinear motion.

Single-crystal silicon has superior mechanical characteristics compared to that of steel. The sensors are fabricated from a stack of three micromachined silicon wafers bonded together. After singulation, the top wafer forms the cap of the sensor and the bottom layer the base. The middle layer contains the proofmass, suspension beams, and reference frame. The resistors are ion-implanted in strain sensitive locations on the suspension beams in order to form a four-leg fully-active Wheatstone bridge configuration. Since the resistive gages are implanted into the silicon, there is no concern about adhesive bonding creep.

CONCLUSION

Field testing has demonstrated that mechanical damping offers the ability to acquire high definition, low frequency vibration measurements down to DC in severe dynamic environments. Measurement Specialties offers product families of both fluid and gas damped piezoresistive bridge accelerometers, as well as high order electronic filtering, whose advantages and disadvantages must be understood by the user in order to achieve valid results.

AUTHOR

Tom Connolly has been involved in transducer design since 1982. He has held the position of Senior Design Engineer at the Vibration Design Center of Measurement Specialties, Inc. (MEAS) in Aliso Viejo, California since January 2007 where he is responsible for the development and qualification of accelerometers using piezoresistive and piezoelectric technologies. Over a span of twenty years prior to MEAS, he was further involved in vibration sensor design while working for PCB Piezotronics and Endevco where he advanced to Engineering Manager of Silicon Products. His transducer development experience also includes the application of variable capacitance MEMS, variable reluctance, inductive proximity, Hall effect, and magnetoresistive technologies for speed and position sensing in military/aerospace, industrial, and automotive applications. He received his Bachelors of Electrical Engineering degree from Cleveland State University, Ohio, in 1978. He earned his Masters of Business Administration from California State University, Fullerton, in 1993. He currently has a patent pending for a unique DC response transducer that features on-board user actuated auto-zero. Contact tom.connolly@meas-spec.com.

Efficiency comparison of CMS vibroacoustic formulations for uncertain damped problems

Morvan OUISSE and Emeline SADOULET-REBOUL

Abstract When dealing with internal vibroacoustics, many formulations are available. The classical (u,p) approach uses physical variables (displacement of the structure, pressure in acoustic cavity), and alternatives exist based on a displacement or velocity potential variable instead of the acoustic pressure in the fluid. Each formulation has its own advantages and drawbacks which are addressed in this paper in the context of Component Mode Synthesis for model reduction, but globally all formulations exhibit the same behavior. Thus, the decoupled mode bases which are classically considered for CMS are identical in all formulations providing that the static pressure is not included in the formulation. So, the question addressed in this work deals with the strategies to take the static response of the fluid domain into account in the projection and on the ability of each formulation to adapt to these strategies. Many options are presented for each of the formulations and are applied for two study cases: a shoe box, that is a parallepipedic cavity and a curved box with a more complex geometry.

1 Introduction

This paper is mainly focused on analyses of acoustic cavities closed by elastic structures, in presence of absorbing materials. In particular, for optimization or uncertainties propagation purposes, strategies of model reduction are addressed. The classical $(\mathbf{u}, p)$ approach uses physical variables (displacement of the structure, pressure in acoustic cavity), and alternatives exist based on a displacement or velocity potential

---

Morvan Ouisse
FEMTO-ST Applied Mechanics, University of Franche-Comté, 24, rue de l'épitaphe, 25000 Besançon - France, e-mail: morvan.ouisse@univ-fcomte.fr

Emeline Sadoulet-Reboul
FEMTO-ST Applied Mechanics, University of Franche-Comté, 24, rue de l'épitaphe, 25000 Besançon - France, e-mail: emeline.sadoulet-reboul@univ-fcomte.fr

T. Proulx (ed.), *Sensors, Instrumentation and Special Topics, Volume 6*, Conference Proceedings of the Society for Experimental Mechanics Series 9,
DOI 10.1007/978-1-4419-9507-0_17, © The Society for Experimental Mechanics, Inc. 2011

variable instead of the acoustic pressure in the fluid [7]. In the context of model reduction, it can be shown that in terms of convergence properties, the main point is related to the availability of the formulation to include static effects of the acoustic cavity. This is due to the fact that whatever the formulation is, the acoustic modes are identical, thus implying equivalent convergence properties using a Ritz based method. The main topic addressed here is then to focus on the ability of the method to take into account the static acoustic mode, since, as indicated in the literature, this mode is theoretically not required [8], while it helps to converge [2]. We propose here an illustration to this fact, together with a new formulation that can naturally include static effect. In a second step, it will be shown that using residue corrections [1, 12] is very efficient to improve convergence with only a few additional computational cost.

2 Formulation of structural-acoustic problem

2.1 Coupled formulation

This part recalls the basic equations of the coupled problem, which are classically available in literature [5, 7, 10].

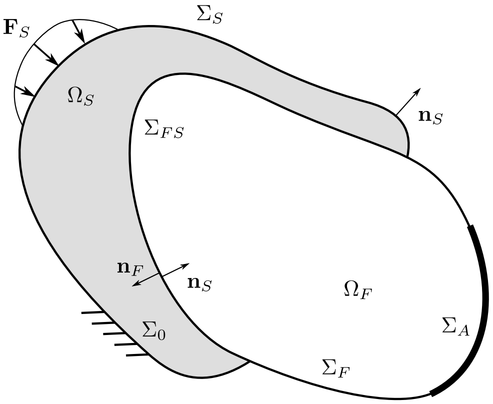

Fig. 1 Description of vibroacoustic problem

The internal vibroacoustic problem which is considered in this paper is presented in figure 1. Let Ω_F be the fluid domain, Ω_S the structural domain. The partition of boundaries is done according to the mechanical conditions: Σ_{FS} is the structural-acoustic coupling surface, Σ_F is the part of the acoustic border on which a Neumann condition is applied, corresponding to a rigid wall (a homogeneous Dirichlet condition could also be considered without loss of generality), Σ_A is the part of the acoustic border on which a Robin condition is considered, corresponding typically to an absorbing material, Σ_S is the structural boundary on which a Neumann condition is applied, corresponding to a prescribed force, Σ_0 is the structural boundary on which a homogeneous Dirichlet condition is applied, corresponding to a clamped area. $\mathbf{n}_S$ and $\mathbf{n}_F$ are respectively the outgoing unit normals of structural and fluid domain.

The physical variables which are used to describe the behavior of the system are the displacement $\mathbf{u}$ for the structure and the acoustic pressure p for the fluid.

For the structural part, the linearized strain tensor is denoted as $\varepsilon(\mathbf{u})$ and the associated stress tensor is denoted as $\sigma(\mathbf{u})$. The choice of acoustic pressure p to describe the fluid behavior instead of a fluid displacement vector field reduces the number of degrees of freedom and avoids the discretization of the fluid irrotationality constraint. This is valid while $\omega \neq 0$. The particular case $\omega = 0$ will be discussed in the next section.

The variational formulation of this problem consists in finding $\mathbf{u}$ and p in $\mathscr{C}_{\mathbf{u}} = \left\{\mathbf{u} \in [H^1(\Omega_S)]^3 \,/\, \mathbf{u} = \mathbf{0} \,\text{on}\, \Sigma_0\right\} \times \mathscr{C}_p = \left\{p \in H^1(\Omega_F)\right\}$ such that,
for all $(\delta\mathbf{u}, \delta p) \in \mathscr{C}_{\mathbf{u}} \times \mathscr{C}_p$:

$$\begin{cases} \displaystyle\int_{\Omega_S} \sigma(\mathbf{u}) : \varepsilon(\delta\mathbf{u})\, d\Omega - \omega^2 \int_{\Omega_S} \rho_S \mathbf{u} \cdot \delta\mathbf{u}\, d\Omega \\ \qquad\qquad \displaystyle - \int_{\Sigma_{FS}} p\, \mathbf{n}_F \cdot \delta\mathbf{u}\, d\Sigma = \int_{\Sigma_S} \mathbf{F}_S \cdot \delta\mathbf{u}\, d\Sigma, & (a) \\ \displaystyle\frac{1}{\rho_F} \int_{\Omega_F} \nabla p \cdot \nabla \delta p\, d\Omega - \frac{\omega^2}{\rho_F c^2} \int_{\Omega_F} p \delta p\, d\Omega \\ \qquad\qquad \displaystyle -\omega^2 \int_{\Sigma_{FS}} \mathbf{u} \cdot \mathbf{n}_F\, \delta p\, d\Sigma + \frac{i\omega}{Z_a(\omega)} \int_{\Sigma_A} p \delta p\, d\Sigma = 0, & (b) \end{cases} \tag{1}$$

where ρ_S is the structure mass density, $\mathbf{F}_S$ is the complex amplitude of the force exciting the structure at frequency ω, c is the sound speed in the fluid and ρ_F the mass density of the fluid at rest. $Z_a(\omega)$ is the complex impedance of absorbing material. The FE discretization of this variational formulation can be written as:

$$\begin{cases} [K_S]\{U\} - \omega^2 [M_S]\{U\} - [L]\{P\} = \{F_S\}, & (a) \\ [K_F]\{P\} - \omega^2 [M_F]\{P\} - \omega^2 [L]^T \{U\} + \frac{i\omega}{Z_a(\omega)} [A_F]\{P\} = \{0\}, & (b) \end{cases} \tag{2}$$

or

$$\left(\begin{bmatrix} K_S & -L \\ 0 & K_F \end{bmatrix} - \omega^2 \begin{bmatrix} M_S & 0 \\ L^T & M_F \end{bmatrix} + \frac{i\omega}{Z_a(\omega)} \begin{bmatrix} 0 & 0 \\ 0 & A_F \end{bmatrix} \right) \begin{Bmatrix} U \\ P \end{Bmatrix} = \begin{Bmatrix} F_S \\ 0 \end{Bmatrix}, \tag{3}$$

where:

$$\begin{aligned} [K_S] &\to \int_{\Omega_S} \sigma(\mathbf{u}) : \varepsilon(\delta\mathbf{u})\, d\Omega, & [M_S] &\to \int_{\Omega_S} \rho_S \mathbf{u} \cdot \delta\mathbf{u}\, d\Omega, \\ [K_F] &\to \frac{1}{\rho_F} \int_{\Omega_F} \nabla p \cdot \nabla \delta p\, d\Omega, & [M_F] &\to \frac{1}{\rho_F c^2} \int_{\Omega_F} p \delta p\, d\Omega, \\ [L] &\to \int_{\Sigma_{FS}} p\, \mathbf{n}_F \cdot \delta\mathbf{u}\, d\Sigma, & [A_F] &\to \int_{\Sigma_A} p \delta p\, d\Sigma. \end{aligned} \tag{4}$$

N.B. For a sake of clarity, no structural damping is considered in the weak formulations and associated FE discretizations presented here, but it can naturally be integrated in the formulations.

2.2 Considerations about the static case

As indicated in reference [8], the considered problem is not valid for $\omega = 0$ since when the frequency tends to 0, the "movement" of the fluid tends to static irrotational motion. In that case, the pressure can be decomposed in two terms:

$$p = p^S + \tilde{p}, \tag{5}$$

where $\tilde{p}$ is a dynamic pressure and p^S is a so-called static pressure, which is constant in space and differs from the static solution which could be obtained by extending the considered problem (2) to $\omega = 0$, since it would result in a static pressure which is constant in space but undetermined in amplitude. The uniqueness of $\tilde{p}$ is guaranteed by the condition

$$\int_{\Omega_F} \tilde{p} d\Omega = 0. \tag{6}$$

If Σ_F is rigid, the static pressure can be directly derived from the normal displacement of the structure:

$$p^S = -\rho_F \frac{c^2}{V_F} \int_{\Sigma_{FS}} \mathbf{u} \cdot \mathbf{n}_F d\Sigma - \rho_F \frac{c^2}{V_F} \int_{\Sigma_A} \mathbf{u}^F \cdot \mathbf{n}_F d\Sigma, \tag{7}$$

where V_F is the measure of the volume occupied by Ω_F. This means that several ways can be considered to solve the considered problem using a displacement/pressure formulation. The variable which describes the movement of the structure is the displacement $\mathbf{u}$, while for the fluid one can use the following strategies:

- use of pressure p for fluid description. This formulation has been presented in section 2.1, it is not valid for $\omega = 0$.
- use of dynamic pressure $\tilde{p}$ for fluid description. This formulation is valid for $\omega = 0$. The constraint (6) has to be considered to solve the problem. In particular, in a finite elements context, this constraint has to be discretized and included in the final system. The total pressure p is then obtained by summing $\tilde{p}$ and p^S which comes from equation (7). This requires in particular the discretization of p^S from equation (7) in which $\mathbf{u}^F \cdot \mathbf{n}_F$ must be expressed on Σ_A in function of the dynamic pressure $\tilde{p}$ using the impedance condition. The corresponding system has large expressions and exhibits no special interest comparing to other strategies.
- use of both dynamic pressure $\tilde{p}$ and static pressure p^S for fluid description. This formulation is valid for $\omega = 0$. The authors did not found any mention of this possibility in the literature, even if a $(\mathbf{u}, \tilde{p}, \varphi, p^S)$ formulation can be found in

[3]. To obtain this formulation, the constraint (6) and the equation (7) have to be considered and discretized. The total pressure p is then obtained by summing $\tilde{p}$ and p^S.

Following this approach, one can define the subspace $\mathscr{C}_{\tilde{p}} = \left\{ \tilde{p} \in \mathscr{C}_p \,/\, \int_{\Omega_F} \tilde{p}\, d\Omega = 0 \right\}$. In a weak form, one has then to find $\mathbf{u}$, $\tilde{p}$ and p^S in $\mathscr{C}_{\mathbf{u}}$, $\mathscr{C}_{\tilde{p}}$ and $\mathscr{R}$ such as, for all $(\delta\mathbf{u}, \delta\tilde{p}, \delta p^S) \in \mathscr{C}_{\mathbf{u}} \times \mathscr{C}_{\tilde{p}} \times \mathscr{R}$:

$$\begin{cases} \displaystyle\int_{\Omega_S} \boldsymbol{\sigma}(\mathbf{u}) : \boldsymbol{\varepsilon}(\delta\mathbf{u})\, d\Omega - \omega^2 \int_{\Omega_S} \rho_S \mathbf{u} \cdot \delta\mathbf{u}\, d\Omega \\ \qquad\qquad \displaystyle - \int_{\Sigma_{FS}} \tilde{p}\, \mathbf{n}_F \cdot \delta\mathbf{u}\, d\Sigma - \int_{\Sigma_{FS}} p^S\, \mathbf{n}_F \cdot \delta\mathbf{u}\, d\Sigma = \int_{\Sigma_S} \mathbf{F}_S \cdot \delta\mathbf{u}\, d\Sigma, \; (a) \\ \displaystyle \frac{1}{\rho_F} \int_{\Omega_F} \nabla\tilde{p} \cdot \nabla\delta\tilde{p}\, d\Omega - \frac{\omega^2}{\rho_F c^2} \int_{\Omega_F} \tilde{p}\delta\tilde{p}\, d\Omega - \omega^2 \int_{\Sigma_{FS}} \mathbf{u} \cdot \mathbf{n}_F\, \delta\tilde{p}\, d\Sigma \\ \qquad\qquad \displaystyle + \frac{i\omega}{Z_a(\omega)} \int_{\Sigma_A} \tilde{p}\delta\tilde{p}\, d\Sigma + \frac{i\omega}{Z_a(\omega)} p^S \int_{\Sigma_A} \delta\tilde{p}\, d\Sigma = 0, \qquad (b) \\ \displaystyle \frac{1}{\rho_F c^2} p^S V_F \delta p^S + \int_{\Sigma_{FS}} \mathbf{u} \cdot \mathbf{n}_F\, d\Sigma\, \delta p^S \\ \qquad\qquad \displaystyle + \frac{1}{i\omega Z_a(\omega)} \int_{\Sigma_A} \tilde{p}\, d\Sigma\, \delta p^S + \frac{1}{i\omega Z_a(\omega)} p^S S_A \delta p^S = 0, \qquad (c) \end{cases} \tag{8}$$

where V_F is the volume of the fluid domain and S_A the surface of the absorbing area. The corresponding finite element formulation can be written as:

$$\left(\begin{bmatrix} K_S & -L & -\ell \\ 0 & K_F & 0 \\ \ell^T & 0 & \frac{V_F}{\rho_F c^2} \end{bmatrix} - \omega^2 \begin{bmatrix} M_S & 0 & 0 \\ L^T & M_F & 0 \\ 0 & 0 & 0 \end{bmatrix} + \frac{i\omega}{Z_a(\omega)} \begin{bmatrix} 0 & 0 & 0 \\ 0 & A_F & a_F \\ 0 & \frac{-1}{\omega^2} a_F^T & \frac{-1}{\omega^2} S_A \end{bmatrix} \right) \begin{Bmatrix} U \\ \tilde{P} \\ p^S \end{Bmatrix} = \begin{Bmatrix} F_S \\ 0 \\ 0 \end{Bmatrix}, \tag{9}$$

where the acoustic displacement potential dofs $\tilde{P}$ are associated to $\tilde{p}$ and:

$$[a_F] \rightarrow p^S \int_{\Sigma_A} \delta\tilde{p}\, d\Sigma, \;\; [\ell] \rightarrow p^S \int_{\Sigma_{FS}} \delta\mathbf{u} \cdot \mathbf{n}_F\, d\Sigma. \tag{10}$$

One should emphasize that this system must be solved under the constraint $\int_{\Omega_F} \tilde{p} d\Omega = 0$, which corresponds to

$$[C]^T \{\tilde{P}\} = 0 \tag{11}$$

where

$$[C] \rightarrow \int_{\Omega_F} \tilde{p} d\Omega. \tag{12}$$

One should emphasize that this system can be easily symmetrized by dividing the equations related to dynamic fluid dofs by ω^2 and changing sign on the last line.

Equivalent $(\mathbf{u},\varphi,p^S)$, $(\mathbf{u},\psi,p^S)$ can also be derived in the same way using velocity or displacement potentials φ and ψ.

3 Model reduction of structural-acoustic problem

3.1 Classical reduction using decoupled basis

In a generic way, all previous problems can be written as:

$$[K-\omega^2M+\frac{i\omega}{Z_a(\omega)}A]\{Y\}=\{F\}, \tag{13}$$

where $\{Y\}$ includes a partition of structural and acoustic dofs. In this generic notation, the matrices can possibly depend on frequency. A very classical way to reduce the size of the harmonic problem is to search the response on a given vectorial space, typically built from the associated undamped problem. In our case, on can define :

- the *in vacuo* structural modes, which are the normal modes of the structure without wet surface (i.e. for which Σ_{FS} is replaced with a free surface), these modes have shapes that can be stored in the structural modal matrix T_S;
- the *blocked* acoustic modes, which are the normal modes of the cavity in which both Σ_{FS} and Σ_A are replaced by rigid wall conditions. The associated shapes are stored in the acoustic modal matrix T_F.

One should emphasize that the decoupled mode shapes are identical in all formulations providing that the static pressure is not included in the formulation. The global projection matrix is then built as:

$$[T]=\begin{bmatrix} T_S & 0 \\ 0 & T_F \end{bmatrix} \tag{14}$$

One can reduce now the initial problem using the projection $\{Y\}=[T]\{q\}$ with $\{q\}=\begin{Bmatrix} q_S \\ q_F \end{Bmatrix}$:

$$[\bar{K}-\omega^2\bar{M}+\frac{i\omega}{Z_a(\omega)}\bar{A}]\{q\}=\{\bar{F}\}, \tag{15}$$

where:

$$[\bar{K}]=[T^TKT], \quad [\bar{M}]=[T^TMT], \quad [\bar{A}]=[T^TAT], \quad \{\bar{F}\}=[T^T]\{F\}. \tag{16}$$

3.2 Considerations about the static case

Concerning the remarks presented in the previous section about the static case, one should underline that in literature, the constraint (6) is generally omitted in the FE formulation. This is valid since the acoustic modes are calculated with rigid boundary conditions, which implies that they automatically verify the constraint. On the other side, for a full model computation, the constraint must be taken into account for proper estimation of the low frequency content of the response.
Several strategies are available to take into account static response of the fluid domain in the projection:

- The mode p_0 can simply be added in the Ritz basis, even if this is not correct in a mathematical point of view, as indicated in [8].
- The proposed $(\mathbf{u}, p, p^S)$ formulation can be used without condensation of p^S.
- The impact of p^S on the structure can be evaluated using elastic modes, as indicated in [9]. In this case, its contribution is interpreted in terms of added mass and stiffness. $M_C = \sum_{\alpha=1}^{n} \frac{\rho_F}{\omega_\alpha^2} L P_\alpha P_\alpha^T L^T$ is the added mass matrix and K_C is the added stiffness matrix obtained by the discretization of $p_0^2 \int_{\Sigma_{FS}} \mathbf{u}\cdot\mathbf{n} d\Sigma \int_{\Sigma_{FS}} \mathbf{n}\delta\mathbf{u} dS$. In this case the reduction of the structural part is performed using the modified structural eigenvalue problem including added effects on the structure [6, 9]. It should be emphasized that this approach leads to convenient formulation without considering the acoustic absorbing area Σ_a. When Σ_a, characterized by Z_a, is present, the methodology used to derive the previous system leads to complex relationships which have no special interest compared to the alternative ways to take into account the static behavior of the fluid cavity.

3.3 Description of the test structures

In order to illustrate the convergence properties of the reduced models, one will exhibit the results coming from two models. The first one, called *shoe box*, is a parallelepiped cavity, with 5 rigid faces, closed by an elastic simply supported plate. This model has a very simple geometry in order that anyone can easily reproduce the results presented here. The second one, called *curved box*, has a more complex geometry, which induces couplings between space directions for the modal shapes of the cavity.

3.3.1 The shoe box

The shoe box is an acoustic cavity ($c = 342.2\, m.s^{-1}$, $\rho = 1.213\, kg.m^{-3}$) with size $0.654 \times 0.527 \times 0.6 m^3$, closed by a simply supported plate, made of aluminum ($E = 7.2 \times 10^{10}\, Pa$, $\nu = 0.3$, $\rho = 2700\, kg.m^{-3}$ with a thickness of 3 mm. It has 3 non parallel sides covered by an absorbing layer. The excitation force is a normal point force located at coordinates (0.19075,0.197625) on the plate. The geometry and one of the coupled modes is presented in figure 2.

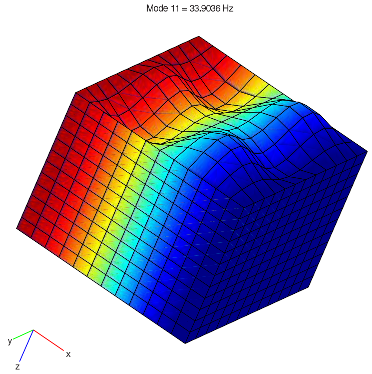

Fig. 2 The shoe box, example of coupled mode (color: acoustic pressure, shape: displacement)

3.3.2 The curved box

The curved box has a more complex geometry, which is illustrated in figure 3. The upper face of the box is an elastic plate, and an absorbing layer covers the lower face. The structural excitation is distributed on a surface which is about 1/20th of the structural area.

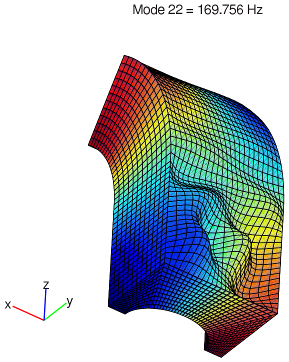

Fig. 3 The curved box, example of coupled mode (color: acoustic pressure, shape: displacement)

3.4 Results concerning the convergence of the $(\mathbf{u}, p)$ formulation

In this part we are interested in the convergence properties of the $(\mathbf{u}, p)$ formulation when the number of modes in the fluid basis increases. The first model of interest is the shoe box. The figure 4 shows frequency evolution of indicators when the absorbing area is not considered, while the figure 5 corresponds to similar results with absorbing area. On both figures, three results are shown: the reference curve (full model), and two curves corresponding to reduced models, one of them corresponding to reduction without the static acoustic mode, while the last one includes the static mode, either by added mass and stiffness for the "undamped" case, or by simply adding a constant vector in the fluid Ritz basis for the "damped" case. In all cases, the system includes dissipation since the structural part is considered to have a complex Young's modulus $E(1+i\eta)$ where $\eta = 4\%$. It can be observed that, in

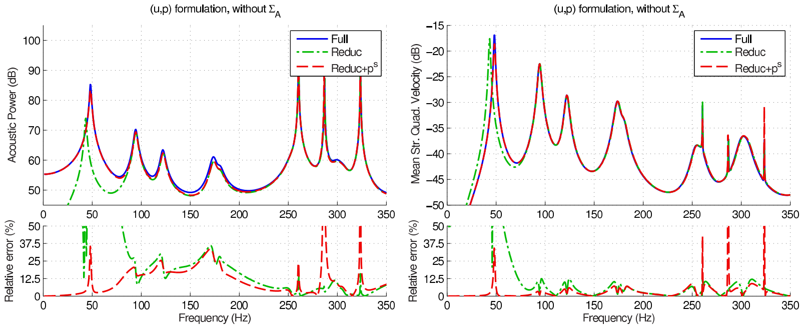

Fig. 4 Indicators for $(\mathbf{u}, p)$ formulation without Σ_A, including or not the static mode

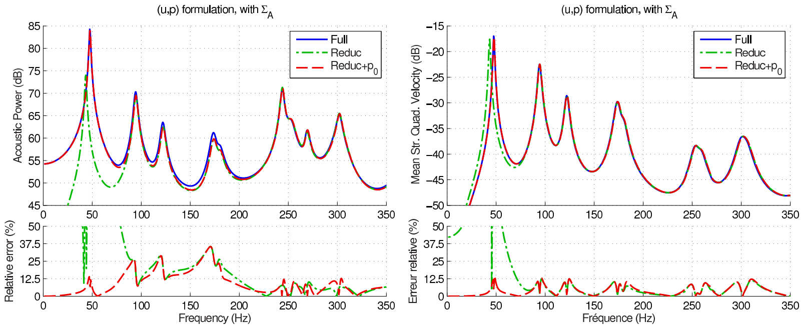

Fig. 5 Indicators for $(\mathbf{u}, p)$ formulation with Σ_A, including or not the static mode

both cases, the reduced models are not able to properly estimate the low frequency behavior of the coupled system if the acoustic static mode is not considered in the

projection. In the middle part of the frequency range of interest, the error (in linear scale) can still be large even if the static mode is considered, particularly in the acoustic domain. This is due to missing information in the fluid basis, which is not rich enough to properly represent the acoustic behavior of the system. In these calculations, 50 structural modes have been considered for T_S (up to 1493 Hz). In this case, using 200 structural modes and a static residual associated to the point force has no effect on the results in the frequency range of interest.
The missing informations are clearly associated to the fluid basis, since the modes have been estimated using rigid boundary conditions, which makes very difficult for the pressure to converge towards continuity on the coupling area and on the absorbing area. As illustrated in figure 6, the convergence is very low. This figure shows the evolution of acoutic power estimated by the reduced model when the number of modes in the fluid basis increases.

A more systematic study can be performed to evaluate the performance of the reduced basis in terms of convergence related to the number of acoustic modes in the Ritz basis. The figure 7 illustrates the results of this analysis, by showing convergence curves of the mean relative error on indicators on the frequency range of interest, when using the following strategies in the reduction:

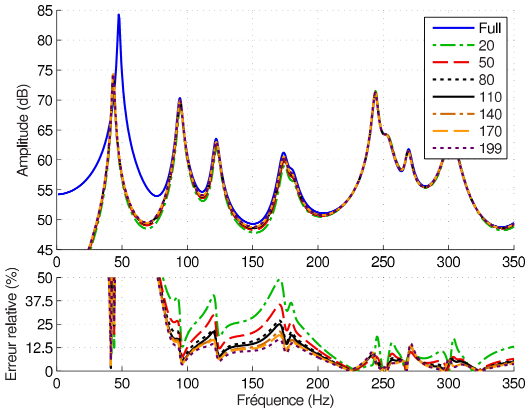

Fig. 6 Example of convergence : acoustic power estimated by reduced model vs. number of modes in the fluid basis

- direct reduction by using only “elastic” acoustic modes (i.e. without p_0 or p^s), referred as “Reduc” in the figure;
- reduction with static acoustic mode directly included in the projecting basis, referred as “Reduc + p_0” in the figure;
- reduction with static acoustic mode considered through added mass and stiffness, referred as “Reduc + p_S” in the figure (this case is only considered on the configuration without absorbing area);
- reduction of $(\mathbf{u}, p, p^S)$ formulation, without considering the static acoustic mode in the projecting basis, this mode being considered through p^S which is kept as a degree of freedom in the model. This case is referred as “$(\mathbf{u}, p, p^S)$ Reduc” in the figure.

The results are presented on both configurations (with or without the absorbing layer in the cavity). It can clearly be observed that:

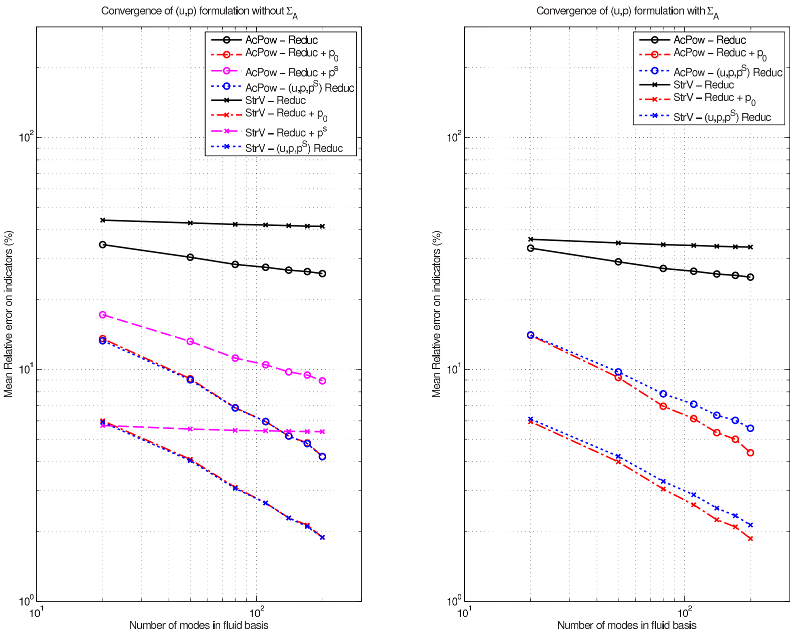

Fig. 7 Convergence of $(\mathbf{u}, p)$ for the shoe box

- in all cases, the convergence rate is very low;
- the direct reduction by using only “elastic” acoustic modes leads to large errors, it is then clear that including static contribution for the fluid part is necessary for correct estimation of low-frequency content of the responses;
- considering static contribution through added mass and stiffness is efficient for a low number of modes, but the convergence is very low, due to the fact that the added mass is evaluated from modal reduction and that no information is provided in the fluid domain to improve convergence;
- the best convergence rate corresponds to direct inclusion of constant vector p_0 in the fluid basis and also to projection using the $(\mathbf{u}, p, p^S)$ formulation. In both cases, the mean error on quadratic velocity (resp. acoustic power) reduces from 6% (resp. 10.5%) for 20 modes in the fluid basis to 1% (resp. 3%) for 200 modes.

There is no fundamental difference between the analysis performed with or without the absorbing layer in the fluid domain. The small difference (1% in mean value) which can be observed is due to the fact that the exact value of static pressure given in equation (7) is better estimated by the contribution of projection of p_0 in the response than by the reduction of $(\mathbf{u}, p, p^S)$ formulation, which implies a projection of (7) on the modes of interest. The results on the curved box clearly exhibit similar

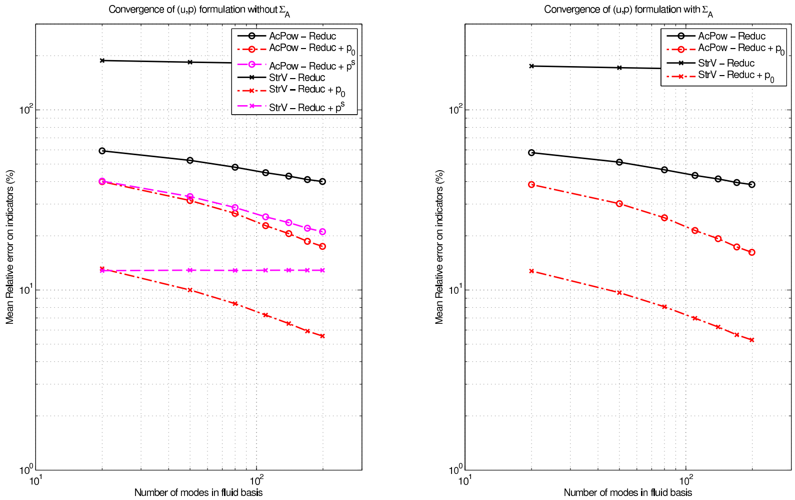

Fig. 8 Convergence of $(\mathbf{u}, p)$ for the curved box

trends, as illustrated in figure 8, which indicates that above results are not specific to the simple geometry of the shoe box case or to the fact that point source is used in this case: more complex geometry together with distributed excitation lead to similar results.

As a conclusion, it has been illustrated that including the static acoustic cavity mode in the Ritz basis, even if this is not required in theory, helps to improve convergence of reduced model. The convergence is equivalent to the one obtained with a new $(\mathbf{u}, p, p^S)$ formulation which includes rigorously the static effects at the price of a little more computation cost (assembly of terms corresponding to an additional dof in the full model). This new formulation provides a nonsingular stiffness matrix, which can be interesting for estimation of static residuals. Nevertheless, if the application does not require a definite stiffness matrix, the analyst can use the cheapest strategy for model reduction, which is the simple addition of the rigid cavity mode in the projecting basis.

4 Strategies for bases enrichment

In this section, two approaches are considered to enrich the decoupled bases in order to illustrate the efficiency of bases enrichment using residual information instead of completing Ritz bases with uncoupled modes.

4.1 Residue iterations

Residue iterations consist in evaluating the error in the estimation of the response, and building associate vectors to enrich the basis [4]. This iterative approach can be summarized as follows. Starting from a decoupled projecting basis, at step j of the iterative procedure, the basis T_j is used to project the unknown dofs vector: $\{q_j\} = [T_j]\{Y_j\}$, where

$$\{q_j\} = [\bar{K} - \omega^2 \bar{M} + \frac{i\omega}{Z_a(\omega)} \bar{A}]^{-1} \{\bar{F}\}. \tag{17}$$

The residue at iteration j is then evaluated:

$$\{R_j\} = [K_0]^{-1} [K - \omega^2 M + \frac{i\omega}{Z_a(\omega)} A] \{Y_j\} - \{F\}, \tag{18}$$

where K_0 is a matrix representative of the stiffness of the problem. It can typically be either K or a filtered version of it. $\{R_j\}$ being complex and frequency-dependent, T_j is combined with real and imaginary parts of $\{R_j\}$ taken at several frequency steps (in particular those corresponding to the largest errors in the response estimation). The new projecting basis T_{j+1} is finally obtained from the principal directions of the set of vectors using a singular value decomposition. This strategy is very general and can take into account any frequency dependency of system's characteristics.

4.2 Robust bases

The vibroacoustic robust bases [12] correspond to a non-iterative procedure and also start from uncoupled bases which are enriched to take into account the effect of the moving structure on the fluid and of the presence of an absorbing material. For weak vibroacoustic coupling (i.e. with light fluid like air), the approach leads to enrichment of the fluid part only and T_F is enriched by ΔT_{Fs} and ΔT_{Fa}:

$$\begin{aligned} \Delta T_{Fs} &= \left(K_F - \omega_c^2 M_F\right)^{-1} L^T T_S, \\ \Delta T_{Fa} &= \left(K_F - \omega_c^2 M_F\right)^{-1} A_F T_F, \end{aligned} \tag{19}$$

where ω_c is a reference frequency (or a set of references) in the band of interest. An orthogonalization is obviously required to ensure good conditioning of the procedure. The approach can also deal with strong coupling and parametric changes, in particular for uncertainties propagation. These points are not discussed here. Compared with the residue iteration, one can qualitatively expect a solution which is equivalent to the one obtained after one full iteration, but with a lower computational time since only one resolution of the problem is required. For more difficult cases, in particular if only a few modes are kept in the uncoupled bases, the residue iteration technique will surely lead to more precise results after few iterations.

4.3 Numerical results

Figures 9 and 10 show improvement of convergence of reduced model when above residue terms are added to the projecting bases. In the simulations, 50 modes have been considered in both structural and acoustic bases. The results are shown in terms of relative errors, and indicate that both procedures lead to almost similar error reduction. The global error is very small in both cases. The calculation cost is of course higher for the iterative procedure that requires a little more calculation effort, but allows new iterations to improve results if the convergence is not achieved yet, which is not the case for the robust basis.

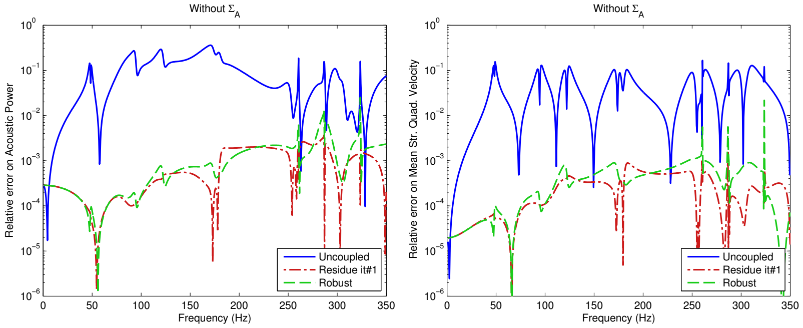

Fig. 9 Comparison of results errors (shoe box) compared with full response for uncoupled basis, residue iteration (after first iteration), robust basis. Case without absorbing area.

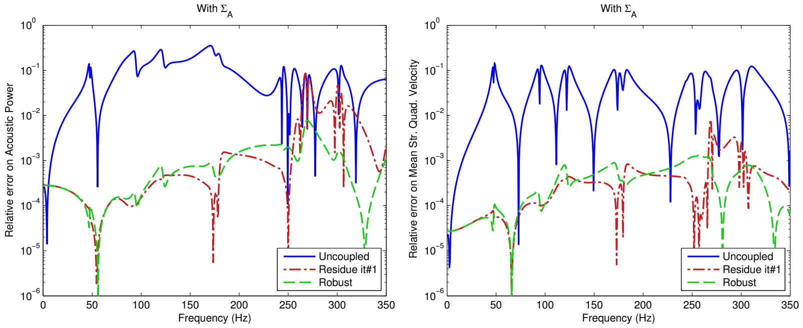

Fig. 10 Comparison of results errors (shoe box) compared with full response for uncoupled basis, residue iteration (after first iteration), robust basis. Case with absorbing area.

4.4 Conclusions

In this paper, it has been shown that the consideration of static effects of cavity was mandatory to obtain precise results concerning the vibroacoustic response of damped systems. For model reduction purpose, including the static mode by itself helps improving convergence in a fast and easy way. A new $(\mathbf{u}, p, p^S)$ formulation has been proposed to automatically include static effects in a proper way, leading to definite reduced stiffness matrix. Finally, efficiency of residual terms added to the uncoupled bases is demonstrated using two different methodologies that allows great improvement of the convergence, even in presence of absorbing layers in the fluid cavity.

References

1. Balmès, E.: Model reduction for system with frequency dependent damping properties. Proceedings of International Modal Analysis Conference pp. 223–229 (1997)
2. Herrmann, J., Maess, M., Gaul, L.: Substructuring including interface reduction for the efficient vibro-acoustic simulation of fluid-filled piping systems. Mechanical Systems and Signal Processing **24**(1), 153 – 163 (2010). DOI 10.1016/j.ymssp.2009.05.003
3. Kehr-Candille, V., Ohayon, R.: New advances in computational structural mechanics, chap. Elasto-acoustic damped vibrations finite element and modal reduction methods, pp. 321–334. Elsevier Science Publishers Ltd., London (1992)
4. Kergourlay, G., Balmes, E., Clouteau, D.: Model reduction for efficient FEM/BEM coupling. In: ISMA, vol. 3, pp. 1167–1174. Citeseer (2001)
5. Lesueur, C.: Rayonnement acoustique des structures, vibroacoustique, interactions fluide-structures. Eyrolles (1988)
6. Morand, H.J.P., Ohayon, R.: Interactions fluide-structure. Masson (1992)
7. Morand, H.J.P., Ohayon, R., Bauer, R.: Fluid structure interaction. John Wiley (1995)
8. Ohayon, R.: Reduced models for fluid-structure interaction problems. International Journal for Numerical Methods in Engineering **60**, 139–152 (2004)
9. Ohayon, R.: Linear vibrations of structures coupled with an internal fluid. In: Eccomas School, 3-7 May 2006, Ibiza Spain (2006)
10. Ohayon, R., Soize, C.: Structural acoustics and vibration. AP (1998)
11. Tournour, M., Atalla, N.: Pseudostatic corrections for the forced vibroacoustic response of a structure-cavity system. Journal of the Acoustical Society of America **170**, 2379–2386 (2000)
12. Tran, Q.H., Ouisse, M., Bouhaddi, N.: A robust component mode synthesis method for stochastic damped vibroacoustics. Mechanical Systems and Signal Processing **24**(1), 164 – 181 (2010). DOI 10.1016/j.ymssp.2009.06.016

Nonlinear Parameteric Health Monitoring for Vibrating Structures Under Non-Stationary Excitation

Timothy A. Doughty, Assistant Professor, University of Portland, 5000 N Willamette Blvd, Portland OR 97203, doughty@up.edu

Natalie S. Higgins, University of Portland, 5000 N Willamette Blvd, Portland OR 97203, higgins11@up.edu

Abstract

Nonlinear system identification has been used to predict and monitor cracks as they form, propagate, and eventually cause the catastrophic failure of a vibrating cantilevered beam. The Continuous Time based system identification technique allows for estimation of model parameters based on collected stimulus and response data. For this study the estimated cubic stiffness term in the model is mapped as a function of time. The purpose of this investigation is to strengthen results from a previous study [1] through repetition, and to expand the scope of this system identification technique. This study mainly explores the effectiveness of using non-stationary excitation in the identification process, with an understanding that in implementation on real systems the selection input amplitude and frequency may not be readily controlled. Additionally, the robustness of this method is demonstrated in direct comparison to a well-accepted linear-based approach. The results show this method to be successful with little prior knowledge of the accurate model form or parametric values for the systems being studied.

Introduction

Failure in oscillating systems is often the result of crack initiation and growth as the system experiences fatigue. Assessing damage as it initiates and evolves is of great interest, as it can prevent failure. Nondestructive evaluation (NDE) has received a great deal of attention in recent decades; see Doebling, et al [2] for a comprehensive review. Most of the methods in use involve linear models, though the phenomenon is well understood to be nonlinear [3-7]. Additionally, many of the current studies involve systems with pre-existing and pre-determined damage [8-10]. While the nonlinear nature of cracks in vibrating structure has long been studied [11], nonlinear NDE methods in crack detection for vibrating systems continues to advance the field [12-14].

This study is motivated by an understanding that all physical systems are nonlinear. If the linear model is assumed changes in system behavior can misidentify failing systems. NDEs that, for example, monitor the natural frequency of a system over time will often use that change as an indication of plastic deformation or crack initiation. Nonlinear models explain the change in apparent natural frequency for a healthy system whose level of excitation is simply varied. For this reason, we start with a nonlinear model. The nonlinear model can explain a wealth of behavior –both linear and nonlinear, but when the nature of the nonlinearity changes, the model will too. Monitoring this change serves as an early indicator of the onset of failure.

For this study system identification is performed on a cantilevered beam which is excited near its second natural frequency. Collected forcing and response data is used with the Continuous Time identification method, which has been shown to indicate the model's nonlinear variations [15]. Both the linear and nonlinear model parameters associated with an established nonlinear model for the system are estimated. A healthy beam is excited over a range of frequencies around

T. Proulx (ed.), *Sensors, Instrumentation and Special Topics, Volume 6*, Conference Proceedings of the Society for Experimental Mechanics Series 9, DOI 10.1007/978-1-4419-9507-0_18, © The Society for Experimental Mechanics, Inc. 2011

resonance to populate the nonlinear model. The evolution of the nonlinear parameter estimate is then plotted over time as the beam is allowed to oscillate from an initially healthy state through failure due to crack initiation and growth.

This work is the continuation of an on-going study. In previous work, the method has been successful at detecting damage significantly prior to failure, even without a strong understanding of the model form or the accuracy of the values estimated by the system identification. A sensitivity study was done to determine the number and location of the steady-state records to be used in the initial identification of the healthy beam's nonlinear model. Similarly, a study was performed on the benefit of using complete nonlinear models with correct linear parameters. Emphasis here is given to the use of time-varying input data with a demonstration of how linear models can misidentify failing systems.

Theoretical Model Development

The study presented here is on a horizontally mounted cantilevered beam subjected to vertical excitation. The excitation is at a frequency which is near the beam's second natural frequency, allowing the spatial dependence of the model to be assumed. The theoretical configuration is shown in Figure 1.

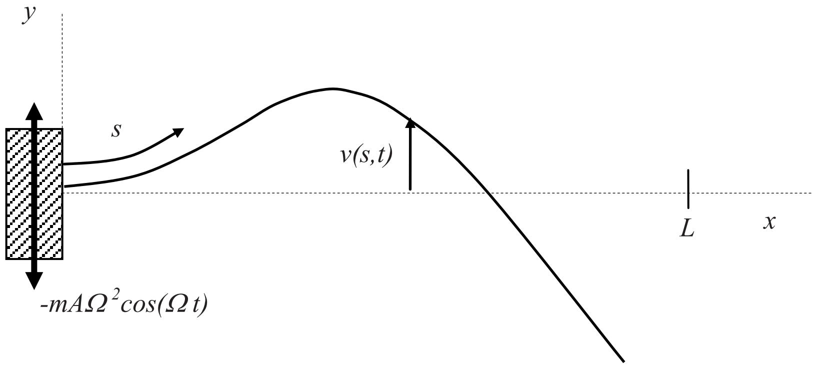

Fig. 1 Theoretical Configuration for Base Excited Cantilevered Beam Demonstrating the Second Mode Shape

In this representation *v* is the beam's vertical displacement, *m* is mass per unit length, *c* is damping per unit length, D_ξ is the bending stiffness, *A* is the amplitude of base displacement, *Ω* is the frequency of excitation, *t* is time, *s* is a reference variable, and *L* is the beam length.

The partial differential equation model for the transverse displacement of a cantilevered beam with nonlinear bending stiffness developed in [16] is given with the following partial differential equation and associated boundary conditions:

$$m\ddot{v} + c\dot{v} + D_{\xi}\left\{v^{iv} + \left[v'\left(v'v''\right)'\right]'\right\} = -mA\Omega^{2}\cos\left(\Omega t\right), \tag{1}$$

$$v(0,t) = v'(0,t) = v''(L,t) = v'''(L,t) = 0\,. \tag{2}$$

In the case of modal excitation, the spatial dependence is assumed known. Letting $v(s,t) = a(t)\bullet\phi(s)$, where $\phi(s)$ an orthonormalized mode shape which satisfies the stated boundary conditions, the nonlinear partial differential equation can be reduced to the form:

$$m\ddot{a} + c\dot{a} + ka + \alpha a^{3} = F(t)\,, \tag{3}$$

where:

$$k = \left\{ D_\xi \int_0^L \phi \phi^{iv} ds \right\}, \tag{4}$$

$$\alpha = \left\{ D_\xi \int_0^L \phi \phi''^3 + 4\phi\phi'\phi''\phi''' + \phi\phi'^2\phi^{iv} ds \right\}, \tag{5}$$

and:

$$F(t) = \int_0^L \phi ds \left(-mA\Omega^2 \right) \cos(\Omega t). \tag{6}$$

With this nonlinear model of the system, a collection of input $F(t)$ and response $a(t)$ can be used to estimate our system parameters. Note that if the nonlinear term, α, is set to zero, the result is the standard linear model for a forced mass-spring-damper system.

System Identification

The linear system parameters lend themselves to estimation through theoretical relationships or simple experimental validation. Both m and D_ξ can be estimated from tabulated material properties and the beam's geometry. With the mode shape, $\phi(s)$, known, stiffness k can be determined with Equation 4. Preliminary testing was done to determine the remaining terms in the linear model for the beam being studied. This includes an estimate of the beam's linear natural frequency and damping through the free decay of the beam excited in its second mode.

Nonlinear system identification is inherently more complex. In short, the system must be excited in a way that pronounces the nonlinearities so that information-rich data can be used in identification. Even with suitable collected data, the method of identification is not obvious. Nonlinear differential equations typically have no analytic solution, and so the formulation of algorithms is dependent on the method of approximating the solution to the governing model. While the methods of Multiple Time Scales and Harmonic Balance have both proven to be effective tools for identifying nonlinear model parameters [17], the Continuous Time method was chosen here for its ease of application and for its acceptance of transient time data. It can be applied to non-harmonic excitations and does not require an asymptotic approximation in implementation.

For Continuous Time based system identification, the forcing and response signals are measured. An accelerometer is used in this study, and this is integrated to yield velocity and displacement vectors. The displacement vector is cubed and the state vectors are then collected in a matrix relation which can be solved in a least squares sense for parameter estimates. Arranging Equation 3 we have:

$$\begin{bmatrix} \ddot{a}(t) & \dot{a}(t) & a(t) & a(t)^3 \end{bmatrix} \begin{bmatrix} m & c & k & \alpha \end{bmatrix}^T = F(t) \tag{7}$$

and

$$\left\{ a(t)^3 \right\} \left[\alpha \right] = \left\{ F(t) - m\ddot{a}(t) - c\dot{a}(t) - ka(t) \right\} \tag{8}$$

Equation 7 allows for the direct estimation of the parameter vector. With the linear parameters known, Equation 7 is easily rearranged to make α the only unknown in the matrix relation, which can then be estimated by solving Equation 8 in a least squares sense where the state vectors are concatenated steady state time responses from select excitation frequencies.

Though this approach does not correspond to curve fitting the nonlinear frequency response function, as the analytic form of this function is not known, it is useful to recognize that collecting steady state data for one sinusoidal forcing frequency would give poor parameter estimates as the data would only give one point along the frequency response trend line. For this reason, steady state data records are collected over a range of frequencies so as to better define the system parameters. Here, we are using steady state input and response data from a harmonically excited system, though this is not necessary for application of this method. Data records were chosen at frequencies near the resonant frequency and on either side. Simulations have shown that data from these regions can be used to accurately identify similar nonlinear models [18, 19].

Streaming data from the periodic excitation at one near-resonance frequency is used to update one of the state entries in the system identification code. When this data indicates a fundamental change in the system, the result is a change in the estimated nonlinear term. In general application, changes in system response that are due to changes in system input will not notably change the estimation of the nonlinear parameters. In this study, the amplitude of the forcing function is varied to confirm that this change in the system input will not significantly change the estimated nonlinear term.

Experiments

This investigation is composed of two experiments: collecting more fatigue data to strengthen the results from the previous paper [1], and varying the system input to determine the effects of non-stationary excitation on the identification process.

The experimental configuration used for observing the initiation and failure of the cantilevered beam for both experiments is given in Figures 2 and 3. As in a previous investigation of the same nature, 6061 Aluminum bar stock with dimensions 12.7 x 1.59 x 500mm was excited with a 45N shaker over a range of frequencies around the second natural frequency of the beam. A standard function generator was used to excite the shaker. LabVIEW was used in conjunction with National Instruments data acquisition to record the accelerations at the base and on the beam. The beam's acceleration was differenced from the base acceleration, and then scaled according to the accelerometer's calibration and the spatial location along the beam; the accelerometer was located 0.045m from the clamped end. The base acceleration was multiplied by mass and then scaled with the mode shape in accordance with Equation 6. These were then treated as the system's output and input, respectively. The signals from the accelerometers were amplified and filtered to remove any high frequency noise. This filtering was done by fitting the signals with sinusoids using MATLAB and keeping only the fundamental frequency for data analysis.

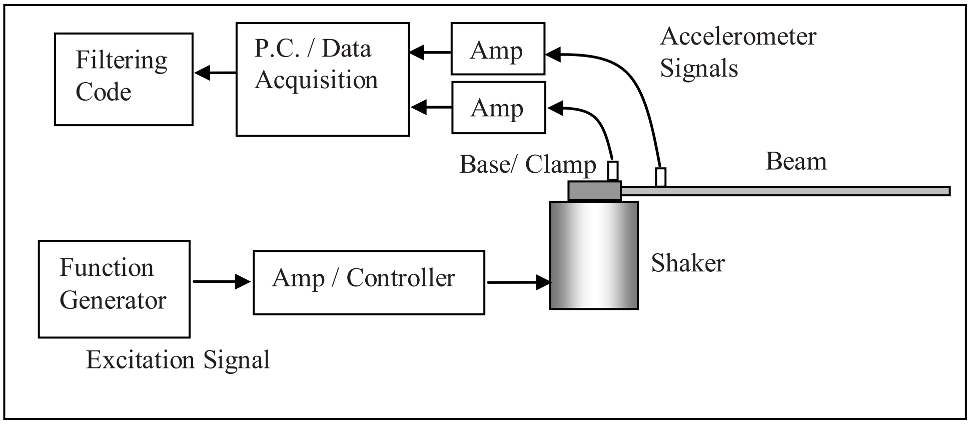

Fig. 2 Experimental Configuration for Fatigue Testing

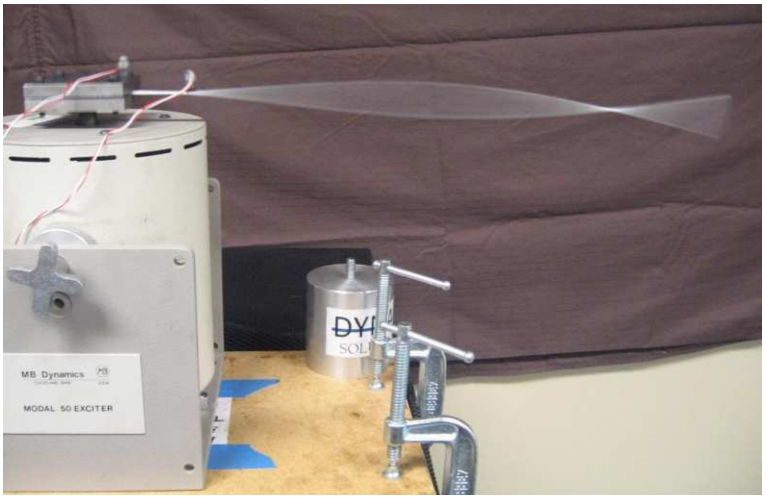

Fig. 3 Beam Vibrating at Second Natural Mode during Fatigue Testing

In both experiments a beam was secured to the base clamp and subjected to an impulse test, allowing for a rough estimate of the system's resonant frequencies. Exciting the system near its second natural frequency gave a sense of appropriate settings for data acquisition and, by removing the base excitation and recording the decay data, logarithmic decrement was used to estimate the damping associated with mode two. Mass and stiffness can be treated as known for the aluminum used, leaving the cubic stiffness as the only remaining parameter to be estimated.

Initial sweeps of the excitation frequency indicated pronounced nonlinearities in the systems response for this level of forcing. Sweeping in both increasing and decreasing frequency allowed for identification of the nonlinear and two-solution regions of beam response. The sweep indicated the expected hardening spring effect, where the maximum response amplitude tends to the left as the excitation amplitude is increased.

For the fatigue tests a single sine wave excitation was used to generate input and output data. The sample rate for all data collection was chosen to be 1 kHz. With the system resonance near 195 rad/sec, excitation frequencies were chosen at 182.22, 186.00, 189.74, 193.53, 197.29, and 201.12 rad/sec. At each of these six frequencies near resonance, two seconds of data was recorded, corresponding to approximately 60 periods of steady state response. These acceleration signals were then scaled, according to both accelerometer calibration and dependence on the mode shape, and integrated appropriately for entry into the system identification matrices.

For the first experiment, the beam was excited near resonance and allowed to shake until failure. The frequency chosen was 193.71 rad/s, which produced a large amplitude response. Data from this excitation was collected continually and used to update the final entry in the system identification matrix, each time replacing the previous 2 seconds from the same excitation frequency.

For the second experiment, a new beam was excited also at 193.71 rad/s. First, it was forced with a medium amplitude and left to shake for several minutes. Then the amplitude was increased and the beam was left to shake at this relatively high amplitude for three minutes. Next the beam was forced at a relatively low amplitude for three minutes and then excited back at the high amplitude for an additional four minutes. Finally the forcing was returned to a medium amplitude and the beam was left to shake until failure. Except for the variation in amplitude, the procedure for the second experiment was identical to that of the first experiment. For this beam's analysis the steady state data at six frequencies near resonance was used from the first experiment. The use of a "set" of typical steady-state data files for a structure was done to determine if, in implementation, one could expect reasonable performance of the method without having to generate unique excitation and response data for each beam being tested.

Results

During experimentation the cantilever beams usually broke at the clamped end. This failure behavior was expected because the clamp restricted the beams movement, causing greater stress at that end. Figure 4 shows a typical beam fracture.

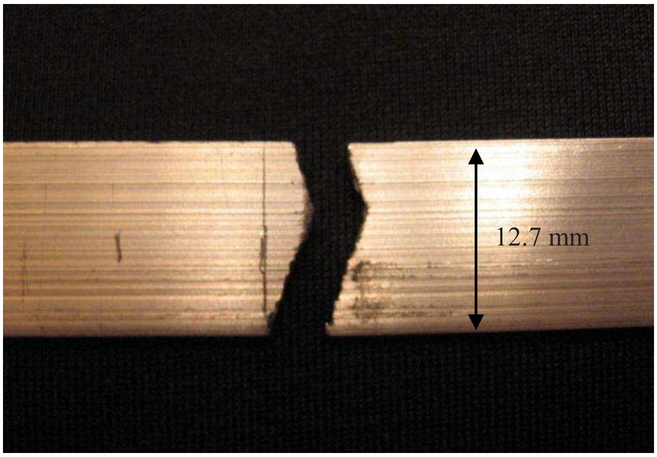

Fig. 4 Broken Beam Resulting from Fatigue Testing

The data from the first experiment was analyzed and the resulting trend of the nonlinear parameter is shown in Figure 5.

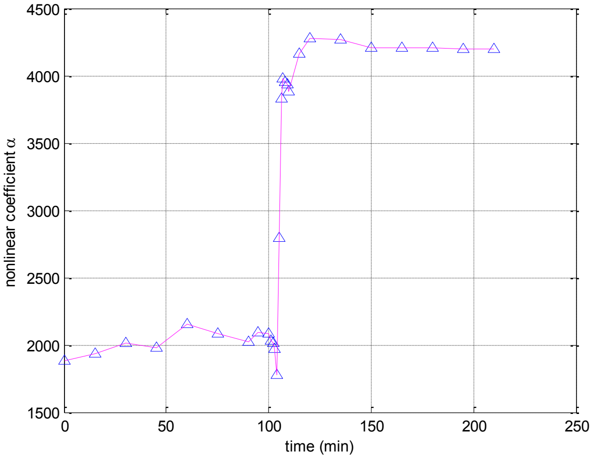

Fig. 5 Mapping of Estimated Nonlinear Stiffness during Fatigue Test

As can been seen in Figure 5, the nonlinear coefficient, α, remains relatively constant in the first 100 minutes of its life, jumps drastically over a short period of time, and finally levels off for the remainder of its life. This jump at around 105 minutes is an indication that the beam is beginning to fatigue. This warning occurs approximately halfway into its life.

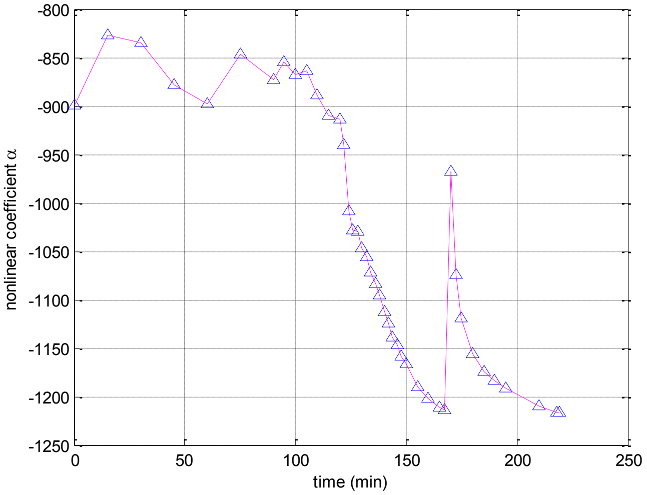

Fig. 6 Mapping of Estimated Nonlinear Stiffness during Fatigue Testing for Beam from Last Study [1]

In the previous study [1] the methodology identified changes in system behavior approximately 120 minutes into its 218 minute life. The important thing to notice in the comparison of Figure 5 and Figure 6 is that the magnitude of the nonlinear parameter changes significantly over a relatively short period of time, indicating the onset of failure.

The trend of the nonlinear parameter, α, resulting from the second experiment is shown in Figure 7.

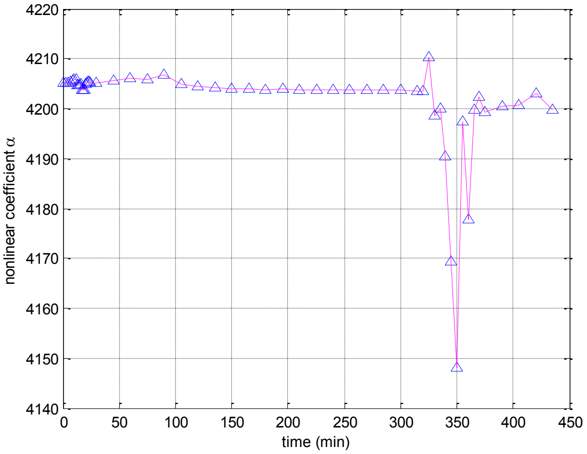

Fig. 7 Mapping of Estimated Nonlinear Stiffness during Fatigue Test with Non-Stationary Excitation

Figure 7 shows that the nonlinear parameter for this experiment is relatively constant for the first 320 minutes, and then spikes downward over a short period of time and finally levels off for the rest of the beam's life. This spike gives approximately an 85 minute warning of fatigue failure for a 435 minute life. Another important characteristic of this nonlinear trend is the cluster of data points near the beginning of the beam's life. These points represent the values of alpha when the amplitude of the forcing was increased and reduced. Notice that these points fit well with the rest of the trend and that this varying of the excitation did not produce a spike, drop, or jump in the nonlinear parameter, though we know that varying the excitation amplitude will result in a varying natural frequency for systems with this cubic nonlinearity.

Conclusions

The application of Continuous Time based nonlinear system identification to detecting crack initiation and growth has been shown in previous work to be effective. Over the course of a fatigue test to failure, the nonlinear system parameter was shown to initially remain constant with some observable error bound. Prior to the system's failure a shift in the nonlinear parameter was detected indicating the material properties were changing. For the beam from the first experiment the nonlinear parameter jumped up. In a previous study this parameter jumped down. In the second experiment, the nonlinear parameter jumped down and then back up. In all three cases the parameter jumped significantly, allowing for the prediction of fatigue failure.

The results from the second experiment, in which the amplitude of excitation was varied, showed that the nonlinear parameter was not affected significantly by non-stationary excitation in the form of varying excitation amplitude. Due to the system's nonlinearity, its natural frequency is dependent on the amplitude of excitation. In previous studies where the system was assumed to be linear, this change in natural frequency because of the system's inherent nonlinearity can trigger a "false alarm" of fatigue. In this investigation, the lack of a significant change in the nonlinear parameter as the input was varied shows that this system identification process is immune to "false alarms" of this nature. Also, the fact that the failure of one beam was successfully predicted by using the steady state data at six frequencies near resonance for an identical beam shows the robustness of this method. These successful results support the argument that in practice the steady state data of this nature would only need to be collected once for a system, and could then be applied to any similar system.

Though still in development, this method holds definite promise for systems requiring health-monitoring during use. Future studies will focus on different forms of non-stationary excitation and an emphasis will be given exploiting false triggers using linear models on the same data.

References

[1] Doughty, T. A. and Higgins, N. S., "Effect of Nonlinear Parametric Model Accuracy in Crack Prediction and Detection", SEM Annual Conference & Exposition on Experimental and Applied Mechanics, Indianapolis, 2010.

[2] Doebling, Scott W., Farrar, C. R., and Prime, M. B., "A Summary of Vibration-Based Damage Identification Methods," Shock Vibration Digest 30, 1998, pp. 91 -105.

[3] Khiem, N.T., Lien, T.V., "Multi-Crack Detection for Beam by the Natural Frequencies," Journal of Sound & Vibration 273, May 2004, pp.175-185.

[4] Loutridis, S. Douka, E., Hadjileontiadis, L.J., "Forced Vibration Behavior and Crack Detection of Cracked Beams Using Instantaneous Frequency," NDT & E International 38, July 2005: 411-419.

[5] Lee, YY, Liew K. M., "Detection of Damage Locations in a Beam using the Wavelet Analysis," International Journal of Structural Stability and Dynamics 1, 2001, pp. 455-465.

[6] Gudmundson, P., "Changes in Modal Parameters Resulting from Small Cracks," Proceedings of the International Modal Analysis Conference and Exhibit 2, 1984, pp. 690-697.

[7] Kim, Jeong-Tae, Ryu, Yeon-Sun, Cho Hyun-Man, Stubbs, N., "Damage Identification in Beam-Type Structures: Frequency-Based Method vs. Mode-shape Based Method," Engineering Structures 25, 2003, pp. 57-67.

[8] Leonard, F., Lanteigne, J., Lalonde, S., Turcotte, Y., “Free-Vibration of a Cracked Cantilever Beam and Crack Detection,” Mechanical Systems and Signal Processing 15, May 2001, pp. 529-548.

[9] Saavedra, P.N., Cuitino, L.A., “Crack Detection and Vibration Behavior of Cracked Beams,” Computers and Structures. 79 (2001): 1451-1459.

[10] Kim, J.T., Stubbs, N., “Crack Detection in Beam-Type Structures Using Frequency Data,” Journal of Sound and Vibration 259, January 2003, pp.145-161.

[11] Ding, J.L., Pazhouh, J., Lin, S.B., Burton, T.D., “Damage Characterization by Vibration Test,” Scripta Metallurgica et Materialia 30, 1994, pp. 839-834.

[12] Sih, G.C., Tzou, D.Y., “Mechanics of Nonlinear Crack Growth: Effects of Specimen Size and Loading Step,” Martinus Nijhoff Publications, 1984, pp. 155-169.

[13] Bovsunovsky, A. and Bovsunovsky, O., “Crack Detection in Beams by Means of the Driving Force Parameters Variation at Non-Linear Resonance Vibrations”, Key Engineering Materials, v 347, Damage Assessment of Structures VII, 2007, pp. 413-420.

[14] Andreaus, U., Casini, P., Vestroni, F., “Nonlinear Features In The Dynamic Response of a Cracked Beam Under Harmonic Forcing,” Proceedings of the ASME International Design Engineering Technical Conferences and Computers and Information in Engineering Conference - DETC2005, v 6 C, 5th International Conference on Multibody Systems, Nonlinear Dynamics, and Control, 2005, pp. 2083-2089.

[15] Wowk, V., *Machinery Vibration Measurement and Analysis*, McGraw Hill, Inc. New York, 1991.

[16] Crespo da Silva, M. R. M. and Glynn, C. C., “Nonlinear Flexural-Flexural-Torsional Dynamics of Inextensional Beams, II. Forced Motions,” International Journal of Solids and Structures 6, 1978, pp. 449-461.

[17] Doughty, Timothy A., Davies, P., Bajaj, A. K., “A Comparison of Three Techniques Using Steady-State Data to Identify Nonlinear Modal Behavior of an Externally Excited Cantilever Beam,” Journal of Sound and Vibration, 249(4), 2002, pp. 785-813.

[18] Doughty, Timothy A., *System Identification of Modes in Nonlinear Structures*. PhD Thesis, Ray W. Herrick Laboratories, School of Mechanical Engineering, Purdue University, 2002.

[19] Doughty, T. A. and Leineweber, M. J., “Investigating Nonlinear Models for Health Monitoring in Vibrating Structures”, ASME International Mechanical Engineering Congress and Exposition, November 2009.

Displacement Based Approach for a Robust Operational Modal Analysis

Gerardo De Canio[1], Palle Andersen[2], Ivan Roselli[1], Marialuisa Mongelli[1], Enrico Esposito[3]

1 ENEA-Italian Natonal Agency for new technologies, energy and sustainable economic development, Via Anguillarese, 301 00123 S.M di Galeria, Roma, Italy

2 Structural Vibration Solutions A/S, NOVI Science Park, Niels Jernes Vej 10, DK-9220 Aalborg, Denmark.

3 Artemis srl c/o Polytechnic University of Marche Via Brecce Bianche 60131-Ancona (Italy)

ABSTRACT

Robust estimation of the dynamic modal parameters of structures during shaking table experiments is done by means of efficient time domain data-driven Crystal Clear Stochastic Subspace Identification (CC-SSI) of vibration data recorded by a new, innovative, high resolution 3-D optical movement detection and analysis tool tracking the dynamic displacement of several selected points of the structures during the dynamic tests of natural (earthquake) and artificial (mechanical) induced vibrations. The measure of the displacements is a crucial task for the numerical and experimental studies in structural dynamics, especially within the displacement based approach in seismic design and calculations. The innovative monitoring technique measures 3 axial absolute displacements with easy and fast test set-up, high accuracy and the possibility to link the 3D-motion time histories of the tracked markers with CAD drawings of the structure and validate the FE models in real time experimental data assimilation.

T. Proulx (ed.), *Sensors, Instrumentation and Special Topics, Volume 6*, Conference Proceedings of the Society for Experimental Mechanics Series 9,
DOI 10.1007/978-1-4419-9507-0_19, © The Society for Experimental Mechanics, Inc. 2011

1 Introduction

Estimation of the dynamic modal parameters of structures is the prior activity to be performed, in laboratory or in situ, to validate the empirical or numerical models for verification of the capacity to withdraw the dynamic forces induced by mechanical vibrations or earthquakes. For laboratory experiments, powerful test facilities are needed to apply the required amount of input energy on large scale models of civil, industrial and cultural heritage structures. In this paper is discussed the use of an efficient time domain data-driven Crystal Clear Stochastic Subspace Identification (CC-SSI) during the shaking table experiments of two structures: the 1/6 scaled mock-up of a structural macro element of a church and a model representative of a 5 storey steel frame building. For the results reported herein the 6 Degree of Freedom (6DOF) 4x4 m shaking table at the ENEA C.R. Casaccia, Italy has been used. The identification of the structural parameters has been processed by the software ARTeMIS Extractor Pro.

Beside the traditional sensors (accelerometers, LVDT, strain gauges) used during the shaking table tests, the displacement data have been acquired by a new, high resolution 3-D optical movement detection and analysis tool. Its purpose is to track the absolute coordinates of several selected points of the structures during the shaking table tests This system uses twelve Infrared Cameras to measure accurate 3-D positions of hundred of markers placed on the structure during the seismic tests [2]. The innovative monitoring technique allows measuring 3 axial absolute displacements x(t), y(t), z(t) with easy and fast test set-up, high accuracy and the possibility to link the 3D-motion time histories of the tracked markers with CAD drawings of the structure and validate the FE models in real time experimental data assimilation [3]. The new monitoring system has been tested during several shaking table experiments for the estimation of the modal parameters of structures and components prior the seismic qualification for mechanical, transportation and nuclear industry.

The possibility to synchronize visible and infrared cameras allows the remote participation and control of the shaking table tests in a networking configuration of distributed experiments [4]. The conceptual structure of this networking configuration within the virtual framework DySCo (structural Dynamic, numerical Simulation, qualification tests and vibration Control) is shown in the fig.1.1.

As the experimentation goes on, remote users have the possibility to interact step by step with the operator. The connection to DySCo is provided by the ENEA grid of numerical computation, the results are shared in real time via Internet among the partners of the experiment.

The fig. 1.1 displays the images shared during the seismic tests of the drum of the vaults of the San Nicolò l'Arena of Catania (Italy). It is a critical macro structure of the church which needed a preventive anti seismic intervention of restoration. The assimilation of the marker's displacements in the FEM allowed the validation of the numerical model of the drum-vault system for successive analyses. Images and data were shared in real time by the ENEA GRID with the partners of the experiment, see the fig 1.1 and fig.1.2 for the shared experiment tool.

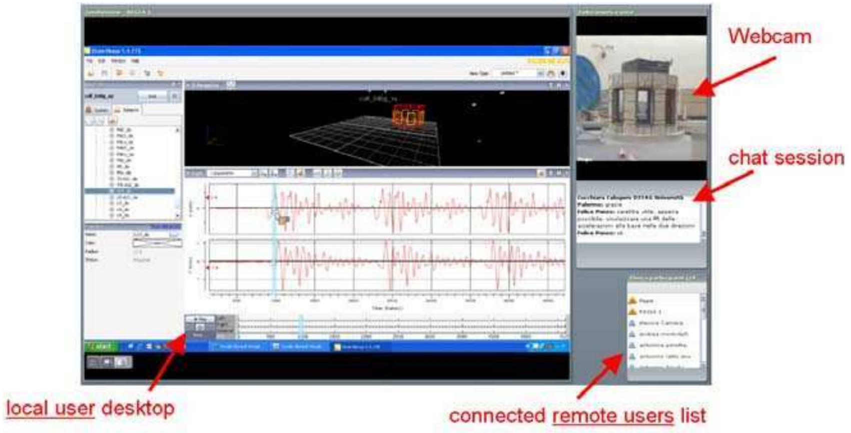

Fig. 1.1 Images shared during the seismic tests of the drum-vault model of the San Nicolò l'Arena Church, Catania (Italy).

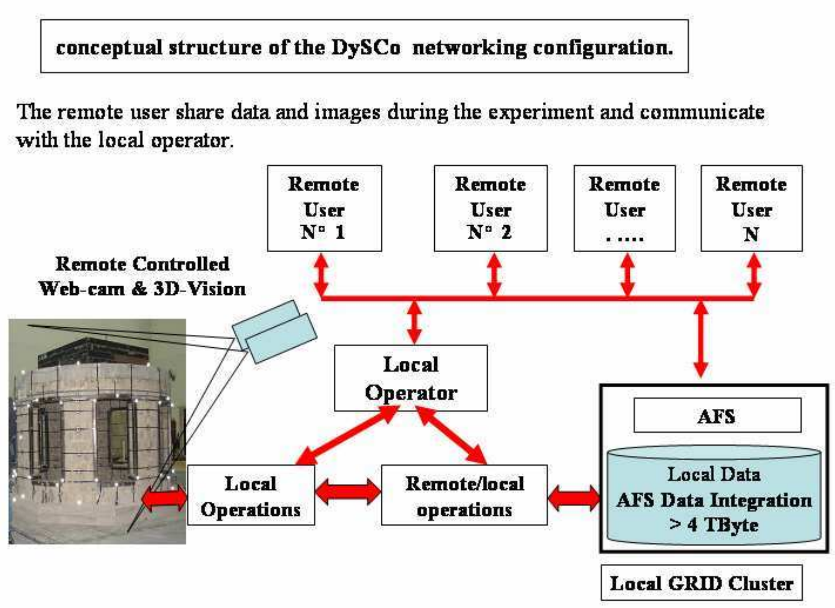
conceptual structure of the DySCo networking configuration.

The remote user share data and images during the experiment and communicate with the local operator.

Fig. 1.2 The possibility to synchronize visible and infrared cameras allows the remote participation to the shaking table tests in a networking configuration of distributed experiments.

2 Estimation of the dynamic modal parameters of a masonry structural macro element

Structural rehabilitation of historical monumental buildings is very difficult and mainly involves two kinds of problems: the former is related to the knowledge of the mechanical characteristics and of the state of damage; the latter involves the artistic values and is related to its architectural interests and the value of the contents in the building.

The masonry structure analyzed herein is the slender drum with large windows sustaining the dome of the S. Nicolò l'Arena church, Catania, Italy [1].The drum was heavy damaged and an experimental test campaign was carried out in order to design the optimal conservative restoration. A reduced 1:6 scale model of the drum-dome system was built to be subjected to dynamic tests and different kinds of reversible devices for the improvement of the structural behavior were experienced. The model with reinforcement frames in the fig. 2.1-a was positioned on the shaking table and monitored with markers at the node of the FEM model as represented in the fig. 2.1-b and submitted to a three times repeated seismic input corresponding to an event recorded in the Colfiorito area (italy) during the 1997 Umbria-Marche earthquake.

The test was concluded when cracks appeared in the pier sears. The cracks was horizontal and translated towards the middle of the piers.

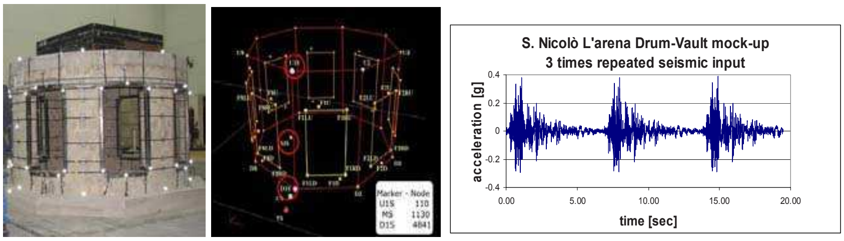

Fig. 2.1-a) Drum-vault reduced scale structural macro element; Fig. 2.1-b) Wire frame reconstruction of the 3D_vision motion detection; Fig. 2.1- c) The seismic input for the shaking table experiments was the 3 times repeated accelerograms recorded at Colfiorito, italy during the 1997 Umbria Marche earthquake.

The seismic input at the base of the shaking table was the 3 times repeated accelerograms recorded at Colfiorito, Italy during the 1997 Umbria Marche earthquake. During the experiment the absolute displacements of the markers were recorded by the 3D_vision system and analyzed by the Crystal Clear Stochastic Subspace Identification (CC-SSI) to identify the modal parameters. The fig. 2.2 displays the ARTEMIS geometry and the first three modes identified by the CC-SSI analysis [5]. The first mode at 2.18 Hz is not a physical mode of the structure, it is the base table motion at the dominant frequency of the earthquake with rigid motion of the drum-vault macro element; the second is the first flexural mode of the drum-vault at 6.31 Hz responsible of the vault damages and the third mode is the torsion mode at 13.91 Hz. responsible of the damages of the large windows.

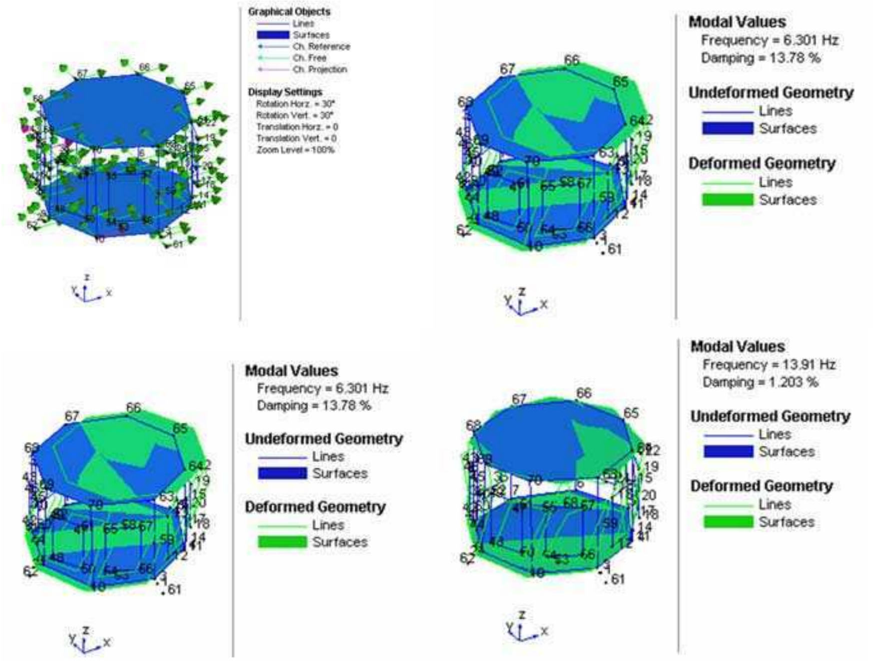

Fig. 2.2-a) X,Y acquisition channels of the markers displacements for the CC-SSI; Fig. 2.2-b) Translational mode associated at the shaking table dominant frequency;Fig.2.2- c) First flexural mode of the drum-vault;Fig.2.2- d) First torsion mode of the drum-vault

The natural frequencies and damping ratios values are displayed on the right side of the figures 2.2-a, 2.2-b and 2.2-c The modal parameters estimation was realized in two range of frequency: the first two modes at low frequencies in the range 0-10 Hz, the third mode in the range 10-20 Hz. The resulting stabilization diagrams are displayed in the fig. 2.3 and fig.2.4

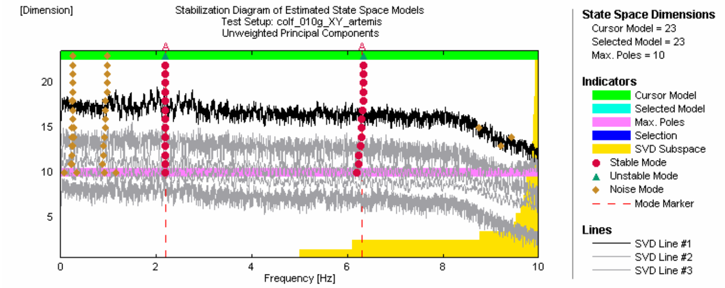

Fig. 2.3 Stabilization diagram of the low frequency estimated state space models.

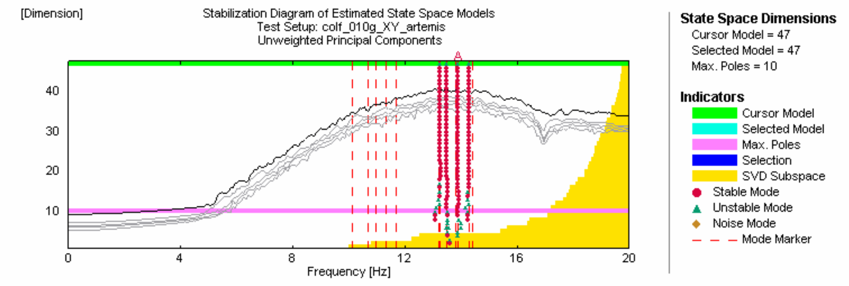

Fig. 2.4 Stabilization diagram of the estimated high frequency state space model.

The results of the displacement based approach for the CC-SSI identification were used to validate the Finite Element Model of the vault - drum macro element and the results of the numerical calculation of the modal model are given in the fig. 2.5: the fig. 2.5-a is the numerical flexural mode at 4.18 Hz , the fig. 2.5-b is the numerical torsion mode at 14.90 Hz and the fig. 2.5-c displays the normalized strain energy patterns associated at the torsion mode.

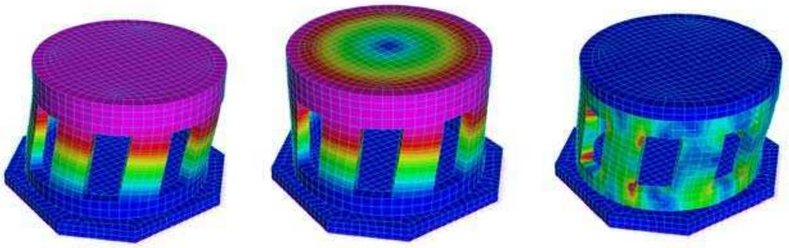

Fig. 2.5-a) Numerical flexural mode at 4.18Hz; Fig. 2.5-b) Numerical torsion mode at 14.90 Hz; Fig.2.5-c) Associated pattern of the normalized strain energy.

3 Estimation of the dynamic modal parameters of a steel frame building

The second experimental campaign was carried out on a 5 storey steel frame structure weighting 2ton. The estimation of the modal parameters has been performed imposing a white noise time history at the base of the table; the displacements data of the markers were recorded by the 3D_vision displacement tool and analyzed by ARTEMIS CC-SSI.

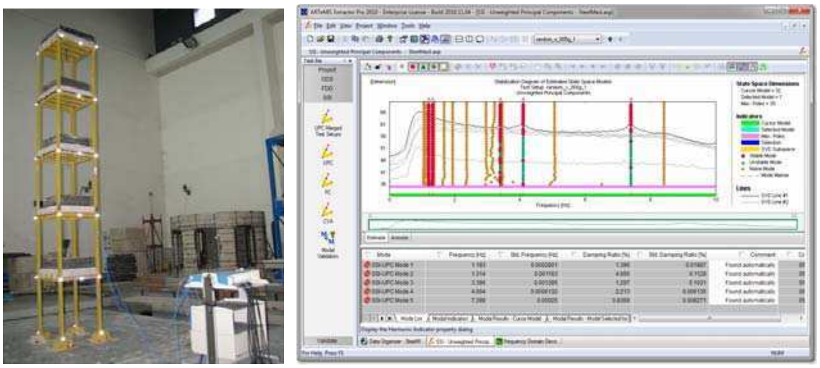

Fig. 3.1 a) Steel frame on the shaking table for the structural identification tests; Fig.3.1-b)Stabilization diagram of the CC-SSI estimated modes.

The Fig. 3.1-a displays the 5 storey steel frame positioned on the shaking table for the structural identification tests. The drum-vault model analyzed in the previous chapter is also visible. The stabilization diagram of the estimated modal parameters is in Fig.3.1-b; note that mode 2 in the stabilization diagram shows too high damping and its mode shape doesn't look good due to high noise, therefore has not been validated. Mode shapes and frequencies of the first four modes of the structure are shown in the Fig.3.2-a,b,c,d.

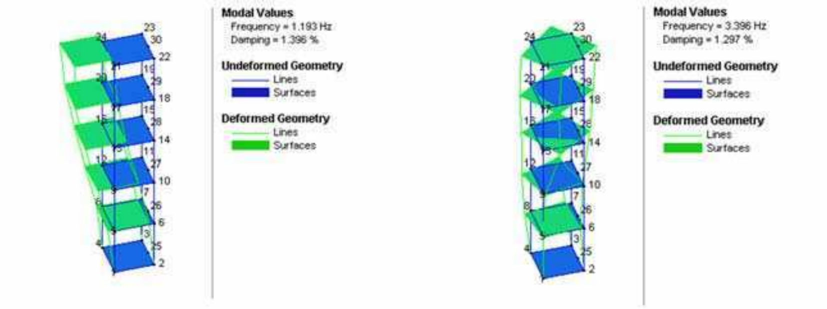

Fig. 3.2 a) 1st flexural mode shape at 1.193 Hz; b) Torsion mode shape at 3.396 Hz.

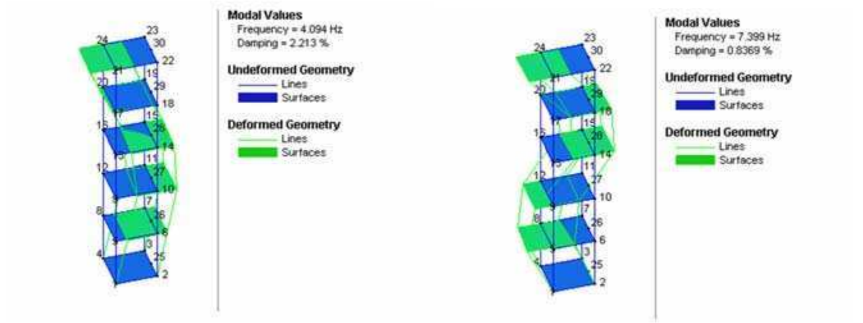

Fig. 3.2 c) 2nd flexural mode shape at 4.094 Hz; d) 3rd flexural mode shape at 7.399Hz.

The results of the CC-SSI analysis of the displacements data have been compared with the Frequency Response Function (FRF) between the accelerations recorded at the base table and top of the structure

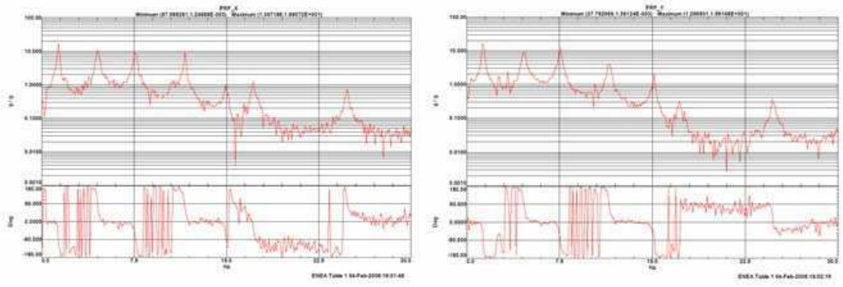

Fig. 3.3: a)FRF_X (A5_X/At_X); b)FRF_Y (A5_Y/At_Y).

The graphs in the fig. 3.3 represent the frequency response functions FRF_X (fig. 3.3-a) and FRF_Y (fig. 3.3-b) between base and top of the structure. The first three peaks of the FRFs agree with the CC-SSI flexural modes at 1.193Hz, 4.094 Hz and 7.399 Hz. Also the first torsion mode at 3.396 Hz has its signature in the FRF graphs, (see fig. 3.3-b).

Table 3.1 comparison between modal parameters estimations by CC-SSI and FRF analysis

Mode	CC-SSI Frequency Hz	CC-SSI Damping. %	FRF Frequency Hz	FRF Damping. %
1st flexural	1.190	1.396	1.35	1.90
1st Torsion	3.396	1.297	3.40	0.92
2ndflexural	4.094	2.213	4.68	1.62
3rdflexural	7.399	0.834	7.58	0.73

Conclusions

The modal parameters estimation of two structures has been performed by means of efficient time domain data-driven Crystal Clear Stochastic Subspace Identification (CC-SSI) of the displacements data recorded by a new, innovative, high resolution 3-D optical movement detection and analysis tool, tracking the dynamic displacements of several selected points of the structures during the shaking table tests. The two structures were a 1:6 reduced scale model representative of the drum-vault macro element of a church and a 5 storey steel frame structure. The validation of Finite Elements models of the structures by means of data assimilation during the shaking table tests and the comparison of the estimated modal parameters with the numerical modal analysis calculation and the FRF analysis of the experimental data showed the robustness of the modal parameters estimation.

Acknowledgments

The Authors wishes to thank Francesco Di Biagio for his contribution to the 3D_vision data acquisition and networking; Alessandro Colucci for the shaking table tests, Massimiliano Baldini, Stefano Bonifazi and Alessandro Picca for their precious contribution to the test set ups and laboratory organization.

REFERENCES

[1] Zingone G, De Canio G, Cavaleri A (2006) On the improvement of monumental structure safety: a case study III European Conference on Computational Mechanics Solids, Structures and Coupled Problems in Engineering C.A. Mota Soares et.al. (eds.) Lisbon, Portugal, 5–8 June 2006

[2] De Canio G, Caponero M, Colucci A, Roselli I (2008). Innovative high resolution 3-d vision and optical fiber sensors for data acquisition during experimental earthquake tests The 14th World Conference on Earthquake Engineering October 12-17, 2008, Beijing, China.

[3] Mongelli ML, De Canio G, Roselli I, Colucci A, Tatì A (2010) 3D motion capture and FEM analysis for shaking table tests at ENEA Casaccia Research Center" 14 ECEE Aug. 30 - Sept 3 2010, Ohrid, Macedonia

[4] Roselli I, Mencuccini I, Mongelli ML, Beone F, De Canio G, Di Biagio F (2010) The DySCo virtual lab for Seismic and Vibration Tests at the ENEA Casaccia R.C. 14 ECEE Aug. 30 - Sept 3 2010, Ohrid, Macedonia.

[5] Dohler M,Andersen P and Mevel L (2010) Data Merging for Multi-Setup Operational Modal Analysis with Data-Driven SSI. 28th International Modal Analysis Conference (IMAC) Jacksonville, Florida USA, 2010.

Effect of systematic FRF errors on matrix inversion based vibro-acoustic analysis methods

Peter Gajdatsy[1], Paul Sas[1], Wim Desmet[1], Karl Janssens[2], Herman Van der Auweraer[2]

[1] Katholieke Universiteit Leuven, Dept. PMA, Celestijnenlaan 300B, 3001 Leuven, Belgium

[2] LMS International, Interleuvenlaan 68, 3001 Leuven, Belgium; herman.vanderauweraer@lmsintl.com

ABSTRACT

The establishment of a non-parametric system description in terms of a Frequency Response Function matrix is an essential step in many structural and vibro-acoustic analysis approaches such as Modal Analysis, Load Identification, Transfer Path Analysis and Substructuring. A crucial step in many of these applications is the inversion of a matrix of this FRF matrix.

Several studies have been reported on the influence of stochastic FRF errors on this matrix inversion, leading to the use of a pseudo-inverse approach, SVD truncation, regularization etc. but little is known about the effect of systematic errors, such as amplitude or frequency shifts and inter-FRF inconsistencies on the matrix inversion result. The present paper investigates the effect of selected systematic FRF measurement errors on applications involving matrix inversion, with emphasis on the Transfer Path Analysis method. The subject is reviewed through analytical considerations and through simulations on a reference numerical model (the Garteur model). In particular, the sensitivity of two Transfer Path Analysis methods with respect to the studied systematic errors is analyzed and considerations on increasing the robustness of these methods are derived.

1. Introduction

The Frequency Response Function is one of the main non-parametric system modeling functions in mechanical engineering. It allows establishing a black-box description of a linear time-invariant system based on input-output measurements. For mechanical structural systems, such description typically takes the form of a large FRF matrix between the forces at a limited set of input locations and velocity or acceleration responses at a large grid of output locations. This dataset can be further processed into a parametric model based on modal parameters, where reciprocity allows to build a full (square input/output) system model. In other applications, the non-parametric FRF matrix is used as the actual system model and the model validity remains confined to the relation between the considered critical input and output locations.

In most of these applications, an inversion of one or more of the FRF matrices involved in building the system model need to be inverted. In FRF-based substructuring, this is done on the FRF matrix in the coupling degrees of freedom to express the flexibility. In applications such as Load Identification [1, 2], Transfer Path Analysis [3, 4]and Operational Path Analysis [5, 6], this inversion is done on a specific "test"-matrix which is established to derive input (or reference) functions which can then be used as load estimates and can be applied as inputs to the propagation system model.

The accuracy of this matrix inversion process is hence of great relevance to the validity and applicability of the analysis methodologies. The topic has hence been the subject of many research efforts, which essentially focused on the effect of random errors. For example, Starkey et al. [7], Tschudi [8], Mas et al. [9], Blau [10-12], and

T. Proulx (ed.), *Sensors, Instrumentation and Special Topics, Volume 6*, Conference Proceedings of the Society for Experimental Mechanics Series 9, DOI 10.1007/978-1-4419-9507-0_20, © The Society for Experimental Mechanics, Inc. 2011

Thite et al. [13-15] studied this problem and revealed the susceptibility of FRF based inverse methods to random errors. They described various mathematical tools, such as regularization, pseudo-inversion using truncated SVD etc, for reducing the negative effects of these errors and making the methods practicable. These approaches allowed to adequately address noise related problems typically associated with the use of sensing and data acquisition systems, where the impact of measurement noise, while in some cases significant, can be described well by considering these as stochastic errors. Improvement in low-noise sensor and measurement systems and high resolution data acquisition systems has contributed to make these errors less prominent than in the past.

Systematic FRF errors have essentially been addressed form the point of view of amplitude and phase effects related to sensor calibration and orientation errors, excitation errors, and global mass loading effects [16]. Tönshoff et al. [17] and Hendrickx [18] analyzed the effect of misaligned excitation, Dossing [19] describes the effect of mass loading and McConnel [20] discusses the interaction of forces transducers with the test structure. In most cases, the problem remains confined to errors in amplitude levels which are comparable to the errors at the input.

A more fundamental problem arises when, due to some of these errors, the FRF matrix becomes inconsistent, implying that the various elements of the FRF matrix correspond to different underlying system models. The main reason for this phenomenon is that in some of the FRF small frequency shifts occur (in a subset of the FRF, or in a different degree over the set of FRFs), which are not only propagated into small shifts in the modal parameters, but lead to fundamental processing problems in the use of estimation algorithms and matrix inversion. Causes for these shifts may be changing mass loading and/or temperature shifts or changing excitation constraints during the test, more specifically between consecutive phases of a test (e.g. between FRF “patches”).

The effect of these inconsistency errors is well known in modal analysis and has been discussed e.g. by Van der Auweraer [21] and Cauberghe [22]. Also when further processing the modal data, as in numerical model updating this problem has been studied, e.g. by Dascotte [23]. The impact of FRF inconsistencies on the matrix inversion process, and hence on the accuracy of methods such as Transfer Path Analysis, is however less well understood. This will be the topic of the present study. It will be shown that small inconsistency errors may have a major impact on the FRF matrix inversion and consequently on the final analysis result such as the path contribution analysis. Two FRF matrix inversion based TPA approaches are investigated using a reference simulation model: the classical matrix inversion TPA and the OPAX TPA [3, 4].

2. The effect of an inconsistent FRF set in matrix inversion transfer path analysis

In inverse force identification methods, such as matrix inversion transfer path analysis, the FRFs are organized into a frequency dependent 3D matrix, $\mathbf{H}(\omega)$, the columns and the rows representing the force – response relationships and the third dimension representing the frequency dependence of the FRF’s. During the matrix inversion process each frequency bin is treated independently, therefore a shift on one or more of the FRF’s is equivalent to modifying the elements of the matrix, leading to a different result. Fig. 1 displays two FRF curves illustrating the effect of shifted resonance frequencies. Comparing the original and the shifted curve, the difference is clearly visible. The biggest change is found at the resonance frequency, marked by the double arrow.

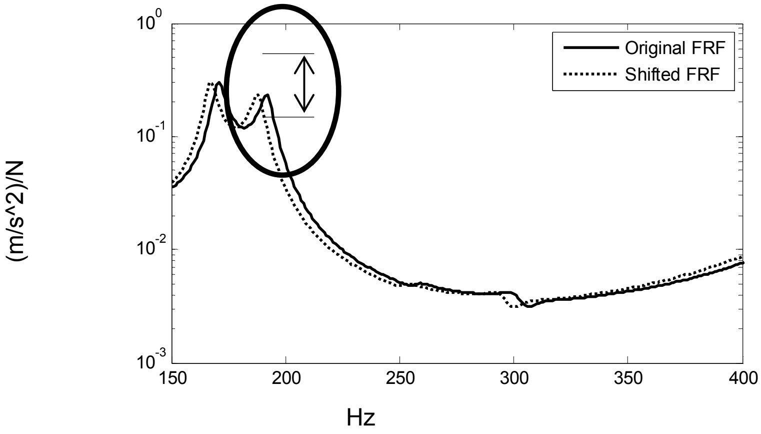

Fig. 1. Resonance frequency shift effect on the FRF amplitude

For a single frequency the FRF matrix can be represented graphically. **Fig. 2** shows the amplitude at one frequency of an example system consisting of 6 inputs (columns) and 18 outputs (rows). The colors represent the magnitude of the matrix elements in dB scale. The left hand side plot shows the original matrix, the middle one the perturbed matrix of the system where eleven FRF's were perturbed by introducing a resonance frequency shift, and the right hand side the difference between the two. The effect is very limited.

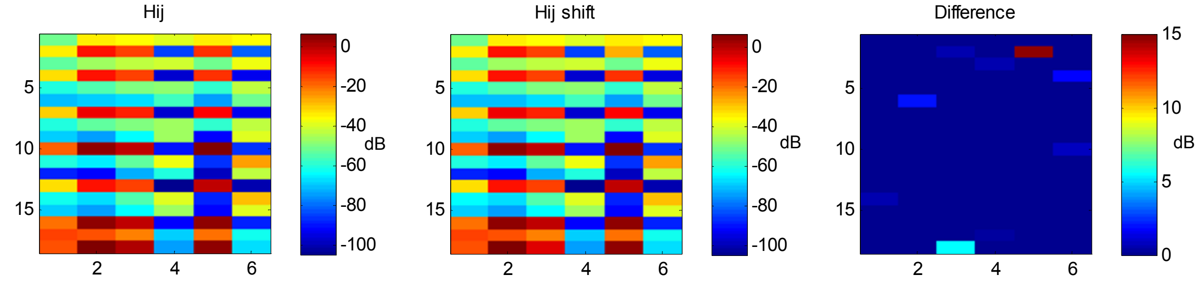

Fig. 2. Original (left), perturbed (center) and error (right) FRF matrices at a given frequency

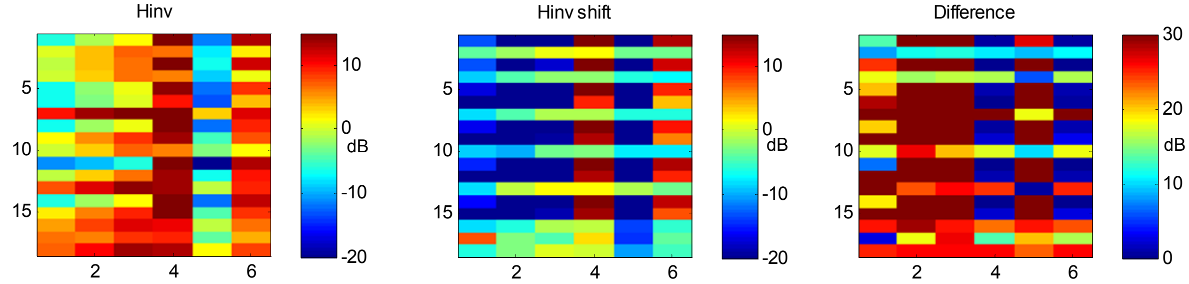

Fig. 3. FRF matrices after inversion: original (left), perturbed (center) and difference (right)

Fig. 3 shows the same two matrices after the inversion. It is clear that despite having only small differences before inversion, the inverted matrices are significantly different. This shows that even a relatively small amount of inconsistency can have a profound effect on the inversion. When used in a context of force estimation (as in TPA), by multiplying the inverted FRF with operational response measurements, this error will highly affect the force estimate values, as is illustrated in **Fig. 4** for the example system. The left hand side shows the unperturbed results, while the right side the results obtained with the inconsistent FRF dataset. The difference between the two plots is obvious.

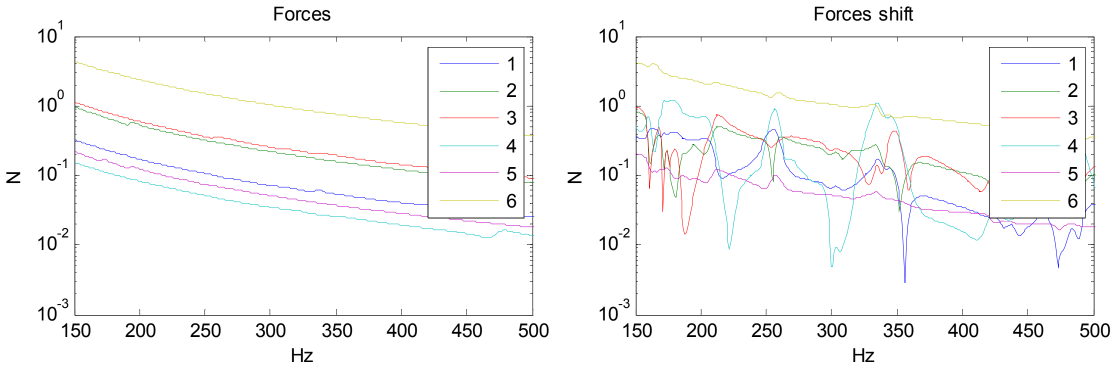

Fig. 4. Force estimates based on the original (left) and the perturbed (right) FRF dataset

3. Simulation setup

3.1. The Garteur model

To study the effects of inconsistencies on matrix inversion and path contribution analysis, a numerical simulation TPA study was conducted. The model which was used is the FE model of the Garteur SM-AG19 Structure [24], shown on **Fig. 5**, from which simulated operational data and the corresponding FRF datasets were obtained.

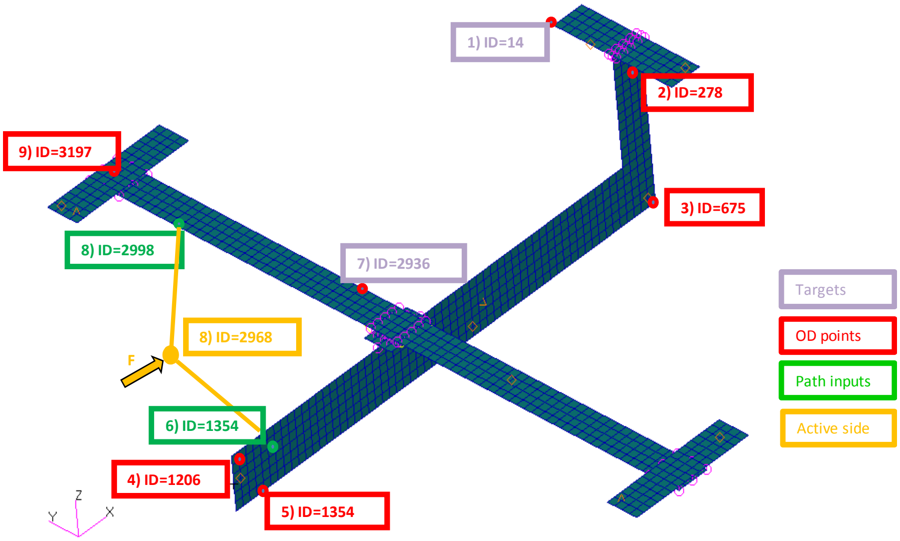

Fig. 5. The Garteur FE model used for the TPA measurement simulation

The TPA dataset consisted of the operational data and FRF's for the following DOF's:

- 3 target DOF's (1z , 7x, 7y)
- 6 input DOF's (6x, 6y, 6z, 8x, 8y, 8z)
- 12 additional overdetermination response DOF's for the matrix inversion

These DOF's were selected from a larger set to obtain a well-conditioned set of FRF's in the frequency range between 150Hz and 500Hz. During the operational simulations a mass-spring system is connected to the structure to emulate the presence of an active component. The 1 DOF springs are connected through the 3 translational DOF's at the two input points (point 8) and 6) in Figure 5.) To simulate the excitation of the structure by the active component, a unit random force is applied on the mass, separately in each principal direction. The values of the spring stiffnesses and the mass are chosen such that the resonance frequency of the spring-mass system would be below the frequency range of the analysis. The FRF's from the input points to the target and overdetermination points were obtained by applying a unit force separately in the 3 translational DOF's at both inputs. During these simulations the active component was removed from the model.

3.2. Analysis performance

During the transfer path analysis the two FRF based TPA methods, matrix inversion and OPAX, were examined w.r.t three features, representative for TPA analysis.

Correct identification of dominant path

The fundamental goal of transfer path analysis is to identify the most contributing path and correct frequency region of the dominant peak on that path for a given engine order or frequency range. The first quality indicator is hence the identification efficiency of the dominant path, **Eq. (1)** over a series of analysis.

$$\eta_{id} = \frac{correctly\ identified\ dominant\ path}{number\ of\ simulation\ runs} \tag{1}$$

Average error on dominant peak

The second indicator, the average error on the dominant peak level, provides a quantitative evaluation of the effects caused by systematic errors. This indicator is calculated according to **Eq. (2)**, only taking into account those runs in which the most contributing path is correctly identified. The dB values are used in this calculation.

$$\bar{e}_{peak} = \sum_{i=1}^{k} \frac{\left| y_{ref} - y_i \right|}{k} \tag{2}$$

Path ranking

The third important requirement for any TPA method is that it should provide a correct ranking of the significant contributing paths. During the following simulations every path within a range of 10 dB relative the dominant path is considered to be important.

Two frequency regions

During the calculation of these three quality indicators, the path contribution results were split into 2 frequency ranges: 150-250Hz and 250-500Hz for all 3 targets, resulting in a total of 6 analysis cases. It was ensured that there was at least one dominant peak in each analysis case. The quality indicators were first calculated separately for each analysis case and then averaged in order to arrive to a single representative value.

3.3. Generation of inconsistent FRF datasets

To examine the effects of inconsistency 51 FRF datasets were created:

- 1 baseline dataset with the original parameters of the Garteur model
- 50 other datasets in which the Young's modulus is varied for the steel components of the model. The Young modulus variation was such that the shift of frequency peaks uniformly varies between ±1% for the first 10 datasets, ±2% for the next 10 datasets, and so on, up to ±5% in the last 10 datasets.

Varying the amount of inconsistency in the FRF set

An increasing amount of inconsistency is introduced into the simulation by replacing more and more FRF's in the baseline dataset by the corresponding FRF's from the perturbed datasets. In each step 200 simulation runs are performed. Within each run both the positions of the replaced FRF's, and the dataset from which each FRF is taken, are randomly chosen.

4. Simulation results for inconsistent FRF dataset

4.1 Analysis purposes

Dominant path identification efficiency

Both TPA methods are sensitive to an inconsistent FRF dataset as it can be observed in the results shown in **Fig. 6**. However the OPAX method proves to be more robust than the classical MI method.

Fig. 7 zooms in on the results of the first 10% range, where the high sensitivity of MI to systematic errors is even more visible. Note, that the x axis shows the number of perturbed paths and not the relative amount as on the previous figure. Already in the case of just a single erroneous FRF, MI fails to correctly identify the dominant path in more than 10% of the simulation runs. Using the same data, OPAX still achieves very high accuracy.

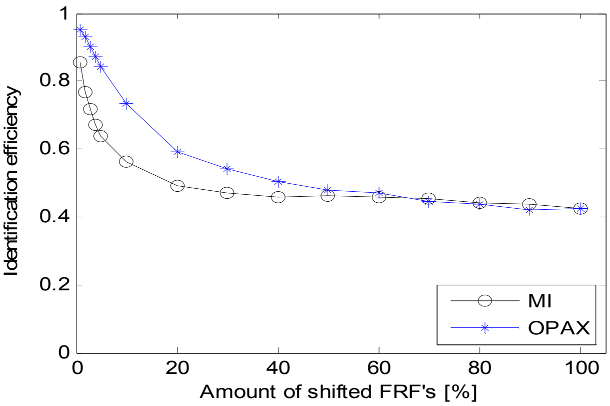

Fig. 6. Dominant path identification efficiency in the presence of inconsistency in the FRF set

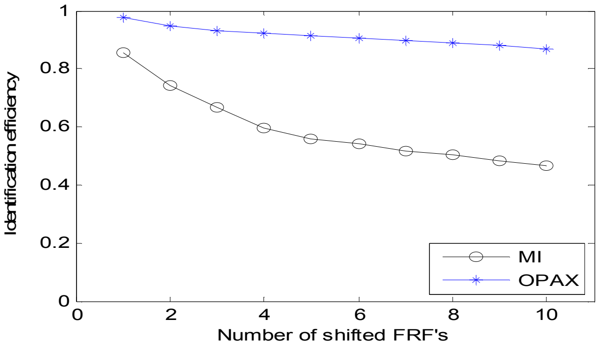

Fig. 7. Close up on the results of Figure 6 for the first 10% range

Observed asymptotic behavior

The reason for the asymptotic behavior observed in **Fig. 6** is that two of the six analysis cases have a strongly dominant path whose contribution is at least 20dB higher than the other paths. This means that very large errors are necessary in order to influence this path, therefore, it remains correctly identified as the dominant path in nearly all simulation runs. **Fig. 8** below illustrates this case for the 250-400Hz frequency range at target point 1. The highest peak on the dominant path 6 can easily be observed. Despite the fact that the difference between the reference and the perturbed PPC plot is quite evident, the dominant peak is 19.5dB higher than the next most contributing path. Such a big difference makes this analysis case more resistant to the errors on the FRF's.

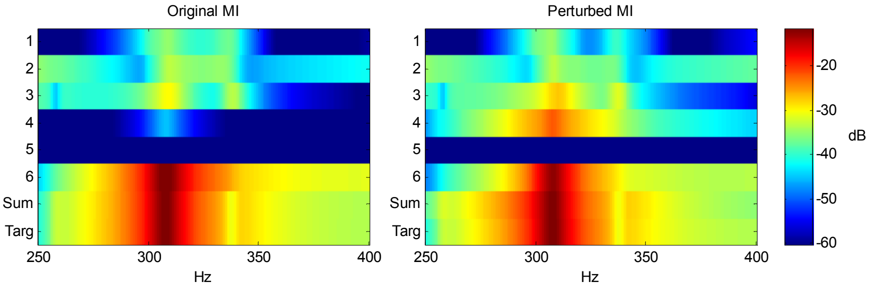

Fig. 8. Example for a highly dominant path. Left: reference, right: perturbed dataset.

Fig. 9 shows a more typical scenario, when most of the paths contribute to the target response. In such a case, even small errors on the FRF's can result in an incorrect identification of the most important path. This is clearly visible in the figure: the value of the dominant peak on path 6 decreases and paths 2 to 4 become the most important contributors.

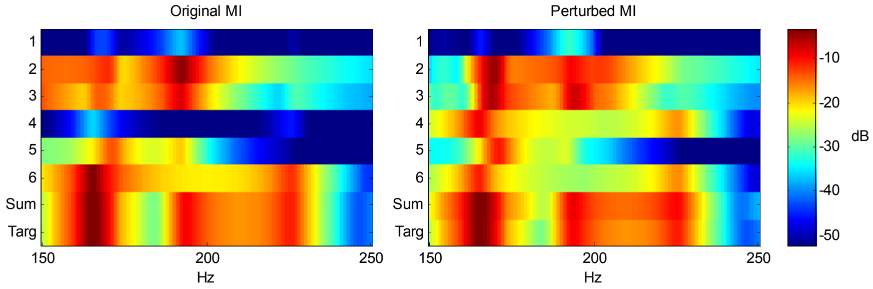

Fig. 9. Example for a more typical, even distribution of contributing paths. Left: reference, right: perturbed dataset.

Path ranking and Average error on dominant peak

Fig. 10 shows the normalized results of the identification efficiency for correct path ranking. OPAX performs better than matrix inversion TPA also in this aspect, proving to be more robust against inconsistent FRF data.

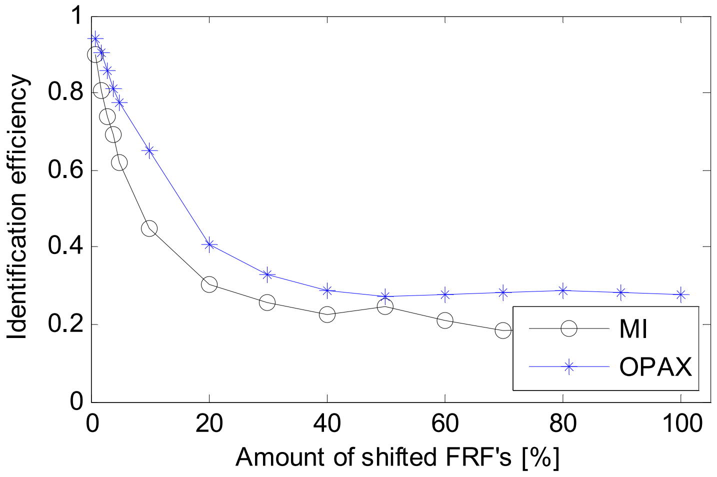

Fig. 10. Identification efficiency for correct path ranking

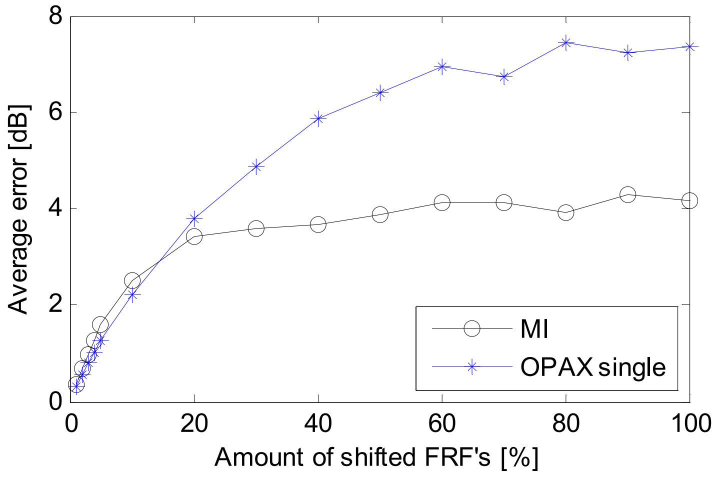

Fig. 11. Average error on the dominant peak

For small errors the average error on the dominant peak is nearly equal (**Fig. 11**). For a higher amount of perturbed FRF's the two methods behave differently. It can be observed that the MI results display an asymptotic behavior. The reason for this is that the average error is only calculated for the correctly identified peaks, therefore it can be expected that when the error on the dominant peak is very high, then the dominant peak is not identified correctly. For this reason large errors get excluded from this calculation. On the other hand the OPAX results behave differently because OPAX is basically a least squares curve fitting approach: it finds the best fit to all indicators. As a consequence, although the overall error on the paths increases, the most dominant features, such as the highest contributor among the paths, can still be correctly identified.

4.2. A quantitative analysis

The previous part of this section has shown that matrix inversion based TPA methods are quite sensitive to inconsistency in the FRF datasets. However, from a practical point of view it would be useful to know how much inconsistency can be allowed in a TPA dataset. In this paper we have chosen the ratio between the number of perturbed FRF's over the number of baseline FRF's as a measure of inconsistency. It was furthermore assumed that having a 95% dominant path identification efficiency is an acceptable performance.

Therefore, in the simulations the quality of the TPA analysis was examined with respect to two factors: 1) the magnitude of the frequency shift and 2) the frequency resolution of the FRF's. To examine the first factor, the amount of frequency shift in the perturbed FRF's was varied between ±1% and ±5% in 5 steps. Furthermore, it was expected that using FRF's with lower frequency resolution might lessen the negative effects of inconsistency. To examine this second factor the resolution of the FRF's was reduced to 3, 5, 7, 9 and 11Hz in the simulation. Further reduction in the resolution does not make sense since the FRF's lose their character, because wider bands would include multiple resonance peaks. The results of this analysis are presented in the following figures.

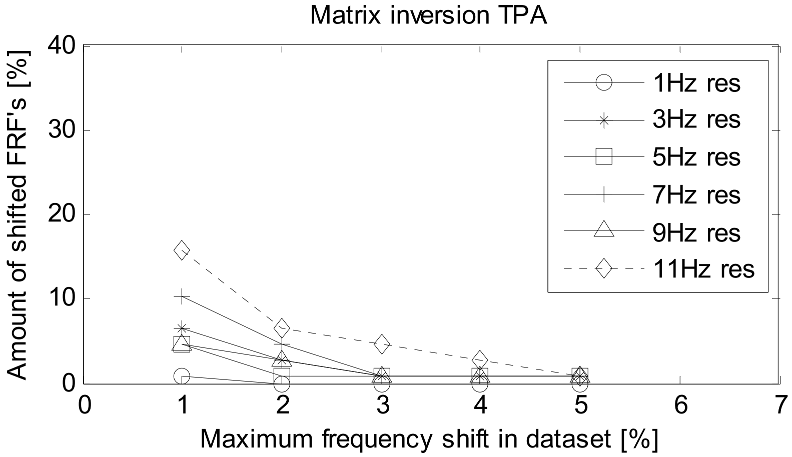

Fig. 12. The sensitivity of matrix inversion TPA to the amount of inconsistency in the FRF dataset, in function of the maximum frequency shift in the perturbed FRF's

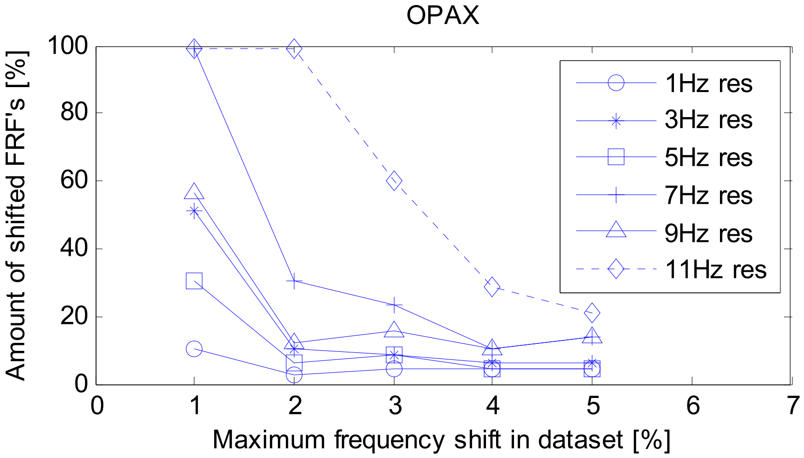

Fig. 13. The sensitivity of OPAX to the amount of inconsistency in the FRF dataset, in function of the maximum frequency shift in the perturbed FRF's. Note the different y-axis!

The following observations can be made:

- Reducing the frequency resolution of the FRF's improves the robustness of both methods.
- The classical matrix inversion TPA method is more sensitive to inconsistency in the FRF:
  - Even with small (1%) frequency shifts in the FRF data, the presence of 10-20% inconsistency yields incorrect analysis results
  - This behavior gets worse with increasing frequency shift, e.g. in the presence of 5% frequency shift, the introduction of even 1% perturbed FRF's yields incorrect results
- At the same time the OPAX method proved to be more robust.

Conclusions

FRF models are widely used in mechanical engineering for a variety of applications. Inverting such an FRF model is a key element of methods such as Transfer Path Analysis and FRF based substructuring. While the effect of random FRF errors on the inversion result has been studied extensively, the impact of systematic errors has been studied only for a limited class of errors such as calibration and orientation errors and the absence of rotational degree of freedom FRF's. In this paper, the effect of frequency shift errors, leading to inconsistent FRF matrices was investigated. A numerical reference model was used to perform a parametric study. The main conclusion is that inconsistencies in the FRF matrix may lead to significant errors in the estimation of loads using matrix inversion procedures, with all consequences to applications such as transfer path analysis. Important deviations in the contributions, ultimately leading to incorrect dominant path identification and incorrect path ranking may be the result.

Acknowledgements

Peter Gajdatsy, performed his research as an early stage researcher at LMS International and K.U.Leuven under the Smart Structures Marie Curie Research Training Network (MRTN-CT-2006-035559). The financial support of the European Commission is gratefully acknowledged.

References

[1] G. Desanghere, “Identification of external forces based on frequency response measurements”, in *Proc. 8-th International Seminar on Modal Analysis*, Leuven, Belgium, 1983.

[2] M. Ohlrich and A. Crone: An equivalent force description of gear-box sources applied in prediction of structural vibrational in wind turbines. In *Pro.Inter-Noise 88, the International Conference on Noise Control Engineering*, Avignon, France, 1988, pp. 479-484.

[3] H. Van der Auweraer, P. Mas, S. Dom, A. Vecchio, K. Janssens and P. Van de Ponseele, “Transfer Path Analysis in the critical path of vehicle refinement: the role of fast, hybrid and operational path analysis”, in *Proc. SAE Noise and Vibration Conf.*, May 14-17, 2007, SAE paper no. 2007-01-2352.

[4] K. Janssens, P. Gajdatsy, L. Gielen, P. Mas, L. Britte, W. Desmet and H. Van der Auweraer, “OPAX: a new transfer path analysis method based on parametric load models”, Accepted for publication in Mechanical Systems and Signal Processing, 2010

[5] P. Gajdatsy, K. Janssens, W. Desmet and H. Van der Auweraer, “Application of the transmissibility concept in transfer path analysis”, Mechanical Systems and Signal Processing, vol. 24, no. 7, pp. 1963-1976, Oct. 2010.

[6] D. de Klerk and A. Osipov, “operational transfer path analysis: theory, guidelines and tire noise applications”, Mechanical Systems and Signal Processing, vol. 24, no. 7, pp. 1950-1962, Oct. 2010.

[7] J.M. Starkey and G.L. Merrill, "On the ill-conditioned nature of indirect force-measurement techniques," *Journal of Modal Analysis*, vol. 4, no. 3, pp. 103-108, July 1989.

[8] H. R. Tschudi, "Le methdode des voies de transmission des forces - une alternative interessante par rapport aux essais de demontage," in Unikeller Conference, 1991.

[9] P. Mas, P. Sas, and K Wyckaert, "Indirect force identification based upon impedace matrix inversion: a study on statistical and deterministical accuracy," in *ISMA 19*, Leuven, Belgium, September, 1994.

[10] M. Blau, "Force spectra identification by FRF matrix inversion: A sensor placement criterion," Journal of the Acoustical Society of America, vol. 105, no. 2, p. 970, 1999.

[11] M. Blau, "Inverse force synthesis: state of the art and future research," in InterNoise 2000, Nice, France, 27-30 August 2000.

[12] M. Blau, "Indirect Measurement of Multiple Excitation Force Spectra by FRF Matrix Inversion: Influence of Errors in Statistical Estimates of FRFs and Response Spectra," Acta Acustica united with Acustica, vol. 85, no. 4, pp. 464-479, July/August 1999.

[13] A.N. Thite and Thompson D.J., "Selection of response measurement locations to improve inverse force determination," Applied Acoustics, vol. 67, no. 8, pp. 797-818, August 2006.

[14] A.N. Thite and D.J. Thompson, "The quantification of structure-borne transmission paths by inverse methods. Part 1: Improved singular value rejection methods," Journal of Sound and Vibration, vol. 264, no. 2, pp. 411-431, July 2003.

[15] A.N. Thite and D.J. Thompson, "The quantification of structure-borne transmissionpaths by inverse methods. Part 2: Use of regularization techniques," Journal of Sound and Vibration, vol. 264, no. 2, pp. 433-451, July 2003.

[16] H. Van der Auweraer, S. Donders and B. Peeters, "Importance of Uncertainty in Identifying and Using Modal Models", in *Proc. Managing Uncertainty in Noise Measurement and Prediction Symposium*, 27-29 June 2005, Le Mans, France

[17] H.K. Tönshoff and D. Ahlborn, "Sensor orientation errors in frequency response function measurements," The Int. Journal of Analytical and Experimental Modal Analysis, vol. 8, no. 3, pp. 219-227, July 1993.

[18] W Hendrickx, "Accurate vehicle FRF measurements for indirect force determination based upon matrix inversion," in *Proc. ISMA 19*, Leuven, Belgium, 1994, pp. 1037-1048.

[19] O. Dossing, "Prediction of transducer mass-loading effects and identification of dynamic mass," in *Proc. of 9th IMAC*, Firenze, Italy, Apr. 15-18, 1991, pp. 306-311.

[20] K.G. McConnel, "Interaction of force transducers with their test environment," in *Proc. 10th IMAC*, San Diego, CA, USA, Feb 3-7, 1992, pp. 1309-1316.

[21] H. Van der Auweraer, W. Leurs, P. Mas, and Hermans L., "On the problem of obtaining consistent estimates from multi-patch modal tests," in *Proc. ISMA 25*, Leuven, Belgium, Sept. 13-15, 2000

[22] B. Cauberghe, P. Guillaume, B. Dierckx, and Verboven P., "Identification of modal parameters from inconsistent data," in *Proc. 20th IMAC*, Los Angeles, CA, USA, 4-7 February, 2002.

[23] E. Dascotte, "The Use of FE Model Updating and Probabilistic Analysis for Dealing with Uncertainty in Structural Dynamics Simulation," in *Proc. JMAC*, Tokyo, Japan, Sept. 10-13, 2003.

[24] M. Degener and M. Hermes, "Round vibration test and finite element analysis of the Garteur SM-AG19 testbed," DLR - German Aerospace Research Establishment, Institute for Aeroelasticity, Technical Report IB 232-96 J 08 October 1996.

Peri-Prosthetic Fracture Vibration Testing

Jesse Cruce[1], Jenny Erwin[2], Kevin Remick[3], Phillip Cornwell[4], R. Michael Meneghini[5], Joe Racanelli[6]

[1]Oklahoma State University, Stillwater, OK 74078
[2]Middlebury College, Middlebury, VT 05753
[3]University of Illinois Urbana-Champaign, Champaign, IL 61820
[4]Dept of Mechanical Engineering, Rose-Hulman Institute of Technology, Terre Haute, IN 47803
[5]Indiana Clinic, Indiana University Department of Orthopaedic Surgery, Indianapolis, IN 46202
[6]Stryker Orthopaedics, Mahway, NJ 07430

Abstract

The purpose of this study was to establish a test setup and vibration analysis method to predict femoral stem seating and prevent bone fracture using accelerometer and force response data from an instrumented stem and impactor. This study builds upon earlier studies to identify a means to supplement a surgeon's tactile and auditory senses by using damage identification techniques normally used for civil and mechanical structures. Testing was conducted using foam cortical shell sawbones prepared for stems of different geometries. Each stem was instrumented with an accelerometer. Two impactor designs were compared: a monolithic impactor and a two-piece impactor, each with an integrated load cell and accelerometer. Acceleration and force measurements were taken in the direction of impaction. Comparisons between different methods of applying an impacting force were made, including a drop tower and a surgical hammer. The effect of varying compliance on the data was also investigated. The ultimate goal of this study was to assist in the design of an integrated portable data acquisition system capable of being used in future cadaveric testing. This paper will discuss the experimental setup and the subsequent results of the comparisons made between impactors, prosthetic geometries, compliances, and impact methods. The results of this study can be used for both future replicate testing as well as in a cadaveric environment.

Introduction

Osteoarthritis, the most common form of arthritis, is a degenerative condition caused by the breakdown of cartilage in one or more joints, and most commonly affects the spine, hips, knees, and hands. Joints affected by this condition become painful and experience a loss of mobility [1]. Advanced stages of osteoarthritis of the hip can be treated with total hip arthroplasty (artificial hip replacement). Currently, orthopedic surgeons perform approximately 235,000 total hip replacements in the United States each year [2]. In cemented hip arthroplasty, the surgeon removes the femoral head and reams the femur out to an area larger than the prosthesis, which is held to the bone using bone cement. Alternatively, in uncemented hip arthroplasty, the surgeon impacts a prosthesis, which is slightly larger than the reamed area, into the femoral canal. This procedure relies on residual stresses from the press fit for stability [3]. Seating is defined as the point when these stresses have reached a high enough point to prevent micromotion of the implant. However, femoral fracture will occur if these stresses exceed the maximum hoop stress of the bone. Unrecognized fractures during surgery may allow the implant to move during recovery, inhibiting the growth of bone into the prosthesis [4]. These fractures occur in one of two locations: proximally, near the femoral neck, and distally, near the tip of the prosthesis [5]. Currently, surgeons rely on auditory and tactile feedback during implantation to determine seating [6].

The use of minimally invasive surgery has become an increasingly popular technique for many procedures, including hip replacements [6] [7]. The smaller incision length causes less soft tissue and muscular damage, resulting in less blood loss, decreased hospital stays, diminished post-operative pain, and a more rapid rehabilitation and recovery time [6][7][8]. However, this procedure is not without problems. The reduction in

T. Proulx (ed.), *Sensors, Instrumentation and Special Topics, Volume 6*, Conference Proceedings of the Society for Experimental Mechanics Series 9, DOI 10.1007/978-1-4419-9507-0_21, © The Society for Experimental Mechanics, Inc. 2011

incision size may decrease the tactile and auditory feedback surgeons rely on to determine seating during the procedure; anecdotal evidence suggests an increase in intraoperative fractures due to this decrease in incision size [6].

Cadaveric studies have been conducted to characterize these fractures using strain gages and photoelastic coatings [3]. These studies focused on quantifying the magnitude of the hoop stresses. The monitoring of vibrations during impaction has been explored as a means of determining implant seating. Giardini et al. [9] measured acceleration of the prosthesis during impaction into a PVC pipe designed to roughly simulate hip arthroplasty. The test was then repeated using a commercially available replicate composite femur. By monitoring the change in the global Holder Exponent, Giardini's data indicated that the possibility exists for developing a method to determine seating. In Abou-Trabi et al. [10], five replicate composite femurs were impacted. Acceleration data and impedance measurements with a PZT patch were taken. Abou-Trabi found several metrics that held potential for determining seating, including the normal of acceleration divided by the normal of the force. Crisman et al. [11] continued this research with cadaveric testing. Unfortunately, the metrics that appeared promising when using composite femurs did not work well with the cadaveric data. Only the time to 99% total norm showed promise as a metric to determine seating. This metric measures the time it takes for a signal from a single impact to obtain 99% of its total norm during the given time interval.

This study continues previous research on methods to identify seating, but focuses more on developing a test protocol that has better control, consistency, and repeatability of the data and results. Developing a mounting system with compliance that better mimics the conditions found in the operating room was also a focus of this study. Comparisons between using a weighted drop tower, which provided a consistent force between successive impacts, and using a surgical hammer, as actually used in orthopedic surgery, were also made. A larger number of replicate femurs were used for this study (26 replicates) than in previous studies.

Experimental Setup and Procedure

This study compared the seating, force, and vibration characteristics of two types of prosthesis geometries: the Secure-Fit Max (132 deg neck, size 10, cat# 6051-1035S) and the Accolade TMZF Cementless Femoral Stem (132 deg neck, size 4.5, cat# 6020-4535.) These two designs are shown in Figure 1. Two different impactor designs were also investigated: the Monolithic and the Two-Piece bolt, as shown in Figure 2. The purpose of comparing the impactor designs was to determine whether using a removable accelerometer mount on the Two-Piece bolt had a significant impact on the data. A removable, bolted mount such as this could easily be implemented on the impactors currently in use by orthopedic surgeons.

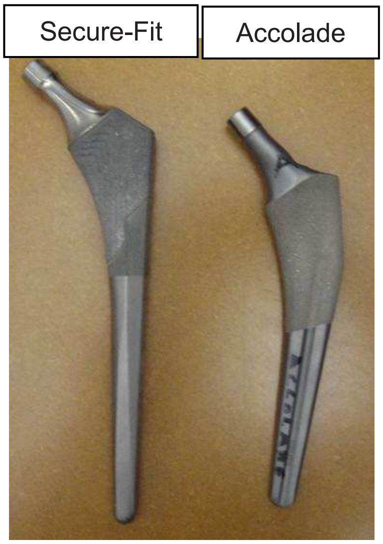

Figure 1: The two geometries of prostheses used.

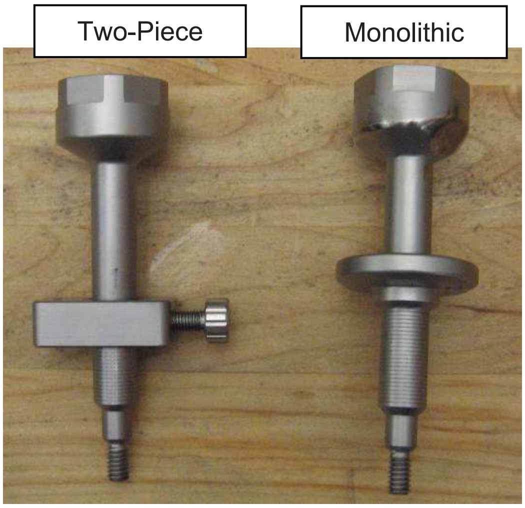

Figure 2: The two impactor designs investigated.

This study used foam cortical shell sawbones (Pacific Research Laboratories, Inc., Vashon, Washington, Model 1130.) A practicing orthopedic surgeon removed the femoral head, then reamed and broached the replicates in accordance with the geometry and size of prosthesis to be used. The bottom half of each replicate femur was removed for convenience. Due to clearance issues, approximately 1 cm of the greater trocanter was removed from replicates used for testing the Accolade prosthesis.

Two Kistler 8742A10 accelerometers were attached to the prosthesis/impactor assembly, as shown in Figure 3. Both accelerometers had a nominal sensitivity of 0.5 mV/g, a measurement range of ±10,000 g's and a frequency range of 1 to 10,000 Hz. One accelerometer, referred to as instrument-mounted for the remainder of this paper, was attached to the impactor, and the other accelerometer, referred to as stem-mounted, was attached to the prosthesis. The accelerometers measured motion in the axial direction only, and were wrench-tightened into tapped holes, to help ensure a solid connection. A Kistler 9176B force transducer was also wrench tightened onto the top of the impactor at the point of impact. The force transducer had a sensitivity of 3.5 pC/N and an amplitude range of -16 to 60 kN.

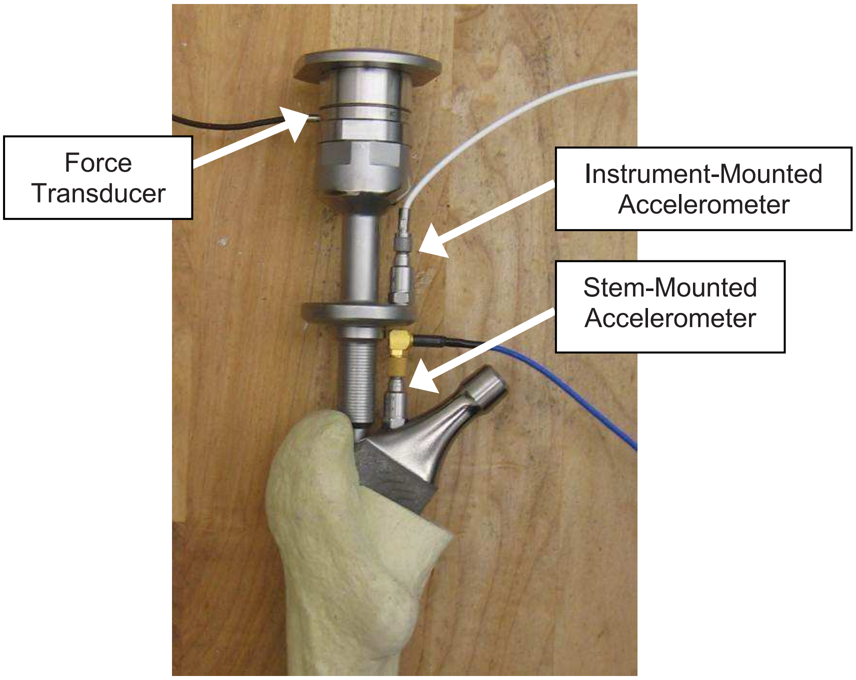

Figure 3: Instrumentation used for the impactor-prosthesis assembly

Each accelerometer was connected to a Kistler 5118B2 power supply/coupler. The force transducer was connected to a Kistler 5010 dual mode amplifier. Both power supplies and the amplifier were connected to a National Instruments NI PXI-2042Q DAQ, which ran a LABVIEW VI to log the data. For each impact, the data acquisition system collected 25,000 data points at a rate of 200 kHz, corresponding to a time of 0.125 seconds. The accelerometers triggered the system, which recorded 500 pre-trigger points.

This study also evaluated the differences between two methods of impacting the prosthesis into the replicate femurs. For the first method, a drop tower assembly, as shown in Figure 4, was used. The sliding beam, added weight, and impacting head of the drop tower had a total mass of 12.18 kg. A pull stop mounted on the sliding rail enabled the drop tower to fall from a constant height for each impact, thereby providing a consistent force input for each test. Two springs were attached from the sliding beam to the horizontal cross bar at the top of the drop tower assembly using a metal wire. The purpose of these springs was to prevent multiple hits from the drop tower. The second method for applying the impact force was using a surgical hammer, as shown in Figure 5.

A guide for the femur was designed and produced by rapid prototyping to constrain the motion of the femur to the axial direction. This guide was held stationary by a vertically mounted vice. Piping insulation was cut to create inserts, which were placed inside the guide. This configuration allowed the femur to slide in the axial direction as well as experience small rotations about the axial axis, helping remove the effects of the vice and drop tower from the femur/prosthesis system. In order to characterize the effects of the compliance on the data, three different compliance setups were compared, hereafter referred to as "soft", "medium", and "hard." The soft compliance consisted of a polymer surgical pad (Mayo Stand Cover, Action Products, Inc., Hagerstown, Maryland, Model No. 40717), which was folded and placed beneath each replicate femur. A neoprene rubber pad was placed between the surgical pad and femur in order to prevent possible damage to the surgical pad from repeated testing (McMaster-Carr Supply Company, Robinson, New Jersey, Part Number: 8568K666, Durometer: 40A). The medium stiffness compliance setup consisted of 6 silicon rubber pads of 3 different durometers (McMaster-Carr, Part Number: 86045K19. Durometers 40A, 50A, and 60A; two of each) that were stacked beneath the end of the replicate femur. The final setup, referred to as the hard compliance, consisted of 3 steel plates placed beneath the replicate femur.

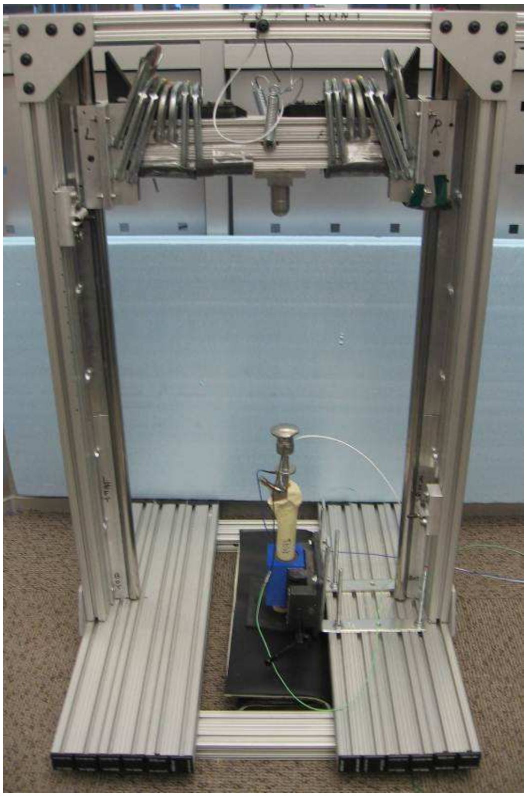

Figure 4: Drop tower assembly

Each test began with the insertion of the prosthesis into the replicate femur. The prosthesis was inserted as far as possible by hand, as per the current practice of orthopedic surgeons, and a position measurement was taken using calipers. For tests using the drop tower, the femur and guide were positioned in the vice and the drop tower impact head was centered on the force transducer. Preliminary testing was used to determine the height of the drop tower above the femur-impactor assembly necessary to apply a target peak force of 12,000 N for the Secure-Fit prosthesis when the soft compliance was used. The drop tower sliding beam was then released, and the data acquisition system recorded force and acceleration time histories for the impact. The position measurement was taken again, and the process repeated. The implant was defined to be seated after two conditions were met. First, the top of the porous metal on the prosthesis sank to within 3 mm above the cut on the replicate femur. Then, impacts continued until the prosthesis moved less than 0.5 mm for three successive impacts. If the implant continued to move more than 0.5 mm, then seating was defined to be when the porous metal on the implant sank to a depth of one mm below the cut on the replicate.

Figure 5: The surgical hammer

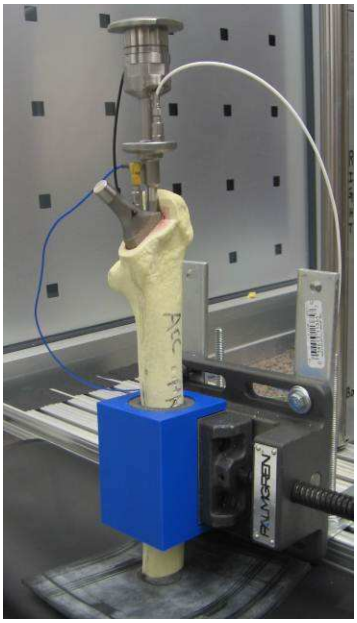

Figure 6: The guide, vice, and surgical pad that provided support for the replicate femur.

Preliminary testing indicated that the Secure-Fit prosthesis with the soft compliance required a larger drop height to become seated than the Accolade prosthesis or the Secure-Fit with different compliance configurations. If this larger drop height was used with the Accolade prosthesis or medium compliance, it resulted in the prosthesis becoming seated in unrealistically few impacts. In order to obtain more data up to seating, the pull stop on the drop tower was lowered several inches when testing these configurations. The pull stop was then raised in one inch intervals until it reached the height used for testing the Secure-Fit prosthesis with the soft compliance. From here, the impacts continued until seating occurred.

After the prosthesis was defined to be seated, the springs were removed and further impacts were applied in order to take the system to fracture. Removal of the springs was necessary because the assembly with the springs attached could not provide the larger impulse required to fracture the replicate femurs. The first impact with no springs was performed at a height lower than that used with the springs because without springs larger impulses were achievable at lower drop heights. After removing the springs, the release mechanism and sliding beam of the drop tower were raised in intervals of one inch until either the replicate femur fractured or the maximum height of the drop tower was reached.

Tests using the surgical hammer involved applying impacts that had a peak force between 20,000 to 25,000 N until the porous section of the prosthesis reached 3 mm above the cut on the replicate femur, as with the drop tower. The seating range was defined to be from this point until the prosthesis was 1 mm below the cut. Due to the variable nature of the hammer impacts, the protocol used to define seating for the drop tower would not work, as the prosthesis continued to sink while in the seating range. Therefore, only a seating range, not a specific seating hit, was noted.

After the prosthesis passed the seating range, as defined above, the impact peak force was increased to approximately 40,000 N. The test continued until one of three things occurred: the sinking of the prosthesis was minimal between successive impacts, clearance issues between the impactor and the replicate prevented further sinking, or the replicate fractured.

For tests using the surgical hammer, the replicate femurs were also gripped by hand immediately below the lesser trocanter. Doing so aided in lining up the surgical hammer with the impactor during hits. A preliminary test, in which the replicates were not gripped, determined that this additional support had no measurable effects on the resultant data.

In order to better characterize and understand the nature of the impacts from both the drop tower and surgical hammer, a high-speed camera (Photron USA, Inc, San Diego, California. Fastcam-512 PCI) was used to film several of the tests. The camera recorded the impacts at a rate of 2000 frames per second. The videos were then compared to the force and accelerometer data; this process matched peaks in the data with the events seen in the videos.

Results and Discussion

Excitation Methods

The type of excitation was the first testing variable examined. Figure 7 shows typical force and acceleration time histories for both the drop tower and hammer impaction tests of a system with the soft compliance. Impacts from both the drop tower and the surgical hammer result in several peaks in the force and acceleration data. For the drop tower, the first impact occurred over a very short time, approximately 0.2 ms; a smaller secondary peak occurred around 5 ms later, followed by a longer hump of significantly less force but lasting approximately 40 ms. High speed video footage of the impacts showed that the drop tower cross-head briefly separated from the impactor-prosthesis assembly after the initial impact, striking it again at the second peak in the force data. The drop tower cross-head and impactor then remained in contact until the force reduced back to zero after the longer hump, at approximately 45 ms after the initial impact. These three features in the force time histories for the drop tower appeared consistently in all subsequent tests. Although the surgical hammer also experienced multiple impacts, there existed much more variation in the magnitude and location of the secondary peaks. High speed video footage also showed larger variation between successive hammer impacts. In some impacts, the hammer bounced off the impactor-replicate assembly and struck it again, often several times. In others, the hammer deflected down the side of the impactor after the initial impact.

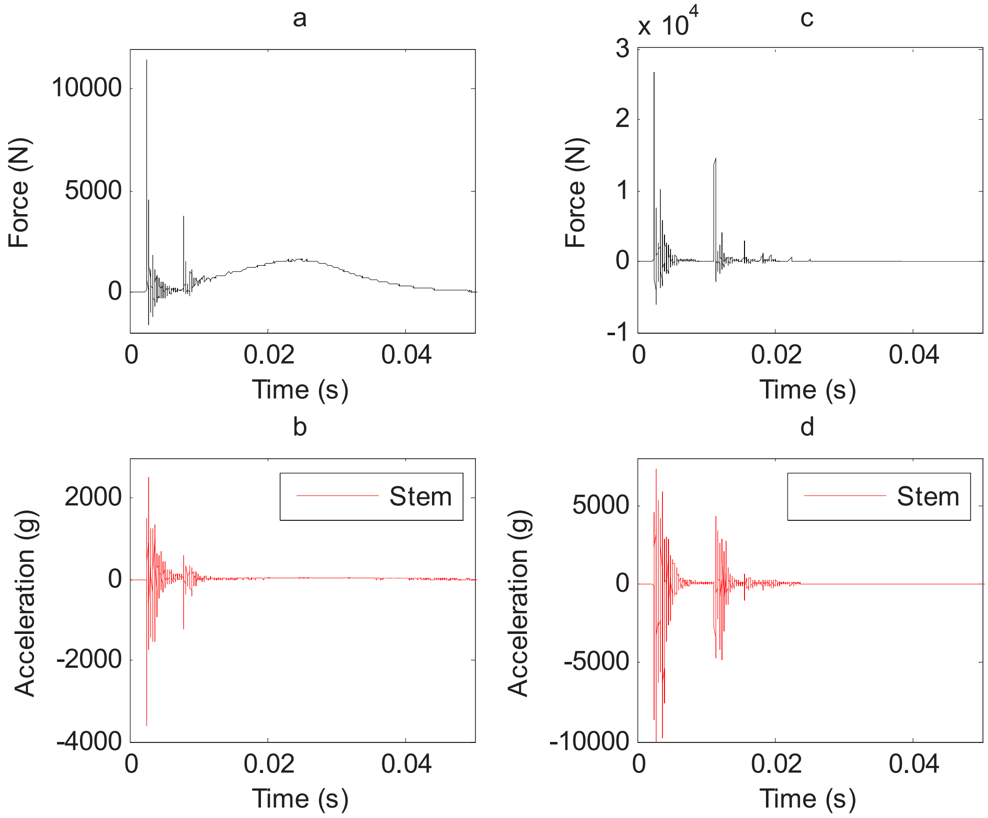

Figure 7: Typical force and acceleration time histories for (a & b) the drop tower with springs and (c & d) the surgical hammer

Despite the differences seen in the force time histories between the two methods of impaction, the initial peaks in the data were very similar. Figure 8 shows a close-up of the initial impact peak for a typical hit from both the drop tower and surgical hammer. As can be seen, even though the impact hammer had a significantly larger peak force, the total length of time over which the peak occurred is approximately the same. This was typical for all tests performed with identical compliances, regardless of the impaction method.

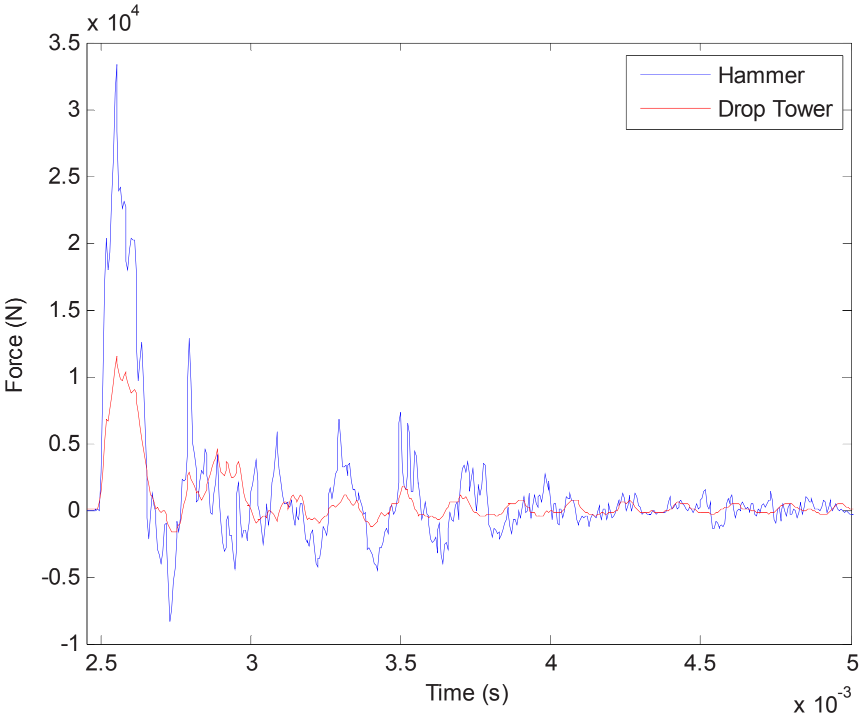

Figure 8: Close-up of the first peak in the force time histories for the hammer and drop tower.

Variation of the location of the second peak in the force time histories existed within each test between successive impacts, as seen in Figure 9. With the exception of the fourth impact, the location of the second peak shifts to the right with each successive impact, indicating that there was a larger time interval between the initial and second impacts.

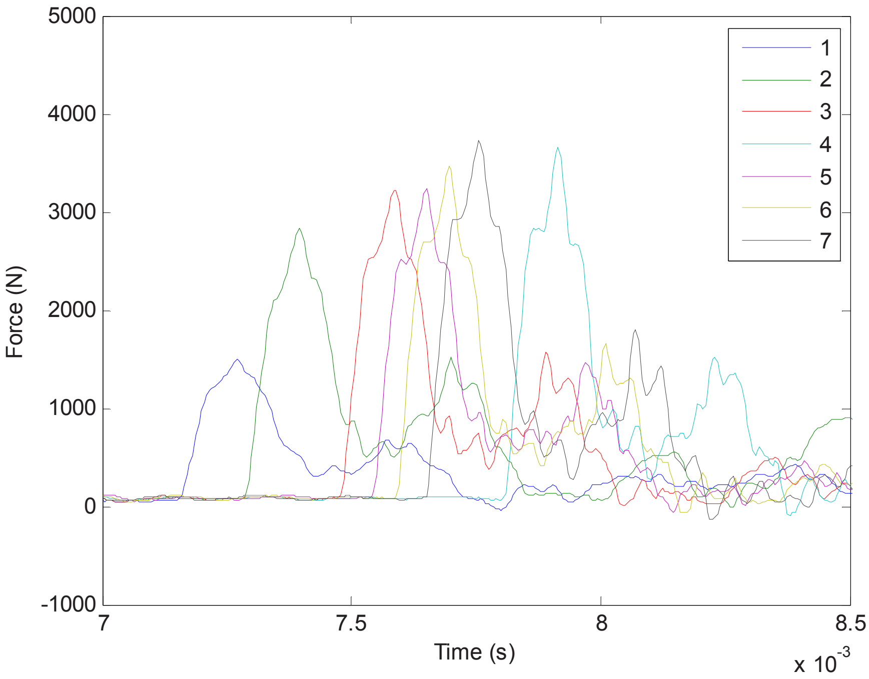

Figure 9: Close-up of the second peak in the force time histories for the first seven impacts in a single test using the drop tower

There were significant differences between the forces and impulses imparted by the various excitation methods, as shown in Table 1. Although the peak force for the surgical hammer was much higher than for any of the drop tower configurations, the total impulse imparted into the prosthesis-replicate system was much lower. Table 1 shows that increasing the mass of the drop tower (with springs) increased both the peak force and the impulse. Removing the springs also increased the peak force and the impulse. From Figure 10, it is clear that the impulse imparted by the surgical hammer varied greatly between subsequent impacts, whereas for the drop tower, the impulse remained relatively constant up to seating, increased when the springs were removed, and then increased gradually as the drop height was increased until fracture.

Table 1: Comparison of resulting peak force and impulse for various methods of impaction

Impaction method	Peak Force	Impulse
Drop tower with springs, mass = 4.22 kg	9.5 kN	11 N-s
Drop tower with springs, mass = 12.2 kg	12 kN	35 N-s
Hammer	40 kN	5 N-s
Drop tower, no springs, mass = 12.2 kg	13.5 kN	45 N-s

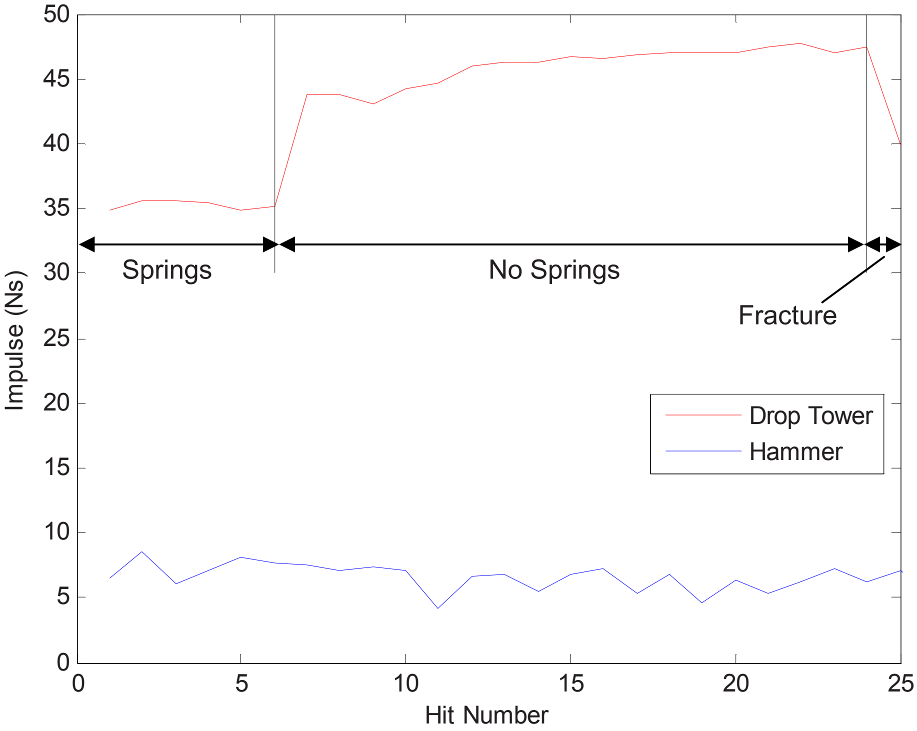

Figure 10: Comparison of the impulse imparted by the surgical hammer versus the drop tower.

For the drop tower impacts, a longer hump with a smaller peak force followed the second peak. High speed video footage showed that the prosthesis sank into the replicate femur during this hump. Analysis of the force data indicated that this hump was also the time period during which most of the impulse was imparted by the drop tower into the prosthesis-replicate system. Figure 11 shows three typical force time histories that occurred for a single test: one for the drop tower with springs, one for the drop tower with no springs, and the force time history of the impact in which the replicate femur fractured. For tests in which the femur fractured, the fractures occurred near the middle of this hump as shown in Figure 11 by the significant drop in the force. This drop is a further indication that most of the imparted impulse, as well as the primary sinking motion of the prosthesis, occured during this hump. Figure 11 also shows that removing the springs from the drop tower resulted in a larger peak magnitude of the hump, but the location and width remained approximately the same. In Figure 11 slight variations also existed in the drop height. The “no springs” configuration was performed at a drop height of one inch lower than the “with springs” configuration, while the “fracture” configuration was performed at one inch higher than that of the “with springs” configuration. As seen in the figure, though the drop height was decreased between the “with springs” and the “no springs” configurations, the peak magnitude of the hump still increased, indicating the removal of the springs had a larger effect on the hump than the drop height.

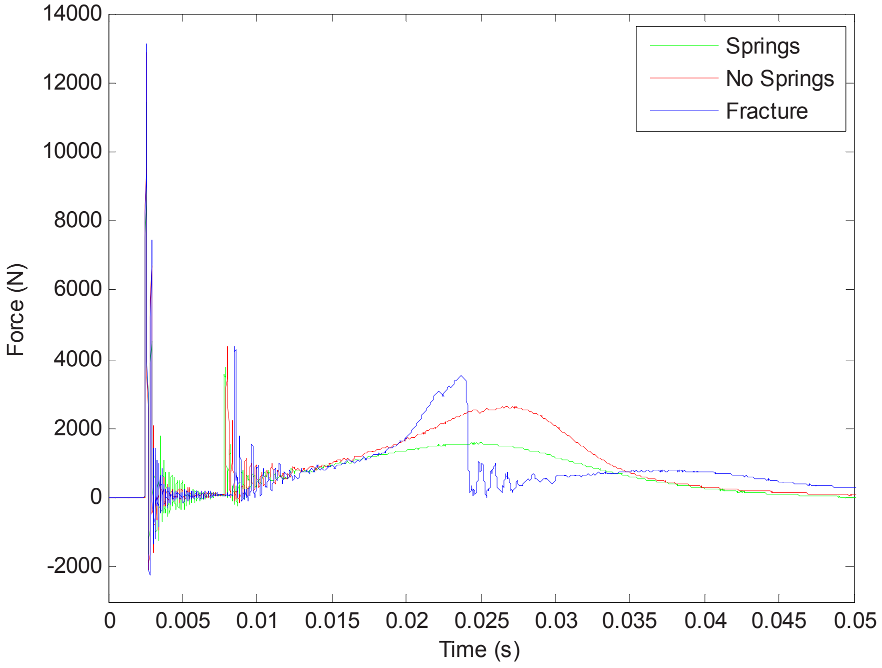

Figure 11: Close-up of the second peak and hump for the drop tower with and without springs.

The force data for the surgical hammer occasionally showed a small hump. This hump seemed to only appear for impacts in which the prosthesis sank significantly into the replicate. Figure 12 shows the force time histories for two different surgical hammer impacts: one in which the prosthesis sank and the force data showed a hump, and the other in which the prosthesis moved only marginally and the force data showed little or no hump. However, even when the hump was present in the force data from the surgical hammer, it was significantly smaller than the hump that appeared when the drop tower was used. Because most of the impulse imparted by the drop tower occurred during the hump, the significantly smaller hump from the surgical hammer also results in a much smaller impulse from this excitation method.

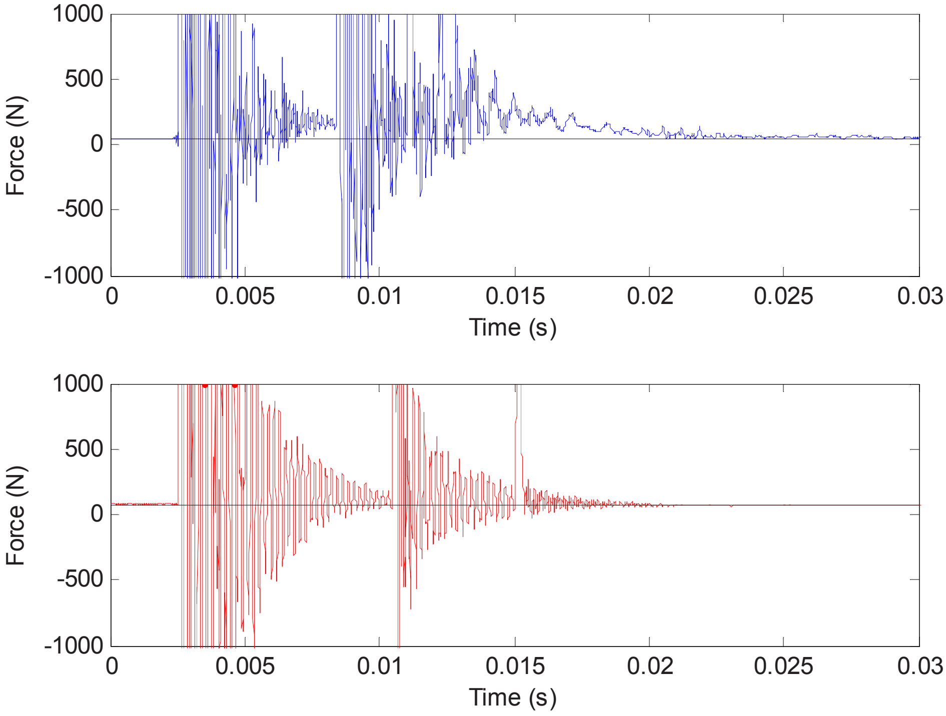

Figure 12: Close-ups of force time histories for two surgical hammer impacts with the same setup configuration. Top: The prosthesis sank. Bottom: Movement of the prosthesis was minimal.

After early tests determined that the original drop tower configuration with a sliding arm mass of 4.22 kg could not provided enough impulse to seat the Secure-Fit prostheses on the soft compliance, more mass was added to the drop tower, bringing its mass to 12.18 kg. This configuration was used for the remainder of the testing. Increasing the mass increased the peak impact force from 9500 N up to 12,000 N, as well as increasing the peak magnitude of the hump after the second force peak, as shown in Figure 13. This figure shows three typical time histories corresponding to three different sliding arm masses. The increased mass resulted in an increase of the impulse from around 11 N-s to 35 N-s. Figure 14 shows the peak force and impulse for typical time histories using the drop tower with various sliding arm masses, the drop tower with no springs, and the surgical hammer. Clearly, as the mass was increased, the magnitude of the peak force of the initial impact increased slightly, while the impulse increased significantly.

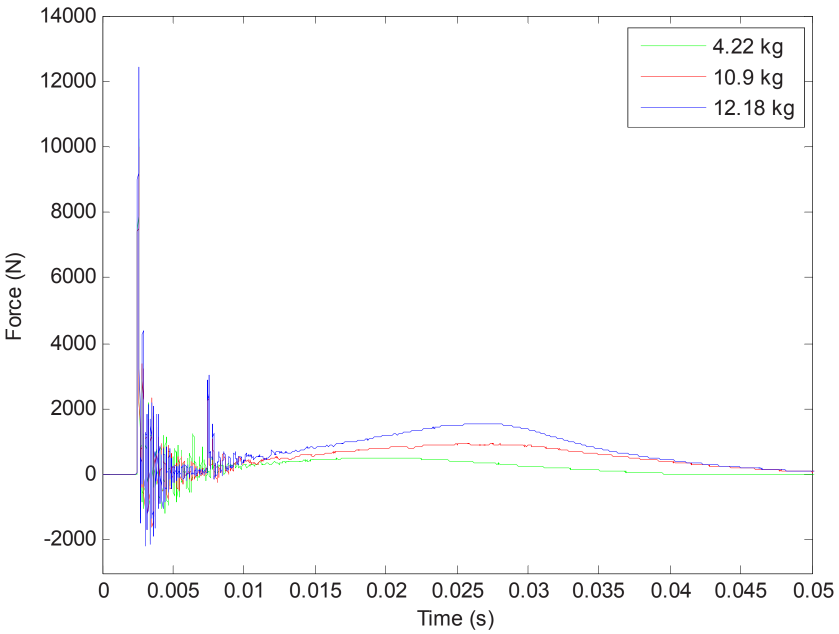

Figure 13: Force-Time history for typical impacts for three different mass configurations.

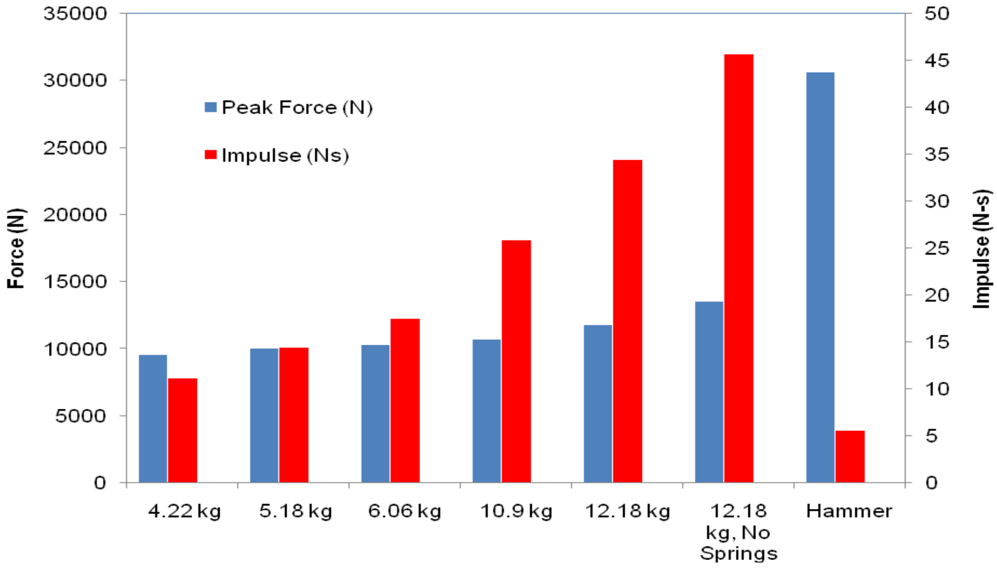

Figure 14: The change in peak force and impulse for various types of forcing

Compliance

The next variable studied was the compliance used beneath the replicate femurs. The drop tower was used with two of the three compliances examined in this study: the surgical pad (soft) and the 6 silicon pads (medium.) High speed camera footage of tests using the soft compliance indicated that the hump in the force time history that followed the second peak was the result of the interaction of the prosthesis-replicate system with the compliance. Figure 15 shows two frames from the high speed camera video corresponding to immediately before impact and at the point of maximum deformation of the compliance pads. The prosthesis-replicate system was found to deflect by several centimeters into the surgical pad. The maximum deflection occurred at the peak of the hump in the force time history. Video evidence suggested that after the initial impact, the replicate system deflected into the surgical pad faster than the drop tower head was falling, and the second impact occurred when the drop tower head caught back up with the impactor head.

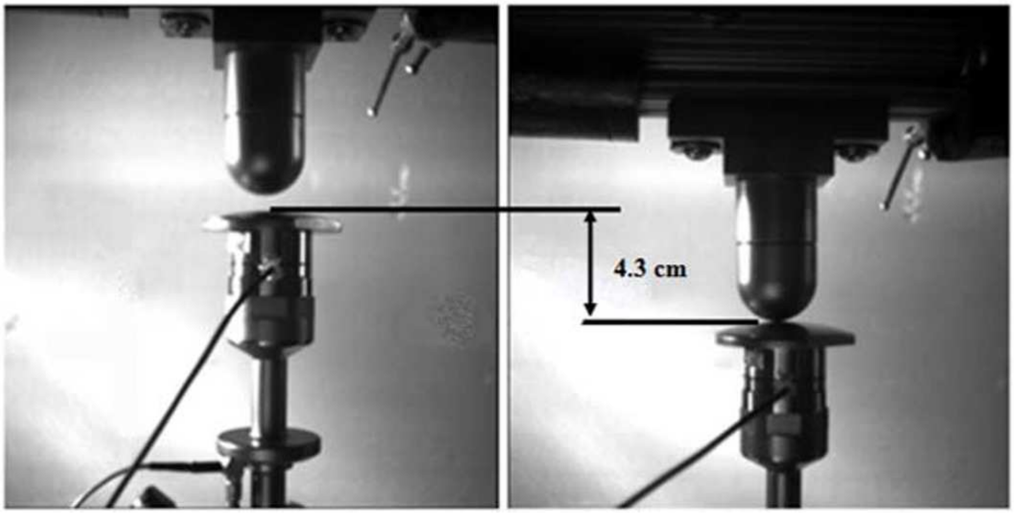

Figure 15: High speed video footage of the drop tower striking the impactor. Left: Just before impact. Right: At the bottom of the prosthes-replicate system's motion. Only 0.040 cm of the motion came from the prosthesis sinking into the replicate femur.

Typical time histories for tests performed using the drop tower with the soft and medium compliances are shown in Figure 16. The medium compliance resulted in a slight increase in the impulse from about 35 N-s to 38 N-s, and very little change in the initial impact peak force. The magnitude of the secondary impact remained unchanged, but the peak shifted to the left when using the medium compliance, indicating the impact occurred sooner after the initial impact than it did when using the soft compliance. The longer hump following the second impact peak was also shifted in time when using the stiffer compliance. The peak of the hump was increased in magnitude and occurred closer to the second impact peak, and the time interval over which the hump occurred was reduced. High speed video footage showed that the prosthesis-replicate system deflected less into the stiffer compliance.

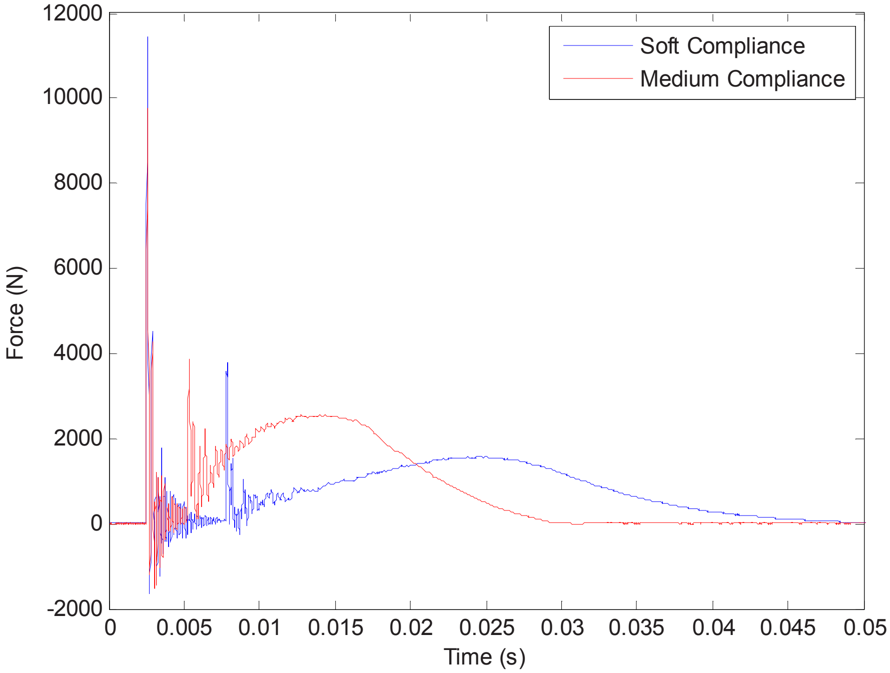

Figure 16: Effects of compliance on the force data for the drop tower

The location of the prosthesis as a function of hit number, as measured from the location where the porous section was flush with the cut on the replicate, is shown in Figure 17. This figure shows the results from two tests using different compliances. Using a stiffer compliance with the drop tower clearly had a significant effect on the seating and fracture characteristics of the prosthesis. A stiffer compliance resulted in the prosthesis sinking and fracturing much faster with fewer hits. In Figure 17 it can be seen that the system with the medium compliance became seated on the second impact, and fractured on the third. Both tests were performed with the Secure-Fit prosthesis geometry, and the drop tower was released from the same height with identical mass and spring configurations.

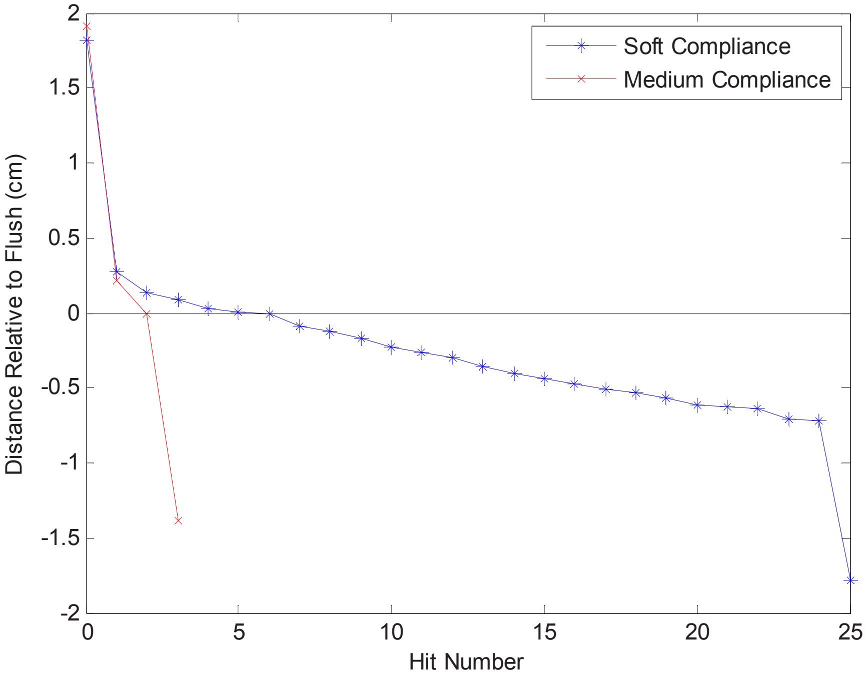

Figure 17: Effects of compliance on sinking rate of the prostheses for the drop tower

Compliance also had an effect on the force data and sinking characteristics when using the surgical hammer. Figure 18 shows typical time histories for tests using the surgical hammer with the Secure-Fit prosthesis and three different compliances. The stiffer compliances caused the secondary impact peaks to shift to the left (occurring sooner after the initial impact.) Figure 19 shows the location of the prosthesis as a function of hit number, as measured from the location where the porous section of the prosthesis was flush with the cut on the replicate femur. From this figure, it is clear that using the soft compliance resulted in a much slower sinking rate than when using the medium or hard compliances. The stiffer compliances also caused the prosthesis to sink further into the replicate femurs – over 12 mm past flush in the case of the hard compliance.

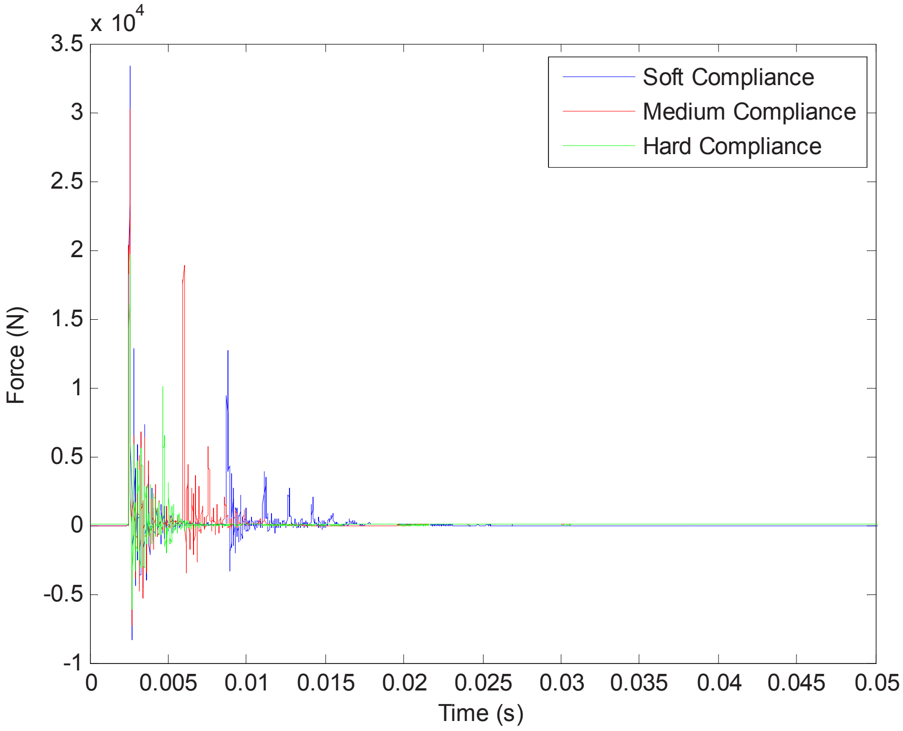

Figure 18: Effects of compliance on the surgical hammer force data.

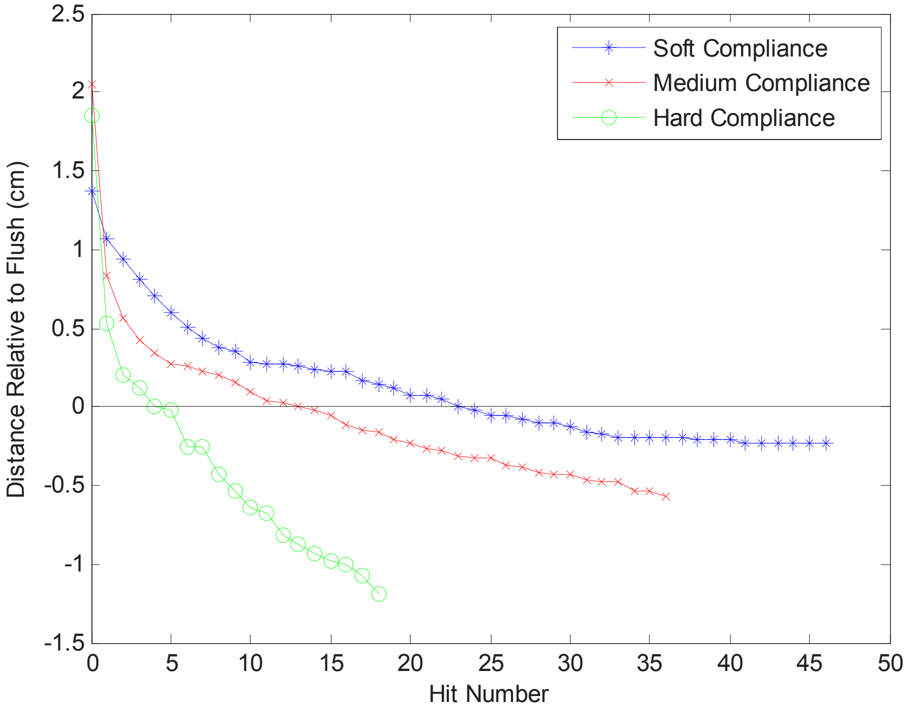

Figure 19: Effects of compliance on sinking rate of the prostheses for the surgical hammer

Impactors

There were no significant differences in the force data obtained using the monolithic and the two-piece impactors. However, a difference did exist in the instrument mounted accelerometer responses between the two impactor designs. Figure 20 shows typical accelerometer time histories for the stem and instrument accelerometers for the monolithic and two-piece impactor designs when using the drop tower with the soft compliance. For the monolithic impactor, both the stem and instrument accelerometers gave responses that appeared fairly similar to each other, but for the two-piece impactor, significant differences existed between the two accelerometer responses. For the two-piece design, the instrument accelerometer typically had a smaller peak acceleration and more high frequency content. Figure 21 shows the frequency response functions (FRFs) for the three hits corresponding to seating using both the stem and instrument accelerometers for both impactor designs. The larger high frequency components for the two-piece design are clearly evident in this figure.

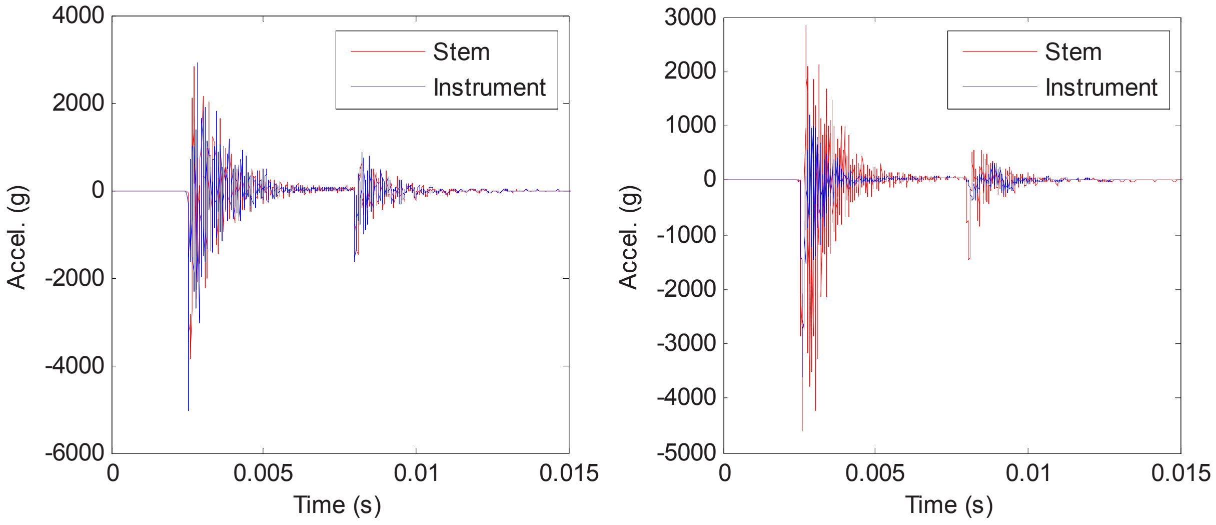

Figure 20: Typical accelerometer response for (Left) the monolithic impactor and (Right) the two-piece.

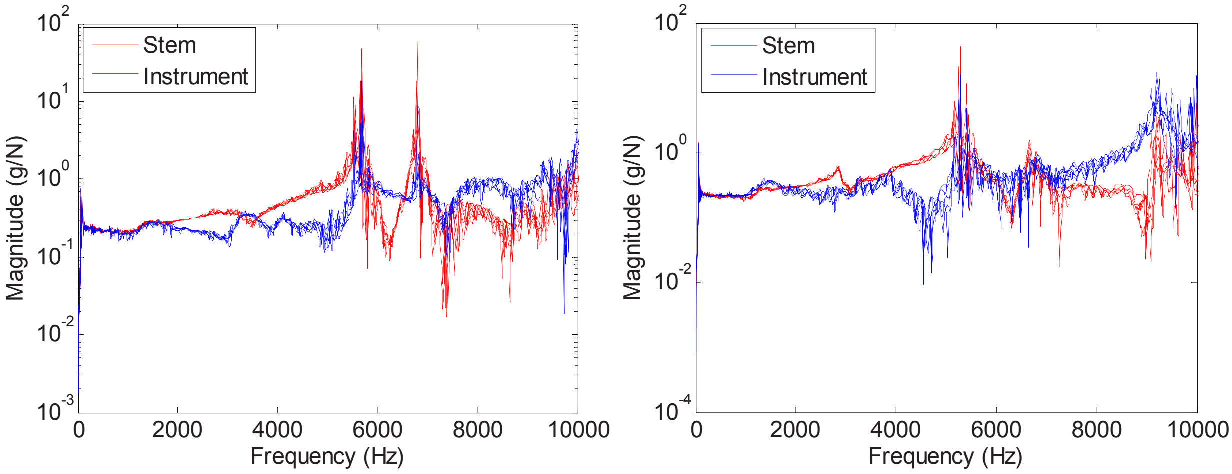

Figure 21: FRF's for both accelerometers on (Left) the monolithic impactor and (Right) the two-piece.

The difference in the response between the stem and instrument accelerometers is further quantified in Table 2. In this table, the average maximum acceleration is the average of the peak of the accelerometer response for the first ten impacts of each test. All of the tests were performed with the drop tower, and the average peak magnitude of the force was similar between tests with the same mass configuration of the drop tower. As shown in the table, for the monolithic impactors, there was very little difference in the magnitude of the average maximum acceleration for the instrument and stem accelerometers. However, significant differences existed between the average maximum accelerations recorded by the two accelerometers on the two-piece impactor. The peak accelerations measured by the instrument accelerometer were over 25% smaller than those measured by the stem accelerometers. This difference in accelerometer responses was most likely due to the presence of the additional mechanical connection in the impactor-prosthesis system for the two-piece impactor.

Table 2: Comparison of the monolithic and two-piece impactors

Mass of Drop Tower	Impactor	Ave Peak Force (N)	Average maximum acceleration for instrument ± one standard deviation (g)	Average maximum acceleration for stem ± one standard deviation (g)	⁄ difference
4.22 kg	Monolithic	5730	2500 ± 110	2470 ± 160	1.2
	Monolithic	5920	2590 ± 140	2590 ± 120	0
	Two-Piece	6000	1980 ± 80	2470 ± 90	−24.7
12.18 kg	Monolithic	11,300	4630 ± 170	4200 ± 160	9.3
	Two-Piece	10,300	3270 ± 90	4280 ± 150	−30.9

The two-piece impactor used in this study had several problems as compared to the monolithic. The screw on the two-piece bolt was initially tightened before each test. During early testing, however, the force of the impacts caused the accelerometer mount to slip, resulting in inaccurate accelerometer measurements. This problem was solved by drilling a hole into the body of the impactor into which the screw could be tightened. During subsequent testing, though, it was found that the screw became loose between hits, requiring it to be retightened with a wrench after every impact. This mechanical connection between the accelerometer mount and the rest of the impactor had an effect on the instrument acceleration output, making the data much noisier and therefore potentially less reliable for use in evaluating prosthesis seating.

Prosthesis Geometries

Differences in sinking and fracture characteristics existed between the Accolade and Secure-Fit prosthesis geometries. Figure 22 shows the location of the prosthesis, as measured from the point where the prosthesis was flush with the cut on the replicate, as a function of hit number for two tests using the Accolade geometry and three tests using the Secure-Fit. As seen in Figure 22, the first several hits caused the implants to move significantly, regardless of the prosthesis used. After that, the Secure-Fit prosthesis became seated as defined by the protocol, while the Accolade continued to sink. After seating, the Accolade prostheses sank further into the replicates at a much faster rate than the Secure-Fit prostheses. Both types of prostheses continued sinking past flush at least 5 mm before the replicate fractured (if it did fracture.) In addition, the Accolade prostheses were significantly less likely to fracture the replicate than the Secure-Fits. Of the twelve Accolade prostheses tested, four resulted in fracture, while of the thirteen Secure-Fits tested, nine resulted in fracture, as shown in Table 3, which summarizes the fractures as a function of compliance, impactor, and method of impact.

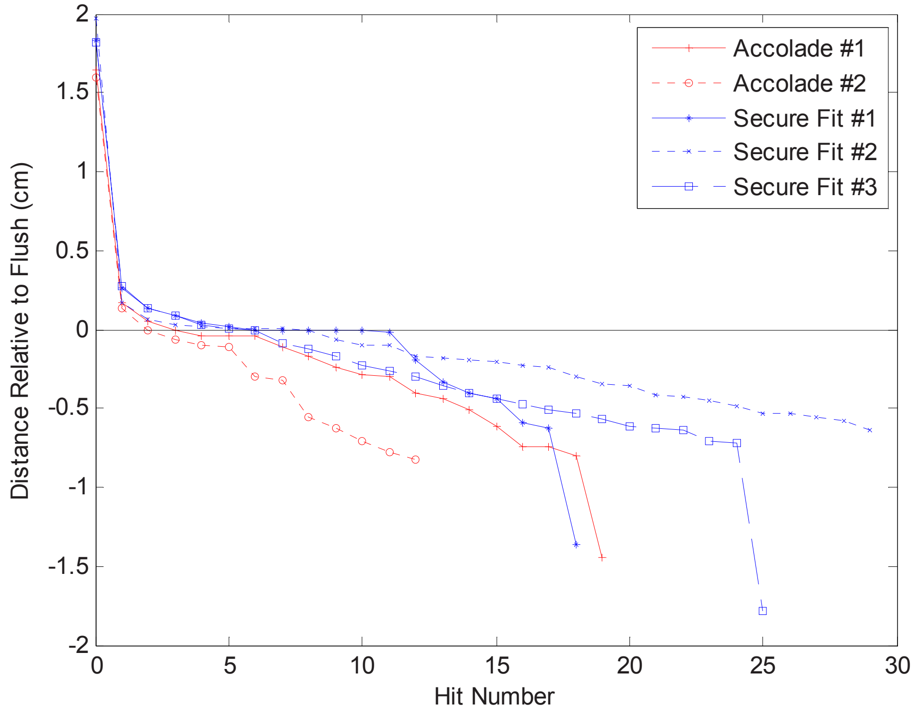

Figure 22: Comparison of the sinking characteristics of both Accolade and Secure-FIt prosthesis geometries of five typical tests using the soft compliance.

Table 3: Summary of fractures by setup configuration

Test configuration		Impaction Method	Number Fractured	Percentage
Soft Compliance	Secure-Fit	Drop Tower	4/5	80⁄
		Hammer	0/3	0⁄
	Accolade	Drop Tower	1/2	50⁄
		Hammer	2/5	40⁄
Medium Compliance	Secure-Fit	Drop Tower	2/2	100⁄
		Hammer	2/2	100⁄
	Accolade	Drop Tower	0/3	0⁄
		Hammer	0/1	0⁄
Hard Compliance	Secure-Fit	Drop Tower	NA	NA
		Hammer	1/1	100⁄
	Accolade	Drop Tower	NA	NA
		Hammer	1/1	100⁄

For all of the tests, the prosthesis sank into the replicate significantly past the point where human bones would typically fracture. Often, the test had to be stopped because the prosthesis sank to the point where clearance issues between the impactor and the replicate prevented further motion of the prosthesis. There also existed significant variability in the replicates themselves, that is, tests with identical setups had very different results; some replicates would fracture, while others would not. Furthermore, when the replicate femurs did fracture, these fractures were not similar to the fractures encountered during orthopedic surgery. Most surgical fractures occur either proximally on the intertrochanteric ridge or distally, near the tip of the prosthesis [5]. In four of the tests performed in this study, however, the femur fractured on the greater trocanter, possibly due to interference by the impactor. Other replicates did experience fractures on the femoral neck. Though these fractures occured in the same location as those common in orthopedic surgery, the fractures experienced by the replicates were much more catastrophic and resulted in significant displacement of the femur, as shown in Figure 23.

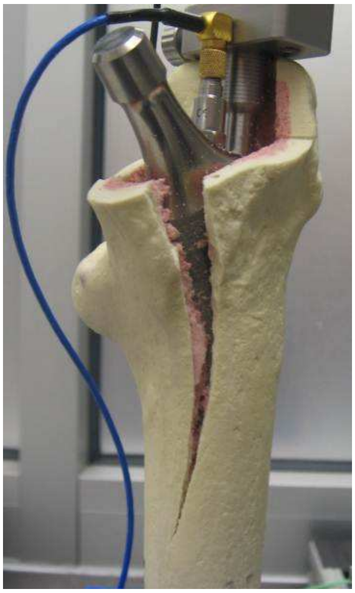

Figure 23: Catastrophic fracture of a replicate femur used in this study

Conclusion

This study found that a significant difference exists between the two methods of impacting the prosthesis. Testing using the drop tower was repeatable, as the drop tower provided a very consistent force input between successive impacts. This repeatability made the drop tower useful when examining other characteristics of the system, such as characterizing the hump after the second peak in the force data. However, the input force and impulse from the drop tower are not comparable to those from the surgical hammer, and are therefore not particularly realistic. Although the surgical hammer was more realistic, tests performed with it were much less repeatable, as it is nearly impossible to maintain a consistent force and impulse between successive hammer impacts. Despite these inconsistencies, it is recommended that future fracture studies utilize the surgical hammer. Should a drop tower be used in future testing, it is important that the differences between it and the hammer be understood. A redesign of the drop tower may be necessary to make testing with it more realistic.

This study also showed that compliance had a significant effect on the sinking and fracture characteristics of the prosthesis into the replicate femur. Harder compliance caused the prosthesis to sink into the replicate at a much faster rate than with softer compliances. Further research is needed in order to understand and model the compliance a real bone would have during surgery.

The instrument accelerometer mounted on the two-piece impactor recorded smaller peak accelerations than the stem mounted accelerometer, in contrast to both accelerometers for the monolithic impactor design. The data for the two-piece instrument accelerometer also appeared to have more high frequency components. Due to these problems, it is recommended that either only a monolithic impactor be used for future testing or that the two-piece impactor be redesigned to ensure a more solid connection between the accelerometer mount and the impactor body.

The foam cortical shell sawbones used as replicate femurs in this study were not good for seating and fracture studies. The sawbones were more elastic than real bones, and as a result, the prosthesis sank very far into the replicate without fracturing, which is not reasonable to expect with actual femurs. When the replicates did fracture, these fractures were often significantly different than those encountered during orthopedic surgery.

This study focused on the development of a test setup and protocol that could be used for future testing, but did not evaluate any metrics for determining seating. These metrics should be examined in future testing, both of replicate femurs as well as in a cadaveric environment.

References

[1] Arthritis Foundation, website: http://www.arthritis.org, 2010.

[2] American Academy of Orthopedic Surgeons, “The Burden of Musculoskeletal Diseases in the United States,” website: http://www.aaos.org/, 2008.

[3] Jasty, M., Henshaw, R., O’Conner, D., and Harris, D. “High Assembly Strains and Femoral Fracture Produced During Insertion of Uncemented Femoral Components, A Cadaver Study,” *The Journal of* Arthroplasty, 8(50) pp. 479-487, 1992.

[4] Falez, F., Santori, N., and Panegrossi, G. “Intraoperative Type 1 Proximal Femoral Fractures: Influence on the Stability of Hydroxyapatite-Coated Femoral Components,” *Journal of Antroplasty*, 13(6) pp 653-659, 1998.

[5] Schwartz, J.T., Mayer, J.G., and Engh, C.A., “Femoral Fracture During Non-Cemented Total Hip Arthroplasty,” *The Journal of Bone and Joint Surgery*, 71 pp 1135-1142, 1989.

[6] Berry, D. J., Berger, R. A., Callaghan, J. J., Lawrence, D. D., Duwelius, P. J., Hartzband, M. A., Lieberman, J. R., and Mears, D. C. “Symposium: Minimally Invasive Total Hip Arthroplasty. Development, Early Results, and a Critical Analysis,” *Journal of Bone and Joint Surgery* (Am.) 85(11) pp. 2235-2246, 2003.

[7] Berger, R. A., Jacobs, J. J., Meneghini, R. M., Della Valle, C., Paprosky, W., and Rosenberg, A. G. “Rapid Rehabilitation and Recovery with Minimally Invasive Total Hip Arthroplasty,” *Clinical Orthopaedics and Related Research*. 429 pp. 239-247. 2004.

[8] Berger, R. A. “Total Hip Arthroplasty Using the Minimally Invasive Two-Incision Approach.” *Clinical Orthopaedics and Related Research*. 417 pp. 232-241. 2003.

[9] Giardini, S., Laney, D., Rutherford, A., and Farrar, C. “Monitoring Femoral Component Insertion in Cementless Total Hip Arthroplasty,” *Proceedings of the 23rd IMAC Conference on Structural Dynamics*, Orlando, FL, 2005.

[10] Abou-Trabi, D., Guthrie, M., Moore, H., Cornwell, P., Rosenberg, A. G., and Meneghini, R. M. “Monitoring Femoral Component Insertion During Uncemented Total Hip Arthroplasty,” *Proceedings of the 24th IMAC Conference on Structural Dynamics,* St. Louis, MO, January, 2006.

[11] Crisman, A., Yoder, N. ,McCuskey, M., Meneghini, M., and Cornwell, P. “Femoral Component Insertion Monitoring Using Human Cadaveric Specimens,” *Proceedings of the 25th IMAC Conference on Structural Dynamics*, Orlando, FL, February, 2007.

Performance Comparison of Fiber Optic Tips in Interferometric Displacement Measurements

Rick Grahn [a], Hussain Karimi [b], Kyle Wilson [c], Erik Moro [d], Anthony Puckett [d]

[a] University of New Mexico, 4000 University Dr., Albuquerque, NM 87131

[b] University of California San Diego, 9500 Gilman Dr., La Jolla, CA 92093

[c] Rose-Hulman Institute of Technology, 5500 Wabash Ave., Terra Heute, IN 47803

[d] Los Alamos National Laboratory, Los Alamos, NM 87545

ABSTRACT
Fiber optic displacement sensors have many potential advantages over traditional displacement measurement techniques, including small size, immunity to electromagnetic interference, electrical isolation, and high resolution. In this report, we focus on an interferometric fiber optic sensor, where the gap between the fiber tip and the device under test forms a Fabry-Perot resonant cavity. An optical interrogator measures the reflected intensity at wavelengths ranging from 1510 to 1590 nm. The spacing between resonant frequencies allows us to determine the distance from the tip to the device under test. We consider ferrule connector angled physical contact (FC/APC), ferrule connector ultra physical contact (FC/UPC) and unpolished cleaved tips and compare their influence on sensor performance. A plane wave propagation model is proposed for predicting tip effects. Comparisons are made on the basis of sensor measurement range, resolution, and sensitivity to changes in test conditions. In this paper, we discuss the experimental setup, detail our analysis, and present test results with recommendations for the applications of each tip.

Motivation

Fiber optic displacement sensors present many advantages over common electro-mechanical sensing devices due to their light-weight characteristics, immunity towards electromagnetic interference, non-spark emitting application, robustness, and potential for extremely high resolution [1], [2]. These traits make them well suited for applications in the structural health monitoring field. There are three types of fiber optic sensing techniques that are implemented in different industries for various applications: intensity-based, frequency-based, and phase-based approaches. Phase-based approaches take advantage of the wave properties of light and are employed here to take displacement measurements as an extrinsic Fabry-Perot interferometer.

Background

Optical fibers are similar to electrical wires in that they serve as media for transportation. Electrical wires carry particulate electrons flowing through a metal. Optical fibers, however, carry photons which must be treated as propagating waves. Waves propagating through a waveguide behave differently than flowing particles. Figure 1 displays a simplified diagram showing two major components: the cladding and the core. The core is the center portion which actually transmits the photons. The cladding is present to ensure total internal reflection which confines the light to the core. Total internal reflection refers to the phenomena of light reflection, rather than refraction (bending), through

T. Proulx (ed.), *Sensors, Instrumentation and Special Topics, Volume 6*, Conference Proceedings of the Society for Experimental Mechanics Series 9, DOI 10.1007/978-1-4419-9507-0_22, © The Society for Experimental Mechanics, Inc. 2011

a medium. The speed of light varies through different materials which results in refraction whenever passing from one medium to another. However, when the angle of approach reaches a maximum, known as the critical angle, the incident light waves completely reflect symmetric about the normal to the surface. The critical angle can be calculated as

$$\theta_c = \sin^{-1}\left(\frac{n_{cl}}{n_{co}}\right) \tag{1}$$

where n_{cl} and n_{co} are the indices of refraction for the cladding and core, respectively.

Furthermore, the waves can be made up of different transverse modes. That is to say that light of a particular wavelength can propagate through the fiber at more than one angle of incidence. However, by limiting the diameter of the core, it is possible to create single-mode fibers. These fibers allow only a single mode of light to traverse the core, which aids significantly in the analysis phase of measurements. This project is solely concerned with single-mode fibers.

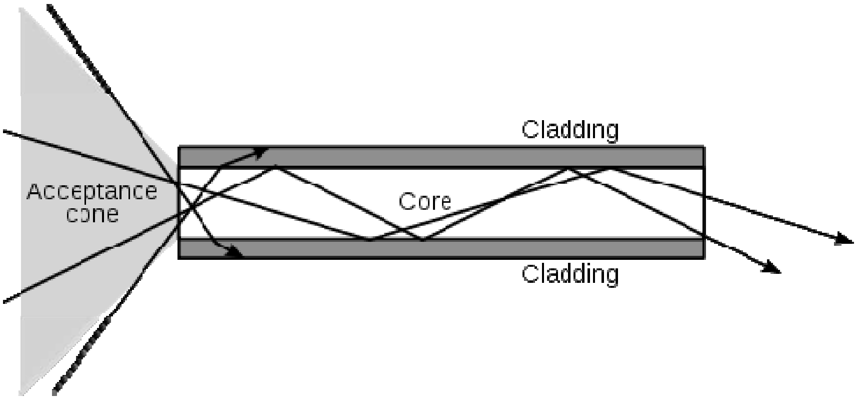

Figure 1. A simple diagram of total internal reflection within an optical fiber is shown [3].

Fabry-Perot interferometers (FPI's) can be used to measure the displacement between the tip of a fiber and the target surface. An FPI can be simply set up by placing an optical fiber aimed towards a flat surface of interest. Light waves exit the fiber tip and traverse the gap between the fiber and the target. A portion of the light is reflected off the target and re-enters the fiber. Remembering that light can be treated as a wave, the phenomena of interference must be considered. Light of wavelengths which can fit evenly within the cavity will resonate and interfere constructively, whereas those that do not fit will interfere destructively (Figure 2) [4]. Sifting through the geometry, one can find that those resonance wavelengths can be described by

$$2L = n\lambda \tag{2}$$

where L is the cavity length, n is a positive integer, and λ is the resonant wavelength, related to the frequency by $\lambda = c/f$ where c is the speed of light. This is allows us to write the resonant frequencies as

$$f_n = n\frac{c}{2L}. \tag{3}$$

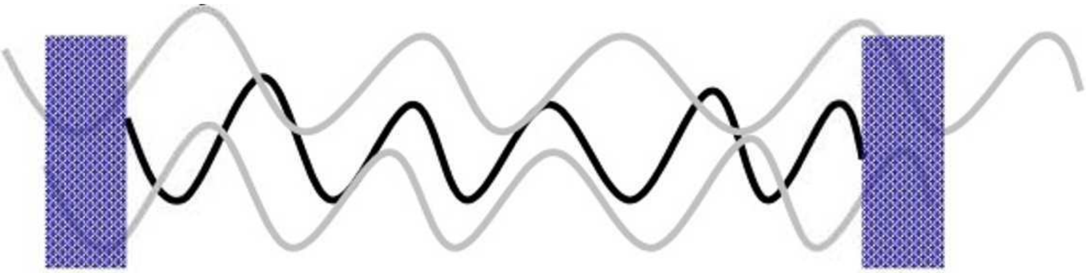

Figure 2. Wave Propagation in a resonant cavity. The black wave resonates whereas the grey waves do not [5].

By sweeping through a range of frequencies at a given gap size and analyzing the intensity of the reflected light waves as a function of frequency, it is possible to determine the frequencies of light which resonate within the cavity. The frequencies that resonate will be measured at much greater powers than those which do not, resulting in peaks. Similarly, the anti-resonance frequencies occur at intervals $1/2n+1/4$ and can be seen as troughs. A typical graph of the power-frequency curve extracted from the hardware is shown in Figure 3. Subsequently a fast Fourier transform reveals the frequency at which resonance occurs. A Fourier transform of the data in Figure 3 is shown in Figure 4. It is well understood that performing a Fourier analysis takes the data from the time domain into the frequency domain. However, the raw data in this case is power as a function of frequency. The Fourier transform then reveals the *frequency of frequencies*. The analysis yields those frequencies of variation in intensity which is most prominent; in other words, those frequencies which are the most frequent. We are looking for the frequency of greatest magnitude, known as the free spectral range (FSR), Δf. Comparing this to the wavelengths projected through the fiber, one can then determine the exact length of the resonance cavity, which is simply the distance between the fiber optic and the target

$$L = \frac{c}{2\Delta f}\,. \tag{4}$$

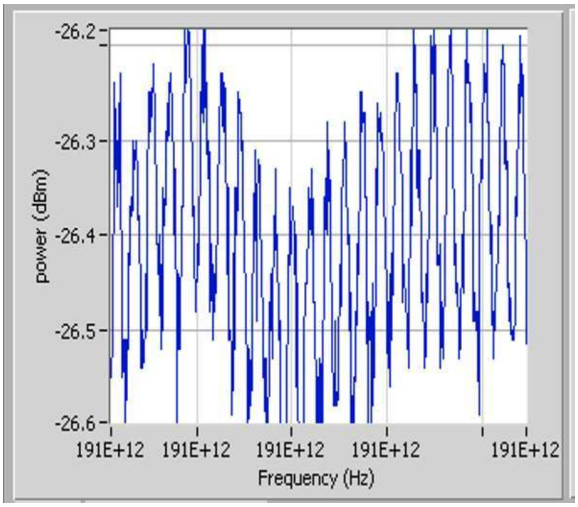

Figure 3. Measured power is shown as a function of optical frequency.

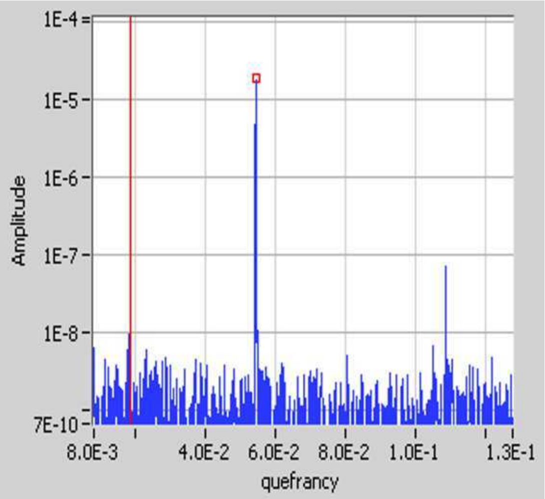

Figure 4. A Fourier transform of the data from Figure 3 is displayed.

Our purpose is to examine the tips of optical fibers, particularly with regard to their ability to take displacement measurements. FC/UPC and FC/APC tips are commercially available and are therefore investigated here, along with cleaved tips which are easily replaced in the field (Figure 5). The FC/UPC tip is polished at a zero degree angle from the vertical, while the FC/APC tip is polished at an eight degree angle. When light is incident upon the fiber tip, some light is transmitted out of the fiber, while a percentage of light is reflected back into the fiber. The back reflected light contributes to the overall noise of the signal because it is creating a signal that we are not interested in measuring. The FC/APC is designed so that the back-reflected light will not reflect straight back, but reflect back at an angle steeper than the critical angle, so that the light is lost into the cladding. However, the angle will also reduce the amount of signal reentering the fiber tip [6]. This study examines the results of the competing effects.

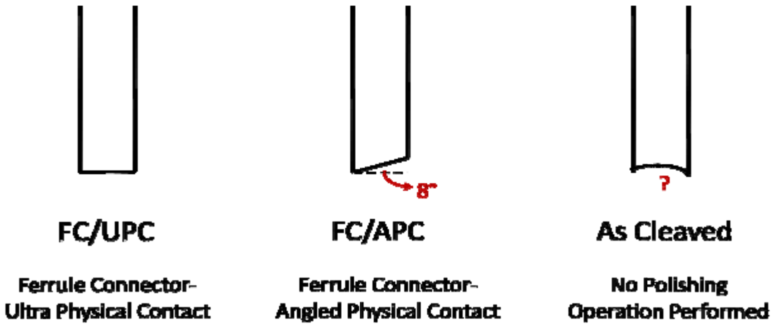

Figure 5. A geometrical comparison of fiber tips is shown.

Experimental Setup

The physical setup is shown in Figure 6. The sm125-500 Optical Sensing Interrogator by Micron Optics Inc is the source of the infrared laser as well as the power reader of incoming waves. It emits a laser in the IR spectrum between wavelengths of 1510-1590 nm. The hardware sweeps through this frequency range at a rate of 2 Hz. The laser propagates through a SMF-28e fiber [7] to an adjustable stage manually positioned with a micrometer. The stage displaces away from the target surface made of aluminum with 95% reflectivity in our range of the IR. The index of refraction was estimated using a thorough analysis of this parameter as a function of atmospheric factors [8]. The power readings from the interrogator are sent via Ethernet to a computer running a LabVIEW VI to handle the data acquisition algorithm. At each cavity length, the power-wavelength data is stored and an FFT is used to determine the FSR which in turn yields the inferred cavity length by (4).

The front panel of the interrogator has four FC/APC fiber jacks. To test the sensor performance of the angled fiber tips, a single cable with double ended angled tips was attached directly from the laser source to the stage. Testing the FC/UPC fibers, however, required intermediate connections since only angled tips can join to the sm125. The interconverting patch bundles were obtained from Timbercon.

The metal plates which make up the measurement apparatus are made of polished aluminum. One is firmly attached to the breadboard table while the other is attached to the movable stage. Care is taken to ensure that the plates are parallel. The moving plate has an array of ferrule connectors on it to accept either flat or angled fiber connectors. Finally, a micrometer is attached to the stage so that it can be manually moved with an accuracy of 1 μm.

Tests on distance range are performed by incrementally moving the stage farther away from the target plate until the free spectral range is no longer discernable. Stage movement was measured with the micrometer, allowing quantitative comparisons of the displacements as measured by both the sensor and the micrometer.

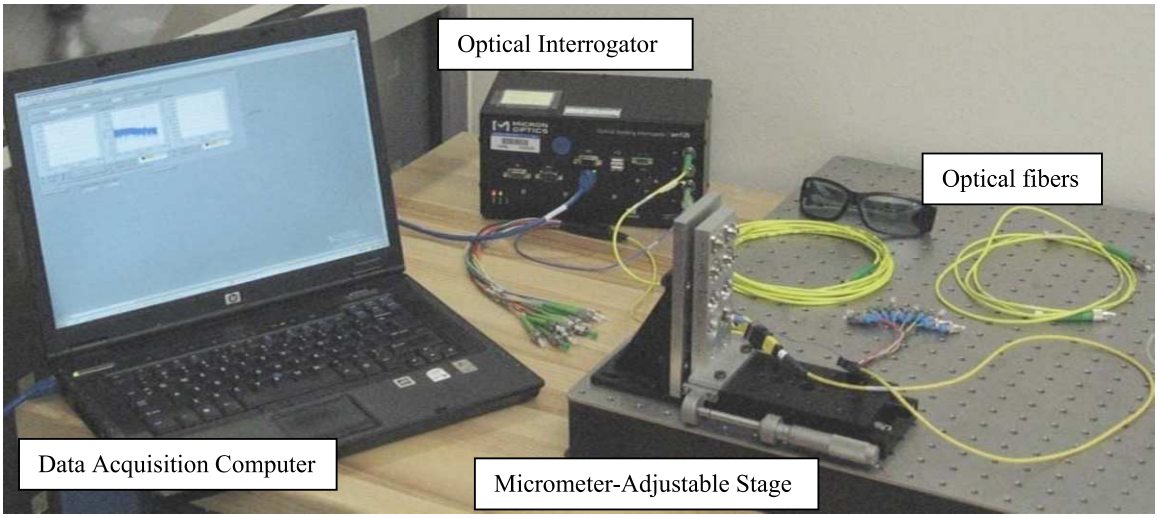

Figure 6. This is the experimental setup that was used.

To test cleaved tips, a fiber with one FC/APC end is stripped down to the cladding/core region. A high-precision Fujikura cleaver then cuts through the two remaining layers of the fiber for a near flat finish. Since the stage as configured above only accepts FC jacks, the cleaved tips were clamped down as shown in Figure 7.

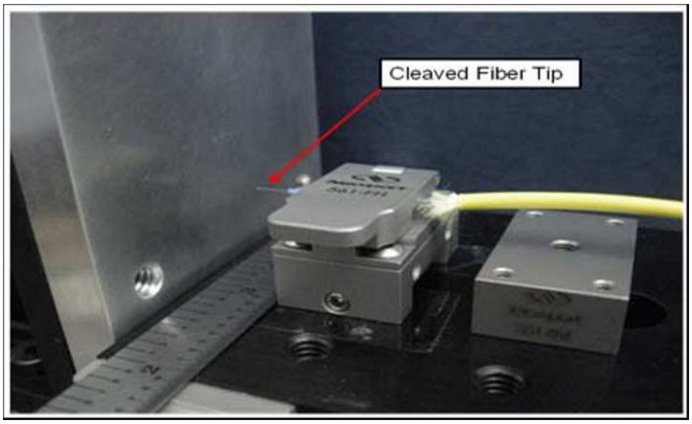

Figure 7. The mounting the mechanism used for the cleaved tip is shown here.

Signal and Noise Floor

The first data set was collected with all three tips (flat, angled, and cleaved) at a 3mm initial displacement incremented by 50 µm until range was lost. The initial displacement was due to the offset between the embedded fiber on the stage and the target surface.

Since the information content in the signal is encoded in the oscillations rather than in the raw signal amplitude, we are interested in the amplitude of oscillation. To eliminate effects of power variability with frequency, we subtract off the baseline so that the oscillations are mostly zero-centered. In order to do so, a fourth-order polynomial was fit to the raw data to quantify the baseline of the power-frequency data to account for the power variation with frequency. Then the baseline is subtracted from the raw data and the RMS amplitude is calculated according to

$$\sqrt{\frac{\sum_{i=1}^{N}\left(P_i - P(f)\right)^2}{N}} \tag{5}$$

where P_i is the measured power at a given frequency, $P(f)$ is the curve fit, and N is the total number of data points. This RMS is taken as the signal strength metric and computed for every increment in cavity length. Typical graphs of the process are shown in Figure 8.

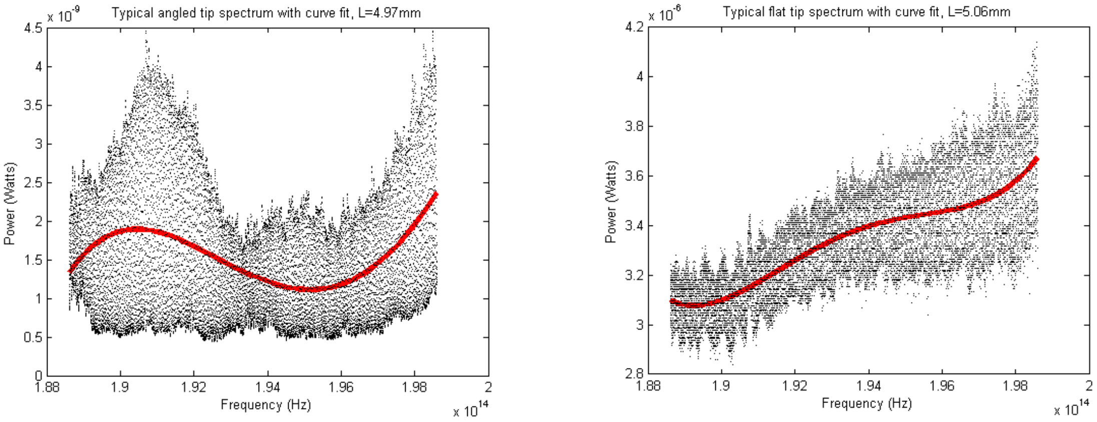

(a) (b)

Figure 8. Raw data is shown, for both the angled (a) and flat (b) tips, with the corresponding polynomial fits (in red).

The noise spectra are obtained using a mirror to reflect light away from the fiber tip, preventing any signal from being coupled back into the fiber. The resulting spectra are considered the noise; measurements which do not contribute to the actual signal. In the same way as for the signal, the RMS of the noise is calculated which allows us to compare the signal to the noise.

The RMS amplitude decreases against cavity length as expected since the cone of light emitted from the fiber grows. As the signal RMS approaches the noise RMS, the accuracy of the measurement declines until the signal is completely immersed in noise, at which point the range has been exceeded. Here, the measurement loses several orders of magnitude in accuracy and the free spectral range of the cavity is no longer the most prominent frequency component observable.

Figure 9 illustrates how the RMS power varies with cavity distance. The red line in each plot represents the noise floor. For statistical significance, three noise-floor measurements were taken during each test as described above.

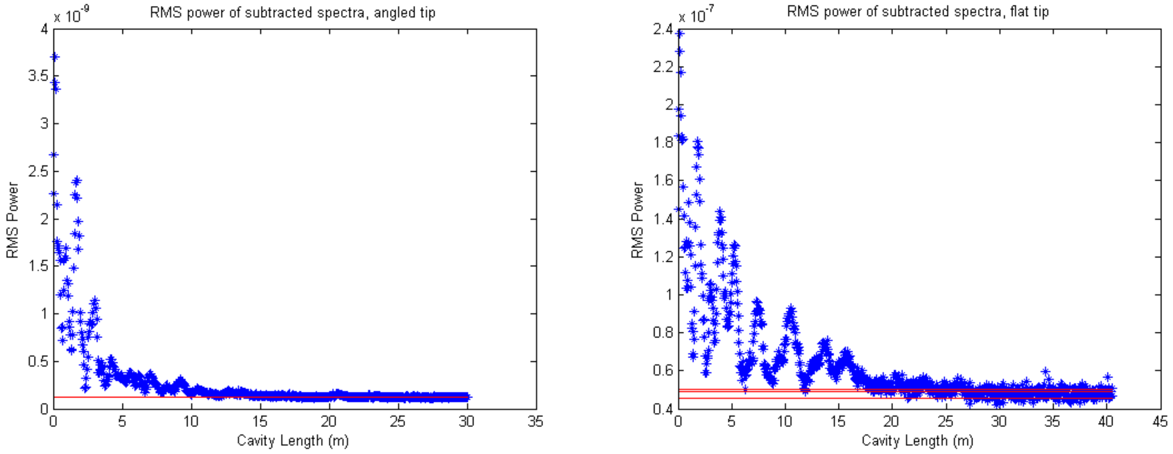

(a) (b)

Figure 9. RMS is calculated as a function of cavity length for the angled (a) and flat (b) tips. The red line is the noise floor.

Range and Accuracy

To resolve the range of the different fiber tips, we plot the calculated gap length against the micrometer reading. Knowing the initial offset and expecting it to remain constant, we observe a horizontal line at the offset for accurate measurements. The range is determined by the distance at which the measurement strays from the constant offset. From Figure 10 (a), we ascertain the range to be 23 mm as the measurement drops off from the expected value. Figure 10 (b) shows a zoomed in plot of (a) to how the accuracy varied within range.

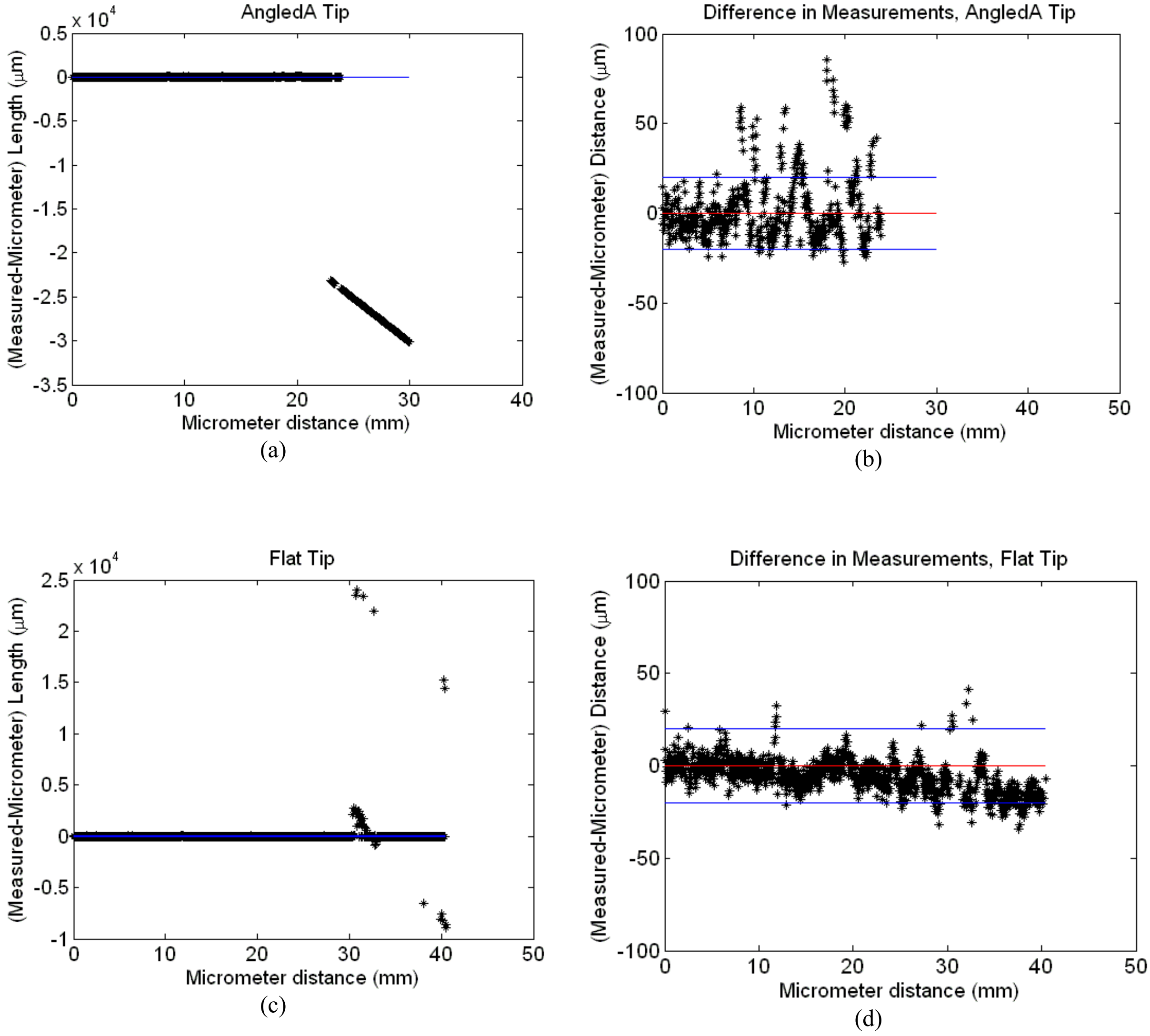

(a) (b)

(c) (d)

Figure 10. The difference between the calculated distance and the micrometer reading is shown for angled (a) and flat (c) tips. Detailed views of (a) and (c) are shown in (b) and (d) respectively.

The accuracy is determined by observing the maximum uncertainty in the measurement. To do so, we calculate the maximum and the minimum difference between the expected value at each cavity length increment and the initial offset. This is a running curve, accounting for all the previous length measurements. The accuracy is plotted up to the respective ranges of the fiber tips in Figure 11. As expected, the accuracy decreases as the stage is displaced further out from the target surface. The angled tips performed relatively poorly in both range and accuracy, whereas the flat tip yielded the most accurate results. The cleaved tips performed surprisingly well in range and slightly worse in accuracy. A closer visual inspection of the cleaved tips (Figure 12) reveals their similarity to the flat tip. This in turn can account for the performance characteristics of the cleaved tips.

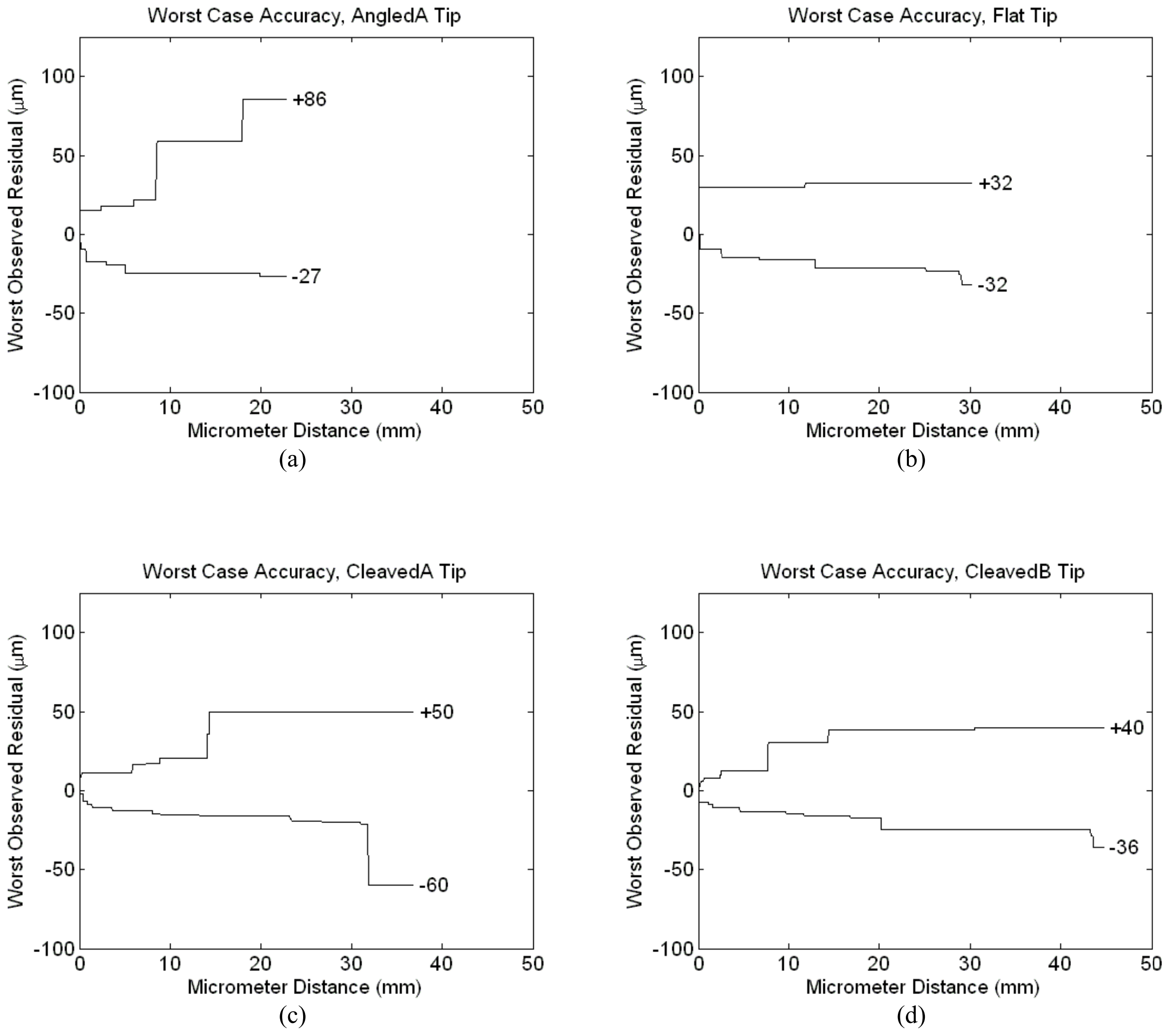

(a) (b) (c) (d)

Figure 11. The accuracy of four fiber tips is calculated from their corresponding resolution. The results from commercially available angled and flat tips are shown in (a) and (b) respectively. The results from two separate cleaved tips are shown in (c) and (d).

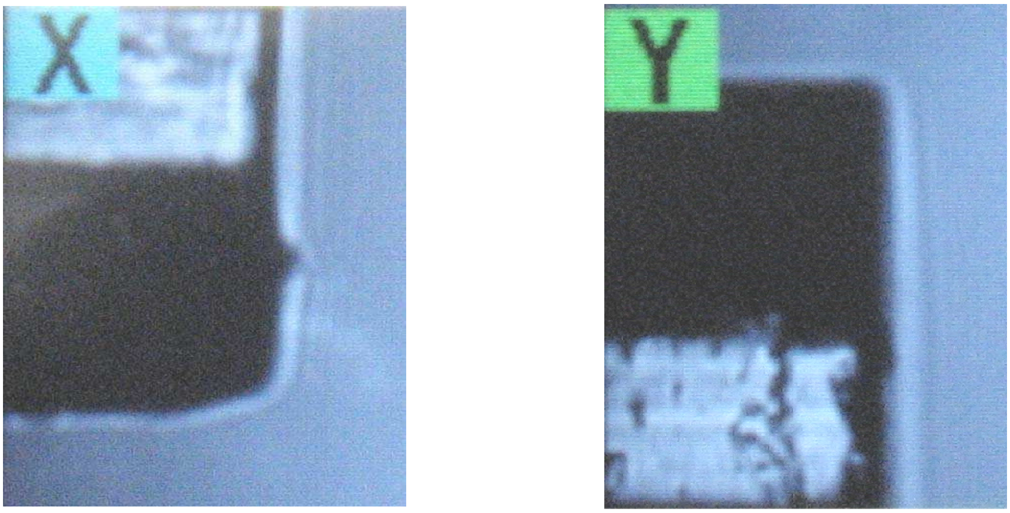

Figure 12. Close up photographs of cleaved fiber tips give an indication of cleave quality.

Conclusions

From the collected data and its analysis, we conclude that the flat FC/UPC tips are best suited for accurate measurements; however the cleaved tips perform slightly worse in accuracy, but better in range. The angled tips, although suffering less from back reflection, also receive less signal from the target surface. Thus it performs worst in both categories of performance.

Referring to Figure 9, oscillations in the RMS plot as a function of cavity length have been observed. We have been unable to find mathematical models to account for these oscillations with varying wavelengths. Another interesting observation is the recovery of accuracy shown in Figure 10. After the first few bad measurements, some data yield accurate cavity lengths before losing range once again. While both these phenomena are interesting, no explanation is proposed in the present work.

References

[1] Sagrario, D. and Mead, P., "Axial and angular displacement fiber-optic sensor," *Applied Optics*, 37 (28). 6748-6754 (1998).

[2] Huang, H. and Tata, U., "Simulation, implementation, and analysis of an optical fiber bundle distance sensor with single mode illumination," *Applied Optics*, 47 (9). 1302-1309 (2008).

[3] http://en.wikipedia.org/wiki/Fiber_optics

[4] Kogelnik, H. and Li, T., "Laser Beams and Resonators," *Applied Optics*, 5 (10). 1550-1567 (1966).

[5] http://ultracold.physics.berkeley.edu/pmwiki/Main/FluctuationBolometer

[6] Kowalevicz, A. and Bucholtz, F., "Beam Divergence from an SMF-28 Optical Fiber," Naval Research Laboratory, NRL/MR/5650—06-8996 (2006)

[7] "Corning SMF-28 Optical Fiber Product Information," Corning Incorporated (2005). Available: http://www.corning.com/assets/0/433/573/583/09573389-147D-4CBC-B55F-18C817D5F800.pdf.

[8] Stone, J. and Zimmerman, J., "Index of refraction of air," National Institute of Standards and Technology Manufacturing Engineering Laboratory: U.S. Department of Commerce (2001). Available: http://emtoolbox.nist.gov/Wavelength/ Edlen.asp.

Development of Polymer ‘Chips’ used in Medical Diagnostics

**Zachary G. Brush[1], Laura M. Schultz[2], Justin W. Vanness[3],
Kevin M. Farinholt[4], Stephen A. Sarles[5], Donald J. Leo[5]**

[1]Department of Engineering Science, Trinity University (San Antonio)
[2]Department of Civil Engineering, Georgia Institute of Technology
[3]Department of Mechanical Engineering, Michigan Technological University
[4]Applied Engineering & Technology Division, Los Alamos National Laboratory
[5]Center for Intelligent Material Systems and Structures, Virginia Tech

ABSTRACT

In recent years, there has been growing interest in creating bio-inspired devices that feature artificial bilayer lipid membranes (BLM), or lipid bilayers. These membranes can be tailored to mimic the structure and transport properties of cellular walls and can be used to selectively transport ions and other species between aqueous volumes. One application of this research is the formation of a standardized BLM contained within a portable and disposable housing for use in medical diagnostics. This concept utilizes a flexible polymer ‘chip’ that has internal compartments for housing both an organic solvent and an aqueous solution, which contains phospholipid molecules, proteins, and specific analyte molecules. The formation of a BLM within the chip enables integration of the chip into an electronic reader to perform diagnostic measurements of the sample. A key element of the bilayer formation process requires a single aqueous volume to first be separated into multiple volumes such that it can then be reattached to form a bilayer at the interface. This process, called the regulated attachment method, relies on the geometry of the deformable ‘chip’ to separate and reattach the aqueous contents held inside by opening and closing an aperture that divides adjacent compartments through the application of mechanical force. The purpose of this research is to develop an optimized chip that provides a controllable method for initially separating the aqueous phase via dynamic excitation. This study focuses on two specific aspects: designing an efficient excitation method for separating the aqueous volume, and optimizing the geometry of the chip to decrease the required input energy and better target the location and duration of the separation. Finite Element (FE) models are used to optimize the chip geometry and to identify suitable excitation signals. A series of experimental studies are also presented to validate the FE models.

1. INTRODUCTION

Artificial materials that capitalize on the characteristics of living cells are at the forefront of biomedical research today. One specific focus is the creation of an artificial bilayer lipid membrane (BLM), or lipid bilayer, to selectively sense and transport a variety of chemical and biological molecules. By inserting biological molecules, such as proteins, with known functions into the BLM, scientists can tailor the molecular composition of the membrane for a given application (Figure 1a). A specific advantage of using proteins reconstituted into a lipid bilayer as a transduction mechanism is the ability to sense interactions between analyte molecules and either proteins or the

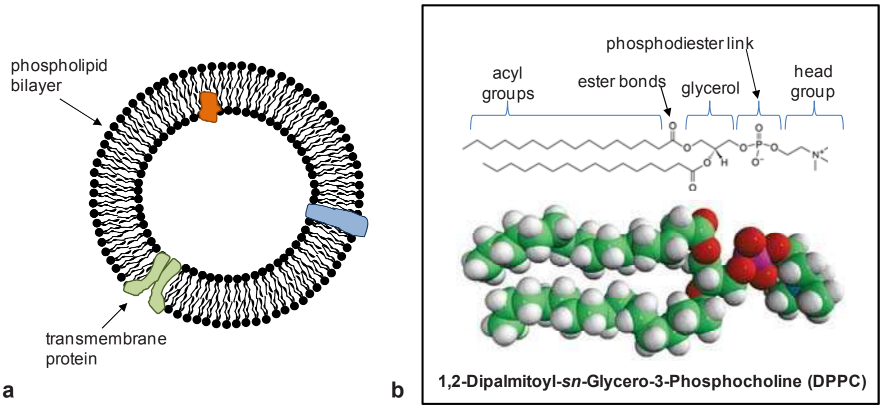

Figure 1: A bilayer lipid membrane (BLM) provides an environment for hosting functional biological molecules such as proteins (a). The ambiphilic chemical structures of phospholipid molecules allow ordered assemblies, such as lipid bilayers, to be constructed via self-assembly process (b).

T. Proulx (ed.), *Sensors, Instrumentation and Special Topics, Volume 6*, Conference Proceedings of the Society for Experimental Mechanics Series 9,
DOI 10.1007/978-1-4419-9507-0_23, © The Society for Experimental Mechanics, Inc. 2011

bilayer at the single molecule level[1]. Consequently, BLMs hold great promise for developing new types of chemical and medical diagnostic platforms for identifying drug-target interactions[2], detecting disease markers, and sensing toxins in very low concentrations[3]. Furthermore, with the similarity in chemical structure and organization to the membranes of living cells, it may be possible to connect artificial membranes to living tissues for reconstructive or therapeutic purposes.

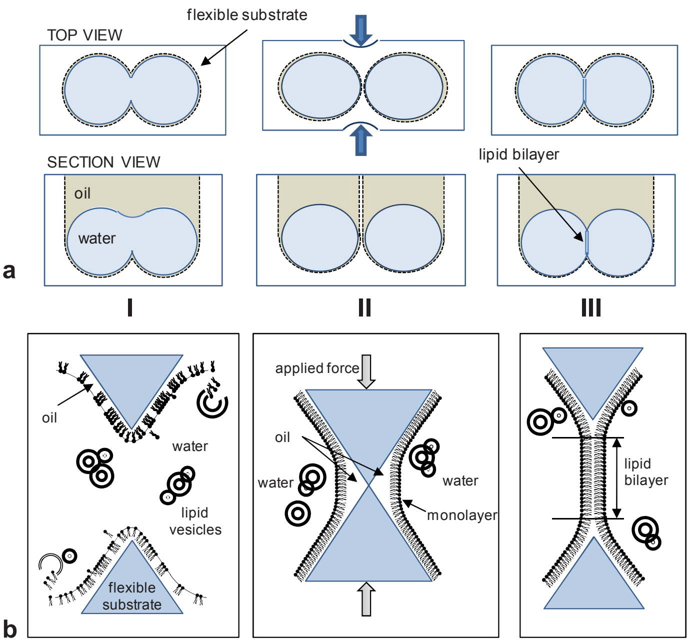

Figure 2: RAM produces lipid bilayers within flexible substrates by first separating an aqueous volume surrounded by oil and then reattaching the lipid-encased aqueous volumes through the application of a mechanical force (a). The self-assembly of lipid monolayers at an oil/water interface in the compartments of the substrate enable bilayer formation upon contact of the two volumes (b).

The characteristic building blocks of a BLM are phospholipid molecules. Phospholipids have an ambiphilic structure in which the head group is hydrophilic and the tail group is hydrophobic (Figure 1b). In the presence of water, phospholipids will self-assemble into organized structures, including a bilayer, in order to minimize contact between the hydrophobic regions of the molecules and the surrounding water. Sarles and Leo recently developed a technique for bilayer formation called the regulated attachment method (RAM), in which aqueous volumes containing phospholipids are surrounded by an immiscible oil phase and contained within a solid substrate[4]. Bilayer formation within the substrate is initiated by first separating the aqueous volume into multiple volumes that reside in adjacent compartments of the substrate (Figure 2a). Self-assembly of a lipid monolayer following separation produces lipid-encased aqueous volumes that when brought into physical contact lead to the spontaneous formation of a lipid bilayer. The geometry of the substrate is designed such that the application of a force on the substrate closes a dividing aperture between the adjacent compartments, providing a method for separating the aqueous volume. The bilayer forms upon relaxation of the applied force, which reopens the aperture and allows the lipid-encased aqueous volumes to come into contact (Figure 2b). Protein molecules incorporated into the aqueous volume either prior to or following BLM formation[4] self-insert into the bilayer that is formed and act as the sensory elements for a variety of analyte screening applications.

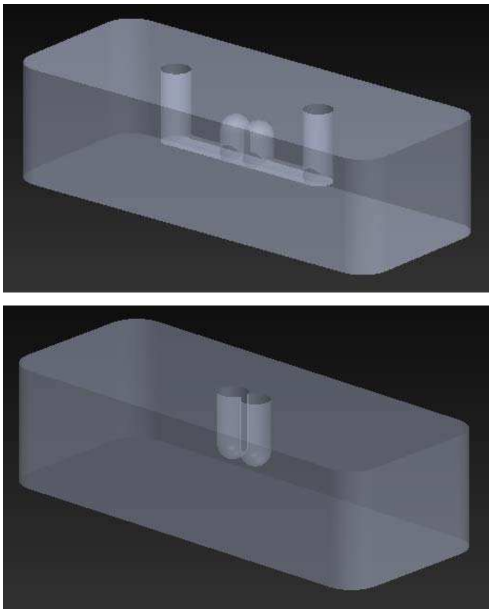

Figure 3: Internal features of the polymer chip with encapsulated (left) and open (right) well designs. Encapsulated wells rely on heavier oils to confine the aqueous phases in the central cavities, whereas open well designs relies on lighter oils.

A key advantage of the regulated attachment is the simplicity by which a durable lipid bilayer can be formed within the flexible substrate. As a result, the design and fabrication of fully-enclosed substrates (examples shown in Figure 3) that enable bilayer formation can lead to new types of portable and disposable medical diagnostic platforms. In such an application, the liquid components, including the oil and aqueous phase which contains phospholipids, proteins, and salt, are first loaded into the substrate prior to use. The analyte solution of interest can be incorporated separately into the substrate where it will mix with the standard lipid solution, or these solutions can be premixed prior to injection into the device. The substrate is then manipulated, either through an applied mechanical force or some other form of excitation, to separate the aqueous volume into two regions in adjacent compartments. Following bilayer formation, electrical measurements performed on the interface provide information such as identification or concentration of the analyte as well as properties of proteins in the bilayer.

To date, the polymer substrate, or 'chip,' has been manually pinched to close the aperture that divides the aqueous volume in the compartments. However, other methods for exciting the chip may enable more efficient and spatially

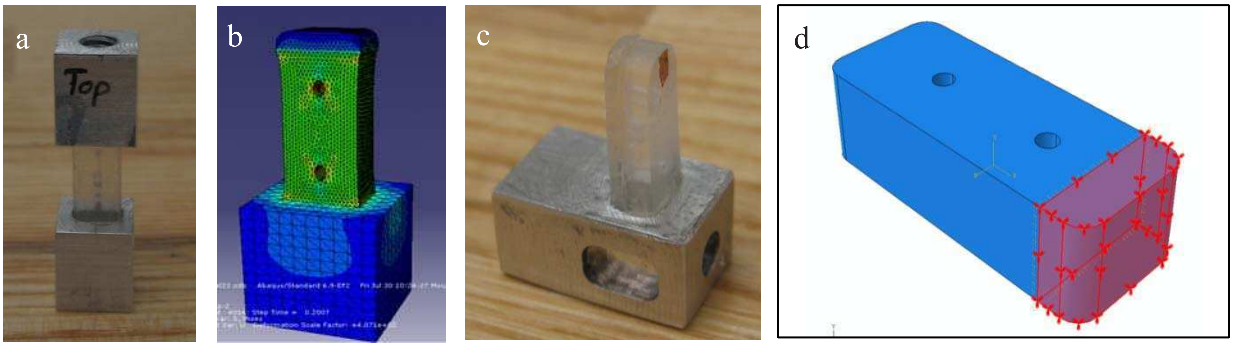

Figure 4: (a) vertical excitation aluminum fixture with mass, (b) ABAQUS model of vertical excitation with mass, (c) fixed-free horizontal excitation aluminum fixture, (d) ABAQUS model of fixed-free horizontal excitation

localized methods for opening and closing the internal apertures of the chip. The objective of this research is to study the modal behavior of the polymer chip such that one could excite the chip at specific frequencies and control the exact deformation of the interface between these wells. The scope of the project will then be expanded to include the optimization of the excitation method and the geometry of the polymer chip to decrease the required input energy and better target the separation of the bilayer lipid membrane.

2. DYNAMIC EXCITATION FEASIBILITY AND MODEL DEVELOPMENT

In the first stage of the project, an electromagnetic shaker was used to determine whether dynamic excitations could provide a viable method for BLM separation. During this stage of the project the original chip geometry remained unaltered throughout testing. The first step in the study was to identify specific frequencies that would be used to excite the physical chip. To accomplish this task, the assembly was first modeled within ABAQUS 6.9 using the material and geometric properties specified by researchers at Virginia Tech. Several end conditions were considered in the ABAQUS simulations to represent the fixture attachments to the electromagnetic shaker. Base excitations were simulated through a prescribed sinusoidal acceleration driving function. Frequencies from the simulation that predict maximum closure of the well interface were then tested on the physical chip. For comparison purposes the tip response of the polymer samples were measured using a Keyence LC 2430 laser displacement vibrometer.

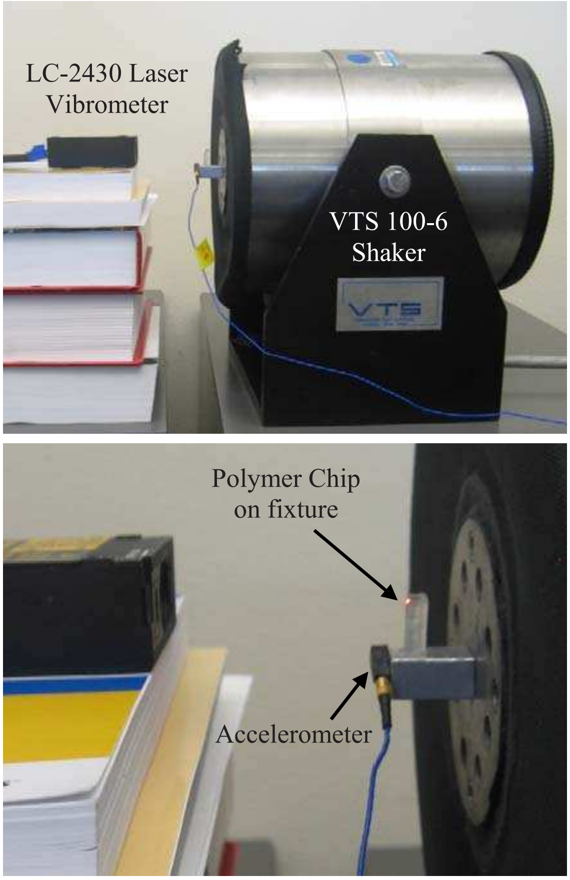

Figure 5: Experimental test setup used to excite the cantilevered polymer chip samples.

In order to verify that the ABAQUS model was an accurate representation of the physical chip behavior, two different base fixtures were fabricated to provide fixed-free boundary conditions specified in the ABAQUS simulation (Figure 4a-4d). To test the chip, sine chirp voltages were generated using a RTS Pro Photon 3.31 analyzer, and are used to excite the VTS 100-6 electromagnetic shaker, producing base accelerations for the fixture and chip. The acceleration input to the chip was recorded by a PCB 352C22 accelerometer that was mounted directly to the fixture. This measured acceleration signal was used as the input signal in characterizing the frequency response of each chip sample, and was also used as the real time input acceleration data for each of the ABAQUS simulations. Experimental displacement data for the chip was recorded using a Keyence LC 2430 laser vibrometer focused on reflective copper tape placed on the surface of the chip (Figure 5). Displacement measurements were then processed through a MATLAB function that determines the single-sided magnitude of the recorded displacement at the same frequency as the input acceleration. This magnitude plot was found by taking the fast Fourier transform (FFT) of the displacement measurements and finding the magnitude of the signal at the same frequency as our desired acceleration. The magnitude of the signal, in volts, was then multiplied by the sensitivity of the laser vibrometer (100µm/V) to obtain the maximum displacement of the chip from its initial position (as the DFT represents the single sided response spectra). It was necessary to transform the data into the frequency domain to assure that the recorded displacements were solely due to the shaker excitation and not sensor noise from the laser vibrometer. In an earlier control test, it was determined that even with the shaker turned off the laser vibrometer recorded some displacement (Figure 6). This measurement was an inherent product of the laser and not due to physical motion of the chip, and when transformed into the frequency domain, it produced significant peaks at frequencies around 100Hz and below. For each test the time domain data was transformed into a DFT plot and the displacement peak at the excitation frequency was recorded. By picking the amplitude at the excitation frequency, one is assured that the amplitude is a product of the excitation and not laser vibrometer noise.

The resonant frequencies from the aforementioned vibration tests were used to experimentally determine the damping value for the system, a key parameter in the finite element model. Damping values were first estimated using the Half-Power Bandwidth Method over 9 peaks, but since the DFT for the system did not contain sharp response peaks, damping was also calculated using a least squares polynomial fit method[5]. Based on these results, an average damping value of 13.0 ± 2.4% (90% confidence) was established and utilized within our ABAQUS model. In addition to damping, material properties greatly affect the accuracy of computer models. Because of this, it was important that the density and elastic modulus of the polymer chip be correctly characterized. The polymer samples used in this study were composed of polydimethylsiloxane (PDMS), a silicone whose material properties are greatly dependent on the duration and temperature used during the hardening process[6]. To properly characterize the density of each chip, the volume was calculated using the solid model of the polymer chip molds, while the mass was experimentally measured and averaged using eight separate PDMS samples (Table 1).

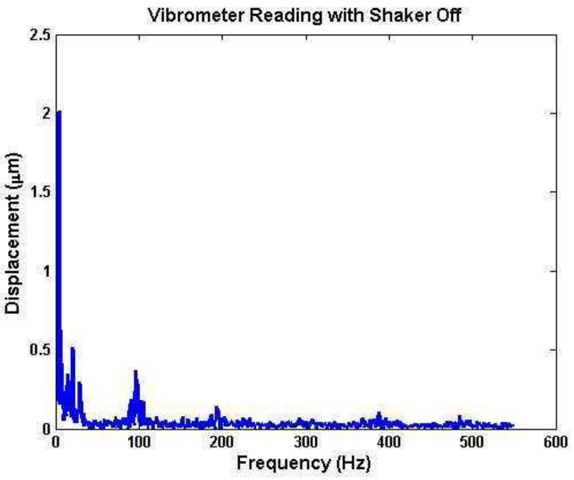

Figure 6: Graph showing the frequency response spectrum of the vibrometer with the shaker turned off

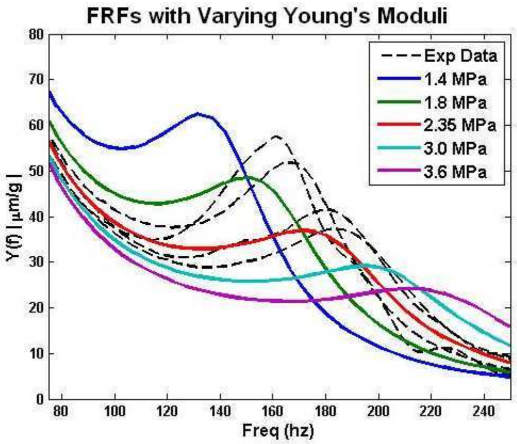

Figure 7: Frequency response functions of a fixed-free chip with varying Young's Moduli versus the experimental data collected in this configuration. All other model variables are at their final values.

The elastic modulus (E) of the chip was more difficult to determine experimentally as PDMS is a non-linear material in which the value of E varies with increasing load[5]. Thus, it is not beneficial to conduct a standard load-deflection test as one would for a linear elastic material. To determine a value for the elastic modulus which is valid over the range of acceleration amplitudes used in this experiment, the exact same loading conditions were used for both testing and modeling. To replicate the exact loading on the polymer chip, the measured acceleration data was prescribed as the base excitation for the fixed-free end condition of the finite element model in ABAQUS (Figure 7). In order to determine the value of E, the modulus value was incrementally changed within the horizontal excitation model (Figure 4d) until the resulting displacement at specific

Table 1: Summary of the mass, volume and density characteristics of the PDMS chip

Average Values and Variability of PDMS Chip Material and Geometric Properties						
	Mass (g)	Length (mm)	Height (mm)	Width (mm)	Volume (mm^3)	Density (g/mm^3)
Average Values (not including nominal value)	0.3149	14.79	4.06	6.17	361	8.80E-04
Standard Deviation (not including nominal value)	0.0395	0.27	0.56	0.16	56	9.7E-05

nodes of the ABAQUS model fell within the range of those measured experimentally (Figure 7). It is understood that this method for determining the elastic modulus depends heavily on the certainty of all other parameters within the model, including damping, density, boundary conditions and prescribed excitation, so some variability in the data is expected (see appendix for discussion of modeling confidence). Multiple tests were conducted with different chips to get a bound on the variability of the physical response, which was also dependent on chip to chip variance in material properties and the quality of adhesion of the chip to the fixture (Figure 8). Given the variability in the test data, the proposed elastic modulus of 2.35MPa shown in Figure 7 is accurate enough to predict a range of frequencies to achieve specific mode shapes of the chip.

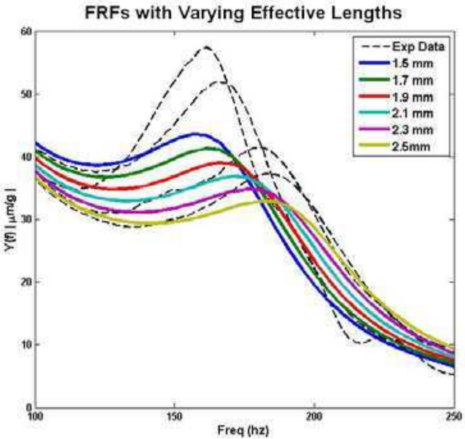

Figure 8: Frequency response functions of a fixed-free chip with varying effective chip protrusion lengths versus the experimental data collected in this configuration. All other model variables are at their final values.

It was necessary to illustrate that the experimentally determined value of elastic modulus accurately characterized the polymer chip for fixture configurations other than the horizontally excited fixed-free condition used in the calibration. Because of this, four more tests were run using a vertically excited fixed-free end condition. Two different chips were placed in the vertical fixture, shaken, removed from the fixture, re-glued and shaken again (Figure 9). The displacements recorded from these four tests are then compared to the predictions from the ABAQUS FE model of the vertically excited chip. The displacement predictions obtained in ABAQUS using the experimentally determined elastic modulus were seen to fall within the range of the experimental results. With an accurate analytical representation of the polymer chip established, design and testing of different chip geometries within the ABAQUS model could be commenced. (For further discussion of model accuracy including mesh convergence and quantified experimental and model error, see Appendix)

3. OPTIMIZATION OF INDIVIDUAL CHIP GEOMETRY

The objective of the second phase of this project was to design a chip geometry that provides sufficient deformation to separate the test wells using dynamic excitation from the electromagnetic shaker. A fixture is considered to be optimal if the BLM can be consistently separated with minimal input energy to the shaker. Because of the correlation between experimental displacements and those predicted in the FE model, it is assumed that the deformation of the inner wells of the polymer chip behaves in a similar manner to the separation predicted by the FE model. Thus preliminary design and simulation of the fixtures is conducted within ABAQUS. The best mode of deformation for forming the BLM is the longitudinal stretching mode, as seen in Figure 10. The first natural frequency of the original chip design (Figure 3Figure 4) was much higher than

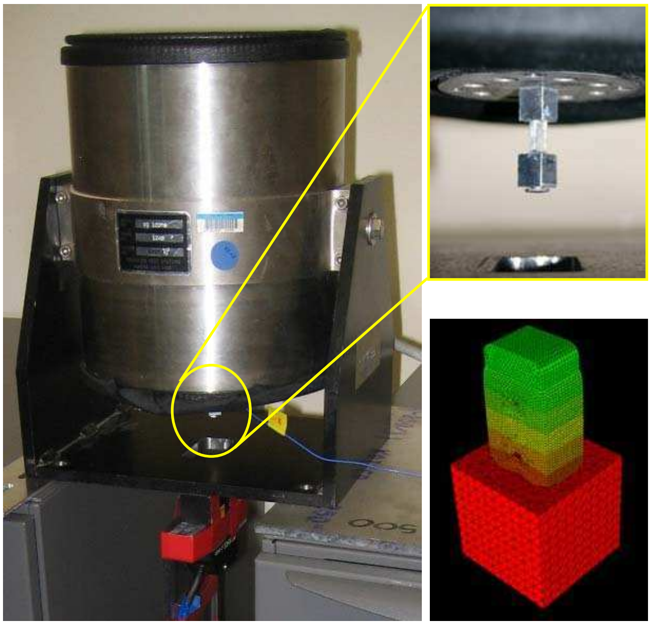

Figure 9: Test set up for the vertical excitation, along with the ABAQUS model of the vertical excitation.

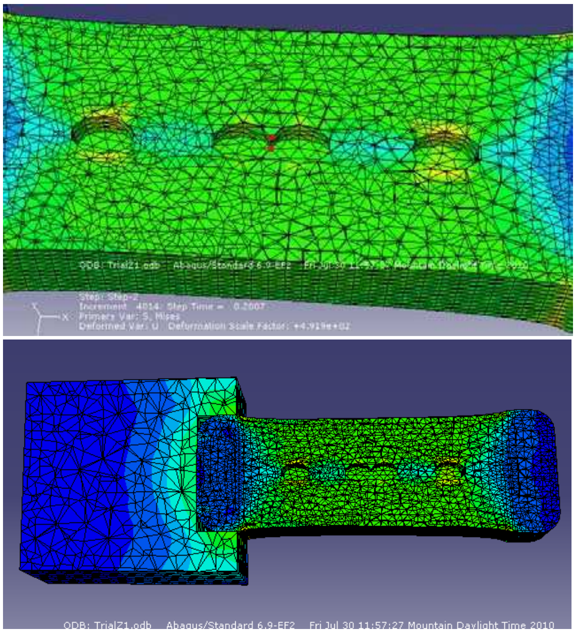
ODB: TrialZ1.odb Abaqus/Standard 6.9-EF2 Fri Jul 30 11:57:27 Mountain Daylight Time 2010

Figure 10: Longitudinal stretching mode of the polymer chip as predicted in ABAQUS

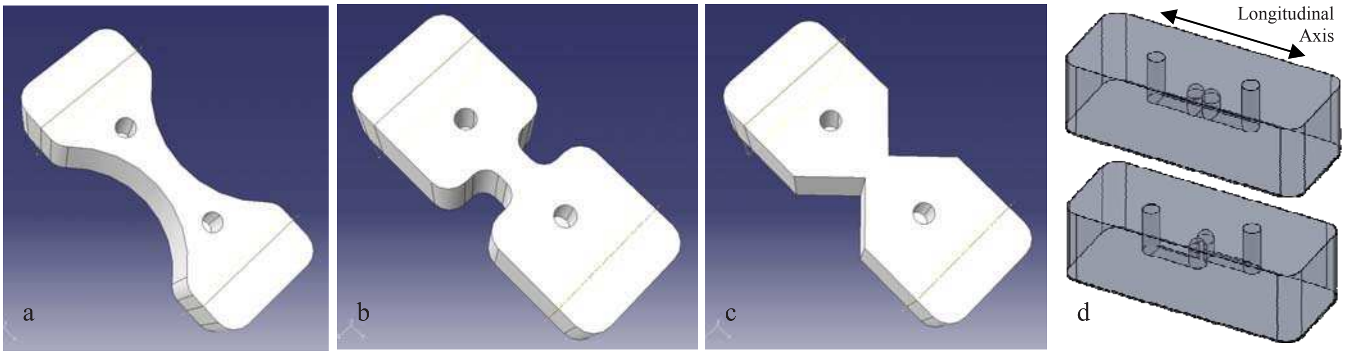

Figure 11: Notch geometries considered during chip optimization: a.) rounded notch, b.) rectangular notch, c.) V-notch and d.) in-line v. rotated well orientations. In-line wells are aligned along the longitudinal axis of the polymer chip.

desired, and only offered small restrictions in the aperture width. Therefore, several variations in the chip geometry were proposed to decrease the sample stiffness, thereby reducing the required excitation frequency and increasing the amplitude of well deformation.

To obtain the maximum amount of deformation near the BLM aperture, three methods of tapering the chip near the well aperture were considered: a rounded notch (Figure 11a), a rectangular notch (Figure 11b), and a v-notch (Figure 11c). In addition to the modified geometries considered in Figure 11a-c, simulations were also conducted with in-line and rotated well designs (Figure 11d). Five combinations were simulated in ABAQUS using the same input voltage, and the minimum aperture width was recorded. The designs that result in the smallest aperture width for a given voltage were considered most efficient (Figure 12a and Figure 12b). Using the results from this preliminary study, an optimized geometry was designed using a filleted v-notch chip with rotated wells (Figure 13a). An open-well design was also implemented, which greatly reduced the thickness of the chip in order to further decrease the natural frequency of the chip. The results from the finalized geometry are summarized in Figure 12b and Figure 13b.

One aspect of the testing that should be noted is that longitudinally excited samples were oriented in a vertical direction with an applied mass mounted to the free end of the polymer chip. In the final implementation of this chip design, samples would need to be oriented in a horizontal direction, to ensure that aqueous and oil phases remain in the proper orientation within the chip wells. Therefore, the final proposed design will incorporate a linear slide or low friction bearing to allow the chips to slide freely when excited in a horizontal direction.

4. EXPANSION TO MULTI-INTERFACE DESIGN

Researchers are very interested in the possibility of expanding the chip design to include multiple bilayer formation sites such that a variety of tests could be conducted within several BLMs contained across a single chip. By tuning the system's

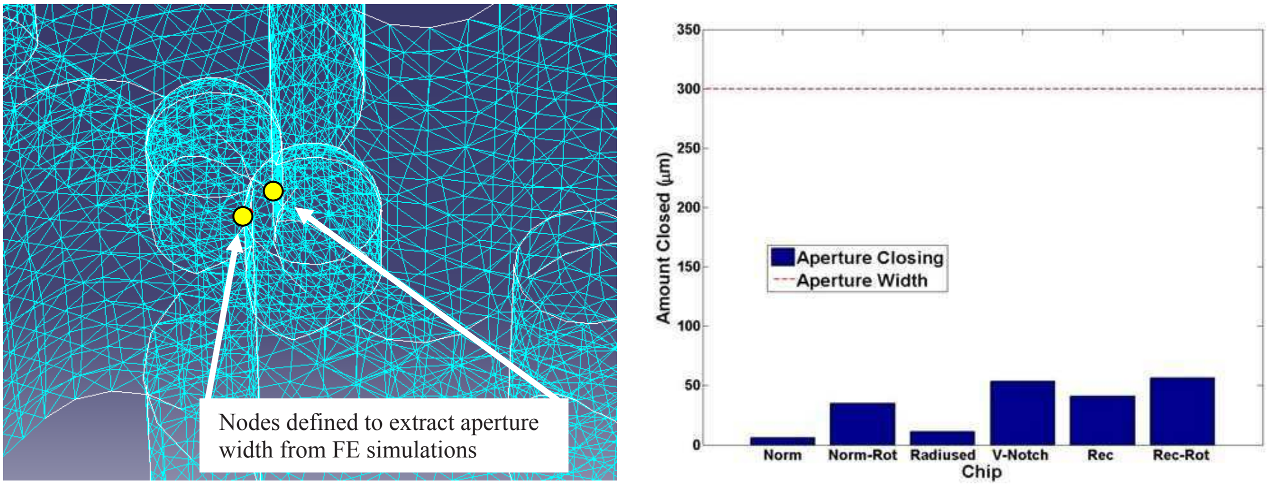

Figure 12: Aperture widths were monitored using a.) two representative nodes defined within the ABAQUS simulations and were monitored for each of the chip geometries. 13b.) presents a comparison of the simulation results for each configuration.

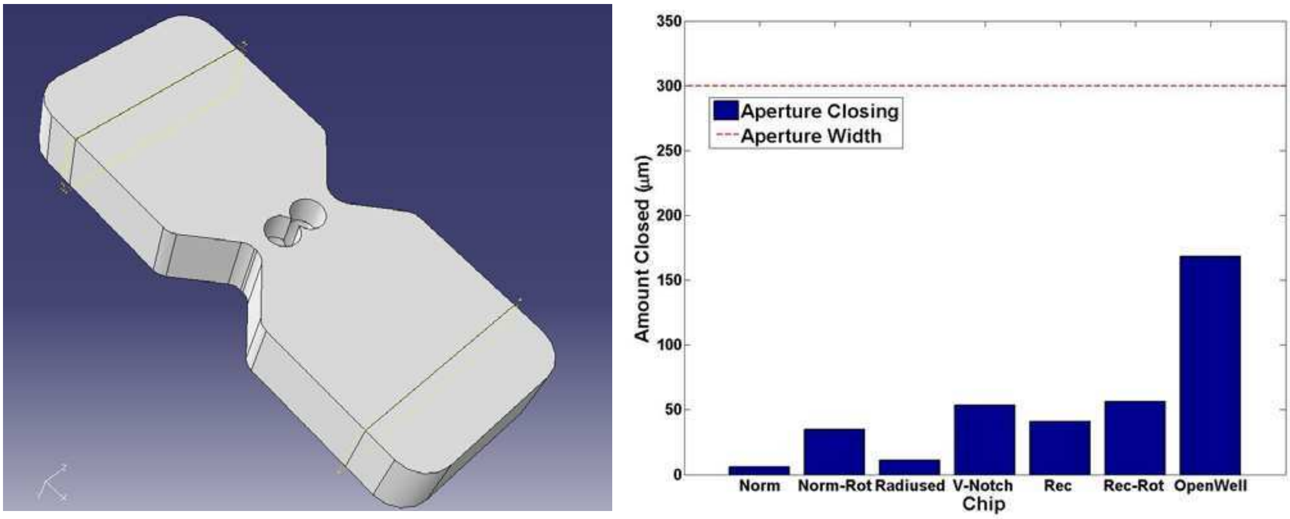

Figure 13a: Optimized geometry that uses a rotated well configuration with a filleted V-notch design. b) This design provides 50% closure of the aperture during excitation.

geometry, the natural frequencies of specific wells could be excited independently to form specific BLMs without closing the well interfaces on other locations along the chip. To accomplish this, an eight-well polymeric substrate that features four individual bilayer formation sites (i.e. four two-well designs) arranged symmetrically along two parallel legs of the substrate. The geometry of each two-well site is based on the optimized two-well design discussed previously. Added masses are incorporated into the center of each leg (shown in Figure 14) such that the resonant properties of each leg can be tuned independently, where the mass-loaded legs represent idealized spring-mass systems. Diamond shape masses are chosen to concentrate stiffness near the aperture and create a concentration of energy. Locally there is less polymeric material between the mass and the aperture to dissipate energy, which also increases the deformation of the wells. In order to separate the natural frequencies of the two sides of the system, the relative size and density of the applied masses was varied until there was significant separation in frequency between the mode shapes of each half of the system.

5. SUMMARY AND CONCLUSIONS

The goal of this investigation has been the dynamic characterization and optimization of polymer chips used in the formation of bilayer lipid membranes for biomedical research devices. In this preliminary study we have demonstrated our ability to model the macroscopic response of existing chip designs, incorporating several material and experimental uncertainties into the modeling approach to quantify our confidence in the analytical predictions. A thorough analysis of key material properties has demonstrated that the predictions fall within the chip-to-chip variabilities observed in the laboratory. Existing

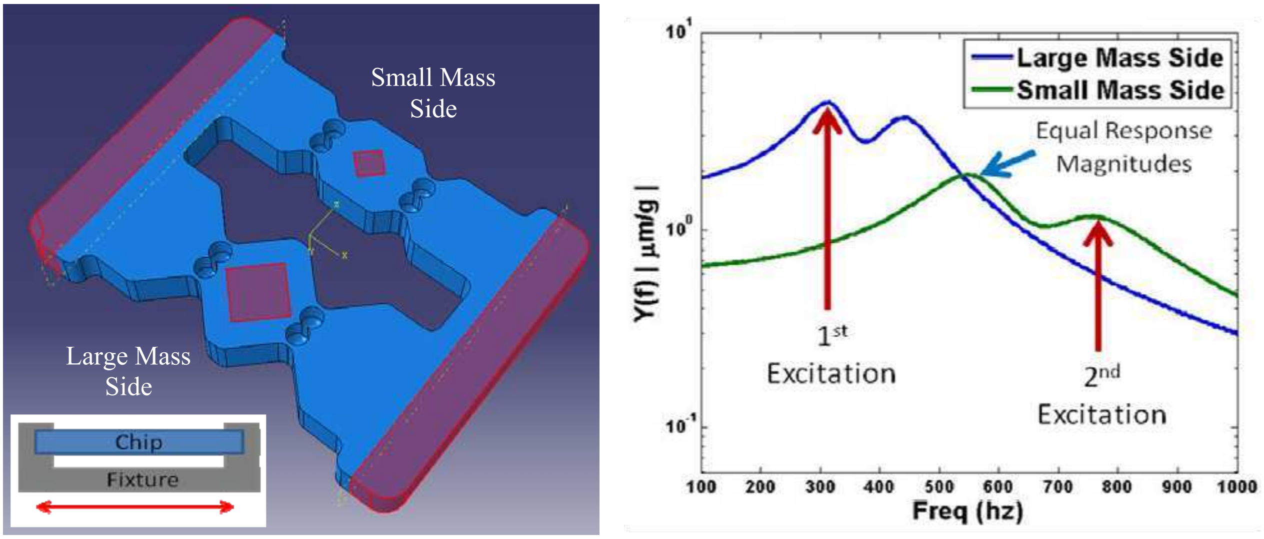

Figure 14: The proposed multi-interface geometry that provides selective excitation frequencies.

polymer chip designs were modeled in ABAQUS' finite element software, and the dynamic response predictions were compared with experimental results for both cantilevered and longitudinally excited samples. Following the development of a suitable FE model that could predict the response characteristics for the existing polymer chip design, a series of analytical studies were conducted to investigate alternative chip geometries that could be used to increase compliance the well interface where bilayer lipid membranes are formed. Several geometric features were considered in this analysis, including: rounded-, rectangular-, and V-notch geometries, as well as in-line versus rotate well orientations, and embedded versus open-well chip designs. It was found that the V-notch geometry with rotated, open-wells provided the largest deformations near the interface where BLM formation is desired. Analytical predictions indicate that we could obtain 50-55% closure of the aperture using small dynamic excitation signals with this design. Future experimental characterizations of this modified design are intended to demonstrate whether this is sufficient to separate the aqueous volumes and provide reliable formation of BLMs at the well interface. Following the validation of the single-interface design, more work will focus on the development of multi-interface fixture designs, and the results are expected to be presented in future publications of this work.

REFERENCES

[1] H. Bayley and P. S. Cremer, "Stochastic Sensors Inspired by Biology,"

Table A2: Experimentally Determined Properties of PDMS Chips

	Mass* (g)	Length (mm)	Height (mm)	Width (mm)	Total Vol. (mm^3)	Inner Vol.** (mm^3)	Actual Vol. (mm^3)	Density*** (g/mm^3)
Nominal	0.360	15	4	6	360	10.2	349.8	1.03E-03
Chip 1	0.3389	14.75	4.27	6.30	396	10.2	386	8.78E-04
Chip 2	0.3510	14.85	4.02	6.07	362	10.2	352	9.97E-04
Chip 3	0.3187	14.85	3.69	6.09	334	10.2	324	9.85E-04
Chip 4	0.3257	15.31	4.84	6.26	464	10.2	454	7.18E-04
Chip 5	0.3503	14.74	4.08	6.44	387	10.2	377	9.29E-04
Chip 6	0.2292	14.69	3.01	6.21	275	10.2	264	8.67E-04
Chip7	0.3041	14.79	4.59	5.98	406	10.2	396	7.68E-04
Chip8	0.3010	14.33	3.99	6.04	345	10.2	335	8.98E-04

*The nominal mass is based on the given value for PDMS density and the nominal actual volume.

**Inner volume is the difference between the nominal total volume of the chip (LxWxH) and the ABAQUS predicted volume based on nominal chip dimensions. We cannot actually test this value, so it is assumed to not vary significantly from chip to chip.

***Nominal density is found in Sylgard 184 PDMS Material Safety Data Sheet (1). Other chip densities are based on measured chip masses and actual volumes.

APPENDIX B: MESH CONVERGENCE ANALYSIS

In any FE model it is necessary to determine that the characteristic mesh size chosen for the simulation yields results that are within the regime of convergence. Within this region solutions are meaningful as they approach a definitive value if an infinitely small mesh size were possible. Outside of this region, solutions which are yielded from the model may be anomalies that are not representative of the actual solution to which the computer simulation is approaching. In order to determine that the mesh size used in this study was indeed within the asymptotic region of convergence, solutions from 5 different mesh sizes were fit via a non-linear least squares error method to the form:

$$0 = Y_{actual} + \beta \Delta X^{p} - Y(\Delta X),$$

where Y_{actual} is the solution to which the model is approaching and ΔX, $Y(\Delta X)$ are the mesh size and the solution given from a particular trial, and β and p are variables found via the least squares solution.[7]

If one is within the region of asymptotic convergence p should ideally be a positive number greater than or equal to 1.0. For a linear element, p will ideally be near 1.0 and for a quadratic element p would ideally be 2.0. If the solutions from the mesh sizes chosen yields a negative value, an extremely large value, or a value significantly less than 1.0, the mesh sizes chosen are not within the asymptotic regime of convergence and the predicted Y_{actual} from the method explained in section a is not valid. Finer mesh sizes should be chosen and the process repeated until the chosen mesh size for the model lies within the convergent regime.

Preliminary mesh convergence tests were run on a simplified model (which did not include the internal voids of the chip) to determine the influence of choosing tetrahedral vs. quadratic elements. From the results it is evident that the choice of tetrahedral elements to speed computations does not significantly impact the actual result towards which the model is converging.

Table B1: Solutions for various mesh sizes on simplified chip geometry

Block Mesh Convergence- 1st Natural Frequency			
	.3 mm	.33 mm	.363 mm
Quadratic Elements	178.7	178.84	178.93
	.2 mm	.25 mm	.3125 mm
Tetrahedral Elements	181.14	182.26	183.77

Table B2: Mesh convergence study comparing the influence of tetrahedral vs. quadratic elements

Element Type	Beta	p-Values	Convergence
Quadratic Elements	-7.213	0.2276*	173.2191
Tetrahedral Elements	27.7502	1.339	177.9236

*Note that the p-value for the Quadratic element model was not ideal, as we were unable to run a finer mesh as it exceeded the node limitations of the computer used for simulation

Table B3: Solutions for various mesh sizes on full chip geometry with tetrahedral elements

Chip Model Convergence- Tetrahedral Elements						
	.3 mm	.4 mm	.5 mm	.533 mm	.6 mm	.711 mm
Model	178.7	179.12	179.51	179.62	179.81	180.33

Table B4: Mesh convergence study of full chip geometry with tetrahedral elements

Element Type	Beta	p-Values	Convergence
Model	-3.8562	1.0124	177.574

Since the predicted solution for the first natural frequency was 2.71% greater using tetrahedral elements instead of quadratic and the variation in first natural frequency for the physical chip was 6.26%. It was determined that tetrahedral elements were appropriate for predictions of natural frequency. Next a mesh refinement study was conducted on the full model and it was determined that the choice of a 0.3mm characteristic mesh size was within the regime of convergence and yields a solution that is 0.634% greater than the solution to which the model is converging (Table B3 and Table B4). Combining the two sources of error, element choice (2.71%) and discretization error (0.634%) yields an overall over prediction for natural frequency of 3.34% from the ideal model composed of infinitesimal quadratic elements. Note that this error is relatively small in comparison to the variation in test data, and the model's predicted natural frequency falls within the bounds of the tested results.

It is noted that error will propagate through to higher frequency responses, as the mesh refinement study was conducted only on the predicted frequency of the first natural mode of the system. But due to the damping in the system, the first mode was the only one which had a pronounced response. Most of the frequencies of interest are within this lower frequency domain, so the model error is not expected to increase significantly for the other testing configurations.

Acoustic Fluid-Structure Interaction of Cars and Ships (Tutorial)

Lothar Gaul

Abstract Acoustic fluid-structure interaction is a common issue in automotive applications. An example is the pressure-induced structure-borne sound of piping and exhaust systems. Efficient model order reduction and substructuring techniques accelerate the finite element analysis and enable the vibro-acoustic optimization of such complex systems with acoustic fluid-structure interaction. This tutorial reviews the application of the Craig-Bampton and Rubin method to fluid-structure coupled systems and presents two automotive applications. First, a fluid-filled brake-pipe system is assembled by substructures according to the Craig-Bampton method. Fluid and structural partitions are fully coupled in order to capture the interaction between the pipe shell and the heavy fluid inside the pipe. Second, a rear muffler with an air-borne excitation is analyzed. Here, the Rubin and the Craig-Bampton method are used to separately compute the uncoupled component modes of both the acoustic and structural domain. These modes are then used to compute a reduced model which incorporates full acoustic-structure coupling. For both applications, transfer functions are computed and compared to the results of dynamic measurements.

The vibro-acoustic behavior of ship-like structures is noticeably influenced by the surrounding water and thus represents a multi-field problem. In this tutorial, fast boundary element methods are applied for the semi-infinite fluid domain. As an advantage, the Sommerfeld radiation condition is satisfied in an exact way and only the boundary, i.e. the ship hull, has to be discretized. To overcome the draw-back of fully populated matrices, fast boundary element methods are applied. The focus is on the comparison of the multipole method with hierarchical matrices, which are set up by adaptive cross approximation. In both cases, a half-space fundamental solution is used to incorporate the water surface, which is treated as pressure-free. The structural domain is discretized with the finite element method. A binary interface to the commercial finite element package ANSYS is used to import the mass and stiff-

---

Lothar Gaul
Institute of Applied and Experimental Mechanics, University of Stuttgart, Pfaffenwaldring 9, 70569 Stuttgart, Germany e-mail: gaul@iam.uni-stuttgart.de

T. Proulx (ed.), *Sensors, Instrumentation and Special Topics, Volume 6*, Conference Proceedings of the Society for Experimental Mechanics Series 9, DOI 10.1007/978-1-4419-9507-0_24, © The Society for Experimental Mechanics, Inc. 2011

ness matrices. The coupled problems are formulated as Schur complements, which are solved by a combination of iterative and direct solvers. Depending on the applied fast boundary element method, different strategies arise for the preconditioning and the overall solution. The applicability of these approaches is demonstrated using a realistic model problem.

1 Introduction

This tutorial explains various phenomena of acoustic fluid-structure interaction and shows how to efficiently model the two-field problem. In general, heavy fluids such as water, oil, fuel or brake fluid influence the structural field and vice versa. Moreover, strong coupling is observed if acoustic fluids interact with thin or slender structures. Important fluid-structure interaction phenomena in practical applications are

- shift of natural frequencies,
- change of wave number and fluid wave speed,
- pressure-induced vibrations,
- sound radiation.

The above mentioned phenomena are present in automotive and ship applications such as fluid-filled brake/fuel pipes, exhaust systems or partly immersed ship hulls. The considered applications are characterized by a negligible mean flow (Mach number $<< 1$), which allows the use of the linear wave equation for a fluid at rest to describe the acoustic field. To predict the hydro- and vibro-acoustic behavior of these industrial examples, three-dimensional models including full coupling of the two-field problem are needed. Appropriate coupling conditions are

- the linear Euler equation enforcing continuity of particle velocities in the normal direction at the fluid-structure interface,
- the reaction force axiom enforcing equilibrium.

In the presence of a heavy fluid, the natural frequencies of longitudinal and flexural wave types in the structure are shifted due to the added mass or the added stiffness effect (shift to lower or higher frequencies, respectively). The torsional wave is not influenced by the acoustic field since no deflection in the normal direction at the fluid-structure interface occurs.

Pressure-induced vibrations are a common problem in automotive piping systems, where oscillating pressure pulsations excite the flexible pipe shell due to fluid-structure coupling. To predict the resulting vibration levels, adequate damping models are needed. The use of a complex wave number is required to model fluid damping. In thin fluid-filled pipes, friction effects close to the pipe wall are the dominant damping mechanism.

In general, two types of structure-acoustic problems can be distinguished. The interior acoustic problem is characterized by an acoustic fluid which is surrounded by a flexible structure. A typical exterior acoustic problem is the sound radiation of vibrating structures in the exterior acoustic field. It is particularly important to account for flexural vibrations, which are predominantly responsible for noise and vibration harshness (NVH). Simulation methods for both problems are briefly described in the following.

2 Interior Acoustic Problem

The finite element method (FEM) is considered as the appropriate discretization method to investigate the dynamics of the interior vibro-acoustic problem since only a finite volume has to be discretized. However, large-scale examples require model reduction techniques to accelerate the computation times. The application of the Craig-Bampton method to the vibro-acoustic problem including an additional reduction of the remaining interface degrees of freedom leads to a considerable model reduction. Dynamic substructuring techniques are particularly efficient for systems with repeating substructures, since the corresponding component system matrices and the reduction basis has to be computed only once. The simulation technique is applied to fluid-filled automotive piping systems. Computed transfer functions are validated by a hydraulic test bench operating in the kHz-range.

It is observed, that for structures with a high impedance mismatch between the structure and the contained fluid, the coupled natural frequencies and eigenvectors are altered only marginally compared to the uncoupled ones. Therefore, in such a case, the reduced-order model is constructed by using the uncoupled eigenvectors, since they span approximately the same subspace as the coupled eigenvectors. This is equivalent to reducing each domain separately. However, the reduced-order model is still a fully coupled system. This approach has the advantage that for each domain the favorable reduction method may be applied. For instance, the Rubin method may be used for the reduction of the structural partition and the Craig-Bampton method may be applied to reduce the fluid partition. This combined approach is applied to a rear muffler with an air-borne excitation.

3 Exterior Acoustic Problem

The boundary element method (BEM) is well-suited for the solution of exterior acoustic problems since the Sommerfeld radiation condition is intrinsically fulfilled. Another advantage of the BEM is that only the boundary of the structure has to be discretized, which reduces the effort of mesh generation. To overcome the drawback of high memory consumption due to fully populated system matrices, fast BE methods are used, such as the fast multilevel multipole BEM as well as the concept of hierarchical matrices. FE-BE coupling schemes are developed for ship applications, where the ship hull is influenced by the surrounding water and vice versa. Due to the large fluid-structure interface, the reduction of interface degrees of freedom is an important step to obtain moderate computation times.

Fast BE methods are also used to compute the sound radiation of automotive structures such as a rear muffler of an exhaust system. Here, both an interior and an exterior acoustic problem have to be solved. The feedback of the exterior acoustic pressure on the vibrating structure may be neglected as long as the impedance mismatch between the two fields is large enough (e.g. stiffened structures surrounded by air).

4 Content of Tutorial and Selected Publications

The tutorial will consist of the following parts:

1. Introduction/Motivation
2. Acoustic Fluid-Structure Coupling
3. Finite Element Method
4. Dynamic Substructuring of the Two-Field Problem
5. Fast Boundary Element Method for the Exterior Acoustic Problem
6. Automotive Applications along with Experimental Techniques
7. Ship Applications
8. Conclusion

The topics of the tutorial are taken from articles and archival publications of the tutor and his co-workers focused on fluid-structure interaction problems. Selected recent publications including abstracts are listed in the following.

1. M. Fischer and L. Gaul: Fast BEM-FEM mortar coupling for acoustic-structure interaction
   International Journal for Numerical Methods in Engineering 62: 1677-1690, 2005
   A coupling algorithm based on Lagrange multipliers is proposed for the simulation of structure-acoustic field interaction. Finite plate elements are coupled to a Galerkin boundary element formulation of the acoustic domain. The interface pressure is interpolated as a Lagrange multiplier, thus, allowing the coupling of non-matching grids. The resulting saddle-point problem is solved by an approximate Uzawa-type scheme in which the matrix-vector products of the boundary element operators are evaluated efficiently by the fast multipole boundary element method. The algorithm is demonstrated on the example of a cavity-backed elastic panel.

2. L. Gaul and M. Fischer: Large-scale simulations of acoustic-structure interaction using the fast multipole BEM
   ZAMM 86: 4-17, 2006
   For the simulation of acoustic-structure interaction problems, the coupled field

equations must be solved. The structure is commonly discretized using finite elements, whereas for the acoustic field the boundary element method (BEM) is favorable. A mortar BEM-FEM coupling algorithm is developed that allows the combination of non-conforming meshes. The high flexibility for the choice of discretizations offers a high efficiency, since specialized shape functions and adaptive mesh refinement can be used in the subdomains. The mortar coupling algorithm yields a saddle point problem that is solved using a preconditioned inexact Uzawa algorithm. The iterative solver enables the use of the fast multipole BEM and thus coupled simulations on large boundary element models.

3. M. Maess and L. Gaul: Substructuring and model reduction of pipe components interacting with acoustic fluids
   Mechanical Systems and Signal Processing 20: 45-64, 2006
   This paper presents a model reduction and substructure technique for reduced dynamical models of fluid-filled pipe components. Both linear acoustical domain and structural domain are modelled by finite elements (FE), and they are fully coupled by a fluidstructure interface. The discretised dynamic FE-equations, which use the acoustic pressure as field variable in the fluid, render both non-symmetric mass and stiffness matrices due to the FSIcoupling. Since the partial solutions to the eigenproblem of the coupled system are of special interest, either numerical preconditioning or non-dimensionalisation of the physical quantities is performed to improve the condition and to accelerate the numerical computation. An iterative subspace solver is adopted to generate a sufficient approximate of the low-frequency eigenspace of the constrained problem. Model reduction for component mode synthesis uses constraint modes together with the computed eigenspace. Single-point constraints for the nodal degrees of freedom hold at the interface between substructures. The null space resulting from a QR-decomposition of the single-point constraints at the interface is used as explicit coupling matrix to prevent the deterioration of the conditioning. Partitioning of the reduction space and coupling matrices leads to a structure of the coupled global system matrices, which is similar to the original system structure in physical quantities. Therefore, the iterative subspace eigensolver is used again for numerical modal analysis. Modal analysis is performed for a pipe segment assembled by fully coupled two-field substructures. The results are compared to the results obtained from the full model and to experimentally determined mode shapes.

4. M. Maess , J. Herrmann and L. Gaul: Finite element analysis of guided waves in fluid-filled corrugated pipes
   Journal of the Acoustical Society of America 121: 1313-1323, 2007
   Free wave propagation in fluid-filled corrugated pipes is analyzed using finite element methods in combination with a wave-based approach. By combining discretized models with a wave-based approach, complex mechanism of wave motion in the three-dimensional waveguide is fully included. The pipes are treated as waveguides having periodic properties in the direction of wave propagation.

The analysis of these guided waves leads to dispersion curves which show the strong frequency-dependency of the different wave modes. The method also allows the inclusion of coupling between fluid-borne and structure-borne wave modes which occur at the acoustic-structure interface. Phase and group velocities of the wave modes are derived in postprocessing steps. Additionally, the energy ratio of the fluid-domain and solid-domain vibrational energies is computed. Finally, linear damping models are included in order to explore wave mode attenuation.

5. D. Brunner, M. Junge and L. Gaul: A comparison of FE-BE coupling schemes for large scale problems with fluid-structure interaction
International Journal of Numerical Methods in Engineering 77: 664-688, 2008
To predict the sound radiation of structures, both a structural problem and an acoustic problem have to be solved. In case of thin structures and dense fluids, a strong coupling scheme between the two problems is essential, since the feedback of the acoustic pressure onto the structure is not negligible. In this paper, the structural part is modeled with the finite element (FE) method. An interface to a commercial FE package is set up to import the structural matrices. The exterior acoustic problem is efficiently modeled with the Galerkin boundary element (BE) method. To overcome the well-known drawback of fully populated system matrices, the fast multipole method is applied. Different coupling formulations are investigated. They are either based on the Burton-Miller approach or use a mortar coupling scheme. For all cases, iterative solvers with different preconditioners are used. The efficiency with respect to their memory consumption and computation time is compared for a simple model problem. At the end of the paper, a more complex structure is simulated.

6. M. Junge, D. Brunner, J. Becker and L. Gaul: Interface reduction for the Craig-Bampton and Rubin Method applied to FE-BE coupling with a large fluid-structure interface
International Journal of Numerical Methods in Engineering 77: 1731-1752, 2009
Component mode-based model-order reduction (MOR) methods like the Craig-Bampton method or the Rubin method are known to be limited to structures with small coupling interfaces. This paper investigates two interface-reduction methods for application of MOR to systems with large coupling interfaces: for the Craig-Bampton method a direct reduction method based on strain energy considerations is investigated. Additionally, for the Rubin method an iterative reduction scheme is proposed, which incrementally constructs the reduction basis. Hereby, attachment modes are tested if they sufficiently enlarge the spanned subspace of the current reduction basis. If so, the m-orthogonal part is used to augment the basis. The methods are applied to FE-BE coupled systems in order to predict the vibro-acoustic behavior of structures, which are partly immersed in water. Hereby, a strong coupling scheme is employed, since for dense fluids the feedback of the acoustic pressure onto the structure is not negligible. For two exam-

ple structures, the efficiency of the reduction methods with respect to numerical effort, memory consumption and computation time is compared with the exact full-order solution.

7. J. Herrmann, M. Maess and L. Gaul: Substructuring including interface reduction for the efficient vibro-acoustic simulation of fluid-filled piping systems
   Mechanical Systems and Signal Processing 24: 153-163, 2010
   The operation of pumps and valves leads to strong acoustic excitation in fluid-filled piping systems. Efficient substructuring and model order reduction strategies are required for the sound prediction in piping systems, and in order to reduce the sound transmission to attached components, such as the floor panel in vehicles, for example. This research presents a finite element based automatic substructuring and component mode synthesis technique, which is a combination of an extended Craig-Bampton method for fluid-structure coupled piping systems and a novel, consecutive interface reduction. Hereby, the remaining interface degrees of freedom between different substructures are further reduced using appropriate Ritz vectors. The proposed model order reduction strategy accelerates the computation of transfer functions in fluid-filled extended piping systems. In order to validate the simulation results, experimental results are obtained by a hydraulic test bench for dynamic measurements, where fluid pulsation is induced by piezo-driven transducers. The observed fluid-structure interaction phenomena correspond to the predictions by the proposed computation approach.

THE TESTING BEHIND THE TEST FACILITY: THE ACOUSTIC DESIGN OF THE NASA GLENN RESEARCH CENTER'S WORLD-CLASS REVERBERANT ACOUSTIC TEST FACILITY

William O. Hughes, Mark E. McNelis, Aron D. Hozman, and Anne M. McNelis

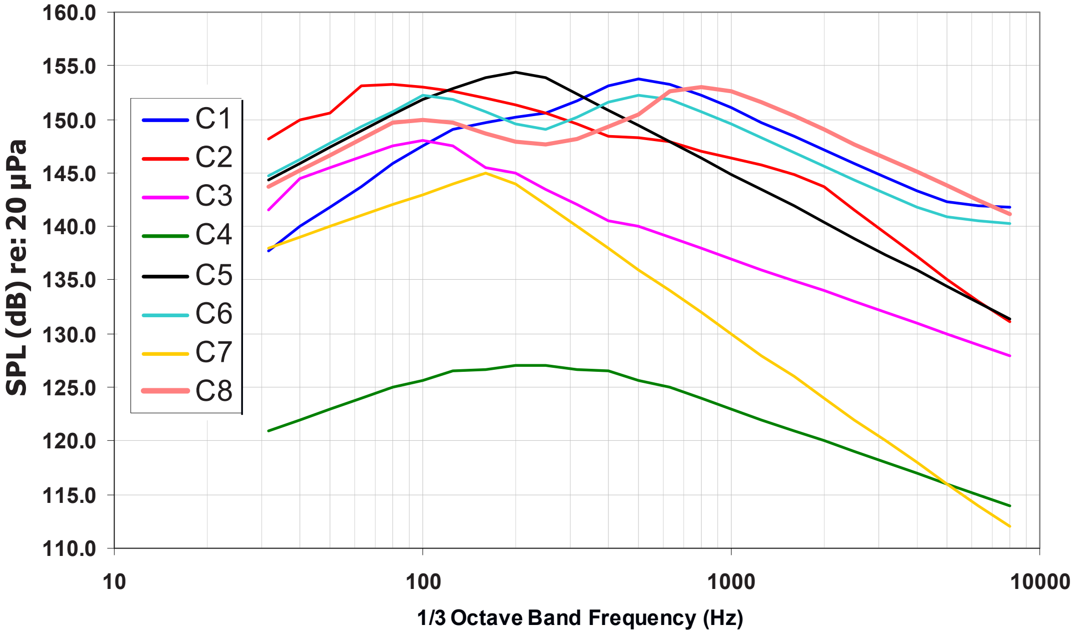

Figure 1. Acoustic Test Spectra Requirements

3. RATF Chamber Sizing and Initial Acoustic Modulator Selection

The physical size of the RATF was determined from the maximum available space within the SPF, along with following guidelines on proper room ratios and good acoustic test practices. Benham and Aiolos ultimately designed a reverberant acoustic test chamber with the following dimensions: 47.5-ft long x 37.5-ft wide x 57-ft high. After accounting for the main chamber door jamb structure the resulting chamber volume is 101,189 ft^3.

The next design issue was to determine the number and type of acoustic modulators or noise generators that would be needed to create the enormous sound power necessary to sustain the high SPL in this large chamber volume. Prior to the "C" acoustic spectra requirements becoming effective in September 2008, six other spectra were originally required including three spectra whose characteristics and SPL were very similar to the C2 spectra. As seen in Fig. 1, C2 is particularly challenging due to its very high SPL at frequencies below 100 Hz. This need led Benham and Aiolos to initially select the TEAM Corporation (TEAM) modulators known as the MK-VI and MK-VII, and propose using horns with three different cut-off frequencies (25, 35 and 50 Hz) for the RATF design. The TEAM modulators, although not widely utilized within the reverberant acoustic industry, are especially effective at the low frequencies (at or below the 125 Hz OTOB) with a rated modulator acoustic power of 150 kW (kilowatts) and 200 kW, respectively.

Although the TEAM modulators have been in service for over 50 years, there was not much acoustic characterization data available on them. To obtain characterization data, and to qualify and mitigate any associated risk, Aiolos, jointly with staff at the National Research Council of Canada (NRC) designed and conducted a test program at the Ottawa NRC reverberant acoustic test facility.

4. Initial NRC Testing, Part 1 (Aiolos):

- Date: December 2007 to January 2008
- Location: Reverberant acoustic chamber at the NRC, Ottawa, Ontario, Canada. NRC's chamber is 32-ft L x 22.6-ft W x 26.3-ft H, with a volume of ~ 19,000 ft^3.
- Objectives: a) Validate the acoustic performance and obtain operating parameters of the TEAM modulators, b) Obtain acoustic test data to benchmark RATF's acoustic predictions.
- Equipment: a) MK-VI and MK-VII modulators, b) 25 Hz and 100 Hz horns
- Findings: a) MK-VI and MK-VII modulators achieved the published acoustic power, b) No major impact of modulator supply pressure on acoustic performance was observed, c) Two modulators operating simultaneously on two horns, result in the same acoustic output as the acoustic sum of two modulators operating individually, d) Results for two modulators operating on one horn via a Y-adaptor produced less than the expected doubling, e) The modulator's output varied linearly with input gain, f) The modulator's bias setting (a measure of the force required to hold the modulator valve closed) requires further exploration to optimize its effect on noise generation, g) Two modulator shaft failures occurred.

- Go-forward plan: a) The TEAM modulator's performance, especially at low frequencies, showed promise for meeting the RATF requirements, b) Need for additional understanding of affect of bias, c) Need to instrument the modulator shaft to understand modulator failure that was then believed to be due to assembly workmanship.

5. Initial NRC Testing, Part 2 (Aiolos):

- Date: April 2008
- Location: Reverberant acoustic chamber at the NRC, Ottawa, Ontario, Canada
- Objectives: a) Examine quantitative relation of bias to modulator efficiency and spectral control, b) Utilize various spectral input signal shapes for open loop testing, c) Add gas accumulator to stabilize supply gas pressure variations, d) Instrument TEAM modulator shaft with strain gauges to provide data to assess previous shaft failures.
- Equipment: a) MK-VI, MK-VII modulators, b) 25 Hz, 100 Hz and 200 Hz horns
- Findings: a) Confirmed minimal effect of gas supply pressure, b) TEAM modulators were controllable from the 25 Hz to 500 Hz OTOB, c) Optimal bias setting produced peak acoustic performance, d) Demonstrated excellent repeatability in acoustic performance, e) Performance between the 630 Hz to 800 Hz OTOB is due to nonlinear spillover and flow noise, f) Performance with the 200 Hz horn was poor due to inadequate connections and subsequent gas flow problems, and g) One additional modulator shaft failure occurred.
- Go-forward plan: a) TEAM Modulators controllability, repeatability and acoustic performance is sufficient for RATF design, especially at low to mid frequencies, b) Shaft failures of TEAM modulators pointed to reliability issues and need to reanalyze and redesign shaft.

6. Redstone Testing (NASA):

Due to the TEAM modulator's shaft reliability issues, the lack of credible data from a high frequency horn (greater than 100 Hz), and continuing external questions on the controllability and acoustic performance of the TEAM modulators, NASA GRC performed its own independent test program to obtain additional acoustic test data and experience with the TEAM modulator [3]. Since the U.S. Army's Redstone Arsenal has many years of experience with the TEAM modulator it was chosen by NASA GRC as the test site.

- Date: May 2008
- Location: Reverberant acoustic chamber at the U.S. Army Redstone Technical Test Center (RTTC) in Huntsville, AL, USA. The Redstone Arsenal chamber is 28.5-ft L x 24.3-ft W x 18.0-ft H, with a volume of ~ 12,500 ft^3.
- Objectives: a) Obtain independent verification of the TEAM modulator acoustic performance (controllability, shape-ability, and repeatability), b) Collect data on two additional horn sizes (50 Hz and 167 Hz), c) Compare the response of the TEAM modulator in two facilities (RTTC and NRC), d) Compare the response of the TEAM MK-VI and the Wyle Laboratories' WAS3000 modulators at the same facility (RTTC).
- Equipment: a) MK-VI modulator, b) WAS3000 modulator, c) 50 Hz and 167 Hz horns
- Findings: a) Confirmed the NRC test findings of controllability, shape-ability and repeatability for the TEAM modulator, b) TEAM modulator performed well with the 167 Hz horn, c) Test data validated the analytical scaling procedures for using data in one chamber to predict the response in a different chamber, d) Test data confirmed superposition of modulators' output, e) The acoustic output of the MK-VI TEAM modulator was higher than that of the WAS3000 modulator by 6-7 dB at 25 Hz to 100 Hz OTOB; similar from 125 Hz to 1000 Hz OTOB; and higher by 2-3 dB from 1000 Hz to 8000 Hz OTOB due to non-linear spillover. Both modulators allowed the generation of shaped spectra by controlling the input signal from 50 Hz to 630 Hz.
- Go-forward plan: a) Pending a successful resolution of TEAM Modulator shaft failures, incorporate TEAM modulators into the RATF design, b) In addition to previously planned use of low frequency horns, incorporate 160 Hz horn for RATF design.

7. Phase 1 Testing at NRC (Aiolos):

Once the C-curve acoustic requirements (Fig. 1) replaced the original acoustic requirements in September 2008 it became necessary to revisit the previous horn selection and related acoustic design, and augment the TEAM noise generators with additional high frequency sources. Additionally, test verification of the closed loop control of the TEAM modulators was planned as part of a new two-phase test program. Finally, the TEAM modulator shaft was extensively redesigned to avoid fatigue life issues and this new design and its performance needed to be test verified.

- Date: March - April 2009

- Location: Reverberant acoustic chamber at NRC, Ottawa, Ontario, Canada
- Objectives: a) Examine the acoustic performance of impinging gas jets, proposed as one alternative to the required high frequency noise sources, including their controllability, and other design features such as impinging plates and means for minimizing screech tones, b) Reconfirm TEAM modulator's acoustic performance and life reliability with new shaft design, c) Perform closed loop control of a single TEAM modulator, and d) Quantify the dynamic range of the TEAM modulator.
- Equipment: a) MK-VI and MK-VII modulators, b) 25 Hz and 160 Hz horns, c) Gas jets with various nozzle diameters, adjustable support frames, impingement plates, reflectors and chevrons
- Findings: a) Gas jets were able to produce high sound pressure levels but generally only in the presence of intense screech tonal noise. Reduction of screech tones was possible using vortex tabs and chevrons at the nozzle exit but at the expense of significantly reduced OASPL. The expected benefit of impinging plates to amplify sound, and reflectors to reduce the screech tones were not observed [4, 5]. Significantly more jets than originally expected, and accompanying gas flow, would be needed to satisfy RATF requirements, b) Endurance testing of the TEAM modulator demonstrated that the shaft problem was resolved through the redesign; the measured stress levels were greatly reduced and very close to the predicted levels by TEAM Corporation, c) Testing also confirmed that the shaft redesign caused no significant change in the acoustic performance, d) Closed loop control testing of the TEAM modulator with the NRC control software was successful, e) The dynamic range was found to be ~ 6-9 dB for the MK-VI and ~ 9-12 dB for the MK-VII modulators.
- Go-forward plan: a) Incorporate TEAM modulators into RATF design, b) To add robustness to the RATF design to handle future spectra, increase the number of horns types (incorporate several different horn cutoff frequencies for RATF design), c) Gas jets are not to be incorporated, but instead evaluate the proposal to incorporate the Wyle WAS5000 modulator (similar to Ling EPT-200 modulator), d) Aiolos to proceed with contract to select acoustic control system (ACS) for RATF and to demonstrate the ACS performance in the Phase 2 testing at NRC.

8. Phase 2 Testing at NRC (Aiolos):

- Date: October 2009
- Location: Reverberant acoustic chamber at NRC, Ottawa, Ontario, Canada
- Objectives: a) Characterize the Wyle Laboratories WAS5000 modulator acoustic performance in a similar manner as the TEAM modulator, including investigating the use of an extension spool between the WAS5000 modulator and horn, b) Demonstrate the operation of the m+p International ACS, including the simultaneous closed loop control of the three modulators (TEAM MK VI and MK VII, Wyle WAS5000).
- Equipment: a) MK-VII modulator on 25 Hz horn, b) MK VI modulator on 100 Hz horn, c) WAS5000 modulator on 250 Hz horn, d) m+p International ACS
- Findings: a) WAS5000 modulator's acoustic performance met or exceeded the expectations going into this test, b) The spool piece is not needed, c) The m+p ACS performed very well controlling three modulators simultaneously meeting the specified test tolerances, stability and ramp-up rates. Given the fact that there were only 3 modulators and 3 horns the ACS exceeded expectations in demonstrating compliance to a variety of acoustic spectra, including the scaled down C-curve acoustic spectral shapes.
- Go-forward plan: a) Incorporate the WAS5000 modulators on a 250 Hz horn into the RATF design, b) Incorporate the m+p ACS system into the RATF design.

9. Paint Absorption Testing at Owens Corning (NASA):

The last remaining key parameter to benchmark was the acoustic absorption of the RATF chamber. In particular, the acoustic absorption of the wall paint planned by Benham for the RATF interior surfaces is an important factor to the RATF's SPL at the mid to high frequencies (200 Hz to 3000 Hz OTOB). NASA wanted to measure this absorption [6, 7] for the Benham selected paint as part of the NASA risk mitigation efforts to further establish confidence in the RATF predictions. Cambridge Collaborative Incorporated (CCI) led and performed this test for NASA.

- Date: February – March 2010
- Location: Small reverberant acoustic chamber at Owens Corning's Acoustic Research Center, Granville, OH. The Owens Corning chamber is 20.9-ft L x 14.7-ft W x 12.7-ft H, with a volume of ~ 3,900 ft^3.
- Objectives: a) Measure the acoustic absorption of the Owens Corning chamber painted with the proposed RATF paint. b) Compare results with expectations and values used in Aiolos' SPL predictions for RATF.
- Equipment: a) Chamber coated with Benham proposed RATF paint, b) B&K (Bruel and Kjaer) sound source, c) Loudspeakers

- Findings: a) Measured test data and subsequent decay rate analysis indicates that the selected paint has absorption characteristics consistent with expectations and with predicted analytical values used by Aiolos for their RATF acoustic predictions and design.
- Go-forward plan: a) Approve the paint selected by Benham for use in RATF chamber.

10. Conclusions:

From the beginning, Benham, Aiolos and NASA have agreed that it was important to ground the acoustic predictions of the RATF chamber with actual test data. This was especially important given the extreme SPL required for RATF, as well as the lack of available performance data for the TEAM MK-VI and MK-VII and the Wyle WAS5000 acoustic modulators. Therefore as explained in this paper, numerous and extensive test programs were completed to obtain the necessary test data to benchmark the RATF acoustic predictions. These test series have provided NASA with the confidence to proceed with the Benham and Aiolos design for RATF.

The overall layout and key properties of the RATF chamber and horn room are illustrated in Figure 2. There will be a total of 36 modulators and 36 horns to produce the acoustic power to meet the RATF requirements. The RATF design has eleven (11) MK-VII modulators distributed on the 25, 35, 50 and 80 Hz horns, twelve (12) MK-VI modulators distributed on the 100 and 160 Hz horns, and thirteen (13) WAS5000 modulators on the 250 Hz horns. In order to meet the gaseous nitrogen (GN2) flow rate needs for these 36 modulators a vaporizer capable of a GN2 flow rate of 72,000 SCFM (standard cubic feet per minute) will be used.

Due to physical limitations within the SPF all the horns will be located on the shared horn room/test chamber wall. The final layout of the 36 horns is shown in Figure 3. If it ever becomes necessary to increase the number of horns/modulators, there are scarring plans which will allow for an additional seven (7) WAS5000 modulators to be installed, as well as additional horn room wall space for future expansion. The chamber walls, ceiling and foundation have been designed and built to withstand up to 166 dB OASPL.

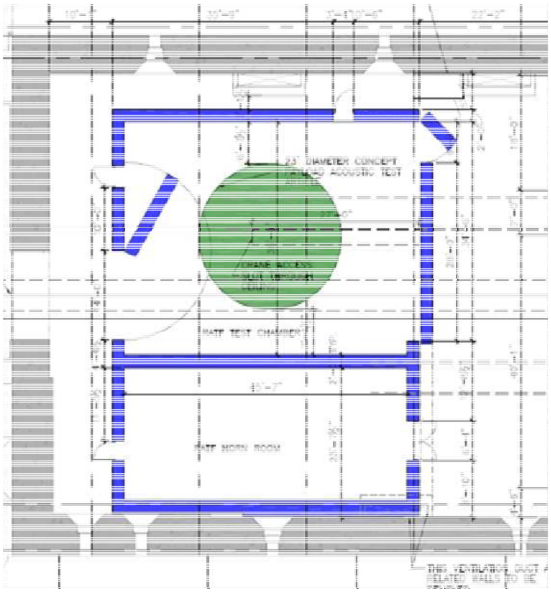

	Chamber Properties
Chamber Size	47.5 ft L x 37.5 ft W x 57 ft H
Chamber Volume	101,189 ft^3
Acoustic Modulators	23 TEAM Modulators & 13 WAS 5000 Modulators
Horns	36 (grouped at 7 different horn cut-off frequencies)
Nominal GN$_2$ flow rate	72,000 scfm
Main Door Opening	34.5 ft wide
Number of Main Doors	2
Door Type	Sliding and hinged
OASPL, empty	163 dB OASPL

Figure 2. RATF Acoustic Design

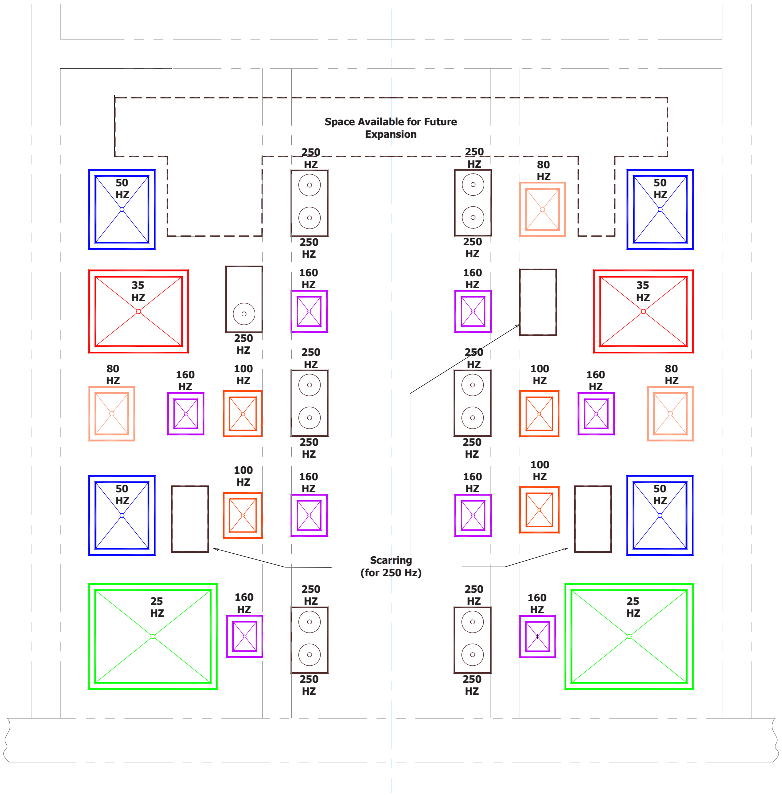

Figure 3. **RATF Horn Wall Layout**

Benham is scheduled to complete the construction of the RATF by early autumn 2010. There will then be a period of several months where Benham will complete their verification testing of the facility, prior to turning the RATF over to NASA. NASA then plans on performing a series of internal tests, with an “available for customer testing” target date of the autumn of 2011.

NASA has high confidence that through the extensive series of acoustic tests summarized in this paper, the RATF will perform to its expected requirements. It is anticipated that the most difficult acoustic spectra to meet will be the C8 curve (spectra with two peaks at 100 Hz and 800 Hz), especially between 1000 to 2000 Hz. Due to its combination of very high chamber sound pressure levels and large volume, the RATF will be the world’s most powerful reverberant acoustic test facility.

ACKNOWLEDGEMENTS

The authors would like to acknowledge the NASA SET Project Office for their continuing support and funding for the test programs discussed in this paper. The extensive contributions of the following organizations and individuals are particularly worthy of mention for their substantial role in this testing and the test data analysis effort:

- Benham Companies, LLC: Neil Waggoner, Josh Loehrke
- Aiolos Engineering Corporation: Ralph Leitner, Dr. Gary Elfstrom, Dr. Ramani Ramakrishnan, Alex Holzwarth, Sergio Raimondo
- TEAM Corporation: Bob Tauscher, Bill Woyski, Chon Mech
- Wyle Laboratories: Dr. Costa Glaretas, Chito Hermoso
- m+p International: Al Prosuk, Guido Bossaert
- Cambridge Collaborative Incorporated: Dr. Jerry Manning, Dr. Patricia Manning
- National Research Council: Dr. David Zimcik, Dr. Anant Grewal, Dr. Eric Chen, Viresh Wickramasinghe, Brent Lawrie, Luc Hurtubise
- Redstone Technical Test Center: Dr. Mike Hale
- Owens Corning: Kevin Herreman, Don Hill

REFERENCES

[1] W.O. Hughes, M.E. McNelis, A.D. Hozman, and A.M. McNelis, “Status and Design Features of the new NASA

GRC Reverberant Acoustic Test Facility (RATF)”,

Detection of Damage in Space Frame Structures with L-shaped Beams and Bolted Joints Using Changes in Natural Frequencies

K. He and W.D. Zhu

Abstract It is difficult to use conventional non-destructive testing methods to detect damage, such as loosening of bolted connections, in a space frame structure due to the complexity of the structure and the nature of the possible damage. A vibration-based method that uses changes in the natural frequencies of a structure to detect the locations and extent of damage in it has the advantage of being able to detect various types of damage in the structure. Since the vibration-based method is model-based, applying it to a space frame structure with L-shaped beams and bolted joints will face challenges ranging from the development of accurate dynamic models for the structures to that of a robust damage detection algorithm for severely under-determined, nonlinear least-square problems under the effects of relatively large modeling error and measurement noise. With the development of the modeling techniques for fillets in thin-walled beams (He and Zhu, 2009, "Modeling of Fillets in Thin-Walled Beams Using Shell/Plate and Beam Finite Elements," ASME J. Vibr. Acoust., 131(5), p. 051002) and bolted joints (He and Zhu, "Finite Element Modeling of Structures with L-shaped Beams and Bolted Joints," ASME J. Vibr. Acoust., in press) by the authors, accurate physics-based models of space frame structures can be developed with a reasonable model size. A new damage detection algorithm that uses a trust-region search strategy combined with a logistic function transformation is developed to improve the robustness of the vibration-based damage detection method. The new algorithm can ensure global convergence of the iterations

---

K. He
Graduate Research Assistant
Department of Mechanical Engineering, University of Maryland, Baltimore County
1000 Hilltop Circle Baltimore, MD 21250,
email:hekun1@umbc.edu

W.D. Zhu
Professor; Corresponding Author
Department of Mechanical Engineering, University of Maryland, Baltimore County
1000 Hilltop Circle Baltimore, MD 21250,
email:wzhu@umbc.edu

T. Proulx (ed.), *Sensors, Instrumentation and Special Topics, Volume 6*, Conference Proceedings of the Society for Experimental Mechanics Series 9,
DOI 10.1007/978-1-4419-9507-0_26, © The Society for Experimental Mechanics, Inc. 2011

and minimize the effects of modeling error and measurement noise. The damage detection method developed is experimentally validated on an aluminum three-bay space frame structure with L-shaped beams and bolted joints. Three types of introduced damage, including joint damage, member damage, and boundary damage, were successfully detected. In the numerical simulation where there is no modeling error and measurement noise, the almost exact locations and extent of damage can be detected.

1 Introduction

Space frame structures are widely used engineering structures and have been frequently used in the studies on structural damage detection. Typical damage in a space frame structure includes distortions of beam members and defects and degradations at its joints and boundaries. It is difficult to use the conventional nondestructive testing (NDT) methods, such as penetrant testing, ultrasonic testing, and electromagnetic testing, to detect damage in a space frame structure, since there is no obvious material loss associated with the damage, and the material of the structure is naturally discontinuous at its joints and boundaries. The topological complexity of a space frame structure also increases the difficulty of implementing conventional NDT methods since these methods often require local access to the test structure.

As global damage detection methods, the vibration-based methods that use changes in vibration characteristics of a structure, such as natural frequencies, mode shapes, and frequency response functions (FRFs), to detect the locations and extent of damage in the structure can overcome the disadvantages of the conventional NDT methods. Because the vibration characteristics can be remotely measured at a few locations of the test structure, there is no need to locally inspect the test structure in vibration-based damage detection. Also, because the vibration-based damage detection methods utilize the relations between the vibration characteristics of a structure and the physical properties such as the mass density and the stiffness of the structure, they aim to detect the changes in the physical properties caused by damage, regardless of specific types of damage. Hence they can be used to detect various types of damage in a structure, including those that occur at its joints and boundaries.

While the vibration-based damage detection methods have been widely investigated [1], most of the research focuses on detection of damage in simple structures such as beams and plates. Application of the vibration-based methods to such complex structures as space frame structures with thin-walled beams and bolted joints has not been fully investigated. Lim and Kashangak [2] developed a two-stage approach that uses changes in the natural frequencies and mode shapes to detect damage in an eight-bay space truss. The locations of damage were detected in the first stage using changes in the measured mode shapes, and the extent of damage was determined in the second stage using changes in the measure natural frequencies and mode shapes. Wu and Li [3] used changes in the natural frequencies to detect damage in a benchmark steel space frame structure. A two-stage eigen-sensitivity-based finite element (FE) model updating method was first used to update the connection stiffness of the base-line FE model of the benchmark space frame; the same method was then used to detect introduced damage in the structure. Sorohan [4] also used FE model updating methods to detect damage in an eight-bay space truss with free boundaries. The measured eigen-parameters and FRFs were first used to update the base-line FE model of the truss; damage detection was then conducted to identify the locations and extent of damage using the measured data. Because the vibration-based damage detection algorithms mentioned above originate from the FE model updating algorithms, an accurate FE model of the structure under investigation is required before damage detection can be conducted.

While it is not difficult to develop an accurate FE model of a simple structure such as a beam or plate, it is difficult to develop an accurate FE model of a complex structure such as a space frame structure with thin-walled beams and boltded joints. The effect of relatively large modeling error is the major obstacle that prevents the vibration-based damage detection methods from being applied to complex structures. The effect of modeling error can be reduced from two aspects: i) developing a more accurate FE model, which is associated with the so-called forward problem, and ii) enhancing the robustness of the damage detection algorithm by reducing the sensitivity of a damage detection algorithm to the presence of modeling error and measurement noise, which is associated with the so-called inverse problem. Sections 1.1 and 1.2 will address in detail the issues associated with the forward and inverse problems in vibration-based damage detection. Because it is much easier to measure the natural frequencies of a structure than the mode shapes, and the accuracy of the natural frequency measurement is higher than that of the mode shape measurement [5], only changes in the natural frequencies are used in damage detection in this work. As will be shown in the numerical simulation and experimental damage detection, changes in the natural frequencies can provide sufficient information about the locations and extent of damage, as long as a sufficient number of natural frequencies are used.

1.1 The Forward Problem

As defined in Ref. [1], the forward problem in damage detection refers to the calculation of the changes in the vibration characteristics caused by damage. When only the natural frequencies are used in damage detection, the changes in the natural frequencies are calculated by comparing the measured natural frequencies to the predicted ones generated by a FE model. Both the changes in the natural frequencies caused by damage and those due to modeling error and measurement noise are included in the forward problem. To obtain meaningful results in damage detection, the modeling error must be minimized so that the changes in the natural frequencies due to it are smaller than those caused by damage. To achieve this, the base-line FE model of a test structure is often updated using the measured data before damage detection is conducted [2, 3, 4]. Updating the base-line model can improve the accuracy of the model if the major modeling error is caused by the inaccuracy of the parameters to be updated[6]. However, selection of the parameters to be updated can be difficult, especially when the structure under investigation is complex. For model-based damage detection, the FE model should be physics-based so that it can accurately predict the vibration characteristics of the test structure at both the undamaged and damaged statuses. If the parameters to be updated are not properly selected, the model updating can result in a FE model with less physical meaning than the one before updating even though it can accurately reproduce the measured data used in the updating [5]. For a space frame structure with simple slender beam members and relatively small joints, as the case in Refs. [2, 4], it is reasonable to attribute the modeling error to its joints since the beam members can usually be accurately modeled, and to choose the connection stiffnesses at the joints as the parameters to be updated [6]. However, the space frames used in many engineering structures are usually more complex than those previously studied. A practical space frame structure usually consists of thin-walled (e.g., L-shaped or I-shaped) beams connected by bolted joints. To avoid buckling, the length-to-width ratios of the beam members are usually relatively small; the sizes of the bolted joints are relatively large due to safety concerns. Due the bending-torsion coupled vibrations of the short L-shaped and I-shaped beams [7], it is difficult to accurately model them using simple beam elements in the FE model. Also, a large bolted joint cannot be accurately modeled by a simple connection stiffness in the FE model [8]. The model updating strategy used in Refs. [2, 3, 4] is not applicable to complex space frame structures, and the FE models of these structures need to be improved in a physics-based way.

With the modeling techniques for fillets in thin-walled beams [7] and bolted joints [8] developed by the authors, space frame structures with thin-walled beams and bolted joints can be accurately modeled with a reasonable model size, as shown in Section 2; the modeling error for the natural frequencies can be reduced to a minimum level.

1.2 The Inverse Problem

The inverse problem in vibration-based damage detection refers to identification of the locations, and sometimes extent, of damage from changes in the vibration characteristics [1]. There are many approaches to formulate the inverse problem [1]; a typical approach to solve the inverse problem associated with damage detection is the so-called parametric methods [6], where damage detection is conducted on a parametric FE model of a test structure. While the parametric methods associated with damage detection essentially originate from FE model updating [5], and both the FE model updating and the damage detection inverse problem can be formulated as a nonlinear least-square problem, the numbers of parameters involved in the two problems usually differ, with the former usually being an over-determined problem and the latter an under-determined problem, as indicated below, which leads to different strategies to solve for the problems.

Because only a limited number of natural frequencies, mode shapes, and FRFs measured from a test structure can be accurately predicted by the FE model of the structure, the number of measured data that can be used in model updating and damage detection is limited. In the FE model updating, because the number of uncertainties associated with the base-line model is limited, the number of parameters to be updated is less than that of the measured data; the problem is over-determined [6]. In damage detection, unless the locations of damage are known, the number of parameters representing potential damage is usually greater than that of the measured data; the problem is under-determined. To solve a small residual nonlinear least-square problem associated with model updating [5], the Gauss-Newton method was used in Ref. [5] as it can avoid calculation of the second-order derivative of the objective function and has a rapid convergence speed [9]. While the Gauss-Newton method works efficiently for an over-determined nonlinear least-square problem, it has natural disadvantages for an under-determined problem due to the following two reasons. First, the Gauss-Newton method cannot ensure global convergence of the iterative algorithm when the nonlinear least-square problem is under-determined. In an iterative algorithm, the angle between the search direction and the negative gradient of the objective function should be uniformly bounded away from $\frac{\pi}{2}$ to ensure that the iterations will converge to a stationary point of the objective function [9]. Due to the rank-deficiency of the Jacobian matrix, the search direction generated by the Gauss-Newton method cannot always satisfy this condition. Second, the Gauss-Newton method is sensitive to the presence of modeling error and measurement noise. Because there is an infinite number of solutions at each iteration for an under-determined problem, a unique solution must be determined using a form of regularization to ensure convergence of the iterative algorithm [6]. Use of the Moore-Penrose inverse is a typical regularization approach to solve for a unique search step at each iteration, and it will lead to a solution with a minimum change to the starting point [5]. However, because the search step calculated by the Moore-Penrose inverse is controlled by the smallest singular values of the Jacobian matrix, use of the Moore-Penrose inverse will amplify the effects of modeling error and measurement noise, especially when the condition number of the Jacobian matrix is relatively large [5]. For damage detection of complex space frame structures, where modeling error is relatively large and the problem can be severely under-determined, the inverse algorithm using the Gauss-Newton method combined with the Moore-Penrose inverse would not be sufficiently robust, as illustrated in Section 3.1.

To avoid the above problems, the locations and extent of damage in a complex structure were separately detected in two stages [2, 3, 4, 10]. Since the locations of damage were determined in the first stage using the measured mode shapes or other measured data [2, 3, 4], the number of parameters to be identified in the second stage was significantly reduced and the problem became over-determined. Because a two-stage method usually requires accurate measurement of mode shapes [2, 3, 4], which usually incurs a relatively large error (over 10%) [11], it is difficult to apply it to a complex space frame structure, especially when damage in the structure is small.

Also, because a two-stage method involves intensive computation to eliminate damage location parameters [10], it requires considerable computational resources to detect damage in a structure with a large model size.

To resolve these problems, a trust-region optimization method called the Levenberg-Marquardt (LM) method, is used in this work, in conjunction with a logistic function transformation to convert the constrained nonlinear least-square problem to an uncnstrained one. Because the trust-region search strategy restricts the length of the search step at each iteration, use of the LM method can avoid an extraordinarily long search step caused by an ill-conditioned Jacobian matrix and control the amplification of modeling error and measurement noise. More importantly, use of the LM method can ensure global convergence of the iterative algorithm if the radius of the trust region is properly selected. The LM method will be discussed in detail in Section 3.2. The damage detection algorithm developed is applied in Section 4 to a three-bay space frame structure with L-shaped beams and bolted joints. It can successfully detect damage introduced to a beam member, a bolted joint, and a boundary of the structure.

2 Physics-Based Modeling of a Space Frame Structure with L-shaped Beams and Bolted Joints

To study damage detection of complex space frame structures, a three-bay space frame structure with L-shaped beams and bolted joints was fabricated in the authors' laboratory (Fig. 1). The structure is made of 6061-T651 aluminum with the density $\rho = 2731.4\ kg/m^3$, Poisson's ratio $\nu = 0.33$, and elastic modulus $E = 68.9$ GPa. The height, width, and depth of the space frame structure are 1.849 m, 0.511 m, and 0.611 m, respectively. It consists of 12 vertical, thin-walled L-shaped beams, 12 horizontal rectangular beams, and two diagonal rectangular beams. The L-shaped beams and the horizontal beams are connected by 12 bolted joints. The width and thickness of the rectangular beams are 0.0381 m and 0.0127 m respectively; the lengths of the longer horizontal and diagonal beams are 0.586 m and 0.755 m respectively, and those of the shorter ones are 0.486 m and 0.650 m respectively. The bolts (Hex Head $M10 \times 35 - 8.8$) are made of steel with an elastic modulus $E_b = 210$ GPa. The four lowest L-shaped beams are bolted to a plate through four cubes, and the length of each side of the cubes is 0.0402 m. The plate, whose thickness, width, and depth are 0.0108 m, 0.5 m, and 0.6 m, respectively, is bolted to the ground through four bolts, as shown in Fig. 1. Note that the plate is not in contact with the ground surface; three washers with a thickness of 0.0024 m and a radius of 0.0135 m are inserted between the plate and the ground on each bolt mounted to the ground.

The natural frequencies of the structure were measured by 27 PCB U352C66 accelerometers. Two accelerometers were placed at each of the 12 bolted joints that connect the L-shaped beams and the horizontal beams, to measure the vibrations of the structure in two perpendicular horizontal directions. Two accelerometers were placed at the middle of two perpendicular horizontal beams at the top of the structure, and the other accelerometer was placed on the bottom plate (Fig. 1). A PCB 086C03 impact hammer with a plastic tip was used to impact two perpendicular horizontal beams at the top of the structure to excite the vibrations of the structure in two perpendicular horizontal directions. Five impact tests were averaged at either excitation location to ensure repeatable results with a good coherence. The measured data were collected and analyzed using an LMS 36-channel spectrum analyzer with the LMS Test.Lab 9B modal analysis software.

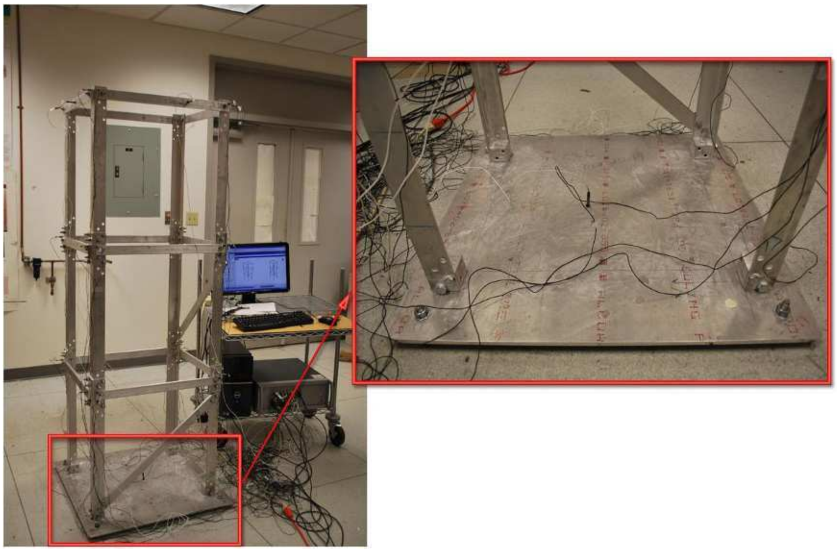

Fig. 1 An aluminum three-bay space frame structure with L-shaped beams and bolted joints, and an enlarged view of its lower boundaries

2.1 *Modeling of Fillets in L-shaped Beams*

As mentioned in Section 1.1, modeling a complex space frame structure using simple beam elements will lead to a large modeling error due to the bending-torsion coupled vibrations of an L-shaped beam and the complexity of the bolted joints. While the bending-torsion coupled vibrations of an L-shaped beam can be captured by a shell element model, it is difficult to model the fillet, which is used to reduce stress concentration in the L-shaped beam, using only shell elements [7]. The effect of the fillet on the linear vibration of the L-shaped beam usually cannot be neglected in the FE model [7].

To resolve this problem, a simple beam and shell element model for fillets in thin-walled beams was developed by the authors [7]. The equivalent stiffness of a fillet can be decomposed into the in-plane stiffness and the out-of-plane stiffness, which can be assumed to be uncoupled and separately calculated [7]. The in-plane stiffness is associated with the cross-sectional deformation and the out-of-plane stiffness is associated with the bending and torsional stiffness of an L-shaped beam. The equivalent in-plane stiffness can be calculated by modeling half of the fillet as a curved cantilever beam subjected to a shear force and a bending moment at the tangent section of the half fillet (Fig. 2(a)), and the equivalent out-of-plane stiffness can be obtained by calculating the area moments of inertia and the torsional stiffness factor associated with the fillet area [7]. In the FE model of the L-shaped beam, the two stiffnesses of the fillet can be modeled using shell and beam elements (Fig. 2). The shell elements are used to mainly capture the in-plane stiffness although they also provide some out-of-plane stiffness; the beam elements are used to compensate for the out-of-plane stiffness that is not fully represented by the shell elements (Fig. 2(b)). The length and thickness of the shell elements are determined by matching the rotational displacement of a tangent section of the fillet with that calculated from the curved beam model under the same shear force and bending moment. The area moments of inertia of the beam elements are calculated by subtracting the area moments of inertia associated with the shell elements from that of the actual fillet area. The torsional stiffness factor of the beam elements is obtained by matching the torsional displacement of the beam elements with that of the fillet area subjected to the same torques at the tangent sections of the fillet [7].

With the fillet accurately modeled, a shell and beam element model of the L-shaped beam was developed using SDTools [12] (Fig. 2(b)) to capture its bending-torsioncoupled vibrations. The natural frequencies and mode shapes of the L-shaped beam predicted by the shell and beam element model developed have essentially the same accuracy as that of an intensive solid element model that has ten times more degrees-of-freedom (DOFs).

2.2 *Modeling of Bolted Connections*

A bolted joint in the middle of the space frame structure in Fig. 1 contains ten bolted connections, and the size of the bolted joint is approximately one fifth of that of an L-shaped beam; the effect of the bolted joint cannot be simply modeled by a connection stiffness in the FE model [8]. A more intensive model of the bolted joint needs to be developed. Direct modeling of a bolted connection in a bolted joint of the space frame structure in Fig. 1 is difficult due to its complex nonlinear behaviors and the uncertainties of the parameters such as the clamping forces, the contact interface properties, and the assembling pre-stresses. Direct simulation of the nonlinear behaviors of a bolted joint will encounter some challenges in experimental parameter identification and the numerical calculation in structural dynamic analysis [8, 13].

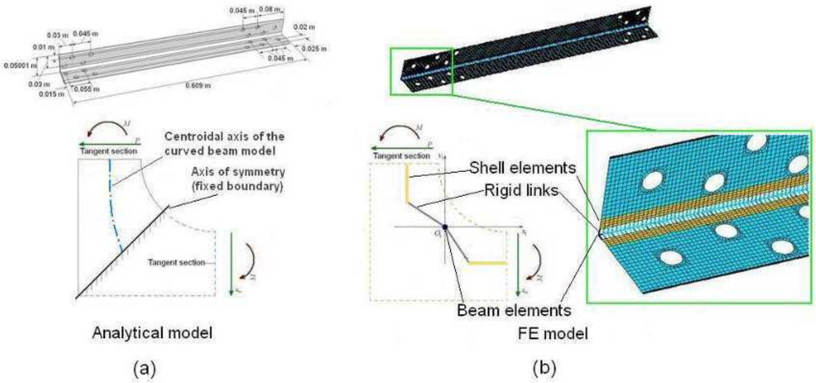

Fig. 2 (a) An analytical model of the fillet in an L-shaped beam whose dimensions are shown, and (b) its shell and beam element model

To resolve the problem associated with the modeling of a relatively large bolted joint, a simple, yet accurate, linear model of a bolted connection was developed by the authors [8]. In the FE model of a bolted joint that connects two L-shaped beams through a bracket (Fig. 3), the walls of the L-shaped beams and the bracket are modeled using shell elements, and a bolted connection is modeled by a solid cylinder [8]. The length of the cylinder is the sum of the length of the gap between the shell elements that represent an L-shaped beam and the bracket and that of the extruded part of the bolt outside the bracket surface. The radius and the material properties of the cylinder are the parameters that need to be determined. It was observed from the numerical simulation that the natural frequencies are more sensitive to the changes in the radius of the cylinder than the elastic and shear moduli [8]. The radius of the cylinder, which is the radius of the effective area of the bolted connection, can be approximated by the radius of the static contact area of the two clamped components under a sufficiently large clamping force, which can be calculated from an intensive contact model using ABAQUS 6.7-1; the resulting radius is 0.01043 m [8]. From the numerical simulation, it was also observed that the contact area is not sensitive to the changes in the contact interface properties and the material properties of the clamped components, and will remain a constant once the clamping force is greater than a threshold value; hence the FE model will be valid as long as the bolted connection is tightened and the clamping force is sufficiently large compared to potential external loading [8].

The elastic modulus of the cylinder can be obtained by matching the axial stiffness of the cylinder with that of the bolted connection calculated using the Rotsher's pressure cone method [14]; the calculated elastic modulus of the cylinder is 1.17 times the material elastic modulus [8]. For a tightened bolted connection, the shear modulus of the cylinder is set to be that of the material shear modulus of the clamped components, since the slip between them is neglected in the linear model of the bolted connection [8]. In addition, rigid-link constraints that can restrict the relative translational motion between the corners of the L-shaped beams and the bracket, and prevent the penetration between the clamped components, are included in the FE model (Fig. 3) [8]. With the parameters of the cylinder determined, the stiffness effect of a bolted connection in can be accurately modeled. The mass effect of a bolted connection is modeled by changing the mass density of the solid cylinder in the FE model, so that the mass of the cylinder equals that of the bolted connection [8].

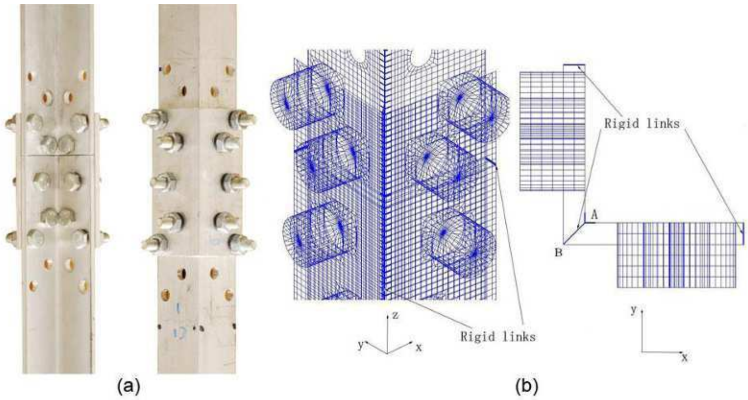

Fig. 3 (a) A bolted joint that connects two L-shaped beams through a bracket, and (b) its FE model from SDTools, with a bolted connection modeled by a solid cylinder

2.3 Modeling of the Space Frame Structure

With the challenges associated with the modeling of fillets in L-shaped beams and bolted joints resolved, an accurate FE model of the space frame structure in Fig. 1 was developed using SDTools (Fig. 4). The bottom plate and the rectangular beams are modeled by shell elements. The cubes, which are modeled by hexahedron solid elements, are fully connected to the plate and the lowest L-shaped beams through rigid links in the FE model. There are no brackets at the four bolted joints at the top of the structure; the rectangular beams are directly bolted on the flanges of the L-shaped beams. The radius of the effective area of these bolted connections is the same as that of a bolted connection in Fig. 3, since the thickness of the flange of the L-shaped beam is smaller than those of the rectangular beam and the bracket, and the radius of the static contact area is controlled by the thinner clamped component [8]. The radius of the effective area of the bolted connections that are used to mount the bottom plate to the ground is the radius of the washers between the plate and the ground, which is 0.01004 m. The elastic moduli of the solid cylinders for the bolted connections at the top of the structure and those at the boundaries are calculated to be $1.22E$. There are three clamped components in a bolted connection that connects a horizontal rectangular beam to a bracket and an L-shaped beam; the elastic modulus of the solid cylinder between the center planes of the rectangular beam and the bracket is $1.32E$, and that between the center planes of the bracket and the L-shaped beam is $1.27E$. There are $223,296$ DOFs in the FE model of the space frame structure. The natural frequencies calculated from the FE model are compared to the measure ones for the first 30 modes, as shown in Table 1; the maximum error is 1.86%.

When eight bolted connections in a bolted joint are loosened to hand-tight, as indicated in Fig. 4, the maximum change in the measured natural frequencies is 8.36% for the first 30 modes (1). By reducing the elastic and shear moduli of the solid cylinders corresponding to the loosened bolted connections, the FE model developed can still accurately model the space frame structure. When the elastic and shear moduli of the solid cylinders are reduced to 3.41% of their original values, the maximum error between the calculated and measured natural frequencies is 1.82% for the first 30 modes (Table 1).

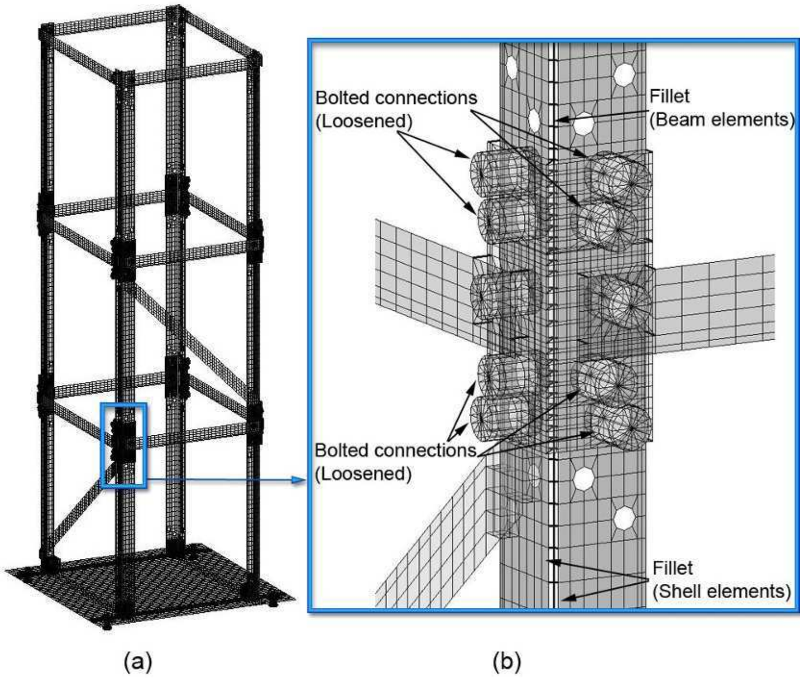

Fig. 4 (a) The FE model of the space frame structure in Fig. 1, and (b) an enlarged view of a bolted joint, where eight bolted connections are later loosened to hand-tight

Table 1 The measured (Exp) and calculated (FEM) natural frequencies of the first 30 modes of the space frame structure in Fig. 1 with all bolted joints tightened (undamaged) and eight bolted connections in a bolted joint loosened to hand-tight (Fig. 4) (damaged)

	Undamaged			Damaged			
Mode	Exp (Hz)	FEM (Hz)	Error	Exp (Hz)	FEM (Hz)	Error	Change
1	17.847	18.137	1.62%	17.656	17.794	0.78%	-1.07%
2	20.690	20.414	-1.33%	19.146	19.402	1.34%	-7.46%
3	28.031	28.088	0.20%	25.689	26.156	1.82%	-8.36%
4	39.031	38.367	-1.70%	38.133	37.470	-1.74%	-2.30%
5	57.695	58.102	0.71%	56.489	56.871	0.68%	-2.09%
6	61.215	60.892	-0.53%	60.114	60.215	0.17%	-1.80%
7	73.809	74.863	1.43%	72.481	73.337	1.18%	-1.80%
8	80.398	80.232	-0.21%	79.737	80.017	0.35%	-0.82%
9	88.476	88.548	0.08%	87.250	87.551	0.34%	-1.39%
10	90.649	90.863	0.24%	90.054	90.521	0.52%	-0.66%
11	93.839	94.233	0.42%	92.413	93.114	0.76%	-1.52%
12	98.522	98.394	-0.13%	96.288	96.949	0.69%	-2.27%
13	108.559	108.361	-0.18%	105.234	105.619	0.37%	-3.06%
14	115.100	144.841	-0.24%	112.425	113.210	0.70%	-2.32%
15	126.888	125.744	-0.90%	122.437	120.203	-1.82%	-3.51%
16	129.707	129.071	-1.26%	125.722	124.638	-0.86%	-3.07%
17	137.472	135.328	-1.56%	134.254	134.559	0.23%	-2.34%
18	148.130	146.295	-1.24%	145.327	144.804	-0.36%	-1.89%
19	150.431	149.123	-0.87%	148.733	147.108	-1.09%	-1.13%
20	157.488	157.504	0.01%	153.045	154.230	0.77%	-2.82%
21	161.676	161.293	-0.24%	161.925	160.016	-1.18%	0.15%
22	165.153	166.449	0.78%	165.045	164.083	-0.58%	-0.07%
23	168.036	167.465	-0.34%	168.080	165.259	-1.68%	0.03%
24	181.142	180.334	-0.45%	181.032	179.906	-0.62%	-0.06%
25	187.13	183.650	-1.86%	182.246	182.577	0.18%	-2.61%
26	192.408	189.267	-1.63%	186.243	184.114	-1.14%	-3.20%
27	198.522	197.591	-0.47%	197.072	196.494	-0.29%	-0.73%
28	209.405	207.822	-0.76%	209.659	207.563	-1.00%	0.12%
29	215.103	213.014	-0.97%	215.315	212.893	-1.12%	0.10%
30	217.930	216.117	-0.83%	216.898	213.689	-1.48%	-0.47%

3 Eigen-Sensitivity-Based Damage Detection Algorithm

Because the natural frequencies of a test structure and their first-order derivatives with respect to the parameters representing possible damage in the structure are used in damage detection, the algorithm used to solve the inverse problem is refered to as an eigen-sensitivity-based damage detection algorithm. Consider a test structure, e.g., a cantilever beam as shown in Fig. 5. Since damage can be anywhere in the cantilever beam, the beam is divided into many sections with each section corresponding to a possible damage location. The length of a section represents the minimum size of a possible damage at the corresponding location; it can range from the size of an element in the FE model to that of many elements. While smaller sections can provide a more accurate representation of damage, the size of a section does not need to be too small since the minimum size of detectable damage depends on the amount of damage information contained in the natural frequencies used in damage detection; decreasing the size of a section will also increase the number of damage locations to be identified. The size of a section should be properly selected, so that the natural frequencies used in damage detection have distinguishable sensitivities to damage represented by each section. While the length of each section does not need to be the same, a similar length of each section will be helpful as the sensitivities of the natural frequencies to the damage at each section can have a similar order of magnitude.

The stiffness of the $i-$th section can be represented by a non-dimensional stiffness parameter $0 < G_i \leq 1$, where $i = 1, 2, \ldots, n$, with $G_i = 1$ and $G_i = 0$ indicating that the $i-$th section is undamaged and fully damaged respectively. The stiffness of the entire beam can be represented by the vector $\mathbf{G} = [G_1\ G_2\ \ldots\ G_n]^{\mathrm{T}}$, where the superscript T denotes the transpose of a matrix. The m calculated natural frequencies of the test structure $\omega = [\omega_1(\mathbf{G})\ \omega_2(\mathbf{G})\ \ldots\ \omega_m(\mathbf{G})]^{\mathrm{T}}$, where a subscript denotes a mode number, are nonlinear functions of the stiffness parameters $\mathbf{G}$. With the m measured natural frequencies of the test structure ω_j^d, where $j = 1, 2, \ldots, m$, the damage detection algorithm will determine what changes in $\mathbf{G}$ can generate the changes in the natural frequencies due to damage. Since the number of the stiffness parameters n is usually greater than the number of the measured natural frequencies m used for damage detection, the problem is under-determined. Hence the damage detection problem can be formulated as an under-determined nonlinear least-square problem with bounded constraints, which minimizes the objective function:

$$Q(\mathbf{G}) = \frac{1}{2}\sum_{j=1}^{m}[\frac{\lambda_j(\mathbf{G}) - \lambda_j^d}{\lambda_j^d}]^2 = \frac{1}{2}\sum_{j=1}^{m} r_j^2 = \frac{1}{2}\mathbf{r}^{\mathrm{T}}\mathbf{r} \tag{1}$$

where $\lambda_j(\mathbf{G}) = \omega_j^2(\mathbf{G})$ and $\lambda_j^d = (\omega_j^d)^2$ are the $j-$th calculated and measured eigenvalues of the test structure respectively. Note that the relative changes in the natural frequencies, i.e., $r_j = \frac{\lambda_j - \lambda_j^d}{\lambda_j^d}$, are used here to obtain better numerical performance. When the stiffness parameters of the structure are identified, both the locations and extent of damage are known.

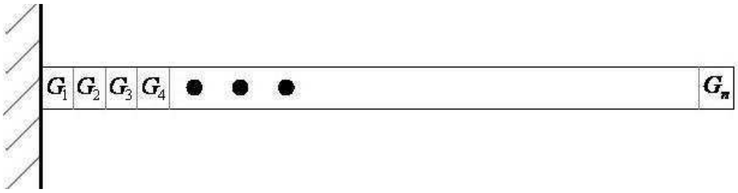

Fig. 5 A cantilever beam whose stiffness is represented by a set of non-dimensional stiffness parameters **G**

To make use of the available methods for solving nonlinear least-square problems [9], which are usually designed for unconstrained problems, a logistic function transformation is introduced to convert the constrained nonlinear least-square problem here to an unconstrained one:

$$G_i = \frac{1}{1+e^{-aS_i}},\ i = 1, 2, \ldots, n \tag{2}$$

where $a > 0$ is the index of the logistic function, which can be adjusted to change the convergence speed of the iterative algorithm; a is set to be 1 in this work. The transformation in Eq. (2) converts the search domain of G_i that is bounded between 0 and 1 to a new search domain of S_i that can vary from $-\infty$ to ∞. The objective function of the inverse problem becomes

$$Q(\mathbf{S}) = \frac{1}{2}\sum_{j=1}^{m}[\frac{\lambda_j(\mathbf{S})-\lambda_j^d}{\lambda_j^d}]^2 = \frac{1}{2}\sum_{j=1}^{m} r_j(\mathbf{S})^2 = \frac{1}{2}\mathbf{r}^{\mathrm{T}}(\mathbf{S})\mathbf{r}(\mathbf{S}) \tag{3}$$

where $\mathbf{S} = [S_1\ S_2\ \ldots\ S_n]^{\mathrm{T}}$.

A nonlinear least-square problem is usually iteratively solved using a Newton-type method [9]. The objective function in Eq. (3) is approximated by a second-order Taylor expansion around a selected initial point $\mathbf{S}_0$ [9]:

$$M(\mathbf{S}) = Q(\mathbf{S}_0) + \nabla Q(\mathbf{S}_0)(\mathbf{S}-\mathbf{S}_0) + \frac{1}{2}(\mathbf{S}-\mathbf{S}_0)^{\mathrm{T}}\nabla^2 Q(\mathbf{S}_0)(\mathbf{S}-\mathbf{S}_0) \tag{4}$$

where

$$\nabla Q(\mathbf{S}) = [\sum_{i=1}^{m} r_i\frac{\partial r_i}{\partial S_1}\ \sum_{i=1}^{m} r_i\frac{\partial r_i}{\partial S_2}\ \cdots\ \sum_{i=1}^{m} r_i\frac{\partial r_i}{\partial S_n}]^{\mathrm{T}} = \mathbf{J}^{\mathrm{T}}\mathbf{r} \tag{5}$$

is the first-order derivative of the objective function with respect to $\mathbf{S}$, in which $\mathbf{J} = [\frac{\partial r_i}{\partial S_j}]\ (i = 1, 2, \ldots, m;\ j = 1, 2, \ldots, n)$ is the Jacobian matrix, and

$$\nabla^2 Q(\mathbf{S}) = \mathbf{J}^{\mathrm{T}}\mathbf{J} + \sum_{q=1}^{m} r_q[\frac{\partial^2 r_q}{\partial S_i \partial S_j}], \quad \mathrm{i} = 1, 2, \ldots, n; j = 1, 2, \ldots, n \tag{6}$$

is the second-order derivative of the objective function with respect to $\mathbf{S}$. A stationary point of $M(\mathbf{S})$, $\mathbf{S}_1$, in the neighborhood of $\mathbf{S}_0$ can be found by setting

$$\nabla M(\mathbf{S}_1) = \nabla Q(\mathbf{S}_0) + \nabla^2 Q(\mathbf{S}_0)(\mathbf{S}_1-\mathbf{S}_0) = 0 \tag{7}$$

By replacing the subscripts 0 and 1 in Eq. (7) with k and $k+1$ respectively, where k denotes the current iteration number, and iteratively solving Eq. (7), a solution of the nonlinear least-square problem, which is a stationary point of the objective function in Eq. (3) near the initial point $\mathbf{S}_0$, can be found.

3.1 Gauss-Newton Method

Due to the special forms of ∇Q in Eq. (5) and $\nabla^2 Q$ in Eq. (6) in the nonlinear least-square problem, the first-order derivative and the first term of the second-order derivative of the objective function can be easily obtained by calculating the Jacobian matrix **J**. In the Newton method, much computational resource is spent on calculating the second term in Eq. (6) in order to obtain the second-order derivative of the objective function. In fact, because of the small residuals, i.e., r_j are small, the second term in Eq. (6) is negligible compared to the first term $\mathbf{J}^{\mathrm{T}}\mathbf{J}$ [9, 15]; hence $\nabla^2 Q(\mathbf{S})$ can be approximated by $\mathbf{J}^{\mathrm{T}}\mathbf{J}$, and Eq. (7) becomes

$$\nabla M(\mathbf{S}_{\mathrm{k+1}}) = \mathbf{J}^{\mathrm{T}}\mathbf{r} + \mathbf{J}^{\mathrm{T}}\mathbf{J}(\mathbf{S}_{\mathrm{k+1}} - \mathbf{S}_{\mathrm{k}}) = 0 \tag{8}$$

which happens to be the normal equation of the linear least-square problem:

$$\mathrm{Min}\, f(\mathbf{dS}) = \frac{1}{2}\|\mathbf{JdS} + \mathbf{r}\|^2 \tag{9}$$

where $\mathbf{dS} = \mathbf{S}_{\mathrm{k+1}} - \mathbf{S}_{\mathrm{k}}$ and $\|\bullet\|$ is the Euclidean norm, since $\nabla f(\mathbf{dS}) = \mathbf{J}^{\mathrm{T}}\mathbf{r} + \mathbf{J}^{\mathrm{T}}\mathbf{JdS}$. Solving an under-determined linear least-square problem becomes solving

$$\mathbf{JdS} + \mathbf{r} = 0 \tag{10}$$

There are an infinite number of solutions for Eq. (10), and a minimum-norm solution can be obtained from

$$\mathbf{dS} = -\mathbf{J}^{+}\mathbf{r} \tag{11}$$

where the superscript + denote the Moore-Penrose inverse. The above method is the Gauss-Newton method, which is essentially the method used in Ref. [16]; it is a typical line-search strategy for solving a small residual nonlinear least-square problem.

In the damage detection application, the Jacobian matrix **J** can be obtained by differentiating the eigen-equation with respect to **S** [5]. The eigen-equation of a stationary test structure is

$$(\mathbf{K} - \lambda_j \mathbf{M})\phi_j = 0, \quad j = 1, 2, \ldots m \tag{12}$$

where **K** and **M** are the stiffness and mass matrices of the test structure in the FE model respectively, and ϕ_j is the $j-$th mass-normalized eigenvector, satisfying $\phi_j^{\mathrm{T}}\mathbf{M}\phi_j = \mathbf{I}$, in which **I** is an identity matrix. Differentiating Eq. (12) with respect to S_i yields

$$(\mathbf{K} - \lambda_j \mathbf{M})\frac{\partial \phi_j}{\partial S_i} + [\frac{\partial \mathbf{K}}{\partial S_i} - \lambda_j \frac{\partial \mathbf{M}}{\partial S_i} - \frac{\partial \lambda_j}{\partial S_i}\mathbf{M}]\phi_j = 0 \tag{13}$$

Premultiplying both sides of Eq. (13) by ϕ_j^{T} yields

$$\phi_j^{\mathrm{T}}(\mathbf{K}-\lambda_j\mathbf{M})\frac{\partial\phi_j}{\partial S_i} = -\phi_j^{\mathrm{T}}[\frac{\partial\mathbf{K}}{\partial S_i} - \lambda_j\frac{\partial\mathbf{M}}{\partial S_i} - \frac{\partial\lambda_j}{\partial S_i}\mathbf{M}]\phi_j \tag{14}$$

Since $\mathbf{K}$ and $\mathbf{M}$ are symmetric matrices, $\phi_j^{\mathrm{T}}(\mathbf{K}-\lambda_j\mathbf{M}) = 0$ and Eq. (14) becomes

$$\frac{\partial\lambda_j}{\partial S_i} = -\phi_j^{\mathrm{T}}[\frac{\partial\mathbf{K}}{\partial S_i} - \lambda_j\frac{\partial\mathbf{M}}{\partial S_i}]\phi_j \tag{15}$$

With $\frac{\partial\lambda_j}{\partial S_i}$ calculated above, entries of $\mathbf{J}$ can be obtained:

$$J_{ij} = \frac{\partial r_i}{\partial S_j} = \frac{\partial\lambda_i}{\lambda_i^d\partial S_j} \tag{16}$$

If mass loss due to damage can be neglected, the partial derivative of $\mathbf{M}$ with respect to S_i in Eq. (15) vanishes. Also, by Eq. (2),

$$\frac{\partial\mathbf{K}}{\partial S_i} = \frac{\partial\mathbf{K}}{\partial G_i}\frac{\partial G_i}{\partial S_i} = \frac{\partial\mathbf{K}}{\partial G_i}\frac{-ae^{-aS_i}}{(1+e^{-aS_i})^2} \tag{17}$$

Since $\mathbf{K}$ is a linear function of G_i, $\frac{\partial\mathbf{K}}{\partial G_i}$ is a constant matrix and remains unchanged at each iteration, which can significantly reduce the computational cost in calculating the Jacobian matrix at each iteration.

While the Gauss-Newton method has a rapid convergence speed and is more efficient than the Newton method in solving a nonlinear least-square problem, it has two drawbacks when the problem is under-determined. First, using the Gauss-Newton method cannot ensure that the iterations will converge to a stationary point of the objective function [9]. The cosine of the angle θ between the search direction $\mathbf{dS}$ calculated using the Gauss-Newton method and the negative gradient of the objective function is [9]

$$cos\theta = -\frac{(\nabla Q)^{\mathrm{T}}\mathbf{dS}}{\|\mathbf{dS}\|\|\nabla Q\|} \tag{18}$$

By Eqs. (5) and (8), $\nabla Q^{\mathrm{T}} = -\mathbf{dS}^{\mathrm{T}}\mathbf{J}^{\mathrm{T}}\mathbf{J}$; hence

$$cos\theta = \frac{\mathbf{dS}^{\mathrm{T}}\mathbf{J}^{\mathrm{T}}\mathbf{JdS}}{\|\mathbf{dS}\|\|\mathbf{J}^{\mathrm{T}}\mathbf{r}\|} = \frac{\|\mathbf{JdS}\|^2}{\|\mathbf{dS}\|\|\mathbf{J}^{\mathrm{T}}\mathbf{JdS}\|} \tag{19}$$

When $\mathbf{J}$ has a full rank, which usually holds for a determined or over-determined problem, for any non-zero real vector $\mathbf{z}$, there exists a constant $\gamma > 0$ such that [9]

$$\|\mathbf{Jz}\| \geq \gamma\|\mathbf{z}\| \tag{20}$$

Also, because $\mathbf{r}(\mathbf{S})$ is a bounded continuous function of $\mathbf{S}$ in the damage detection application, $\mathbf{J}$ is bounded, which means that there is a constant $\beta > 0$ such that $\|\mathbf{J}\| = \|\mathbf{J}^{\mathrm{T}}\| \leq \beta$. Hence

$$cos\theta = \frac{\|\mathbf{JdS}\|^2}{\|\mathbf{dS}\|\|\mathbf{J}^{\mathrm{T}}\mathbf{JdS}\|} \geq \frac{\gamma^2\|\mathbf{dS}\|^2}{\beta^2\|\mathbf{dS}\|^2} = \frac{\gamma^2}{\beta^2} > 0$$

and $0 \leq \theta < \frac{\pi}{2}$. However, when **J** is rank-deficient as the case for an under-determined problem, Eq. (20) cannot be satisfied, and θ cannot be uniformly bounded away from $\frac{\pi}{2}$. Hence the Gauss-Newton search direction can be perpendicular to the negative gradient of the objective function at some iteration, and the further iterations would make no progress in minimizing the objective function. If the Gauss-Newton method is used to solve an under-determined nonlinear least-square problem, only a weak global convergence can be achieved [9, 15]:

$$\underset{\mathrm{k}\to\infty}{lim}[\nabla^2 Q(\mathbf{S}_\mathrm{k})]^\mathrm{T}\nabla Q(\mathbf{S}_\mathrm{k}) = 0 \tag{21}$$

Second, using the Moore-Penrose inverse to calculate the search step in the Gauss-Newton method will amplify modeling error and measurement noise. The Moore-Penrose inverse essentially uses the singular value decomposition (SVD) [5]. The SVD of **J** is

$$\mathbf{J} = \mathbf{USV}^\mathrm{T} = \mathbf{U}\begin{bmatrix}\Lambda & 0\end{bmatrix}\begin{bmatrix}V_1^\mathrm{T}\\ V_2^\mathrm{T}\end{bmatrix} \tag{22}$$

where **U** and **V** are $m \times m$ and $n \times n$ unitary matrices respectively, with $\mathbf{V}_1$ containing the first m columns of **V** and $\mathbf{V}_2$ the other $n-m$ columns; and Λ is a $m \times m$ diagonal matrix, with the diagonal entries $\sigma_1 \geq \sigma_2 \geq \cdots \geq \sigma_m > 0$ being the singular values of **J**. The Gauss-Newton search step calculated using the Moore-Penrose inverse of **J** is

$$\mathbf{dS} = -\mathbf{J}^+\mathbf{r} = -\mathbf{V}_1\Lambda^{-1}\mathbf{U}^\mathrm{T}\mathbf{r} = -\sum_{i=1}^{m}\frac{u_i^\mathrm{T} v_i}{\sigma_i}\mathbf{r} \tag{23}$$

where u_i and v_i are the $i-th$ columns of **U** and $\mathbf{V_1}$ respectively. When the condition number of **J** is relatively large, i.e., $\frac{\sigma_1}{\sigma_m} \gg 1$, **dS** is controlled by its smallest singular values [5, 9], which can amplify small perturbations in **r**, u_i, and v_i that are mainly introduced by modeling error and measurement noise. Hence the ill-conditioning of **J** can reduce the robustness of the damage detection algorithm.

The lack of global convergence in solving an under-determined problem can be overcome by monitoring the angle θ at each iteration. If the search direction is perpendicular to the negative gradient of the objective function at some iteration, it can be replaced by a selected search direction that is not perpendicular to the $-\nabla Q$, e.g., the steepest descent direction. While this approach can ensure global convergence for an under-determined problem, extra calculation is required at each iteration, and the convergence speed of the algorithm can be slower than that of the Gauss-Newton method. The error-amplification problem of the Gauss-Newton method can be overcome by removing the smallest singular values of **J** to reduce its condition number [16]. However, some valuable information contained in these singular values can also be lost. It is also difficult to determine the number of the singular values that should be removed.

3.2 LM Method

The LM method provides a perfect resolution for the two problems associated with the Gauss-Newton method [9]. Instead of using a line search strategy as in the Gauss-Newton method, in which the direction and the magnitude of each search step are simultaneously determined by solving Eq. (11), the LM method uses a trust-region search strategy to solve a nonlinear least-square problem. The magnitude of each search step is restricted to a spherical region in the search domain with a prescribed radius, so that within each step, approximation of the objective function $Q(\mathbf{S})$ by the quadratic function $M(\mathbf{S})$ is acceptable. The direction of the search is then selected with the magnitude constraint. Because the LM method still uses $\mathbf{J}^{\mathrm{T}}\mathbf{J}$ to approximate the second-order derivative of the objective function, it solves a linear least-square problem similar to that of the Gauss-Newton method in Eq. (9) at each iteration:

$$\mathrm{Min}\, f(\mathbf{dS}) = \frac{1}{2}\|\mathbf{JdS}+\mathbf{r}\|^2 \qquad \text{subject to } \|\mathbf{dS}\| \leq \triangle \tag{24}$$

where $\triangle > 0$ is the radius of the trust region. If the solution of Eq. (11) lies strictly inside the trust region, the solution also satisfy Eq. (24), and the Gauss-Newton step is acceptable at the current iteration. Otherwise, a new solution of Eq. (24) needs to be calculated. Equation (11) can be solved by finding a parameter $t \geq 0$ and $\mathbf{dS}$, satisfying [9]

$$\begin{cases} t(\triangle - \|\mathbf{dS}\|) = 0 \\ (\mathbf{J}^{\mathrm{T}}\mathbf{J} + t\mathbf{I})\mathbf{dS} = -\mathbf{J}^{\mathrm{T}}\mathbf{r} \end{cases} \tag{25}$$

As shown in Ref. [9], the LM method can ensure that the iterations will converge to a stationary point of the objective function for an under-determined problem, if the following inequality is satisfied:

$$M(\mathbf{S}_k) - M(\mathbf{S}_{k+1}) \geq c_1 \|\mathbf{J}^{\mathrm{T}}(S_k)\mathbf{r}(S_k)\| \min(\triangle_k, \frac{\|\mathbf{J}^{\mathrm{T}}(\mathbf{S}_k)\mathbf{r}(\mathbf{S}_k)\|}{\|\mathbf{J}^{\mathrm{T}}(\mathbf{S}_k)\mathbf{J}(\mathbf{S}_k)\|}) \tag{26}$$

where $c_1 > 0$ is a constant. The above inequality implies that if the radius of the trust region is selected to be smaller than the magnitude of the Gauss-Newton search step and achieve sufficient descent in $M(\mathbf{S})$, global convergence can be ensured. Comparing the second equation in Eq. (25) to Eq. (8), one finds that there is an extra term $t\mathbf{I}$ being introduced to the LM method. Since adding this term to Eq. (8) is a typical regularization method to solve an ill-conditioned problem [5], along with the magnitude restriction equation in the first equation in Eq. (25), the LM method can more efficiently solve an ill-conditioned under-determined problem, and reduce the effects of modeling error and measurement noise in the damage detection application.

Figure 6 shows the flow chart of the LM method. The initial trust region radius is set to be five times the initial magnitude of $\mathbf{G}$ in this work. The selection of the radius of a trust region is evaluated at each iteration by an index $\rho = \frac{Q(\mathbf{S}_{\mathrm{k}})-Q(\mathbf{S}_{\mathrm{k+1}})}{M(\mathbf{S}_{\mathrm{k}})-M(\mathbf{S}_{\mathrm{k+1}})}$. If $\rho \gg 1$, which means that the objective function $Q(\mathbf{S}_{\mathrm{k+1}})$ has a much larger descent than its quadratic approximation $M(\mathbf{S}_{\mathrm{k+1}})$, the selection of the radius is acceptable but too conservative at the current iteration, and the radius needs to be increased in the next iteration. If $0 < \rho \ll 1$, which means that $M(\mathbf{S}_{\mathrm{k+1}})$ has a much larger descent than $Q(\mathbf{S}_{\mathrm{k+1}})$, the selection of the radius is acceptable but too aggressive at the current iteration, and the radius needs to be decreased in the next iteration. If ρ is close to 1, i.e., $0.75 < \rho < 1.25$, the selection of the radius is appropriate at the current iteration, and the radius can be used in the next iteration. If $\rho < 0$, which means that $Q(\mathbf{S}_{\mathrm{k+1}})$ has a descent direction opposite to that of its quadratic approximation, the selection of the radius is not acceptable at the current iteration, and the radius needs to be decreased in the next iteration. The iterations will be terminated when the first-order derivative of $M(\mathbf{S}_{\mathrm{k}})$ or the radius of the trust region $\triangle$ is sufficiently small. Note that the part inside the dashed-line box in Fig. 6 is the core of the trust-region search strategy, without which the algorithm becomes the Gauss-Newton method.

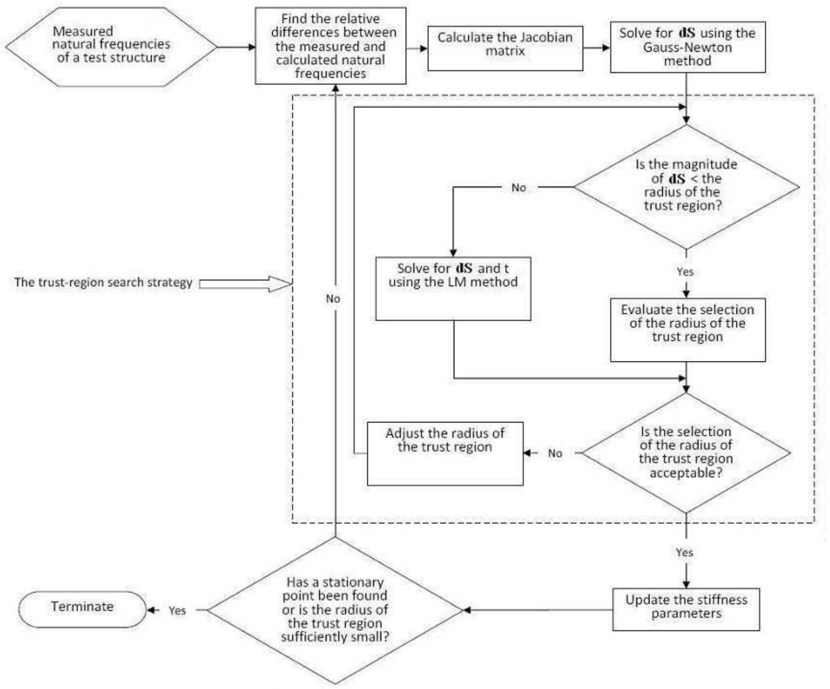
Measured natural frequencies of a test structure
Find the relative differences between the measured and calculated natural frequencies
Calculate the Jacobian matrix
Solve for dS using the Gauss-Newton method
Is the magnitude of dS < the radius of the trust region?
No
Yes
Solve for dS and t using the LM method
Evaluate the selection of the radius of the trust region
The trust-region search strategy
No
Adjust the radius of the trust region
No
Is the selection of the radius of the trust region acceptable?
Yes
Update the stiffness parameters
Has a stationary point been found or is the radius of the trust region sufficiently small?
Yes
Terminate

Fig. 6 Flowchart of the damage detection algorithm using the LM method

4 Detection of Damage in the Space Frame Structure

The damage detection algorithm developed in Section 3 using the LM method is used to detect various types of damage in the space frame structure in Fig. 1. The structure is divided into 39 element groups (Fig. 7) in the FE model, where the groups are similar to the sections in the cantilever beam in Fig. 5. Each solid cylinder that models a bolted connection connecting the bottom plate to the ground is represented by a group (groups 1-4). The bottom plate is represented by a group (group 5). Each of the L-shaped beams and the horizontal and diagonal beams is represented by a group (groups 6-8, 11-13, 16-18, 21-23, 26-39). The eight solid cylinders representing the eight bolted connections that connect the L-shaped beams and the bracket, in each of the eight bolted joints in the middle of the structure, are grouped together and represented by a stiffness parameter (groups 9, 10, 14, 15, 19, 20, 24, 25).

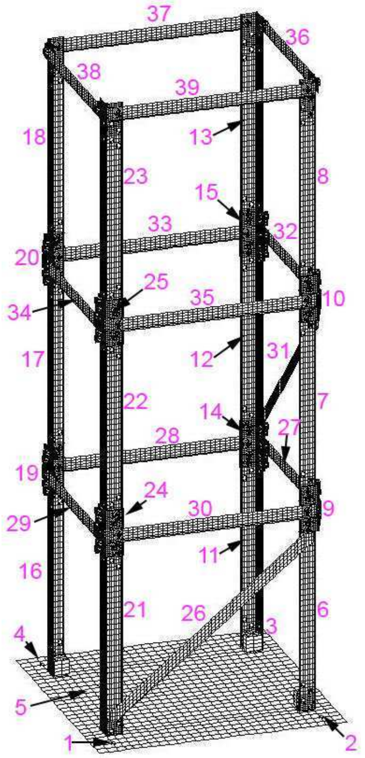

Fig. 7 Element groups in the FE model of the space frame structure in Fig. 1

4.1 Numerical Simulation

The numerical simulation is first conducted to detect a member damage in the space frame structure in Fig. 7. Damage is introduced to the structure by reducing the nondimensional stiffness parameter of a horizontal beam (the group 30 in Fig. 7) to 35% of its original value. The natural frequencies of the first 10 modes are used to detect the damage. The introduced damage causes a maximum 4.24% change in the natural frequencies of the the first 10 modes. In all the damage detection cases in this work, the iteration starts from $S_i = 0$, i.e., $G_i = 0.5$. The iterations are terminated in all the numerical simulation cases in this work when the radius of the trust region $\triangle$ is less than 1×10^{-5} times the initial magnitude of $\mathbf{G}$ or $\|\nabla Q(\mathbf{S})\|$ is less than 1×10^{-3}. After 24 iterations, the almost exact locations and extent of the introduced damage are detected, as shown in Fig. 8; the maximum resultant residual is 7.1048×10^{-5}. In the second case, damage is introduced to a bolted joint in the space frame structure (the group 24 in Fig. 7) by reducing the corresponding nondimensional stiffness parameter to 5% of its original value. The natural frequencies of the first 14 modes are used to detect the damage. The introduced damage causes a maximum 3.15% change in the natural frequencies of the first 14 modes. After 23 iterations, the almost exact locations and extent of the introduced damaged are detected (Fig. 9); the maximum resultant residual is 4.9849×10^{-5}. In the third case, damage is introduced to a bolted connection that connects the bottom plate to the ground (the group 3 in Fig. 7) by reducing the corresponding nondimensional stiffness parameter to 15% of its original value. The natural frequencies of the first nine modes are used to detect the damage. The introduced damage causes a maximum 4.35% change in the natural frequencies of the the first nine modes. After 23 iteration, the almost exact locations and extent of the introduced damaged are detected (Fig. 10); the maximum resultant residual is 4.1409×10^{-5}.

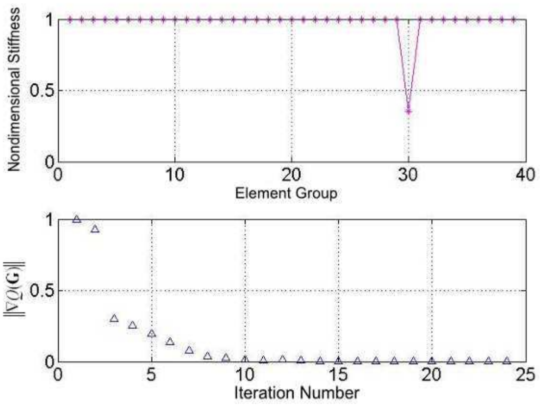

Fig. 8 The numerical damage detection result of the space frame structure in Fig. 7 with a 35% stiffness reduction introduced to a horizontal beam member (the group 30 in Fig. 7)

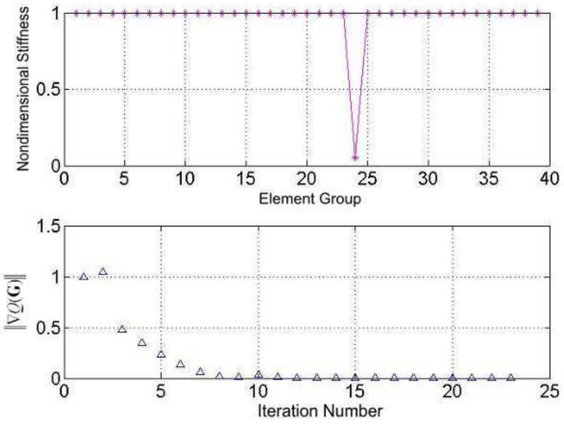

Fig. 9 The numerical damage detection result of the space frame structure in Fig. 7 with damage introduced to a bolted joint (the group 24 in Fig. 7)

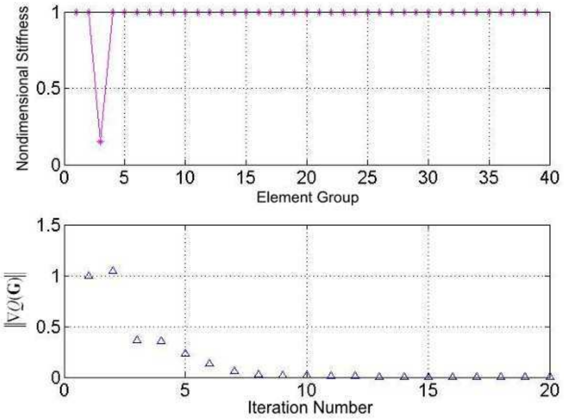

Fig. 10 The numerical damage detection result of the space frame structure in Fig. 7 with damage introduced to a bolted connection that connects the bottom plate to the ground (the group 3 in Fig. 7)

4.2 Experimental Damage Detection

The experimental damage detection was first conducted on the undamaged space frame structure in Fig. 1 for a false positive study. The first 22 measured natural frequencies were used to detect any potential damage. The iterations are terminated in experimental damage detection in this work when $\triangle$ is less than 1×10^{-5} times the initial magnitude of $\mathbf{G}$ or $\|\nabla Q(\mathbf{S})\|$ is less than 1×10^{-2}. The algorithm was terminated after 48 iterations (Fig. 11); the maximum resultant residual was 1.8176×10^{-2}. Note that the algorithm did not make a noticeable progress after the 20th iteration, and the iterations could be terminated earlier by loosening the termination criterion. The experimental damage detection result indicates that there was no obvious damage in the structure since the maximum resultant stiffness reduction was less than 0.02%. The second case was to detect damage in a beam member. The damage was introduced to the structure in Fig. 1 by almost fully loosening the upper bolted connection of a diagonal beam (the group 26 in Fig. 7); the diagonal beam did not provide any stiffness to the space frame structure, but retained its mass effect on the vibration of the structure. The first 14 measured natural frequencies were used to detect the damage. The maximum change in the natural frequencies caused by the damage was 4.18% for the first 14 modes. The location and extent of the introduced damage were detected after 14 iterations (Fig. 12); the maximum resultant residual was 0.2905×10^{-2}. The resultant stiffness at the damage location was 1.23% of its original value. The third case was to detect loosening of a bolted joint. The damage was introduced to the structure in Fig. 1 by loosening eight bolted connections in a bolted joint (the group 9 in Fig. 7) to hand-tight (Fig. 4); note that the two bolted connections that connect the two horizontal beams to the bracket and the L-shaped beam remained tightened, and loosening them would reduce the stiffness effects of the two horizontal beams. The first 10 measured natural frequencies were used to detect the damage. The maximum change in the natural frequencies caused by the damage was 8.36% for the first 10 modes. The location and extent of the introduced damage were detected after 15 iterations; the maximum resultant residual was 1.0932×10^{-2}. The resultant stiffness at the damage location was 3.37% of its original value. The fourth case was to detect damage at a lower boundary of the space frame structure. The damage was introduced to the structure in Fig. 1 by loosening one of the four bolted connections that connected the bottom plate to the ground (the group 4 in Fig. 7) to hand-tight. The first nine measured natural frequencies were used to detect the damage. The maximum change in the natural frequencies caused by the damage was 4.35% for the first nine modes. The location and extent of the introduced damage were detected after 12 iterations; the maximum resultant residual was 1.8216×10^{-2}. The resultant stiffness at the damage location was 10.91% of its original value. For the second through fourth cases, when a similar damage is introduced to the FE model of the space frame structure in the numerical simulation, the almost exact location and extent of damage can be detected in each case (Figs. 12-14).

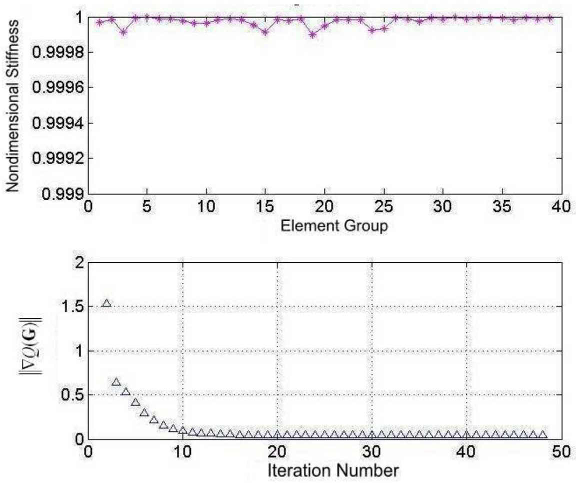

Fig. 11 The experimental damage detection result for the undamaged space frame structure in Figs. 1 and 7

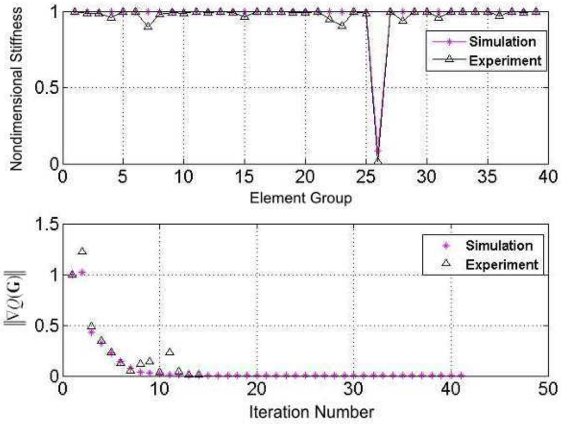

Fig. 12 The experimental and numerical damage detection results for the space space frame structure in Figs. 1 and 7, with the upper bolted connection of a diagonal beam (the group 26 in Fig. 7) loosened to hand-tight

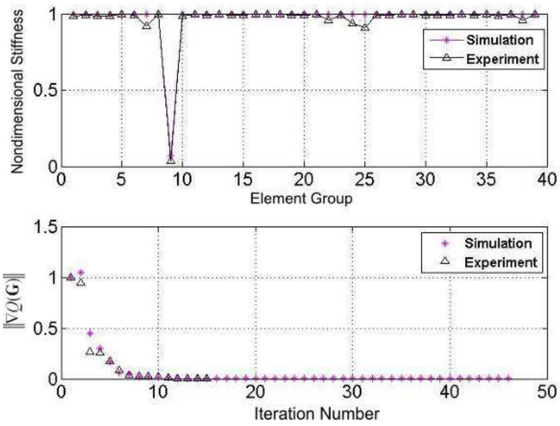

Fig. 13 The experimental and numerical damage detection results for the space space frame structure in Figs. 1 and 7, with eight bolted connections in a bolted joint (the group 9 in Fig. 7) loosened to hand-tight

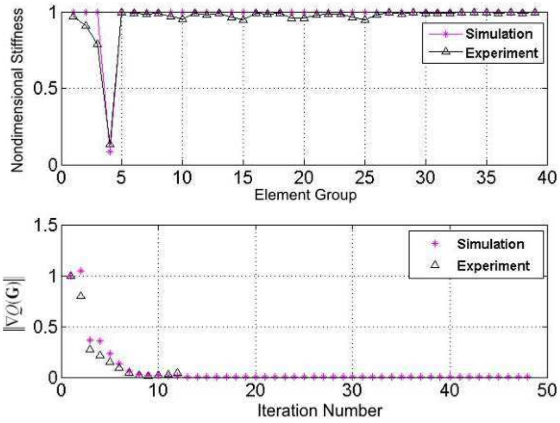

Fig. 14 The experimental and numerical damage detection results for the space space frame structure in Figs. 1 and 7, with a bolted connection that connects the bottom plate to the ground (the group 4 in Fig. 7) loosened to hand-tight

5 Conclusion

A robust vibration-based damage detection method that uses changes in natural frequencies to detect various types of damage in space frame structures with L-shaped beams and bolted joints is developed in this work. With the authors' previous studies on the modeling of fillets in thin-walled beams [7] and bolted joints [8], the forward problem associated with the vibration-based damage detection method can be resolved. An accurate FE model of a three-bay space frame structure with a reasonable model size was developed, which makes it feasible to detect a small damage in the structure. A new algorithm that uses the LM method combined with a logistic function transformation to solve a severely under-determined nonlinear least-square problem associated with the inverse problem is developed. Because the LM method adopts a trust-region search strategy, it can minimize the effects of relatively large modeling error and measurement noise that inherently exist in damage detection of complex space frame structures. The LM method can also ensure global convergence of the iterative algorithm. Experimental damage detection was successfully conducted on the three-bay space frame structure to detect a joint damage, a member damage, and a boundary damage. In the numerical simulation where there is no modeling error and measurement noise, the almost exact locations and extent of damage can always be detected when a sufficient number of natural frequencies are used.

6 Acknowledgement

This work is supported by the National Science Foundation through Grant No. CMS-0600559 and the American Society for Nondestructive Testing (ASNT) through the 2007 ASNT Fellowship Award.

References

1. Doebling, S. W., Farrar, C. R., Prime, M. B. and Shevitz, D. W., “Damage Identification and Health Monitoring of Structural and Mechanical Systems From Changes in Their Vibration Characteristics: A Literature Review,” Los Alamos National Laboratory, Report No. LA-13070-MS, 1996.
2. Lim, T. W. and Kashangak, T. A. L., “Structural Damage Detection of Space Truss Structures Using Best Achievable Eigenvectors,” AIAA Journal, 32(5), pp. 1049-1057, 1994.
3. Wu, J. R. and Li, Q. S., “Structural Parameter Identification and Damage Detection for a Steel Structure using a Two-Stage Finite Element Model Updating Method,” Journal of Constructional Steel Research, 62, pp. 231-239, 2006.
4. Sorohan, S. T., “Finite Element Model Updating and Damage Detection on a Truss Structure,” U. P. B. Sci. Bull., Series D, 66(1), pp. 47-62, 2004.
5. Friswell, M. I. and Mottershead, J. E., “Finite Element Model Updating in Structure Dynamics,” Netherlands, Kluwer Academic Publishers, pp.79-96, pp. 158-172, 1995.
6. Friswell, M. I. and Penny, J. E. T., “Is Damage Location Using Vibration Measurements Practical?” Proceedings of EUROMECH 365 International Workshop: DAMAS 97, Structural Damage Assessment Using Advanced Signal Processing Procedures, Sheffield, UK, 1997.
7. He, K. and Zhu, W. D., “Modeling of Fillets in Thin-Walled Beams Using Shell/Plate and Beam Finite Elements,” ASME Journal of Vibration and Acoustics, 131(5), p. 051002, 2009.
8. He, K. and Zhu, W.D. , “Finite Element Modeling of Structures with L-shaped Beams and Bolted Joints,” ASME Journal of Vibration and Acoustics, in press.
9. Nocedal, J. and Wright, S. J., Numerical Optimization, New York, Springer-Verlag, pp. 252-270, 1999.

10. Friswell, M. I., Penny, J. T. and Garvey, S. D., “ Parameter Subset Selection in Damage Location,” Inverse Problem in Engineering, 5, pp. 189-215, 1997.
11. D. J. Ewins, Modal Testing: Theory, Practice and Application, 2nd Edition, Research Studies Press Ltd., Baldock, Hertfordshire, UK, 2000.
12. Blmes, E., Bianchi,J. P., and Leclre, J. M., Structural Dynamics Toolbox, Users Guide, Version 6.1, Scientific Software Group, Paris, France, 2009.
13. D. J. Segalman, Status and Integrated Road-Map for Joints Modeling Research, Sandia National Laboratories, 2003.
14. Shigley, J. E., and Mischke, C .R., Mechanical Engineering Design, 5th Edition, McGraw-Hill, Inc., New York, 1989.
15. Galantai, A., The Theory of Newton’s Method, Journal of Computational and Applied Mathematics, 124, pp. 25-44, 2000.
16. Xu, G. Y., W. D. Zhu and B. H. Emory, “Experimental and Numerical Investigation of Structural Damage Detection Using Changes in Natural Frequencies,” ASME Journal of Vibration and Acoustics, 129(6), pp. 686-700, 2007.

Steels for Caribbean Steel Drums

Soren E. Maloney
Metal Industries Company Limited
Century Drive, Trincity Industrial Estate,Macoya, Trinidad and Tobago, West Indies
Email: smaloney@mic.co.tt

ABSTRACT

The Caribbean steel drum also known as the pan or steelpan is a percussion instrument which has its beginnings in the twin island Republic of Trinidad and Tobago. The instrument surfaced around WWII and for more than seven decades a majority of pan makers have continued to fabricate these instruments from used 55 gallon oil barrels. Barrel material which is predominantly low-carbon steel has long been the de-facto material for the production of these instruments in part due to its low cost and high availability in addition to having tuning methods centred on its usage. The manufacture of oil barrels is a regulated industry with standards that stipulate the grade of low-carbon steel that is to be used for the construction of oil containers. These grades of steels may not be entirely suitable for pan making and at times grades of steels which do not conform to the specifications for drum making may be deliberately or ignorantly used. Currently, there is no material standard for Caribbean steel drums. In this work, three low carbon steels were examined and compared on the basis of vibration damping properties. The results indicate that a pan standard must incorporate specifications on chemical composition and vibration properties for the recommended steels.

1. Introduction

An important facet of the vibrational behaviour of percussion instruments and by extension any vibrating structure is the effect of damping. Particularly in musical instruments, the level of damping, be it material or non-material, contributes in large part to the quality of the sound produced by the instrument. This work generally considered material damping, and the work reported on in this paper focused specifically on the effect of the steelpan production regime on material damping in steel sheet that could be used to fabricate Caribbean steel drums. This was pursued in an attempt to contribute another dimension to the work done in previous research. Previous work, mainly by Murr *et al.* [1] and Ferreyra *et al.* [2] concentrated on how other material properties such as hardness and yield strength were affected by pan production stages and carbon content, with the aim of identifying optimum process parameters that would produce the requisite properties that facilitated the production of high quality steel drums.

A major portion of this work took the form of an experimental programme in which test structures were put through steps similar to pan production, followed by vibration damping measurements at each step. The overall investigation consisted of two segments. The **first segment** (Fig. 1) was an experimental simulation that mirrored portions of the pan production process. In this section, test structures were fabricated from low-carbon steel sheet that had comparable chemical composition to steel sheet used in fabricating oil drums. These structures were put through identical stages of the steelpan production process. The test structures herein were rectangular steel strips, and "*test structure*", "*test strip*" and "*rectangular strip*" will be used interchangeably throughout this chapter. Before conducting experiments on these test structures a finite element (FE) vibration analysis was performed to determine mode shapes, natural frequencies and suitable impact locations to be used during experimental modal testing. The **second segment** (see Fig. 1) of this work also involved a simulation of the pan production process but test structures were constructed from bake hardenable (BH) and interstitial free (IF) steel sheets. In this section the damping properties extracted from the BH and IF steel strips were compared with those of the rectangular strips extracted from the low-carbon sheet steel.

Some predictions were made about the expected outcomes of the various tests that were conducted, based on the earlier literature on damping in metals. For instance Zener [3] reported on the effects of cold working and heat treatment on metals (steel, brass and copper) and found the material damping to increase with cold forming and to decrease with subsequent heat treatment of cold formed metal specimens. However, this decrease in material damping with heat treatment only occurred up

T. Proulx (ed.), *Sensors, Instrumentation and Special Topics, Volume 6*, Conference Proceedings of the Society for Experimental Mechanics Series 9, DOI 10.1007/978-1-4419-9507-0_27, © The Society for Experimental Mechanics, Inc. 2011

to the recrystallization temperature of the metal, beyond which the material damping increased. Zener [3] also noted that there was no noticeable change in hardness for cold formed metal samples heated up to the recrystallization temperature. Nowick [4], Hikata *et al.* [5] and Granato *et al.* [6] all showed that room temperature plastic deformation led to a decrease in the elastic modulus of a material. However, the elastic modulus and the internal friction recovered provided the plastic strain was only small (0.4 – 4%) [4,6]. This subsequent recovery of the elastic modulus and internal friction after room temperature deformation is known as the Köster effect [4]. The strains that were used in the experiments (10%-50%) done in this work far exceed 4% which means that any recovery that occurs may not be total and there may be a permanent decrease in the elastic modulus of the sheet metal after cold forming.

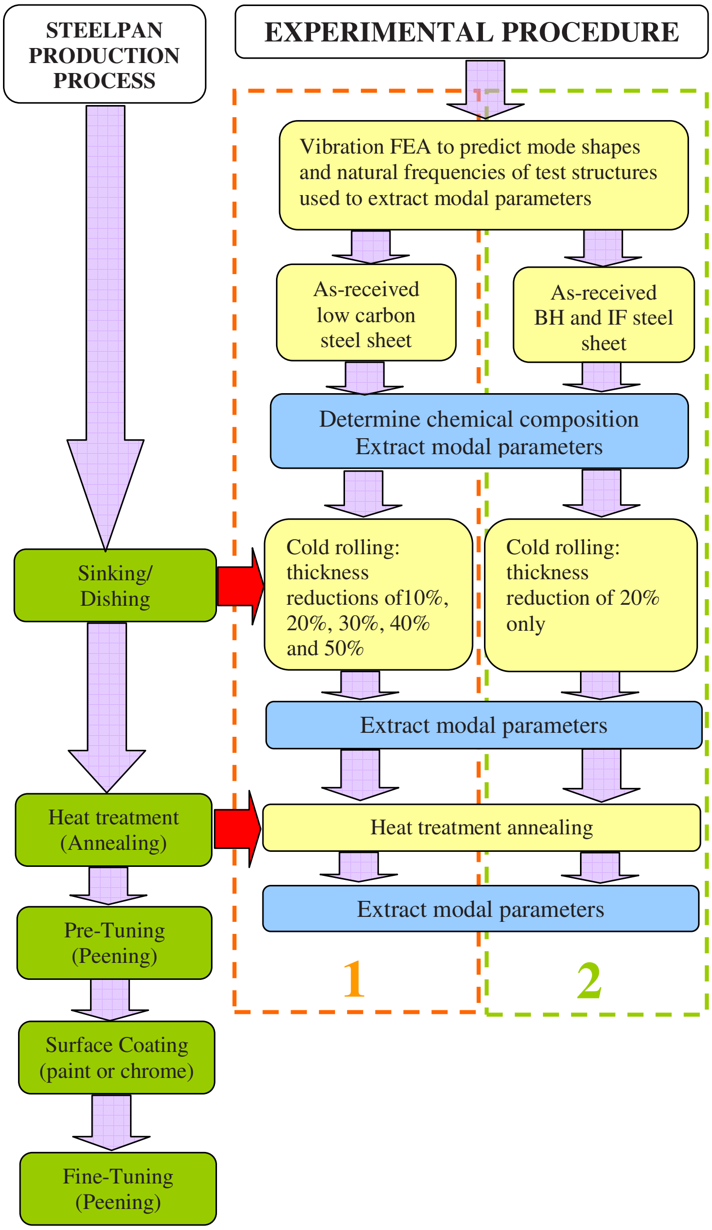
STEELPAN PRODUCTION PROCESS
EXPERIMENTAL PROCEDURE
Vibration FEA to predict mode shapes and natural frequencies of test structures used to extract modal parameters
As-received low carbon steel sheet
As-received BH and IF steel sheet
Determine chemical composition
Extract modal parameters
Sinking/ Dishing
Cold rolling: thickness reductions of10%, 20%, 30%, 40% and 50%
Cold rolling: thickness reduction of 20% only
Extract modal parameters
Heat treatment (Annealing)
Heat treatment annealing
Extract modal parameters
Pre-Tuning (Peening)
1
2
Surface Coating (paint or chrome)
Fine-Tuning (Peening)

Fig. 1 *Experimental Methodology: 1) Experiment with low-carbon steel; 2) Experiment with BH and IF steels*

There are a variety of terms which are used to denote material damping which include: logarithmic decrement (δ), loss factor (η), loss angle (φ), damping ratio (ς), quality factor (Q) and specific damping capacity (ψ). Damping was reported using the quality factor (Q) which was defined in Chapter 4. Bert [7] gives a comprehensive overview on the mathematical models and the experimental techniques used for measuring some of these damping quantities. The experimental techniques used for the measurement of material damping generally fall into one of the following categories: (a) vibration amplitude decay; use of either frequency domain modal analysis or time domain decay rate methods, (b) steady state measurement of input energy and stored energy; (c) wave propagation methods [7-9]. Free-vibration decay methods (time and frequency domain) were employed primarily because they are the most accurate and appropriate for this range of damping i.e. low damping. Another attractive feature of these methods are the relative simplicity with which they could be conducted and the required instrumentation required for conducting these methods were also easily accessible.

The objectives of this investigation were to: (1) understand how the various manufacturing stages influenced the material damping properties of low-carbon steel sheet used for the production of steelpans; (2) to determine an optimum heat treatment regime for steelpans using material damping measurements; (3) to identify mechanisms responsible for damping changes in the steel used and (4) to determine the effect of carbon content on the damping properties by comparing the material damping properties in BH and IF steel grades to the low-carbon steel.

2. Experimental Procedure

Caribbean steelpans are predominantly produced from steel sheets hence the experimental investigations were mainly conducted on low-carbon sheet steels (see Table 1).

Table 1 *Chemical Composition (wt %)*

Material (Steel sheet)	Nominal Thickness (mm)	C	Si	Mn	P	S	Al	N	Ti	VHN†
Low-Carbon	0.86	0.061	0.02	0.34	0.019	0.017	0.03	0.0055	-	107
IF – HS	1.02	0.0021	0.004	0.05	0.012	0.005	0.035	0.0021	0.062	90
BH	0.82	0.0035	0.04	0.32	0.036	0.005	0.048	0.0018	-	128

Note: 0.061% carbon steel will be referred to as low-carbon steel throughout this paper

† Vickers Hardness Number in the as-received condition

2.1 Fabrication of test structures

In this section, the fabrication of the test structures is described. The test structures or rectangular strips used in this work were mainly extracted from steel sheet in the as-received and cold-rolled conditions. The initial step in the preparation of these structures required that the mill rolling direction in the as-received steel sheet be identified. Cold rolling of the sheet was done in the same direction as the mill rolling direction. Samples of dimensions 180mm x 50mm were cut from the 0.86mm thick, low-carbon steel parent material and rolled to the following thickness reductions: 10%, 20%, 30%, 40% and 50%. These percentages were chosen because recent work by Murr *et al.* [1] has shown the cold reduction in a 570mm diameter soprano pan dish to vary from approximately 10% thickness reduction at the steelpan rim to as much as 50% reduction at the dish base.

A sheet-metal rolling machine was used and the desired cold reduction was achieved by multi-pass rolling and progressive adjustment of the distance between the roller surfaces. Seventy 0.061wt.% carbon steel rectangular strips of dimensions 150mm x 15mm were extracted, with a guillotine, from the larger cold-rolled samples with a batch of 35 for annealing and air-cooling and the remainder for annealing and water quenching. Each batch was subdivided into 7 groups of 5 – each group having a strip at one of the percentage reductions mentioned earlier. A pair of strips was also extracted from the low-carbon steel sheet in the as-received condition. Test structures extracted in the as-received condition were used to measure the damping of the steel in the as-received state. Although the BH and IF steel test structures were fabricated in an identical manner, detailed description will be given further on when the use of these steels is introduced.

2.2 Finite Element Predictions

Before conducting experimental modal tests on the cold-rolled steel strips, approximations of the natural frequencies and mode shapes of the first ten modes of the rectangular strips were predicted using the software ABAQUS [10]. The modal parameters were computed by using the material properties: ρ=7800kgm^{-3}, E=210GPa and υ=0.28. The strips were modeled in ABAQUS® using 4-noded shell elements (S4R) since the ratios t/L << 1/10. The resulting mode shapes were used to approximate node line positions (see Table 2).

Table 2: *Mode shapes with node line positions and impact and suspension locations*

Mode	Mode shape with node line positions (x, y) mm	Mode	Mode shape with node line positions (x, y) mm
1) B1	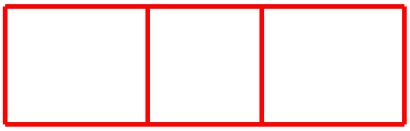 *x* = 34; 116	**6) T2**	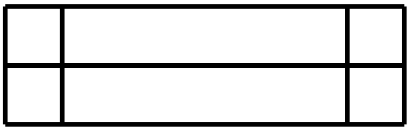 *x* = 38; 112 *y* = 7.5
2) B2	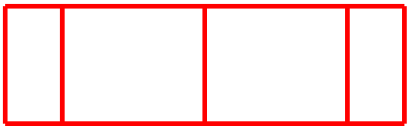 *x* = 20; 75; 130	**7) B5**	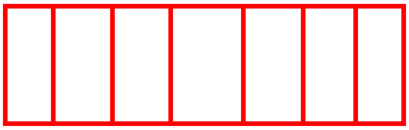 *x* = 9; 34; 61; 89; 116; 141
3) B3	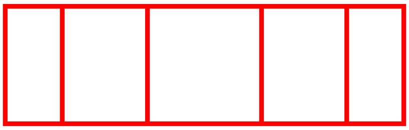 *x* = 14; 53; 97; 136	**8) T3**	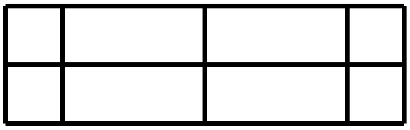 *x* = 25; 75; 125 *y* = 7.5
4) T1	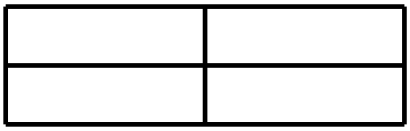 *x* = 75; *y* = 7.5	**9) B6**	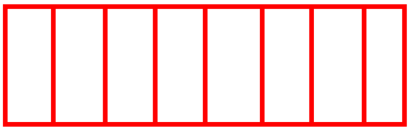 *x* = 7; 29; 52; 75; 98; 121; 143
5) B4	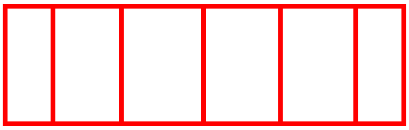 *x* = 11; 42; 75; 109; 139	**10)T4**	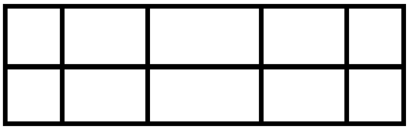 *x* = 18; 54; 96; 132 *y* = 7.5
P	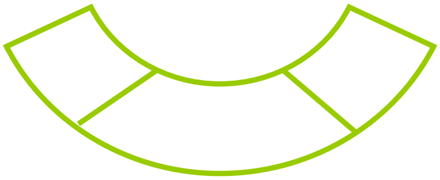		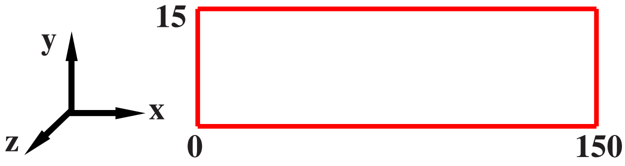

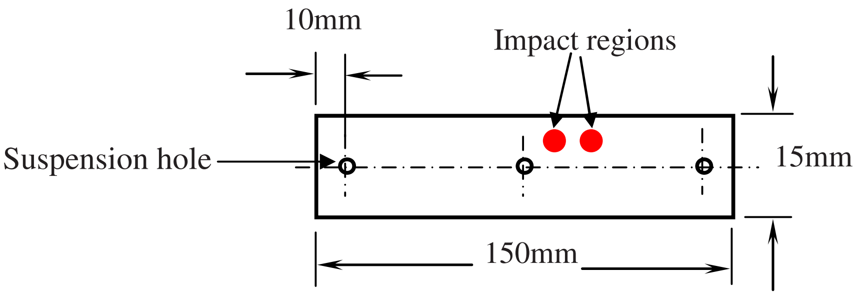

Notes: B – bending mode (**Red**); T – torsional mode (**Black**); P – in-plane mode (**Green**); in-plane modes are not used in this work; Impact locations at *x* = 83 or 100 and *y* = 10 – in some instances both positions were used to excite all the modes of interest; **Diagrams are not drawn to scale**

This information was also used to predict suitable impact zones which were set at x=83 and x=100 (see Table 2) such that the modes of interest could be easily excited. Locations at which holes could be drilled to facilitate suspension of the strips in a free-free configuration were chosen at 10mm from either side and at the middle of the strips (see Table 2). The mode shapes are identical for the first seven modes of all the strips. In-plane modes were not considered in this work since the plane of vibration of these modes was in the same plane as the suspension supports.

2.3 Experimental Modal Testing: Low-Carbon Steels

A schematic of the experimental set-up and hardware used along with the signal flow for experimental modal testing is shown in Fig. 2. The first modal tests were conducted on the strips in their cold rolled condition. The strips were supported at both ends in a free-free configuration using nylon thread. Excitation was provided by a miniature impulse hammer on a pendulum fixture and the response was recorded by a laser vibrometer. In this experiment all the strips were excited from behind (Fig. 2). Impact locations were at 8mm or 25mm (see Table 2) from the center of the strip. Sometimes both locations were used in order to obtain all the modes of interest. Only the first ten modes in the frequency range up to 4 kHz were considered. The Logging frequency used was 50 kHz for an acquisition time of 5s and 10 averages were used to produce the coherence. Clipped and truncated signals were discarded.

2.4 Damping Measurements

Damping measurements are reported using the quality factor ‘Q’. Damping measurements were extracted by two methods: (a) circle fit of the Nyquist plot and (b) using sonogram analysis. The Nyquist plot which required consideration of the frequency range in the immediate vicinity of the resonance peak was better suited for structures with higher damping as a sufficient number of points in the vicinity of the resonance peak can be obtained for the construction of the Nyquist plot. The rectangular strips had very low damping and the sonogram analysis offered a better alternative as there was an insufficient number of points in the vicinity of the resonance peak to allow a circle fit to be used that would provide reliable results. The sonogram algorithm allowed the damping of several modes in the desired bandwidth to be obtained simultaneously as compared with circle fitting in which the damping can only be determined for one resonant frequency at a time. For the rectangular test strips, the temporal decay rates of the modes of interest were calculated using the sonogram analysis. The sonogram takes a series of short FFTs of overlapping data segments. Peaks were found, and the best fitting exponential decays were calculated on the basis of the variation of each peak height with time. The analysis also displayed a measure of the fit quality which enabled poor data to be excluded from the measurements. When extracting the quality factor, a number of 10 trials were taken and an average rate (Q-factor) was calculated.

For preliminary vibration tests involving the rectangular strips a small microphone was used to validate damping measurements collected using the laser vibrometer. In this test the microphone was positioned in the near field (approximately 2cm from strip surface) – just to the front of the impact zone. The damping measurements collected using a microphone and a laser vibrometer simultaneously, exhibited good agreement. However, the microphone was not used to collect response data throughout the experiment as it regularly recorded unwanted background noise. An accelerometer was also not used to measure the response of the rectangular strips as its mass and damping along with that of its cable would have perturbed the behaviour of the light weight strips significantly. Reflective tape was initially used to improve the reflectivity of the laser-beam on the strip surface and hence the signal to noise ratio of the vibration measurements. However, the application of a small patch (approx. 5mm x 5mm) of reflective tape was found to significantly increase the damping (lower Q-factors) of the test strips. Reflective dust did not have this effect and was therefore used in all modal tests.

2.5 Suspension configuration and rigid body modes

The sensitivity of damping to suspension configuration is crucial particularly in free-free arrangements. To determine the sensitivity of damping to support configuration, test structures in free-free modal tests were suspended in different ways. The configuration that gave the lowest damping (highest Q-factors) was adopted throughout the modal test. The configuration with the strip suspended simultaneously from both sides gave the lowest damping and was therefore adopted throughout the experiment.

Although rigid body modes were not of interest in the modal tests conducted it is suggested that for an acceptable suspension method, the highest rigid body mode frequency should be less than 10-20% of that of the lowest bending mode. When conducting free-free modal tests this was used as a simple check to provide a measure of how well the supports used approximated that of a free-free condition.

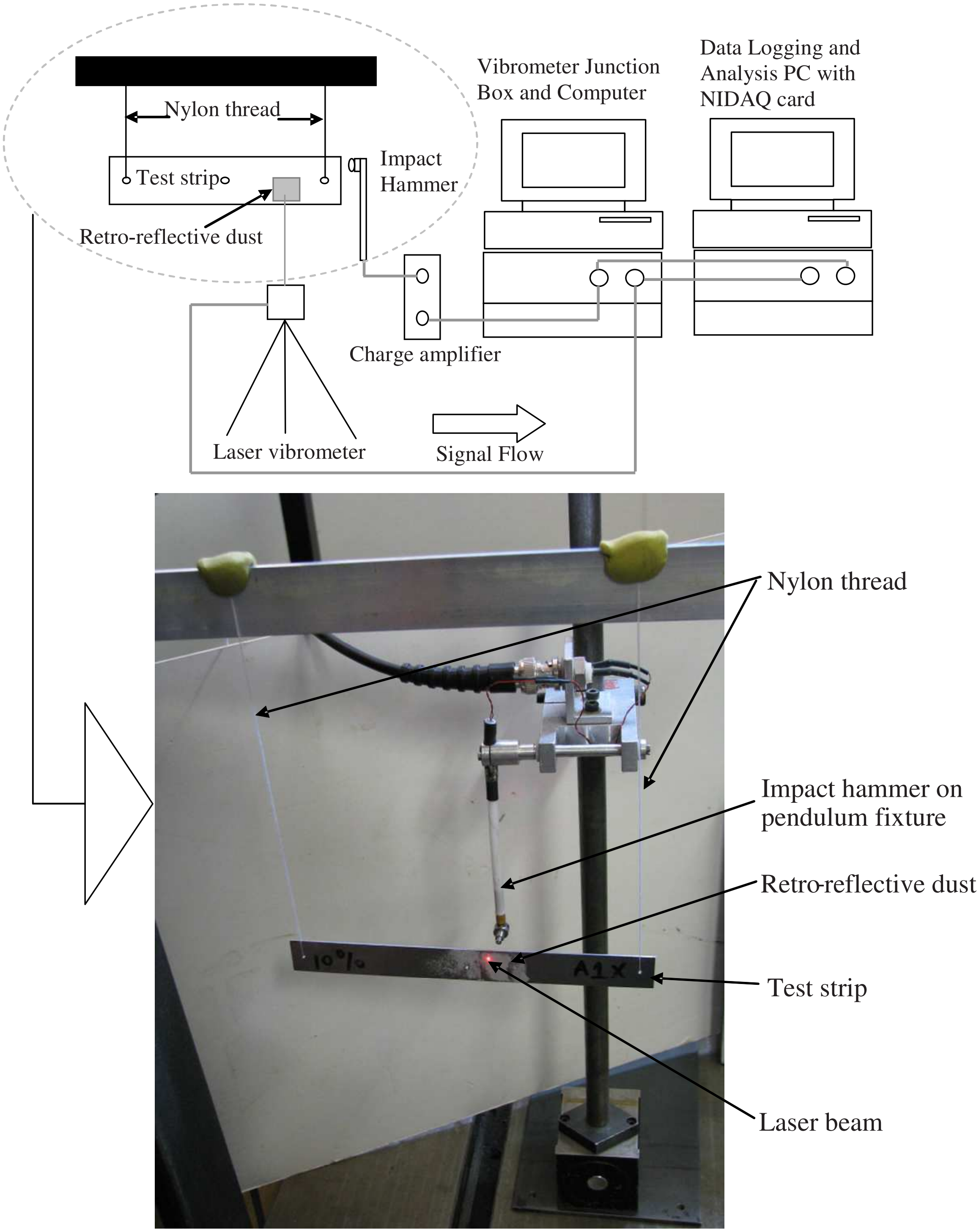

Fig. 2 *Experimental set-up for vibration tests. Strips were tested using two free-free configurations to ascertain the influence of the supports on damping properties: horizontal (shown here) and suspended solely from the center. The impact hammer is located behind the test strip.*

2.6 Heat treatment annealing

After extracting damping measurements from the cold-rolled, low-carbon rectangular strips, all the strips were heat treated. Each group in a batch was annealed using a Lenton 3000W furnace (max temp. 1200˚C) and held at one of the following temperatures for 10 minutes: 200˚C, 250˚C, 300˚C, 350˚C, 400˚C, 450˚C and 500˚C. Air cooled strips were wrapped in stainless steel foil so as to minimize surface oxidation. Strips to be water quenched were not wrapped but were heated in a metal basket which allowed for quick removal from the furnace for subsequent quenching in a nearby water filled basin. All strips were kept in a desiccator whenever they were not in use so as to minimize surface rusting. After heat treatment, damping measurements were again extracted from the test structures.

2.7 Experimental Modal Testing: IF and BH steels

Rectangular strips of dimensions 150mm x 15mm were extracted from cold-rolled bake hardenable and interstitial free steels of chemical composition given in Table 1. A total of 18 strips were prepared, nine BH and nine IF. In each batch, seven strips (one for each annealing temperature: 200˚C, 250˚C, 300˚C, 350˚C, 400˚C, 450˚C and 500˚C) were extracted along the rolling direction from sheet that had been cold reduced by 20% of the nominal thickness. The other two strips were extracted from the material in the as received condition (along rolling and transverse directions). For heat treatment (annealing), the strips were wrapped in stainless steel foil and held in a furnace at the respective temperature for 10 minutes before extracting and cooling normally in air to room temperature. Strips were allowed to cool in wrapping before removing. Material damping (Q-factor) was extracted from the BH and IF strips in the as received material, after cold reduction, and after annealing using the same equipment and settings as that used for the extraction of damping in the low-carbon strips.

3. Results

It is necessary to recall that a low Q-factor value corresponds to high damping and *vice-versa*. Fig. 3a shows the material damping in the as-received material for each steel type used in this work. Note that the damping was generally low, with the bulk of the modes having Q-factors greater than 1000. The damping in the 0.061 wt% carbon and IF steel strips were comparable, particularly for frequencies above 1 kHz, whereas damping in the BH as-received condition is lower than that of the low carbon and IF as-received material for all modes.

Fig. 3b shows the effect of cold rolling on damping in the first 8 flexural modes of the low-carbon steel strips. Damping for the first 8 modes was shown, as the 9th or 10th modes for some of the strips were in-plane modes. As predicted from the literature, damping increased (lower Q-factor) as the percentage cold reduction (thickness reduction) increased. Note also that the largest increase in damping for the majority of the modes was seen for the first 10% of thickness reduction after which the increase in damping was minimal. The first mode however, did not show such a trend: damping in cold rolled strips was comparable to damping in the as-received condition.

Before outlining the trends, one of the most notable observations was the audible difference in the duration of the strip vibrations after impact. Strips annealed at much higher temperatures rang for longer indicating a decrease in damping with increase in annealing temperature. This shows that the damping changes being investigated here are of an order to have clearly audible consequences, and to be relevant to musical instruments.

In this paper, the effect of heat treatment on the damping in the first ten modes up to 4 kHz of each test group for the low carbon test structures were examined. This bandwidth was selected as it is the frequency range in which the musical notes on the soprano pan are situated. Before highlighting the findings it is first necessary to state that all tests reported on in this paper were conducted at room temperature. Temperatures listed on any graphs were temperatures at which annealing was conducted and not temperatures at which experimental measurements were taken. In the frequency band of major interest, up to 4 kHz, similar trends were observed in the variation of damping with annealing temperature across air-cooled and water quenched test groups for all the low-carbon test strips. However, only a sample is shown in this paper (see Fig. 4, Fig. 5a and b and Fig. 6) . It is therefore reasonable to use a single group to highlight these trends. Consider the 10% air cooled test set in Fig 4. The following trends were observed:

- The Q-factor for each mode increased to a maximum value which occurred between 350°C and 400°C before plateauing: There was minimal change in damping beyond 400°C. This is a general trend which was observed with the other test groups. This combination suggests 2 different damping mechanisms added together: one constant, the other with a power law.

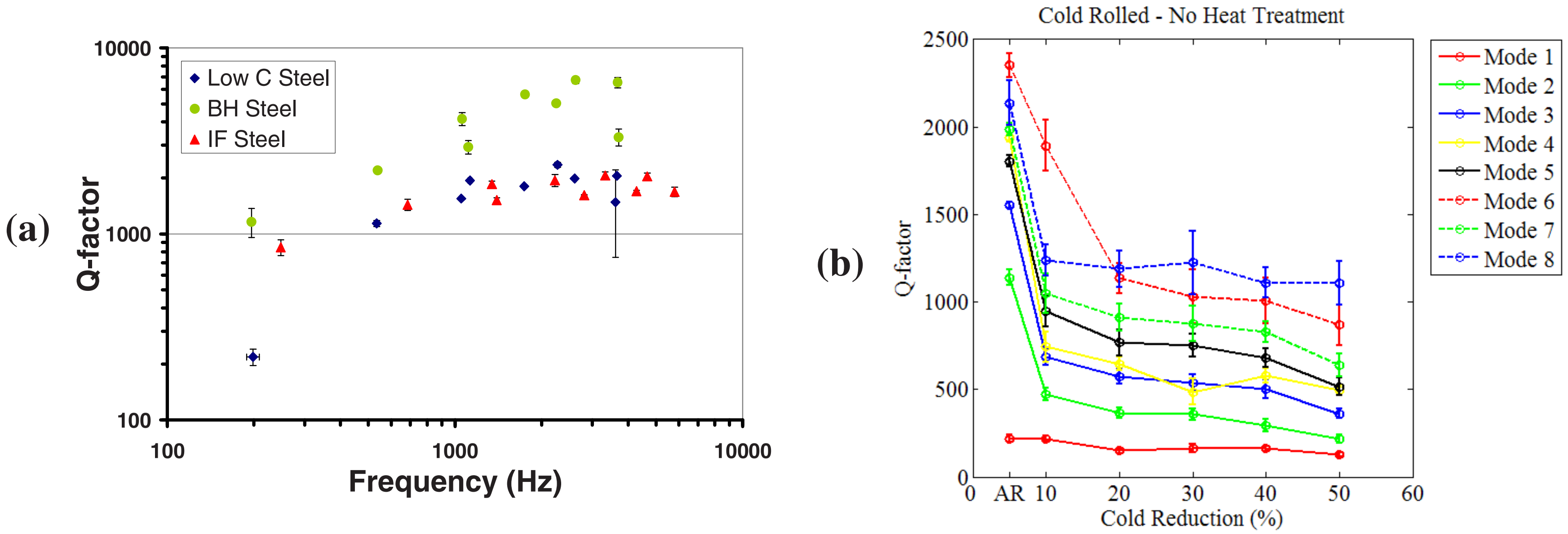

Fig. 3 ***(a)*** *Damping for first ten modes in as received material;* ***(b)*** *Effect of cold rolling on damping in low carbon steel; AR – as received*

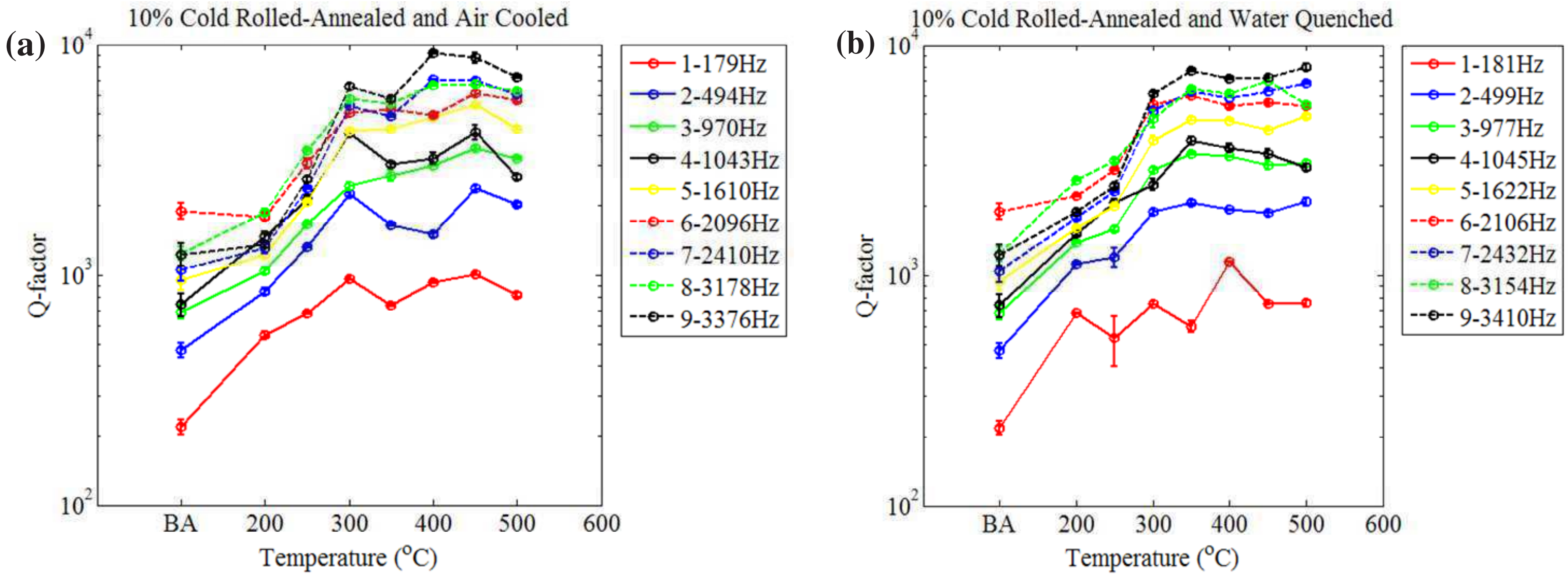

Fig. 4 *10% reduced low-carbon steel strips **(a)** air-cooled and **(b)** water quenched ; BA – cold rolled condition before being annealed*

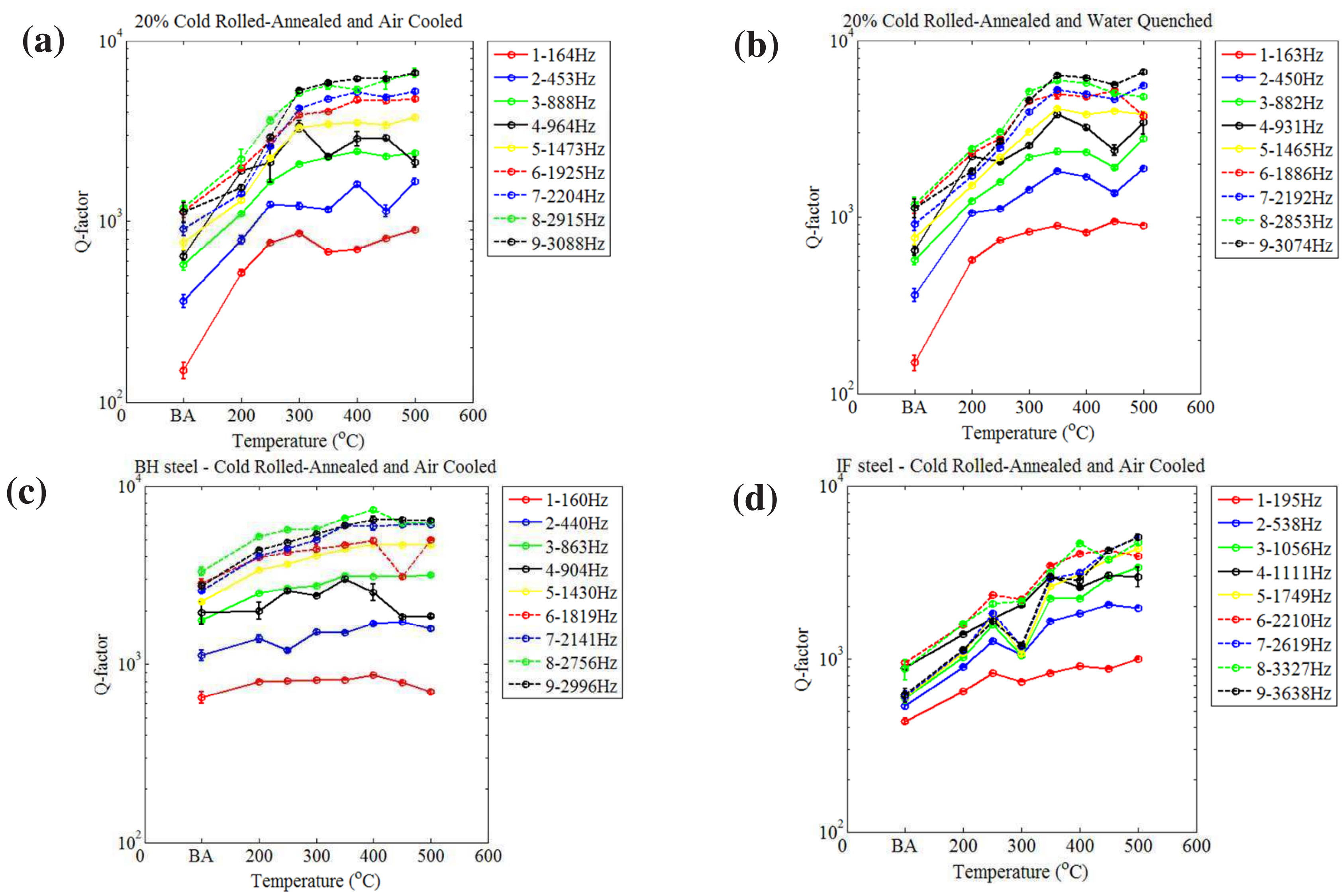

Fig. 5 *20% reduced Low-carbon steel **(a)** air cooled **(b)** water quenched; **(c)** 20% reduced BH steel; **(d)** 20% reduced IF steel; BA – cold-rolled condition before being annealed*

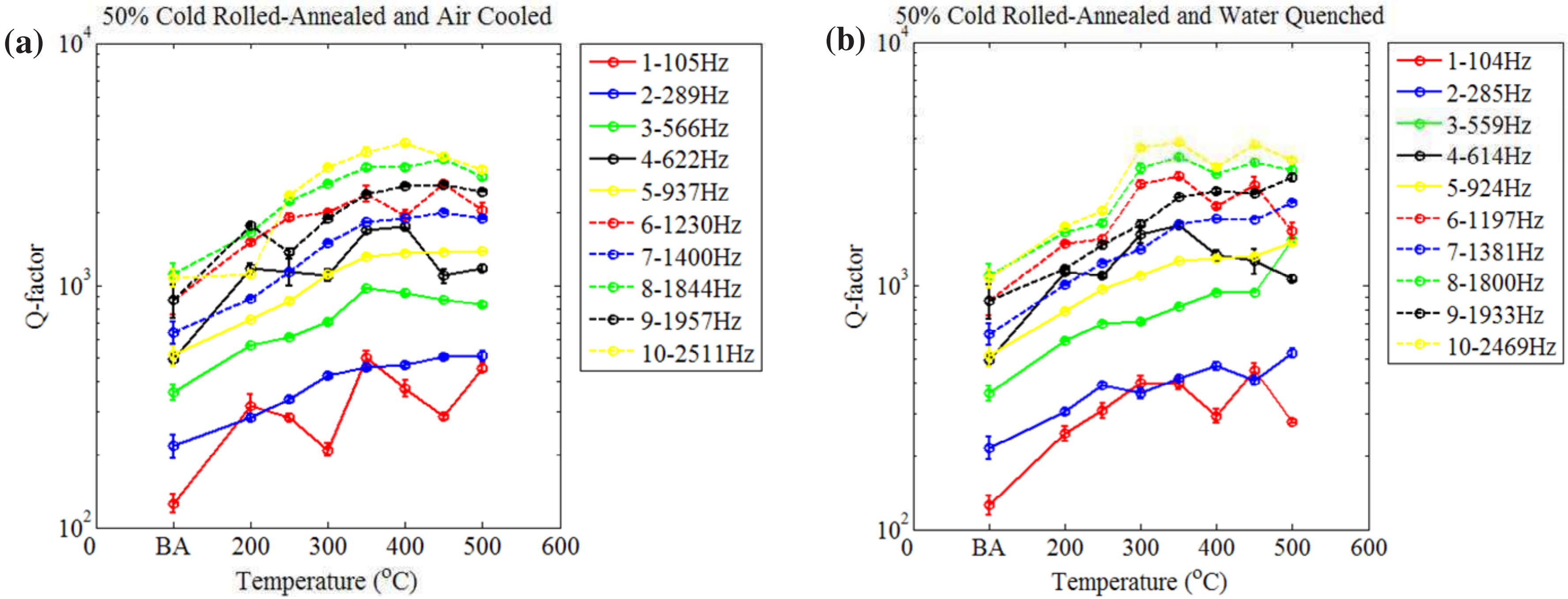

Fig. 6 *50% reduced low-carbon steel strips* ***(a)*** *air-cooled and* ***(b)*** *water quenched ; BA – cold rolled condition before being annealed*

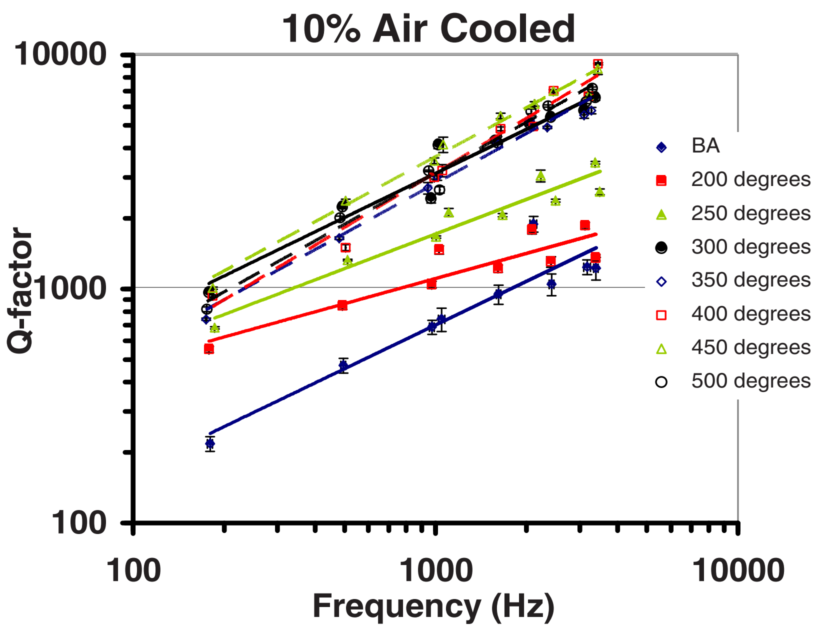

Fig. 7 *Damping-frequency fits for 10% reduced strips*

- The largest *Q*-factor (lowest damping) values occurred in 10% reduced strips air cooled and water quenched (Fig. 4a and b). In these groups the 9th mode *Q*-factors approached the order of 8000 to 9000 but as percentage reduction increased the maximum levels of damping achieved in corresponding modes decreased. For instance, consider the selection of the 5th mode *Q*-factors in air cooled groups from 10% to 50% reduction. The maximum *Q*-factor values for these modes are approximately 5000, 3500, 2800, 2200 and 1400 respectively. This general trend is seen for all air cooled and water quenched strips.

Consider the *Q*-factors of identical modes of the 10% air cooled and 10% water quenched strips (Fig. 4a and b). Their values are in close proximity, and this pattern is also generally seen for other air cooled and water quenched test groups. This suggests there is no significant difference in damping between air cooled and water quenched strips.

Another consistent characteristic was found in the *Q*-factor values for bending and torsional modes for the low carbon steel strips. The modes 1, 2, 3, 5, 7 and 9 for the majority of strips were pure bending modes while modes 4, 6, 8 and 10 were usually torsional with the exception of a few instances where there was an in-plane modes, see With reference to the 10% reduced strips test-group, it was apparent that the *Q*-factor values for the bending modes followed a sequence such that the *Q*-factor of a successive bending mode was higher than the previous bending mode. However, the torsional modes appeared to have a different pattern that did not fit in with the sequence of *Q*-factors for the bending modes. For instance, (see Fig. 4a and b) the 6th and 8th modes had the highest *Q*-factors in the range BA (before annealing or after cold rolling) to 300°C. In most cases, the highest *Q*-factors were recorded for torsional modes. These patterns may be due to a difference between the complex Young's modulus and complex shear modulus.

To highlight the trends observed with respect to the damping variation with frequency, the low-carbon, 10% air cooled *Q*-factor versus frequency plots was considered (see Fig. 7). There are significant differences between strips heated up to 250°C and strips before heat treatment or after cold reduction (designated BA). At 300°C and beyond, however, the log-log fits began to cluster. This general trend was also observed for the other air cooled and water quenched low-carbon strips. The temperature at which this clustering begun (i.e. 300°C) corresponded to the temperature beyond which damping plateaued or became independent of annealing temperature. The data can be well fitted by the form $Q = \beta f^{\alpha}$ where Q is the material damping, f is the natural frequency and β and α are constants. There was reasonably good fit for this power-law relationship as indicated by the R^2 values (see Table 3 and Table 4). The α values were generally between 0.60 and 0.80.

Table 3 *Power law fit values for 10% and 20% reduced low-carbon, BH and IF steel strips*

Strip	**10% Air Cooled**			**10% Water Cooled**			**20% Air Cooled**			**20% Water Cooled**			**BH 20% Air Cooled**			**IF 20% Air Cooled**		
T(°C)	β	α	R^2	β	α	R^2	β	α	R^2	β	α	R^2	β	α	R^2	β	α	R^2
BA	9.6	0.62	**0.88**	9.6	0.62	**0.88**	5.0	0.69	**0.97**	5.0	0.69	**0.97**	45.1	0.54	**0.97**	189.3	0.17	**0.40**
200	94.0	0.35	**0.81**	93.9	0.40	**0.92**	61.9	0.43	**0.79**	76.0	0.43	**0.78**	30.0	0.64	**0.97**	201.2	0.24	**0.64**
250	57.4	0.49	**0.93**	37.0	0.55	**0.92**	60.9	0.50	**0.96**	63.1	0.48	**0.95**	22.9	0.69	**0.97**	203.4	0.29	**0.81**
300	41.1	0.62	**0.95**	23.4	0.69	**0.96**	28.2	0.65	**0.95**	31.7	0.63	**0.98**	24.6	0.69	**0.99**	225.4	0.24	**0.36**
350	20.6	0.71	**0.98**	10.7	0.82	**0.96**	11.7	0.78	**0.99**	30.8	0.69	**0.97**	20.1	0.73	**0.98**	100.7	0.44	**0.85**
400	14.5	0.77	**0.97**	42.0	0.63	**0.99**	18.0	0.72	**0.99**	24.2	0.69	**0.99**	20.0	0.74	**0.98**	86.5	0.47	**0.85**
450	29.2	0.70	**0.98**	14.8	0.77	**0.99**	15.9	0.74	**0.97**	27.7	0.67	**0.94**	21.0	0.71	**0.90**	68.5	0.52	**0.91**
500	20.6	0.72	**0.98**	16.1	0.76	**0.97**	21.3	0.71	**0.97**	38.7	0.63	**0.96**	12.5	0.79	**0.95**	59.9	0.55	**0.95**

Table 4 *Power law fit values for 30%, 40% and 50% reduced low-carbon, BH and IF steel strips*

Strip	**30% Air Cooled**			**30% Water Cooled**			**40% Air Cooled**			**40% Water Cooled**			**50% Air Cooled**			**50% Water Cooled**		
T(°C)	β	α	R^2	β	α	R^2	β	α	R^2	β	α	R^2	β	α	R^2	β	α	R^2
BA	6.5	0.66	**0.98**	6.5	0.66	**0.98**	6.8	0.66	**0.98**	6.8	0.66	**0.98**	4.4	0.71	**0.96**	4.4	0.71	**0.96**
200	54.0	0.44	**0.87**	19.1	0.59	**0.90**	46.7	0.47	**0.86**	24.4	0.54	**0.88**	18.3	0.57	**0.74**	11.4	0.64	**0.86**
250	23.0	0.61	**0.96**	35.2	0.53	**0.93**	16.5	0.63	**0.89**	17.7	0.63	**0.91**	9.1	0.70	**0.87**	15.7	0.62	**0.91**
300	23.8	0.64	**0.91**	19.9	0.68	**0.99**	9.2	0.76	**0.99**	7.5	0.79	**0.97**	3.9	0.84	**0.96**	9.5	0.73	**0.80**
350	19.2	0.68	**0.97**	15.1	0.74	**0.97**	14.3	0.72	**0.91**	6.9	0.81	**0.99**	16.4	0.67	**0.85**	8.3	0.77	**0.86**
400	12.4	0.75	**0.96**	11.9	0.77	**0.99**	7.1	0.85	**0.81**	12.4	0.74	**0.93**	9.3	0.75	**0.91**	7.2	0.78	**0.96**
450	18.2	0.71	**0.98**	13.7	0.75	**0.99**	8.2	0.79	**0.96**	20.4	0.68	**0.92**	5.1	0.84	**0.96**	10.0	0.74	**0.88**
500	16.7	0.72	**0.97**	18.1	0.72	**0.90**	7.4	0.81	**0.96**	8.6	0.79	**0.99**	15.0	0.67	**0.92**	6.8	0.80	**0.96**

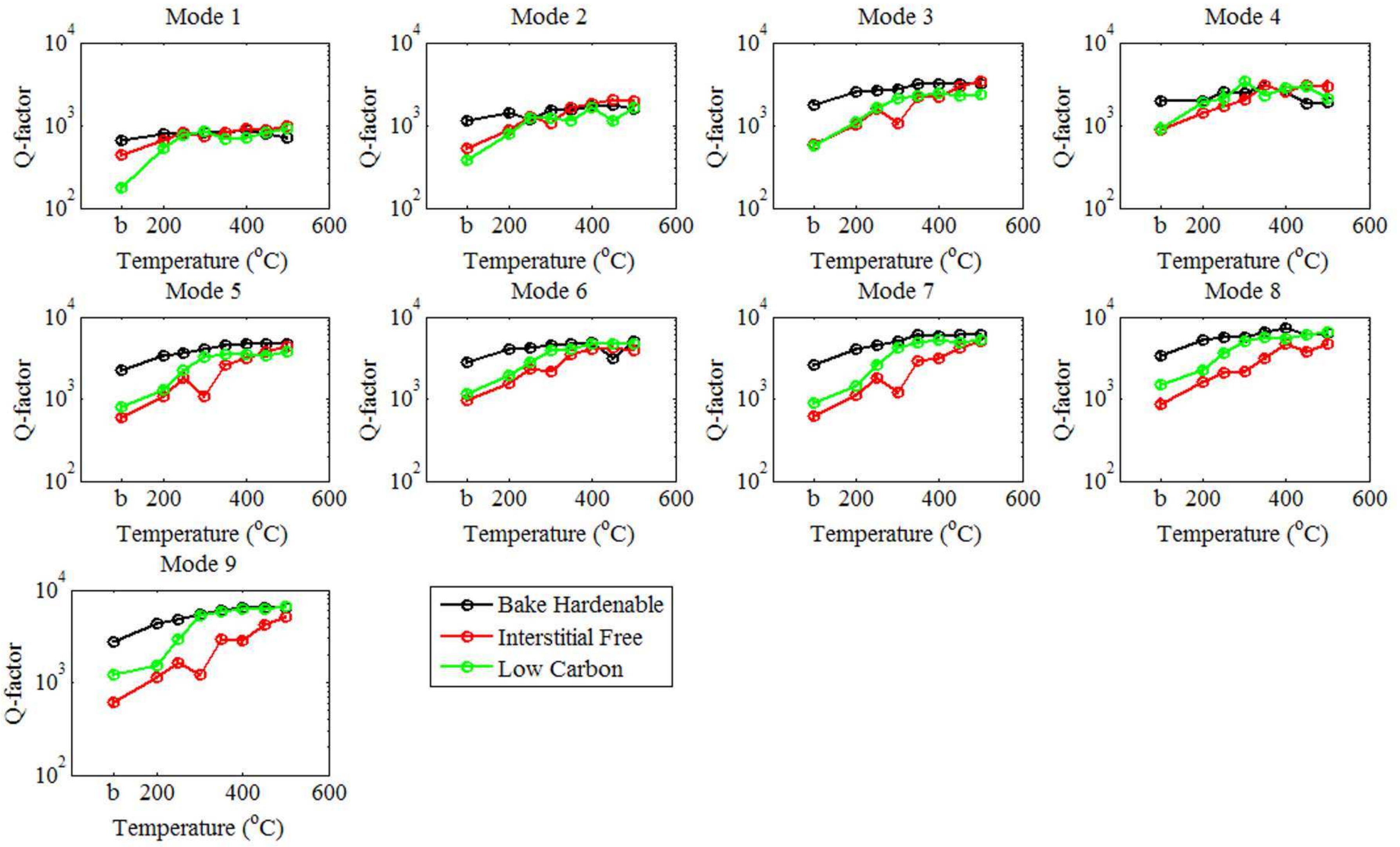

Fig. 8 *Modal damping comparison among 20% cold-rolled carbon strips: The data for these plots were taken from Fig. 5(a), (c) and (d)*

3.1 Damping in BH, IF and Low-Carbon Steel Compared

Fig. 5a, c and d are plots which illustrate the effect of annealing temperature on damping in the 20% cold rolled low carbon, bake hardenable and interstitial free steels. It was noted that:

- Damping in the BH steel could almost be described as independent of annealing temperature, particularly for annealing temperatures beyond 300°C. The majority of the plots in this graph (Fig. 5c) resemble the plateau region of the low carbon steel plots in Fig. 5a. Compare also the rates of increase in *Q*-factor for annealing temperatures up to 250°C between the low carbon and BH steels (Fig. 5a and c). The rate of *Q*-factor increase in this range was much lower for the BH steel than the earlier results for low-carbon steel (see Fig. 5a and c).

- With respect to the IF steel (Fig. 5d), modal *Q*-factors increased (damping decreased) with minimal indication of plateauing and the damping in this case appeared to be dependent on annealing temperature.

- On comparing the *Q*-factor versus natural frequency fits for the 20% cold-rolled BH, IF and low carbon steels, it was discovered that: (1) a much better fit was obtained between *Q*-factor and frequency for the BH steel as indicated by the R^2 values in Table 3 and (2) the range of values obtained for the coefficient α was comparable to the range of α values obtained for the low carbon steels at annealing temperature 300°C and above (see both Table 3 and Table 4) while this was not the case for the IF steel.

A closer examination of the *Q*-factor versus annealing temperature plots for the 20% cold-rolled low-carbon, BH and IF steels shown in Fig. 5a, b and c was made by comparing the damping in each of the nine modes. This is shown in Fig. 8. The following findings were:

- Overall the modes in the BH steel generally maintained the lowest damping (highest *Q*'s) throughout the range of annealing temperatures. However damping in the low carbon and BH steels were comparable for annealing temperatures beyond 300°C. It is significant to highlight that the BH steel which has significantly lower carbon content than the low-carbon steel (see Table 1) displayed comparable or higher *Q*'s than the low carbon steel. It was expected that the *Q*-factors would have been in the following order: low-carbon >BH>IF from highest to lowest. The observed trend will be discussed further on.

- The IF and low-carbon steels had comparable damping at lower annealing temperatures and in the cold-rolled state.

- Overall, the highest damping (lowest *Q*'s) were recorded for the IF steels particularly in the higher modes – see modes 5 to 9.

4. DISCUSSION

It is first important to highlight that the material damping trends observed in each part of the experimental simulation with the low-carbon steel test-structures were in good agreement with the expectations at the onset of this investigation. These expected outcomes were listed at the beginning of this paper. Two important outcomes were: (1) that material damping would increase with cold rolling but (2) would recover (or revert to levels comparable to damping in the as received material condition) on subsequent heat treatment of the cold rolled test structures. These and other deductions were realised and will be discussed in more detail.

More recently, work by Murr *et al.*[1] and Ferreyra *et al.*[2,11] focused on the effect of the steelpan making process on the metallurgical and acoustic properties of several drum steels which had different carbon and residual element contents. While these studies recommend a range for carbon content and an optimum heat treatment temperature, the acoustic analysis did not consider the damping properties of the steels tested but instead focused on the effect of the pan making process on the frequency spectra of replica steelpan notes. Unarguably, the works of Murr *et al.* [1] and Ferreyra *et al.*[2] have contributed significantly to a better understanding of the behaviour of low-carbon steels in the pan making process but the intent of these works were not towards the development of a specification in any form.

The development of specifications for the standardization of materials for the steelpan should initially consider low-carbon steels. Low-carbon steel has long been the *de-facto* material for pan making, primarily through the use of oil barrels which are primarily constructed from low carbon steel. However, the manufacture of tight-head barrels is regulated by standards [12,13] which specify the grade of low-carbon steel sheet to be used for their construction. These grades of steels were not specified with the intention that the containers would be used primarily or subsequently for musical instruments and may or may not be suitable for pan making.

The increase in damping with cold reduction was primarily attributed to the increase in dislocation density. This is widely reported on in the literature [14-16]. One highlight of this work was the vibration damping trends exhibited by the low carbon, IF and BH steels with annealing heat treatment. With regard to the low carbon steel, the first trend was the expected increase and plateauing of the Q-factors values among water quenched and air cooled test specimens. This plateauing of Q-factor values typically began between the annealing temperatures of 300°C and 400°C. This temperature range also corresponded to the temperature range (300°C and 400°C) between which the return of the yield point effect was manifested in the tensile specimens, as indicated by a very sharp upper yield point[1]. The onset of the return of the yield point was also accompanied by increased yield strength and decreased ductility (elongation) which are both indicators of strain ageing. This development indicated that strain ageing may be in part or majorly responsible for the damping trends (the plateauing) observed in the low carbon steel test structures.

Another trend was found with the relationships obtained by considering the plots between the natural frequencies and the damping of the low carbon test strips where $Q = \beta f^{\alpha}$. The values for the coefficient of α for test strips heated beyond 300°C were typically between 0.60 and 0.80. It is not certain whether this relationship is a characteristic of the strain ageing phenomenon in low-carbon steels. Efforts to locate comparable information were difficult: data for a range of low-carbon steels need to be gathered and analysed before any conclusions can be made. It may be that this information may be useful for the development of a quality control criterion for ensuring that selected low-carbon steels meet the vibration damping requirements for steelpan making. However, the application of this relationship to steelpan production is not immediately apparent and further research is therefore recommended.

In order to substantiate the deduction that strain ageing was primarily or at least in part responsible for the damping trends observed with annealing heat treatment, the material damping in 20% cold reduced and annealed BH and IF steels were compared to the 20% cold reduced air cooled low-carbon steel strips. The concept behind using these steels (BH and IF) was that they possess very minute quantities of interstitial atoms (carbon and nitrogen) (see Table 1) and therefore the degree of strain ageing which accompanied the heat treatment of cold-rolled samples of these steels would be modest or almost negligible in comparison to the strain ageing that may occur in the low-carbon steel. The IF steel sheet used in this work contained Titanium (Table 1) which further reduces the carbon and nitrogen in solution through the formation of stable carbides and nitrides. On this premise, it was therefore reasonable to expect that the highest damping (lowest Q-factor values) would be manifested by the BH and IF steels. This expectation was not entirely realised but in most cases (see Fig. 8) the IF steel displayed the lowest Q-factors. This finding could be accepted as a confirmation of the deduction. Although the BH steel was also expected to exhibit comparable damping to the IF steel but instead manifested the lightest damping among the group of steels, was an indication that very minute contents of interstitial atoms could have major effects on damping properties and that vibration damping in low and ultra-low carbon steels may not be very sensitive to carbon content. Further work needs to be conducted in order to establish how sensitive material damping is to carbon content in low and ultra-low carbon steels.

There were also comparable findings between the low carbon and BH steel Q-factor-natural frequency plots. For the fit $Q = \beta f^{\alpha}$, the coefficient α for the BH strips also fell between the values 0f 0.60 and 0.80 while this was not the case for the IF steel (see Table 3 and Table 4). In the case of the IF steel the deviation from this trend may be due to the presence of Ti which reduces the amount of C and N in solution.

5. Conclusions

- As expected and in agreement with earlier literature on damping, cold rolling resulted in a decrease in material damping; annealing heat treatment resulted in damping recovery while surface coating lead to a material damping decrease.
- There was no apparent difference in the damping trends in test structures that were air cooled or water quenched.
- The coinciding of the temperature ranges at which the stabilisation (plateauing) of material damping occurred and at which there was an onset of strain ageing suggested that an annealing temperature between 300°C and 400°C would be appropriate for the heat treatment of pans.

---

[1] Tensile tests accompanied vibration tests but the results are not shown here.

- Strain ageing may be largely responsible for the stabilisation (plateauing) of the material damping in the annealing temperature range 300°C to 400°C.

References

[1] Murr, L.E., E. Ferreyra, J.G. Maldonado, E.A. Trillo, S. Pappu, C. Kennedy, J. de Alba, M. Posada, D.P. Russell, and J.L. White, *Materials science and metallurgy of the Caribbean steel drum. Part I. Fabrication, deformation phenomena and acoustic fundamentals.* Journal of Materials Science, 1999. **34**(5): p. 967-979.

[2] Ferreyra, E., J.G. Maldonado, L.E. Murr, S. Pappu, E.A. Trillo, C. Kennedy, M. Posada, J. de Alba, R. Chitre, and D.P. Russell, *Materials science and metallurgy of the Caribbean steel drum. Part II. Heat treatment, microstructures, hardness profiles and tuning effects.* Journal of Materials Science, 1999. **34**(5): p. 981-996.

[3] Zener, C., *Internal Friction in Solids IV. Relation Between Cold Work and Internal Friction.* Physical Review, 1938. **53**(7): p. 582-586.

[4] Nowick, A.S., *On the interpretation of "low-temperature" recovery phenomena in cold-worked metals.* Acta Metallurgica, 1955. **3**(4): p. 312-321.

[5] Hikata, A., R. Truell, A. Granato, B. Chick, and K. Lucke, *Sensitivity of Ultrasonic Attenuation and Velocity Changes to Plastic Deformation and Recovery in Aluminum.* Journal of Applied Physics, 1956. **27**(4): p. 396-404.

[6] Granato, A., A. Hikata, and K. Lücke, *Recovery of damping and modulus changes following plastic deformation.* Acta Metallurgica, 1958. **6**(7): p. 470-480.

[7] Bert, C.W., *Material damping: An introductory review of mathematic measures and experimental technique.* Journal of Sound and Vibration, 1973. **29**(2): p. 129-153.

[8] Bloss, B. and M.D. Rao, *Measurement of damping in structures by the power input method.* Experimental Techniques, 2002. **26**(3): p. 30-32.

[9] Nashif, A.D., D.I.G. Jones, and J.P. Henderson, *Vibration Damping*. 1985, New York: John Wiley & Sons, Inc.

[10] SIMULIA, *Abaqus, Getting started with Abaqus, Version 6.7*. Interactive ed. 2007.

[11] Ferreyra, E., L.E. Murr, D.P. Russell, and J.F. Bingert, *Elastic interactions and the metallurgical and acoustic effects of carbon in the Caribbean steel drum.* Materials Characterization, 2001. **47**(5): p. 325-363.

[12] *ASTM International A366/A 366M - 97$^{\epsilon 1}$: Standard specification for commercial steel (CS) sheet, Carbon (0.15 Maximum Percent) Cold Rolled*. 1998.

[13] *United Nations Designation UN1A1-101-01: Carbon steel tight head 55-gallon drum specification*. 2001.

[14] Eshelby, J.D., *Dislocations as a Cause of Mechanical Damping in Metals.* Proceedings of the Royal Society of London. Series A, Mathematical and Physical Sciences, 1949. **197**(1050): p. 396-416.

[15] Johnson, W., *Dislocation damping after plastic deformation in interstitial-free and carbon steels.* Journal of Alloys and Compounds, 2000. **310**(1-2): p. 423-426.

[16] Wilks, J., *Dislocation damping in metals.* British Journal of Applied Physics, 1965. **16**(5): p. 587-603.